frontiers | Research Topics

Tumor microenvironment, inflammation, and resistance to immunotherapies

Edited by
Apostolos Zaravinos, Julie Decock and Giuseppina Comito

Published in
Frontiers in Immunology
Frontiers in Oncology

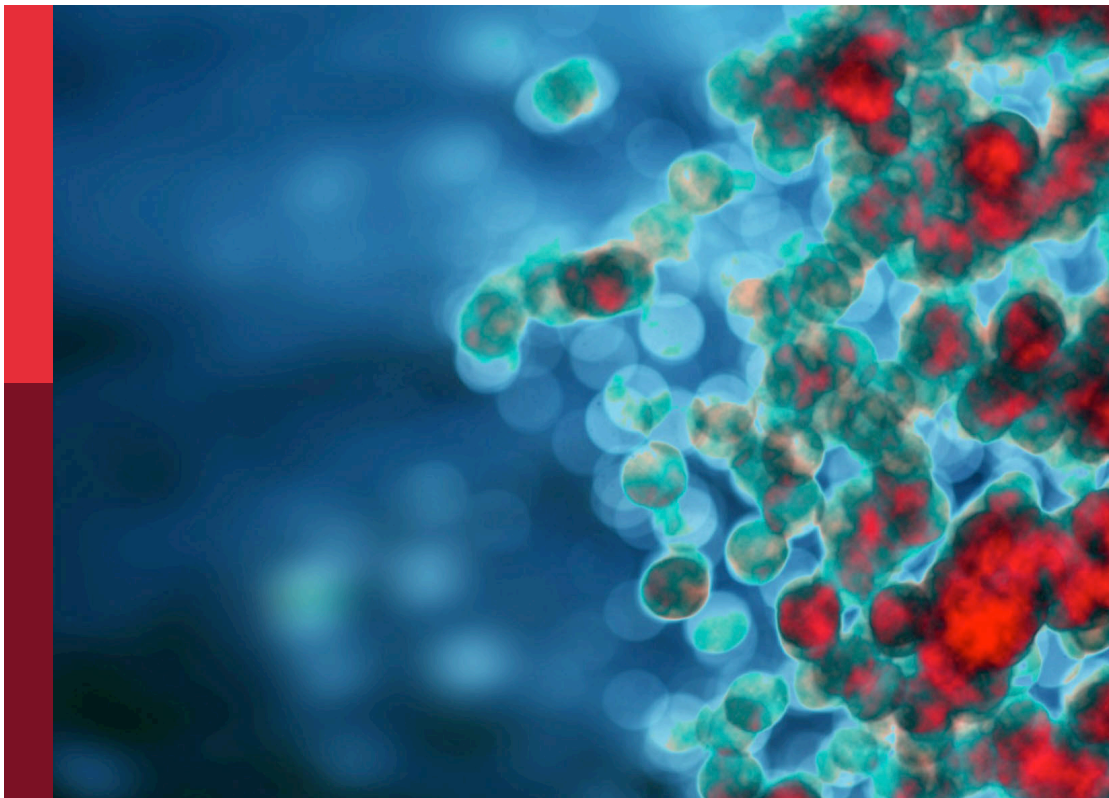

ISSN 1664-8714
ISBN 978-2-8325-2712-2
DOI 10.3389/978-2-8325-2712-2

About Frontiers

Frontiers is more than just an open access publisher of scholarly articles: it is a pioneering approach to the world of academia, radically improving the way scholarly research is managed. The grand vision of Frontiers is a world where all people have an equal opportunity to seek, share and generate knowledge. Frontiers provides immediate and permanent online open access to all its publications, but this alone is not enough to realize our grand goals.

Frontiers journal series

The Frontiers journal series is a multi-tier and interdisciplinary set of open-access, online journals, promising a paradigm shift from the current review, selection and dissemination processes in academic publishing. All Frontiers journals are driven by researchers for researchers; therefore, they constitute a service to the scholarly community. At the same time, the *Frontiers journal series* operates on a revolutionary invention, the tiered publishing system, initially addressing specific communities of scholars, and gradually climbing up to broader public understanding, thus serving the interests of the lay society, too.

Dedication to quality

Each Frontiers article is a landmark of the highest quality, thanks to genuinely collaborative interactions between authors and review editors, who include some of the world's best academicians. Research must be certified by peers before entering a stream of knowledge that may eventually reach the public - and shape society; therefore, Frontiers only applies the most rigorous and unbiased reviews. Frontiers revolutionizes research publishing by freely delivering the most outstanding research, evaluated with no bias from both the academic and social point of view. By applying the most advanced information technologies, Frontiers is catapulting scholarly publishing into a new generation.

What are Frontiers Research Topics?

Frontiers Research Topics are very popular trademarks of the *Frontiers journals series*: they are collections of at least ten articles, all centered on a particular subject. With their unique mix of varied contributions from Original Research to Review Articles, Frontiers Research Topics unify the most influential researchers, the latest key findings and historical advances in a hot research area.

Find out more on how to host your own Frontiers Research Topic or contribute to one as an author by contacting the Frontiers editorial office: frontiersin.org/about/contact

Tumor microenvironment, inflammation, and resistance to immunotherapies

Topic editors

Apostolos Zaravinos — European University Cyprus, Cyprus
Julie Decock — Hamad bin Khalifa University, Qatar
Giuseppina Comito — University of Florence, Italy

Citation

Zaravinos, A., Decock, J., Comito, G., eds. (2023). *Tumor microenvironment, inflammation, and resistance to immunotherapies*. Lausanne: Frontiers Media SA. doi: 10.3389/978-2-8325-2712-2

Table of contents

frontiers | Frontiers in Oncology

TYPE Editorial
PUBLISHED 31 May 2023
DOI 10.3389/fonc.2023.1215332

OPEN ACCESS

EDITED AND REVIEWED BY
Fernando Torres Andón,
Institute of Biomedical Research of A Coruña (INIBIC), Spain

*CORRESPONDENCE
Apostolos Zaravinos
a.zaravinos@euc.ac.cy
Julie Decock
juliedecock80@gmail.com

RECEIVED 01 May 2023
ACCEPTED 23 May 2023
PUBLISHED 31 May 2023

CITATION
Decock J, Comito G and Zaravinos A (2023) Editorial: Tumor microenvironment, inflammation, and resistance to immunotherapies.
Front. Oncol. 13:1215332.
doi: 10.3389/fonc.2023.1215332

Editorial: Tumor microenvironment, inflammation, and resistance to immunotherapies

Julie Decock[1,2]*, Giuseppina Comito[3] and Apostolos Zaravinos[4,5]*

[1]Translational Cancer and Immunity Center (TCIC), Qatar Biomedical Research Institute (QBRI), Hamad Bin Khalifa University (HBKU), Qatar Foundation (QF), Doha, Qatar, [2]College of Health and Life Sciences (CHLS), Hamad Bin Khalifa University (HBKU), Qatar Foundation (QF), Doha, Qatar, [3]Department of Experimental and Clinical Biomedical Sciences, School of Mathematical, Physical and Natural Sciences, University of Florence, Florence, Italy, [4]Department of Life Sciences, School of Sciences, European University Cyprus, Nicosia, Cyprus, [5]Cancer Genetics, Genomics and Systems Biology Laboratory, Basic and Translational Cancer Research Center (BTCRC), Nicosia, Cyprus

KEYWORDS

tumor microenvironment, inflammation, resistance, immunotherapies, immunosuppression, cancer

Editorial on the Research Topic
Tumor microenvironment, inflammation, and resistance to immunotherapies

The tumor microenvironment (TME) refers to the complex ecosystem surrounding a tumor, including stromal cells, blood vessels, extracellular matrix, and different types of immune cells such as T-cells, B-cells, dendritic cells, neutrophils, natural killer cells, myeloid-derived suppressor cells, and tumor-associated macrophages. Cancer cells exploit the inflammatory mechanisms present in the TME to promote their growth and survival. In turn, immunotherapies, including immune checkpoint inhibition (ICI), adoptive cell transfer (ACT), and genetically-modified T-cell receptor (TCR) and chimeric antigen receptor (CAR-T) based therapies, aim to modulate the immune system to better recognize and eliminate cancer cells. However, the molecular profile of cancer cells affect the TME, hampering the response to these therapies. The causes of immunotherapy resistance remain unclear, but immune dysregulation within the TME, the tumor mutational landscape, inflammation, hypoxia, and epithelial-mesenchymal transition (EMT) have been implicated. Understanding the key immunosuppressive and resistance mechanisms associated with the TME is crucial to develop new therapeutic strategies, limit immune escape, and tailor effective treatments.

This Research Topic aims to provide new insights into the interplay of cancer cells and immune cells within the TME and its impact on resistance to immunotherapeutic approaches.

One of the major mechanisms by which tumor cells can shape the tumor-immune microenvironment in favor of tumor progression is through increased infiltration and polarization of immunosuppressive cells. Here, Cai et al. demonstrated that cancer cell lines release branched-chain α-ketoacids (BCKAs) that affect macrophage polarization in a MCT1-dependent manner whereby α-ketoisocaproate (KIC) and α-keto-β-methylvalerate

(KMV) induce pro-tumoral polarization of macrophages whereas α-ketoisovalerate (KIV) exert a pro-inflammatory effect on macrophages, suggesting that cancer-derived BCKAs should be selectively targeted to optimize the anti-tumor immune response. In turn, Qin et al. found that the serine protease PRSS23 is associated with worse prognosis in gastric cancer, supports tumor cell proliferation and invasion, and promotes infiltration of immunosuppressive M2-type macrophages through increased expression and secretion of FGF2. On the other hand, Geng et al. demonstrated how expression of the tumor suppressor RARRES1 could be exploited to enhance the recruitment of anti-tumorigenic type 1 macrophages and reduce the viability of kidney renal clear cell carcinoma cells (KIRC). Although KIRC is the most frequently diagnosed subtype of renal cell carcinoma, the need for diagnostic biomarkers remains unmet and was addressed by Wang et al. who established a 13-gene diagnostic model using cell death-related genes. While NK cells been mostly investigated in relation to their direct anti-tumorigenic functions, Lindsay et al. show that NK cells also play an important role in the maturation of antigen presenting cells during immune responses to early-stage tumors, reducing the development of anergic T cells and improving tumor control and T cell responses.

Given the complexity and dynamic nature of the tumor-immune microenvironment, major efforts are invested towards the identification of biomarkers that can predict the immune composition and contexture of tumors. For instance, Zhong et al. found that elevated expression of FAM110A was associated with the expression of multiple immune checkpoint genes and abundance of tumor-infiltrating immune cells across multiple types of cancer, especially in liver hepatocellular carcinoma. The diverse roles of immune checkpoints in different immune cells were reviewed in more detail by Guo et al. who highlighted the importance of gaining a better understanding of immune checkpoint expression in relation to immune checkpoint blockade. Further, An et al. defined a gene signature score for tertiary lymphoid structures in bladder cancer that correlates with immune cell infiltration, and predicts clinical outcome and response to immunotherapy and chemotherapy. In a second bladder cancer study in this Research Topic, Chang et al. identified a novel immune and inflammatory responses signature (IIRS) that could independently predict overall survival, immunotherapy and chemotherapy response and classify patients with poor clinical and histopathological features. In addition, Georgoulias and Zaravinos examined the expression of various immune receptors, immune-cell fractions, immune-related signatures and mutational signatures across cutaneous melanomas with diverse tumor mutation burdens (TMB) and found that patients with low TMB who are considered to be less responsive to immunotherapy could still benefit from immune-based interventions thanks to pre-existing T-cell immunity. Furthermore, Fang et al. identified a prognostic gene signature associated with iron-dependent regulated cell death, ferroptosis, in triple negative breast cancer which strongly correlated with immunological features and could predict response to anti-cancer treatment. Finally, Kimm et al. observed alterations in the composition of monocyte subpopulations and abundance of monocytic myeloid-derived suppressor cells (mMDSCs) following interstitial brachytherapy or radiofrequency ablation of hepatocellular carcinoma, suggesting that liquid biopsy of monocytes may provide information on the inflammatory response to local ablation.

In addition to modulation of the cellular components of the tumor microenvironment, dysregulation of the extracellular matrix can impact anti-tumor immunity. Here, Donelan et al. discuss how hyaluronan-enriched stroma contributes to tumor growth and progression through the promotion of cancer inflammation, angiogenesis and tumor-associated immune suppression. In this context, Nath et al. demonstrated that inflammation in the bone marrow of N-ethyl-N-nitrosourea-induced leukemic mice could be reduced by treatment with ethanolic olive leaves extract, thereby decreasing the expression of anti-apoptotic proteins.

Overall, the studies in this Research Topic collectively improve our current understanding of the key mechanisms involved in resistance to immunotherapeutic approaches and highlight potential prognostic biomarkers for treatment response. These findings can inform the development of new therapeutic strategies to overcome resistance and improve patient outcomes.

Author contributions

AZ, JD and GC contributed to writing the manuscript. All the authors proofread the manuscript and approved the submitted version.

Funding

This work was supported by a grant from the Qatar Biomedical Research Institute (#VR94-IGP3-2020), awarded to JD.

Acknowledgments

We would like to thank all the authors who contributed their original work to our RT and the reviewers for their valuable comments. We also thank the Frontiers Editorial Office for providing us with the opportunity to host this RT.

Conflict of interest

The authors declare that the research was conducted in the absence of any commercial or financial relationships that could be construed as a potential conflict of interest.

Publisher's note

frontiers | Frontiers in Immunology

TYPE Original Research
PUBLISHED 15 September 2022
DOI 10.3389/fimmu.2022.955841

OPEN ACCESS

EDITED BY
Julie Decock,
Qatar Biomedical Research Institute, Qatar

REVIEWED BY
Dominic C. Voon,
Kanazawa University, Japan
Runwei Yan,
The First Affiliated Hospital of Nanchang University, China

*CORRESPONDENCE
Shanshan Qin
qinss77@163.com
Dandan Li
lidandan_cup@163.com

SPECIALTY SECTION
This article was submitted to Cancer Immunity and Immunotherapy, a section of the journal Frontiers in Immunology

RECEIVED 29 May 2022
ACCEPTED 16 August 2022
PUBLISHED 15 September 2022

CITATION
Qin S, Wang Z, Huang C, Huang P and Li D (2022) Serine protease PRSS23 drives gastric cancer by enhancing tumor associated macrophage infiltration *via* FGF2. *Front. Immunol.* 13:955841. doi: 10.3389/fimmu.2022.955841

Serine protease PRSS23 drives gastric cancer by enhancing tumor associated macrophage infiltration *via* FGF2

Shanshan Qin[1,2]*, Zidi Wang[2], Congcong Huang[1,2], Pan Huang[1,2] and Dandan Li[1,2]*

[1]Hubei Key Laboratory of Embryonic Stem Cell Research, School of Basic Medical Sciences, Hubei University of Medicine, Shiyan, China, [2]Laboratory of Tumor Biology, Academy of Bio-Medicine Research, Hubei University of Medicine, Shiyan, China

Serine proteases has been considered to be closely associated with the inflammatory response and tumor progression. As a novel serine protease, the biological function of PRSS23 is rarely studied in cancers. In this study, the prognostic significance of PRSS23 was analyzed in two-independent gastric cancer (GC) cohorts. PRSS23 overexpression was clinically correlated with poor prognosis and macrophage infiltration of GC patients. Loss-of-function study verified that PRSS23 plays oncogenic role in GC. RNA-seq, qRT-PCR, western blotting and ELISA assay confirmed that serine protease PRSS23 positively regulated FGF2 expression and secretion. Single-cell analysis and gene expression correlation analysis showed that PRSS23 and FGF2 were high expressed in fibroblasts, and highly co-expressed with the biomarkers of tumor associated macrophages (TAMs), cancer-associated fibroblasts (CAFs) and mesenchymal cells. Functional analysis confirmed PRSS23/FGF2 was required for TAM infiltration. Rescue assay further verified that PRSS23 promotes GC progression and TAM infiltration through FGF2. Survival analysis showed that high infiltration of M1-macrophage predicted favorable prognosis, while high infiltration level of M2-macrophage predicted poor prognosis in GC. Our finding highlights that PRSS23 promotes TAM infiltration through regulating FGF2 expression and secretion, thereby resulting in a poor prognosis.

KEYWORDS

serine protease PRSS23, FGF2, macrophage infiltration, TAM, gastric cancer

Introduction

Gastric cancer (GC) is a heterogeneous tumor with the third highest mortality rate worldwide (1). There are about 1.089 million new cases of gastric cancer worldwide in 2020, of which about 478,508 cases occurred in China (2, 3). Though current treatments for patients have been greatly improved, the prognosis remains unoptimistic to date due to the inconvenience of early diagnosis of GC (4). Besides, the molecular mechanisms underlying GC progression remain unclear (5–8). Hence, it is urgent and necessary to explore novel potential biomarkers and their molecular mechanisms to better understand the pathophysiology of gastric malignancies.

Serine proteases play critical roles in the digestion, blood coagulation fertilization, fibrinolysis, cell apoptosis and differentiation, angiogenesis (9). Recently, emerging evidence have showed that serine proteases play essential roles in tumor progression. For examples, Serine protease PRSS8 suppresses colorectal carcinogenesis and metastasis by inhibiting epithelial mesenchymal transition (EMT) signaling (10, 11). Serine protease PRSS3 was found to function as an oncogene in stomach cancer, lung cancer and colon cancer (12–14). However, as a conserved member of the trypsin family of serine proteases (15), the biological function of serine protease PRSS23 remains largely unknown in cancers.

Tumor-associated macrophages (TAMs) have been reported to be independent prognostic biomarker in cancers, including GC (16–18). Increasing studies have reported that TAMs exert pro-tumor effects by inhibiting antitumor immune responses (19). TAMs closely resemble the M2-macrophages, both of which highly express classic biomarkers of M2 macrophage, such as CD163, MSR1, and MRC1 (20–22). Fibroblast growth factor 2 (FGF2), secreted by cancer-associated fibroblast (CAFs), was reported to be required for tumor cell growth in lung cancer (23). Recently, multiple independent studies have reported a critical role of FGF2 in TAM infiltration, which implied a pro-tumor role of FGF2 in tumor progression (24–26).

In this study, a novel role of serine protease PRSS23 in immune infiltration was disclosed in GC. PRSS23 overexpression was positively associated with poor prognosis and macrophage infiltration in GC. PRSS23 functions as an oncogene in GC by enhancing tumor associated macrophage infiltration *via* FGF2. Our data highlights that the upregulation of PRSS23/FGF2 may be critical for macrophage infiltration in pan-cancer.

Materials and methods

Prognostic analysis and single-cell analysis

The gene expression profile of GSE62254 used in this study was downloaded from the Gene Expression Omnibus (GEO) in the NCBI web server. The clinical information of GC patients from GSE62254 cohort was download as descripted previously (27). The gene expression data and the clinical information of GC patients were obtained from the Cancer Genome Atlas (TCGA) database. Expression level of per gene was calculated from log2 of FPKM-UQ value. Single-cell analysis used in this study was obtained from the Human Protein Atlas (HPA) dataset (https://www.proteinatlas.org/).

Immune infiltration analysis

The TIMER database can used to estimate the immune infiltration levels of B cells, CD4+ T cells, CD8+ T cells, Neutrophils, Macrophages and Dendritic cells. The CIBERSORT method can used to estimate the immune infiltration of 24 immune cell types. The quanTIseq method can used to estimate the immune infiltration of 10 immune cell types, including M1 and M2 macrophages. These algorithms provide powerful correlation analysis and survival analysis regarding different types of immune cells. The gene module allows users to select any gene of interest and visualize the correlation of its expression with immune infiltration level in diverse cancer types. The survival module allows users to explore the clinical relevance of one or more tumor immune subsets, with the flexibility to correct for multiple covariates in a multivariable Cox proportional hazard model. The gene expression level in different immune cell types between stomach cancer and normal stomach tissues was analyzed using GEPIA 2021 web tool.

Cell culture and cell transfection

For cell culture, all cell lines used in this study were cultured in DMEM medium containing 10% fetal bovine serum (FBS) at 37 °C in 5% CO_2. The siRNAs targeting PRSS23 were purchased from Genepharma (Shanghai, China). The sequence of 2 siRNAs targeting PRSS23 were listed as follows. siRNA#1: 5'-GCGGCAGAUUUAUGGCUAUTT-3', siRNA#2: 5'-CCAGAUUUGCUAUUGGAUUTT-3'. For cell transfection, the GC cells were plated into a six-well plate. After the cell density reaches 30-50% the next day, siRNAs were transfected into GC cells using Lipofectamine 2000 (Invitrogen) according to the manufacturer's instructions.

THP-1-derived TAMs

THP-1 cells were used to induce TAMs *in vitro* as described previously (28–30). Briefly, macrophages were induced from THP-1 cells by treatment with PMA (Sigma, 100 ng/mL) for 24 hours. Then, these THP-1 derived macrophages were re-placed into a six-well

transwell plate. At the same time, HGC-27 cells were cultured as usually on the 0.4-μm porous membrane of upper chamber. After 24 hours, we co-cultured HGC-27 cells with THP-1-derived macrophages. Then 48 hours later, macrophages were collected for RNA extraction and other experiments.

Quantitative RT-PCR assay

At 48 hours post-transfection, GC cells were directly harvested using Trizol reagent (Invitrogen, USA) and the total RNA was extracted according to the manufacturer's instructions. The contaminated gDNA in total RNA was removed using RNase-free DNase I (Roche) for 20 minutes (31). cDNA was obtained using the PrimeScript™ RT reagent Kit (Perfect Real Time, Takara). The qPCR analysis was performed on Bio-Rad CFX Manager 3.1 real-time PCR system. The specific primers used in this study were synthesized by Wcgene Biotech (Shanghai, China). FGF2-F: 5'-GAAAAGGCAAGATGCAGGAG-3', FGF2-R: 5'-ACGTG AGAGCAGAGCATGTG-3'; PRSS23-F: 5'-GGGGGAT TTTCTGCTTGTCT-3', PRSS23-R: 5'- TGGAGACCTCCC TTCTTCCT-3'; ACTIN-F: 5'-ATCGTCCACCGCAAATGC TTCTA-3', ACTIN-R: 5'-AGCCATGCCAATCTCATCTTGTT-3' $2^{-\Delta\Delta Ct}$ method was used to determine gene expression quantification.

Western blotting assay

The western blotting assay was performed as previously described (1). In brief, after 72h transfected with siRNAs, GC cells were lysed in RIPA buffer added 1 mM PMSF. Approximately 100 μg of total protein was electrophoresed through 10% SDS polyacrylamide gels and were then transferred to a PVDF membrane (Millipone). The FGF2 antibody (A11488) and PRSS23 (A17092) antibody was purchased from Abclonal company (Wuhan, China).

RNA sequencing

After transfection of 2 siRNAs targeting PRSS23 in AGS cells, total RNA was extracted and send to Lifegenes company (Shanghai, China) to perform RNA sequencing. A total amount of 1.5 μg RNA per sample was used as input material for the RNA sample preparations. The RNA-seq data used in this study was uploaded in the GEO dataset (GSE204725).

Statistical analysis

The P values for PRSS23 expression analysis of different subtypes of GC were estimated using Mann–Whitney nonparametric test. The P values of survival curves were analyzed using the log-rank test. Pearson correlation analysis was used for the correlation test of the two groups of data. For quantitative RT-PCR, the P values were analyzed using ANOVA. $P < 0.05$ considered statistically significant.

Results

Serine protease PRSS23 overexpression predicts poor prognosis in GC

To reveal the biological function of PRSS23 in GC, we firstly analyzed its expression pattern in GC and normal stomach tissues. The Human Protein Atlas (HPA) contains large quantity of immunohistochemistry (IHC) images of different proteins in normal human tissues and cancer tissues (32). Therefore, we first evaluated the protein expression of PRSS23 in normal and cancer tissue of stomach using the HPA web tool (Figure 1A). The results showed that PRSS23 protein was mainly located in cytoplasmic and was relatively highly expressed in GC tissue compared to the normal stomach tissue. In addition, two independent GC cohort (GSE54129 and TCGA_STAD) containing normal tissues and cancer tissues were included into our study. The results showed that PRSS23 expression was also significantly upregulated in the GSE54129 cohort (Figures 1B, C).

To understand the significance of PRSS23 overexpression in GC, we analyzed the prognostic value of PRSS23 in two independent GC cohort (TCGA_STAD and GSE62254). In the TCGA_STAD cohort, PRSS23 expression in diffuse GC tissues was higher than that in intestinal GC tissues (Figure 1D). Poorly differentiated GC tissues tended to have relatively high expression of PRSS23 (Figure 1E). Furthermore, PRSS23 expression level was positively correlated to T stages of GC patients (Figure 1F). However, there was no significant difference in the expression of PRSS23 in GC tissues with or without lymph node metastasis or distant metastasis (Figures 1G, H). In addition, we also noted that PRSS23 expression was significantly decreased in the GC patients with radiation therapy, compared to the GC patients without radiation therapy (Figure 1I). Survival analysis showed that PRSS23 overexpression predicted poor prognosis (Figures 1J, K).

Similarly, in GSE62254 cohort, PRSS23 was also relatively high expressed in the diffuse or MLH1+ GC tissues (Figures 2A, B). Furthermore, PRSS23 was positively correlated with the degree of malignancy in GC (Figures 2C, D), but has no significant changes in GC patients with different N/M stages (Figures 2E, F). Survival analysis in GSE62254 cohort also showed that PRSS23 predicted poor prognosis in GC (Figures 2G, H). Taken together, PRSS23 functions as an oncogene and can be served as a prognostic biomarker in GC.

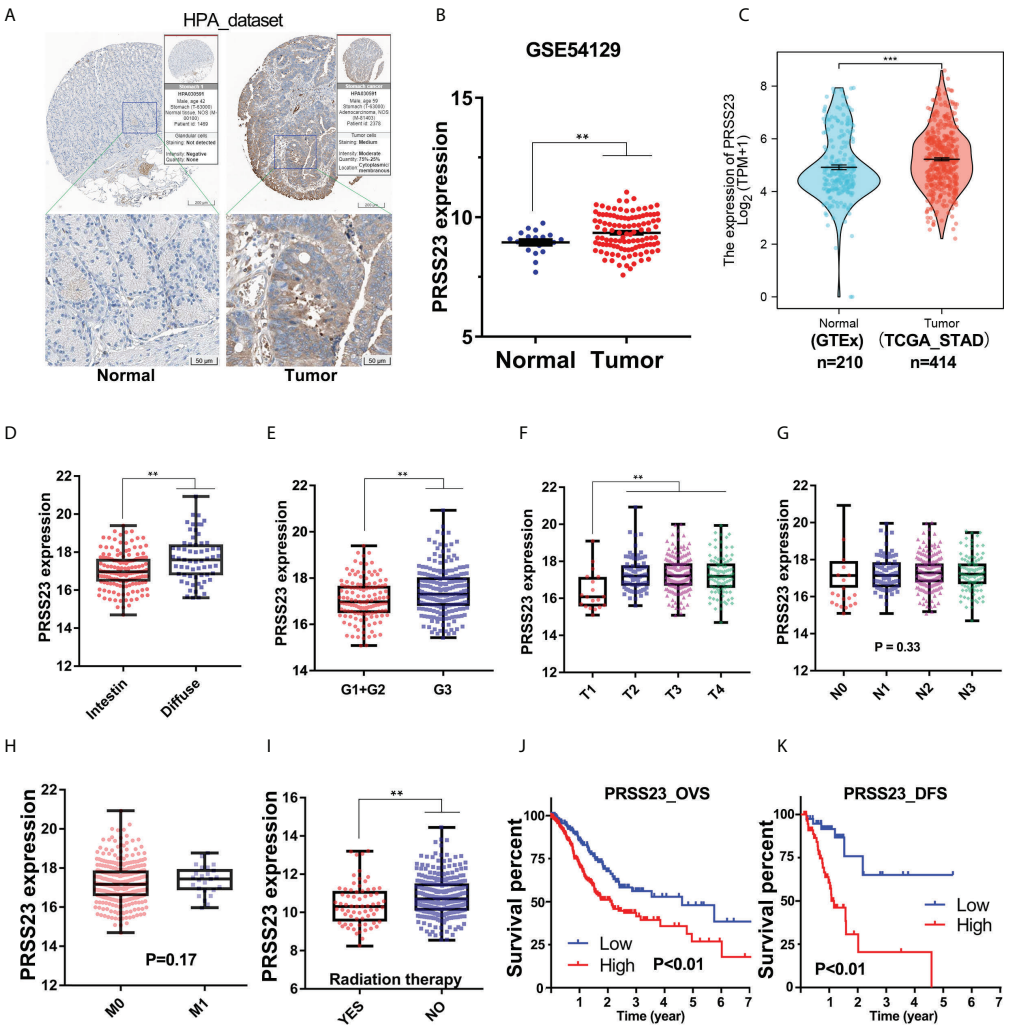

FIGURE 1
The clinical significance of PRSS23 overexpression was analyzed in the GC cohort from TCGA. **(A)** Differences in the immunostaining of PRSS23 between normal tissues and cancerous tissues in GC. **(B, C)** PRSS23 was overexpressed in cancerous tissues in the GSE54129 and TCGA_STAD cohort. **(D)** Differences in PRSS23 expression between intestinal and diffuse tissues of GC. **(E)** PRSS23 expression in GC tissues with different differentiation stages. **(F–H)** PRSS23 expression level in different TNM-stages of GC tissues. **(I)** PRSS23 was lowly expressed in GC patients with radiation therapy. **(J, K)**: PRSS23 overexpression predicted shorter overall survival time and disease-free survival time in GC. **, P < 0.01, ***, P < 0.001.

PRSS23 knockdown inhibits GC cell proliferation and invasion

Since clinical analysis implied an oncogenic role of PRSS23 in GC, we further validated the biological function of PRSS23 *in vitro*. Given PRSS23 was overexpressed in GC tissues, we hence considered performing loss-of-function study to verify the biological function of PRSS23 in GC. Firstly, we verified the RNA interference efficiency of PRSS23 depletion in GC cell lines by qPCR assay (Figure 3A). Next, the cell proliferation assay showed that PRSS23 depletion caused a strong inhibition of cell growth (Figure 3B). After knocking down PRSS23 expression for 72 hours in GC cell lines, we checked the cell morphology with an optical microscope. The results showed that PRSS23 knockdown significantly decreased the proliferation of GC cells (Figure 3C). At the same time, we also determined the effect of PRSS23 knockdown on the metastasis of GC cells. In the scratch wound healing assays, the migration of GC cells that silenced PRSS23 was significantly slower than that of control GC cells (Figures 3D–F). In transwell invasion assays, the numbers of GC cells that invaded through the Matrigel were decreased in the PRSS23 silencing group than the control group (Figures 3G, H). These data demonstrated a tumor-promoting role of PRSS23 in GC.

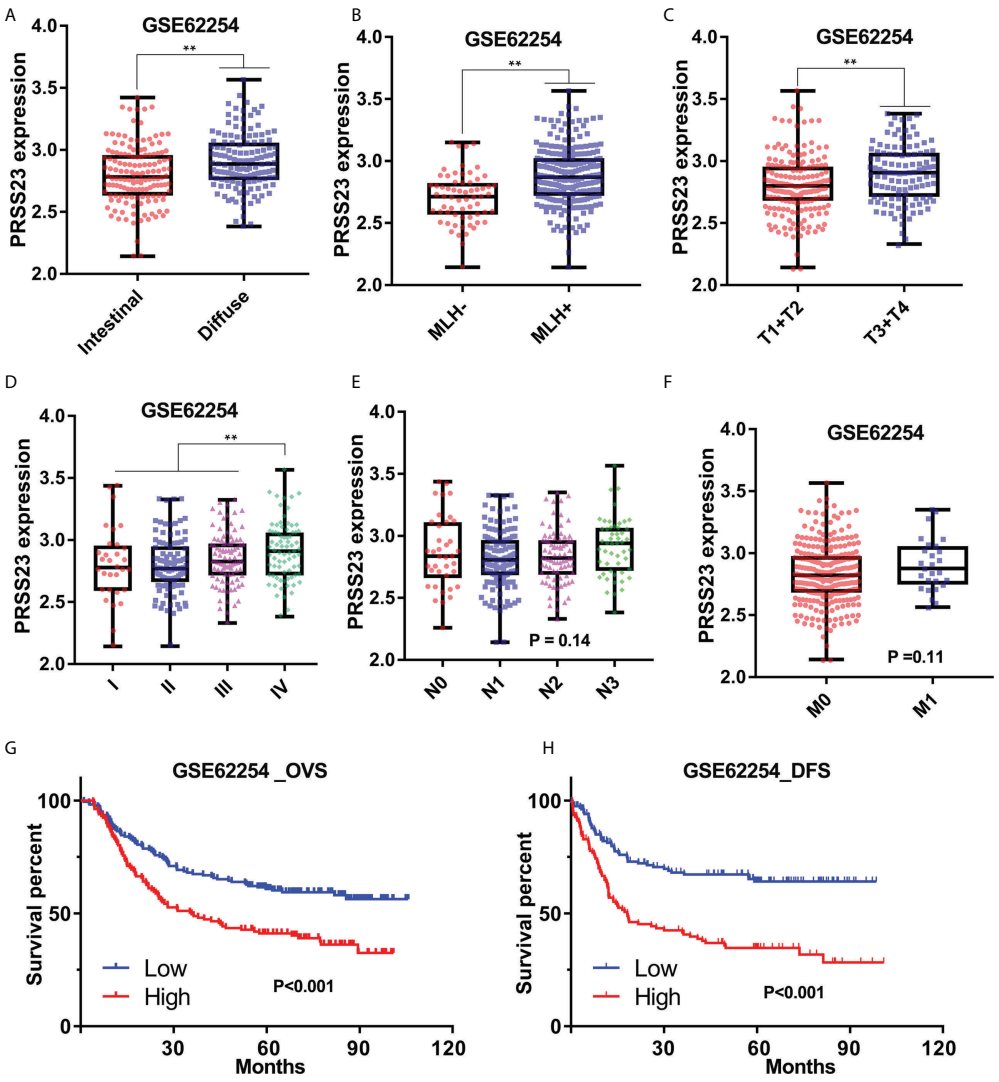

FIGURE 2
The prognostic significance of PRSS23 overexpression was analyzed in the GC cohort from GSE62254. **(A)** Differences in PRSS23 expression between intestinal and diffuse tissues of GC. **(B)** PRSS23 was highly expressed in GC patients with positive MLH1 expression. **(C–F)** PRSS23 expression level in different TNM-stages and Pathologic stages of GC tissues. **(G, H)** PRSS23 overexpression predicted shorter overall survival time and disease-free survival time in GC. **, P < 0.01.

PRSS23 is positively associated with macrophage infiltration

Increasing studies have reported that immunity infiltration level is an independent predictor of survival and sentinel lymph node status in cancers (33). In order to clarify the biological role PRSS23 in immune infiltration, two different algorithms, including TIMER (34) and CIBERSORT (35), were performed to analyze the RNA-seq data of GC samples from TCGA (Figure 4A). The TIMER method contains 6 immune cell types and the CIBERSORT method contains 24 immune cell types. The infiltration level of each immune cells was evaluated by the enrichment score calculated by TIMER and CIBERSORT. Then, the correlation between PRSS23 expression level and infiltration level of each immune cell was analyzed in GC. According to immune infiltration analysis by TIMER, PRSS23 was most associated with macrophage infiltration (Figure 4B). Likewise, immune infiltration analysis by CIBERSORT showed that PRSS23 was most associated with macrophage and NK cell infiltration (Figure 4C). Scatter plots for the correlation between PRSS23 and macrophage infiltration based on two algorithms are shown in Figures 4D, E respectively.

Interestingly, after adjusting the clinical factors, both of the two algorithms indicated that GC patients with higher level of

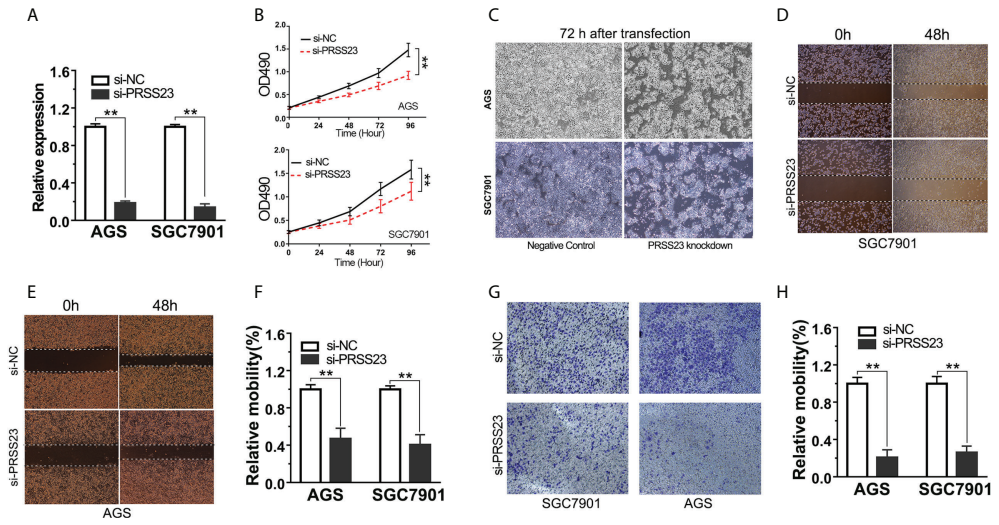

FIGURE 3
PRSS23 knockdown significantly decreased GC cell proliferation and invasion. **(A)** The efficiency of PRSS23 knockdown was determined in GC cell lines. **(B)** The effect of PRSS23 knockdown on GC cell growth was determined by MTT assay. **(C)** The morphology of gastric cancer cells after knockdown of PRSS23 for 72 hours. **(D, E)** Wound healing assays showed that PRSS23 knockdown inhibits GC cells migration. **(F)** The statistical data of the migrated cells. **(G)** The effects of PRSS23 knockdown on GC cells invasion were assessed by transwell assays. **(H)** The statistical data of the invasive cells. **, $P < 0.01$.

Macrophage infiltration tends to possess a shorter overall survival time (Figures 4F, G). These results suggested that PRSS23 may promote GC by affecting macrophage infiltration.

PRSS23 knockdown decreased the expression level of FGF2 in GC

To figure out the molecular mechanism of PRSS23 in macrophage infiltration and GC progression, we conducted transcriptome sequencing studies (GSE204725) in GC cells between PRSS23-depleted group and control group. After analysis of the RNA-seq data, genes with the most significant fold change in expression (log2FC>0.8) after PRSS23 knockdown are listed in the heatmap (Figure 5A). A total of 67 genes were downregulated and 38 genes were upregulated after knockdown of PRSS23 in GC. RNA-seq analysis revealed that FGF2, which is involved in regulating macrophage polarization, was greatly decreased after PRSS23 knockdown. In addition, fibroblast growth factor-binding protein (FGFBP1), which was reported to play essential roles in regulating FGF2 secretion (36–38), was also greatly decreased after knockdown of PRSS23. Thus, we speculated that PRSS23 might regulate TAMs infiltration by regulate FGF2 secretion.

Multiple independent experiments were performed to validate the regulation of FGF2 by PRSS23 in GC. First, RNA-seq data showed that the expression of PRSS23 and FGF2 were both decreased in PRSS23-depleted GC cells (Figures 5B, C). Consistently, the qRT-PCR assay further confirmed that PRSS23 knockdown decreased the FGF2 expression in two GC cell lines (Figures 5D, E). Besides, gene expression correlation analysis also showed that PRSS23 and FGF2 were highly co-expressed in GC tissues from TCGA (Figure 5F). Furthermore, PRSS23 knockdown greatly reduced the protein level of FGF2 (Figure 5G). Given FGF2 was a secreted protein, we also examined the effect of PRSS23 knockdown on FGF2 secretion by ELISA. The ELISA assay showed that PRSS23 knockdown significantly hindered secreted FGF2 level (Figures 5H, I).

PRSS23/FGF2 axis positively regulates tumor associated macrophage infiltration

To further validate the role of FGF2 in macrophage infiltration, immune infiltration analysis by two different algorithms was conducted. The results confirmed that FGF2 was positively associated with macrophage infiltration in GC (Figures 6A, B). Besides, survival analysis showed that overexpression of FGF2 predicted poor prognosis in GC (Figures 6C–E). Single-cell RNA-seq analysis revealed that FGF2 and PRSS23 were predominantly expressed in gastric fibroblasts and highly co-expressed in normal gastric tissue (Figures 6F, G). Consistently, both FGF2 and PRSS23 were closely related to EMT signaling and highly co-expressed with biomarkers of CAFs and mesenchymal cells (Figures S1A-D). Thus, we speculated that PRSS23 may regulate macrophage

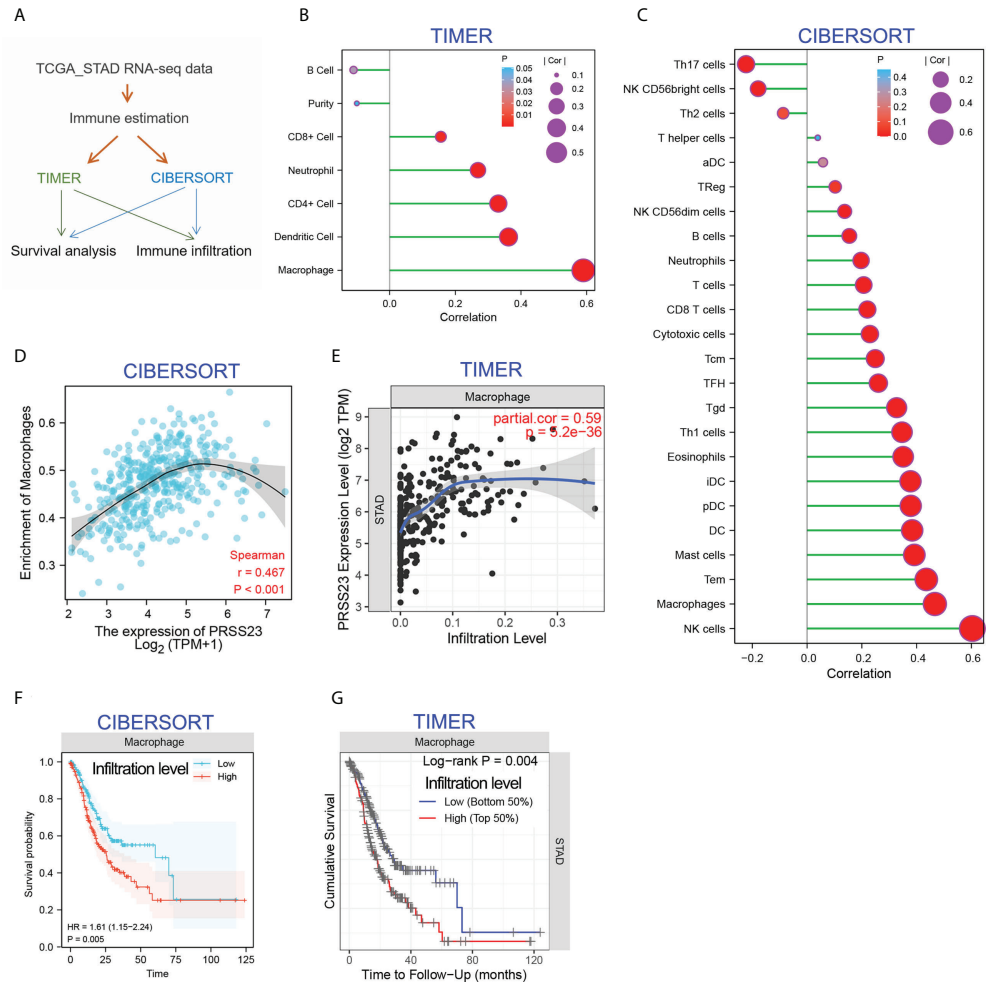

FIGURE 4
PRSS23 is associated with macrophage infiltration in GC. **(A)** Immune estimation analysis was conducted using two different methods. **(B, C)** The correlation between PRSS23 expression and immune infiltration was analyzed using TIMER and CIBERSORT methods. **(D, E)** The correlation between PRSS23 expression and macrophage infiltration was analyzed using TIMER and CIBERSORT methods. **(F, G)** Survival analysis using CIBERSORT or TIMER indicated that higher level of macrophage infiltration predicted poorer prognosis in GC.

infiltration *via* regulating FGF2 secretion in fibroblasts or mesenchymal cells.

As described above, FGF2 has been shown to play a critical role in TAMs infiltration (39–41). Multiple surface molecules (such as CD163, MSR1 (CD204), MRC1 (CD206), CSF1R, CD40 and CD81) and secreted factors (such as IL10, PDGFB and CCL2) have been reported to be well-known biomarkers of TAM/M2 (20, 42). Hence, we conducted the gene expression correlation analysis between PRSS23/FGF2 and these M2/TAM biomarkers. The results showed that both PRSS23 and FGF2 were highly co-expressed with M2/TAM biomarker genes (Figures 7A, B). Besides, we further analyzed the expression level of PRSS23/FGF2 in monocytes and different stages of macrophages. The results showed that both PRSS23 and FGF2 were significantly overexpressed in M2 macrophage, which is highly similar to tumor associated macrophage (Figures 7C, D).

Considering high level of secreted FGF2 would have a more pronounced effect in regulating macrophage polarization, we herein selected a GC cell line HGC-27 with relatively high expression of FGF2 for co-culture with THP-1 cells (Figure 7E). Then, we examined the expression of popular M2/TAM biomarkers in TAM-like cells by qRT-PCR assay. Both MSR1 (CD206) and IL10 were greatly upregulated in the TAM-like cells, suggested that we successfully induced TAM cells (Figure 7F). Consistent with previous immune infiltration analysis, both FGF2 and PRSS23 were significantly upregulated in TAM-like cells (Figure 7G). More importantly, knockdown of either PRSS23 or FGF2 significantly reduced the survival rate of TAM-like cells, indicating that both PRSS23 and FGF2 were

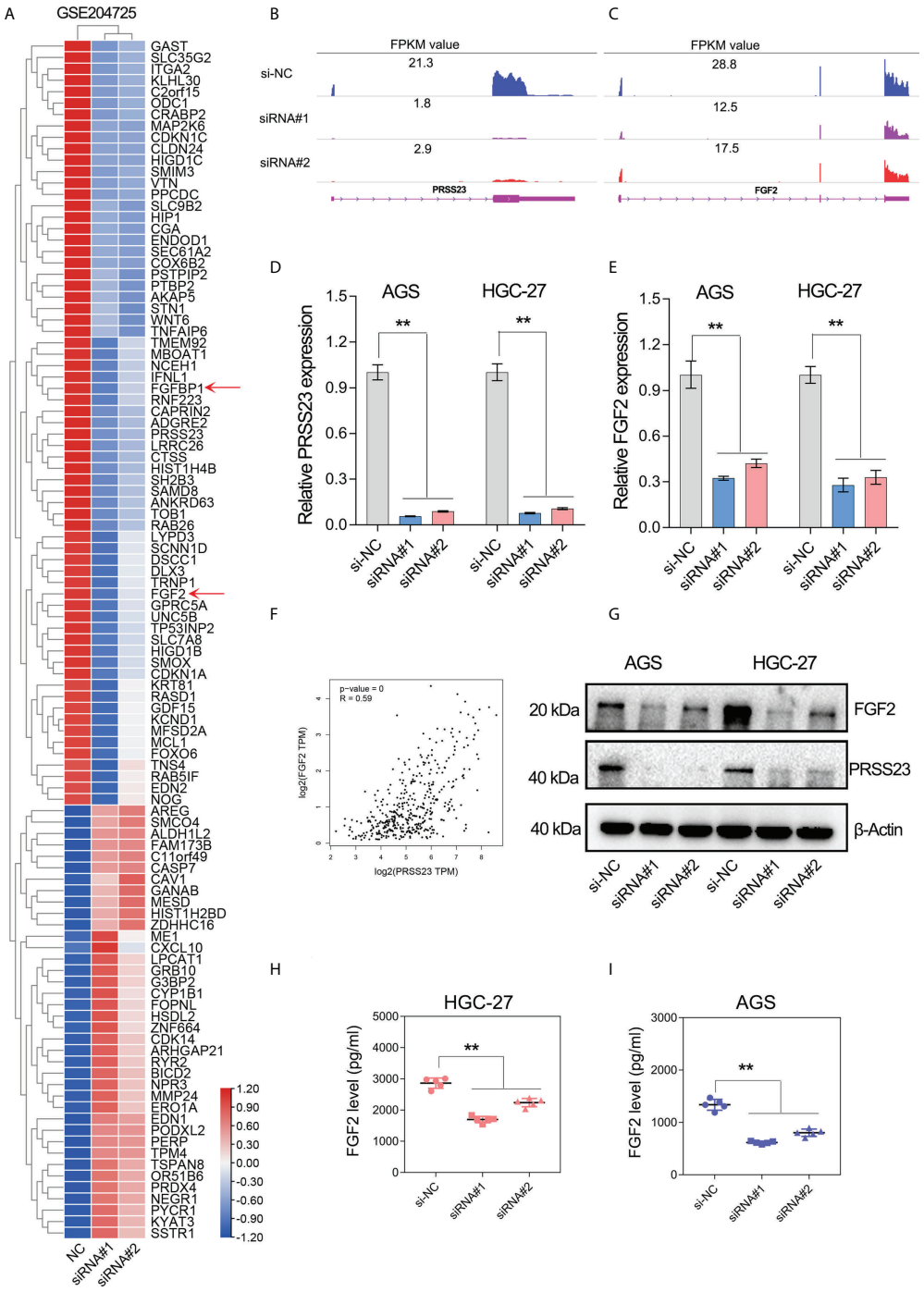

FIGURE 5
PRSS23 knockdown decreased FGF2 expression and secretion in GC. **(A)** RNA-seq studies were conducted in GC cells transfected with siRNAs targeting PRSS23. The most significantly altered genes upon PRSS23 knockdown were shown in the heatmap. **(B, C)** The transcripts abundance of PRSS23 and FGF2 in PRSS23-depleted GC cells was detected by RNA-seq. The normalized expression (FPKM value) of PRSS23 and FGF2 were shown in the plot. **(D)** The knockdown efficiency of PRSS23 in GC cell lines was examined by qRT-PCR assay. **(E)** The effect of PRSS23 knockdown on FGF2 expression in GC cell lines were examined by qRT-PCR assay. **(F)** PRSS23 and FGF2 were highly co-expressed in GC. **(G)** The effect of PRSS23 knockdown on FGF2 protein level in GC cell lines were examined by western blotting assay. (**H, I**) ELISA assay showed that PRSS23 knockdown significantly decreased secreted FGF2 level in GC cell lines. **, $P < 0.01$.

10.3389/fimmu.2022.955841

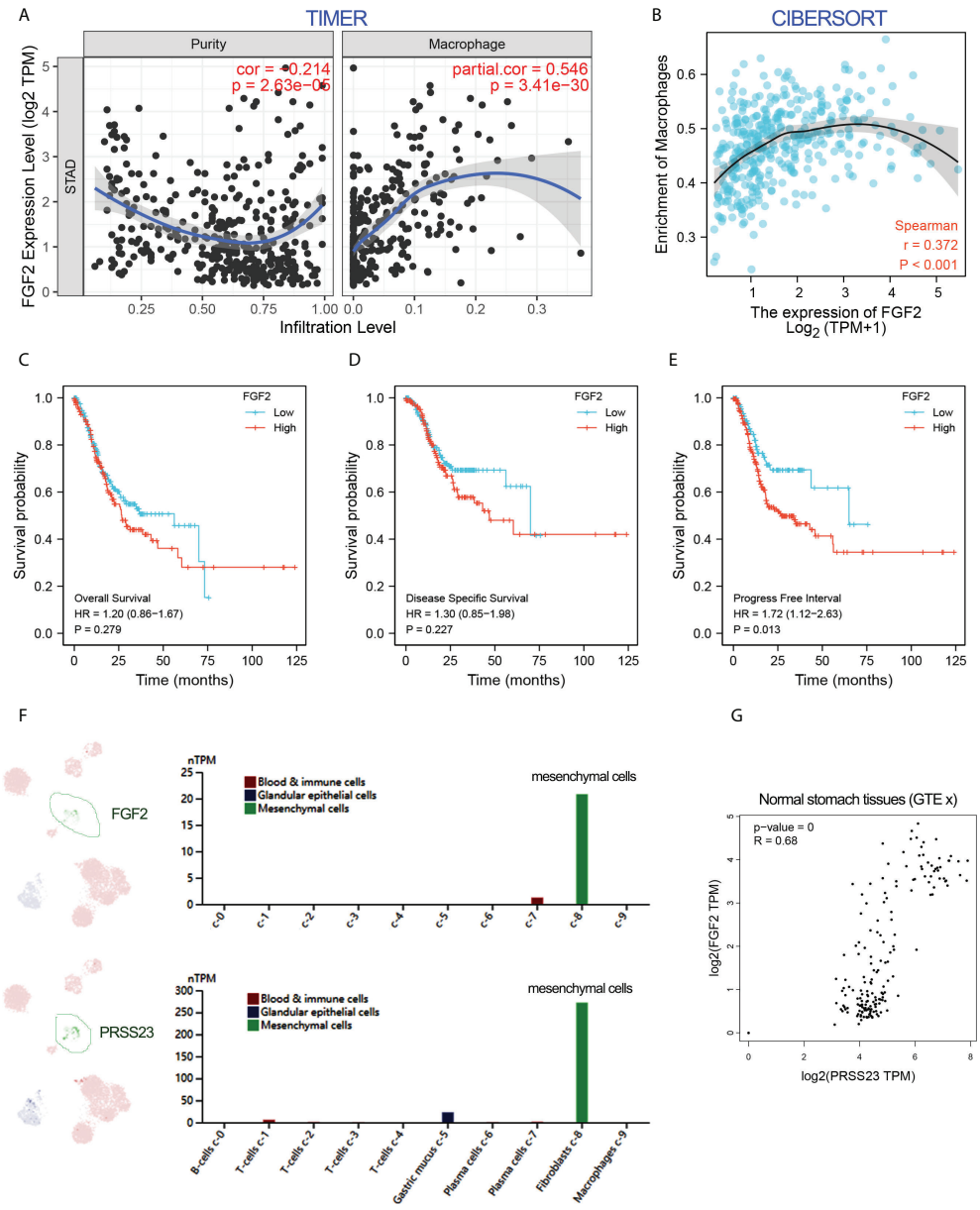

FIGURE 6
FGF2 showed a positive association with macrophage infiltration and PRSS23 expression. **(A, B)** The correlation between FGF2 expression and immune infiltration was analyzed using TIMER and CIBERSORT methods. **(C–E)** FGF2 overexpression predicted poor overall survival, disease-specific survival and progress-free survival in GC from TCGA dataset. **(F)** Single-cell analysis showed that PRSS23 and FGF2 were both highly expressed in mesenchymal GC cells. **(G)** FGF2 and PRSS23 were highly co-expressed in normal stomach tissues.

required for TAM macrophage infiltration (Figure 7H). Furthermore, rescue assay confirmed FGF2 overexpression can recovery the inhibitory effect of PRSS23 depletion on cell survival rate of TAM-like cells or cell proliferation of GC cells (Figures 7H, I).

As a serine protease, PRSS23 may play a role in FGF2 processing and secretion by directly cleaving FGF2 proteins. Immunoblotting assay showed that PRSS23 knockdown mainly downregulating 18kDa FGF2 expression (Figures 8A, B). However, there is no new FGF2 band generated, even under conditions where Brefeldin A blocked FGF2 secretion (Figures 8A, B).

FGF2 has been reported to bind all 4 FGF receptors (FGFR1-4) (43). Gene expression correlation analysis showed that FGF2 expression was positively associated with FGFR1/2, but negatively associated with FGFR3/4 expression (Figure 8C).

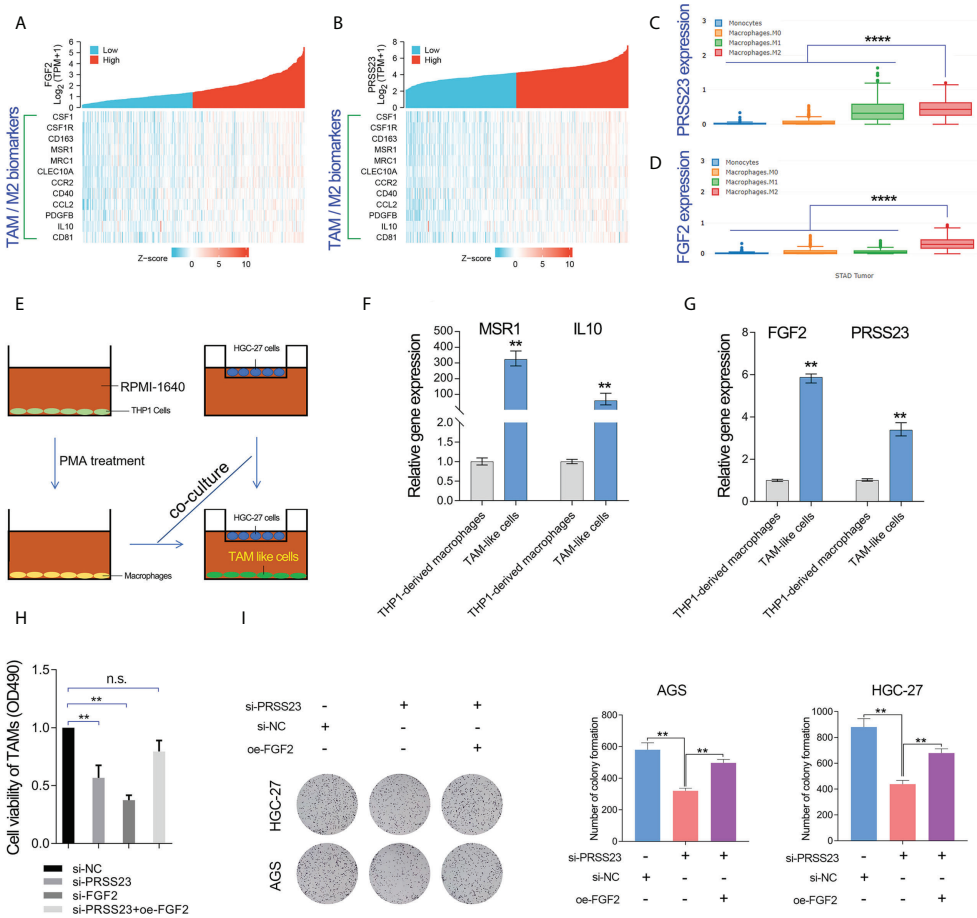

FIGURE 7
PRSS23 enhances TAM infiltration by regulating FGF2 expression and secretion. **(A)** The gene expression correlation between FGF2 and the well-known biomarker genes of TAM/M2 macrophage was analyzed. **(B)** The gene expression correlation between PRSS23 and the well-known biomarker genes of TAM/M2 macrophage was analyzed. **(C, D)** PRSS23 and FGF2 was upregulated in M2 macrophages. **(E)** The TAM-like cells were induced by co-culturing with HGC-27 cells and THP-1 derived macrophages. **(F)** The well-known biomarkers of TAM/M2 macrophages were greatly upregulated. **(G)** Both FGF2 and PRSS23 were significantly upregulated in TAM-like cells. **(H)** Overexpression of FGF2 rescued the inhibitory effect of survival of TAM-like cells by PRSS23 depletion. **(I)** Overexpression of FGF2 rescued the inhibitory effect of GC cell proliferation by PRSS23 depletion. **p < 0.01, ****p < 0.0001, ns means no significant..

Besides, clinical analysis showed that FGF2 and FGFR1 were highly expressed in diffuse GC, FGFR3 and FGFR4 were lowly expressed in diffuse GC (Figures 8D, E). Although there were several studies have reported that FGFR2 was amplified in diffuse GC, our data herein showed that FGFR2 expression has no significant change between diffuse GC and intestinal GC. That may be due to the low frequency (approximately 4-10%) of FGFR2 amplification events in diffuse GC (44–46). Survival analysis showed that FGFR1 overexpression predicted poor prognosis, FGFR3 overexpression predicted favorable prognosis. These results implied that there may be a FGF2/FGFR1 autorinal loop in GC (Figure 8F).

Several studies have reported that FGF2 can act in autocrine modes by binding to FGFR1 (47–49). Since FGF2 mRNA and protein level were both downregulated after PRSS23 knockdown, we thus further identified if PRSS23 knockdown downregulated FGF2 mRNA level by affecting FGF2 in an autocrinal manner. In other words, it's possible that the reduced secreted FGF2 by PRSS23 knockdown may in turn regulate FGF2 transcription *via* an autocrinal loop. Thus, we performed exogenous recombinant FGF2 protein treatment in HGC-27 cells. The results showed that recombinant FGF2 significantly upregulated FGFR1 expression but has no significant effects on FGF2 and FGFR2/3/4 expression in GC (Figure 8G).

Macrophage infiltration can be divided into M1 macrophage infiltration and M2 macrophage infiltration. To this end, we used the quanTIseq algorithm to distinguish M1 macrophages from M2 macrophages (50), and further analyzed the correlation between M1 or M2 macrophage infiltration and the prognosis of GC patients (Figures 9A, B). The results showed that GC

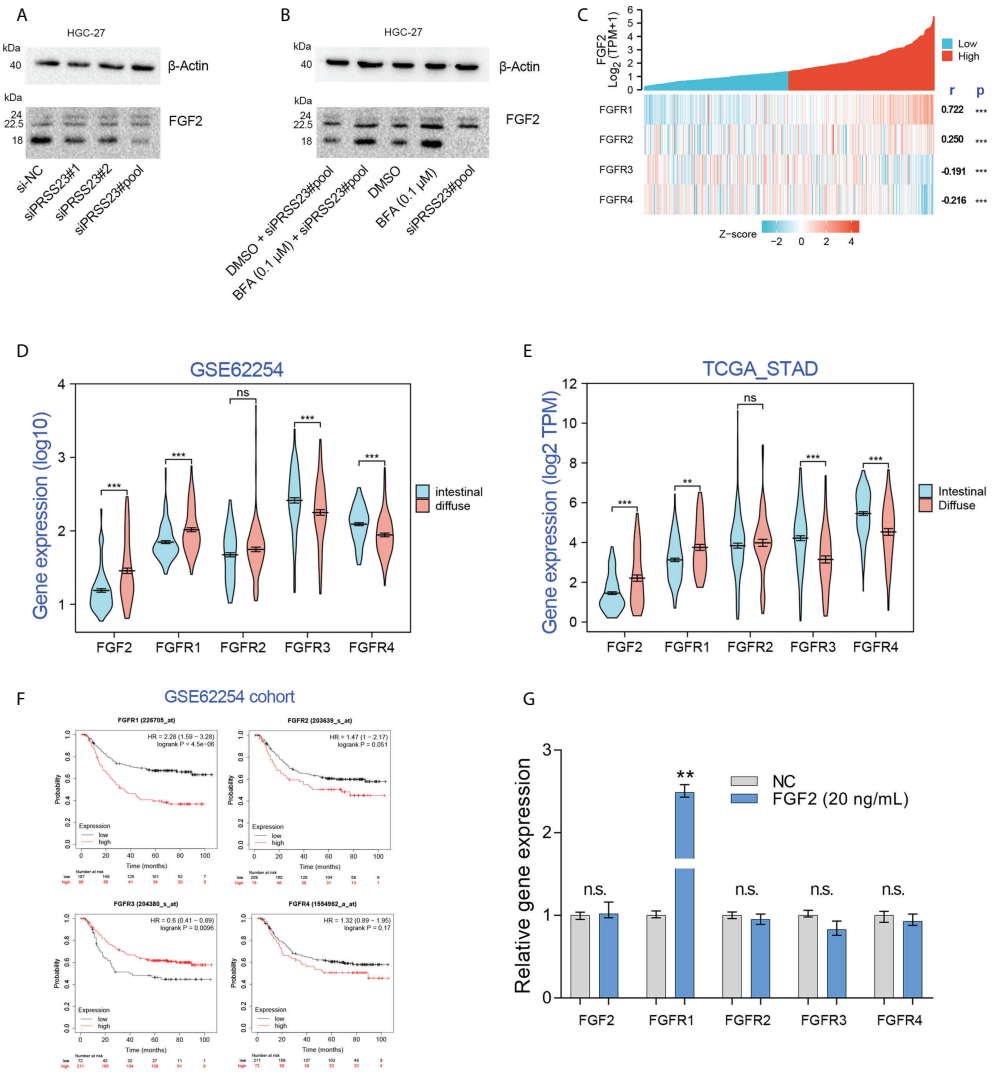

FIGURE 8
Exogenous recombinant FGF2 significantly upregulated FGFR1 expression in GC. **(A)** Western blotting assay confirmed that PRSS23 knockdown mainly affected low weight molecular FGF2 (18 kDa) expression in GC. **(B)** The experiments combining blockade of FGF2 secretion by Brefeldin A (BFA) with PRSS23 knockdown were performed. **(C)** The gene expression correlation between FGF2 and its receptors in TCGA_STAD cohort. **(D, E)** The expression levels of FGF2/FGFR1/2/3/4 were analyzed in two independent GC cohorts. **(F)** Survival analysis of FGF2/FGFR1/2/3/4 in GSE62254 cohort. **(G)** The expression levels of FGF2/FGFR1/2/3/4 were determined by qRT-PCR after treatment with recombinant FGF2 in HGC-27 cells. **p < 0.01, ***p < 0.001, ns means no significant..

patients with higher M1 macrophage infiltration tends to possess a longer overall survival time (p=0.04), while GC patients with higher M2 macrophage infiltration tends to possess a shorter overall survival time (p<0.01). Given FGF2 suppressed M1 macrophage polarization but promoted M2 macrophage polarization, we mapped the working model of PRSS23 in promoting GC progression (Figure 9C).

In GC, serine protease PRSS23 was overexpressed, thereby promoting the expression and secretion of FGF2. Increased level of FGF2 in turn promotes TAMs polarization and infiltration, leading to poor prognosis in GC. This study reveals for the first time the biological function of PRSS23 in macrophage infiltration, which may have implications for immunotherapy of GC.

Discussion

Gastric cancer is a common malignancy characterized by significant clinical heterogeneity and remains the fourth most common cause of death resulting from cancer worldwide (51). The intratumor heterogeneity determines the differences in drug resistance, treatment methods and prognosis of different

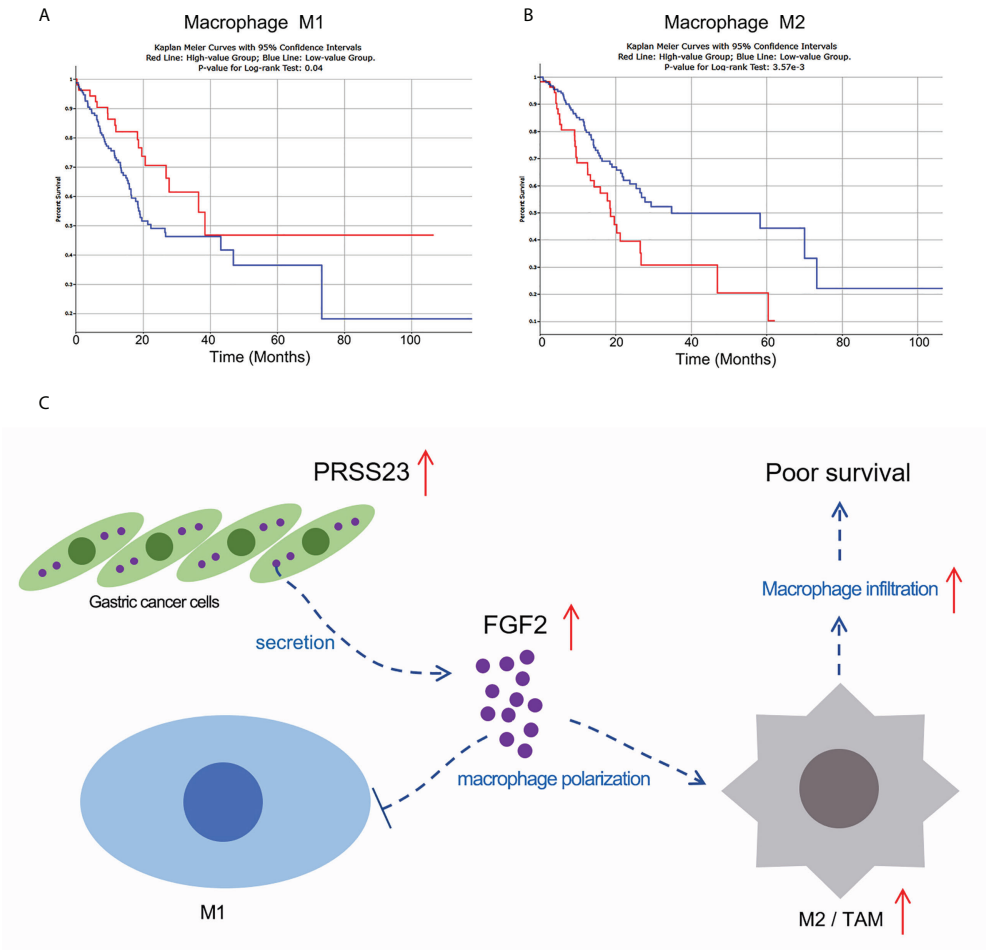

FIGURE 9
Working model of PRSS23/FGF2 axis in regulating macrophage infiltration. **(A)** High level of M1 macrophage infiltration predicted favorable prognosis in GC. **(B)** High level of M2 macrophage infiltration predicted poor prognosis in GC. **(C)** Working model of PRSS23/FGF2 axis in macrophage infiltration. PRSS23 was overexpressed in GC, which enhanced the expression and secretion of FGF2. Meanwhile, FGF2 upregulation drives macrophage polarized towards M2/TAM phenotype, thereby resulting poor prognosis in GC. Taken together, PRSS23 promotes TAM/M2 macrophage infiltration through positively regulating FGF2 expression and secretion.

patients. Biomarkers are one of the important ways to distinguish tumor heterogeneity. Therefore, the development of novel biomarker genes is of great significance to the diagnosis, treatment and prognosis of tumors.

In this study, the clinical value of PRSS23 was analyzed in two independent cohorts. PRSS23 overexpression showed a significant correlation with malignant progression and poor prognosis of GC, suggested PRSS23 can be served as an ideal prognostic biomarker for GC. Loss-of-function study had confirmed that PRSS23 functioned oncogenic roles in GC progression, which fits well with another reported evidence that PRSS23 knockdown inhibits gastric tumorigenesis (52).

Previous study had reported Fgf2 was secreted by CAFs in mice (23). Likewise, single-cell analysis also showed that FGF2 was specifically expressed in fibroblasts of human stomach. So, what is the role of FGF2 secreted by fibroblasts? Several studies have reported the critical role of FGF2 in macrophage infiltration and polarization. Knockout of Fgf2 in mice significantly decreased macrophage infiltration (40). Likewise, Im et al. have found that TAMs were polarized towards an inflammatory (M1) phenotype in the Fgf2 knockout mice (24). Similarly, Takase et al. also reported that FGF2/FGFR1 axis was required for TAM infiltration in esophageal cancer (25). These data proved that FGF2 promotes macrophage polarization towards an M2/TAM phenotype. FGFBP1 was reported to be a secreted heparin proteins that reversibly bind FGF1 and FGF2, releasing them from the extracellular matrix and increasing the local levels of free ligand available for receptor binding (53). In other words, FGFBP1 contributes to FGF2 secretion, enhancing its binding to the receptors (FGFR1/2/3/4) (43).

In the present work, a novel role of the serine protease PRSS23 in macrophage infiltration was uncovered in GC. Through high-throughput RNA sequencing, we noted that serine protease PRSS23 was involved into positively regulating FGF2/FGFBP1 expression. Consistently, our subsequent qRT-PCR, western blotting and ELISA assay showed that PRSS23 depletion significantly decreased FGF2 expression and secretion. More importantly, HGC-27 cells and THP-1-derived macrophages co-culture assay further confirmed that PRSS23 promoted TAM infiltration in GC through regulating FGF2 expression and secretion.

Although our findings demonstrate the positive regulation of FGF2 expression and secretion by PRSS23, a non-negligible limitation of our work lies in how exactly PRSS23 regulates FGF2/FGFBP1 expression. Previous studies have reported that although most of FGFs are secreted proteins with cleavable amino terminal portions, FGF1 and FGF2 have no secretion sequences, although they are found in the extracellular compartment (18). In addition, considering that FGF2 mRNA was also decreased by PRSS23 knockdown, this strongly implies that FGF2 was not a direct substrate protein of PRSS23.

Previous publications had reported that ED-71 and its analogues (1, 25-dihydroxyvitamin D3) suppressed expression of FGFBP1/FGF2 by upregulating IκBα (NFKBIA), a critical regulator of NF-κB pathway (54–56). However, according to our RNA-seq data, NFKBIA expression was slightly downregulated in PRSS23-depleted GC cells. The molecular mechanism of how PRSS23 regulates FGF2 expression remains to be further investigated.

TAMs have very similar phenotypes with M2 macrophages, which functioned oncogenic roles in tumor progression (57–59). While M1 macrophages with pro-inflammation functions played tumor-suppressive roles in tumor progression (60). Herein, after differentiation of M1 and M2 macrophages by the quanTIseq algorithm (50), we analyzed the relationship between M1 or M2 macrophage infiltration and the survival of GC patients from TCGA. The results showed that M1 macrophage infiltration predicted favorable prognosis, while M2 macrophage infiltration predicted poor prognosis in GC, suggested M1 and M2 macrophage play opposite roles in GC progression (Figures 9A, B). Therefore, we thought PRSS23 plays critical roles in GC progression by enhancing TAMs infiltration *via* FGF2.

Conclusion

In summary, PRSS23 was overexpressed and showed a significant correlation with poor prognosis, macrophage infiltration. Mechanismly, PRSS23 promotes tumor associated macrophage infiltration by regulating FGF2 expression and secretion. Our finding highlights that PRSS23/FGF2 was a novel signaling axis involved into regulating TAMs infiltration and GC progression.

Data availability statement

The datasets presented in this study can be found in online repositories. The names of the repository/repositories and accession number(s) can be found in the article/Supplementary Material.

Author contributions

SQ, and DL conceived and designed the study. SQ wrote the paper. DL performed most of the experiments. PH, CH, and ZW carried out initial data analyses and performed partial of the experiments. All authors contributed to drafting the manuscript. All authors have read and approved the final submitted manuscript.

Funding

This study was supported by grants from the National Natural Science Foundation of China (82203829, 82273451 and 81802375); Hubei Provincial Natural Science Foundation (2022CFB for DL and SQ), the Faculty Development Grants from Hubei University of Medicine (2020QDJZR024 to CH and 2020QDJZR012 to PH) and the Grants of Open-Ended Design Project from Hubei Key Laboratory of Embryonic Stem Cell Research (no. 2021ESOF021).

Conflict of interest

The authors declare that the research was conducted in the absence of any commercial or financial relationships that could be construed as a potential conflict of interest.

Publisher's note

Supplementary material

The Supplementary Material for this article can be found online at: https://www.frontiersin.org/articles/10.3389/fimmu.2022.955841/full#supplementary-material

SUPPLEMENTARY FIGURE 1
Both of PRSS23 and FGF2 were highly co-expressed with biomarkers of mesenchymal cells and cancer-associated fibroblasts in GC. **(A, B)** PRSS23 or FGF2 expression was positively correlated with the expression of mesenchymal biomarkers, but negatively correlated with the expression of epithelial biomarkers in GC. **(C, D)** PRSS23 or FGF2 was highly co-expressed with classic biomarkers of cancer-associated fibroblasts (CAFs) in GC.

References

1. Li D, Xu M, Wang Z, Huang P, Huang C, Chen Z, et al. The EMT-induced lncRNA NR2F1-AS1 positively modulates NR2F1 expression and drives gastric cancer *via* miR-29a-3p/VAMP7 axis. *Cell Death Dis* (2022) 13(1):1–10:84. doi: 10.1038/s41419-022-04540-2

2. Siegel RL, Miller KD, Fuchs HE, Jemal A. Cancer statistics, 2021. *Ca-Cancer J Clin* (2021) 71(1):7–33. doi: 10.3322/caac.21654

3. Zheng R, Zhang S, Zeng H, Wang S, Sun K, Chen R, et al. Cancer incidence and mortality in China, 2016. *J Natl Cancer Cent* (2022) 2(1):1–9. doi: 10.1016/j.jncc.2022.02.002

4. Wang JJ, Zhang MX, Hu XH, She JJ, Sun RN, Qin SS, et al. miRNA-194 predicts favorable prognosis in gastric cancer and inhibits gastric cancer cell growth by targeting CCND1. *FEBS Open Bio* (2021) 11(7):1814–26. doi: 10.1002/2211-5463.13125

5. Shah BK, Khanal A, Hewett Y. Second primary malignancies in adults with gastric cancer - a US population-based study. *Front Oncol* (2016) 6. doi: 10.3389/fonc.2016.00082

6. Li DD, Wang JJ, Zhang MX, Hu XH, She JJ, Qiu XM, et al. LncRNA MAGI2-AS3 is regulated by BRD4 and promotes gastric cancer progression *via* maintaining ZEB1 overexpression by sponging miR-141/200a. *Mol Ther-Nucl Acids* (2020) 19:109–23. doi: 10.1016/j.omtn.2019.11.003

7. Li DD, She JJ, Hu XH, Zhang MX, Sun RN, Qin SS. The ELF3-regulated lncRNA UBE2CP3 is over-stabilized by RNA-RNA interactions and drives gastric cancer metastasis *via* miR-138-5p/ITGA2 axis. *Oncogene* (2021). doi: 10.1038/s41388-021-01948-6

8. Li D, Cheng P, Wang J, Qiu X, Zhang X, Xu L, et al. IRF6 is directly regulated by ZEB1 and ELF3, and predicts a favorable prognosis in gastric cancer. *Front Oncol* (2019) 9:220. doi: 10.3389/fonc.2019.00220

9. Barzkar N, Khan Z, Jahromi ST, Pourmozaffar S, Gozari M, Nahavandi R. A critical review on marine serine protease and its inhibitors: A new wave of drugs? *Int J Biol Macromol* (2021) 170:674–87. doi: 10.1016/j.ijbiomac.2020.12.134

10. Bao YH, Guo YC, Yang YQ, Wei XN, Zhang SS, Zhang YM, et al. PRSS8 suppresses colorectal carcinogenesis and metastasis. *Oncogene* 40(10):1922–4. doi: 10.1038/s41388-018-0453-3

11. Bao YH, Li K, Wang Q, Guo YC, Han RF, Chen ZG, et al. Characterization of a novel tumor suppressor PRSS8 in colorectal cancer. *Cancer Res* (2015) 75 (15_Supplement). doi: 10.1158/1538-7445.AM2015-2044

12. Ma H, Hockla A, Mehner C, Coban M, Papo N, Radisky DC, et al. PRSS3/Mesotrypsin and kallikrein-related peptidase 5 are associated with poor prognosis and contribute to tumor cell invasion and growth in lung adenocarcinoma. *Sci Rep-Uk* (2019) 9(1844). doi: 10.1038/s41598-018-38362-0

13. Wang F, Hu YL, Feng Y, Guo YB, Liu YF, Mao QS, et al. High-level expression of PRSS3 correlates with metastasis and poor prognosis in patients with gastric cancer. *J Surg Oncol* (2019) 119(8):1108–21. doi: 10.1002/jso.25448

14. Zhang QY, Wang JH, Huang D, Liu G. High expression of PRSS3 indicates unfavorable clinical outcomes in colon adenocarcinoma. *Appl Immunohisto M M* (2021) 29(8):564–9. doi: 10.1097/PAI.0000000000000921

15. Chen H-W, Tzeng C-RJF. The novel serine proteases, prtn3 and prss23, in murine blastocyst development and hatching. *Fertility and Sterility* (2007) 88:S312. doi: 10.1016/j.fertnstert.2007.07.1049

16. Räihä MR, PAJCd P. Tumor-associated macrophages (TAMs) as biomarkers for gastric cancer: a review. *Chronic Dis Transl Med* (2018) 4 (3):156–63. doi: 10.1016/j.cdtm.2018.07.001

17. Tang X. Tumor-associated macrophages as potential diagnostic and prognostic biomarkers in breast cancer. *Cancer letters* (2013) 332(1):3–10. doi: 10.1016/j.canlet.2013.01.024

18. Feng Q, Chang W, Mao Y, He G, Zheng P, Tang W, et al. Tumor-associated macrophages as prognostic and predictive biomarkers for postoperative adjuvant chemotherapy in patients with stage II colon cancer. *Clinical Cancer Research* (2019) 25(13):3896–907. doi: 10.1158/1078-0432.CCR-18-2076

19. Yang L, YJJoh Z. Tumor-associated macrophages: from basic research to clinical application. *Journal of hematology & oncology* (2017) 10(1):1–12. doi: 10.1186/s13045-017-0430-2

20. Pan Y, Yu Y, Wang X, Zhang T. Tumor-associated macrophages in tumor immunity. *Frontiers in immunology* (2020) 11:. doi: 10.3389/fimmu.2020.583084

21. Zhou J, Tang Z, Gao S, Li C, Feng Y, Zhou X. Tumor-associated macrophages: recent insights and therapies. *Frontiers in Oncology* (2020) 10:188. doi: 10.3389/fonc.2020.00188

22. Wu K, Lin K, Li X, Yuan X, Xu P, Ni P, et al. Redefining tumor-associated macrophage subpopulations and functions in the tumor microenvironment. *Frontiers in immunology* (2020) 11:. doi: 10.3389/fimmu.2020.01731

23. Hegab AE, Ozaki M, Kameyama N, Gao J, Kagawa S, Yasuda H, et al. Effect of FGF/FGFR pathway blocking on lung adenocarcinoma and its cancer-associated fibroblasts. *the Journal of Pathology* (2019) 249(2):193–205. doi: 10.1002/path.5290

24. Im JH, Buzzelli JN, Jones K, Franchini F, Gordon-Weeks A, Markelc B, et al. FGF2 alters macrophage polarization, tumour immunity and growth and can be targeted during radiotherapy. *Nat Commun* (2020) 11(1):1–14. doi: 10.1038/s41467-020-17914-x

25. Takase N, Koma Y, Urakawa N, Nishio M, Arai N, Akiyama H, et al. NCAM- and FGF-2-mediated FGFR1 signaling in the tumor microenvironment of esophageal cancer regulates the survival and migration of tumor-associated macrophages and cancer cells. *Cancer Lett* (2016) 380(1):47–58. doi: 10.1016/j.canlet.2016.06.009

26. Wang Y, Sun Q, Ye Y, Sun X, Xie S, Zhan Y, et al. FGF-2 signaling in nasopharyngeal carcinoma modulates pericyte-macrophage crosstalk and metastasis. *JCI Insight* (2022) 7(10):e157874. doi: 10.1172/jci.insight.157874

27. Cristescu R, Lee J, Nebozhyn M, Kim KM, Ting JC, Wong SS, et al. Molecular analysis of gastric cancer identifies subtypes associated with distinct clinical outcomes. *Nat Med* (2015) 21(5):449–56. doi: 10.1038/nm.3850

28. Zhang X, Zhu M, Hong Z, Chen C. Co-Culturing polarized M2 thp-1-derived macrophages enhance stemness of lung adenocarcinoma A549 cells. *Ann Transl Med* (2021) 9(8):709. doi: 10.21037/atm-21-1256

29. Dehai C, Bo P, Qiang T, Lihua S, Fang L, Shi J, et al. Enhanced invasion of lung adenocarcinoma cells after co-culture with THP-1-derived macrophages *via* the induction of EMT by IL-6. *Immunol Lett* (2014) 160(1):1–10. doi: 10.1016/j.imlet.2014.03.004

30. Wei R, Zhu WW, Yu GY, Wang X, Gao C, Zhou X, et al. S100 calcium-binding protein A9 from tumor-associated macrophage enhances cancer stem cell-like properties of hepatocellular carcinoma. *Int J Cancer* (2021) 148(5):1233–44. doi: 10.1002/ijc.33371

31. Qin SS, Tang YH, Chen YP, Wu PZ, Li MR, Wu GJ, et al. Overexpression of the starch phosphorylase-like gene (PHO3) in lotus japonicus has a profound effect on the growth of plants and reduction of transitory starch accumulation. *Front Plant Sci* (2016) 7. doi: 10.3389/fpls.2016.01315

32. Issac Niwas S, Andreas KRS, Virginie U, Palanisamy P, Caroline K, Martin S, et al. Automated classification of immunostaining patterns in breast tissue from the human protein atlas. *J Pathol Inform* (2013) 4(Suppl):S14. doi: 10.4103/2153-3539.109881

33. Dai D, Liu L, Huang H, Chen S, Chen B, Cao J, et al. Nomograms to predict the density of tumor-infiltrating lymphocytes in patients with high-grade serous ovarian cancer. *Front Oncol* (2021) 11:148. doi: 10.3389/fonc.2021.590414

34. Li TW, Fan JY, Wang BB, Traugh N, Chen QM, Liu JS, et al. TIMER: A web server for comprehensive analysis of tumor-infiltrating immune cells. *Cancer Res* (2017) 77(21):E108–10. doi: 10.1158/0008-5472.CAN-17-0307

35. Newman AM, Liu CL, Green MR, Gentles AJ, Feng WG, Xu Y, et al. Robust enumeration of cell subsets from tissue expression profiles. *Nat Methods* (2015) 12 (5):453. doi: 10.1038/nmeth.3337

36. Czubayko F, Liaudet-Coopman ED, Aigner A, Tuveson AT, Berchem GJ, Wellstein A. A secreted FGF-binding protein can serve as the angiogenic switch in human cancer. *Nature medicine* (1997) 3(10):1137–40. doi: 10.1038/nm1097-1137

37. Tassi E, Al-Attar A, Aigner A, Swift MR, McDonnell K, Karavanov A, et al. Enhancement of fibroblast growth factor (FGF) activity by an FGF-binding protein. *Journal of Biological Chemistry* (2001) 276(43):40247–53. doi: 10.1074/jbc.M104933200

38. Shintani T, Higaki M, Okamoto TJC. Heparin-binding protein 17/Fibroblast growth factor-binding protein-1 knockout inhibits proliferation and induces differentiation of squamous cell carcinoma cells. *Cancers* (2021) 13(11). doi: 10.3390/cancers13112684

39. Wang P, Xu LJ, Qin JJ, Zhang L, Zhuang GH. MicroRNA-155 inversely correlates with esophageal cancer progression through regulating tumor-associated macrophage FGF2 expression. *Biochem Bioph Res Co* (2018) 503(2):452–8. doi: 10.1016/j.bbrc.2018.04.094

40. Liang WJ, Wang Q, Ma H, Yan WJ, Yang JJ. Knockout of low molecular weight FGF2 attenuates atherosclerosis by reducing macrophage infiltration and oxidative stress in mice. *Cell Physiol Biochem* (2018) 45(4):1434–43. doi: 10.1159/000487569

41. Huang JK, Ma L, Song WH, Lu BY, Huang YB, Dong HM, et al. LncRNA-MALAT1 promotes angiogenesis of thyroid cancer by modulating tumor-associated macrophage FGF2 protein secretion. *J Cell Biochem* (2017) 118 (12):4821–30. doi: 10.1002/jcb.26153

42. Chávez-Galán L, Olleros ML, Vesin D, Garcia I. Much more than M1 and M2 macrophages, there are also CD169+ and TCR+ macrophages. (2015) 6:. doi: 10.3389/fimmu.2015.00263

43. Helsten T, Schwaederle M, Kurzrock RJC, Reviews M. Fibroblast growth factor receptor signaling in hereditary and neoplastic disease: biologic and clinical implications. (2015) 34(3):479–96. doi: 10.1007/s10555-015-9579-8

44. Wang H, Lu J, Tang J, Chen S, He K, Jiang X, et al. Establishment of patient-derived gastric cancer xenografts: a useful tool for preclinical evaluation of targeted therapies involving alterations in HER-2, MET and FGFR2 signaling pathways. (2017) 17(1):1–11. doi: 10.1186/s12885-017-3177-9

45. Lau WM, Teng E, Huang KK, Tan JW, Das K, Zang Z, et al. Acquired resistance to FGFR inhibitor in diffuse-type gastric cancer through an AKT-independent PKC-mediated phosphorylation of GSK3β. (2018) 17(1):232–42. doi: 10.1158/1535-7163.MCT-17-0367

46. Sase H, Nakanishi Y, Aida S, Horiguchi-Takei K, Akiyama N, Fujii T, et al. Acquired JHDM1D–BRAF fusion confers resistance to FGFR inhibition in FGFR2-amplified gastric CancerResistant mechanism to FGFR inhibition in gastric cancer. (2018) 17(10):2217–25. doi: 10.1158/1535-7163.MCT-17-1022

47. Terai H, Soejima K, Yasuda H, Nakayama S, Hamamoto J, Arai D, et al. Activation of the FGF2-FGFR1 autocrine pathway: A novel mechanism of acquired resistance to gefitinib in NSCLCAcquired resistance to gefitinib by FGF2–FGFR1 autocrine loop. (2013) 11(7):759–67. doi: 10.1158/1541-7786.MCR-12-0652

48. Lefevre G, Babchia N, Calipel A, Mouriaux F, Faussat A-M, Mrzyk S, et al. Activation of the FGF2/FGFR1 autocrine loop for cell proliferation and survival in uveal melanoma cells. (2009) 50(3):1047–57. doi: 10.1167/iovs.08-2378

49. Cen M, Yao Y, Cui L, Yang G, Lu G, Fang L, et al. Honokiol induces apoptosis of lung squamous cell carcinoma by targeting FGF2-FGFR1 autocrine loop. (2018) 7(12):6205–18. doi: 10.1002/cam4.1846

50. Plattner C, Finotello F, Rieder D. Deconvoluting tumor-infiltrating immune cells from RNA-seq data using quanTIseq. *Method Enzymol* (2020) 636:261–85. doi: 10.1016/bs.mie.2019.05.056

51. Zhang L, Liu Q, K-w L, Z-y Q, G-x Z, L-t S, et al. SHARPIN stabilizes β-catenin through a linear ubiquitination-independent manner to support gastric tumorigenesis. *Gastric Cancer* (2021) 24(2):402–16. doi: 10.1007/s10120-020-01138-5

52. Han B, Yang Y, Chen J, He XX, Lv NH, Yan RW. PRSS23 knockdown inhibits gastric tumorigenesis through EIF2 signaling. *Pharmacol Res* (2019) 142:50–7. doi: 10.1016/j.phrs.2019.02.008

53. Wu D, Kan M, Sato GH, Okamoto T, Sato JD. Characterization and molecular cloning of a putative binding protein for heparin-binding growth factors. *Journal of Biological Chemistry* (1991) 266(25):16778–85. doi: 10.1016/S0021-9258(18)55368-0

54. Rosli S, Shintani T, Hayashido Y, Toratani S, Usui E, TJTJoSB O, et al. 1α, 25 (OH) 2D3 down-regulates HBp17/FGFBP-1 expression *via* NF-κB pathway. *The Journal of Steroid Biochemistry and Molecular Biology* (2013) 136:98–101. doi: 10.1016/j.jsbmb.2012.10.011

55. Rosli S, Shintani T, Toratani S, Usui E, Okamoto TJIVC, Biology-Animal D. 1α, 25 (OH) 2D3 inhibits FGF-2 release from oral squamous cell carcinoma cells through down-regulation of HBp17/FGFBP-1. *In Vitro Cellular & Developmental Biology - Animal* (2014) 50(9):802–6. doi: 10.1007/s11626-014-9787-5

56. Shintani T, Takatsu F, Rosli S, Usui E, Hamada A, Sumi K, et al. Eldecalcitol (ED-71), an analog of 1α, 25 (OH) 2D3, inhibits the growth of squamous cell carcinoma (SCC) cells *in vitro* and *in vivo* by down-regulating expression of heparin-binding protein 17/fibroblast growth factor-binding protein-1 (HBp17/FGFBP-1) and FGF-2. *Cancers* (2017) 53(9):810–7. doi: 10.3390/cancers13112684

57. Jayasingam SD, Citartan M, Thang TH, Zin AAM, Ang KC, Ch'ng ES. Evaluating the polarization of tumor-associated macrophages into M1 and M2 phenotypes in human cancer tissue: Technicalities and challenges in routine clinical practice. *Front Oncol* (2020) 9. doi: 10.3389/fonc.2019.01512

58. Liu JY, Geng XF, Hou JX, Wu GS. New insights into M1/M2 macrophages: key modulators in cancer progression. *Cancer Cell Int* (2021) 21(1):389. doi: 10.1186/s12935-021-02089-2

59. Yuan A, Hsiao YJ, Chen HY, Chen HW, Ho CC, Chen YY, et al. Opposite effects of M1 and M2 macrophage subtypes on lung cancer progression. *Sci Rep-Uk* (2015) 5:14273. doi: 10.1038/srep14273

60. Utomo L, Bastiaansen-Jenniskens YM, Verhaar JA, van Osch GJ. Cartilage degeneration is exacerbated by pro-inflammatory (M1) macrophages but not inhibited by anti-inflammatory (M2) macrophages *in vitro*. *Osteoarthr Cartil* (2016) 24:S34–S5. doi: 10.1016/j.joca.2016.01.087

frontiers | Frontiers in Immunology

TYPE Systematic Review
PUBLISHED 27 September 2022
DOI 10.3389/fimmu.2022.971278

OPEN ACCESS

EDITED BY
Julie Decock,
Qatar Biomedical Research Institute, Qatar

REVIEWED BY
James McCarthy,
University of Minnesota Twin Cities, United States
Spyros S. Skandalis,
University of Patras, Greece

*CORRESPONDENCE
Sergei Kusmartsev
sakus61@ufl.edu

SPECIALTY SECTION
This article was submitted to Cancer Immunity and Immunotherapy, a section of the journal Frontiers in Immunology

RECEIVED 16 June 2022
ACCEPTED 07 September 2022
PUBLISHED 27 September 2022

CITATION
Donelan W, Dominguez-Gutierrez PR and Kusmartsev S (2022) Deregulated hyaluronan metabolism in the tumor microenvironment drives cancer inflammation and tumor-associated immune suppression.
Front. Immunol. 13:971278.
doi: 10.3389/fimmu.2022.971278

Deregulated hyaluronan metabolism in the tumor microenvironment drives cancer inflammation and tumor-associated immune suppression

William Donelan, Paul R. Dominguez-Gutierrez and Sergei Kusmartsev*

Department of Urology, University of Florida, College of Medicine, Gainesville, FL, United States

Hyaluronan (HA) is known to be a prominent component of the extracellular matrix in tumors, and many solid cancers are characterized by aberrant HA metabolism resulting in increased production in tumor tissue. HA has been implicated in regulating a variety of cellular functions in tumor cells and tumor-associated stromal cells, suggesting that altered HA metabolism can influence tumor growth and malignancy at multiple levels. Importantly, increased HA production in cancer is associated with enhanced HA degradation due to high levels of expression and activity of hyaluronidases (Hyal). Understanding the complex molecular and cellular mechanisms involved in abnormal HA metabolism and catabolism in solid cancers could have important implications for the design of future cancer therapeutic approaches. It appears that extensive crosstalk between immune cells and HA-enriched stroma contributes to tumor growth and progression in several ways. Specifically, the interaction of tumor-recruited Hyal2-expressing myeloid-derived suppressor cells (MDSCs) of bone marrow origin with HA-producing cancer-associated fibroblasts and epithelial tumor cells results in enhanced HA degradation and accumulation of small pro-inflammatory HA fragments, which further drives cancer-related inflammation. In addition, hyaluronan-enriched stroma supports the transition of tumor-recruited Hyal2$^+$MDSCs to the PD-L1$^+$ tumor-associated macrophages leading to the formation of an immunosuppressive and tolerogenic tumor microenvironment. In this review, we aim to discuss the contribution of tumor-associated HA to cancer inflammation, angiogenesis, and tumor-associated immune suppression. We also highlight the recent findings related to the enhanced HA degradation in the tumor microenvironment.

KEYWORDS

tumor microenvironment, HYAL2, hyaluronan degradation, PD-L1, MDSC, tumor-associated macrophages, cancer inflammation, tumor-associated immune suppression

Biology of hyaluronan

Synthesis and degradation of HA

Hyaluronan, also called hyaluronic acid (HA), is a member of the glycosaminoglycan family of polysaccharides synthesized at the cell surface. Distributed widely through vertebrate connective, epithelial, and neural tissues, interactions between HA and the extracellular matrix (ECM) regulate cellular processes involved in embryonic development, tissue healing, inflammation, and tumor progression (1–3). HA is synthesized as an unbranched polymer of repeating disaccharides of glucuronic acid and *N*-acetylglucosamine. Normal physiological HA polymers consist of 2,000-25,000 disaccharides with molecular masses in the range of 10^6 – 10^7 kDa and polymer lengths of 2-25μm. HA is synthesized at the cell membrane as an unmodified polysaccharide by one of three hyaluronan synthases (HAS): HAS1, HAS2, or HAS3.

These transmembrane enzymes initiate synthesis on the inner side of the cell membrane and extrude HA onto the outer cell surface or into the ECM. HAS2 produces the largest HA polymers and is responsible for the majority of HA synthesis. Cell surface HA binding proteins, such as CD44 and RHAMM, anchor the matrix to the cell (4, 5). The degradation of HA is catalyzed by hyaluronidase enzymes (6, 7). Hyal1 and Hyal2 are the major hyaluronidases that are expressed in most tissues and hydrolyze the linkage between *N*-acetylglucosamine and glucuronic acid to generate HA fragments (8). Cell surface GPI-anchored Hyal2 degrades high molecular weight HA into intermediate molecular weight fragments of 20 kDa. In a concerted effort, HA fragments are further hydrolyzed by Hyal1 in endo-lysosomal compartments generating oligosaccharides.

HA function and turnover in normal tissues and organs

HA has numerous biological functions both structurally and in terms of cell signaling. HA is an important constituent of the ECM that plays a role in the lubrication of joints and maintaining connective tissue integrity (1, 3). The biophysical properties of HA such as high hydration capacity contribute to tissue homeostasis and the structural integrity of the interstitial space which is critical for cellular remodeling. The transmembrane protein CD44 is considered the principal receptor for HA (2). CD44 expression is upregulated by growth factors and pro-inflammatory cytokines such as IL-1, epidermal growth factor (EGF), and transforming growth factor-beta (TGF-β). HA-CD44 interactions regulate key cellular functions including cell-cell adhesion, cellular migration, and receptor-mediated HA internalization and degradation. RHAMM is another key HA receptor that is present at the cell surface and also has isoforms that are localized to the cytoplasm and nucleus. HA-RHAMM interactions mediate cellular migration, cytoskeleton rearrangement, and intracellular signal transduction. HA-induced signal transduction *via* interactions with CD44 and RHAMM is mediated through a variety of cell signaling pathways including protein kinase C, focal adhesion kinase (FAK), mitogen-activated protein kinases (MAPKs), nuclear factor NF-κB, RAS, phosphatidylinositol kinase (PI3K), tyrosine kinases, and cytoskeletal components (1, 2). Under normal homeostatic conditions, the synthesis and degradation of HA are well balanced, but a shift towards increased degradation of HA occurs during pathological conditions (2).

Hyaluronan metabolism in cancer

Enhanced HA synthesis in tumors

Multiple studies have demonstrated that cancers are associated with elevated levels of HA, and human tumors typically have higher HA concentrations than in healthy tissues (2, 3). Human breast, lung, prostate, ovarian, nephroblastomas, and colon cancer are considered to be enriched with HA (1, 2). In these tumors, HA may support tumor growth by stimulating anchorage-independent growth and proliferation of tumor cells. Elevated HA levels have been identified in the urine of patients with bladder carcinomas (9). Not surprisingly, elevated expression of hyaluronan synthases have been identified in bladder cancer tissue and HAS1 is a predictor of tumor recurrence and disease-specific survival (10, 11). *In vivo* studies have confirmed that highly invasive and aggressive breast cancer cell lines express significantly elevated levels of HAS2 (12, 13). Additionally, clinical studies and experiments using mouse models have further found that expression of HAS2 in breast cancer tissues is associated with metastasis and reduced overall survival (14, 15). Enhanced HA synthesis and degradation are evident in the microenvironment of several tumor types and affect tumor growth, cell motility, and metastasis (2, 3).

In experimental tumor models, the overexpression of HA synthases leads to increased HA levels and accelerated tumor growth *in vivo*. The level of HA expression by tumors also correlates well with metastatic progression. For example, high levels of HA are found in the tumor stroma of patients with prostate cancer and are associated with metastasis (16, 17). Supporting these tumor-promoting functions of enhanced HA synthesis, experimental evidence demonstrates that suppression of HAS, reduction of HA synthesis using inhibitors, or use of HA binding molecules have been shown to impair tumor growth and reduce metastasis in several *in vitro* and *in vivo* models (3). Abnormal activation of CD44 and RHAMM cell signaling pathways can lead to malignant behavior, and HA interactions with cell surface receptors CD44 and RHAMM promote tumor

progression by affecting cell proliferation, migration, and angiogenesis (2).

Enhanced HA degradation in tumors

HA turnover is key to understanding the role of HA metabolism in tumor progression (1–3). HA is continually turned over in normal tissues, but the degradation products are rapidly cleared. In contrast, several types of cancer, including breast, prostate, bladder, melanoma, and lung cancers, are characterized by enhanced HA degradation (2, 3 and Figure 1). It is important to understand that HA degradation in the tumor microenvironment is a complex process that involves not only the tumor but also tumor-associated cells. The tumor stroma, which consists of an extracellular matrix and many non-cancer cell types contains an abundance of degraded HA compared to adjacent normal tissue. Bladder cancer progression is associated with enhanced expression of both Hyal2 and Hyal1 (11, 18), and Hyal2 gene expression is significantly increased in patients with progressive versus non-progressive bladder cancer. Elevated hyaluronidase expression and activity in tumor tissues lead to the accumulation of small HA fragments with low molecular weight.

The dual nature of hyaluronan

The size of HA fragments is important for biological activity: high molecular-weight hyaluronan (HMW-HA), a major component of the extracellular matrix, is anti-oncogenic, which exerts anti-inflammatory and wound-healing activities. Evidence of anti-oncogenic properties of HMW-HA comes from the fact that naked mole rats show unusual resistance to cancer and the maximal lifespan of these mice exceeds 30 years (19). Analysis of HA produced by fibroblasts from naked mole rats revealed that its molecular size is five-time higher than human or mouse HA. Naked mole-rat tissues contain larger HA polymers and less detectable fragmentation than tissues of the more tumor-susceptible mouse. Knocking down the expression of hyaluronan synthase or overexpressing the HA-degrading enzyme, Hyal2, naked mole-rat cells become susceptible to malignant transformation and readily form tumors. A recent study demonstrated that at the molecular level, HMW-HA-mediated signaling through the CD44 receptor engages the tumor-suppressive Hippo pathway (20). Thus, recruitment of the polarity-regulating kinase PAR1b by the CD44 intracellular domain results in disruption of the Hippo signaling-inhibitory PAR1b-MST complex. Once liberated from PAR1b, MST activates Hippo signaling.

In contrast, the low-molecular-weight hyaluronan (LMW-HA) is pro-oncogenic. Thus, the HA fragments with low molecular weight produced in a hyaluronidase-dependent manner, inhibited Hippo signaling by competing with HMW-HA for CD44 binding (20). Tumor growth frequently is associated with enhanced HA degradation and the accumulation of small HA fragments with low molecular weight. The LMW-HA has been shown to promote tumor growth in a multifaceted manner by stimulating cancer inflammation, angiogenesis, and spreading of metastatic tumor cells (21–26).

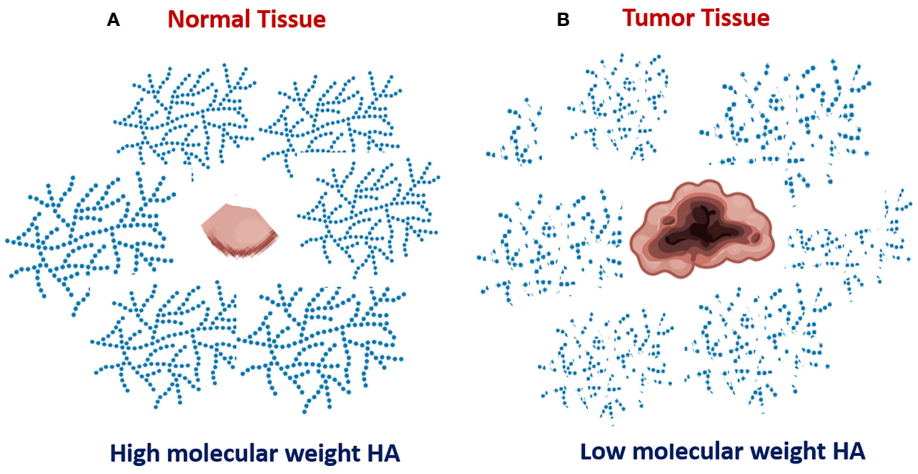

FIGURE 1
Increased degradation of extracellular hyaluronan in tumor tissue. Normal non-malignant bladder tissue produce HA with mostly high molecular weight **(A)**. In contrast, the tumor bladder tissue is characterized by enhanced HA degradation and accumulation of tumor-associated HA with low molecular weight **(B)**.

Effects of LMW-HA accumulation in cancer

LMW-HA and cancer-related inflammation

Cancer-related inflammation is one of the hallmarks of tumor growth (27). Increased production of various inflammatory factors (chemokines, cytokines, bioactive lipids, etc) in tumor tissue supports constant mobilization and recruitment of immunosuppressive cells, precursors of endothelial cells, and cancer-associated fibroblasts which are needed for tumor growth. Increased degradation of hyaluronan in cancer tissue leads to the accumulation of HA fragments with small molecular weight, which is associated with elevated production of multiple cytokines, chemokines, and pro-angiogenic factors (1–3, 18, 28). Mechanistically, the LMW-HA elicits pro-inflammatory responses by modulating the toll-like receptor-4 (TLR-4) and activating the nuclear factor kappa B (NF-kB). In contrast, the HMW-HA manifests an anti-inflammatory effect by inhibiting NF-kB activation (29). During inflammation, HA can be degraded by hyaluronidases or cleaved by reactive oxygen species (ROS) (30–32). HA uptake and fragmentation by macrophages are thought to be important for the resolution of inflammation (24). The molecular weight of HA directly influences the immune macrophage activation (33, 34). According to these studies, the high-molecular-weight HA greater than 1,000 kDa exerts antiangiogenic, immunosuppressive, and anti-inflammatory effects that are important in wound healing, embryogenesis, and ovulation. In contrast, both medium-molecular weight HA and low-molecular-weight HA are pro-inflammatory, pro-angiogenic, and pro-tumor (34). HA added to LPS stimulated chondrocytes responded differently according to the HA molecular weight (32). Lee et al. demonstrated that HA fragments with molecular weight less than 50 kDa significantly increased iNOS production while medium MW-HA (1000 kDa) did not affect iNOS; however, HMW-HA (5000 kDa) significantly reduced iNOS in LPS-stimulated chondrocytes. A similar result was observed in LPS- stimulated macrophages where LMW-HA led to increases in iNOS, TNF-α, IL-6, IL-1β, TGF-β1, IL-10, IL-11, CCL2, and Arg1; however, in unstimulated macrophages, IL-10 significantly up-regulated by HMW-HA (24). Furthermore, LMW-HA increases several cytokines such as MMP-12, plasminogen activator inhibitor-1 (35, 36), CCL2 (MCP-1), CCL3 (MIP-1a), CCL4 (MIP-1β), keratinocyte chemoattractant, interleukins IL-8, and IL-12 by macrophages (37–39). Additionally, LMW-HA elicits the irreversible phenotypic and functional maturation of human dendritic cells (40, 41). In the model for acute lung injury to epithelium causes the production of inflammatory cytokines and chemokines resulting in the influx of neutrophils filled by macrophages to the site with further increase of cytokines and modulation of the extracellular matrix such as HA, collagen, fibronectin. Mechanistically, the low molecular weight HA fragments bind to the CD44, RHAMM, and Toll-like receptors (5, 26, 42–44). Stimulation of TLR2/TLR4 results in enhanced production of inflammatory cytokines and chemokines. In addition, LMW-HA is a potent stimulant of arachidonic acid release in a time- and dose-dependent manner, inducing cPLA$_2$α, ERK1/2, p38, and JNK phosphorylation, as well as activated COX2 expression and PGE$_2$ production in primary human monocytes, murine RAW 264.7, and wild type bone marrow-derived macrophages. Specific cPLA$_2$α inhibitors blocked HA-induced arachidonic acid release and PGE$_2$ production in all of these cells (26). It is interesting to note that HMW-HA can significantly diminish TLR4, TLR2, MyD88, and NF-kB expression (45).

LMW-HA and tumor angiogenesis

Multiple studies have demonstrated that both HMW-HA and LMW-HA are potent regulators of angiogenesis signaling, mainly by influencing endothelial cell (EC) behavior. One of the first studies demonstrated that partial degradation products of HA produced by the action of testicular hyaluronidase induced an angiogenic response, such as the formation of new blood vessels in the chick chorioallantoic membrane. Further fractionation of the digestion products showed that the activity was restricted to LMW-HA fragments between 4 and 25 disaccharides in length (46). More recently published studies indicate that LMW-HA stimulates vascular EC proliferation, migration, and tubule formation *in vitro*, as well as in various *in vivo* models of angiogenesis. In contrast, the HMW-HA displays anti-angiogenic properties by inhibiting EC proliferation, motility, and sprout formation (47–50). Since CD44 as well as RHAMM, two main receptors for HA, are present on the surface of the endothelial cells, both anti-RHAMM and anti-CD44 antibodies blocked the EC's ability to form tubule-like structures in matrigel. Both CD44 and RHAMM stimulated by HA oligomers create a complex with ERK 1/2, which leads to the constitutive activation of ERK 1/2 and increased cell motility of invasive breast cancer cells (49). Similar ERK 1/2 pathway activation by LMW-HA has also been demonstrated in other tumor cell lines including ECs, such as human umbilical vein ECs (HUVECs), human microvessels endothelial cells, and human pulmonary artery ECs (49). Additionally, LMW-HA promotes the proliferation of HUVECs and ECs *via* ezrin, a linkage protein between the plasma membrane and actin skeleton that interacts with the cellular C-terminus of the CD44 receptor. In wound healing, CXCL12 stimulates angiogenesis by activating CXCR4 present on the EC surface and significantly increased cell migration, and induced faster-wound closure in wound closure assays. By pre-incubating with HMW-HA, the wound closure rate was significantly increased. *In vitro* studies have shown that CXCR4 activation by CXCL12 was significantly increased in HUVECs pretreated with HMW-HA; however, LMW-HA pre-incubation blocked CXCL12 signaling.

LMW-HA and cancer metastasis

It appears that enhanced HA degradation is associated with tumor cell spreading. For example, accumulation of LMW-HA in tumor interstitial fluid correlates with lymphatic invasion and lymph node metastasis (51). Analysis of 176 serum specimens from breast cancer patients revealed (52) that level of serum LMW-HA but not total HA significantly correlated with lymph nodes metastasis, suggesting that serum LMW-HA may represent an indicator for metastasis development and prognosis for breast cancer progression. In addition, LMW-HA has been reported to induce cancer cell invasion by enhancing cancer cell motility (53).

Mechanistically, the HA receptors CD44s and RHAMM serve as mediators of HA-dependent development of metastasis (54). These receptors contribute to tumor progression *via* major pathways including the MAPK (MEK1, ERK1, 2) and SRC/FAK pathways that promote expression of an oncogenic transcriptome required for tumor cell survival, migration invasion, proliferation, and resistance to apoptosis (54).

CD44 co-localizes with HAS enzymes in lipid rafts where it is clustered by high molecular weight HA polymers and functions as a co-receptor for growth factor receptors to reduce the activation threshold of oncogenic driver signaling networks. For example, these small HA fragments limit oncogenic pathway activation and reverse drug resistance in CD133-positive highly tumorigenic subpopulations of ovarian carcinoma cells (55).

Another HA receptor, RHAMM is consistently overexpressed in many tumors, and its high expression is linked to the progression of multiple solid cancers. Increased expression of RHAMM is associated with castration-resistant disease in patients with prostatic metastases and elevated levels of both HA and RHAMM area are associated with a likelihood of biochemical failure in at-risk cancer patients after prostatectomy (56). Overexpression of RHAMM in breast primary cancer was linked to distant metastases (57), whereas increased RHAMM expression in colorectal cancers at the invasive front of primary tumors is linked to frequent lymphatic invasion, high tumor grade, and nodal metastasis (58).

Mechanisms of HA degradation in the tumor microenvironment

The fragmented forms of HA occur in abundance in various malignancies. These small hyaluronan oligomers are assumed to be largely a result of increased hyaluronidase (Hyal) expression/activity (30). Functional perturbations of HA synthesis in cancer and degradation have revealed active roles of both the HA synthases and Hyals in epithelial tumor cells, stroma, tumor vascular formation, and resistance to chemotherapy (59). Six hyaluronidase-like gene sequences have been identified in humans: Hyal1-6 (6, 7), and two recently discovered enzymes with hyaluronidase activity, termed HYBID (KIAA1199; CEMIP) and TMEM (60, 61). Hyal1 and Hyal2 are the major hyaluronidases expressed in human somatic tissues. It has been proposed that Hyal1 and Hyal2 work together in a concerted effort (6, 62, 63). Hyal2 is a rate-limiting, glycosylphosphatidylinositol-linked (GPI-linked) enzyme that is anchored to the plasma membrane. It cleaves extracellular HMW-HA into intermediate size, 20-kDa HA fragments, or about 50 disaccharide units. The Hyal2-generated HA fragments are internalized, delivered to endosomes, and ultimately to lysosomes, where Hyal1 degrades the 20-kDa fragments to very small tetra-saccharides.

Importantly, both Hyal1 and Hyal2 contribute to intracellular and extracellular catabolism of hyaluronic acid, respectively, in a CD44-dependent manner (64). Several studies have shown that the HA can be internalized by normal, non-malignant cells (chondrocytes, macrophages, keratinocytes, etc.) for degradation and that the endocytosis is mediated *via* cell surface HA receptors. In cancer, the epithelial tumor cells frequently express the membrane-bound Hyal2 and can break down secreted HA into intermediate 20 kDa fragments. Analysis of tumor tissues from cancer patients and experimental animal tumors revealed that tumor cells frequently work together with tumor-recruited myeloid cells including myeloid-derived suppressor cells (MDSCs) and tumor-associated macrophages (TAMs) to break down the extracellular HA into small HA fragments (18, 65, 66). It appears, that tumor-associated myeloid cells have significant amounts of internalized HA and display higher levels of Hyal1 expression as compared to tumor cells. Accordingly, the tumor-associated myeloid cells, and particularly TAMs, are more efficient in breaking down the HMW-HA into small pro-inflammatory and pro-angiogenic HA fragments.

Tumor stroma and hyaluronan metabolism

Tumor stroma supports tumor growth in multiple ways including simulation of proliferation, migration, invasion, promoting cancer-related inflammation, tumor angiogenesis, and also by contributing to tumor-associated immune suppression, resistance to cancer immunotherapy, and chemotherapy (67–72). Major cellular components of tumor stroma include cancer-associated fibroblasts (CAFs), TAMs, and mesenchymal and endothelial cells.

In addition to cells, the tumor stroma also has a highly complex extracellular component such as ECM, which comprises collagens, glycans, proteoglycans, and various secreted proteins such as growth and angiogenic factors, eicosanoids, chemokines, etc (73, 74). The state of tumor stroma is highly dynamic and is constantly being remodeled *via* the recruitment of myeloid cell subsets as well as precursors of endothelial and mesenchymal cells. HA is one of the major ECM components in tumor stroma. HA has been

implicated in regulating a variety of cellular functions in both tumor cells and tumor-associated stromal cells, suggesting that altered HA levels can influence tumor growth and malignancy at multiple levels. Previously published studies have demonstrated that HA increases the proliferation rate of tumor cells *in vitro* and promotes cell survival under anchorage-independent conditions. Stromal HA accumulation is associated with a low immune response and poor prognosis in some cancers (75, 76) Due to the abnormal production of HA and its enhanced degradation in tumor tissues, it is plausible that aberrant HA metabolism in the tumor microenvironment is highly relevant for tumor growth and progression, specifically through stimulation of cancer inflammation, tumor angiogenesis, and modulation of the anti-tumor immune response. HA has frequently been implicated in monocyte/macrophage trafficking and activation. Pathology studies of human cancer specimens suggested that increased numbers of macrophages were correlated with HA accumulation in tumors (77). Also, it has been shown that TAMs preferentially infiltrate tumor tissues in an HA-dependent manner and concomitantly enhance neovascularization and tumor growth (78).

Recently we showed that HA-enriched tumor stroma directly contributes to the development of the immunosuppressive tumor microenvironment by supporting the formation of PD-L1-expressing macrophages (65). Thus, analysis of organotypic tumor tissue-slice cultures, from mice with implanted syngeneic tumors as well as from cancer patients, revealed that tumor-recruited myeloid cells directly interact with stromal cells to form the large PD-L1-expressing cell congregates. Using genetically modified tumor cells, we found that both epithelial tumor cells and vimentin-positive CAFs represent the major sources of HA in the tumor microenvironment. Furthermore, similar cell clusters comprised of HA-producing fibroblast-like cells and F4/80$^+$PD-L1$^+$ macrophages were detected in tumor-draining, but not in distant lymph nodes. Taking together, these findings indicate that the formation of multiple large HA-enriched stromal clusters that support the development of PD-L1-expressing antigen-presenting cells in the tumor microenvironment and draining lymph nodes could contribute to the immune escape and resistance to immunotherapy in cancer.

Tumor-recruited Hyal2$^+$ myeloid cells and degradation of tumor-associated hyaluronan

There are multiple pieces of evidence in various cancer types demonstrating that tumor-associated myeloid cells play pivotal roles in the formation of the immunosuppressive and tolerogenic tumor microenvironment that promotes immune escape and contributes to resistance to cancer immunotherapy. Tumors promote mobilization of myeloid-derived suppressor cells (MDSCs) using various mechanisms primarily from bone marrow and spleen (79, 80). Upon entering tumor tissue MDSCs directly interact with tumor cells. However, the mechanisms of these interactions are not fully understood. It appears that tumor-associated HA mediates the crosstalk between tumor-recruited Hyal2$^+$ MDSCs, tumor cells, and stroma (64). Thus, Hyal2-expressing myeloid cells directly contact HA-producing tumor cells and CAFs. In a non-activated state, the HA-degrading enzyme Hyal2 in myeloid cells resides predominantly in intracellular space. However, upon activation in the tumor microenvironment Hyal2 translocate to the cell membrane, thus enabling the degradation of extracellular HA (Figure 2). The tumor-associated Hyal2-expressing myeloid cells have been detected in close contact with HA-producing CAFs and epithelial tumor cells, leading to enhanced degradation of tumor-

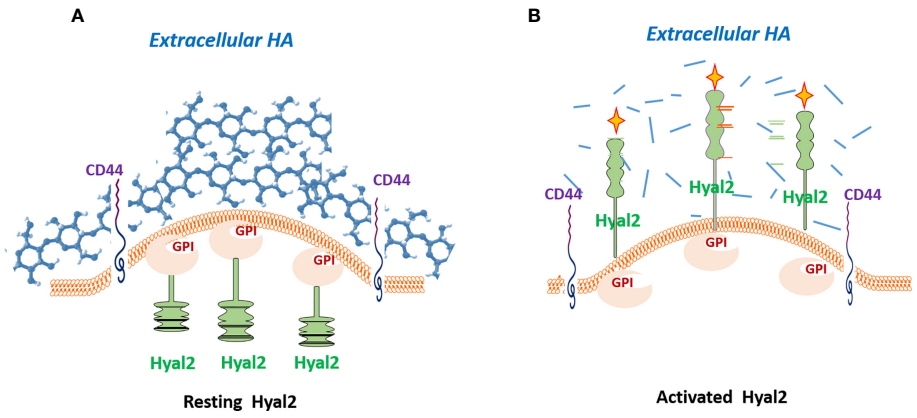

FIGURE 2
Hyal2 translocation is required for the degradation of extracellular hyaluronan. In a quiescent state, the Hyal2 molecule in myeloid cells resides predominantly in intracellular space **(A)**. However, activation of the CD44 signaling pathway results in translocation of Hyal2 to the cellular membrane, enabling the degradation of extracellular HA **(B)**. Depicted yellow crosses indicate the activated status of the enzyme Hyal2.

associated fragmentation of HA in the tumor microenvironment. It should be noted that Hyal2 activity in myeloid cells is regulated by CD44 signaling and IL-1beta (18).

The increased numbers of Hyal2$^+$ MDSCs have been detected in peripheral blood and tumor tissue in patients with bladder and kidney cancers (18, 66). In humans this co-express marker of myeloid cells CD11b and the marker of monocytic MDSCs CD33 (Hyl2$^+$CD33$^+$CD11b$^+$). A similar subset of Hyal2-expressing MDSCs (Hyal2$^+$Gr-1$^+$CD11b$^+$) has been found in tumor-bearing mice (65). Mobilization and tumor recruitment of Hyal2$^+$ myeloid cells results in enhanced HA degradation in tumor tissue, leading to the accumulation of small HA fragments (~20 kDa) in the tumor microenvironment. In addition, the tumor-infiltrating myeloid cells show significantly higher expression of Hyal1 than tumor cells and have the ability to degrade HA into much smaller fragments with a molecular weight of less than 5 kDa (63). The smallest HA fragments exert the strongest pro-inflammatory and pro-angiogenic activities (2, 3, 7, 45).

Importantly, the tumor-recruited Hyal2$^+$ MDSCs also co-express the immunosuppressive ligand PD-L1 (64, 65). In mouse tumor models, upon contact with HA-producing tumor cells or CAFs, Hyal2$^+$ MDSCs can proliferate and differentiate into immunosuppressive macrophages, forming the large PD-L1$^+$ myeloid cell clusters (Figures 3 and 4). Interestingly, during the transition of Hyal2$^+$MDSCs into TAMs, the activity of HA-degrading activity of Hyal2 is reduced, while expression of immunosuppressive ligand PD-L1 is markedly up-regulated. It is still unclear how the degradation of extracellular HA promotes differentiation of Hyal2$^+$Gr-1$^+$PD-L1$^+$ MDSCs into more mature immunosuppressive F4/80$^+$PD-L1$^+$ tumor-associated macrophages. It is plausible that under pro-inflammatory conditions in the tumor microenvironment small HA fragments promote the transition of MDSCs into activated immunosuppressive PD-L1$^+$ macrophages. Collectively, these data indicate that tumor-recruited myeloid cells contribute to tumor growth through degradation of tumor-associated HA, promoting cancer-related inflammation, tumor angiogenesis, and tumor-associated immune suppression.

Conclusions

Understanding the complex molecular and cellular mechanisms involved in abnormal HA metabolism and catabolism in solid cancers could have important implications for the design of future cancer therapeutic approaches. It appears that extensive crosstalk between tumor-associated myeloid cells and HA-enriched stroma contributes to the tumor growth and progression in several ways. Specifically, the interaction of tumor-recruited Hyal2-expressing myeloid cells with HA-producing stromal cells results in enhanced HA degradation and accumulation of small pro-inflammatory and pro-angiogenic HA fragments (18). HA-enriched stroma directly supports the development of PD-L1-expressing macrophages, thus contributing to the formation of the immunosuppressive, tolerogenic microenvironment by creating a PD-L1 shield and

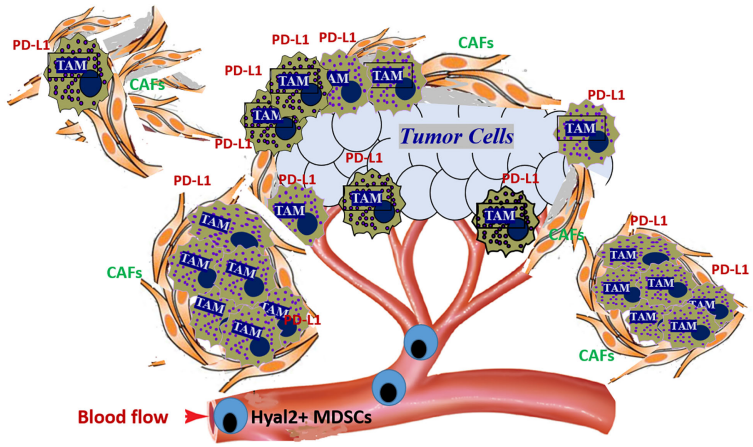

FIGURE 3
Tumor-recruited Hyal2$^+$ MDSCs directly contribute to the development of the immunosuppressive tumor microenvironment by forming PD-L1$^+$ macrophage clusters in the hyaluronan-enriched stroma. Tumors constantly secrete significant amounts of chemokines that attract the Hyal2$^+$ MDSCs from bone marrow. Once recruited to the tumor, Hyal2-expressing myeloid cells start degradation of extracellular HA in the tumor microenvironment. Direct interaction of tumor-recruited myeloid cells with HA-producing cancer-associated fibroblasts (CAFs) and epithelial tumor cells leads to the accumulation of small HA pro-inflammatory and pro-angiogenic fragments. Hyal2$^+$ MDSCs differentiate into immunosuppressive tumor-associated PD-L1$^+$ macrophages (PD-L1$^+$ TAMs), forming large PD-L1-expressing cell clusters in HA-enriched tumor stroma.

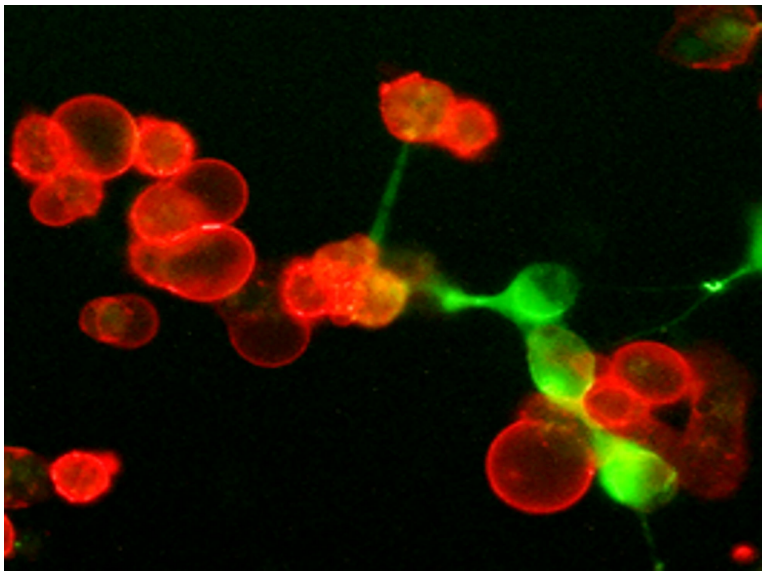

FIGURE 4
Tumor-associated hyaluronan directly supports the development of immunosuppressive PD-L1^{+} macrophages in the tumor microenvironment. Freshly prepared tumor tissue slices were cultured for twenty-four hours. Then cultures were fixed with 4% formaldehyde and stained PD-L1 (red) and HA (green). Representative IF image is shown.

preventing T cell-mediated immune response *via* the PD1/PD-L1 pathway (65, 66). Constant mobilization of bone marrow-derived Hyal2^{+} MDSCs, CAFs, and endothelial cells contribute to the highly dynamic development of tumor stroma, enhances degradation of tumor-associated HA, and further promotes the tumor progression through stimulation of cancer-related inflammation, tumor angiogenesis, and tumor-associated immune suppression. Therefore, the normalization of HA metabolism in the tumor microenvironment could potentially provide a strong beneficial step for improving the efficacy of existing approaches to treat cancer, particularly for cancer immunotherapy.

Data availability statement

The original contributions presented in the study are included in the article/supplementary materials. Further inquiries can be directed to the corresponding author.

Author contributions

WD wrote review materials related to HA metabolism in normal and malignant tissues. PD-G wrote review sections related to the roles of LMW-HA in inflammation and angiogenesis. SK composed the article, wrote review materials related to mechanisms of HA degradation in tumor microenvironment and stroma, wrote abstract, conclusion and prepared Figures. All authors contributed to the article and approved the submitted version.

Funding

This work was supported by James and Ester King Biomedical Research Program, Florida Health Department, award 8JKO5 and 1923 Fund to SK.

Conflict of interest

SK is a founder of K-Lab Therapeutics.

The remaining authors declare that the research was conducted in the absence of any commercial or financial relationships that could be construed as a potential conflict of interest.

Publisher's note

References

1. Toole BP. Hyaluronan: from extracellular glue to pericellular cue. *Nat Rev Cancer* (2004) 4:528–39. doi: 10.1038/nrc1391

2. Girish KS, Kemparaju K. The magic glue hyaluronan and its eraser hyaluronidase: A biological overview. *Life Sci* (2007) 80:1921–43. doi: 10.1016/j.lfs.2007.02.037

3. Schmaus A, Bauer J, Sleeman JP. Sugars in the microenvironment: the sticky problem of HA turnover in tumors. *Cancer Metastasis Rev* (2014) 33:1059–79. doi: 10.1007/s10555-014-9532-2

4. Knudson W, Bartnik E, Knudson CB. Assembly of pericellular matrices by COS-7 cells transfected with CD44 lymphocyte-homing receptor genes. *Proc Natl Acad Sci USA* (1993) 90:4003–7. doi: 10.1073/pnas.90.9.4003

5. Turley EA, Noble PW, Bourguignon LYW. Signaling properties of hyaluronan receptors. *J Biol Chem* (2002) 277:4589–92. doi: 10.1074/jbc.R100038200

6. Csoka AB, Frost GI, Stern R. The six hyaluronidase-like genes in the human and mouse genomes. *Matrix Biol* (2001) 20:499–508. doi: 10.1016/S0945-053X(01)00172-X

7. Csóka AB, Scherer SW, Stern R. Expression analysis of six paralogous human hyaluronidase genes clustered on chromosomes 3p21 and 7q31. *Genomics* (1999) 60:356–61. doi: 10.1006/geno.1999.5876

8. Chanmee T, Ontong P, Itano N. Hyaluronan: A modulator of the tumor microenvironment. *Cancer Lett* (2016) 375:20–30. doi: 10.1016/j.canlet.2016.02.031

9. Lokeshwar VB, Schroeder GL, Selzer MG, Hautmann SH, Posey JT, Duncan RC, et al. Bladder tumor markers for monitoring recurrence and screening comparison of hyaluronic acid-hyaluronidase and BTA-stat tests. *Cancer* (2002) 95:61–72. doi: 10.1002/cncr.10652

10. Golshani R, Hautmann SH, Estrella V, Cohen BL, Kyle CC, Manoharan M, et al. HAS1 expression in bladder cancer and its relation to urinary HA test. *Int J Cancer* (2007) 120:1712–20. doi: 10.1002/ijc.22222

11. Kramer MW, Escudero DO, Lokeshwar SD, Golshani R, Ekwenna OO, Acosta K, et al. Association of hyaluronic acid family members (HAS1, HAS2, and HYAL-1) with bladder cancer diagnosis and prognosis. *Cancer* (2011) 117:1197–209. doi: 10.1002/cncr.25565

12. Li Y, Li L, Brown TJ, Heldin P. Silencing of hyaluronan synthase 2 suppresses the malignant phenotype of invasive breast cancer cells. *Int J Cancer* (2007) 120:2557–67. doi: 10.1002/ijc.22550

13. Udabage L, Brownlee GR, Nilsson SK, Brown TJ. The over-expression of HAS2, hyal-2 and CD44 is implicated in the invasiveness of breast cancer. *Exp Cell Res* (2005) 310:205–17. doi: 10.1016/j.yexcr.2005.07.026

14. Lien H-C, Lee Y-H, Jeng Y-M, Lin C-H, Lu Y-S, Yao Y-T. Differential expression of hyaluronan synthase 2 in breast carcinoma and its biological significance. *Histopathology* (2014) 65:328–39. doi: 10.1111/his.12390

15. Okuda H, Kobayashi A, Xia B, Watabe M, Pai SK, Hirota S, et al. Hyaluronan synthase HAS2 promotes tumor progression in bone by stimulating the interaction of breast cancer stem-like cells with macrophages and stromal cells. *Cancer Res* (2012) 72:537–47. doi: 10.1158/0008-5472.CAN-11-1678

16. Posey JT, Soloway MS, Ekici S, Sofer M, Civantos F, Duncan RC, et al. Evaluation of the prognostic potential of hyaluronic acid and hyaluronidase (HYAL1) for prostate cancer. *Cancer Res* (2003) 63:2638–44. Availabloe at: https://aacrjournals.org/cancerres/article/63/10/2638/509916/Evaluation-ofthe-Prognostic-Potential-of

17. Lipponen P, Aaltomaa S, Tammi R, Tammi M, Agren U, Kosma VM. High stromal hyaluronan level is associated with poor differentiation and metastasis in prostate cancer. *Eur J Cancer* (2001) 37:849–56. doi: 10.1016/S0959-8049(00)00448-2

18. Dominguez-Gutierrez PR, Kwenda EP, Donelan W, O'Malley P, Crispen PL, Kusmartsev S. Hyal2 expression in tumor-associated myeloid cells mediates cancer-related inflammation in bladder cancer. *Cancer Res* (2021) 81:648–57. doi: 10.1158/0008-5472.CAN-20-1144

19. Tian X, Azpurua J, Hine C, Vaidya A, Myakishev-Rempel M, Ablaeva J, et al. High-molecular-mass hyaluronan mediates the cancer resistance of the naked mole rat. *Nature* (2013) 499:346–9. doi: 10.1038/nature12234

20. Ooki T, Murata-Kamiya N, Takahashi-Kanemitsu A, Wu W, Hatakeyama M. High-molecular-weight hyaluronan is a hippo pathway ligand directing cell density-dependent growth inhibition *via* PAR1b. *Dev Cell* (2019) 49:590–604.e9. doi: 10.1016/j.devcel.2019.04.018

21. Bourguignon LYW, Wong G, Earle CA, Xia W. Interaction of low molecular weight hyaluronan with CD44 and toll-like receptors promotes the actin filament-associated protein 110-actin binding and MyD88-NFκB signaling leading to proinflammatory cytokine/chemokine production and breast tumor invasion. *Cytoskeleton (Hoboken)* (2011) 68:671–93. doi: 10.1002/cm.20544

22. Jiang D, Liang J, Noble PW. Hyaluronan as an immune regulator in human diseases. *Physiol Rev* (2011) 91(1):221–64. doi: 10.1152/physrev.00052.2009

23. Tolg C, Messam BJ, McCarthy JB, Nelson AC, Turley EA. Hyaluronan functions in wound repair that are captured to fuel breast cancer progression. *Biomolecules* (2021) 11(11):1551. doi: 10.3390/biom11111551

24. Lee BM, Park SJ, Noh I, Kim C-H. The effects of the molecular weights of hyaluronic acid on the immune responses. *Biomater Res* (2021) 25(1):27. doi: 10.1186/s40824-021-00228-4

25. Liu M, Tolg C, Turley E. Dissecting the dual nature of hyaluronan in the tumor microenvironment. *Front Immunol* (2019) 10:947. doi: 10.3389/fimmu.2019.00947

26. Sokolowska M, Chen LY, Eberlein M, Martinez-Anton A, Liu Y, Alsaaty S, et al. Low molecular weight hyaluronan activates cytosolic phospholipase A2α and eicosanoid production in monocytes and macrophage. *Biol Chem* (2014) 289(7):4470–88. doi: 10.1074/jbc.M113.515106

27. Mantovani A, Allavena P, Sica A and Balkwill F. Cancer-related inflammation. *Nature* (2008) 454:436–44. doi: 10.1038/nature07205

28. Witschen PM, Chafee TS, Brady NJ, Huggins DN, Knutson TP, LaRue RS, et al. Tumor cell associated hyluronan-CD44 signaling promotes pro-tumor inflammation in breast cancer. *Cancers* (2020) 12(5)1325. doi: 10.3390/cancers12051325

29. Campo GM, Avenoso A, Campo S, D'Ascola A, Nastasi G, Calatroni A. Molecular size hyaluronan differently modulates toll-like receptor-4 in LPS-induced inflammation in mouse chondrocytes. *Biochimie* (2010) 92(2):204–15. doi: 10.1016/j.biochi.2009.10.006

30. Stern R. Hyaluronidases in cancer biology. *Semin Cancer Biol* (2008) 18:275–80. doi: 10.1016/j.semcancer.2008.03.017

31. Yang J-M, Kim H-J, Cho B-K. Preparation of antioxidant hydrogel contact lenses based on interpenetrating hyaluronic acid network. *Polymer (Korea)* (2020) 44(1):21–9. pk. doi: 10.7317/pk.2020.44.1.21

32. Bracke KR, Dentener MA, Papakonstantinou E, Vernooy JHJ, Demoor T, Pauwels NS, et al. Enhanced deposition of low-molecular-weight hyaluronan in lungs of cigarette smoke-exposed mice. *Am J Respir Cell Mol Biol* (2010) 42(6):753–61. doi: 10.1165/rcmb.2008-0424OC

33. Rayahin JE, Buhrman JS, Zhang Y, Koh TJ, Gemeinhart RA. High and low molecular weight hyaluronic acid differentially influence macrophage activation. *ACS Biomater Sci Eng* (2015) 1(7):481–93. doi: 10.1021/acsbiomaterials.5b00181

34. D'Agostino A, Stellavato A, Corsuto L, Diana P, Filosa R, La Gatta A, et al. Is molecular size a discriminating factor in hyaluronan interaction with human cells? *Carbohydr Polym* (2017) 157:21–30. doi: 10.1016/j.carbpol.2016.07.125

35. Horton MR, Shapiro S, Bao C, Lowenstein CJ, Noble PW. Induction and regulation of macrophage metalloelastase by hyaluronan fragments in mouse macrophages. *J Immunol* (1999) 162(7):4171–6. Available at: https://www.jimmunol.org/content/162/7/4171

36. Horton MR, Olman MA, Bao C, White KE, Choi AM, Chin BY, et al. Regulation of plasminogen activator inhibitor-1 and urokinase by hyaluronan fragments in mouse macrophages. *Am J Physiol Lung Cell Mol Physiol* (2000) 279(4):L707–15. doi: 10.1152/ajplung.2000.279.4.L707

37. Hodge-Dufour J, Noble PW, Horton MR, Bao C, Wysoka M, Burdick MD, et al. Induction of IL-12 and chemokines by hyaluronan requires adhesion-dependent priming of resident but not elicited macrophages. *J Immunol* (1997) 159(5):2492–500. Available at: https://www.jimmunol.org/content/159/5/2492.long

38. Horton MR, Burdick MD, Strieter RM, Bao C, Noble PW. Regulation of hyaluronan-induced chemokine gene expression by IL-10 and IFN-gamma in mouse macrophages. *J Immunol* (1998) 160(6):3023–30. Available at: https://www.jimmunol.org/content/160/6/3023

39. McKee CM, Penno MB, Cowman M, Burdick MD, Strieter RM, Bao C, et al. Hyaluronan (HA) fragments induce chemokine gene expression in alveolar macrophages. the role of HA size and CD44. *J Clin Invest* (1996) 98(10):2403–13. doi: 10.1172/JCI119054.

40. Termeer C, Benedix F, Sleeman J, Fieber C, Voith U, Ahrens T, et al. Oligosaccharides of hyaluronan activate dendritic cells *via* toll-like receptor 4. *J Exp Med* (2002) 195(1):99–111. doi: 10.1084/jem.20001858

41. Termeer CC, Hennies J, Voith U, Ahrens T, Weiss JM, Prehm P, et al. Oligosaccharides of hyaluronan are potent activators of dendritic cells. *J Immunol* (2000) 165(4):1863–70. doi: 10.4049/jimmunol.165.4.1863

42. Jiang D, Liang J, Fan J, Yu S, Chen S, Luo Y, et al. Regulation of lung injury and repair by toll-like receptors and hyaluronan. *Nat Med* (2005) 11(11):1173–9. doi: 10.1038/nm1315

43. Taylor KR, Yamasaki K, Radek KA, Nardo AD, Goodarzi H, Golenbock D, et al. Recognition of hyaluronan released in sterile injury involves a unique receptor

complex dependent on toll-like receptor 4, CD44, and MD-2. *J Biol Chem* (2007) 282(25):18265–75. doi: 10.1074/jbc.M606352200

44. Taylor KR, Trowbridge JM, Rudisill JA, Termeer CC, Simon JC, Gallo RL. Hyaluronan fragments stimulate endothelial recognition of injury through TLR4. *J Biol Chem* (2004) 279(17):17079–84. doi: 10.1074/jbc.M310859200

45. Campo GM, Avenoso A, Nastasi G, Micali A, Prestipino V, Vaccaro M, et al. Hyaluronan reduces inflammation in experimental arthritis by modulating TLR-2 and TLR-4 cartilage expression. *Biochim Biophys Acta* (2011) 1812(9):1170–81. doi: 10.1016/j.bbadis.2011.06.006

46. West DC, Hampson IN, Arnold F, Kumar S. Angiogenesis induced by degradation products of hyaluronic acid. *Science.* (1985) 228(4705):1324–6. doi: 10.1126/science.2408340

47. Slevin M, Krupinski J, Gaffney J, Matou S, West D, Delisser H, et al. Hyaluronan-mediated angiogenesis in vascular disease: Uncovering RHAMM and CD44 receptor signaling pathways. *Matrix Biol* (2007) 26(1):58–68. doi: 10.1016/j.matbio.2006.08.261

48. Silva AL, Babo PS, Rodrigues MT, Gonçalves AI, Novoa-Carballal R, Pires RA , et al. Hyaluronic acid oligomer immobilization as angiogenic trigger for the neovascularization of TE constructs. *ACS Appl Bio Mater* (2021) 4(8):6023–35. doi: 10.1021/acsabm.1c00291

49. Lokeshwar VB, Selzer MG. Differences in hyaluronic acid-mediated functions and signaling in arterial, microvessel, and vein-derived human endothelial cells. *J Biol Chem* (2000) 275(36):27641–9. doi: 10.1074/jbc.M003084200

50. Fuchs K, Hippe A, Schmaus A, Homey B, Sleeman JP, Orian-Rousseau V. Opposing effects of high- and low-molecular weight hyaluronan on CXCL12-induced CXCR4 signaling depend on CD44. *Cell Death Dis* (2013) 4:e819. doi: 10.1038/cddis.2013.364

51. Schmaus A, Klusmeier S, Rothley M, Dimmler A, Sipos B, Faller G, et al. Accumulation of small hyaluronan oligosaccharides in tumour interstitial fluid correlates with lymphatic invasion and lymph node metastasis. *Br J Cancer* (2014) 111(3):559–67. doi: 10.1038/bjc.2014.332

52. Wu M, Cao M, He Y, Liu Y, Yang C, Du Y, et al. A novel role of low molecular weight hyaluronan in breast cancer metastasis. *FASEB J* (2015) 29:1290–8. doi: 10.1096/fj.14-259978

53. Sugahara KN, Murai T, Nishinakamura H, Kawashima H, Saya H, Miyasaka M, et al. Hyaluronan oligosaccharides induce CD44 cleavage and promote cell migration in CD44-expressing tumor cells. *J Biol Chem* (2003) 281:5861–8. doi: 10.1074/jbc.M506740200

54. Turley EA, Wood DK, McCarthy JB. Carcinoma cell hyaluronan as a "portable" cancerized pro-metastatic microenvironment. *Cancer Res* (2016) 76 (9):2507–12. doi: 10.1158/0008-5472.CAN-15-3114

55. Slomiany MG, Dai L, Tolliver LB, Grass GD, Zeng Y, Toole BP. Inhibition o functional hyaluronan-CD44 interactions in CD133-positive primary human ovarian carcinoma cells by small hyaluronan oligosaccharides. *Clin Cancer Res* (2009) 15:7593–601. doi: 10.1158/1078-0432.CCR-09-2317

56. Rizzardi AE, Vogel RI, Koopmeiners JS, Forster CL, Marston LO, Rosener NK, et al. Elevated hyaluronan and hyaluronan-mediated motility receptor are associated with biochemical failure in patients with intermediate-grade prostate tumors. *Cancer* (2014) 120:1800–9. doi: 10.1002/cncr.28646

57. Wang C, Thor AD, Moore DH2nd, Zhao Y, Kerschmann R, Stern R., et al. The overexpression of RHAMM, hyaluronan-binding protein that regulates RAS signaling, correlates with overexpression of mitogen-activated protein kinase and is significant parameter in breast cancer progression. *Clin Cancer Res* (1998) 4:367–576. Available at: https://aacrjournals.org/clincancerres/article/4/3/567/7638/The-overexpression-of-RHAMM-a-hyaluronan-binding

58. Koelzer VH, Huber B, Mele V, Iezzi G, Trippel M, Karamitopoulou E, et al. Expression of the hyaluronan-mediated motility receptor RHAMM in tumor budding cells identifies aggressive colon cancers. *Hum Pathol* (2015) 46 (11):1573–8. doi: 10.1016/j.humpath.2015.07.010

59. Passi A, Vigetti D, Buraschi S, Iozzo RV. Dissecting the role of hyaluronan synthases in the tumor microenvironment. *FEBS J* (2019) 286(15):2937–49. doi: 10.1111/febs.14847

60. Nagaoka A, Yoshida H, Nakamura S, Morikawa T, Kawabata K, Kobayashi M, et al. Regulation of hyaluronan (HA) metabolism mediated by HYBID (hyaluronan-binding protein involved in HA depolymerization, KIAA1199) and HA synthases in growth factor-stimulated fibroblasts. *J Biol Chem* (2015) 290:30910–3092. doi: 10.1074/jbc.M115.673566

61. Tobisawa Y, Fujita N, Yamamoto H, Ohyama C, Irie F, Yamaguchi YJ. The cell surface hyaluronidase TMEM2 is essential for systemic hyaluronan catabolism and turnover. *J Biol Chem* (2021) 297(5):101281. doi: 10.1016/j.jbc.2021.101281

62. Stern R. Devising a pathway for hyaluronan catabolism: Are we there yet glycobiology. *Glycobiology* (2003) 13:105–15. doi: 10.1093/glycob/cwg112

63. Stern R. Hyaluronan catabolism: a new metabolic pathway. *Eur J Cell Biol* (2004) 83:317–25. doi: 10.1078/0171-9335-00392

64. Harada H, Takahashi M. CD44-dependent intracellular and extracellular catabolism of hyaluronic acid by hyaluronidase-1 and 2. *J Biol Chem* (2007) 282 (8):5597–607. doi: 10.1074/jbc.M608358200

65. Dominguez-Gutierrez PR, Kwenda E, Donelan W, Miranda M, Doty A, O'Malley P, et al. Detection of PD-L1-expressing myeloid cell clusters in the hyaluronan-enriched stroma. *J Immunol* (2022) 208:2829–36. doi: 10.4049/jimmunol.2100026

66. Kusmartsev S, Kwenda E, Dominguez-Gutierrez PR, Crispen PL, O'Malley P. PD-L1$^+$ and Hyal2$^+$ myeloid cells in renal cell carcinoma: A case report. *J Kidney Cancer VHL* (2022) V.9(2):1–6. doi: 10.15586/jkcvhl.v9i2.208.

67. Kraman M, Bambrough PJ, Arnold JN, Roberts EW, Magiera L, Jones JO, et al. Suppression of antitumor immunity by stromal cells expressing fibroblast activation protein-alpha. *Science* (2010) 330:827–30. doi: 10.1126/science.1195300

68. Liguori M, Solinas G, Germano G, Mantovani A, Allavena P. Tumor-associated macrophages as incessant builders and destroyers of the cancer stroma. *Cancers* (2011) 3(4):3740–61. doi: 10.3390/cancers3043740

69. Turley SJ, Cremasco V, Astarita JL. Immunological hallmarks of stromal cells in the tumour microenvironment. *Nat Rev Immunol* (2015) 15(11):669–82. doi: 10.1038/nri3902

70. Sahai E, Astsaturov I, Cukierman E, DeNardo DG, Egeblad M, Evans RM, et al. A framework for advancing our understanding of cancer-associated fibroblasts. *Nat Rev Cancer* (2020) 20:174–86. doi: 10.1038/s41568-019-0238-1

71. Kalluri R. The biology and function of fibroblasts in cancer. *Nat Rev Cancer* (2016) 16:582–98. doi: 10.1038/nrc.2016.73

72. Xiang H, Ramil CP, Hai J, Zhang C, Wang H, Watkins AA, et al. Cancer-associated fibroblasts promote immunosuppression by inducing ROS-generating monocytic MDSCs in lung squamous cell carcinoma. *Cancer Immunol Res* (2020) 8 (4):436–50. doi: 10.1158/2326-6066.CIR-19-0507

73. Brownfield DG, Venugopalan G, Lo A, Mori H, Tanner K, Fletcher DA, et al. Patterned collagen fibers orient branching mammary epithelium through distinct signaling modules. *Curr Biol* (2013) 3(8):703–9. doi: 10.1016/j.cub.2013.03.032

74. Toole BP, Slomiany MG. Hyaluronan: A constitutive regulator of chemoresistance and malignancy in cancer cells. *Semin Cancer Biol* (2008) 4):244–50. doi: 10.1016/j.semcancer.2008.03.009

75. Tahkola K, Ahtiainenm M, Mecklin JP, Kellokumpu I, Laukkarinen J, Tammi M, et al. Stromal hyaluronan accumulation is associated with low immune response and poor prognosis in pancreatic cancer. *Sci Rep* (2021) 11 (1):12216. doi: 10.1038/s41598-021-91796-x

76. Wu W, Chen L, Wang Y, Jin J, Xie X, Zhang J. Hyaluronic acid predicts poor prognosis in breast cancer patients: A protocol for systematic review and meta-analysis. *Medicine* (2020) 99(22):e20438. doi: 10.1097/MD.0000000000020438

77. Tiainen S, Tumelius R, Rilla K, Hamalainen K, Tammi M, Tammi R, et al. High numbers of macrophages, especially M2-like (CD163-positive), correlate with hyaluronan accumulation and poor outcome in breast cancer. *Histopathology* (2015) 66:873–83. doi: 10.1111/his.12607

78. Kobayashi N, Miyoshi S, Mikami T, Koyama H, Kitazawa M, Takeoka M, et al. Hyaluronan deficiency in tumor stroma impairs macrophage trafficking and tumor neovascularization. *Cancer Res* (2010) 70:7073–83. doi: 10.1158/0008-5472.CAN-09-4687

79. Gabrilovich D, Ostrand-Rosenberg S, Bronte V. Coordinated regulation of myeloid cells by tumours. *Nat Rev Immunol* (2012) 12(4):253–68. doi: 10.1038/nri3175

80. Kusmartsev S, Serafini P, Nagaraj S, Kortylewski M. Roles of tumor-recruited myeloid cells in immune evasion in cancer. *Front Immunol* (2021) 12:749605. doi: 10.3389/fimmu.2021.749605

frontiers | Frontiers in Immunology

TYPE Original Research
PUBLISHED 13 October 2022
DOI 10.3389/fimmu.2022.966158

OPEN ACCESS

EDITED BY
Julie Decock,
Qatar Biomedical Research Institute, Qatar

REVIEWED BY
Anna Halama,
Weill Cornell Medicine, Qatar
Apostolos Zaravinos,
European University Cyprus, Cyprus

*CORRESPONDENCE
Wolfram Weckwerth
wolfram.weckwerth@univie.ac.at

SPECIALTY SECTION
This article was submitted to Cancer Immunity and Immunotherapy, a section of the journal Frontiers in Immunology

RECEIVED 10 June 2022
ACCEPTED 12 September 2022
PUBLISHED 13 October 2022

CITATION
Cai Z, Li W, Brenner M, Bahiraii S, Heiss EH and Weckwerth W (2022) Branched-chain ketoacids derived from cancer cells modulate macrophage polarization and metabolic reprogramming. *Front. Immunol.* 13:966158. doi: 10.3389/fimmu.2022.966158

Branched-chain ketoacids derived from cancer cells modulate macrophage polarization and metabolic reprogramming

Zhengnan Cai[1], Wan Li[1], Martin Brenner[1,2], Sheyda Bahiraii[2], Elke H. Heiss[2] and Wolfram Weckwerth[1,3]*

[1]Molecular Systems Biology (MOSYS), Department of Functional and Evolutionary Ecology, University of Vienna, Vienna, Austria, [2]Department of Pharmaceutical Sciences, University of Vienna, Vienna, Austria, [3]Vienna Metabolomics Center (VIME), University of Vienna, Vienna, Austria

Macrophages are prominent immune cells in the tumor microenvironment that can be educated into pro-tumoral phenotype by tumor cells to favor tumor growth and metastasis. The mechanisms that mediate a mutualistic relationship between tumor cells and macrophages remain poorly characterized. Here, we have shown *in vitro* that different human and murine cancer cell lines release branched-chain α-ketoacids (BCKAs) into the extracellular milieu, which influence macrophage polarization in an monocarboxylate transporter 1 (MCT1)-dependent manner. We found that α-ketoisocaproate (KIC) and α-keto-β-methylvalerate (KMV) induced a pro-tumoral macrophage state, whereas α-ketoisovalerate (KIV) exerted a pro-inflammatory effect on macrophages. This process was further investigated by a combined metabolomics/proteomics platform. Uptake of KMV and KIC fueled macrophage tricarboxylic acid (TCA) cycle intermediates and increased polyamine metabolism. Proteomic and pathway analyses revealed that the three BCKAs, especially KMV, exhibited divergent effects on the inflammatory signal pathways, phagocytosis, apoptosis and redox balance. These findings uncover cancer-derived BCKAs as novel determinants for macrophage polarization with potential to be selectively exploited for optimizing antitumor immune responses.

KEYWORDS

macrophage polarization, tumor-associated macrophages, panomics, BCKAs Fc-gamma receptor (FCgR)-mediated phagocytosis, tumor necrosis factor alpha (TNFα)-nuclear factor kappa B (NFκB) -mediated inflammatory pathway, apoptosis

Introduction

Over the past decade, a wealth of preclinical and clinical evidence supports a tumor-promoting role for macrophages in cancer (1). For example, macrophage contents in solid tumors correlate with chemotherapy resistance and a worse prognosis for non-small cell lung carcinoma (NSCLC), breast cancer, pancreatic cancer, glioblastoma, and lymphoma (2–6). Indeed, macrophages were thought to be antitumoral at an early stage of tumor onset, owing to their ability to directly engulf and kill tumor cells or indirectly clear tumor cells through presenting tumor antigens to activate cytotoxic lymphocytes, but once macrophages were influenced by cancer cells, they rapidly adopt an alternative phenotype with an immunosuppressive function that enhances tumor progression and metastasis. Even though there may still be antitumor macrophages present, most macrophages are "educated" to favor tumor growth (7). Thus, understanding how cancer cells govern macrophage phenotype within the tumor microenvironment provides a means to selectively target macrophage reprogramming and improve tumor immune surveillance.

Cancer cell-secreted metabolites within the tumor microenvironment are partially responsible for modulating surrounding immune profiles (8). Lactate is largely produced within the tumor microenvironment by cancers cells exploiting the Warburg effect (aerobic glycolysis) (9), which promotes differentiation and polarization of tumor-associated macrophages towards a pro-tumoral phenotype (M2-like) with elevated expression of arginase-1 (ARG1), pro-tumoral marker *Vegf* and M2 marker genes (*Arg1, Fizz1, Mgl1, Mgl2*) (10). In turn, M2-like macrophages produce immunosuppressive cytokines (IL10) and metabolites such as arginine, ornithine and polyamines, which are essential for the cell division and proliferation of some tumors (11, 12). In addition, tumor cell-derived kynurenine dampened the effector function of macrophages and engaged a pro-tumoral cooperation between macrophages and regulatory T cells (Tregs) (13). TCA cycle intermediate succinate released by lung cancer cells can activate macrophage polarization into an M2-like phenotype, and accelerate cancer cell migration and metastasis (14).

Our initial unpublished metabolomic analysis showed elevated BCKAs levels in the conditioned media (CM) from two lung cancer cell lines (A549 and AE17) compared to non-proliferative cells. Recently, accumulated BCKAs were also found in glioblastoma and can act as substrates for *de novo* synthesis of branched-chain amino acids (BCAAs) in macrophages (15). The three BCKAs are α-ketoisocaproate (KIC), α-keto-β-methylvalerate (KMV), and α-ketoisovalerate (KIV). All are precursors for or generated from essential amino acids leucine, isoleucine, and valine. The reaction is catalyzed by the compartment-specific BCAAs transaminases (cytoplasmic, BCAT1; mitochondrial, BCAT2). Within cells or tissues, BCKAs can either be reversibly transaminated to BCAAs and α-ketoglutarate (α-KG) or catabolized to branched-chain acyl-CoA (R-CoA) that can be further metabolized by multimeric BCKA dehydrogenase enzyme complex (BCKDH) to generate a branched-chain acyl-CoA (R-CoA) that can be further metabolized to acetyl-coenzyme A (acetyl-CoA) or succinyl-CoA, which finally fuel the tricarboxylic acid (TCA) cycle (16) (Figure S1A). BCAT1 and BCAT2 are highly expressed in human tumors such as glioblastoma, acute myeloid leukaemia, lung tumor, breast tumor and pancreatic tumor (17–22). BCAT1 inhibition significantly reduced BCKAs within pancreatic stromal cells (22). Notably, uptake of BCKAs suppressed the phagocytosis of macrophages suggesting an immunosuppressive function of these metabolites (15). In contrast, BCKAs induced upregulation of proinflammatory genes and inflammation-related cytokines in bone marrow-derived macrophages (BMDM) from wild-type and db/db mice (type 2 diabetes) (23). Thus, how BCKAs modulate macrophage phenotype remains controversial and underlying mechanisms and context-dependency are far from being completely understood.

Here, we uncover the role of BCKAs in regulating macrophage activation and metabolic reprogramming. We found that a panel of selected cancer cells secrete all three BCKAs to different extents, of which KIV exhibited an effect on pro-inflammatory (M1-like) macrophage polarization while KIC and KMV showed an effect on pro-tumoral (M2-like) macrophage polarization. Combined BCKAs promoted M2-like polarization and was closer to tumor setting. Proteomic analyses revealed that KMV stimulation affected Fc-gamma receptor (FcγR)-mediated phagocytosis, tumor necrosis factor-alpha (TNFα)-nuclear factor kappa B (NFκB)-mediated inflammatory pathway and apoptosis. Further metabolomics analyses indicated that cancer-derived BCKAs were used for augmenting TCA cycle intermediates. KIC and KMV also contributed to enhanced polyamine metabolism in macrophages. Hence, preventing the release of BCKAs by cancer cells, and selectively targeting KMV or KIC in the tumor microenvironment would benefit antitumor immunity.

Results

Cancer cell-derived BCKAs modulate macrophage polarization *via* MCT1

To examine whether cancer cell-derived BCKAs can modulate macrophage activation, we first measured concentrations of KIV, KIC and KMV in the conditioned media (CM) from 9 equally seeded cancer cell lines (6 human cancer cell lines and 3 murine cancer cell lines), as well as immortalized bone marrow derived-macrophages (iBMDM) and BMDM. Both iBMDM and BMDM consumed a few BCAAs and released a low quantity of BCKAs (Figures 1A, B). In contrast, accumulated BCKAs were detected in cancer CM,

which is consistent with the consumption of BCAAs by cancer cells (Figure 1C). The contents of the three BCKAs varied substantially in each cancer cell CM, where KIV ranges from 15 μM to 80 μM, KIC ranges from 15 μM to 100 μM and KMV ranges from 10 μM to 40 μM. To keep our initial findings consistent, we evaluated the effect of BCKAs and two lung cancer CM (A549 CM and AE17 CM) on macrophage proliferation and polarization (Figure 1D). Both BMDM and iBMDM proliferation rates were significantly enhanced on exposure to A549 CM and AE17 CM (Figures 2A, S1B), probably because of cancer cell-released various cytokines (e.g., macrophage colony-stimulating factor (M-CSF/CSF-1)) and soluble factors that affect macrophage differentiation and proliferation. While stimulation with BCKAs only had little effect on macrophage proliferation even at a concentration of 1 mM (Figures 2B, S1C). Moreover, both iBMDM and BMDM exhibited an increase in expression of (Arginase-1) ARG1 protein and M2 marker genes *Arg1, Mgl1, Mgl2, Mrc1* and a pro-tumoral marker *Vegf* after AE17 CM treatment (Figures 2C, D, S1D, E). BMDM also significantly secreted anti-inflammatory cytokine TGF-β and growth factor VEGF after AE17 CM treatment, whereas proinflammatory cytokines TNF-α and IL6 were slightly reduced (Figure 2F). However, the individual BCKAs differed in their activation of genes and cytokines associated with immune suppression, chronic inflammation, and tumor angiogenesis in macrophages. *Vegf* mRNA expression was increased in both iBMDM and BMDM on stimulation with all three BCKAs, while *Arg1* was only enhanced by KIC and KMV stimulation (Figures 2E, S1F). *Mgl1* and *Mgl2* were solely enhanced by KIV stimulation (Figure 2E). Both KIV and KIC additionally enhanced the proinflammatory (M1-like) marker *Nos2*, while only KIV stimulation also activated *Il1β* and *Il6* (Figures 2E, S1F). KIC and KMV treatment also caused the production of anti-inflammatory cytokine TGF-β and growth factor VEGF (Figure 2F). Similar effects on TGF-β and VEGF production by BCKA pool treatment were observed (Figure 2F). Proinflammatory cytokines IL6 and TNF-α were only increased after KIV treatment while slightly reduced in KMV-treated macrophages (Figure 2F). Interestingly, BCKA pool treatment did not affect TNF-α and modestly reduced IL6 production, which is closer to AE17 CM treatment and probably due to the opposing effects from the other two BCKAs, especially KMV.

The monocarboxylate transporter MCT1 mediates the transport of BCKAs through plasma membranes of Xenopus oocytes and glioblastoma cells (15, 24, 25). We thus investigated whether BCKAs activate macrophage MCT1 expression. RT-quantitative PCR (qPCR) analyses of BMDM showed that BCKAs stimulation has no effect on MCT1 (*Slc16a1*) mRNA level (Figure 2E). However, BCKAs-induced upregulation of *Arg1* and *Vegf* was significantly reduced by the MCT1 inhibitor AZD3965 (Figure 2G). We repeated the same experiments with iBMDM and found similar results (Figure

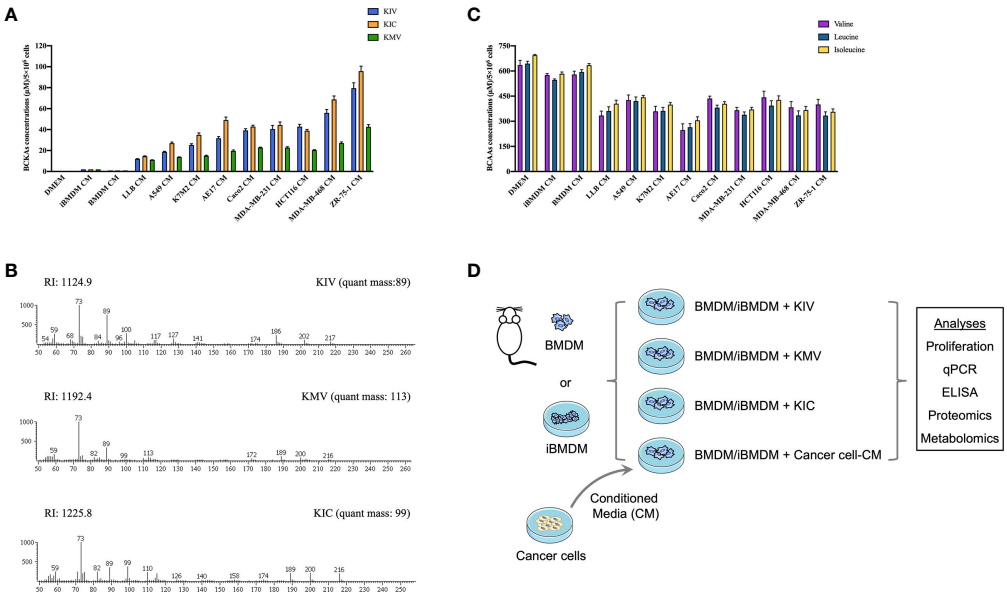

FIGURE 1
Cancer cells consume BCAAs and secrete BCKAs. **(A)**, BCKAs (KIV, KIC and KMV) in the DMEM complete medium or conditioned media (CM) from indicated cells were detected by GC-MS. **(B)**, Representative mass spectra of KIV, KIC and KMV by GC-MS. **(C)**, BCAAs (leucine, isoleucine and valine) in the DMEM complete medium or conditioned media from indicated cells were detected by GC-MS. **(D)**, Diagram of workflow. Conditioned media from cancer cells and three BCKAs were added to BMDM or iBMDM, followed by multiomics analysis. Data in A and C show the mean ± SEM of n = 3 technical experiments.

10.3389/fimmu.2022.966158

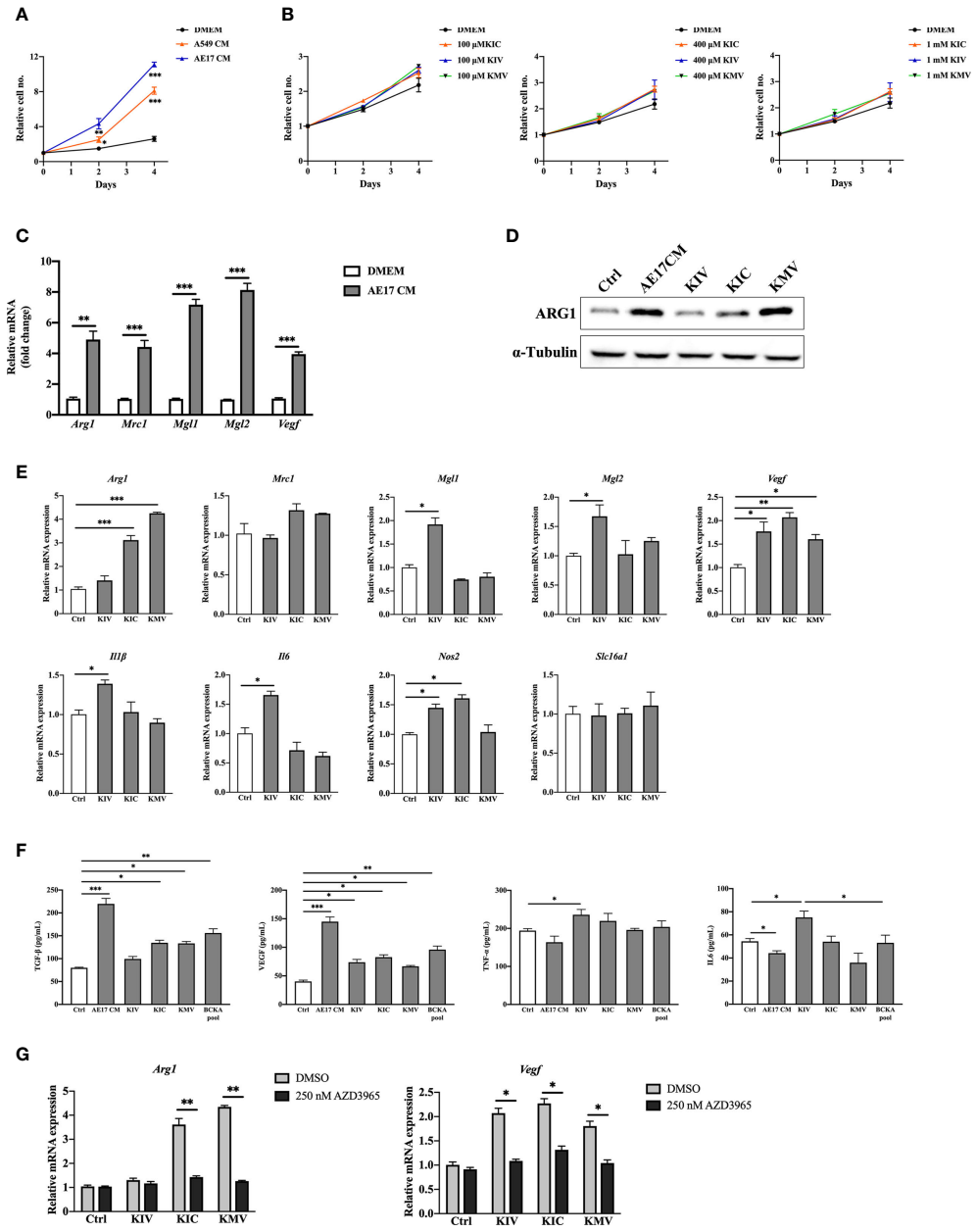

FIGURE 2
BCKAs in cancer cell CM induce murine BMDM polarization. **(A)**, Relative proliferation rate of BMDM grown in DMEM complete medium or indicated cancer cell CM. **(B)**, Relative proliferation rate of BMDM grown in DMEM complete media or equivalent media containing 200 μM KIV or 200 μM KIC or 200 μM KMV (n = 3). **(C)**, mRNA expression of *Arg1*, *Mrc1*, *Mgl1* and *Mgl2* in BMDM was measured by qPCR after incubation with AE17 CM for 24 hours. **(D)**, ARG1 protein level was measured by western blot after incubation with AE17 CM for 24 hours. **(E)**, mRNA expression of *Arg1*, *Mrc1*, *Mgl1*, *Mgl2*, *Vegf*, *Il1β*, *Il6*, *Nos2* and *Slc16a1* was measured in BMDM after stimulation with DMEM (Control), 200 μM KIV, 200 μM KIC and 200 μM KMV, respectively for 24 hours. **(F)**, Cytokines TGF-β, TNF-α, IL6 and growth factor VEGF in BMDMs after the indicated treatments were measured by ELISA kits. **(G)**, mRNA expression of *Arg1* and *Vegf* was measured after pretreatment with the MCT1 inhibitor 250 nM AZD3965 for 1 hour, and stimulation with 200 μM KIV, 200 μM KIC and 200 μM KMV, respectively for 24 hours. Data show the mean ± SEM of n = 3 biological experiments. *$p < 0.05$, **$p < 0.01$, ***$p < 0.001$ (unpaired two-tailed t test).

S1G). Taken together, these data indicate that cancer cell-secreted KIV promote pro-inflammatory macrophage polarization whereas KIC and KMV promote a pro-tumoral phenotype (based on the investigated markers). Although individual BCKAs differed in macrophage polarization, combined BCKAs have a crucial impact on macrophage pro-tumoral polarization and all three BCKAs seem to affect macrophage polarization only after import by MCT1.

Macrophage apoptosis, redox balance and inflammatory functions are significantly altered by KMV stimulation

To investigate the global responses of macrophages to BCKAs, we performed an untargeted MS-based proteomic analysis on iBMDM treated with DMEM (Ctrl), AE17 CM, 200 μM KIC, 200 μM KIV and 200 μM KMV, respectively. Overall, 3512 protein groups were quantified (Table S1) upon data processing (see methods). Next we applied one-way analysis of variance (ANOVA) with an False Discovery Rate (FDR) cutoff (FDR value < 0.05) and found 114 and 130 differentially expressed proteins (DEPs) in the DMEM group and in the combined three BCKAs groups, respectively (Table S1, Figure 3A). Principal component analysis (PCA) reliably distinguished DEPs from three BCKAs groups versus the control group (Figure S2A). Functional analysis indicated that the most enriched categories of BCKAs-upregulated proteins included the cAMP signaling pathway, sphingolipid signaling pathway, autophagy, VEGF signaling pathway, nucleotide synthesis and mitochondrial transport (Figure S2B). Among the top categories of suppressed proteins were RNA splicing, regulation of cytochrome c release, apoptosis, RNA destabilization and TNFα-NFκB pathway (Figure 2B).

Next, we used all DEPs to construct a protein interaction map. Most of these proteins exhibited significant interactions (PPI = 0.00102) (Table S1, Figure 3B). 6 clusters of DEPs were identified by way of k-means analysis and enriched in canonical macrophage functions (Figures 3B, C), including FcγR pathway-mediated phagocytosis (FCGR4, SPHK2, PIK3R1), apoptosis (CASP3, STEAP3, ROCK1, ROCK2, RIPK1, PIK3R1), TNFα-NFκB signaling (NFKB1, RELA, RIPK1, PPP2CA, SPHK2), oxidation-reduction process (CAT, GSR, GPX1), ribosome biogenesis (NOP58, NOP10, NOP14, WDR74), RNA transport (POP1, RAN, NUPL1, TPR, FXR2) and metabolic pathways (CMPK1, GRHPR, GPI, ACSL1, ABCD1, CKB, P4HA1, PFAS, AK1, SGPL1, ATP5H). Of note, KMV stimulation has more obvious alterations in these pathways than KIC and KIV. Furthermore, we compared the top26 node degree of proteins (each protein interacts with at least 10 other proteins) among control and three BCKAs groups (Table S1). We found that apoptosis executor CASP3 was reduced while negative apoptosis regulator PIK3RL was increased by KMV stimulation (Figure 3D), suggesting that KMV stimulation protects macrophages from apoptosis. Similarly, reduced inflammatory regulator NFKB1 and increased negative regulator CAT indicated that KMV stimulation prevented macrophage polarizing into inflammatory tumor suppressive phenotype (Figure 3D), which is in line with our previous qPCR results. In addition, KMV stimulation changed several metabolic pathways such as glycolysis, TCA cycle, purine and pyrimidine nucleotide synthesis, arginine and proline metabolism and sphingolipid metabolism (Figure 3C).

BCKA stimulation elevates metabolites in the TCA cycle and polyamine metabolism

Metabolic reprogramming of macrophages shapes their activation state and function. Our proteomic analysis suggested a plausible metabolic alteration in response to BCKA stimulation, we then decided to examine the metabolome of macrophages after BCKA treatment. Because macrophage metabolism is constantly changing, we harvested unstimulated and iBMDM stimulated with each of the three BCKAs at two-time points: 2 hours (h) for early response and 24 h for the late response. Totally 41 metabolites were identified by GC-MS analysis, including glycolysis, TCA cycle, amino acids metabolism, and polyamine metabolism. Clusters of 2 h groups were notably separated from 24 h by PCA plot (Figure 4A), indicating a dynamic metabolic change within the macrophages. An interesting trend was observed after exposure to BCKAs, where all clusters of late responses of BCKAs groups, especially KIC, have shifted away from the DMEM (control) group (Figure 4A). Indeed, a variety of intracellular metabolites were altered after stimulation with BCKAs, and this difference was more profound at 24 h compared to the DMEM group (Table S2, Figure 4B). Evidently, TCA cycle intermediates α-ketoglutarate (α-KG), succinyl-CoA, succinate, fumarate, and malate are all enhanced by the administration of any of the three BCKAs at both time points. Meanwhile, individual BCKAs treatment significantly increased acetyl-CoA levels, implying that BCKAs can be catabolized by macrophages and contribute to the TCA cycle. Although glutamine and glutamic acid levels were not changed by individual BCKAs treatment (Figures 4B, S3A), increased α-KG may also be from the contribution of BCKA transamination. Thus, our results indicate that BCKAs are taken up and incorporated into the TCA cycle *via* acetyl-CoA, succinyl-CoA, or α-KG (Figures 4B, C). The glycolysis intermediates pyruvate and lactate were enhanced by KMV and KIC at 24 h. In addition, inflammatory-related metabolites itaconate, β-alanine and 2-hydroxyglutarate were enhanced by BCKAs at 24 h (Figure 4B). KIC and KMV also enhanced putrescine, which is the important metabolite of polyamine metabolism (Figure 4D). Moreover, KIC

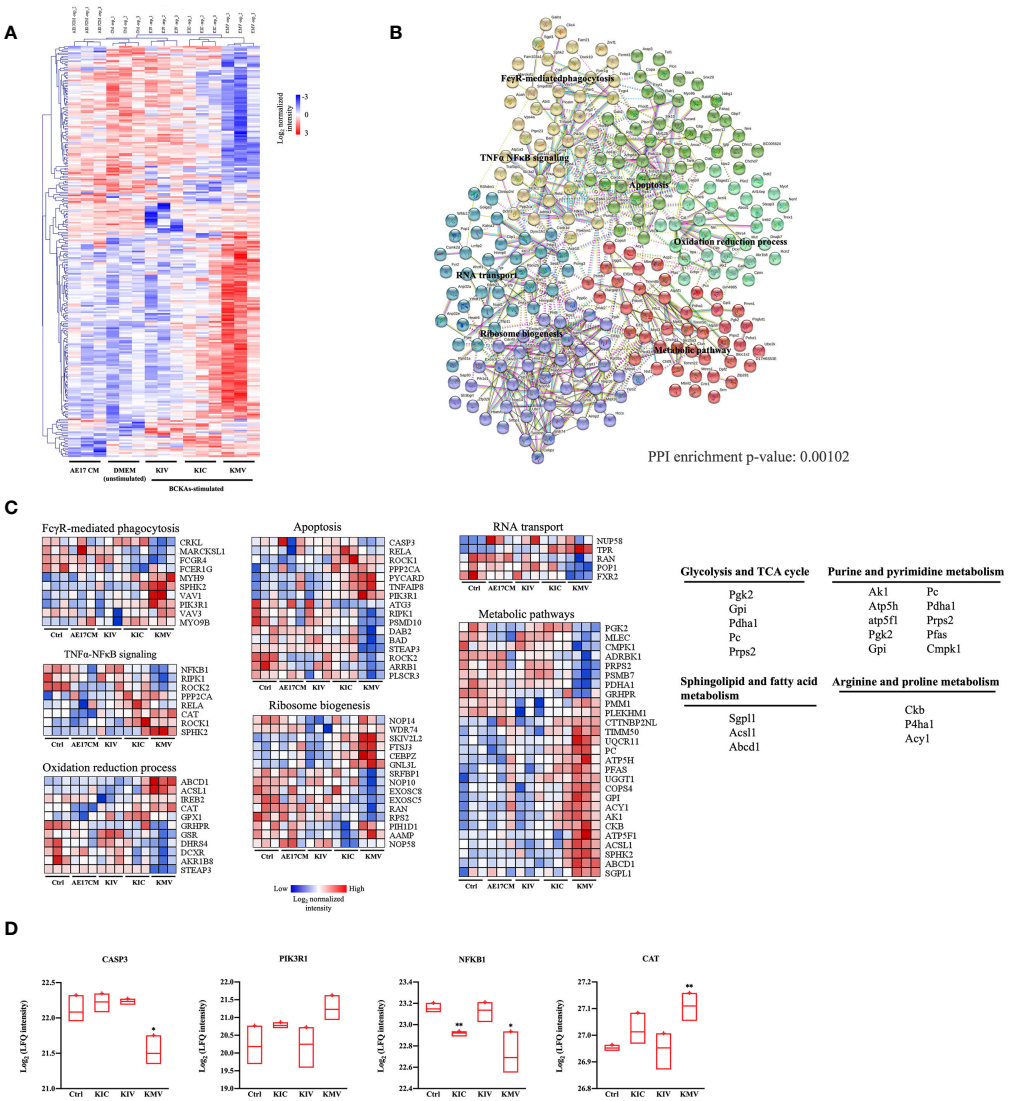

FIGURE 3
Protein signatures of responses to BCKAs stimulation. **(A)**, Heatmap of 243 differentially expressed proteins (one-way ANOVA, FDR q value < 0.05) between unstimulated (DMEM) and three BCKAs-stimulated iBMDM. **(B)**, Protein–protein interaction (PPI) network in differentially expressed proteins shown in A illustrated by STRING (PPI enrichment p-value = 0.00102). Proteins were divided into 6 clusters by k-means clustering method. Each node represents input proteins. Distinct nod colors indicated 1-6 clusters (see Table S1). Edges represent protein-protein associations (evidence). Representative KEGG terms are shown in enriched positions. **(C)**, Heatmap of the protein intensity of selected KEGG terms shown in **(B, D),** Proteomics analysis of CASP3, PIK3R1, NFKB1 and CAT in Ctrl and three BCKAs-stimulated iBMDM. The LFQ intensities were log2 transformed. Data shown the mean ± SEM of n = 3 biological experiments. *$p < 0.05$, **$p < 0.01$ (unpaired two-tailed t test).

stimulation at 24 h significantly activated creatinine, the by-product of energy metabolism and other amino acids tyrosine, alanine, cysteine, phenylalanine, taurine, and lysine (Figure 4B). Of note, a recent study reported that macrophages take up cancer cell-released KIV, KIC and KMV for regenerating valine, leucine and isoleucine (15). However, our metabolic data only revealed an increase in leucine level in the KIC stimulation group (Figure 4B). One possibility is that macrophages utilize regenerated BCAAs from BCKAs instead of extracellular sources (15). Moreover, no intracellular BCKAs were observed after 2 h or 24 h treatment, it is probably because intracellular concentrations of BCKAs are too low to be detected by the mass spectrometer or BCKAs are quickly catabolized and transaminated into the TAC cycle and BCAAs, respectively.

Next, we performed pathway analysis using selected 17 metabolites at 24 h whose FDR was < 0.05 by one-way ANOVA (Table S2). The most enriched metabolic pathways were the TCA cycle (citrate cycle), pyruvate metabolism and

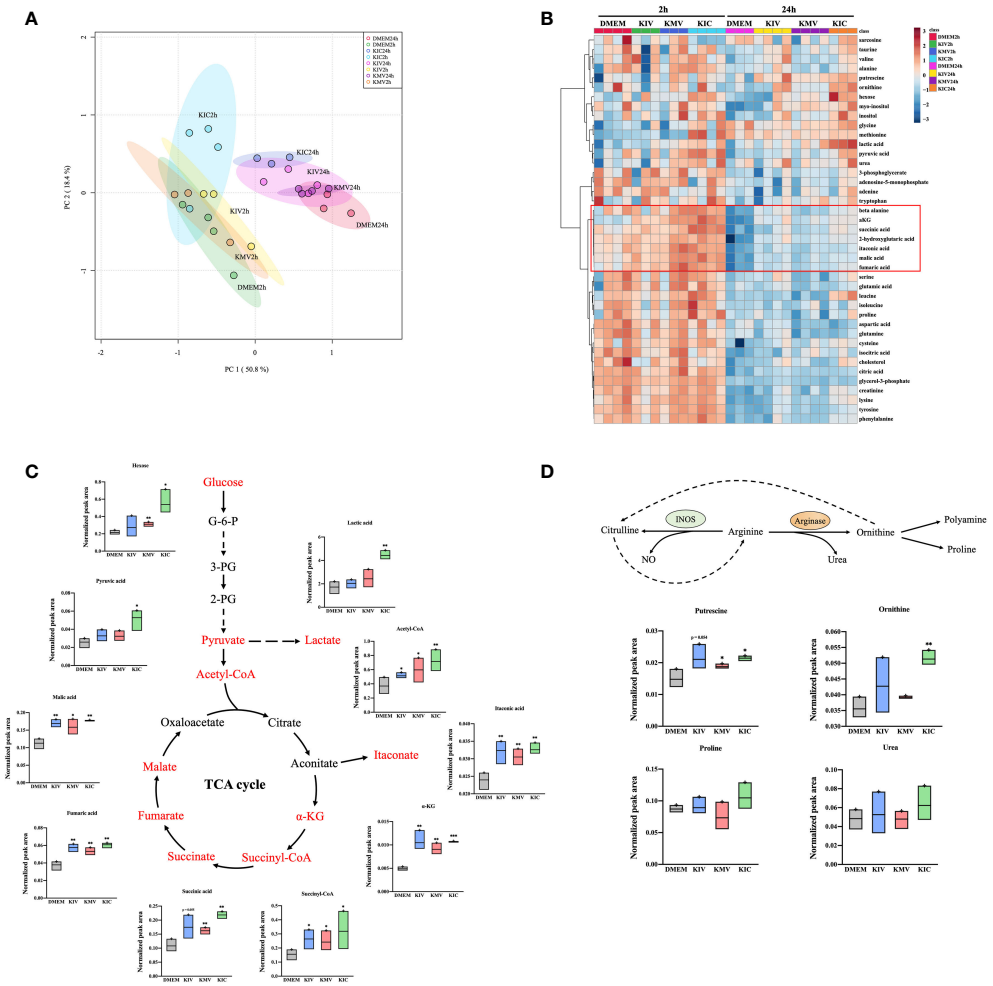

FIGURE 4
BCKAs stimulation enhance TCA cycle and polyamine metabolism in macrophages. **(A)**, PCA analysis of total identified metabolites among DMEM, KIV, KMV and KIC treatment at two time points (2 h and 24 h) is shown. **(B)**, The hierarchal clustering heatmap of identified metabolites upon DMEM and three BCKAs treatment at two time points (2 h and 24 h) is shown. The rows indicate different metabolites, and the columns indicate different conditions. The log-transformed metabolite intensities (normalized to internal standards) were scaled by autoscaling (mean-centering/standard deviation). **(C)**, Schematic representation of the TCA cycle, the corresponding metabolite is shown. **(D)**, Schematic representation of the arginine metabolism at 24 h, the corresponding metabolites from **(B)** are shown. PCA **(A)** and hierarchical clustering **(B)** analysis were applied *via* online tool MetaboAnalyst. Data shown the mean ± SEM of n = 3 or 4 biological experiments. *$p < 0.05$, **$p < 0.01$, ***$p < 0.001$ (unpaired two-tailed t test) (unpaired two-tailed t test).

alanine, aspartate and glutamate metabolism in macrophages (Figure S3B). Taken together, these data provide evidence that administration of BCKAs reprograms macrophage metabolic profiles.

Discussion

The diverse metabolic environment of tumors has long been implied to influence the phenotype of tumor-associated macrophages, rendering them immunosuppressive and contributing to tumor growth and metastasis (10, 14, 26, 27). Here, we demonstrate that cancer cells secreted three BCKAs that are able to influence macrophage polarization and metabolic reprogramming. Previous work has described the importance of BCKAs in favoring tumor growth and accelerating chronic inflammatory disease (22, 23). Our work suggests that three BCKAs exhibit divergent roles in affecting macrophage functional pathways and should be targeted individually to improve anti-tumor immune responses.

Many solid tumor cells rely heavily on amino acids for their proliferation, especially on BCAAs, which they can only derive from the diet or the tumor microenvironment (28, 29). BCKAs are the intermediates of BCAAs catabolism, which can be

exported into extracellular space by MCT1 in glioblastoma (15). Accumulation of BCKAs is also correlated with various diseases including obesity, type 2 diabetes and cardiac dysfunction (30–32). We showed that a panel of cancer cells including breast, colorectal and lung cancer cells consumed BCAAs from media and released high levels of KIV, KIC and KMV. KIC and KMV could induce pro-tumoral polarization of macrophages whereas KIV could exert pro-inflammatory effects on macrophages. MCT1 is well known as the lactate transporter that mediate lactate influx and efflux (33, 34). Tumor-associated macrophages highly expressed MCT1, which is correlated with poor prognosis in breast cancer patients (35). MCT1 also mediated M2-like macrophage polarization instructed by lactate within an ischemic muscle (36). We found that BCKAs influenced macrophage polarization in an MCT1-dependent manner. Considering a higher lactate level was observed in KIC-treated macrophages, our results imply that the antitumor benefits of targeting MCT1 may partially be due to the blocked uptake of cancer-derived BCKAs or KIC-triggered lactate by surrounding immune cells.

Tumor cells have evolved to evade the engulfment by macrophages *via* the expression of anti-phagocytic molecules, leading to immune escape and macrophage repolarization (37). FcγRIV (encoded by gene *Fcgr4*) was recently identified as an important Fc receptor that promotes macrophage-mediated phagocytosis, proinflammatory cytokine production and antigen presentation to T cells (38). Activated *Fcgr4* by Intravenous Igs (IVIg) treatment repolarized M2-like macrophages switch to M1-like macrophages and impaired tumor progression and metastasis (39). Our data revealed that KMV stimulation significantly increased majority of proteins (including phagocytosis negative regulator SPHK2) associated with FcγR-mediated phagocytosis pathway while significantly reduced FCGR4 protein intensity, which may partially explain why BCKAs stimulation suppressed macrophage phagocytosis (15). Transcription factor NFκB has been shown to play a critical role in regulating the expression of proinflammatory mediators, such as nitric oxide (NO) synthase and IL-1β, IL-6 and TNF-α. Interestingly, NFKB1 intensity was decreased by KMV or KIC stimulation but not KIV stimulation. We also found that catalase (CAT) and serine/threonine-protein phosphatase 2A catalytic subunit alpha isoform (PPP2CA) proteins are increased in KMV group. CAT overexpression can inhibit NFκB activation triggered by a peroxisome proliferator and protect liver cells from oxidative damage (40). Similar, PPP2CA is a vital constituent of PP2A and its downregulation by breast cancer cell-derived exosomes activated NFκB signaling pathway in tumor-associated macrophages (41). Our proteomics and qPCR data imply that KMV probably activates CAT and PPP2CA-mediated downregulation of NFκB signal transduction, thereby limiting the expression of proinflammatory genes. However, the causal relationship between this signal axis and KMV-induced macrophage polarization and the detailed experimental validation of the proteomic data remain to be addressed in the future studies.

Recent reports revealed a mutualistic relationship concerning BCAAs metabolism between tumor cells and the tumor microenvironment (15, 22). Cancer-associated fibroblasts-secreted BCKAs can be taken up by pancreatic cancer cells and re-aminated to BCAAs, which are further involved in maintaining cellular protein synthesis, fueling the TCA cycle and increasing oxidative phosphorylation (OXPHOS) (22). In contrast, we did not find an increase of all three BCAAs in macrophages except leucine after BCKAs exposure, but our data showed the enhancement of glycolysis and TCA cycle metabolites upon BCKAs stimulation. Metabolism has been highlighted as a crucial mediator of macrophage activation and polarization (42). It is well known that enhanced glycolysis and accumulated TCA cycle intermediates such as citrate and succinate emerge as typical features of M1-like macrophages (43, 44). KIV, KMV, and KIC treatment all triggered TCA cycle intermediates while only KIV activated proinflammatory cytokines IL6 and TNF-α as well as transcripts of *Il6* and *Il1β*. Combined with our proteomics results, it seems that KMV and KIC, not KIV inhibit the NFκB pathway, which is responsible for the transcription of these proinflammatory cytokines. In M2-like macrophages, arginine is metabolized to urea and polyamines (putrescine and ornithine) by highly expressed ARG1. Increased polyamines have been found to promote tumor growth and blunt effector T cell responses (45, 46). Our results found that KMV and KIC treatment significantly increased putrescine, which supports the role of KMV and KIC on macrophage pro-tumoral polarization. Moreover, mitochondrial OXPHOS and redox homeostasis are essential for both M1-like and M2-like macrophages. M2-like macrophages are crucially dependent on the efficient electron transport chain and OXPHOS to support their energy demands and phenotype, whereas M1-like macrophages shift mitochondria away from ATP production and towards ROS production, which drives IL-1β generation and undermines anti-inflammatory activation (47). Our proteomic results revealed that KIV treatment induced GSR protein expression, which catalyzes GSH synthesis and highlighted the importance of GSH in maintaining cellular redox balance during macrophage proinflammatory activation. Unlike KIV treatment, KMV treatment decreased GSR expression while enhancing another antioxidant enzyme CAT. Thus, redox regulation is associated with BCKAs-induced macrophage polarization, and the complex mechanism remains further investigated.

In summary, we have shown that cancer cells secrete BCKAs into the extracellular milieu, which can affect distinct macrophage polarization by altering proinflammatory and anti-inflammatory phenotype markers. Furthermore, all three BCKAs can fuel TCA cycle metabolite pools. KIC and KMV can also increase immunosuppressive metabolites in macrophages. Proteomics and network analysis identified several canonical

functions significantly altered by KMV treatment of macrophages, including TNFα-NFκB pathway, FcγR-mediated phagocytosis, apoptosis, and redox regulation. We also provide evidence that BCKAs depend on MCT1. These findings highlight the importance of cancer-derived BCKAs for regulating macrophage polarization and metabolism. Studies focusing on the actual net degree of tumor promotion by BCKA-exposed macrophages and its reliance on observed metabolic changes are warranted, most preferably in an appropriate *in vivo* setting.

Materials and methods

Animals

6–8-week-old wild-type C57BL/6JRI mice were purchased from Janvier (France). The animals were kept in a pathogen-free environment. Every procedure was carried out under sterile conditions and according to the regulations of the Ethics Committee for the Care and Use of Laboratory Animals at the Medical University of Vienna.

Cell culture

All cells were cultured at 37°C in a humidified (5% CO2) atmosphere. All cancer cell lines were obtained by ATCC and routinely cultured in Dulbecco's Modified Eagle's Medium (DMEM) high glucose containing 10% heat-inactivated FBS, 2 mM L-glutamine, 100 U/mL penicillin and 100 µg/mL streptomycin (DMEM complete medium). All the cultured cells were tested negative for mycoplasma contamination regularly.

Bone marrow derived macrophages (BMDM) were obtained as previously described (48). Briefly, femurs and tibiae from wild-type C57BL/6JRI mice (Janvier) aged 6 to 8 weeks were flushed and bone marrow (BM) cells collected by centrifugation at 400*g* for 5 min at 4 °C. BM cells were resuspended in BMDM differentiation medium and cultured in non-tissue culture treated petri dishes for 6-7 days. BMDM differentiation medium consists of DMEM high glucose, 10% heat-inactivated FBS, 2 mM L-glutamine, 100 U/mL penicillin and 100 µg/mL streptomycin supplemented with 20% L929-conditioned supernatant. The medium was replaced every 3 days. On day 6 or 7, differentiated BMDM (96% of the cells were positive for F4/80 and CD11b) were washed, harvested, and seeded in the DMEM complete medium for different experiments. iBMDM was kindly provided by Laszlo Nagy (Debrecen University, Hungary) and cultured in iBMDM medium consisting of DMEM high glucose, 10% heat-inactivated FBS, 10% L929-conditioned supernatant, 2 mM L-glutamine, 100 U/mL penicillin and 100 µg/mL streptomycin.

CM preparation

5×10^6 cancer cells or BMDM or iBMDM were seeded in 20 mL DMEM complete medium, and conditioned medium (CM) was collected after 24 h and centrifuged at 410*g*. for 4 min. The supernatant was passed through a 0.22-µm filter to eliminate debris before use.

Proliferation assay

Cancer cells were seeded in 24-well plates (AE17 2×10^4 cells per well, A549 4×10^4 cells per well), BMDM or iBMDM in 12-well plates (4×10^4 cells per well) in DMEM complete media and allowed to grow overnight. Macrophages were then washed with PBS and received fresh medium supplemented with or without indicated concentrations of BCKAs. To maintain constant nutrient levels and remove waste liberated from dead cells, the medium was replaced every 24 h. Live cell numbers were quantitated with the Vi-CELL XR cell counter (BECKMAN). KIV (Cat: HY-W006057) and KMV (Cat: HY-113063) were purchased from MedChemExpress. KIC (Cat: 68255) was purchased from Sigma-Aldrich. All BCKAs are made up in DMEM. The experiment was performed in 3 independent biological replicates.

Metabolomic analysis

Metabolites in the conditioned media (CM) or iBMDM were extracted and analyzed according to previous established method with modifications (48). In brief, iBMDM were seeded at 0.85×10^6 cells per well of a 6-well plate and allowed to attach for overnight. Cells were washed with PBS and received fresh medium supplemented with 200 µM KIV, 200 µM KIC and 200 µM KMV, respectively. After 2 h and 24 h incubation, cells were washed in cooled 0.9% NaCl and extracted in 1 mL/well of 80% methanol with 0.3 nM Pentaerythritol and 2.5 nM Phenyl β-D-glucopyranoside as internal extraction standards. Extraction samples were incubated for 15 min at 4°C, then centrifuged for 10 min at 21,000*g*. The supernatant was transferred to a fresh polypropylene tube and dried in a SpeedVac (Labogene). The cell pellet was lysed by RIPA and used to measure protein levels for normalization purposes. 15 µL of methoxyamine hydrochloride solution (40 mg dissolved in 1 ml pyridine) was added to the dried fraction which was then incubated for 90 min at 30°C. Next, 60 µL of (N-Methyl-N-trimethylsilyltrifluoracetamid) MSTFA was added and incubated for 30 min at 37°C. Reaction mixtures were centrifuged for 10 min and 4°C at 21,000*g* and the supernatants were transferred to glass vials with micro-inserts. Measurement of metabolites was performed using gas chromatography-mass spectrometry (GC-MS) standard

protocols (49). Deconvolution of the total ion chromatogram, peak alignment and integration was performed using the software MS-DIAL v4.7 (50).

To measure the KIC, KIV, KMV, leucine, isoleucine, and valine contents on CM samples, three aliquots (100 µL) were run for each CM. Briefly, 400 µL prechilled methanol containing internal standards was added to 100 µL media samples and kept for 1h at 4°C. The samples were then centrifuged for 10 min and 4°C at 21,000*g*, and the supernatants were transferred to fresh tubes and dried in a SpeedVac. 20 µL methoxyamine hydrochloride solution (40 mg/1 mL pyridine) and 80 µL MSTFA were used for metabolite derivatization. Measurement and data process was performed as described above. Different concentrations of standard compounds were extracted and measured under the same conditions to calculate the standard curves for absolute quantification.

The analysis of cellular acetyl-CoA and succinyl-CoA was performed using microflow liquid chromatography in combination with an Orbitrap Elite mass spectrometer (LC-MS/MS, Thermo Fisher Scientific) system according to Neubauer et al. (51) with some modifications. Briefly, iBMDM was seeded at 0.8×10^6 cells per well of a 6-well plate and allowed to attach for overnight. Cells were washed with PBS and received fresh medium supplemented with 200 µM KIV, 200 µM KIC and 200 µM KMV, respectively. After 24 h incubation, cells were washed in cooled 0.9% NaCl and quenched in 80% methanol (-20°C). The quenched cells were scraped and incubated for 30 min at 4°C, then centrifuged for 10 min at 21,000*g*. The supernatant was transferred to a fresh polypropylene tube and dried in a SpeedVac. MS buffer (20 mM NH_4OAc in mqH_2O and 2% methanol, pH 6.7) was added to the dried fraction and CoA standards which were then centrifuged for 10 min at 21,000*g* and the supernatant was transferred to LC-MS vials. 5 µL of the sample was injected into a Accucore™ Vanquish C-18+ UHPLC column (100 × 2.1 mm; 1.5 µm particle size), equipped with an Accucore™ Defender guards pk4 guard column (150 - C18 10 × 2.1 mm, 2.5 µm particle size (Thermo Fisher Scientific). The mobile phase system consisted of a mixture of solvent A (20 mM NH_4OAc in mqH_2O, pH 6.7) and solvent B (LC-MS grade methanol). A gradient elution method was used for the analysis, 0–1 min 5% B, 1–30 min linear gradient to 85% B, 30-30.1 min 0% B, and 30.1–40 min 0% B. The flow was kept constant at 0.25 mL/min and the column was kept at 30°C throughout the analysis. MS-analysis was performed in positive ion mode with the following parameters: Resolution, 120,000; spray voltage, 3.8 kV; capillary temperature, 350°C; sheath gas, 5; auxiliary gas, 0. The mass scanning range of the MS1 fullscan was set at 350–1200 m/z. The collision energy for collision-induced dissociation (CID) was set at 35 eV. Xcalibur (Thermo Fisher Scientific) and MS-DIAL were used to analyze the data.

Sample preparation for proteomics analysis

Proteomic analyses were performed according to established protocols with modifications (48). Briefly, iBMDM was seeded in DMEM complete medium and allowed to attach for overnight. Cells were stimulated with AE17 CM, 200 µM KIV, 200 µM KIC and 200 µM KMV, respectively. After 24h incubation, cells were washed and harvested in lysis buffer (6M guanidinium chloride (GdmCl), 100 mM Tris pH 8.5, 10 mM tris-(2-carboxyethyl)-phosphin-hydrochloride (TCEP), 40 mM 2-chloroacetamide (CAA)). Lysates were heated for 5 min at 95°C and sonicated with a tip–probe sonicator at 4°C (3 × 30 s of 1 s on and 1 s off at 80% output power). The protein concentration was determined by a BCA assay and adjusted to a concentration of 0.6 µg/µL. 60 µg of protein solution was diluted with 15% aqueous acetonitrile (ACN), and digested with 200:1 (protein:enzyme) LysC at 37°C for 1 h. Then, 10% aqueous ACN in 25 mM Tris (pH 8.5) was added to obtain a final concentration of 0.5 M GdmCl and a final volume of 1000 µL. Samples were incubated with trypsin 50:1 (protein:enzyme) overnight at 37°C. To stop the digestion process, digested peptides were acidified to a final concentration of 1% Trifluoroacetic acid (TFA). The peptides were desalted with MonoSpin C18 columns according to the manufacturer's instruction. The peptides were eluted with 2 × 60 µL ACN and concentrated in a SpeedVac for 1 h at 45°C. Finally, they were reconstituted in MS loading buffer (2% ACN, 0.1% formic acid (FA)) for LC-MS/MS analysis. The experiment was performed in 3-4 biological replicates.

LC-MS-based proteomics

Shotgun proteomics was performed according to established protocols (48). LC-MS/MS runs were performed on the UltiMate 300 system (Thermo Scientific) coupled to a Q-Exactive Plus mass spectrometer (Thermo Scientific) The peptides were separated by reversed-phase chromatography using a binary buffer system consisting of 0.1% FA (buffer A) and 90% ACN with 0.1% FA (buffer B). 2 µg of peptides were loaded on a 50 cm column with a 75 µM inner diameter and 2 µM C18 particles (EASY-spray PepMap, Thermo Fisher) and separated by a 170 min gradient (4-35% buffer B over 110min, 35-90% buffer B over 1 min) at a flowrate of 300 nL/min. MS data were acquired using a data-dependent top-20 method with a maximum injection time of 50 ms, a scan range of 300–1650 m/z, and an AGC target of 3e6. The resolutions of the MS and MS/MS spectra were 70,000 and 17,500, respectively. The AGC for MS/MS acquisition was set to 5e4. The max IT and dynamic exclusion were set to 100 ms and 20s, respectively.

Raw mass spectrometry data were processed with MaxQuant version v2.0.3.1 using the default setting if not stated otherwise (52, 53). Oxidized methionine (M) and acetylation (protein N-term) were selected as variable modifications, and carbamidomethyl (C) as fixed modifications. Three missed cleavages for protein analysis were allowed. Label-free quantitation (LFQ) and "Match between runs" were enabled. Searches were performed against the mouse UniProt FASTA database (March 2021) containing 22,001 sequences. Bioinformatics analysis was performed using Perseus v1.6.6.0 (54) and COVAIN toolbox (55). The proteinGroups output table was used for all proteomic analyses. Reverse proteins, proteins that were only identified by site, and potential contaminants were filtered out. The protein groups were filtered to have at least 70% valid values, reaching a list of 3512 protein groups (Table S1), which were further used for all downstream analyses. Dataset integration was based on gene name. Missing values were imputed using a minimal value model within the COVAIN toolbox. Significantly up-or-downregulated proteins (DEPs) between the three BCKAs groups and the control group were determined by ANOVA (FDR < 0.05) and used for all downstream analyses.

Enrichment analysis

Pathway analysis of metabolomics data was performed using the online tool MetaboAnalyst v5.0 (56). Enrichment analyses of proteomics data were performed using the Cytoscape v3.8.2 (57) module ClueGO v2.5.8 (58). Enrichments were performed using the GO, KEGG, REACTOME and Wiki Pathway databases. Only pathways with $p < 0.05$ and at least a 4 gene overlap were considered for grouping (kappa score 0.4). A protein network was generated with DEPs using STRING v11.5 (59) and selected KEGG pathways (FDR < 0.05) were highlighted.

Cytokine production measurement

Differentiated BMDMs were seeded at a density of 0.9×10^6 cells per well in 6-well plates in 2 mL of DMEM complete medium overnight before the media was either replaced with AE147 CM or was supplemented with 200 µM KIV, 200 µM KMV, 200 µM KIV or BCKA pool. After 24 h, cell-free supernatants were collected. The levels of IL-6 (Sigma, RAB0308-1KT), TNF-α (Sigma, RAB0477-1KT), TGF-β (Invitrogen, BMS608-4) and VEGF (Sigma, RAB0509-1KT) in the supernatants were measured by ELISA kits according to the manufacturer's instructions. The experiment was performed in 3 biological replicates.

Immunoblotting

BMDM or iBMDM were lysed on ice in self-made RIPA lysis buffer supplemented with a proteinase inhibitor cocktail (Sigma; 4693116001). After 10 min incubation on ice the lysates were subjected to sonication with a tip–probe sonicator at 4°C (3-5 s of 1 s on and 1 s off at 80% output power) to effectively shear DNA and reduce viscosity. After centrifugation, the pellet was discarded and the protein concentration in the supernatant was measured by a BCA assay. Equal amounts of denatured lysate were separated by 10% SDS-PAGE and transferred to PVDF membranes. Membranes were blocked in 5% low-fat milk for 1 h at room temperature (RT) and incubated with primary antibodies at 4°C overnight. Membranes were then incubated with HRP-conjugated secondary antibodies for 1 h at RT. The signal was detected using the ECL system (Amersham Biosciences, Cytiva) according to the manufacturer's instructions (iBright FL1500 Imaging System, Thermo Fisher). The primary antibodies used were against ARG1 (Santa Cruz; sc-47715) and α-tubulin (Proteintech; HRP-66031). Appropriate secondary antibodies were from Proteintech. The experiment was performed in 3 biological replicates.

RNA isolation and gene expression analysis

BMDM or iBMDM were washed twice and suspended directly in TRI reagent (Thermo Scientific; 15596026). Total RNA was isolated according to the manufacturer's instructions. Quality and quantity were measured on a Nanodrop (Thermo Scientific). cDNA was synthesized from 1 µg of RNA using the GoScriptTM Reverse Transcription kit (Promega). mRNA levels were determined using the Luna Universal qPCR Master Mix (New England biolab) on a Bio-Rad CFX Connect. The quantification of the results was performed by the comparative Ct (2–ΔΔCt) method. The Ct value for each sample was normalized to the value for the *Rps9* gene. The following primer pairs were used:*Arg1*, ACATTGGCTTGCGAGACGTA, ATCGGCCTTTTCTTCC TTCCC; *Mrc1*, CTCTGTTCAGCTATTGGACGC, CGGAATTT CTGGGATTCAGCTTC; *Rps9*, GCAAGATGAAGCTGGATTAC, GGGATGTTCACCACCTG; *Nos2*, CAGAGGACCCAGAGACA AGC, TGCTGAAACATTTCCTGTGC; *Vegf*, GGCCTCCGAAA CCATGAACT, CTGGGACCACTTGGCATGG; *Mgl1*, TGCAACAGCTGAGGAAGGACTTGA, AACCAATAGCA GCTGCCTTCATGC; *Mgl2*, GCATGAAGGCAGCTGCTATT GGTT, TAGGCCCATCCAGCTAAGCACATT; *Il6*, ACAAAG CCAGAGTCCTTCAGAGAG, TTGGATGGTCTTGGTCCTTA GCCA; *Il1β*, TGGCAACTGTTCCTG, GGAAGCAGCCCTTC ATCTTT; *Slc16a1*, GGGCTAAAGCCACAGTCCAT, TCTGCT AAGTGCCACACAGG. The experiment was performed in 4 independent biological replicates.

Quantification and statistical analysis

Statistical significance was calculated between two groups by student's unpaired t-test. One-way ANOVA with Tukey's HSD post-test was used to calculate statistical significance between multiple groups. Analyses were performed using Microsoft Excel or GraphPad Prism v9. Error bars represent SEM and $p < 0.05$ was considered statistically significant ($*p < 0.05$, $**p < 0.01$, $***p < 0.001$).

Data availability statement

The mass spectrometry-based proteomics data have been deposited at ProteomeXchange Consortium (http://www.proteomexchange.org/) with the accession number PXD032100. Metabolomics data have been deposited to the EMBL-EBI MetaboLights database (https://www.ebi.ac.uk/metabolights) with the identifier MTBLS4497.

Ethics statement

The animal study was reviewed and approved by Ethics Committee for the Care and Use of Laboratory Animals at the Medical University of Vienna.

Author contributions

ZC and WW conceived and designed the study; ZC and WL performed the experiments; MB and SB helped with instruments and techniques; EH provided necessary tools, supervised, and supported experiments; ZC, WL, and WW wrote the manuscript. All the authors read, revised, and agreed on the final version of the manuscript.

Funding

ZC and WL were supported by Ph.D. scholarships provided by China Scholarship Council (CSC) (Grant numbers: 201806500012 and 201908320480). Part of this work was supported by the Austrian Science Fund (FWF; grant number P32600 to EH).

Acknowledgments

We thank Petra Heffeter (Medical University of Vienna, Austria) for providing the C57BL/6JRI mice. We thank Leila Afjehi, Palak Chaturvedi and Florian Schindler (University of Vienna, Austria) for mass spectrometry assistance. We thank Shomaila Mehmood (Anhui University, China) for helpful discussions.

Conflict of interest

The authors declare that the research was conducted in the absence of any commercial or financial relationships that could be construed as a potential conflict of interest.

Publisher's note

Supplementary material

The Supplementary Material for this article can be found online at: https://www.frontiersin.org/articles/10.3389/fimmu.2022.966158/full#supplementary-material

SUPPLEMENTARY FIGURE 1
BCKAs in cancer cell CM induce murine iBMDM polarization. **(A)**, Schematic showing how branched-chain amino acids (BCAAs) (leucine, isoleucine, and valine) are broken and oxidation. BCAA transaminases 1 and 2 (BCAT1/2) transfer nitrogen to a-ketoglutarate (a-KG) to produce glutamine and the specifed BCKAs, which then metabolized by branched-chain a-keto acid dehydrogenase (BCKDH) complex to produce a branched-chain acyl-CoA (R-CoA) that can be further metabolized to the TCA cycle intermediates acetyl-CoA or succinyl-CoA. **(B)**, Relative proliferation rate of iBMDM grown in DMEM complete medium or indicated cancer cell CM. **(C)**, Relative proliferation rate of BMDM grown in DMEM complete media or equivalent media containing 200 μM KIV or 200 μM KIC or 200 μM KMV (n = 3). **(D)**, mRNA expression of *Arg1*, *Mrc1*, *Mgl1* and *Mgl2* in iBMDM was measured by qPCR after incubation with AE17 CM for 24 hours. **(E)**, ARG1 protein level was measured by western blot after incubation with AE17 CM for 24 hours. **(F)**, mRNA expression of *Arg1*, *Vegf*, *Il6*, *Nos2* and *Slc16a1* was measured in iBMDM after stimulation with DMEM (Control), 200 μM KIV, 200 μM KIC and 200 μM KMV, respectively for 24 hours. **(G)**, mRNA expression of *Arg1* and *Vegf* in iBMDM was measured after pretreatment with the MCT1 inhibitor 250 nM AZD3965 for 1 hour, and stimulation with 200 μM KIV, 200 μM KIC and 200 μM KMV, respectively for 24 hours. Data show the mean ± SEM of n = 3 biological experiments. $*p < 0.05$, $**p < 0.01$, $***p < 0.001$ (unpaired two-tailed t test).

SUPPLEMENTARY FIGURE 2
Protein signatures of responses to BCKAs stimulation, related to **(A)**, Principal Component Analysis (PCA) of proteins shown in **(B)**, Selected functional categories (GO, KEGG, REACTOME and Wiki Pathway databases) of BCKAs-stimulated iBMDM versus unstimulated iBMDM. BCKAs upregulated proteins are enriched cAMP signaling pathway, sphingolipid signaling pathway, autophagy, VEGF signaling, purine nucleotide biosynthesis process (left). BCKAs downregulated proteins are enriched in RNA splicing, redox regulation, apoptosis, NF-κB pathway (right). PCA plot was applied *via* toolbox COVAIN (55).

SUPPLEMENTARY FIGURE 3
BCKAs stimulation reprogrammed macrophage metabolism. **(A)**, Glutamine and glutamic acid levels after individual BCKAs treatment were shown. **(B)**, Pathway analysis of 17 metabolites (FDR $p < 0.05$, one-way ANOVA) between control and three BCKA groups at 24 h. First 3 critical pathways are highlighted.

References

1. Pathria P, Louis TL, Varner JA. Targeting tumor-associated macrophages in cancer. *Trends Immunol* (2019) 40:310–27. doi: 10.1016/j.it.2019.02.003

2. Atanasov G, Pötner C, Aust G, Schierle K, Dietel C, Benzing C, et al. TIE2-expressing monocytes and M2-polarized macrophages impact survival and correlate with angiogenesis in adenocarcinoma of the pancreas. *Oncotarget* (2018) 9:29715. doi: 10.18632/oncotarget.25690

3. Sørensen M, Dahlrot R, Boldt H, Hansen S, Kristensen B. Tumour-associated microglia/macrophages predict poor prognosis in high-grade gliomas and correlate with an aggressive tumour subtype. *Neuropathol Appl Neurobiol* (2018) 44:185–206. doi: 10.1111/nan.12428

4. Wang H, Li P, Wang L, Xia Z, Huang H, Lu Y, et al. High numbers of CD68+ tumor-associated macrophages correlate with poor prognosis in extranodal NK/T-cell lymphoma, nasal type. *Ann Hematol* (2015) 94:1535–44. doi: 10.1007/s00277-015-2401-4

5. Zhang W-j, Wang XH, Gao ST, Chen C, Xu XY, Zhou ZH, et al. Tumor-associated macrophages correlate with phenomenon of epithelial-mesenchymal transition and contribute to poor prognosis in triple-negative breast cancer patients. *J Surg Res* (2018) 222:93–101. doi: 10.1016/j.jss.2017.09.035

6. Zheng X, Weigert A, Reu S, Guenther S, Mansouri S, Bassaly B, et al. Spatial density and distribution of tumor-associated macrophages predict survival in non–small cell lung carcinoma. *Cancer Res* (2020) 80:4414–25. doi: 10.1158/0008-5472.CAN-20-0069

7. Lopez-Yrigoyen M, Cassetta L, Pollard JW. Macrophage targeting in cancer. annals of the new York academy of sciences. *Annals of the New York Academy of Sciences* (2021) 1499:18–41. doi: 10.1111/nyas.14377

8. Li F, Simon MC. Cancer cells don't live alone: metabolic communication within tumor microenvironments. *Dev Cell* (2020) 54:183–95. doi: 10.1016/j.devcel.2020.06.018

9. Rabinowitz JD, Enerbäck S. Lactate: the ugly duckling of energy metabolism. *Nat Metab* (2020) 2:566–71. doi: 10.1038/s42255-020-0243-4

10. Colegio OR, Chu N-Q, Szabo AL, Chu T, Rhebergen AM, Jairam V, et al. Functional polarization of tumour-associated macrophages by tumour-derived lactic acid. *Nature* (2014) 513:559–63. doi: 10.1038/nature13490

11. Miller-Fleming L, Olin-Sandoval V, Campbell K, Ralser M. Remaining mysteries of molecular biology: the role of polyamines in the cell. *J Mol Biol* (2015) 427:3389–406. doi: 10.1016/j.jmb.2015.06.020

12. Poillet-Perez L, Xie X, Zhan L, Yang Y, Sharp DW, Hu ZS, et al. Autophagy maintains tumour growth through circulating arginine. *Nature* (2018) 563:569–73. doi: 10.1038/s41586-018-0697-7

13. Campesato LF, Budhu S, Tchaicha J, Weng C-H, Gigoux M, Cohen IJ, et al. Blockade of the AHR restricts a treg-macrophage suppressive axis induced by l-kynurenine. *Nat Commun* (2020) 11:1–11. doi: 10.1038/s41467-020-17750-z

14. Wu J-Y, Huang T-W, Hsieh Y-T, Wang Y-F, Yen C-C, Lee G-L, et al. Cancer-derived succinate promotes macrophage polarization and cancer metastasis *via* succinate receptor. *Mol Cell* (2020) 77:213–27:e215. doi: 10.1016/j.molcel.2019.10.023

15. Silva LS, Poschet G, Nonnenmacher Y, Becker HM, Sapcariu S, Gaupel AC, et al. Branched-chain ketoacids secreted by glioblastoma cells *via* MCT 1 modulate macrophage phenotype. *EMBO Rep* (2017) 18:2172–85. doi: 10.15252/embr.201744154

16. Sivanand S, Vander Heiden MG. Emerging roles for branched-chain amino acid metabolism in cancer. *Cancer Cell* (2020) 37:147–56. doi: 10.1016/j.ccell.2019.12.011

17. Li J-T, Yin M, Wang D, Wang J, Lei M-Z, Zhang Y, et al. BCAT2-mediated BCAA catabolism is critical for development of pancreatic ductal adenocarcinoma. *Nat Cell Biol* (2020) 22:167–74. doi: 10.1038/s41556-019-0455-6

18. Mayers JR, Torrence ME, Danai LV, Papagiannakopoulos T, Davidson SM, Bauer MR, et al. Tissue of origin dictates branched-chain amino acid metabolism in mutant kras-driven cancers. *Science* (2016) 353:1161–5. doi: 10.1126/science.aaf5171

19. Raffel S, Falcone M, Kneisel N, Hansson J, Wang W, Lutz C, et al. BCAT1 restricts αKG levels in AML stem cells leading to IDHmut-like DNA hypermethylation. *Nature* (2017) 551:384–8. doi: 10.1038/nature24294

20. Zhang B, Chen Y, Shi X, Zhou M, Bao L, Hatanpaa KJ, et al. Regulation of branched-chain amino acid metabolism by hypoxia-inducible factor in glioblastoma. *Cell Mol Life Sci* (2021) 78:195–206. doi: 10.1007/s00018-020-03483-1

21. Zhang L, Han J. Branched-chain amino acid transaminase 1 (BCAT1) promotes the growth of breast cancer cells through improving mTOR-mediated mitochondrial biogenesis and function. *Biochem Biophys Res Commun* (2017) 486:224–31. doi: 10.1016/j.bbrc.2017.02.101

22. Zhu Z, Achreja A, Meurs N, Animasahun O, Owen S, Mittal A, et al. Tumour-reprogrammed stromal BCAT1 fuels branched-chain ketoacid dependency in stromal-rich PDAC tumours. *Nat Metab* (2020) 2:775–92. doi: 10.1038/s42255-020-0226-5

23. Liu S, Li L, Lou P, Zhao M, Wang Y, Tang M, et al. Elevated branched-chain α-keto acids exacerbate macrophage oxidative stress and chronic inflammatory damage in type 2 diabetes mellitus. *Free Radical Biol Med* (2021) 175:141–54. doi: 10.1016/j.freeradbiomed.2021.08.240

24. Bröer S, Schneider H-P, Bröer A, Rahman B, Hamprecht B, Deitmer JW. Characterization of the monocarboxylate transporter 1 expressed in xenopus laevis oocytes by changes in cytosolic pH. *Biochem J* (1998) 333:167–74. doi: 10.1042/bj3330167

25. Fox JEM, Meredith D, Halestrap AP. Characterisation of human monocarboxylate transporter 4 substantiates its role in lactic acid efflux from skeletal muscle. *J Physiol* (2000) 529:285. doi: 10.1111/j.1469-7793.2000.00285.x

26. Devalaraja S, To TKJ, Folkert IW, Natesan R, Alam MZ, Li M, et al. Tumor-derived retinoic acid regulates intratumoral monocyte differentiation to promote immune suppression. *Cell* (2020) 180:1098–1114. e1016. doi: 10.1016/j.cell.2020.02.042

27. Goossens P, Rodriguez-Vita J, Etzerodt A, Masse M, Rastoin O, Gouirand V, et al. Membrane cholesterol efflux drives tumor-associated macrophage reprogramming and tumor progression. *Cell Metab* (2019) 29:1376–1389. e1374. doi: 10.1016/j.cmet.2019.02.016

28. Hattori A, Tsunoda M, Konuma T, Kobayashi M, Nagy T, Glushka J, et al. Cancer progression by reprogrammed BCAA metabolism in myeloid leukaemia. *Nature* (2017) 545:500–4. doi: 10.1038/nature22314

29. Peng H, Wang Y, Luo W. Multifaceted role of branched-chain amino acid metabolism in cancer. *Oncogene* (2020) 39:6747–56. doi: 10.1038/s41388-020-01480-z

30. Biswas D, Dao KT, Mercer A, Cowie AM, Duffley L, El Hiani Y, et al. Branched-chain ketoacid overload inhibits insulin action in the muscle. *J Biol Chem* (2020) 295:15597–621. doi: 10.1074/jbc.RA120.013121

31. Menni C, Fauman E, Erte I, Perry JR, Kastenmüller G, Shin S-Y, et al. Biomarkers for type 2 diabetes and impaired fasting glucose using a nontargeted metabolomics approach. *Diabetes* (2013) 62:4270–6. doi: 10.2337/db13-0570

32. She P, Olson KC, Kadota Y, Inukai A, Shimomura Y, Hoppel CL, et al. Leucine and protein metabolism in obese zucker rats. *PloS One* (2013) 8:e59443. doi: 10.1371/journal.pone.0059443

33. Végran F, Boidot R, Michiels C, Sonveaux P, Feron O. Lactate influx through the endothelial cell monocarboxylate transporter MCT1 supports an NF-κB/IL-8 pathway that drives tumor angiogenesis. *Cancer Res* (2011) 71:2550–60. doi: 10.1158/0008-5472.CAN-10-2828

34. Wilde L, Roche M, Domingo-Vidal M, Tanson K, Philp N, Curry J, et al. Metabolic coupling and the reverse warburg effect in cancer: Implications for novel biomarker and anticancer agent development. *Seminars in oncology*. (2017) 44:198–203. doi: 10.1053/j.seminoncol.2017.10.004

35. Li B, Yang Q, Li Z, Xu Z, Sun S, Wu Q, et al. Expression of monocarboxylate transporter 1 in immunosuppressive macrophages is associated with the poor prognosis in breast cancer. *Front Oncol* (2020) 2072. doi: 10.3389/fonc.2020.00207

36. Zhang J, Muri J, Fitzgerald G, Gorski T, Gianni-Barrera R, Masschelein E, et al. Endothelial lactate controls muscle regeneration from ischemia by inducing M2-like macrophage polarization. *Cell Metab* (2020) 31:1136–1153. e1137. doi: 10.1016/j.cmet.2020.05.004

37. Liu M, O'Connor RS, Trefely S, Graham K, Snyder NW, Beatty GL. Metabolic rewiring of macrophages by CpG potentiates clearance of cancer cells and overcomes tumor-expressed CD47– mediated 'don't-eat-me'signal. *Nat Immunol* (2019) 20:265–75. doi: 10.1038/s41590-018-0292-y

38. Hirano M, Davis RS, Fine WD, Nakamura S, Shimizu K, Yagi H, et al. IgEb immune complexes activate macrophages through FcγRIV binding. *Nat Immunol* (2007) 8:762–71. doi: 10.1038/ni1477

39. Domínguez-Soto A, de las Casas-Engel M, Bragado R, Medina-Echeverz J, Aragoneses-Fenoll L, Martín-Gayo E, et al. Intravenous immunoglobulin promotes antitumor responses by modulating macrophage polarization. *J Immunol* (2014) 193:5181–9. doi: 10.4049/jimmunol.1303375

40. Jang B-C, Kim D-H, Park J-W, Kwon TK, Kim S-P, Song D-K, et al. Induction of cyclooxygenase-2 in macrophages by catalase: role of NF-κB and PI3K

signaling pathways. *Biochemical and biophysical research communications* (2004) 316:398–406. doi: 10.1016/j.bbrc.2004.02.060

41. Guo J, Duan Z, Zhang C, Wang W, He H, Liu Y, et al. Mouse 4T1 breast cancer cell–derived exosomes induce proinflammatory cytokine production in macrophages *via* miR-183. *J Immunol* (2020) 205:2916–25. doi: 10.4049/jimmunol.1901104

42. Kelly B, O'neill LA. Metabolic reprogramming in macrophages and dendritic cells in innate immunity. *Cell Res* (2015) 25:771–84. doi: 10.1038/cr.2015.68

43. Infantino V, Convertini P, Cucci L, Panaro MA, Di Noia MA, Calvello R, et al. The mitochondrial citrate carrier: A new player in inflammation. *Biochem J* (2011) 438:433–6. doi: 10.1042/BJ20111275

44. Tannahill G, Curtis A, Adamik J, Palsson-McDermott E, McGettrick A, Goel G, et al. Succinate is an inflammatory signal that induces IL-1β through HIF-1α. *Nature* (2013) 496:238–42. doi: 10.1038/nature11986

45. Chang C-I, Liao JC, Kuo L. Macrophage arginase promotes tumor cell growth and suppresses nitric oxide-mediated tumor cytotoxicity. *Cancer Res* (2001) 61:1100–6.

46. Rodriguez PC, Quiceno DG, Zabaleta J, Ortiz B, Zea AH, Piazuelo MB, et al. Arginase I production in the tumor microenvironment by mature myeloid cells inhibits T-cell receptor expression and antigen-specific T-cell responses. *Cancer Res* (2004) 64:5839–49. doi: 10.1158/0008-5472.CAN-04-0465

47. Van den Bossche J, O'Neill LA, Menon D. Macrophage immunometabolism: where are we (going)? *Trends Immunol* (2017) 38:395–406. doi: 10.1016/j.it.2017.03.001

48. Wilson JL, Nägele T, Linke M, Demel F, Fritsch SD, Mayr HK, et al. Inverse data-driven modeling and multiomics analysis reveals phgdh as a metabolic checkpoint of macrophage polarization and proliferation. *Cell Rep* (2020) 30:1542–1552. e1547. doi: 10.1016/j.celrep.2020.01.011

49. Weckwerth W, Wenzel K, Fiehn O. Process for the integrated extraction, identification and quantification of metabolites, proteins and RNA to reveal their co-regulation in biochemical networks. *Proteomics* (2004) 4:78–83. doi: 10.1002/pmic.200200500

50. Tsugawa H, Cajka T, Kind T, Ma Y, Higgins B, Ikeda K, et al. MS-DIAL: data-independent MS/MS deconvolution for comprehensive metabolome analysis. *Nat Methods* (2015) 12:523–6. doi: 10.1038/nmeth.3393

51. Neubauer S, Chu DB, Marx H, Sauer M, Hann S, Koellensperger G. LC-MS/MS-based analysis of coenzyme a and short-chain acyl-coenzyme a thioesters. *Analytical bioanaly Chem* (2015) 407:6681–8. doi: 10.1007/s00216-015-8825-9

52. Cox J, Mann M. MaxQuant enables high peptide identification rates, individualized ppb-range mass accuracies and proteome-wide protein quantification. *Nat Biotechnol* (2008) 26:1367–72. doi: 10.1038/nbt.1511

53. Cox J, Neuhauser N, Michalski A, Scheltema RA, Olsen JV, Mann M. Andromeda: a peptide search engine integrated into the MaxQuant environment. *J Proteome Res* (2011) 10:1794–805. doi: 10.1021/pr101065j

54. Tyanova S, Temu T, Sinitcyn P, Carlson A, Hein MY, Geiger T, et al. The Perseus computational platform for comprehensive analysis of (prote) omics data. *Nat Methods* (2016) 13:731–40. doi: 10.1038/nmeth.3901

55. Sun X, Weckwerth W. COVAIN: A toolbox for uni-and multivariate statistics, time-series and correlation network analysis and inverse estimation of the differential Jacobian from metabolomics covariance data. *Metabolomics* (2012) 8:81–93. doi: 10.1007/s11306-012-0399-3

56. Pang Z, Chong J, Zhou G, de Lima Morais DA, Chang L, Barrette M, et al. MetaboAnalyst 5.0: narrowing the gap between raw spectra and functional insights. *Nucleic Acids Res* (2021) 49:W388–96. doi: 10.1093/nar/gkab382

57. Shannon P, Markiel A, Ozier O, Baliga NS, Wang JT, Ramage D, et al. Cytoscape: a software environment for integrated models of biomolecular interaction networks. *Genome Res* (2003) 13:2498–504. doi: 10.1101/gr.1239303

58. Bindea G, Mlecnik B, Hackl H, Charoentong P, Tosolini M, Kirilovsky A, et al. ClueGO: a cytoscape plug-in to decipher functionally grouped gene ontology and pathway annotation networks. *Bioinformatics* (2009) 25:1091–3. doi: 10.1093/bioinformatics/btp101

59. Szklarczyk D, Morris JH, Cook H, Kuhn M, Wyder S, Simonovic M, et al. The STRING database in 2017: quality-controlled protein–protein association networks, made broadly accessible. *Nucleic Acids Res* (2017) 45:D362–68. doi: 10.1093/nar/gkw937

frontiers | Frontiers in Immunology

TYPE Original Research
PUBLISHED 24 October 2022
DOI 10.3389/fimmu.2022.982045

OPEN ACCESS

EDITED BY
Julie Decock,
Qatar Biomedical Research Institute, Qatar

REVIEWED BY
Anqun Chen,
Second Xiangya Hospital, Central South University, China
Wolfram Weckwerth,
University of Vienna, Austria

*CORRESPONDENCE
Quan Hong
hongquan@301hospital.com.cn

†These authors have contributed equally to this work

SPECIALTY SECTION
This article was submitted to Cancer Immunity and Immunotherapy, a section of the journal Frontiers in Immunology

RECEIVED 30 June 2022
ACCEPTED 10 October 2022
PUBLISHED 24 October 2022

CITATION
Geng X, Chi K, Liu C, Fu Z, Wang X, Meng L, Wang H, Cai G, Chen X and Hong Q (2022) Interaction of RARRES1 with ICAM1 modulates macrophages to suppress the progression of kidney renal clear cell carcinoma. *Front. Immunol.* 13:982045. doi: 10.3389/fimmu.2022.982045

Interaction of RARRES1 with ICAM1 modulates macrophages to suppress the progression of kidney renal clear cell carcinoma

Xiaodong Geng[1,2,3†], Kun Chi[1,2†], Chao Liu[1,2], Zhangning Fu[1,2], Xu Wang[1,2], Liangliang Meng[4], Hanfeng Wang[5], Guangyan Cai[1,2], Xiangmei Chen[1,2] and Quan Hong[1,2*]

[1]Department of Nephrology, First Medical Center of Chinese People's Liberation Army (PLA) General Hospital, Nephrology Institute of the Chinese People's Liberation Army, State Key Laboratory of Kidney Diseases, National Clinical Research Center for Kidney Diseases, Beijing, China, [2]Beijing Key Laboratory of Kidney Disease Research, Beijing, China, [3]Beidaihe Rehabilitation and Recuperation Center, Chinese People's Liberation Army Joint Logistics Support Force, Qinhuangdao, China, [4]Department of Radiology, First Medical Centre of Chinese People's Liberation Army (PLA) General Hospital, Beijing, China, [5]Department of Urology, Third Medical Center of Chinese People's Liberation Army (PLA) General Hospital, Beijing, China

Background: RARRES1 is a tumor suppressor protein, and its expression is suppressed in various tumor cells. However, whether it participates in the immune response in kidney renal clear cell carcinoma (KIRC) is unknown, and the defined mechanism is not clear. Therefore, the mechanism of RARRES1 in KIRC is worthy of investigation.

Methods: We analysed the expression and function of RARRES1 with The Cancer Genome Atlas (TCGA) database. The Kaplan–Meier curve was adopted to estimate survival. RARRES1-correlated genes were obtained from the UALCAN database and subjected to Gene Ontology (GO) enrichment and protein–protein interaction (PPI) network analyses. The correlation analysis between tumor-infiltrating immune cells and selected genes were performed with TIMER database. We also investigated the possible function of RARRES1 in KIRC by coculturing Caki-1 cells with THP-1 cells. Immunofluorescence assay was performed to study the RARRES1 expression in difference grade KIRC tissues.

Results: The expression of RARRES1 was negatively correlated with survival in KIRC patients. The GO biological process term most significantly enriched with the RARRES1-correlated genes was regulation of cell adhesion. ICAM1, which exhibited a relatively highest correlation with RARRES1, is positively correlated with the infiltration level of macrophages. RARRES1 could enhance the expression of ICAM1 in Caki-1 cells and then induce the activation of M1 THP-1 cells to decrease the viability and induce the apoptosis of Caki-1 cells.

10.3389/fimmu.2022.982045

Conclusion: RARRES1 plays an antitumor role by promoting ICAM1 expression and inducing the activation of M1 macrophages. We offer insights into the molecular mechanism of KIRC and reveal a potential therapeutic target.

KEYWORDS

kidney renal clear cell carcinoma, RARRES1, ICAM1, bioinformatic analyses, M1 macrophages

Introduction

The most common form of renal cancer is known as renal cell carcinoma (RCC). It represents over 90 percent of all renal cancer cases. RCC is an immunogenic tumor characterized by frequent invasion of tumor tissues by immune cells, rare spontaneous regression, and a clinical response to immunotherapy (1). The most aggressive RCC in adults is kidney renal clear cell carcinoma (KIRC) (2). Genetic aberrations and the tumor environment have been indicated to be associated with KIRC. Extensive studies have examined the mechanisms of relapse and metastasis, but the cause and pathogenesis of KIRC is still unknown. It is worth noting that the occurrence and development of KIRC reveal a correlation with its immune microenvironment (3). The characteristic of tumor microenvironment strongly influence disease biology and may influence the response rate to systemic therapy. Targeted immunotherapy is currently an option in first line treatment because KIRC is also considered an immunogenic tumour with high numbers of immune cells (4). Macrophage infiltration in KIRC is associated with prognosis (5). Macrophages are the regulators of tumor immunity and immunotherapy (6). Macrophages can be affected by different factors to polarize toward the M1 or M2 phenotype and thus affect tumor progression (7). It is necessary to unravel the causes and mechanisms to find biomarkers for diagnosis or personalized therapy of KIRC (8).

RARRES1 was described as a retinoid response gene in skin raft cultures and thought to be a transmembrane protein (9). RARRES1 is induced by retinoic acid and expressed in multiple tissues. Research has shown that RARRES1 inhibits tumor cell proliferation or invasion and induces apoptosis of tumor cells (10). RARRES1 has been shown to act as an invasion inhibitor in prostatic tumor cell lines (11). In inflammatory breast cancer, RARRES1 mediates the regulatory cancer invasion cells through the Axl pathway (12). RARRES1 has been described as a cell adhesion molecule that increases cell contact or reduces cell proliferation. Previously, downregulation of RARRES1 has been confirmed in some human cancers (13). RARRES1 is epigenetically silenced by promoter methylation, and its promoter is hypermethylated in prostate, nasopharyngeal, and gastric cancers (14). Hence, understanding the regulatory mechanism and molecular functions of RARRES1 may identify potential targets for the diagnosis and immunotherapy of KIRC.

Materials and methods

Clinical cohorts and RNA-Seq datasets

RNA-seq datasets, including information on the clinical cohorts, were searched from TCGA database (http://cancergenome.nih.gov/). 533 patients of KIRC and 72 controls were enrolled in this study. The clinical features of these data included patient gender, race, age and survival time.

Analysis of RNA-Seq data

Differential expression analysis and survival analysis of Kaplan–Meier(KM) curve were performed to compare the normal control group and KIRC patients using the UALCAN tool (http://ualcan.path.uab.edu/) (15). The bioinformatic analyses of RARRES1-correlated genes included Gene Ontology (GO) enrichment and protein–protein interaction (PPI) analyses with the Metascape analysis tool (http://metascape.org/) (16). All of these analytical tools can be accessed online.

Immune infiltration analysis

Tumor Immune Estimation Resource (TIMER; http://cistrome.shinyapps.io/timer/) (17) was adopted to carry out a comprehensive correlation analysis of RARRES1 expression with the features of tumor-infiltrating immunocytes (TILs) in KIRC. The "Gene module" of TIMER could visualize the correlation of gene expression with immune infiltration level in KIRC. The scatterplots will show the purity-corrected partial Superman's rho value (partial.cor) and statistical significance(P value). The integrated repository portal for tumor-immune system

interactions (TISIDB; http://cis.hku.hk/TISIDB) (18) was used to inspect tumor-immune system interactions for 28 TILs in human cancers. For each cancer type, the relative abundance of TILs were inferred by using gene set variation analysis (GSVA) based on gene expression profile. Spearman correlation analysis was used to assess the relations between RARRES1 and TILs in TISIDB. The correlations between RARRES1 expression and hub gene expression in KIRC were determined using Gene Expression Profiling Interactive Analysis (GEPIA; http://gepia.cancer-pku.cn) and was calculated by Pearson correlation coefficient.

Cell culture and Transwell assay

Both the human KIRC cell line Caki-1 and the human macrophage line THP-1 were purchased from American Type Culture Collection(ATCC company). THP-1 cells and Caki-1 cells were all cultured in Dulbecco's modified Eagle's medium (DMEM) (HyClone™) supplemented with 10% fetal bovine serum (FBS) (Gibco™) at 37°C with 5% CO_2 in a humidified incubator. To assess the interaction between macrophages and RCC cells, Caki-1 cells and THP-1 cells were co-cultured in a Transwell system (0.4 μm pore diamete, Corning Incorporation) in a 6-well plate for 24 h, allowing free diffusion of molecules between the two compartments but not cell translocation. THP-1 cells were seeded in the upper chamber of Transwell system and co-cultured with Caki-1 cells in the bottom chamber.

Induction and identification of macrophages

THP-1 cells were treated with 100 ng/mL PMA (#HY-18739, MCE) for 24 h every 2 days to induce differentiation into M0 macrophages. To induce M1 macrophage polarization, M0 macrophages were exposed to 20 ng/mL IFN-γ(#HY-p7025, MCE) and 100 ng/mL LPS (#HY-D1056, MCE) for 24 h. Cells were collected for qRT-PCR detection and western blot analysis. The markers of M0 macrophage (CD68) and M1 macrophage (CD86) were analyzed by western blot in THP-1 cell. And the markers of M1 macrophage(CD86) was also analyzed by qPCR method.

Lentivirus construction and cell infection

The full-length RARRES1 cDNA fragment was cloned into the lentiviral vector pReceiver-lv185 by Guangzhou FulenGen Co., Ltd; empty vector was regarded as negative control. The pReceiver-RARRES1 lentivirus was produced by 293T cells. Before cell transduction, Caki-1 cells digested into single cell suspension were inoculated into 6-well culture plates and cultured in cell culture incubator. Then, Caki-1 cells were infected with pReceiver-RARRES1 lentivirus(RARRES1-OE group) and empty vector(Vector group) when 70% to 80% confluent respectively; Caki-1 cells without any intervention served as a blank control(control group). Quantitative PCR was used to evaluate the mRNA expression level of RARRES1 and RARRES1 related-ICAM1 in Caki-1 cells.

RNA extraction and quantitative PCR

THP-1 cells (macrophages) or Caki-1 cells (RCC) were grown in 6-well plates. THP-1 cells were cultured for 24 h after being transfected with either control or siRNA-CD11b. Caki-1 cells transfected with control or siRNA-ICAM1 were cultured for another 24 h. TRIzol reagent purchased from Invitrogen Life Technologiesis was used to isolate total RNA from cells. A first-strand reverse transcription kit (Thermo Fisher, Carlsbad, CA) was used to synthesize complementary DNA, and SYBR Green dye mixture (Takara, Kusatsu, JPN) was used for qPCR with the following primers:

RARRES1, 5'-TGGCTTTCCTTGGAAGCTCT-3'(Forward) and 5'-AGGTTTTTCTTACCCACTGCCT-3'(Reverse);
ICAM1, 5'-ACGGAGCTCCCAGTCCTAAT-3' (Forward) and 5'-CTCCTTCTGGGGAAAGGCAG-3' (Reverse);
CD86, 5'-AGCTTTGCTTCTCTGCTGCTGTA-3' (Forward) and 5'-CAGCACCACTGGGGATCCATTT-3' (Reverse);
CD11b, 5'-CCCAATTGTGACCGCAAAGG-3'(Forward) and 5'-GGCAGCTTCATCCCGTACTT-3'(Reverse).

The siRNAs targeting human CD11b and ICAM1 and the NC siRNA (Si-CTRL) were purchased from RiboBio company. The oligonucleotide sequences were as follows:

si-CTRL (Nontargeting), 5'-UUCUCCGAACGUGUCACG UTT-3' (Forward) and 5'-ACGUGACACGUUCGGAGA ATT-3GUGACACGUU (Reverse);
siRNA-CD11b, 5'-AUCAAGAAGGCAAUGUCACUA-3' (Forward) and 5'-GUGACAUUGCCUUCUUGAUUG-3' (Reverse);
siRNA-ICAM1, 5'-UUGAAUAGCACAUUGGUUGGC-3' (Forward) and 5'-CAACCAAUGUGCUAUUCAAAC-3' (Reverse)

ELISA detection of ICAM1

Twenty-four hours after M1 THP-1 cells and Caki-1 cells were cocultured in the Transwell system, the concentration of

ICAM1 in the cell culture supernatant was determined by ELISA following the kit instructions (#ab100688, Abcam).

Co-Immunoprecipitation

THP-1 cells treated in three different ways (THP-1 cells only, THP-1 cells cocultured with Caki-1 cells in transwell system after 24h and THP-1 cells cocultured with RARRES1-overexpression (OE) Caki-1 cells in transwell system after 24h were collected separately. Co-IP assays were carried out using the Pierce CoImmunoprecipitation(Co-IP) Kit (#26149,Thermo Scientific™,MA, USA) according to the manufacture's instruction. The antibodies used were as follows: IP: (Mac-1) CD11b/Integrin αM Polyclonal antibody(#21851-1-AP; Proteintech). The Mac-1 protein expression of THP-1 cells in three groups were tested by western blot analysis. IgG group was used as a negative control. Extracted cell lysates before adding antibodies (imput) were also used as a control for target protein-GAPDH detection.

Immunofluorescent staining

The studies involving human participants were approved by the PLA General Hospital ethics committee (Approval Number S2015-061-01). The patients had provided informed consent when their tissues were stored in the tissue bank. The KIRC tissues which fixed in formalin and made into paraffin embedded tissue blocks were obtained form the tissue bank of PLA General Hospital. Immunofluorescent (IF) staining was performed in KIRC tissues. Briefly, The slices were incubated with indicated primary anti-RARRES1(#MA5-26247, Invitrogen), anti-ICAM-1 (#10831-1-AP, Proteintech) and anti-CD86(#ab239075, Abcam) at 4°C overnight and then incubated with Cy3-conjugated goat anti-rabbit IgG(#A0516, Beytime Biotechnology) secondary antibody or FITC-conjugated goat anti-mouse IgG(#A0568, Beytime Biotechnology) secondary antibody. The nucleus was stained with DAPI and signals were observed using confocal fluorescence microscopy (Olympus). The evaluation was done *via* Image J software.

Cell migration assay

Transwell migration chambers (8.0 μm pore diamete, Corning Incorporated) were used to evaluated the migratory capacity of M1 THP-1 cells. The M1 THP-1 cells and Caki-1 cells were cultured in DMEM medium (HyClone™) supplemented with 10% FBS(Gibco™). M1 THP-1 cells were seed in the upper chambers at 2×10^5 cells/well, and Caki-1 cells were grown in the lower chambers at 15×10^5 cells/well. After incubated for 24h at 37°C in an incubator, the upper chamber was removed, and the cells were fixed with 4% paraformaldehyde. We used a cotton swab to remove cells on the upper surface of the filter membrane. 0.1% crystal violet (#G106, Solarbio) was used to stain the cells migrated to the lower surface. Image J software was used to record migrated cells. Cells were counted and averaged in 5 random fields.

Cell viability assay

Caki-1 cells were cultured in a 96-well plate (2000 cells/well) for 12 h and then cocultured with or without M1 THP-1 cells in the Transwell system for anther 24 h. The culture medium added 10% CCK-8 solution(#CK04, Dojindo) and incubated in 37°C temperature. Cell viability was quantified by evaluating the OD450 with a microplate reader.

Western blot analysis

Total protein extracted from cells were used RIPA buffer. Proteins were separated by 10% SDS-PAGE and then transferred to a PVDF membrane. After blocking by 5% skim milk for one hour, the membrane was incubated with an anti-RARRES1(#MA5-26247, Invitrogen), anti-CD86(#ab239075, Abcam), anti-CD68 (#ab213363, Abcam) and anti-cleaved caspase-3 primary antibody (#ab2302, Abcam). HRG-tagged anti-rabbit IgG (#ab205718, Abcam) was used as the secondary antibody. Immunoreactive bands were detected with the Western blot reagent ECL and the gray values were analyzed with ImageJ software.

Statistical analysis

UALCAN and GEPIA gene expression data were analyzed using Student's t test. Spearman's correlation analysis was used for evaluation of correlation analysis. Database-derived tools were applied to all statistical tests. Statistical analysis was performed with GraphPad Prism 8.0 (GraphPad Software Inc., San Diego, CA, USA). The results are expressed as the mean ± standard deviation of at least 3 independent experiments. One-way ANOVA was performed with the Bonferroni method for multiple comparisons. The t test was used for comparisons between two groups.

Results

RARRES1 was related to the prognosis of KIRC

We analyzed survival rates by the KM curves, which indicated that RARRES1 expression was closely related to

survival time in KIRC patients and that lower RARRES1 expression implied a longer survival time for patients. However, there was no correlation between RARRES1 expression and survival time in KIRP or KICH patients (P>0.05) (Figure 1A). To analyze RARRES1 expression in subgroups, we divided KIRC patients stratified by RARRES1 expression into subgroups based on age, race, sex, pathological grade, and tumor stage. The expression level of RARRES1 was significantly higher in male compared to female patients (p<0.01; Figure 1B). The expression level of RARRES1 in the subgroup of individuals with stage 1 tumors was significantly lower than that in the stage 3/4 subgroups, and the RARRES1 expression level in the stage 2 subgroup was also significantly lower than that in the stage 3 and stage 4 subgroups (p<0.05) (Figure 1C. The expression of RARRES1 was significantly lower in the tumor grade 1 subgroup than in the normal subgroup and the tumor grade 2/3/4 subgroup (P<0.001). In addition, the RARRES1 expression level was significantly lower in the tumor grade 2 and 3 subgroups than in the tumor grade 4 subgroup (Figure 1D). There was no significant difference in RARRES1 expression among the normal control, Caucasian, African-American and Asian populations (p>0.05). (Figure 1E). Patients were separated into four subgroups by age with a 20-year interval, and there was no significant difference among the age 21-40, 41-60, 61-80 and 81-100 subgroups (p>0.05) (Figure 1F). DNA methylation is an epigenetic regulation mechanism involved in gene transcription and tissue development. The methylation level of the RARRES1 gene was decreased in KIRC tissue samples (p<0.0001) (Figure 1G).

Regulation of cell adhesion was the GO biological process most significantly enriched with genes related to RARRES1

As gene regulatory networks suggest genetic risk factors that have functional relationships, we studied the regulatory factors of RARRES1 in KIRC. Figure 2A shows the genes highly coexpressed with RARRES1; 164 genes were positively correlated with RARRES1(dark red dots), and 120 genes were negatively correlated with RARRES1(dark green dots). After that, we used the Metascape analysis tool to analyze RARRES1 and the 284 related genes and found that the main enriched GO biological processes were regulation of cell adhesion, protein maturation, negative regulation of hydrolase activity, negative regulation of response to external stimuli, protein hydroxylation, and positive regulation of cell migration (Figure 2B). A similar effect was seen in PPI networks identified by functional cluster analysis (Figures 2C, D). The GO biological process most significantly enriched with genes related to RARRES1 was regulation of cell adhesion. It is well known that cell adhesion is the first step in cancer metastasis and invasion. Twenty-six genes were included in the GO biological process regulation of cell adhesion: ADA, BCL2, ICAM1 and so on.

Eight hub genes overlapped between the GO term regulation of cell adhesion and immune-related genes

A total of 1640 immune-related genes (IRGs) were downloaded from the ImmPort database. By overlapping these IRGs with the 26 genes involved in the regulation of cell adhesion, which was the GO biological process most significantly enriched with genes related to RARRES1, we finally identified 8 common genes: CALR, ICAM1, CMTM7, CX3CL1, SAA1, PLAUR, IL23A, and IL20RB (Figure 3A). After that, the UALCAN database was used to analyze overall survival rates based on these 8 hub genes, and we found that high expression of these 8 hub genes are associated with poor prognosis(Figure 3B).

ICAM1 had a relatively high correlation with RARRES1 among the 8 hub genes

According to TIMER, a web tool for analyzing immune cell infiltration in TCGA data, we discovered that RARRES1 expression had a negative correlation with tumor purity in KIRC and strong positive correlations with the infiltration of B cells and macrophages. The expression level of RARRES1 was positively correlated with the infiltration levels of B cells (r=0.247, P=8.34e-08), macrophages (r=0.258, P=3.08e-08), neutrophils (r=0.204, P=1.14e-05) and DCs (r=0.215, P=3.55e-06) in KIRC tissues (Figure 4A). In addition, we found that RARRES1 expression was significantly related to the abundance of 28 types of TILs in heterogeneous human cancers (Figure 4B). Regarding B cells and macrophages, RARRES1 expression was significantly related to the numbers of activated B cells Act_B cells; rho=0.348, p<0.001), immature B cells (Imm_B cells; rho=0.323, p<0.001), memory B cells (Mem_B cells; rho=0.304, p<0.001) and macrophages (rho=0.537, p<0.001) (Figure 4C). Among these cells, RARRES1 had the highest correlation with macrophages. We further analyzed the correlations between macrophage infiltration and the expression of the 8 hub genes related to RARRES1. As shown in Table 1, the expression levels of CMTM7, PLAUR, IL23A, and ICAM1 in KIRC tissues were significantly positively correlated with the infiltration of macrophages (p<0.05). We next analyzed the correlations between RARRES1 expression and CMTM7, PLAUR, IL23A, and ICAM1 expression with GEPIA. There was a relatively highest correlation (Spearman correlation coefficient=0.38) between RARRES1 and ICAM1 (CMTM7 = 0.28, PLAUR=0.3, and IL23A=0.31) (Figure 4D).

10.3389/fimmu.2022.982045

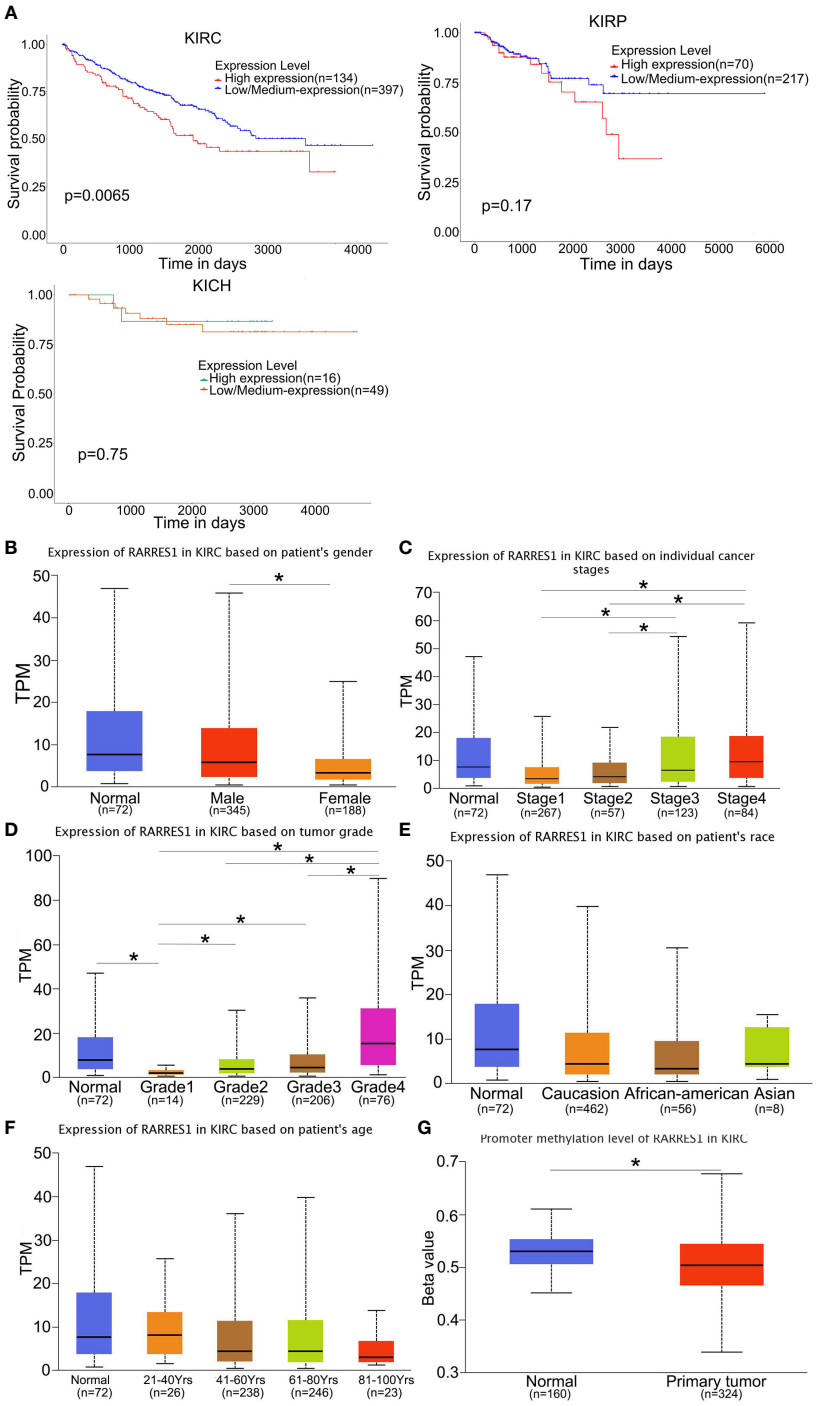

FIGURE 1
RARRES1 expression in KIRC. **(A)** The effect of the RARRES1 expression level on KIRC, KIRP and KICH patient survival was assessed by Kaplan–Meier survival analysis. **(B–G)** The differential expression of RARRES1 in KIRC patients. RARRES1 expression in different subgroups. **(B)** The expression of RARRES1 in male patients was significantly different from that in female patients (p=0.00144). **(C)** The RARRES1 expression level in the stage 1 subgroup was significantly different from those in the stage 3 (p=0.037) and stage 4 (p=0.0017) subgroups. The RARRES1 expression level in the stage 2 subgroup was significantly different from those in the stage 3 (p=0.039) and stage 4 (p=0.0056) subgroups. **(D)** RARRES1 expression in different tumor grades. **(E)** Expression of RARRES1 in KIRC based on race. RARRES1 expression in normal controls was not significantly different from that in Caucasian, African-American and Asian patients (p>0.05). **(F)** Expression of RARRES1 in KIRC based on age. There was no significant difference in RARRES1 expression among the groups (p>0.05). **(G)** The promoter methylation level in the RARRES1 gene was significantly decreased compared with that in normal controls (p < 0.0001) (TPM, transcripts per million). *p<0.05.

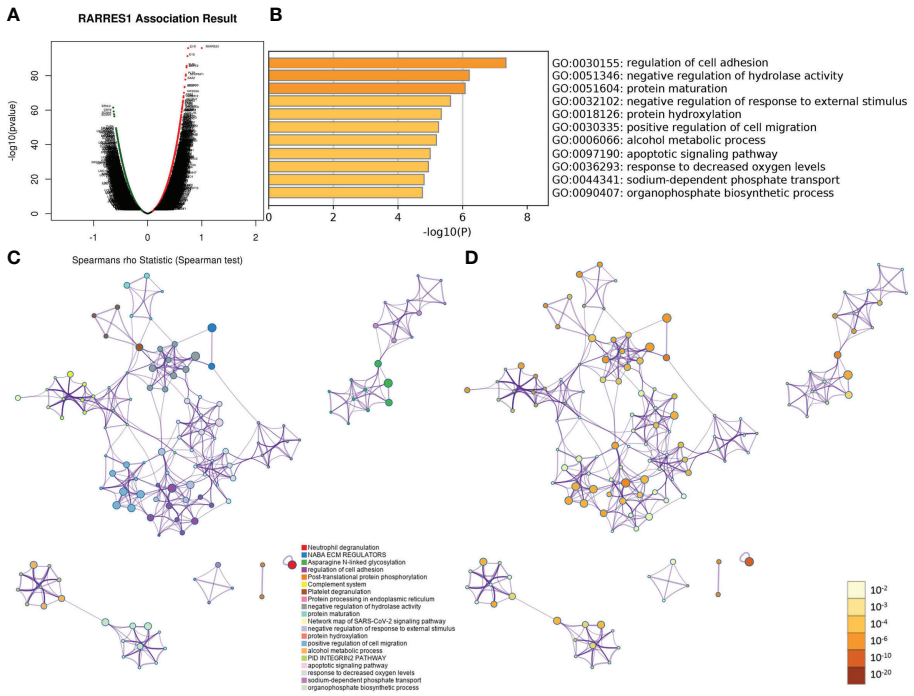

FIGURE 2
GO and PPI analyses of RARRES1-correlated genes. **(A)** The genes highly correlated with RARRES1 identified by Pearson correlation analysis in the KIRC cohort. **(B)** Main GO biological processes of all 284 genes correlated with RARRES1. **(C)** The PPI networks determined by functional cluster analysis. The different colors represent different functional clusters. **(D)** The PPI networks determined by functional cluster analysis. The different colors represent different P values. GO, Gene Ontology. PPI, protein–protein interaction.

ICAM1 was positively correlated with macrophage infiltration in KIRC

Furthermore, we analyzed the ICAM1 expression in KIRC using the UALCAN database. Compared with normal controls group, ICAM1 expression was significantly increased in KIRC patients (Figure 5A). ICAM1 was highly correlated with patient survival, as shown by the KM curves (P<0.001) (Figure 3B). The ICAM1 expression was negatively correlated with tumor purity in KIRC and positively correlated with the infiltration levels of B cells (r=0.339, P=8.28e-14), CD8+ T cells (r=0.174, P=2.57e-04), CD4+ T cells (r=0.182, P=8.56e-05), macrophages (r=0.201, P=1.76e-05), neutrophils (r=0.444, P=1.67e-23), and DCs (r=0.385, P=1.59e-17) in KIRC tissues (Figure 5B). These results also indicated that ICAM1 was closely related to macrophage infiltration in KIRC.

ICAM1 expression and interaction with Mac-1 were induced by RARRES1 overexpression

GEPIA analysis indicated a positive correlation between RARRES1 and ICAM1 expression. To investigate whether RARRES1 overexpression can induce the expression of ICAM1 in RCC (Caki-1) cells, we generated RARRES1 overexpression lentivirus to infect RCC cells. Compared with control cells, RARRES1-overexpressing RCC cells showed significantly upregulated expression of RARRES1 and ICAM1 (Figures 6A, B). It is commonly considered that M1 macrophages contribute to the promotion of inflammation and tumor suppression. To investigate the interaction between M1 macrophages and renal carcinoma cells, THP-1 cells were induced to differentiate with IFN-γ+LPS, which act as activators of the M1 macrophage phenotype. IFN-γ+LPS stimulation increased the expression of CD86 at the mRNA and protein levels, suggesting that the polarization of THP-1 cells toward M1-like macrophages was successfully induced (Figure 6C). Given that Mac-1 (CD11b/CD18), mainly expressed in macrophages, is the receptor for ICAM1, to study whether RARRES1-overexpressing RCC cells can enhance the binding of ICAM1 to Mac-1 in macrophages, we cocultured RARRES1-overexpressing RCC cells and M1 macrophages in a Transwell system. The mRNA expression level of ICAM1 and the concentration of ICAM1 in cell supernatants were significantly increased when RARRES1 was overexpressed in RCC cells (Figures 6D, E). Next, we performed a Co-IP assay to examine the binding of ICAM1 and Mac-1 in macrophages.We found that the expression of Mac-1 in THP-1

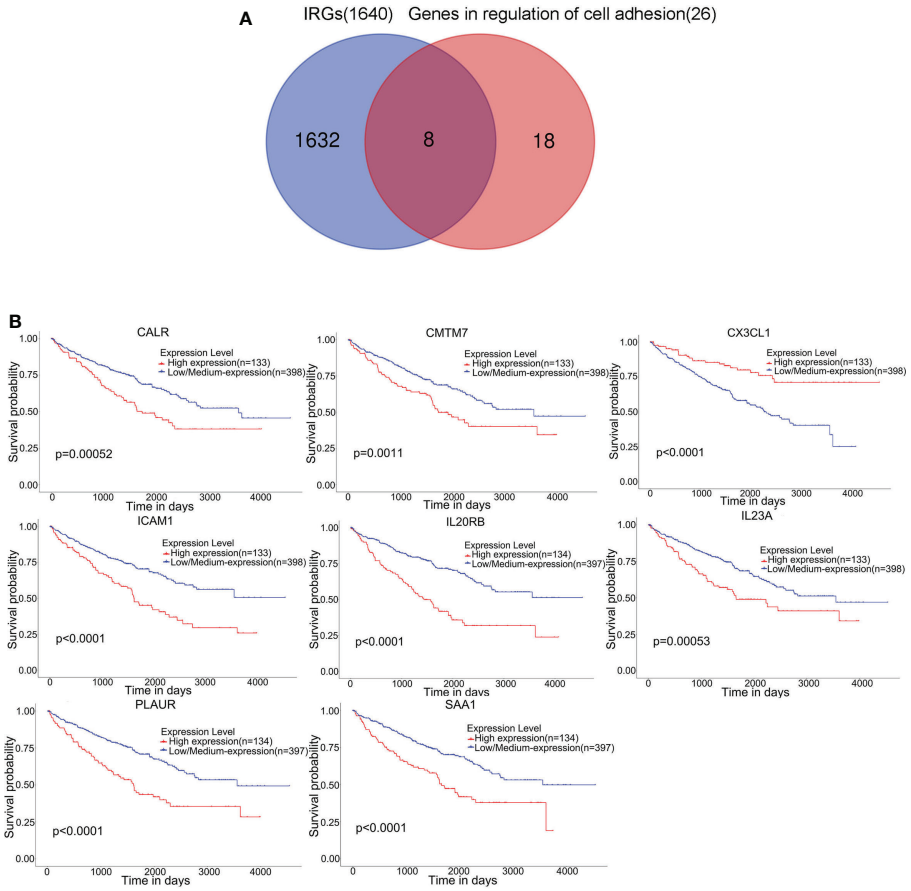

FIGURE 3
Eight hub genes were found in the regulation of cell adhesion GO term and among immune-related genes (IRGs). **(A)** Identification of 8 common genes between the GO biological process regulation of cell adhesion and the set of immune-related genes (IRGs). The different colored regions represent different datasets. The overlapping region indicates overlapping genes. **(B)** Kaplan–Meier survival analysis based on the expression of these 8 hub genes in KIRC was performed with the UALCAN database.

cells did not change when THP-1 cells co-cultured with or without Caki-1 cells and RARRES1-OE Caki-1 cells. But the binding of ICAM1 with Mac-1 on THP-1 cells was increased with after RARRES1 was overexpressed in Caki-1 cells. These results demonstrated that overexpression of RARRES1 in RCC cells promoted the binding of ICAM1 and Mac-1 (Figure 6F).

Validated the expression of RARRES1, ICAM1 and CD86 in KIRC tumor tissue

We also used KIRC samples to verify the correlation between RARRES1, ICAM1 and CD86. we performed immunofluorescence assay with Grade 4 KIRC tissues and Grade 2 KIRC tissues to study the expression difference. We found that the fluorescent signals of RARRES1 were stronger in Grade 4 KIRC tissues. Higher RARRES1 were accompanied by higher ICAM1 staining and higher CD86 staining. On the contrary, lower RARRES1 were accompanied by lower ICAM1 staining and lower CD86 staining. This is consistent with our above results which indicated that higher expression of RARRES1 may lead to more M1 macrophages infiltration (Figure 7).

Knockdown of ICAM1 or Mac-1 decreased the migration potential of macrophages induced by RARRES1 overexpression

To examine whether the Mac-1 and ICAM1 interaction affected the migration potential of macrophages after RARRES1 was overexpressed in RCC cells, we transfected siRNA-CD11b into macrophages and transfected siRNA-ICAM1 into RCC cells. As shown in Figures 8A, B, the mRNA and protein expression levels of CD11b in macrophages and ICAM1 in RCC cells were decreased after siRNA transfection. We assessed the migration

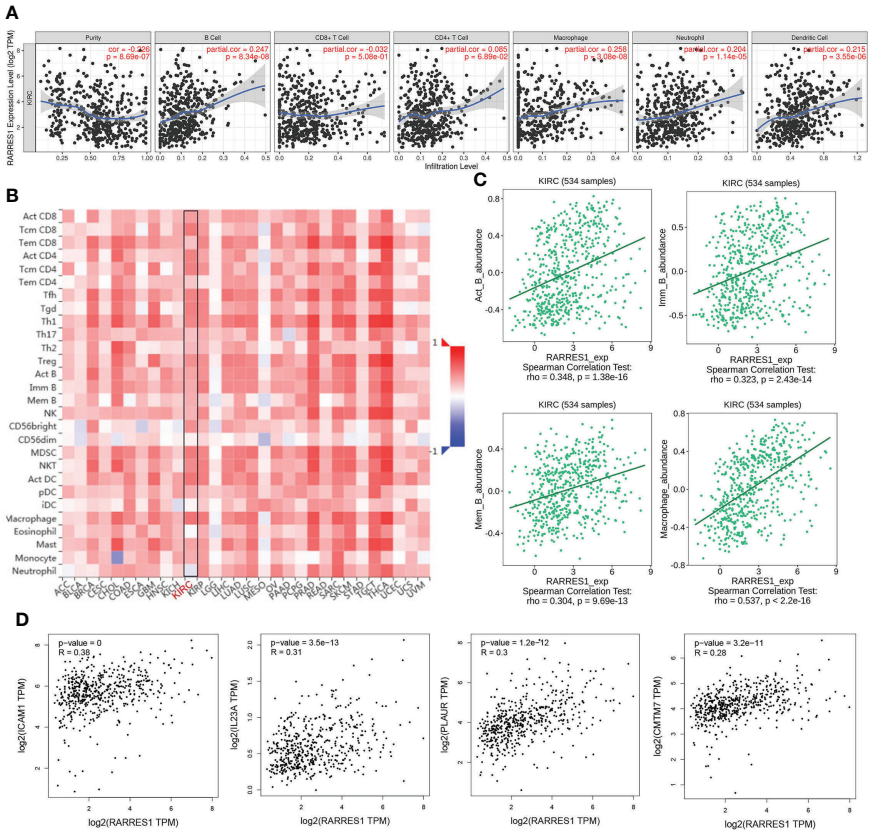

FIGURE 4
Analysis of associations between immune infiltration and the expression of RARRES1 and the 8 hub genes in KIRC. **(A)** Correlation of RARRES1 expression with the numbers of 6 tumor-infiltrating immune cells in KIRC using TIMER. **(B)** Relations between the expression of RARRES1 and the abundance of 28 types of TILs across heterogeneous human cancers. **(C)** RARRES1 expression was significantly correlated with the abundance of activated B cells (Act_B cells; rho=0.348, p<0.001), immature B cells (Imm_B cells; rho=0.323, p<0.001), memory B cells (Mem_B cells; rho=0.304, p<0.001), and macrophages (rho=0.537, p<0.001). **(D)** Correlations between the mRNA expression level of RARRES1 and those of CMTM7, PLAUR, IL23A, and ICAM1 in KIRC were determined using GEPIA.

ability of macrophages by coculture with RCC cells. The migration assay showed that the number of migrated macrophages was significantly increased after coculture with RARRES1-overexpressing RCC cells for 24 h, which demonstrated that RARRES1 overexpression (OE) in RCC cells promoted the migration of macrophages. Furthermore, after coculture with ICAM1-overexpressing (OE) RCC cells for 24 h, the number of migrated macrophages was significantly increased. Then, we evaluated the migration of macrophages after Mac-1 or ICAM1 was inhibited. The number of migrated macrophages was greatly

TABLE 1 Gene expression positively correlates with the infiltration level of macrophages in KIRC tissues.

variable	GENE	partial.cor	P value
Macrophage	ICAM1	0.201318588	1.76E-05
	CMTM7	0.328467814	9.91E-13
	PLAUR	0.271638741	5.11E-09
	IL23A	0.175304878	0.000192199
	CX3CL1	0.074709859	0.114313278
	CALR	0.063240745	0.181499461
	IL20RB	0.039214584	0.407661468
	SAA1	0.029919598	0.527615135

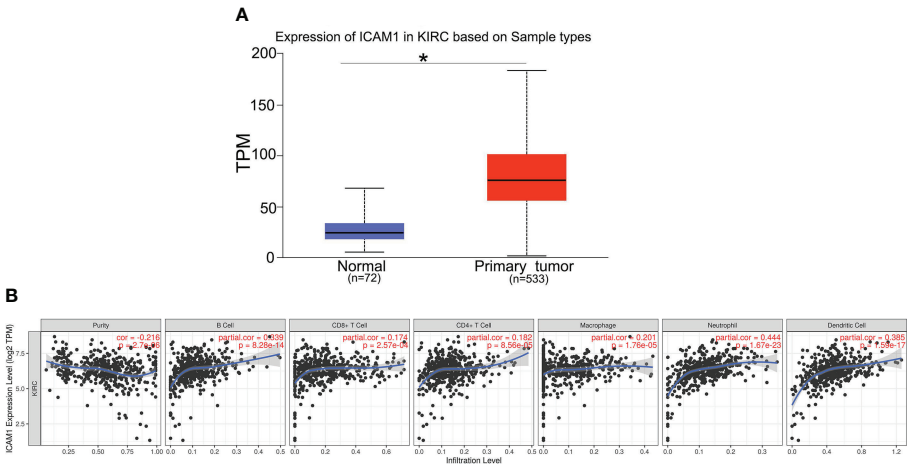

FIGURE 5
Expression of ICAM1 in KIRC patients. **(A)** ICAM1 was upregulated in primary tumors ($p < 0.001$). **(B)** Correlation analysis of ICAM1 expression and infiltration levels of immune cells in KIRC tissues using TIMER. ICAM1 expression in KIRC tissues was negatively correlated with tumor purity and positively correlated with the infiltration levels of B cells, CD8+ T cells, CD4+ T cells, macrophages, neutrophils, and dendritic cells. (KIRC, kidney renal clear cell carcinoma; TPM, transcripts per million.). *p<0.05.

reduced as CD11b was silenced in macrophages or ICAM1 was silenced in RCC cells (p<0.05) (Figure 8C). Taken together, these findings indicated that blockade of Mac-1 in macrophages or ICAM1 in RCC cells decreased macrophage migration induced by RARRES1-OE.

M1-Like macrophages reduced the viability of renal carcinoma cells and induce apoptosis

We cocultured M1 macrophages with RCC cells to determine whether overexpression of RARRES1 can induce M1 macrophage polarization and mediate resistance to tumors. We aimed to explicit the effect of M1 type macrophages on the viability of cancer cells. The CCK-8 assay results showed that M1 macrophages significantly decreased the viability of renal carcinoma cells after being cocultured with RARRES1-overexpressing RCC cells (Figure 9A). In addition, the apoptosis rate of RCC cells was increased after M1 macrophages were cocultured with RARRES1-overexpressing RCC cells. In the RARRES1-overexpressing RCC cell group, the protein expression level of cleaved caspase-3 was significantly increased after co-culture with M1 macrophages compared with that in the group of RCC cells without RARRES1 overexpression (Figure 9B).

Discussion

KIRC is the most common renal tumor. Genetic alterations or epigenetic regulation are involved in the progression and tumor environment of KIRC (19). RARRES1 acted as an invasion suppressor in prostate cancer and triple-negative breast cancer (20, 21). In our research, we assessed the prognostic value of RARRES1 in KIRC and observed that RARRES1 expression was negatively correlated with survival time. In our vitro experiments, we showed that RARRES1 exerts anti-tumor effect on tumor cells through macrophages. This seems inconsistent with KM curve of RARRES1 expression in KIRC. The reason maybe that tumors are abnormal organs composed of multiple cell types and extracellular matrix rather than simply clones of cancer cells (22). In our research, high expression of RARRES1 may indicate high degree of tumor malignancy and RARRES1 is recruiting more macrophages to suppress tumor. But the tumor microenvironment is complex, the tumor suppressor effects of RARRES1 may fail to counteract malignant tumor. These results provide insight into the influence of RARRES1 expression on the disease progression of KIRC through macrophage activation. We sought to determine the mechanism by which RARRES1 exerts a tumor-suppressive effect in KIRC.

Functional enrichment analysis demonstrated that the GO biological process most significantly enriched with genes related to RARRES1 was regulation of cell adhesion. Inflammation as a basic physiological process is a hallmark of various tumors (23). Cancer-associated inflammation involves reciprocal autocrine and paracrine communication among malignant and nonmalignant cells through chemokines, cytokines and prostaglandins. Inflammatory tumor environment combines with genetic alterations that ultimately lead to tumor progression and metastasis (24). Cell adhesion mediates cell–cell crosstalk and exerts an important effect on the inflammatory

10.3389/fimmu.2022.982045

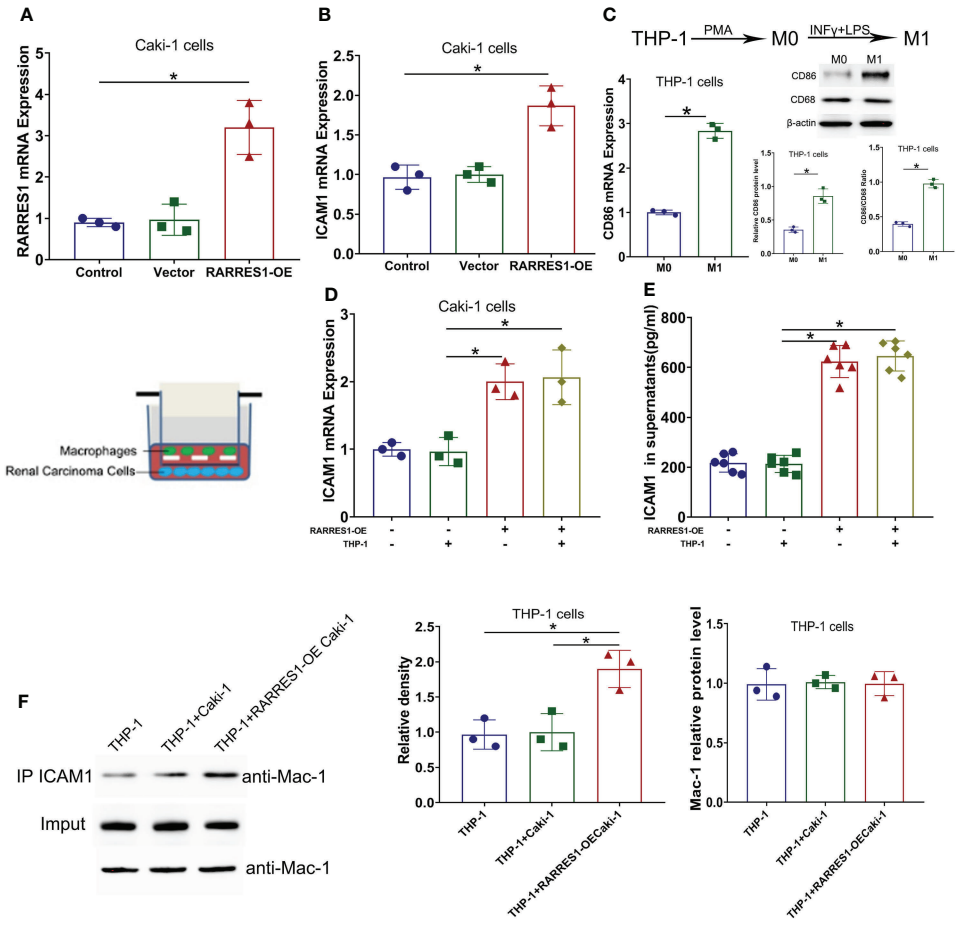

FIGURE 6
ICAM1 expression and interaction with Mac-1 were induced by RARRES1 overexpression. **(A, B)** Relative RARRES1 **(A)** and ICAM1 **(B)** mRNA expression in renal carcinoma cells, as measured by qPCR after transfection. RARRES1 and ICAM1 were significantly upregulated in the RARRES1-OE group; *p < 0.05 compared to the vector group; n = 3 in each group. **(C)** CD86 mRNA and protein expression in THP-1 cells after stimulation with IFN-γ. *p < 0.05 compared to the THP-1 only group. **(D)** ICAM1 mRNA expression in RCC cells cocultured with macrophages. Coculture of RARRES1-overexpressing RCC cells with macrophages induced evident upregulation of ICAM1 in RCC cells. *p < 0.05 **(E)** The level of ICAM1 in cell supernatants was measured by ELISA and was significantly increased after RARRES1 overexpression in RCC cells. *p < 0.05 **(F)** The Co-IP assay showed that overexpression of RARRES1 in RCC cells significantly promoted the interaction of ICAM1 and Mac-1. *p < 0.05.

response. Intercellular adhesion molecule 1 (ICAM1) is regarded as a cell surface glycoprotein which is in the immunoglobulin superfamily that mediates adherence-dependent interactions between cells (25). Different expression levels of ICAM1 have been found in various malignant tumors. In this study, we found that ICAM1 is significantly upregulated in KIRC. ICAM1 can also regulate immune cell-mediated tumor cytotoxicity, thereby improving the prognosis of patients with certain tumors, such as melanoma and oral squamous cell carcinoma (26). Several articles have suggested that patients with ICAM1-positive tumor cells have better clinical outcomes in breast, colorectal, and gastric cancers (27). We analyzed the correlation between RARRES1 and ICAM1 expression. GEPIA analysis indicated that there was a relatively highest correlation between RARRES1 and ICAM1. Thus, we hypothesized that RARRES1 overexpression can upregulate the expression of ICAM1 and inhibit tumorigenesis. In addition, ICAM1 is an adhesion receptor that is best known for regulating immune cell recruitment (28).

Our study reveals that overexpression of RARRES1 can promote ICAM1 expression in RCC cells. In addition, we found that ICAM1 expression was negatively correlated with tumor purity in KIRC and positively correlated with the infiltration level of macrophages in KIRC. Macrophage antigen-1 (Mac-1, CD11b/CD18, CR3), a β2 integrin expressed on macrophages, is a receptor for ICAM1 (29). KIRC is a highly immunogenic tumor type whose tumor cells generate an immunosuppressive environment through multiple immunosuppressive mechanisms. KIRC tumors are surrounded by many inflammatory cells, such as T cells, NK cells, and

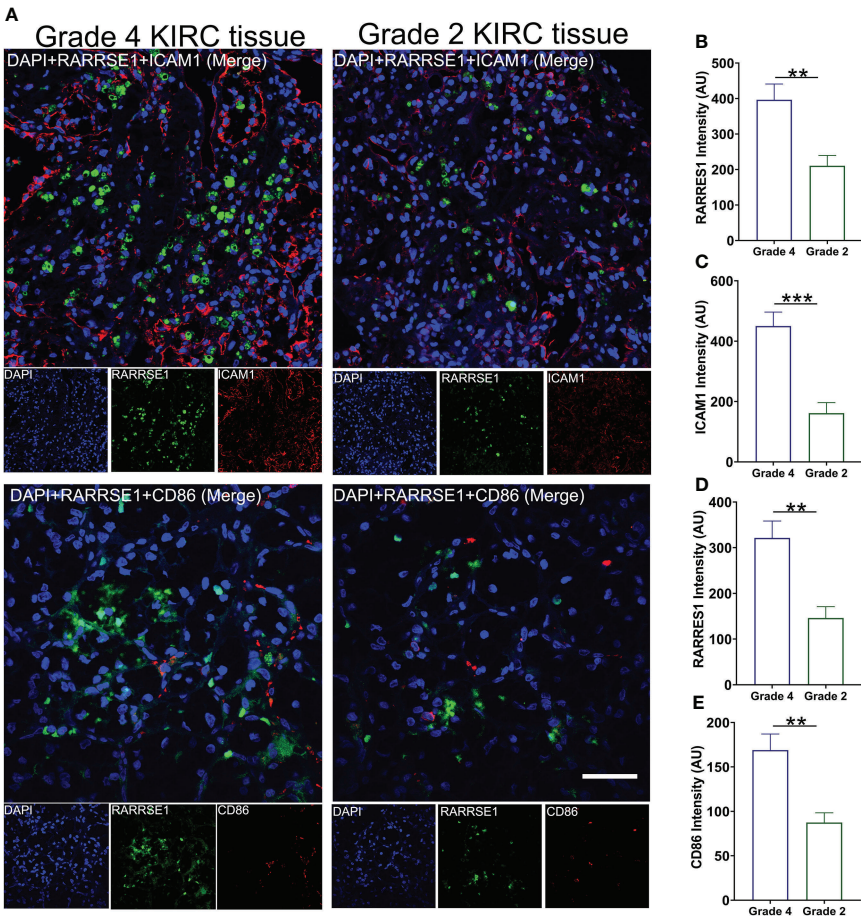

FIGURE 7
Validate the expression of RARRES1, ICAM1 and CD86 in KIRC tumor tissue. **(A)** The immunofluorescence staining of RARRES1, ICAM1 and CD86 in Grade 4 and Grade 2 KIRC samples (Scale bar, 50 μm). Fluorescence intensity of RARRES1 **(B)** combine with ICAM1 **(C)** in Grade 4 and 2 KIRC tissue groups. Fluorescence intensity of RARRES1 **(D)** combine with CD86 **(E)** in Grade 4 and 2 KIRC tissue groups. n = 3 in each group; $^{**}p < 0.01$,$^{***}p < 0.001$.

macrophages (30). This observation could help to design new clinical trials for patients undergoing immunotherapy. Depending on the patterns of M1 and M2 polarization, macrophages probably play either a tumor-promoting role or a antitumor role (31). In RCC cells, M1 macrophage markers are expressed alongside M2 markers in tumor-Associated macrophages(TAM), suggesting that some TAMs can exhibit hybrid phenotypes in some cancers (32). M1-like macrophages are essential tumor suppressor cells that initially act in the inhibition of tumor cell growth in the tumor microenvironment (33).

For the application of novel immunotherapy, macrophage-based therapies could augment macrophage functionalities with antitumor activity (34). We found that both ICAM1 expression in RCC cells and Mac-1 expression in M1 macrophages were upregulated after RARRES1-overexpressing RCC cells were cocultured with macrophages. In addition, RARRES1 overexpression in renal carcinoma cells enhanced the migration potential of M1 macrophages. Blocking Mac-1 in M1 macrophages or ICAM1 in RCC decreased RARRES1-OE-induced M1 macrophage migration. We showed that M1 macrophages more significantly decreased the viability of RARRES1-overexpressing renal carcinoma cells and increased the apoptosis rate of renal carcinoma cells. Collectively, these results indicate that M1 type macrophages perform antitumor functions by decreasing the viability of renal carcinoma cells and inducing their apoptosis. Our results indicated interaction of RARRES1 with ICAM1 modulating macrophages may be a new target for immunotherapy of kidney renal clear cell carcinoma.

In summary, RARRES1 expression is strongly related to cancer progression, survival rate and immune invasion in KIRC patients. According to the bioinformatics analysis and preliminary validation experiments, we suggest that the antitumor effect of RARRES1 is achieved by promoting the expression of ICAM1 and inducing the activation of M1 macrophages. This study offers

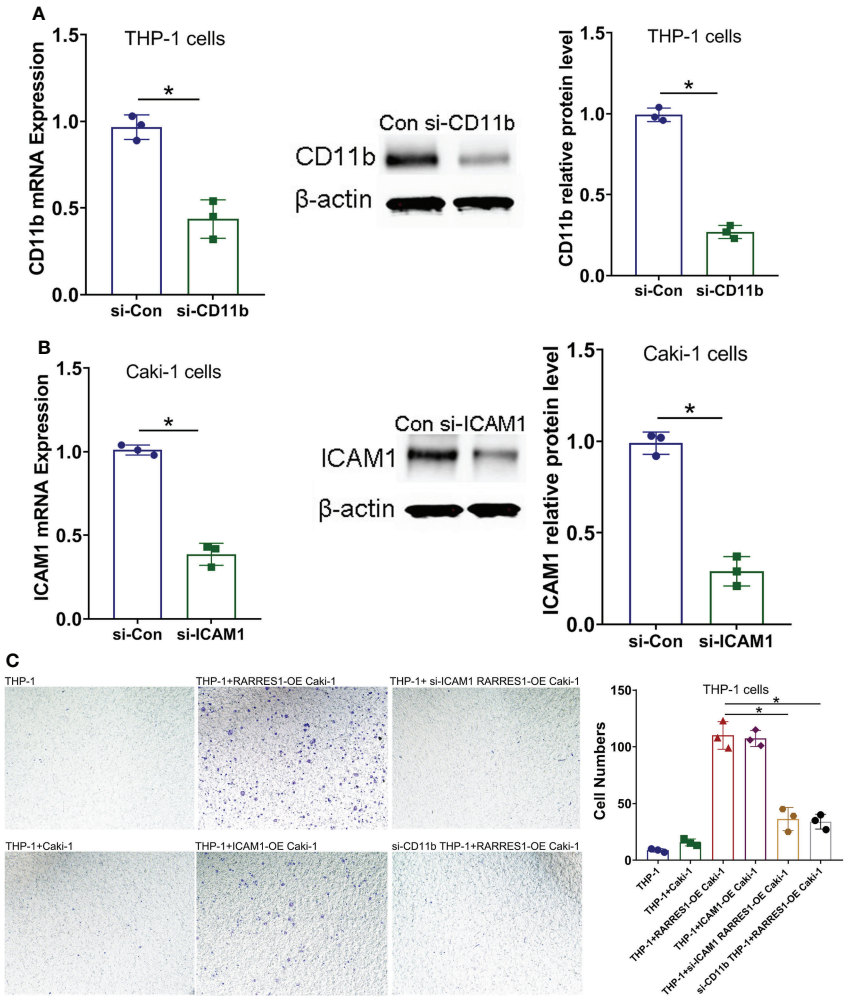

FIGURE 8
Blockade of Mac-1 or ICAM1 decreases the migration potential of macrophages. **(A, B)** The effects of siRNA transfection on Mac-1 (CD11b) and ICAM1 silencing were confirmed by qPCR and Western blot analysis. **(C)** Blockade of Mac-1 (CD11b) in macrophages or ICAM1 in RCC cells decreased RARRES1-OE-induced macrophage migration. The migration potential of macrophages (THP-1 cells) cocultured with renal carcinoma cells (Caki-1) was examined using a Transwell assay (scale bars: 100 μm). *p < 0.05.

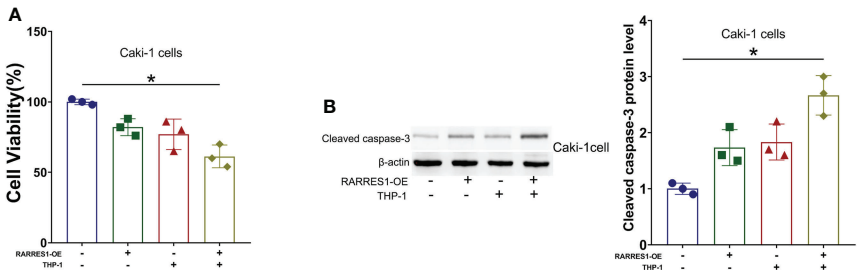

FIGURE 9
RARRES1-overexpressing RCC cell-induced M1 macrophages reduce the viability, induce the apoptosis and suppress the proliferation of renal carcinoma cells. **(A)** Cell viability was evaluated by a CCK-8 assay. **(B)** The level of an apoptosis-related protein (cleaved caspase-3) was measured by Western blot analysis. *p < 0.05.

promising insights for subsequent research to elucidate the molecular pathogenesis of KIRC.

Data availability statement

The datasets presented in this study can be found in online repositories. The names of the repository/repositories and accession numbers can be found within the article/Supplementary Materials.

Ethics statement

The studies involving human participants were reviewed and approved by PLA General Hospital ethics committee. The patients/participants provided their written informed consent to participate in this study. The animal study was reviewed and approved by the Ethics Committee for the Use of Animals of PLA General Hospital.

Author contributions

QH, GC, and XC conceived and designed the experiments. XG, KC, CL, ZF and HW performed the experiments. XW and LM analyzed the data. XG and KC wrote the manuscript. QH revised the manuscript. QH provided funding. All authors contributed to the article and approved the submitted version.

Funding

Project supported by: Fostering Fund of Chinese PLA General Hospital for National Distinguished Young Scholar Science Fund (2019-JQPY-002), National Natural Science Foundation of China (NO.82204744, 82270758 and 82070741) and National Key Research and Development Project (2018YFE0126600).

Conflict of interest

The authors declare that the research was conducted in the absence of any commercial or financial relationships that could be construed as a potential conflict of interest.

Publisher's note

All claims expressed in this article are solely those of the authors and do not necessarily represent those of their affiliated organizations, or those of the publisher, the editors and the reviewers. Any product that may be evaluated in this article, or claim that may be made by its manufacturer, is not guaranteed or endorsed by the publisher.

References

1. Lombardi P, Filetti M, Falcone R, Di Bidino R, Iacovelli R, Ciccarese C, et al. New first-line immunotherapy-based combinations for metastatic renal cell carcinoma: A systematic review and network meta-analysis. *Cancer Treat Rev* (2022) 106:102377. doi: 10.1016/j.ctrv.2022.102377

2. Alaghehbandan R, Perez Montiel D, Luis AS, Hes O. Molecular genetics of renal cell tumors: A practical diagnostic approach. *Cancers (Basel)* (2019) 12(1):85. doi: 10.3390/cancers12010085

3. Sanders C, Hamad ASM, Ng S, Hosni R, Ellinger J, Klumper N, et al. CD103+ tissue resident T-lymphocytes accumulate in lung metastases and are correlated with poor prognosis in ccRCC. *Cancers (Basel)* (2022) 14(6):1541. doi: 10.3390/cancers14061541

4. Zhou P, Liu Z, Hu H, Lu Y, Xiao J, Wang Y, et al. Comprehensive analysis of senescence characteristics defines a novel prognostic signature to guide personalized treatment for clear cell renal cell carcinoma. *Front Immunol* (2022) 13:901671. doi: 10.3389/fimmu.2022.901671

5. Xiong Y, Wang Z, Zhou Q, Zeng H, Zhang H, Liu Z, et al. Identification and validation of dichotomous immune subtypes based on intratumoral immune cells infiltration in clear cell renal cell carcinoma patients. *J Immunother Cancer* (2020) 8(1): e000447. doi: 10.1136/jitc-2019-000447

6. DeNardo DG, Ruffell B. Macrophages as regulators of tumour immunity and immunotherapy. *Nat Rev Immunol* (2019) 19(6):369–82. doi: 10.1038/s41577-019-0127-6

7. Baumann D, Drebant J, Hagele T, Burger L, Serger C, Lauenstein C, et al. p38 MAPK signaling in M1 macrophages results in selective elimination of M2 macrophages by MEK inhibition. *J Immunother Cancer* (2021) 9(7):e002319. doi: 10.1136/jitc-2020-002319

8. Xu WH, Xu Y, Wang J, Wan FN, Wang HK, Cao DL, et al. Prognostic value and immune infiltration of novel signatures in clear cell renal cell carcinoma microenvironment. *Aging (Albany NY)* (2019) 11(17):6999–7020. doi: 10.18632/aging.102233

9. Wang CH, Lu TJ, Wang LK, Wu CC, Chen ML, Kuo CY, et al. Tazarotene-induced gene 1 interacts with polo-like kinase 2 and inhibits cell proliferation in HCT116 colorectal cancer cells. *Cell Biol Int* (2021) 45(11):2347–56. doi: 10.1002/cbin.11681

10. Wang CH, Shyu RY, Wu CC, Chen ML, Lee MC, Lin YY, et al. Tazarotene-induced gene 1 interacts with DNAJC8 and regulates glycolysis in cervical cancer cells. *Mol Cells* (2018) 41(6):562–74. doi: 10.14348/molcells.2018.2347

11. Shyu RY, Wang CH, Wu CC, Chen ML, Lee MC, Wang LK, et al. Tazarotene-induced gene 1 enhanced cervical cell autophagy through transmembrane protein 192. *Mol Cells* (2016) 39(12):877–87. doi: 10.14348/molcells.2016.0161

12. Wang X, Saso H, Iwamoto T, Xia W, Gong Y, Pusztai L, et al. TIG1 promotes the development and progression of inflammatory breast cancer through activation of axl kinase. *Cancer Res* (2013) 73(21):6516–25. doi: 10.1158/0008-5472.CAN-13-0967

13. Oldridge EE, Walker HF, Stower MJ, Simms MS, Mann VM, Collins AT, et al. Retinoic acid represses invasion and stem cell phenotype by induction of the metastasis suppressors RARRES1 and LXN. *Oncogenesis* (2013) 2:e45. doi: 10.1038/oncsis.2013.6

14. Huebner H, Strick R, Wachter DL, Kehl S, Strissel PL, Schneider-Stock R, et al. Hypermethylation and loss of retinoic acid receptor responder 1 expression in human choriocarcinoma. *J Exp Clin Cancer Res* (2017) 36(1):165. doi: 10.1186/s13046-017-0634-x

15. Chandrashekar DS, Bashel B, Balasubramanya SAH, Creighton CJ, Ponce-Rodriguez I, Chakravarthi B, et al. UALCAN: A portal for facilitating tumor

subgroup gene expression and survival analyses. *Neoplasia* (2017) 19(8):649–58. doi: 10.1016/j.neo.2017.05.002

16. Zhou Y, Zhou B, Pache L, Chang M, Khodabakhshi AH, Tanaseichuk O, et al. Metascape provides a biologist-oriented resource for the analysis of systems-level datasets. *Nat Commun* (2019) 10(1):1523. doi: 10.1038/s41467-019-09234-6

17. Li T, Fan J, Wang BB, Traugh N, Chen QM, Liu JS, et al. TIMER: A web server for comprehensive analysis of tumor-infiltrating immune cells. *Cancer Res* (2017) 77(21):e108–10. doi: 10.1158/1538-7445.AM2017-108

18. Ru B, Wong CN, Tong Y, Zhong JY, Zhong SSW, Wu WC, et al. TISIDB: an integrated repository portal for tumor-immune system interactions. *Bioinformatics* (2019) 35(20):4200–2. doi: 10.1093/bioinformatics/btz210

19. Xu WH, Shi SN, Xu Y, Wang J, Wang HK, Cao DL, et al. Prognostic implications of aquaporin 9 expression in clear cell renal cell carcinoma. *J Transl Med* (2019) 17(1):363. doi: 10.1186/s12967-019-2113-y

20. Ropri AS, DeVaux RS, Eng J, Chittur SV, Herschkowitz JI. Cis-acting super-enhancer lncRNAs as biomarkers to early-stage breast cancer. *Breast Cancer Res* (2021) 23(1):101. doi: 10.1186/s13058-021-01479-8

21. Jamali L, Moradi A, Ganji M, Ayati M, Kazeminezhad B, Fazeli Attar Z, et al. Potential prognostic role for SPOP, DAXX, RARRES1, and LAMP2 as an autophagy related genes in prostate cancer. *Urol J* (2020) 17(2):156–63. doi: 10.22037/uj.v0i0.4935

22. Egeblad M, Nakasone ES, Werb Z. Tumors as organs: complex tissues that interface with the entire organism. *Dev Cell* (2010) 18(6):884–901. doi: 10.1016/j.devcel.2010.05.012

23. Sahu M, Suryawanshi H. Immunotherapy: The future of cancer treatment. *J Oral Maxillofac Pathol* (2021) 25(2):371. doi: 10.4103/0973-029X.325257

24. Singh R, Mishra MK, Aggarwal H. Inflammation, immunity, and cancer. *Mediators Inflammation* (2017) 2017:6027305. doi: 10.1155/2017/6027305

25. Bui TM, Wiesolek HL, Sumagin R. ICAM-1: A master regulator of cellular responses in inflammation, injury resolution, and tumorigenesis. *J Leukoc Biol* (2020) 108(3):787–99. doi: 10.1002/JLB.2MR0220-549R

26. Adutler-Lieber S, Friedman N, Geiger B. Expansion and antitumor cytotoxicity of T-cells are augmented by substrate-bound CCL21 and intercellular adhesion molecule 1. *Front Immunol* (2018) 9:1303. doi: 10.3389/fimmu.2018.01303

27. Shi X, Jiang J, Ye X, Liu Y, Wu Q, Wang L. Prognostic prediction and diagnostic role of intercellular adhesion molecule-1 (ICAM1) expression in clear cell renal cell carcinoma. *J Mol Histol* (2014) 45(4):427–34. doi: 10.1007/s10735-014-9568-1

28. Wiesolek HL, Bui TM, Lee JJ, Dalal P, Finkielsztein A, Batra A, et al. Intercellular adhesion molecule 1 functions as an efferocytosis receptor in inflammatory macrophages. *Am J Pathol* (2020) 190(4):874–85. doi: 10.1016/j.ajpath.2019.12.006

29. Podolnikova NP, Hlavackova M, Wu Y, Yakubenko VP, Faust J, Balabiyev A, et al. Interaction between the integrin mac-1 and signal regulatory protein alpha (SIRPalpha) mediates fusion in heterologous cells. *J Biol Chem* (2019) 294(19):7833–49. doi: 10.1074/jbc.RA118.006314

30. Guan Y, Xu F, Tian J, Wang Y, Guo N, Wan Z, et al. Prognostic value of circulating tumor cells and immune-inflammatory cells in patients with renal cell carcinoma. *Urol Oncol* (2022) 40(4):167 e121–167 e132. doi: 10.1016/j.urolonc.2021.12.021

31. Murray PJ, Allen JE, Biswas SK, Fisher EA, Gilroy DW, Goerdt S, et al. et al. macrophage activation and polarization: nomenclature and experimental guidelines. *Immunity* (2014) 41(1):14–20. doi: 10.1016/j.immuni.2014.06.008

32. Guo S, Chen X, Guo C, Wang W. Tumour-associated macrophages heterogeneity drives resistance to clinical therapy. *Expert Rev Mol Med* (2022) 24:e17. doi: 10.1017/erm.2022.8

33. Ge Z, Ding S. The crosstalk between tumor-associated macrophages (TAMs) and tumor cells and the corresponding targeted therapy. *Front Oncol* (2020) 10:590941. doi: 10.3389/fonc.2020.590941

34. Tian L, Lei A, Tan T, Zhu M, Zhang L, Mou H, et al. Macrophage-based combination therapies as a new strategy for cancer immunotherapy. *Kidney Dis (Basel)* (2022) 8(1):26–43. doi: 10.1159/000518664

frontiers | Frontiers in Oncology

TYPE Original Research
PUBLISHED 24 October 2022
DOI 10.3389/fonc.2022.959987

OPEN ACCESS

EDITED BY
Apostolos Zaravinos,
European University Cyprus, Cyprus

REVIEWED BY
Jarek T. Baran,
Jagiellonian University Medical College, Poland
Benjamin Bonavida,
University of California, Los Angeles, United States

*CORRESPONDENCE
Melanie A. Kimm
melanie.kimm@med.uni-muenchen.de

†These authors have contributed equally to this work

SPECIALTY SECTION
This article was submitted to Cancer Immunity and Immunotherapy, a section of the journal Frontiers in Oncology

RECEIVED 02 June 2022
ACCEPTED 03 October 2022
PUBLISHED 24 October 2022

CITATION
Kimm MA, Kästle S, Stechele MMR, Öcal E, Richter L, Ümütlü MR, Schinner R, Öcal O, Salvermoser L, Alunni-Fabbroni M, Seidensticker M, Goldberg SN, Ricke J and Wildgruber M (2022) Early monocyte response following local ablation in hepatocellular carcinoma. *Front. Oncol.* 12:959987. doi: 10.3389/fonc.2022.959987

Early monocyte response following local ablation in hepatocellular carcinoma

Melanie A. Kimm[1*†], Sophia Kästle[1†], Matthias M. R. Stechele[1], Elif Öcal[1], Lisa Richter[2], Muzaffer R. Ümütlü[1], Regina Schinner[1], Osman Öcal[1], Lukas Salvermoser[1], Marianna Alunni-Fabbroni[1], Max Seidensticker[1], S. Nahum Goldberg[3,4,5], Jens Ricke[1] and Moritz Wildgruber[1]

[1]Department of Radiology, University Hospital, Ludwig-Maximilians-Universität München, Munich, Germany, [2]Core Facility Flow Cytometry, Biomedical Center Munich, Ludwig-Maximilians-Universität München, Planegg-Martinsried, Germany, [3]Goldyne Savad Institute of Gene Therapy, Hadassah Hebrew University Hospital, Jerusalem, Israel, [4]Laboratory for Minimally Invasive Tumor Therapies, Department of Radiology, Beth Israel Deaconess Medical Center, Harvard Medical School, Boston, MA, United States, [5]Division of Image-guided Therapy and Interventional Oncology, Department of Radiology, Hadassah Hebrew University Hospital, Jerusalem, Israel

Local ablative therapies are established treatment modalities in the treatment of early- and intermediate-stage hepatocellular carcinoma (HCC). Systemic effects of local ablation on circulating immune cells may contribute to patients' response. Depending on their activation, myeloid cells are able to trigger HCC progression as well as to support anti-tumor immunity. Certain priming of monocytes may already occur while still in the circulation. By using flow cytometry, we analyzed peripheral blood monocyte cell populations from a prospective clinical trial cohort of 21 HCC patients following interstitial brachytherapy (IBT) or radiofrequency ablation (RFA) and investigated alterations in the composition of monocyte subpopulations and monocytic myeloid-derived suppressor cells (mMDSCs) as well as receptors involved in orchestrating monocyte function. We discovered that mMDSC levels increased following both IBT and RFA in virtually all patients. Furthermore, we identified varying alterations in the level of monocyte subpopulations following radiation compared to RFA. (A) Liquid biopsy liquid biopsy of circulating monocytes in the future may provide information on the inflammatory response towards local ablation as part of an orchestrated immune response.

KEYWORDS

hepatocellular carcinoma, local ablation, brachytherapy, radiofrequency ablation, monocytes, flow cytometry

Introduction

Liver cancer is the second leading cause of cancer death worldwide (1). Etiological causes of hepatocellular carcinoma (HCC) include chronic viral infections, high alcohol intake, and increasingly non-alcohol-related steatohepatitis (NASH), whereby the majority of HCC arises in the setting of chronic liver inflammation (2). Clinical decision-making in HCC is further dependent on staging systems that include tumor size and burden as well as liver function (3). The "Barcelona Clinic Liver Cancer" (BCLC) staging system is commonly used to link the prognostic stage of HCC to the best first-line treatment option. In early-stage HCC, curative surgical treatments, such as resection or transplantation, are first-line therapies (4). However, many patients do not fulfill the criteria for surgical treatment options, whereby image-guided local ablative therapies represent an alternative, either as definitive treatment or as a bridging option to transplantation (3).

Radiofrequency ablation (RFA) is a well-established method in interventional oncology and has been proven to be safe and effective for the treatment of early HCC (5, 6), but is limited with respect to a certain tumor size and tumor location. Interstitial brachytherapy (IBT) is a valuable alternative with deposition of an ionizing source (e.g., ^{192}Iridium) within the tumor tissue instead of using external beam radiation, thereby limiting the injury of adjacent non-tumor tissue, which is particularly important in the setting of impaired liver function (7). IBT allows for safe and effective ablation even in patients with tumors larger than 3 cm, and who are not suitable for treatment by RFA or microwave ablation (MWA) (8). Notably, both local ablative therapies are able to induce effects on the local as well as on the systemic immune response (9, 10). Local effects are mainly related to the tumor microenvironment (TME), which is a heterogeneous composition of interacting tumor and non-tumor cells (such as fibroblasts and immune cells) and extracellular matrix components (11). Any change of this highly sensitive cell-to-cell communication mediated by internal or external alterations can support either pro- or anti-tumorigenic immune responses (12). Although it is still puzzling which cell–cell interactions, communication signals, and polarization events within TME of HCC will lead to an anti- or pro-tumorigenic effect, it is well established that myeloid-derived cells such as monocytes, macrophages, and dendritic cells are key players within this theater (13).

In the liver, tissue-resident macrophages (Kupffer cells) play a central role in maintaining liver homeostasis and upon acute liver injury become activated and differentiate into immune-activating or immune-suppressive phagocytes (14). In addition, myeloid cell populations from the peripheral blood [monocytes and myeloid-derived suppressor cells (MDSCs)] are recruited to the site of injury (15, 16). When entering the tissue, monocytes differentiate into macrophages and the TME orchestrates the polarization into certain phenotypes. Whether different ablative treatments induce differences in pre-priming of peripheral blood monocytes is not yet elucidated. This pre-priming of circulating immune cell populations may serve as a predictive or prognostic biomarker for response to targeted treatment or may indicate severity of tissue injury. Recent studies have identified lymphocyte-to-monocyte ratio (LMR), neutrophil-to-monocyte ratio (NMR), and neutrophil-to-lymphocyte ratio (NLR) as potential prognostic markers for survival of HCC patients (17–21). Yet, little is known about possible differences in peripheral blood myeloid cell subpopulations following local ablative therapies, such as IBT and RFA.

Thus, in this study, we aimed to investigate priming of circulating monocytes following local ablation in early- and intermediate-stage HCC.

Material and methods

Patients and study design

Patients were recruited in two prospective clinical trials investigating the image-guided local ablation of early- and intermediate-stage HCC. The analysis consists of 21 patients with HCC. The ESTIMATE trial investigates the effects of IBT, from which 12 patients were recruited. In order to compare the effects after local radiation to RFA, nine patients were included from the THIAMAT trial. An overview of the patients' clinical characteristics is shown in Table 1. Blood samples were obtained at baseline on the day before local ablation as well as 24–48 h post-IBT/RFA.

Ethics

The studies were approved by the local ethics commission of the university hospital (LMU München, Munich, Germany), with German clinical trial register numbers DRKS 00010587 (ESTIMATE) and DRKS 00010560 (THIAMAT). All study protocols were conducted in accordance with the Declaration of Helsinki. Informed consent of each participant was obtained prior to enrollment.

Patient response assessment

Patients were stratified into responders versus non-responders based on previously published criteria for HCC disease stages (4) and eligibility for curative versus palliative

TABLE 1 Clinical characteristics of the study cohort.

		IBT (n = 12)	RFA (n = 9)	p-value
Sex	Female	3	1	0.6030[a]
	Male	9	8	
Age at therapy start[#]		71.50 (7.50)	70.00 (14.00)	1.0000[b]
Cirrhosis		10/12	8/9	1.0000[a]
Child pugh score	A	8	7	0.3865[c]
	B	2	1	
NASH		1/8	2/8	1.0000[a]
Diabetes mellitus Type II		7/12	5/9	1.0000[a]
High alcohol intake		5/8	4/7	1.0000[a]
Viral hepatitis		2/8	1/8	1.0000[a]
Mixed etiology		2/8	2/8	1.0000[a]
Maximal tumor diameter [mm]*		34.73 (± 14.56)	31.93 (± 14.61)	0.6691[d]
⌀ amount of tumors[#]		1.00 (1.00)	2.00 (1.00)	0.0091[b]
BCLC score	BCLC 0/A	2/6	0/3	0.4753[c]
	BCLC B/C	2/2	2/4	
AFP [ng/ml][#]		16.05 (412.85)	8.55 (13.80)	0.9079[b]
Serum albumin [g/dl]*		3.92 (± 0.61)	3.87 (± 0.43)	0.8370[d]
Total bilirubin [mg/dl][#]		0.70 (0.90)	0.80 (0.60)	0.4920[b]
Platelet count [G/L][#]		130.50 (56.00)	114.00 (75.00)	0.9716[b]
Therapy outcome (Responder/Non-Responder)		11/1	7/2	0.5534[a]

The size of tumor lesions was measured as maximal tumor diameter of the largest lesion. AFP, a-fetoprotein; BCLC, Barcelona Clinic Liver Cancer staging system; NASH, non-alcoholic steatohepatitis. [#]median (IQR), *mean (± SD), a, Fisher's exact test, b, Mann–Whitney U-test, c, Chi-square test, d, t-test.

treatments in case of progression. Accordingly, responders were defined as patients showing complete remission for a minimum of 6 months following therapy. Any recurrence seen within 6 months post-therapy or tumor appearance in between a total follow-up period of 24 months greater than 3 cm or >3 tumor lesions classified the patient as a non-responder.

Leukocyte ratios

LMR and NMR were computed as absolute numbers of lymphocytes and neutrophils, respectively, divided by monocytes. NLR was computed as absolute number of neutrophils divided by lymphocytes. Pre- and post-therapy LMR, NMR, and NLR were calculated from absolute numbers of monocytes, lymphocytes, and neutrophils (G/µl). In total, from all 12 ESTIMATE patients and from 7/9 THIAMAT patients, cell numbers were available and analyzed.

PBMC collection and flow cytometry analysis

PBMCs were isolated using a Ficoll-Paque density gradient (Cytiva, Uppsala, Sweden) and cryopreserved until analyzed. The following monoclonal antibodies specific for human antigens were used: anti-CD14-APC (63D3), anti-CD16-PE (B73.1), anti-CD64-PE-Cy7 (10.1), anti-CD86-FITC (BU63), anti-CD163-APC (GHI/61), anti-CD200R-PE (OX-108), anti-HLA-DR-PE-Cy7 (L243), anti-IgG1 (MOPC-21) (all from BioLegend, San Diego, CA, USA), anti-CD11b-PerCP-eFluor®710 (ICRF44), and Fixable Viability Dye-eFluor®780 (all from ThermoFisher Scientific, Waltham, MA, USA). In brief, cells were thawed and resuspended in staining buffer (1× PBS/3% FBS). Staining against surface antigens only (panel 2) or surface antigens and cytoplasmic protein (panel 1, data for intracellular staining not shown) was performed for 30 min at 4°C in the dark. Staining against cytoplasmic protein was performed after cell fixation with 2% PFA. Cells were analyzed on the flow cytometer FACSCanto (BD Biosciences, Immune Cytometry Systems, San Jose, CA, USA), and data were analyzed using FlowJo software version 10 (BD Life Sciences, Ashland, OR, USA). The gates were set based on Fluorescence-minus-one (FMO) and IgG control antibody staining, and the number in each gate represents the percentage of cells. Gating strategy for monocyte subsets and mMDSC (panel 1) is shown in Figure 1A, and gating strategy for the myeloid polarization markers (panel 2) is shown in Figure 1B. Monocyte subsets, CD86+, D163+, and CD200R+ cells were presented as percentage of monocytes; mMDSCs

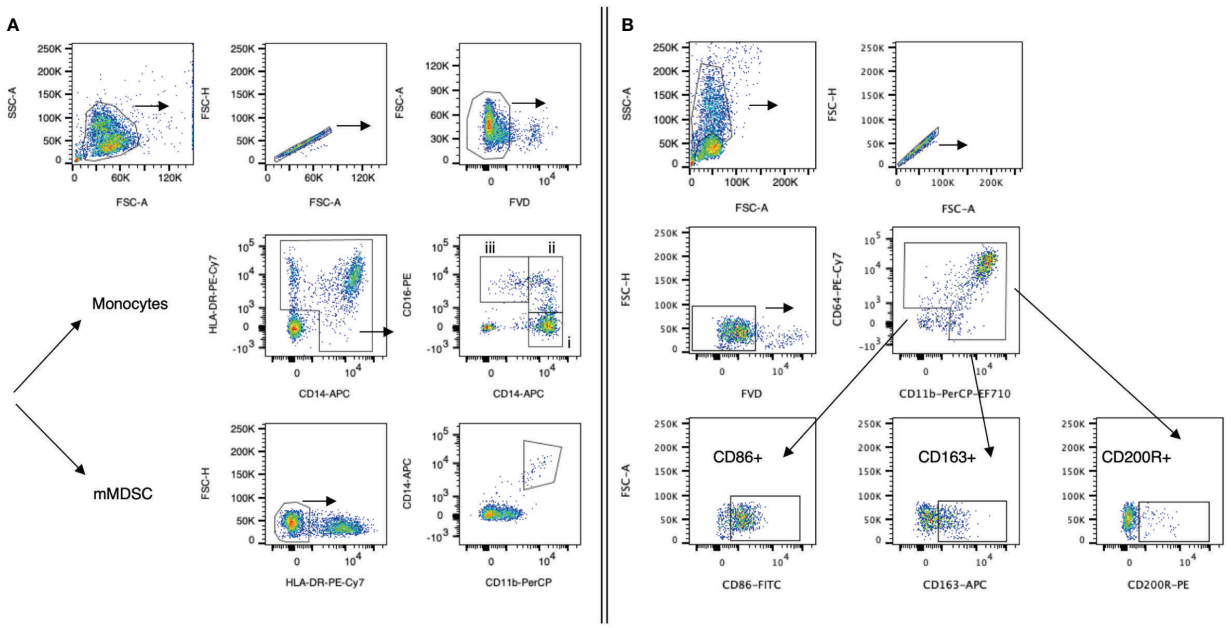

FIGURE 1
Gating strategies for myeloid cell populations. Representative dot plots from one HCC patient. **(A)** Panel 1: Monocytes were defined as HLA-DR+CD14+ cells. Monocyte subsets (classical, intermediate, non-classical; all presented as % frequency of monocytes) were further defined by their expression of CD14 and CD16: (i) classical monocytes (CD14++CD16–), (ii) intermediate monocyte (CD14++CD16+), and (iii) non-classical monocytes (CD14+CD16++). Monocytic MDSCs (mMDSCs) were defined as HLA-DR-CD11b+CD14+ cells (% of live cells). Cells were fixed prior to staining. **(B)** Panel 2: CD11b+CD64+ monocytes were further analyzed for CD86, CD163, and CD200R marker expression. Cells were not fixed prior to staining. Following staining, cells of both panels were fixed with 4% PFA and subsequently analyzed. FVD, Fixable Viability Dye-eFluor®780.

were presented as percentage of viable cells. Monocyte gating strategies and nomenclature were applied following the principles by Ziegler-Heitbrock et al. (22, 23); those for mMDSCs were based on Gabrilovich et al. (24, 25).

Histology

Tumor biopsies were fixed in 3.7% neutral-buffered formaldehyde and embedded in paraffin according to standard protocols. Two-micrometer sections were prepared, and morphology was visualized by standard H&E staining. For immunohistochemistry, the activity of the endogenous peroxidase was blocked with 1% hydrogen peroxide, and after antigen retrieval (citric acid buffer, pH 6) at 100°C, sections were incubated with anti-CD68 (dilution 1:250, clone KP1, ThermoFisher Scientific, Waltham, MA, USA), anti-CD86 (dilution 1:75, clone E2G8P, Cell Signaling Technology, Beverly, CA, USA), and anti-CD163 antibody (dilution 1:250, clone D6U1J, Cell Signaling Technology, Beverly, CA, USA), respectively. This was followed by incubation with EnVision™+Dual Link System-HRP (Dako, Carpinteria, CA, USA). Diaminobenzidine (Cell Signaling Technology, Beverly, CA, USA) was used as a chromogen. Sections were counterstained with 1% Mayer's hematoxylin. Slides were analyzed using a Leica dm2500 microscope equipped with LAS version 4 software (Leica, Germany).

Statistical analysis

Statistical analysis was performed using GraphPad Prism (version 9, GraphPad Software, San Diego, CA, USA) and SAS (version 9.4, SAS Institute Inc., Cary, NC, USA). Normality distribution was determined by the Shapiro–Wilk test. Paired data were analyzed using paired *t*-test or Wilcoxon test. We calculated intraindividual differences delta to take care of the dependencies in the data (pre- and post-treatment values of the same patient) and compared the independent deltas between the two different cohorts using *t*-test or Mann–Whitney *U*-test, depending on normality of data. For analysis of clinical and demographic data, Fisher's exact test, Mann–Whitney *U*-test, *t*-test, and chi-square test were used in dependency of the normal distribution. Non-normally distributed data are presented as

median with interquartile range (IQR), and normally distributed data are presented as mean with standard deviation (SD). A p-value < 0.05 was considered significant.

Results

Patient characteristics of the study cohort

All patients were recruited through the liver clinics in a tertiary care/liver transplant center and diagnosed with HCC based on radiological criteria and biopsy. Patient characteristics and liver function tests at treatment baseline are summarized in Table 1. No significant differences were observed between the two patient cohorts for most of the listed parameters.

Tumor-associated macrophage staining (CD68) of tumor biopsies of nine patients obtained at baseline before local ablation revealed tumor regions with CD163+ cells in all patients. This denoted an inflamed liver microenvironment and immunosuppressive M2-phenotypic TME. In turn, CD86 staining, indicative of M1 polarization of macrophages, was almost completely absent (Figure 2).

Alterations in leukocyte populations and ratios following IBT and RFA

First, we investigated peripheral blood LMR, NMR, and NLR following local ablative therapy IBT and RFA (Figure 3). Both treatments resulted in significant changes in LMR and NMR, IBT additionally in NLR. Following IBT, LMR decreased from 2.06 pre-therapy to 1.85 post-therapy (p = 0.0024) (Figure 3A) while NMR increased from 7.70 to 10.16 (p = 0.0130) (Figure 3B) and NLR increased from 3.38 to 8.26 following treatment (p = 0.0044) (Figure 3C). Strikingly, following RFA, both LMR and NMR dropped close to zero in all patients analyzed, indicating a tremendous increase in monocytes. LMR values decreased post-RFA from 1.95 to 0.19 (p < 0.0001) (Figure 3A), and NMR decreased from 6.60 to 0.70 (p < 0.0001) (Figure 3B). No significant changes were obtained for NLR in patients following RFA (Figure 3C). Detailed specifications are listed in Supplementary Table 1. These results point to the different mode of action between IBT and RFA.

Looking into the distribution of the different leukocyte populations in more detail, we found an increase in monocyte and neutrophil numbers following IBT, while lymphocyte numbers decreased (Figures 3D–F). In contrast, following RFA, only peripheral blood monocytes increased in numbers

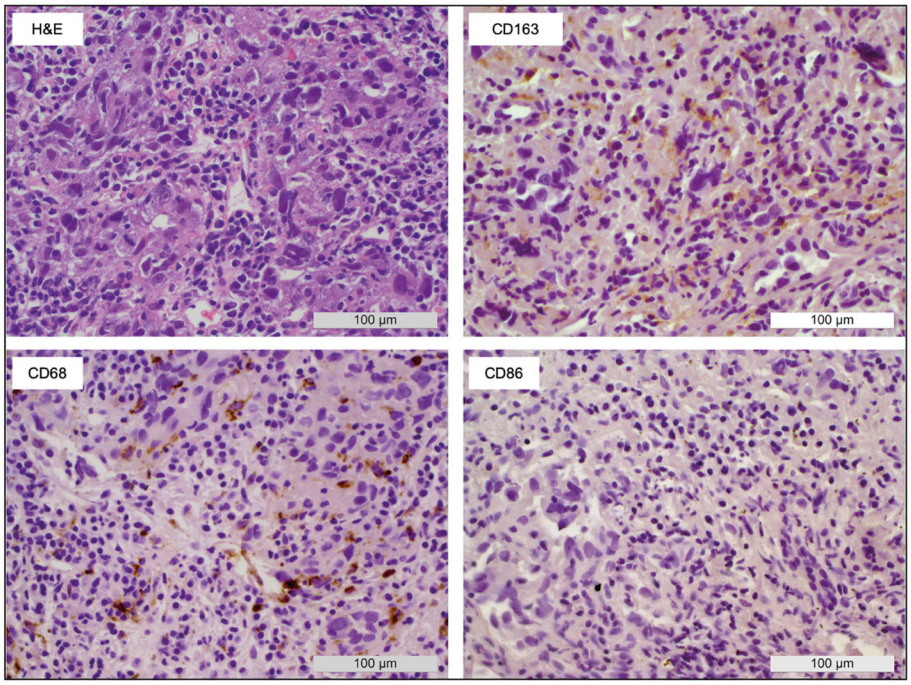

FIGURE 2
Macrophage polarization within HCC biopsies. A representative sample shows the appearance of macrophages in tumor tissue obtained before local ablation. H&E staining as well as CD68 (pan macrophage), CD86 (M1), and CD163 (M2) IHC allowed the identification of large areas with M2-type macrophages (CD163+) whereas M1-type macrophages (CD86+) were almost completely absent.

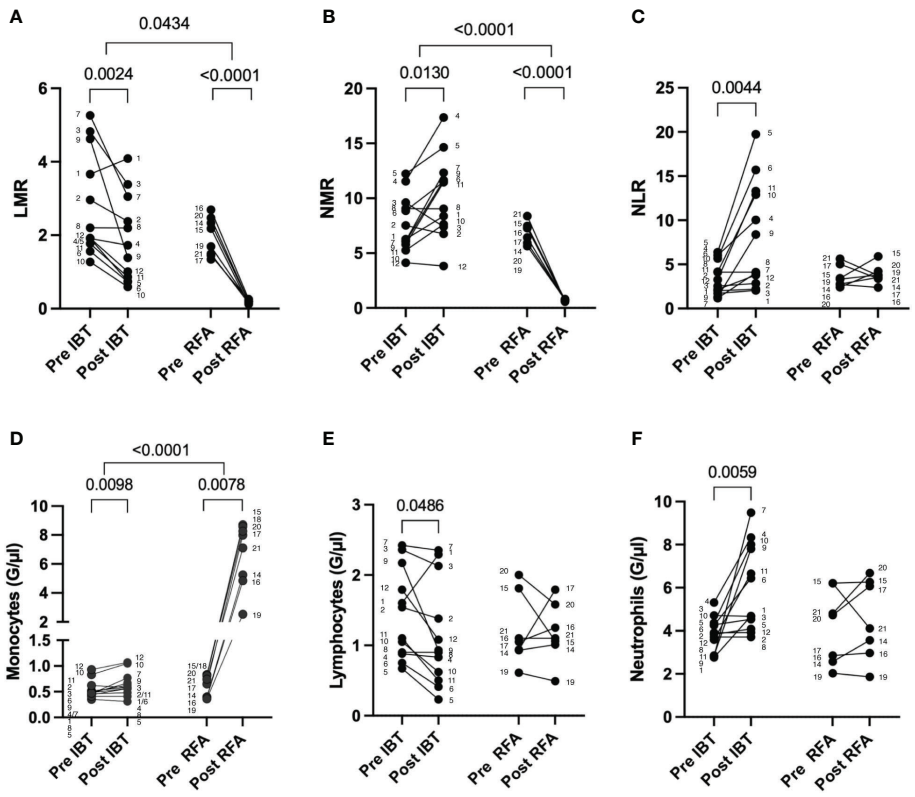

FIGURE 3
Leukocyte changes following different local ablation treatments. Pre and post analysis of **(A)** LMR, **(B)** NMR, **(C)** NLR, **(D)** monocytes, **(E)** lymphocytes, and **(F)** neutrophils. Differential blood values from 12 IBT- and 7 RFA-treated patients were analyzed. Each dot represents an individual patient. Numbers next to dots represent patient IDs and ensure assignment of pre and post values. Data were analyzed using paired *t*-test (IBT: **B, C, E**, and F; RFA: **A–C, E, F**) or Wilcoxon-test (IBT: **A, D**; RFA: **D**). Intraindividual differences were analyzed using unpaired *t*-test **(A, B, D–F)** or Mann–Whitney *U*-test **(C)**. *p*-values < 0.05 indicate statistical significance.

(Figure 3D), whereas lymphocytes and neutrophils showed no significant changes (Figures 3E, F).

Interventional therapy-related dynamics of peripheral blood myeloid cell populations

To gain more insight into treatment-related differences in monocyte subpopulations between radiation-based IBT and heat-based RFA, we analyzed the peripheral blood of 12 IBT- and 9 RFA-treated patients pre- and post-treatment (Figure 4) using flow cytometry. In addition to the three major subpopulations—classical, intermediate, and non-classical monocytes (Figures 4A–C)—we identified mMDSC (Figure 4D) and analyzed the expression of CD86, CD163, and CD200R indicative for monocyte activation and differentiation (Figures 4E–G). Healthy donor data of three non-matched individuals showed no difference for monocyte subpopulations and mMDSC at baseline (Supplementary Figure 1).

Compared to baseline, we found significantly increased fractions of classical monocytes in 11 out of 12 patients following IBT (52% pre vs. 66% post, $p = 0.0027$) (Figure 4A, Supplementary Table 1). Only in patient no. 1 did classical monocyte levels decrease post-IBT; still, the patient responded well to therapy. The most relevant clinical parameter that differed compared to other patients was a chronic hepatitis B infection.

Patients treated with RFA were heterogeneous in regard to classical monocyte proportion (Figure 4A). Only two patients showed an increase in the proportion of classical monocytes following RFA (patient no. 14 and patient no. 18), but no relevant clinical parameters could be clearly correlated to this observation. Furthermore, we determined intraindividual differences (delta) for each patient cohort and analyzed possible differences between the two treatment options. With regard to classical monocyte percentages, we observed significant differences between the two treatments ($p = 0.0027$). Looking at intermediate monocyte frequencies, we saw no significant changes compared to baseline neither for

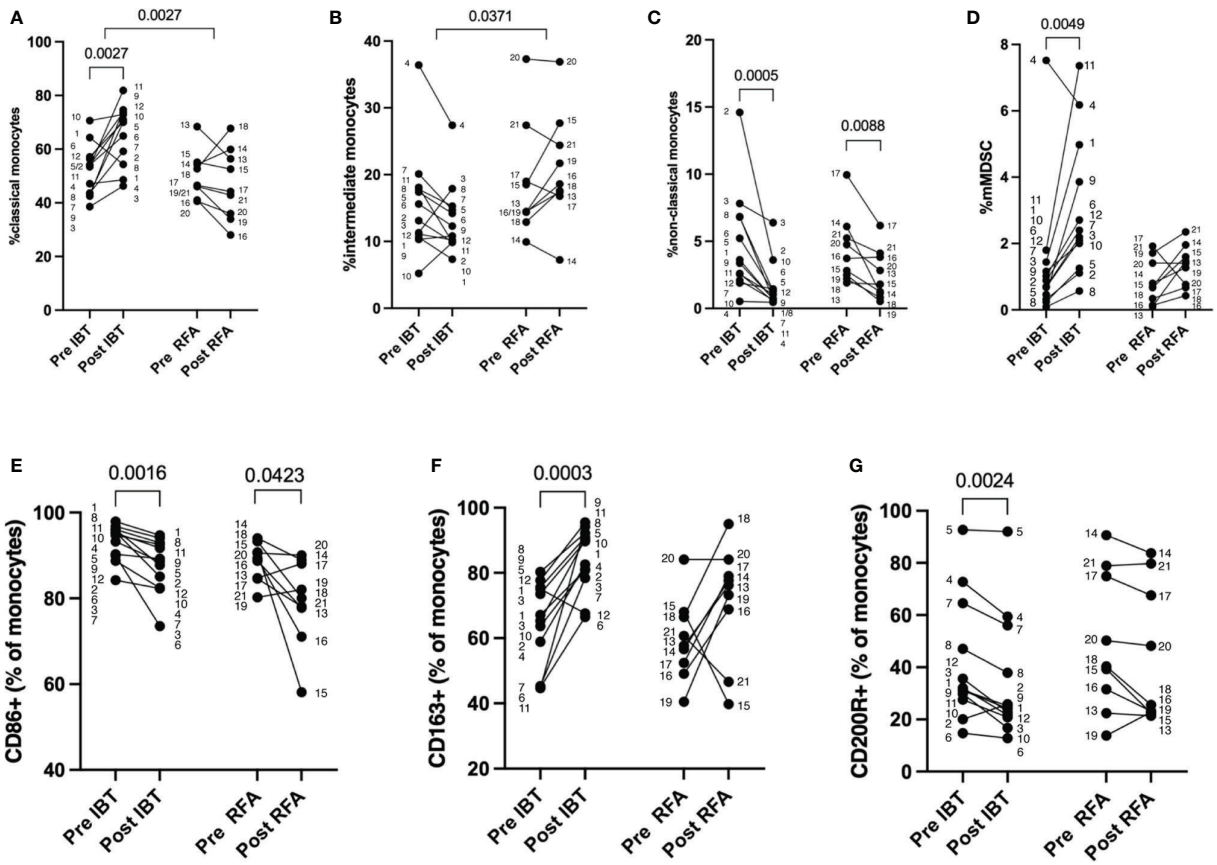

FIGURE 4
Therapy-specific alterations in monocyte cell populations. Percentage of myeloid cells as measured by flow cytometry. Pre and post analysis of 12 IBT- and 9 RFA-treated patients. **(A)** Classical monocytes (CD14++CD16−), **(B)** intermediate monocytes (CD14++CD16+), **(C)** non-classical monocytes (CD14+CD16++), **(D)** mMDSC, **(E)** CD86+, **(F)** CD163+, and **(G)** CD200R+ monocytes (shown as percentage of monocytes). Each dot represents an individual patient. Numbers next to dots represent patient IDs and ensure assignment of pre and post values. Data were analyzed using paired *t*-test (IBT: **A, F**; RFA: **A, C–F**) or Wilcoxon test (IBT: **B–E, G**; RFA: **B, G**). Intraindividual differences were analyzed using unpaired *t*-test **(A, B, D, E)** or Mann–Whitney *U*-test **(C, F, G)**. *p*-values < 0.05 indicate statistical significance.

IBT- nor RFA-treated patients (14% pre vs. 12% post, $p = 0.1294$ and 15% pre vs. 21% post, $p = 0.2031$, respectively) (Figure 4B, Supplementary Table 1). Yet, the comparison between treatment modalities revealed significant difference concerning the proportion of intermediate monocyte population ($p = 0.0371$). While IBT led to decreased intermediate monocyte fractions, they were overall increasing following RFA (Supplementary Table 1). Interestingly, non-classical monocyte levels significantly decreased unrelated to one or the other treatment (IBT: 4% pre vs. 1% post, $p = 0.0005$ and RFA: 5% pre vs. 3% post, $p = 0.0088$) (Figure 4C, Supplementary Table 1) even though the effect was more pronounced following IBT.

Next, we analyzed proportions of peripheral blood mMDSC and detected in virtually all IBT-treated patients significantly increased mMDSC proportions (1% pre- vs. 2% post-therapy, $p = 0.0049$) (Figure 4D, Supplementary Table 1). Only in one patient (patient no. 4) did we observe a decrease in mMDSC following IBT. This patient represents the only non-responder in the IBT-treated patient cohort. Following RFA, we found in 8 patients increasing levels of mMDSC regardless of the response status. One patient had decreasing mMDSC proportion (patient no. 17), and one patient (patient no. 19) showed equal percentages pre- and post-therapy. In comparison to the non-responding patient following IBT, both non-responding patients of the RFA-treated patient cohort showed increasing mMDSC frequencies (all RFA-treated patients: 0.87 pre vs. 1.32 post, $p = 0.1081$). Compared to the other patients, there was no clinically evident cause explaining the decreased mMDSC.

Furthermore, we investigated possible variance in expression of CD86, CD163, and CD200R pre- and post-treatment (Figures 4E–G). The rate of CD86+ monocytes showed a tendency to decrease in both patient cohorts, but not reaching significant differences (IBT: 86% pre vs. 81% post, $p = 0.0772$; RFA: 82% pre vs. 72% post, $p = 0.0508$) (Figure 3E, Supplementary

Table 1). At the same time, we observed a significant increase in scavenger receptor CD163-expressing monocyte proportions following IBT (55% pre vs. 80% post, $p < 0.0001$), and even though not significant, we observed a gain in CD163+ monocyte fraction following RFA (49% pre vs. 62% post, $p = 0.1298$) (Figure 4F, Supplementary Table 1). Only for one IBT-treated patient (patient no. 12) did we observe a decrease in CD163+ monocyte percentages. This result may be explained by an underlying hemochromatosis with a mutation in the HFE gene. Two RFA-treated patients showed decreased CD163+ proportions. Patient no. 15 was classified as a non-responder; patient no. 21 was the only HBV-positive patient within the RFA-treated cohort. When looking at the dynamics of CD200R+ monocyte fractions, we discovered certain differences. Following IBT, CD200R+ monocyte levels significantly decreased (16% pre vs. 10% post, $p = 0.0425$) (Figure 4G, Supplementary Table 1). Only two IBT-treated patients had increasing CD200R+ proportions (patient no. 2 and patient no. 5). We could not identify relevant clinical parameters for patient no. 2 explaining an increase in CD200R+. Patient no. 5, however, has an underlying autoimmune hepatitis. In comparison, we could not detect significant differences in CD200R expression levels in monocytes of RFA-treated patients (Figure 4G) (Supplementary Table 1).

For none of the three markers analyzed did we find a significant difference between the two types of treatment (Figures 4E–G).

Discussion

Liver cancer is an inflammation-associated tumor that develops on the ground of injured liver tissue—cirrhosis. The inflammatory reaction originally intended for tissue repair usually develops towards a chronic condition, which is able to promote tumorigenesis and growth (26). Inflammation is considered a hallmark of cancer and the innate immune response is a major player in orchestrating both the local and systemic response (27). Furthermore, myeloid cells play a critical role in the resolution phase of inflammation (28) and activating myeloid cell populations following therapy could affect patients' response, resulting in positive or negative abscopal effects. The TME plays a decisive role, and its composition mainly determines whether a pro- or anti-tumorigenic environment dominates the scene. Herein, tumor-associated macrophages are one of the most abundant cell types in the TME. They mature from peripheral circulating monocytes and, depending on prevalent mediators, differentiate into pro-inflammatory M1 or anti-inflammatory M2 macrophages. Additionally, under pathological conditions, tissue-resident Kupffer cells become activated and gain either M1 or M2 function (29, 30).

Local ablative therapies have proven effective in the treatment of primary liver tumors and their combination with immunotherapies is currently an increasing focus of research. IBT as locally effective radiotherapy and heat-induced tumor destruction by RFA or microwave ablation represent common forms of interventional tumor therapy (31). Both IBT and RFA are able to induce immunogenic cell death leading to increased antigen presentation and the release of damage-associated molecular patterns (DAMP) due to cell necrosis, which may finally result in an anti-tumorigenic response (32–35). In both types of therapy, next to the destruction of tumor tissue, adjacent liver tissue and vasculature is affected and potentially injured. The associated inflammatory reaction is of interest, as it may contribute to the patient's therapy response beyond the initial tumor destruction. This raises several questions: Is the immune reaction restricted locally or is it possible to detect systemic effects within the peripheral blood? Are there differences in the systemic immune reaction depending on the type of interventional therapy applied? To answer these questions, we analyzed the dynamics of circulating blood monocytes and the expression of monocyte function-related markers using flow cytometry in a cohort of 21 HCC patients treated with either IBT or RFA. Due to the applied study protocols and the prospective character of the studies, our analysis does not include data from patients with the same degree of liver cirrhosis, but without cancer. This is a clear limitation of the herein presented data and future studies shall address this issue in more detail.

We found significant changes in leukocyte ratios LMR, NMR, and NLR that indicate systemic effects following ablation therapy. Furthermore, we detected changes in monocyte proportions, monocyte subpopulations, mMDSCs, and distinct monocyte markers at 24 to 48 h after the respective therapy. The changes occurred independent of the patients' response status, but differed regarding the treatment modality. Noteworthy, the analysis revealed an increase in absolute monocyte numbers that was significantly higher following RFA, compared to IBT treatment. This could indicate the degree of early injury, which initially is more pronounced in RFA compared to IBT, where cell death and necrosis develop in due course. In addition to monocytosis, we noted lymphopenia and neutrophilia following IBT, but not RFA, representing an inflammatory leukogram that is caused by IBT-induced necrosis and thus related to the induction of immunogenic cell death. Hence, differences in leukocyte populations may hint to temporal differences in wound healing phases following either one of the ablative treatments. In addition, RFA and IBT clearly induce different systemic immune reactions, which might correlate to the degree and mode of tissue injury and the associated inflammatory response.

With respect to the different monocyte subsets, we observed a substantial decrease in non-classical monocytes, no matter

which treatment modality was applied. A drop in non-classical monocytes may indicate their migration to the liver, and since non-classical monocytes are associated with wound healing (36, 37), they might be recruited for tissue repair following tumor ablation. Even though classical monocytes are the predominant population, which upon tissue injury is recruited from the blood to the site of injury (38), we noted increased proportions of classical monocytes only following IBT, not after RFA. Classical monocytes have an important function in the initiation and progression of the inflammatory response (39), and differences in the appearance of classical monocyte proportions could be related to radiation-induced cell death, which occurs over an extended time frame of at least several days, while RFA induced cell death is an immediate event. Furthermore, we noted that changes within intermediate monocyte subsets differed significantly between IBT- and RFA-treated patients. Changes in peripheral monocyte subsets may also indicate how fast ablation-induced inflammation resolves (39, 40). A clear limitation of this study is that only one time point after local ablation was sampled. Kinetic studies will be needed to obtain a more precise picture on the recruitment and re-storage of individual monocyte subsets following the different interventional therapies. Such studies are also necessary to better understand how the wound healing phases temporally differ depending on the ablation mode.

The increase in mMDSC fractions observed in both patient cohorts also suggests a treatment-related effect, although the increase in mMDSC was only significant following IBT. Again, this might be the result of the different modes of action and may indicate a stronger inflammatory response post-IBT. Monocytic MDSCs are only found under pathological conditions (40–42), and as they are able to enhance or restore immune reactions, their function is a double-edged sword (43). mMDSC accumulation is commonly linked to a worse prognosis of patients in a wide range of cancers (44). However, given that virtually all treated patients had a good response to ablation (18/21), defined as no recurrence of the disease within 6 months after treatment, we conclude that the mMDSC signature in the peripheral blood that we observed at the given time point is treatment- rather than response-related. Immunosuppression is a critical part during wound healing (45), and the recruitment of mMDSCs following ablative therapy may indicate the healing process. To delineate the role of mMDSC following local ablation, more mechanistic studies, including animal models of local ablation, would be needed. The descriptive character of our study is a clear limitation and more studies are needed to reveal the role of mMDSC following ablative therapies in HCC.

The observation that the proportion of CD163+ monocytes was increased independent of the type of treatment applied was remarkable. CD163 is a scavenger receptor, physiologically involved in the clearance of hemoglobin after red blood cell lysis (46). Changes in CD163+ monocyte proportion could indicate complications, technically as well as those that are hemolysis-related. Hemolysis was described in patients following thermal injury, and the circumstance that hemolysis can lead to acute kidney failure makes CD163 an interesting marker for monitoring patients after ablative treatments. Further studies with higher patient numbers are needed to better understand why radiation-induced injury caused significantly increased CD163+ monocyte fractions whereas thermal-induced injury did not. The tendency of CD86+ monocyte fractions to decrease following ablative treatment suggests a functional shift from an inflammatory environment towards an anti-inflammatory one within the peripheral blood. In complex with CD80, the CD86 receptor interacts with CD28 on T lymphocytes and is part of the full activation of CD4+ T cells. Finally, this leads to CTLA-4 upregulation that competes with CD28 for CD80/86 binding, resulting in the termination of T-cell stimulation. Furthermore, CD86 is a marker for APC activation (47) and CD86 receptor downregulation can lead to an anti-inflammatory and immune-regulatory phenotype (48) and may indicate the presence of a wound healing phase following ablation therapy. With regard to CD200R+ monocytes, we detected decreased fractions following treatment with IBT, but no relevant changes following RFA. CD200–CD200R is a known immunoregulatory checkpoint axis with CD200R mainly expressed on myeloid cells and T cells. It is one key player in regulating immune homeostasis, especially in maintaining immune tolerance (49, 50). We identified in one patient with autoimmune hepatitis (AIH) high CD200R+ monocyte numbers at baseline that further increased following IBT. Recently, CD200R was described as dampening the production of inflammatory cytokines by myeloid cells in healthy people. Nevertheless, in IFN-alpha-mediated inflammation, CD200R can amplify the immune response (51). Type I interferon activation is also described for AIH (52), and it is likely that IBT triggers the induction of IFN-alpha. With regard to immunotherapies and their increasing use in combination with local ablative therapies, the CD200–CD200R axis is of major importance and additional investigations are needed to identify targets harmonizing combinations of both therapy types.

In summary, local ablation by IBT and RFA causes an early systemic innate immune response and modulates myeloid cell populations in the peripheral blood of HCC patients. We demonstrate that IBT leads to changes in levels of several monocyte subpopulations as well as mMDSC and significantly alters expression levels of myeloid markers whereas RFA does less. Future studies are necessary to explore the impact of the therapy-induced innate immune response on tumor cells and how myeloid-targeting immunotherapies could be combined with interventional strategies. Regardless of mechanism, we

hypothesize that radiation-based therapy may be more advantageous when combined with immune-oncology. Thus, in the future, with further validation, addressing myeloid cells and their function may become an adjunct to alter effects of local ablative therapies.

Data availability statement

The datasets generated during and/or analyzed during the current study are available from the corresponding author on reasonable request.

Ethics statement

This study was reviewed and approved by Ethics commission of the University hospital, LMU München, Munich, Germany. The patients/participants provided their written informed consent to participate in this study.

Author contributions

MK, SK, LR, MRS, and MW conceived the experiments. MK, SK, EÖ, MS, and MW carried out the experiments. MK, SK, EÖ, MÜ, OÖ, MRS, MS, and MW analyzed the data. MK, SK, and MW wrote the manuscript. All authors contributed to manuscript revision, read, and approved the submitted version.

Acknowledgments

We would like to thank the Study Center (Department of Radiology, University Hospital, LMU Munich) for the study management and Cheryl Gray for technical assistance.

Conflict of interest

The authors declare that the research was conducted in the absence of any commercial or financial relationships that could be construed as a potential conflict of interest.

Publisher's note

Supplementary material

The Supplementary Material for this article can be found online at: https://www.frontiersin.org/articles/10.3389/fonc.2022.959987/full#supplementary-material

References

1. Sung H, Ferlay J, Siegel RL, Laversanne M, Soerjomataram I, Jemal A, et al. Global cancer statistics 2020: GLOBOCAN estimates of incidence and mortality worldwide for 36 cancers in 185 countries. *CA Cancer J Clin* (2021) 71:209–49. doi: 10.3322/caac.21660

2. Suresh D, Srinivas AN, Kumar DP. Etiology of hepatocellular carcinoma: Special focus on fatty liver disease. *Front Oncol* (2020) 10:601710. doi: 10.3389/fonc.2020.601710

3. EASL. EASL clinical practice guidelines for the management of patients with decompensated cirrhosis. *J Hepatol* (2018) 69:406–60. doi: 10.1016/j.jhep.2018.03.019

4. Reig M, Forner A, Rimola J, Ferrer-Fábrega J, Burrel M, Garcia-Criado A, et al. BCLC strategy for prognosis prediction and treatment recommendation Barcelona clinic liver cancer (BCLC) staging system. the 2022 update. *J Hepatol* (2021) 76:681–93. doi: 10.1016/j.jhep.2021.11.018

5. Öcal O, Rössler D, Ricke J, Seidensticker M. Advances in diagnostic and interventional radiology in hepatocellular carcinoma. *Digest Dis* (2022) 40:458–67. doi: 10.1159/000518101

6. Ikeda K, Kobayashi M, Kawamura Y, Imai N, Seko Y, Hirakawa M, et al. Stage progression of small hepatocellular carcinoma after radical therapy: comparisons of radiofrequency ablation and surgery using the Markov model. *Liver Int* (2011) 31:692–9. doi: 10.1111/j.1478-3231.2011.02480.x

7. He P, Guan S, Ren E, Chen H, Chen H, Peng Y, et al. Precision interventional brachytherapy: A promising strategy toward treatment of malignant tumors. *Front Oncol* (2021) 11:753286. doi: 10.3389/fonc.2021.753286

8. Song Z, Ye J, Wang Y, Li Y, Wang W. Computed tomography-guided iodine-125 brachytherapy for unresectable hepatocellular carcinoma. *J Canc Res Ther* (2019) 15:1553. doi: 10.4103/jcrt.jcrt_629_19

9. Balázs K, Kis E, Badie C, Bogdándi EN, Candéias S, Garcia LC, et al. Radiotherapy-induced changes in the systemic immune and inflammation parameters of head and neck cancer patients. *Cancers* (2019) 11:1324. doi: 10.3390/cancers11091324

10. Shi L, Wang J, Ding N, Zhang Y, Zhu Y, Dong S, et al. Inflammation induced by incomplete radiofrequency ablation accelerates tumor progression and hinders PD-1 immunotherapy. *Nat Commun* (2019) 10:5421. doi: 10.1038/s41467-019-13204-3

11. Franklin RA, Li MO. Ontogeny of tumor-associated macrophages and its implication in cancer regulation. *Trends Cancer* (2016) 2:20–34. doi: 10.1016/j.trecan.2015.11.004

12. Klemm F, Joyce JA. Microenvironmental regulation of therapeutic response in cancer. *Trends Cell Biol* (2015) 25:198–213. doi: 10.1016/j.tcb.2014.11.006

13. Kimm MA, Klenk C, Alunni-Fabbroni M, Kästle S, Stechele M, Ricke J, et al. Tumor-associated macrophages–implications for molecular oncology and imaging. *Biomed* (2021) 9:374. doi: 10.3390/biomedicines9040374

14. Seki E, Minicis SD, Österreicher CH, Kluwe J, Osawa Y, Brenner DA, et al. TLR4 enhances TGF-β signaling and hepatic fibrosis. *Nat Med* (2007) 13:1324–32. doi: 10.1038/nm1663

15. Li P, He K, Li J, Liu Z, Gong J. The role of kupffer cells in hepatic diseases. *Mol Immunol* (2017) 85:222–9. doi: 10.1016/j.molimm.2017.02.018

16. Hammerich L, Tacke F. Emerging roles of myeloid derived suppressor cells in hepatic inflammation and fibrosis. *World J Gastrointest Pathophysiol* (2015) 6:43. doi: 10.4291/wjgp.v6.i3.43

17. Shen Y, Wang H, Chen X, Li W, Chen J. Prognostic significance of lymphocyte-to-monocyte ratio and platelet-to-lymphocyte ratio in patients with hepatocellular carcinoma undergoing transcatheter arterial chemoembolization and radiofrequency ablation. *Oncotargets Ther* (2019) 12:7129–37. doi: 10.2147/ott.s217935

18. Yang Y-T, Jiang J-H, Yang H-J, Wu Z, Xiao Z-M, Xiang B-D. The lymphocyte-to-monocyte ratio is a superior predictor of overall survival compared to established biomarkers in HCC patients undergoing liver resection. *Sci Rep-uk* (2018) 8:2535. doi: 10.1038/s41598-018-20199-2

19. Ha Y, Ali MAM, Petersen MM, Harmsen WS, Therneau TM, Lee HC, et al. Lymphocyte to monocyte ratio-based nomogram for predicting outcomes of hepatocellular carcinoma treated with sorafenib. *Hepatol Int* (2020) 14:776–87. doi: 10.1007/s12072-020-10076-4

20. Li K-J, Xia X-F, Su M, Zhang H, Chen W-H, Zou C-L. Predictive value of lymphocyte-to-monocyte ratio (LMR) and neutrophil-to-lymphocyte ratio (NLR) in patients with oesophageal cancer undergoing concurrent chemoradiotherapy. *BMC Cancer* (2019) 19:1004. doi: 10.1186/s12885-019-6157-4

21. Motomura T, Shirabe K, Mano Y, Muto J, Toshima T, Umemoto Y, et al. Neutrophil–lymphocyte ratio reflects hepatocellular carcinoma recurrence after liver transplantation *via* inflammatory microenvironment. *J Hepatol* (2013) 58:58–64. doi: 10.1016/j.jhep.2012.08.017

22. Ziegler-Heitbrock L, Ancuta P, Crowe S, Dalod M, Grau V, Hart DN, et al. Nomenclature of monocytes and dendritic cells in blood. *Blood* (2010) 116:e74–80. doi: 10.1182/blood-2010-02-258558

23. Ziegler-Heitbrock L. Blood monocytes and their subsets: Established features and open questions. *Front Immunol* (2015) 6:423. doi: 10.3389/fimmu.2015.00423

24. Cassetta L, Baekkevold ES, Brandau S, Bujko A, Cassatella MA, Dorhoi A, et al. Deciphering myeloid-derived suppressor cells: Isolation and markers in humans, mice and non-human primates. *Cancer Immunol Immunother* (2019) 68:687–97. doi: 10.1007/s00262-019-02302-2

25. Bronte V, Brandau S, Chen S-H, Colombo MP, Frey AB, Greten TF, et al. Recommendations for myeloid-derived suppressor cell nomenclature and characterization standards. *Nat Commun* (2016) 7:12150. doi: 10.1038/ncomms12150

26. Endig J, Buitrago-Molina LE, Marhenke S, Reisinger F, Saborowski A, Schütt J, et al. Dual role of the adaptive immune system in liver injury and hepatocellular carcinoma development. *Cancer Cell* (2016) 30:308–23. doi: 10.1016/j.ccell.2016.06.009

27. Cavallo F, Giovanni CD, Nanni P, Forni G, Lollini P-L. 2011: the immune hallmarks of cancer. *Cancer Immunol Immunother: CII* (2011) 60(3):319–26. doi: 10.1007/s00262-010-0968-0

28. Kratofil RM, Kubes P, Deniset JF. Monocyte conversion during inflammation and injury. *Arterioscler Thromb Vasc Biol* (2017) 37:35–42. doi: 10.1161/atvbaha.116.308198

29. Wellenstein MD, de Visser KE. Cancer-Cell-Intrinsic mechanisms shaping the tumor immune landscape. *Immunity* (2018) 48:399–416. doi: 10.1016/j.immuni.2018.03.004

30. Capece D, Fischietti M, Verzella D, Gaggiano A, Cicciarelli G, Tessitore A, et al. The inflammatory microenvironment in hepatocellular carcinoma: A pivotal role for tumor-associated macrophages. *BioMed Res Int* (2013) 2013:187204. doi: 10.1155/2013/187204

31. Aubé C, Bouvier A, Lebigot J, Vervueren L, Cartier V, Oberti F. Radiological treatment of HCC: Interventional radiology at the heart of management. *Diagn Interv Imag* (2015) 96:625–36. doi: 10.1016/j.diii.2015.04.008

32. Galluzzi L, Buqué A, Kepp O, Zitvogel L, Kroemer G. Immunogenic cell death in cancer and infectious disease. *Nat Rev Immunol* (2017) 17:97–111. doi: 10.1038/nri.2016.107

33. Zhu M, Yang M, Zhang J, Yin Y, Fan X, Zhang Y, et al. Immunogenic cell death induction by ionizing radiation. *Front Immunol* (2021) 12:705361. doi: 10.3389/fimmu.2021.705361

34. Wang L, Guan R, Xie L, Liao X, Xiong K, Rees TW, et al. An ER-targeting Iridium(III) complex that induces immunogenic cell death in non-Small-Cell lung cancer. *Angewandte Chemie Int Ed* (2021) 60:4657–65. doi: 10.1002/anie.202013987

35. Walter F, Fuchs F, Gerum S, Rottler MC, Erdelkamp R, Neumann J, et al. HDR brachytherapy and SBRT as bridging therapy to liver transplantation in HCC patients: A single-center experience. *Front Oncol* (2021) 11:717792. doi: 10.3389/fonc.2021.717792

36. Dal-Secco D, Wang J, Zeng Z, Kolaczkowska E, Wong CHY, Petri B, et al. A dynamic spectrum of monocytes arising from the *in situ* reprogramming of CCR2+ monocytes at a site of sterile injury. *J Exp Med* (2015) 212:447–56. doi: 10.1084/jem.20141539

37. Olingy CE, Emeterio CLS, Ogle ME, Krieger JR, Bruce AC, Pfau DD, et al. Non-classical monocytes are biased progenitors of wound healing macrophages during soft tissue injury. *Sci Rep-uk* (2017) 7:447. doi: 10.1038/s41598-017-00477-1

38. Karlmark KR, Weiskirchen R, Zimmermann HW, Gassler N, Ginhoux F, Weber C, et al. Hepatic recruitment of the inflammatory Gr1+ monocyte subset upon liver injury promotes hepatic fibrosis. *Hepatology* (2009) 50:261–74. doi: 10.1002/hep.22950

39. Hamers AAJ, Dinh HQ, Thomas GD, Marcovecchio P, Blatchley A, Nakao CS, et al. Human monocyte heterogeneity as revealed by high-dimensional mass cytometry. *Arterioscler Thromb Vasc Biol* (2019) 39:25–36. doi: 10.1161/atvbaha.118.311022

40. Gabrilovich DI. Myeloid-derived suppressor cells. *Cancer Immunol Res* (2017) 5:3–8. doi: 10.1158/2326-6066.cir-16-0297

41. Grützner E, Stirner R, Arenz L, Athanasoulia AP, Schrödl K, Berking C, et al. Kinetics of human myeloid-derived suppressor cells after blood draw. *J Transl Med* (2016) 14:2. doi: 10.1186/s12967-015-0755-y

42. Ma C, Zhang Q, Greten TF. MDSCs in liver cancer: A critical tumor-promoting player and a potential therapeutic target. *Cell Immunol* (2021) 361:104295. doi: 10.1016/j.cellimm.2021.104295

43. Xu Y, Fang F, Jiao H, Zheng X, Huang L, Yi X, et al. Activated hepatic stellate cells regulate MDSC migration through the SDF-1/CXCR4 axis in an orthotopic mouse model of hepatocellular carcinoma. *Cancer Immunol Immunother* (2019) 68:1959–69. doi: 10.1007/s00262-019-02414-9

44. Veglia F, Sanseviero E, Gabrilovich DI. Myeloid-derived suppressor cells in the era of increasing myeloid cell diversity. *Nat Rev Immunol* (2021) 21(8):485–98. doi: 10.1038/s41577-020-00490-y

45. Kawai H, Oo MW, Tsujigiwa H, Nakano K, Takabatake K, Sukegawa S, et al. Potential role of myeloid-derived suppressor cells in transition from reaction to repair phase of bone healing process. *Int J Med Sci* (2021) 18:1824–30. doi: 10.7150/ijms.51946

46. Kristiansen M, Graversen JH, Jacobsen C, Sonne O, Hoffman H-J, Law SKA, et al. Identification of the haemoglobin scavenger receptor. *Nature* (2001) 409:198–201. doi: 10.1038/35051594

47. Taddio MF, Jaramillo CAC, Runge P, Blanc A, Keller C, Talip Z, et al. *In vivo* imaging of local inflammation: Monitoring LPS-induced CD80/CD86 upregulation by PET. *Mol Imaging Biol* (2021) 23:196–207. doi: 10.1007/s11307-020-01543-3

48. Austermann J, Roth J, Barczyk-Kahlert K. The good and the bad: Monocytes' and macrophages' diverse functions in inflammation. *Cells* (2022) 11:1979. doi: 10.3390/cells11121979

49. Shafiei-Jahani P, Helou DG, Hurrell BP, Howard E, Quach C, Painter JD, et al. CD200–CD200R immune checkpoint engagement regulates ILC2 effector function and ameliorates lung inflammation in asthma. *Nat Commun* (2021) 12:2526. doi: 10.1038/s41467-021-22832-7

50. Rygiel TP, Meyaard L. CD200R signaling in tumor tolerance and inflammation: A tricky balance. *Curr Opin Immunol* (2012) 24:233–8. doi: 10.1016/j.coi.2012.01.002

51. van der Vlist M, Ramos MIP, van den Hoogen LL, Hiddingh S, Timmerman LM, de Hond TAP, et al. Signaling by the inhibitory receptor CD200R is rewired by type I interferon. *Sci Signal* (2021) 14:eabb4324. doi: 10.1126/scisignal.abb4324

52. Tana MM-S, Klepper A, Lyden A, Pisco AO, Phelps M, McGee B, et al. Transcriptomic profiling of blood from autoimmune hepatitis patients reveals potential mechanisms with implications for management. *PloS One* (2022) 17:e0264307. doi: 10.1371/journal.pone.0264307

frontiers | Frontiers in Immunology

TYPE Original Research
PUBLISHED 27 October 2022
DOI 10.3389/fimmu.2022.1008865

OPEN ACCESS

EDITED BY
Apostolos Zaravinos,
European University Cyprus, Cyprus

REVIEWED BY
Qi-Dong Xia,
Huazhong University of Science and Technology, China
Disha Sharma,
Stanford Healthcare, United States
Marat Urmantsev,
Bashkir State Medical University, Russia

*CORRESPONDENCE
Wenqi Wu
wwqwml@163.com
Baoqing Sun
sunbaoqing@vip.163.com
Shujue Li
lishujue@163.com

†These authors have contributed equally to this work and share first authorship

SPECIALTY SECTION
This article was submitted to Cancer Immunity and Immunotherapy, a section of the journal Frontiers in Immunology

RECEIVED 01 August 2022
ACCEPTED 14 October 2022
PUBLISHED 27 October 2022

CITATION
Chang Z, Li R, Zhang J, An L, Zhou G, Lei M, Deng J, Yang R, Song Z, Zhong W, Qi D, Duan X, Li S, Sun B and Wu W (2022) Distinct immune and inflammatory response patterns contribute to the identification of poor prognosis and advanced clinical characters in bladder cancer patients. *Front. Immunol.* 13:1008865. doi: 10.3389/fimmu.2022.1008865

Distinct immune and inflammatory response patterns contribute to the identification of poor prognosis and advanced clinical characters in bladder cancer patients

Zhenglin Chang[1,2,3†], Rongqi Li[4†], Jinhu Zhang[3†], Lingyue An[3†], Gaoxiang Zhou[1,3], Min Lei[3], Jiwang Deng[3], Riwei Yang[3], Zhenfeng Song[2,3], Wen Zhong[3], Defeng Qi[3], Xiaolu Duan[3], Shujue Li[3*], Baoqing Sun[2*] and Wenqi Wu[1,3*]

[1]Department of Urology, The Second Affiliated Hospital of Guangzhou Medical University, Guangzhou, Guangdong, China, [2]Department of Allergy and Clinical Immunology, Department of Laboratory, National Center for Respiratory Medicine, National Clinical Research Center for Respiratory Disease, State Key Laboratory of Respiratory Disease, Guangzhou Institute of Respiratory Health, The First Affiliated Hospital of Guangzhou Medical University, Guangzhou, China, [3]Guangdong Key Laboratory of Urology, The First Affiliated Hospital of Guangzhou Medical University, Guangzhou, China, [4]Department of Hepatobiliary Surgery, Foshan Hospital of Traditional Chinese Medical, Foshan, Guangdong, China

Due to the molecular heterogeneity, most bladder cancer (BLCA) patients show no pathological responses to immunotherapy and chemotherapy yet suffer from their toxicity. This study identified and validated three distinct and stable molecular clusters of BLCA in cross-platform databases based on personalized immune and inflammatory characteristics. H&E-stained histopathology images confirmed the distinct infiltration of immune and inflammatory cells among clusters. Cluster-A was characterized by a favorable prognosis and low immune and inflammatory infiltration but showed the highest abundance of prognosis-related favorable immune cell and inflammatory activity. Cluster-B featured the worst prognosis and high immune infiltration, but numerous unfavorable immune cells exist. Cluster-C had a favorable prognosis and the highest immune and inflammatory infiltration. Based on machine learning, a highly precise predictive model (immune and inflammatory responses signature, IIRS), including FN1, IL10, MYC, CD247, and TLR2, was developed and validated to identify the high IIRS-score group that had a poor prognosis and advanced clinical characteristics. Compared to other published models, IIRS showed the highest AUC in 5 years of overall survival (OS) and a favorable predictive value in predicting 1- and 3- year OS. Moreover, IIRS showed an excellent performance in predicting immunotherapy and chemotherapy's response. According to immunohistochemistry and qRT-PCR, IIRS genes were differentially expressed between tumor tissues with corresponding normal or

adjacent tissues. Finally, immunohistochemical and H&E-stained analyses were performed on the bladder tissues of 13 BLCA patients to further demonstrate that the IIRS score is a valid substitute for IIR patterns and can contribute to identifying patients with poor clinical and histopathology characteristics. In conclusion, we established a novel IIRS depicting an IIR pattern that could independently predict OS and acts as a highly precise predictive biomarker for advanced clinical characters and the responses to immunotherapy and chemotherapy.

KEYWORDS

bladder cancer, chemotherapy, immunotherapy, immune and inflammatory characteristics, unsupervised cluster analysis

Introduction

Bladder Cancer (BLCA) has become an increasingly prominent public health issue worldwide due to its high recurrence rate, high metastatic propensity, and peculiar chemo- and radio-resistance (1, 2). Radical cystectomy can perform well in resecting localized tumors, and cisplatin-based neoadjuvant chemotherapy (NAC) remains the most established perioperative option so far. Nevertheless, the survival probability of patients after an operation is extremely low, and nearly 50% of them will ultimately experience the spread of cancer (3, 4). In the past decade, immunotherapy has evolved as one of the most promising advancements, deeply revolutionizing the therapeutic paradigm of BLCA. Factually, some immune checkpoint inhibitors have already been approved in advanced BLCA (5). Unfortunately, most patients show no pathological responses to immunotherapy and chemotherapy yet suffer from their toxicity. The distinct sensitivity to therapy might primarily be due to the molecular and genetic heterogeneity of the tumor microenvironment (TME) in BLCA (1, 3). Hence, there is an urgent need to identify the potential molecular subtype and develop novel and reliable markers to predict prognosis, chemotherapy, and immunotherapy efficacy for BLCA.

The initiation and progression of tumors not only depend on the genetic heterogeneity of malignant cells but also on the tumor microenvironment (TME) (6). The inflammatory milieu has been considered a pivotal aspect of a tumor, affecting various hallmarks of the tumor, including cell proliferation, angiogenesis, invasion, and metastasis (7, 8). Recently, a growing number of clinical and experimental evidences indicated that the acute inflammatory response could prevent the growth and invasion of the tumor, while chronic inflammation can aid the transformation of malignancy (9–11). Moreover, innate immunity can promote tumorigenesis, while adaptive immunity often restrains through immunosurveillance (7, 9, 12). It is worth noting that immune and inflammatory responses (IIR) play distinct roles in different stages of tumor progression, and the balance of IIR is crucial in restricting the development and progression of malignancy. The normal controlled inflammatory response can activate a specific immune response, resulting in healing (13). Conversely, prolonged and dysregulated inflammation is closely related to immune suppression, thus leading to disease progression (13, 14). The immune and inflammatory process is dynamic and changing over time, reflecting the degree of the normal or abnormal responses of the body. Although increasing research has focused on the molecular characteristics of BLCA based on gene expression patterns of immune or inflammation (15–19), there has been no report of prognosis-related classification that combined immune with inflammatory response patterns. Therefore, it is meaningful to identify the distinct IIR patterns and develop a novel prognosis, immunotherapy, and chemotherapy-related signature based on IIR patterns.

The IIR patterns and IIR-based signature (IIRS) were identified for the first time in this study using two cross-platform BLCA data. In addition, bladder tissues and corresponding clinical characteristics of BLCA patients were collected to validate the clinical application potential of the IIRS-score. These findings will unveil unknown molecular subtypes of TME-related immune and inflammatory responses and make current immunotherapy and chemotherapy strategies more efficient, optimizing the chance of response and reducing the overtreatment of non-responders.

Methods

Dataset acquisition and preparation

The RNA-Seq data of BLCA with matched clinicopathological features were obtained from TCGA database. The microarray data

set GSE32894 with corresponding clinical information was downloaded from the GEO database. IMvigor210 trial, including patients with metastatic urothelial cancer treated with atezolizumab, was obtained from http://research-pub.gene.com/IMvigor210CoreBiologies/. In two data sets, the selection criteria were as follows: (1) have survival data; (2) follow-up ≥ 1 month; (3) pathological diagnosis was BLCA. Finally, 403 BLCA samples of TCGA, 224 of GSE32894, and 348 of IMvigor210 were enrolled in this study.

Identification of immune and inflammatory phenotype-related genes (IIRGs)

We analyzed six inflammation-related gene sets (M3952, M5932, M6910, M17322, M38152, and M39641) from the GSEA database, representing diverse targets from inflammatory cells, cytokines, pathways, and responses. In addition, immune-related genes were picked from the Tracking Tumor Immunophenotype database. These targets were put into the STRING database, and CytoNCA plug-in was applied to sieve the IIRGs.

Identification of the IIR-related patterns by consensus clustering

Based on these identified IIRGs, the consensus clustering method was applied to identify novel IIR patterns in TCGA cohort to classify patients. We limited the clustering algorithm to 'pam' and performed 100 iterations here. Two GEO cohorts were utilized to verify the clustering stability using the same method. To determine the optimal clustering number, we applied the PCA method to extract the data of the consensus matrix, followed by generating the fitting curve using the 'ecdf' method. After calculating the area under the cumulative distribution function (CDF) curve between 0.1 and 0.9, the corresponding K was regarded as the optimal number of clustering according to the minimum area under CDF. The overall survival (OS) among classifications was calculated using the Kaplan-Meier (KM) method. Principal component analysis (PCA) was also utilized to demonstrate expression patterns of IIRGs in different BLCA patients.

Comparison of tumor microenvironment infiltration patterns

Based on the ESTIMATE algorithm, we generated the immune score, stromal score, and tumor purity. We then generated the inflammatory score based on the ssGSEA algorithm using the identified inflammation-related gene sets. Next, CIBERSORTX was applied to evaluate the relative abundances of multiple immune cell types (20). The influence of immune cell types on survives was determined by classifying the patient's samples into high or low groups according to relative expression levels of immune cell types. Cases were divided into two groups based on the relative expression levels of immune cell types, and then the prognoses of BLCA patients with different immune cell expression levels were analyzed by the Kaplan–Meier survival curve. Subsequently, the univariate Cox regression was applied to identify the prognostic-related differentially expressed immune cells among clusters.

Identification of the BLCA-related inflammation activity signature

We established scoring systems to quantify the different inflammatory activity patterns to increase our understanding of cluster-related inflammatory activities. First, 11 signatures of inflammatory activity related to the progression of bladder cancer were selected from the GSEA database (Supplementary Table 1). Then, using a univariate Cox regression model, we performed prognostic analysis on the genes in each signature. Next, genes with significant prognoses ($p<0.05$) were extracted for further analysis. Afterward, PCA was performed to establish inflammatory signatures. Both principal components 1 and 2 were selected as signature scores. Finally, the scores were defined using a method similar to Genomic Grade Index (21, 22):

$$\text{score} = \sum(\text{PC1i} + \text{PC2i})$$

Where i is the expression of inflammatory activity-related genes with a significant prognosis among clusters.

Construction of IIR-based signature (IIRS)

To conduct the quantitative assessment of the IIR pattern of each patient, we constructed a scoring system termed IIRS. First, the "limma" package was utilized to filter the differentially expressed IIRGs (DEIIRGs) among patterns. The optimal IIRS was then established based on the machine learning and Cox regression. We then calculated the IIRS-score (risk-Score) of each patient to predict the prognosis of BLCA and utilized the "survminer" package to determine the optimal cut-off score for the risk. Next, the time-dependent receiver operating characteristic (ROC) curve analysis was conducted to compare the predictive accuracy and other clinicopathological characteristics of IIRS. Moreover, we picked five reported immune or inflammatory signatures to compare the prognostic values (15–19). Finally, the clinical utility was evaluated by decision curve analysis (DCA).

Gene set enrichment analysis of the IIRS genes

Based on the median expression of IIRS genes, 403 BLCA patients were divided into two groups. First, GSEA was conducted to investigate the potential molecular mechanisms of IIRS genes, setting the "c2.cp.kegg.v7.1.-symbols.gmt" as the reference gene set. The top 10 terms of each IIRS gene were obtained after excluding unrelated signaling pathways such as "acute myeloid leukemia" and "endometrial cancer".

Biomarkers for predicting immunotherapy response and chemotherapeutic response

The tumor mutation burden (TMB) of each TCGA-BLCA patient was calculated by Perl script. Then, we divided patients into four groups based on the median cut-offs of IIRS-score and TMB to see if the IIRS-TMB joint diagnosis had a thorough prediction ability. A total of 50 checkpoints were collected from the previously published articles. In addition, IMvigor210 cohorts were included in our study to see if the IIRS could predict clinical response to PD-1 blockers. Moreover, we applied The Cancer Immunome Atlas (TCIA) to detect the immunophenoscore (IPS) of tumor samples, which can predict the clinical response to CTLA-4 and PD-1 blockers. Finally, to provide individualized medication for each BLCA patient, we picked underlying drugs of BLCA in the 'pRRophetic' package according to previously published articles, followed by evaluating the half-maximal inhibitory concentration (IC50) of each drug.

Tumor mutation analysis of DEIIRGs

The single nucleotide variants data of BLCA samples based on the "VarScan" process were obtained from the TCGA database. Mutation data were visualized using the "maftools" package to identify the somatic mutations of the patients with the identified genes of IIRGs.

Quantitative real-time polymerase chain reaction (qRT-PCR)

Three bladder samples of carcinomas and adjacent normal tissues were obtained from BLCA patients who underwent surgery at Guangzhou Medical University's Second Affiliated Hospital (GZhmu2.cohort) without preoperative immunotherapy or chemotherapy. RNA extraction and qRT-PCR were conducted as previously described (22, 23). The PCR primers are described in Supplementary Table 2. The relative expression of IIRS genes was calculated from three technical replicates using the $2^{-\Delta\Delta Ct}$ method.

Hematoxylin and eosin (H&E)

A total of 403 whole-slide H&E-stained histopathology images were obtained from TCGA. Moreover, 14 bladder samples of cancer tissues were obtained from BLCA patients who underwent surgery at Guangzhou Medical University's First Affiliated Hospital (GZhmu1.cohort) without preoperative immunotherapy or chemotherapy. The corresponding clinical information is displayed in Supplementary Table 3. A single tissue was too small to scan and was abandoned for subsequent analysis. All images were observed by a tissue scanner (PathScope 4s, DigiPath, NV, USA) to observe the inflammatory and immune histological changes of bladder tissues. The corresponding score system was performed as previously described (22, 23).

Immunohistochemistry (IHC)

The primary antibodies: CD247 (1:200), TLR2 (1:200), c-MYC (1:500), IL10 (1:200), and FN1 (1:200) were obtained from Proteintech (Rosemont, IL, USA) and were applied for IHC. IHC was conducted as previously described (22, 23). For each IHC-tissue section, five random visual fields were selected for determination. The relative expressions of IIRS genes were obtained by calculating the means of integrated optical density (MOD) using ImageJ software.

Statistical analyses

R and IBM SPSS Statistics were used to conduct statistical analyses. The KM analysis was conducted using the log-rank test. The Hazard Ratio (HR) and 95% confidence interval (CI) were generated using KM and Cox regression. Statistical significance of the comparison between two groups for continuous variables and categorical variables was estimated by Student's T-test or Mann-Whitney-Wilcoxon test and Chi-square test or Fisher's exact tests, respectively. The existence of a correlation between variables was accessed by Spearman correlation analysis. The statistical significance of PCR and IHC were assessed by t-tests or one-way ANOVA with LSD *post hoc* comparisons or Dunnett's T3 *post hoc* tests. A two-tailed P value less than 0.05 was considered statistically significant.

Results

Collection of IIRGs

The workflow is shown in Figure 1. 1193 inflammatory genes and 178 immune genes were enrolled into our analysis (Supplementary Figures 1A, B). After filtering, a total of 85 IIRGs were selected (Supplementary Figures 1C-F, Supplementary Table 4).

Three distant IIR Clusters with different clinical outcomes of BLCA

The optimal clustering division was three based on the minimum area under the CDF curve. The heatmap showed a relatively clear-cut boundary, indicating the reliability of clustering (Figure 2A). KM analysis revealed that patients in Clusters A and C had a survival benefit, while patients in cluster B had the worst outcome (Figure 2B). The PCA distribution patterns represented three different dynamic IIR types and validated three clusters assignment (Figure 2C). Moreover, the hierarchical clustering revealed that the expression of IIRGs among subtypes was significantly different, further verifying the reliability of clustering (Figure 2D). We further confirmed less immune and inflammatory cells infiltration in Cluster A and more infiltration in Cluster C (Figures 2E, F). Finally, two GEO cohorts were applied to prove the repeatability of classification (Supplementary Figures 2A, B).

Existence of diverse tumor microenvironment infiltration among three identified patterns

The ESTIMATE and ssGSEA tools were used to analyze the levels of the immune score, stromal score, tumor purity, and

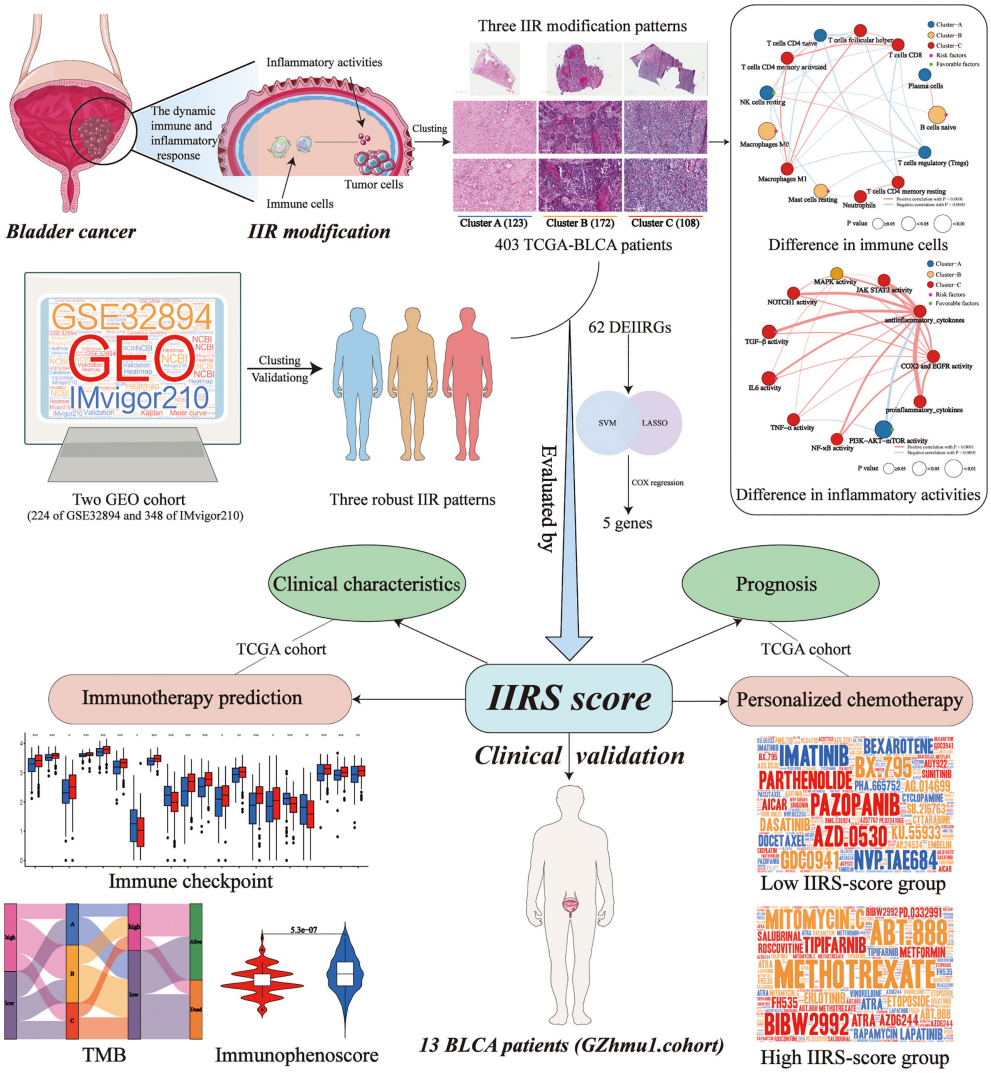

FIGURE 1
The workflow of designed analysis.

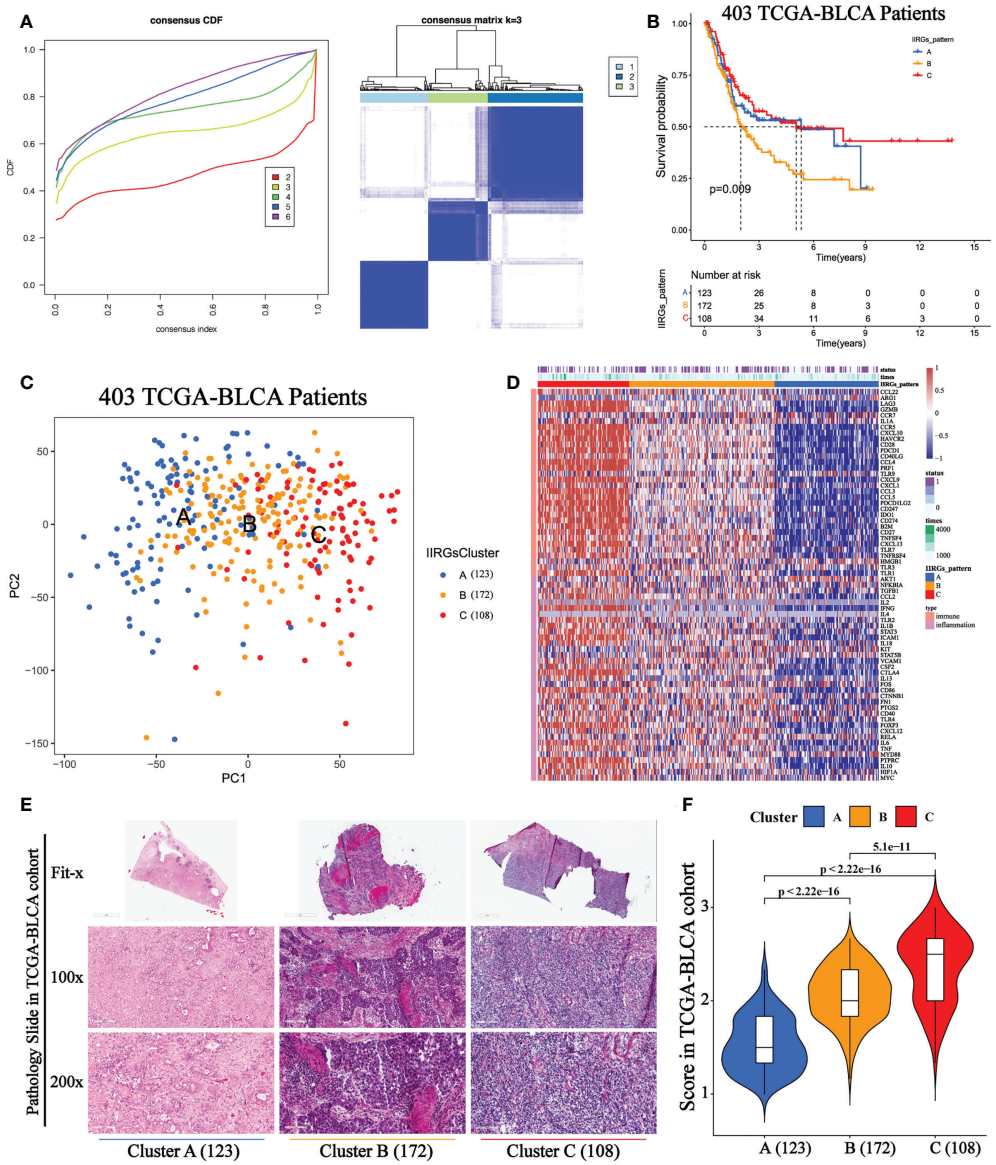

FIGURE 2
Unsupervised consensus cluster analysis of IIRGs in TCGA-BLCA cohort. **(A)** Heatmap of consensus clustering matrix for k =3 and Consensus clustering cumulative distribution function (CDF) for k = 2 to 6. **(B)** KM curves of OS among clusters in BLCA. **(C)** PCA among three IIRG modification patterns. **(D)** Hierarchical clustering of IIRGs in TCGA-BLCA cohort. **(E)** Representative photomicrographs of H&E staining of bladder sections among clusters. **(F)** The One-way ANOVA analysis of histopathological scores among clusters.

inflammation score among clusters (Supplementary Table 5). Cluster A showed the highest tumor purity, while Cluster C referred to the highest inflammation, immune, and stromal scores, further validating the distribution of the three subclasses (Supplementary Figures 3A-D). Subsequently, we noticed that Cluster A showed the highest abundance of NK cells resting, T cells CD4 naïve, T cells regulatory (Tregs), and Plasma cells. On the other hand, cluster B was characterized by immature and resting immune cells, including Macrophages M0, Mast cells resting, and B cells naïve. This can help explain that it did not survive as well as Cluster A or Cluster C. Cluster C was primarily made up of activated immune cells, such as T cells CD8, T cells follicular helper, T cells CD4 memory activated, T cells CD4 memory resting, Neutrophils, and Macrophages M1 (Supplementary Figure 3E).

Cluster B-specific differentially expressed immune cells and inflammatory activity might result in a poor outcome for TCGA-BLCA patients

In order to investigate the mechanisms leading to clinical phenotypic heterogeneity among clusters, univariate Cox regression was conducted to analyze 13 differentially expressed immune cells (Supplementary Table 6). Cluster A-specific NK cells resting were regarded as prognosis-related favorable factors (Figure 3A). While prognosis-related risk factors consisted of Cluster B-derived Macrophages M0, Mast cells resting, and B cells naïve. This might help explain the worst prognosis of cluster B despite having a high immune score. Further KM analysis showed that the high-level group of T cells follicular helper, T cells CD4 memory activated and NK cells resting had significantly higher survival probability than the low-level group (Figures 3B–D). Conversely, the abundance of Macrophages M0, Mast cells resting, T cells CD4 memory resting, and Neutrophils were related to poor prognosis (Figures 3E–H).

Furthermore, we assessed the relationship between clusters and inflammatory activity signatures. Cluster A positively correlated with the higher activity of PI3K-AKT-mTOR (Figure 3I), which was related to favorable prognosis (Supplementary Figure 4A). MAPK activity was regarded as the specific inflammatory activity of cluster B (Figure 3J). Cluster C showed the highest abundance of other inflammatory activities (Figures 3K–S), significantly related to OS (Supplementary Figures 4B-3G). Next, univariate Cox regression was conducted to analyze these differentially expressed inflammatory activities. PI3K-AKT-mTOR was cluster-specific favorable factor, which probably accounts for why Cluster A had a favorable prognosis (Figure 3T).

Construction of the IIRS

We obtained 62 DEIIRGs among clusters (Figure 4A). Univariate and multivariate Cox regression models identified 5 DEIIRGs (Figures 4B, C; Supplementary Figure 4H). The risk score = 1.13822603*Expression (FN1) + 0.50559931*Expression (IL10) + 0.631436*Expression (MYC) – 0.8375582*Expression (CD247) – 0.8336228*Expression (TLR2). GSEA further revealed that the five genes were correlated with immune pathways (Figure 4D).

Genetic alteration of IIRS genes in TCGA-BLCA patients

The waterfall plot revealed 38 mutated DEIIRGs with higher than 0.5% mutation frequencies (Supplementary Figures 5A, B). Notably, TP53 and FN1 were regarded as the most frequently mutated DEIIRGs. Further pathway enrichment indicated that these 38 mutated DEIIRGs were significantly associated with the PD-L1 expression and PD-1 checkpoint pathway in cancer (Supplementary Figure 5C). Next, we unveiled the genetic alteration of IIRS genes. These genes are FN1 (5.34%), TLR2 (0.73%), IL10 (0.49%), MYC (0.49%), and CD247 (0.24%) (Supplementary Figure 5D).

IIRS could predict OS and the IIR patterns

The KM analysis showed that the high IIRS-score group was significantly associated with low survival probability (Figure 4E). After adjusting clinical characteristics, 168 patients with complete clinical information were collected (Supplementary Table 7). The ROC curve revealed a high accuracy of IIRS in predicting the prognosis of BLCA patients, with an AUC of 0.671, 0.719, and 0.790 in 1, 3, and 5 years, respectively, compared to other clinical factors (Figure 4F). Compared to other models, IIRS showed the highest AUC in 5 years and a favorable predictive value in predicting 1- and 3- year OS (Supplementary Figure 4I), which revealed a favorable efficiency of our model in predicting short-term and long-term survival for BLCA patients.

Further, we noticed that patients in Cluster B showed a higher IIRS score than other subclasses (Figure 4G), which might help explain the survival inferiority of Cluster B. Simultaneously, patients in Cluster A showed a lower IIRS score compared to other molecular subclasses. Moreover, a Chi-square test demonstrated a significant difference in IIRS scores among IIR-clusters (Figure 4H). These results indicated that the IIRS had a strong predictive ability for survival prediction and IIR patterns.

Two IIRS subtypes have distinct clinical behaviors

To investigate whether IIRS was related to OS among different clinical subgroups, the log-rank analysis indicated that lower risk scores were associated with favorable clinical characteristics in most subgroups (Supplementary Figures 6A-E).

IIRS showed a good performance in predicting the clinical response of immunotherapy and chemotherapy

TMB has been regarded as an essential biomarker of the clinical response to immunotherapy in BLCA (24). We calculated the TMB value of each patient, and it was used to

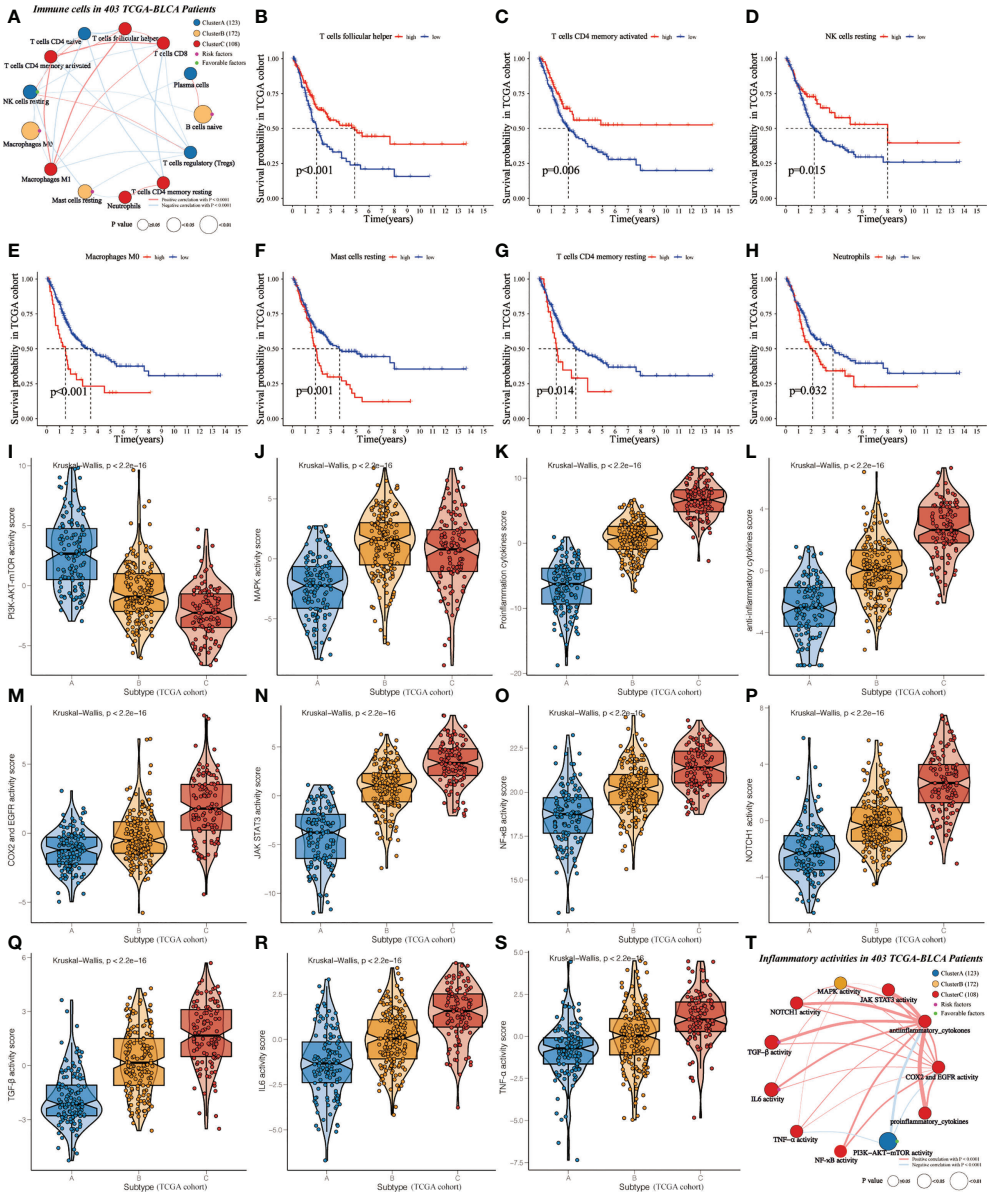

FIGURE 3
Identification of cluster-specific and prognosis-related differentially expressed immune cells and inflammatory activities in TCGA-BLCA cohort. **(A)** Interaction of cluster-specific and prognosis-related differentially expressed immune cells. Cluster A, blue; Cluster B, yellow; Cluster C, red. These circles highlighted in Green (purple) referred to favorable (risk) factors of overall survival. The size of each circle evaluated by Unicox p-values indicated the survival impact of each immune cell. The connection shows the interaction between two immune cells, and the thickness of the lines means the correlation strength among cells. The red (blue) lines represented the positive (negative) correlation. **(B-H)** KM curves were applied to estimate OS for the high- and low-level groups of differentially expressed immune cells. **(I-S)** The violin plots demonstrate the differences in expression levels of various inflammatory activities among clusters. **(T)** Interaction of cluster-specific and prognosis-related differentially expressed inflammatory activities.

analyze the correlation between IIR clusters and IIRS scores (Supplementary Table 8). First, we noticed that patients in Cluster C (Figure 5A) and IIRS low-risk group (Figure 5B) showed the highest TMB values, matching their higher survival probability. The Sankey diagram further revealed that most Cluster B patients had high IIRS scores and low TMB, which was associated with a poor clinical outcome (Figure 5C). The further KM curve indicated that BLCA patients with high TMB showed a higher survival advantage than patients in the low TMB group (Figure 5D). Moreover, a high-TMB/low-IIRS risk score had the highest survival probability, whereas a low-TMB/high-IIRS score showed the worse clinical outcome (Figure 5D).

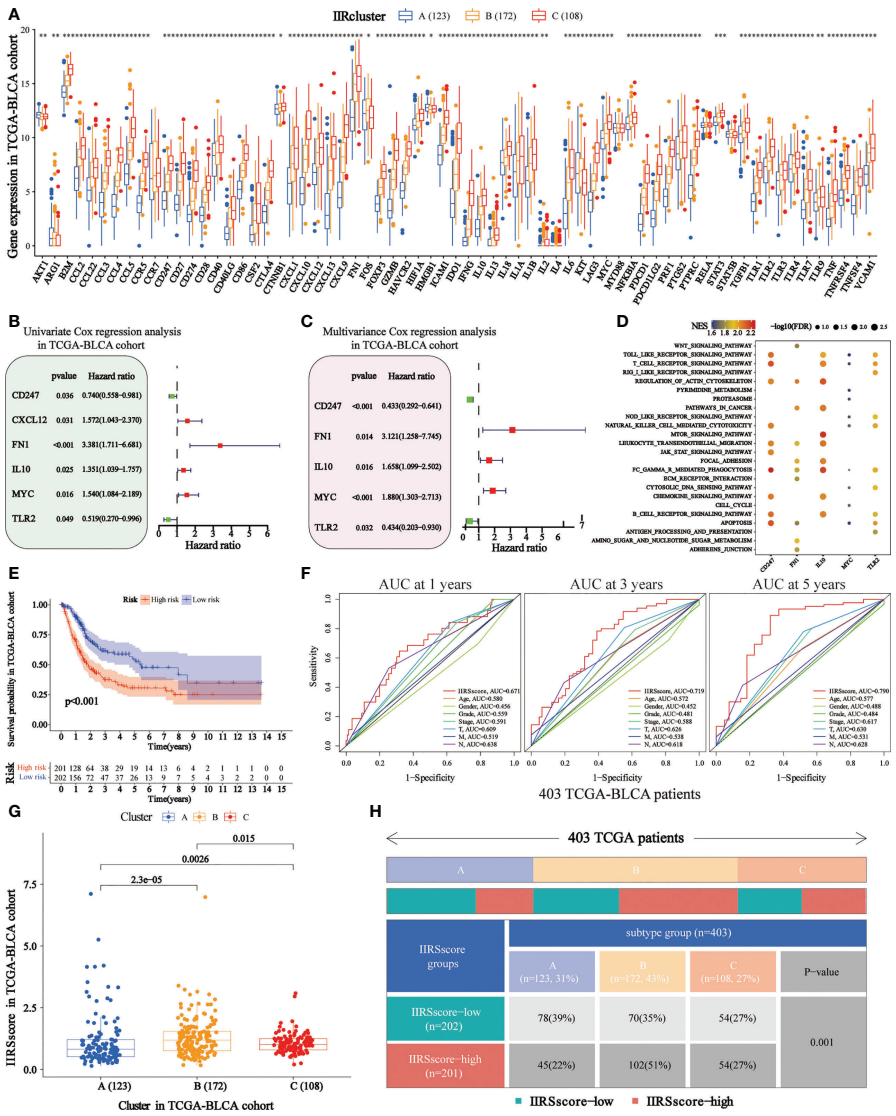

FIGURE 4
Construction of immune and inflammatory phenotype-related gene signature in TCGA-BLCA cohort. **(A)** Differences in the levels of the 85 IIRGs in three subtypes (***P< 0.001; **P< 0.01; *P< 0.05). **(B, C)** Forrest plot depicting the univariate and multivariance Cox regression analysis of DE. **(D)** Enrichment analysis for pathways in the high expression group of the IIRS genes. NES is the normalized enrichment score. **(E)** Survival analyses were applied to evaluate overall survival for the high- and low-risk groups in the TCGA train cohort. **(F)** AUCs (Area under ROC curve) for 1-, 3-, and 5-year OS and the risk score and clinical characteristics ROC curves. **(G)** Distributions of IIRS-score among clusters. **(H)** The Chi-square test was applied to evaluate the difference in immune and inflammatory patterns among patients in the high- and low-IIRS-score groups.

Next, we noticed that almost all differentially expressed checkpoints were significantly upregulated in high IIRS-score groups compared with the low IIRS-score groups (Figures 5E, F).

Immunotherapies represented by PD-1 and CTLA-4 blockade have undoubtedly emerged as a critical breakthrough in BLCA therapy. We found that patients with low IIRS-score showed significant therapeutic advantages compared to those with high IIRS scores in the IMvigor210 cohort (Figure 5G). To further evaluate the relationship between IIRS and the clinical response to CTLA-4 and PD-1 blockers, we calculated the IPS of 402 BLCA patients. The results indicated that the low IIRS score was significantly correlated with CTLA-4 and PD-1 blockers (Figure 5H). Moreover, we noticed that the IC50 of potential majority drugs, including cisplatin, was significantly higher in the low IIRS-score group than in IIRS high-risk patients (Supplementary Figure 7).

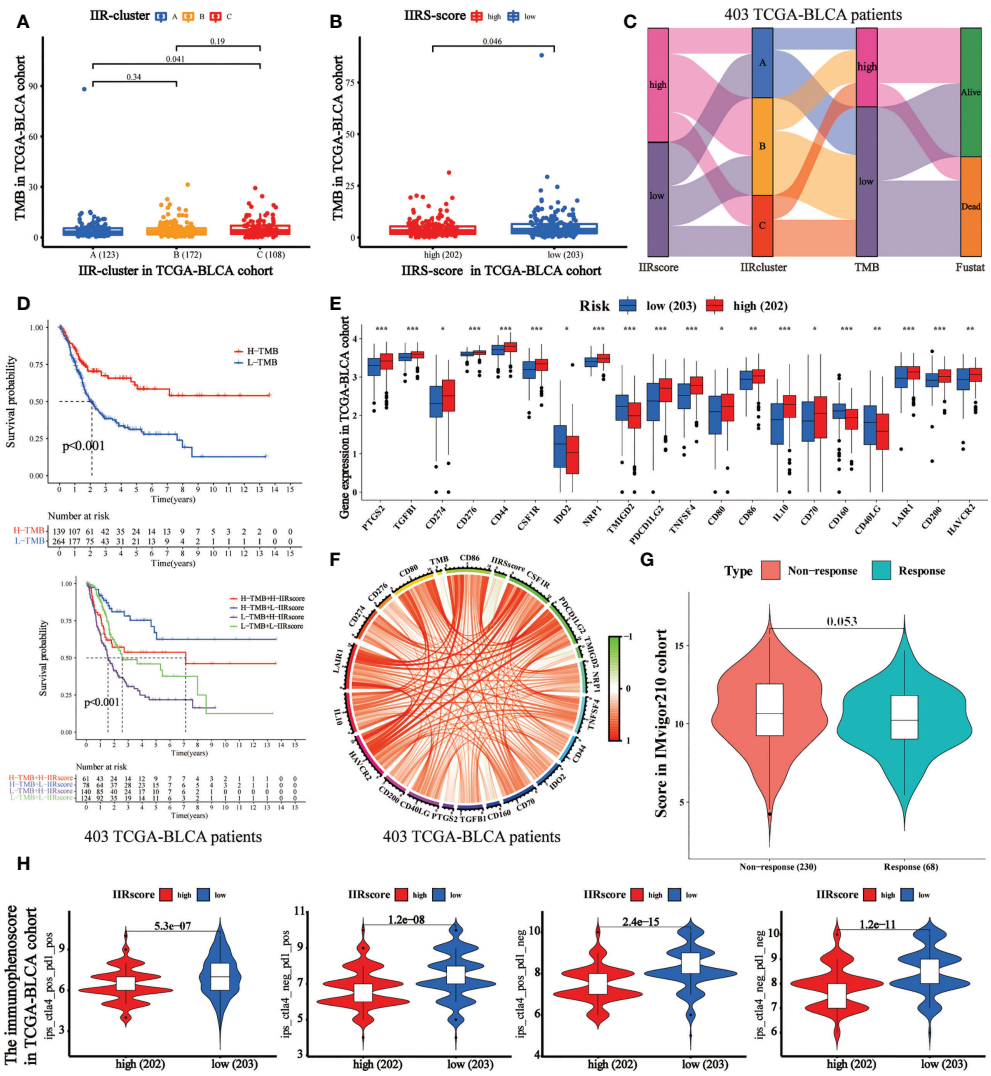

FIGURE 5
Evaluation of the performance of IIRS in the TCGA-BLCA patients' immunotherapy. **(A)** The distribution of the TMB value in different IIR-clusters in TCGA-BLCA patients. **(B)** Differences in the TMB value between high- and low-risk IIRS groups. **(C)** The Sankey diagram was used to visualize the relation between IIR-clusters, IIRS-score groups, and TMB. Each column indicates a characteristic variable, different colors show different types, and lines represent the distribution of the same sample in different characteristic variables. **(D)** KM curves for different groups stratified by TMB or combining IIRS with TMB in the TCGA-BLCA cohort. **(E)** Differences in the expression of immune checkpoints between high- and low-risk IIRS groups. The upper and lower ends of the boxes refer to an interquartile range of values. **(F)** The correlation chord chart displays the mutual correlation among IIRS risk score, TMB, and checkpoints. **(G)** The differences in the clinical response (CR/PR, SD/PD) to anti−PD-1 immunotherapy in high or low IIRS-score groups in the IMvigor210 cohort. **(H)** The differences of the immunophenoscore (IPS) to anti−PD-1 or/and anti−CTLA4 immunotherapy in high or low IIRS-score groups. ***P < 0.001; **P < 0.01; *P < 0.05.

Evaluation of the IIRS genes' expression

According to the histopathological section, the infiltration of immune and inflammatory cells in the high or low IIRS-risk group was significantly different (Figures 6A, B). We further explored the expression of five identified genes in the Human Protein Atlas (HPA) database. Compared with the normal tissues, FN1, IL10, and MYC were highly expressed, while the expression of CD247 was decreased in tumor bladder tissues (Figure 6C). Nevertheless, the HPA database has not included information on TLR2 due to its limited bladder tissues. So, we further evaluated the expression of the five proteins in two cohorts. In the IMvigor210 cohort, FN1, IL10, and MYC expressions in the IIRS high-risk group were significantly upregulated, while CD247 was significantly downregulated (Figure 6D). In the GSE32894 cohort, CD247 in the IIRS low-risk group was significantly upregulated, while MYC was significantly downregulated (Figure 6E). Finally, we evaluated

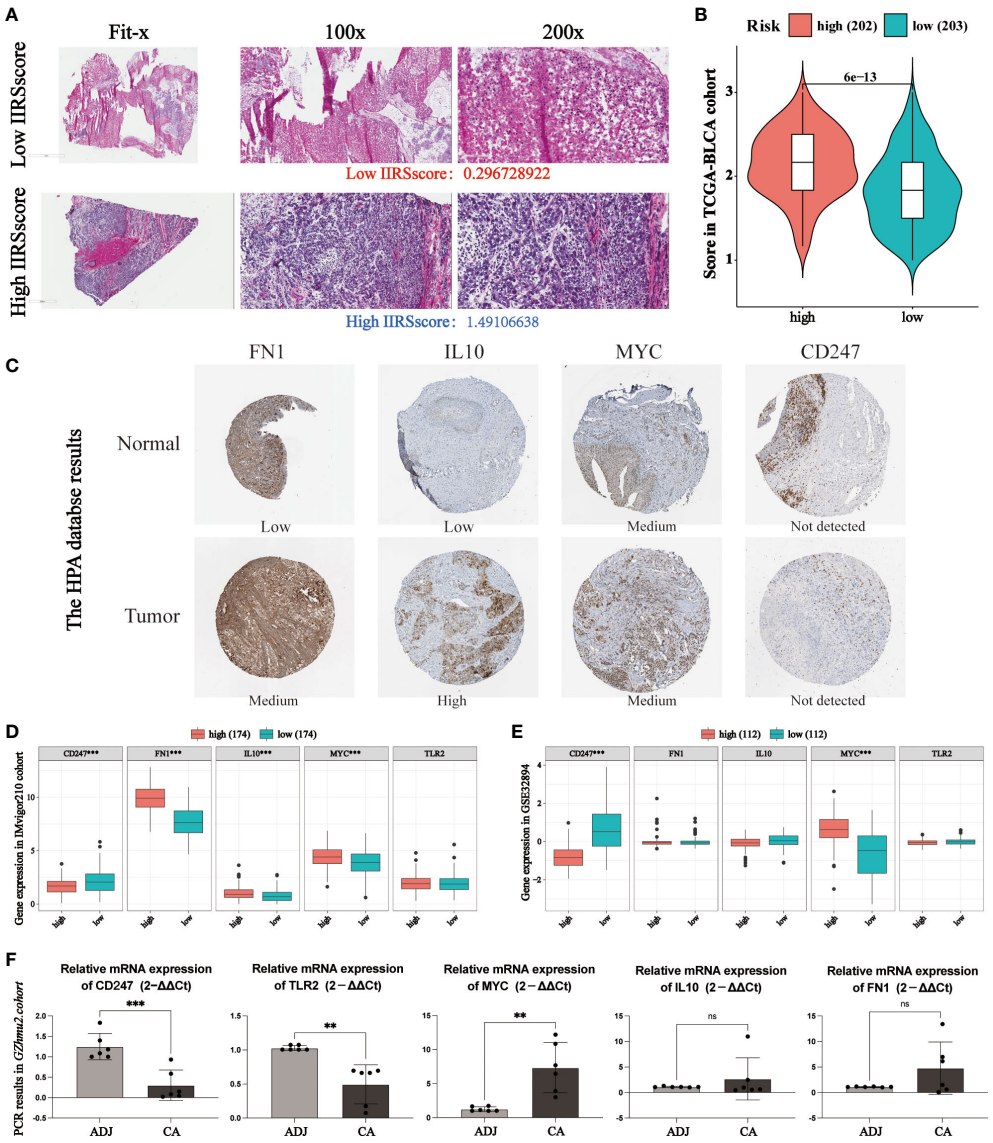

FIGURE 6
Evaluation of the expression of identified IIRS genes. **(A)** Representative photomicrographs of H&E staining of bladder sections between high or low IIRS-score groups. **(B)** Student's T-test of histopathological scores between high or low IIRS-score groups. **(C)** The representative images of the immunohistochemical labeling of the identified genes of IIRGS on bladder tissues. Data were obtained from the human protein atlas (https://www.proteinatlas.org/). **(D, E)** Differences in the levels of the 5 identified genes of IIR signature in GEO cohorts. **(F)** Differences in the levels of the 5 identified genes of IIR signature in bladder cancer (CA) tissues and adjacent (ADJ) normal tissues. ***P < 0.001; **P < 0.01; ns refer to not statistically significant.

the expressions of five identified genes in human bladders. As expected, MYC expressions in the cancer tissues were significantly upregulated, while CD247 and TLR2 were significantly downregulated in the adjacent normal tissues (Figure 6F). These data indicated that IIRS genes were differentially expressed between tumor tissues with corresponding normal or adjacent tissues.

Evaluating the clinical application potential of the IIRS score

To evaluate the clinical application potential of the IIRS score, we first collected 13 bladder tissues of BLCA patients. First, the relative expression of five IIRS genes and the IIRS scores of 13 patients were evaluated by IHC (Supplementary Table 9).

Intriguingly, these patients with higher T and M stages showed increased IIRS scores (Figures 7A–C). Next, the H&E-stained images evaluated the IIR cluster and inflammatory and immune scores of 13 patients (Supplementary Table 10). The HE-scores showed a nearly significant correlation with IIRS-scores (Figure 7D, p=0.0506), indicating that IIRS-score can effectively reflect the inflammatory/immune infiltration of bladder tissues. Furthermore, patients in Cluster B showed the highest IIRS scores than other subclasses (Figure 7E), which further proved that the IIRS score is a valid substitute for IIR patterns.

Discussion

BLCA is one of the most frequent tumors in the urinary tract, with nearly 200,000 deaths reported worldwide annually, which carries a considerable financial and societal debt to countries (1, 2). Along with the growing molecular understanding of tumors, we have realized that BLCA is a heterogeneous disease with diverse oncogenic pathways and unique tumor microenvironment (TME) infiltration characteristics (2, 25). This molecular diversity bestows the

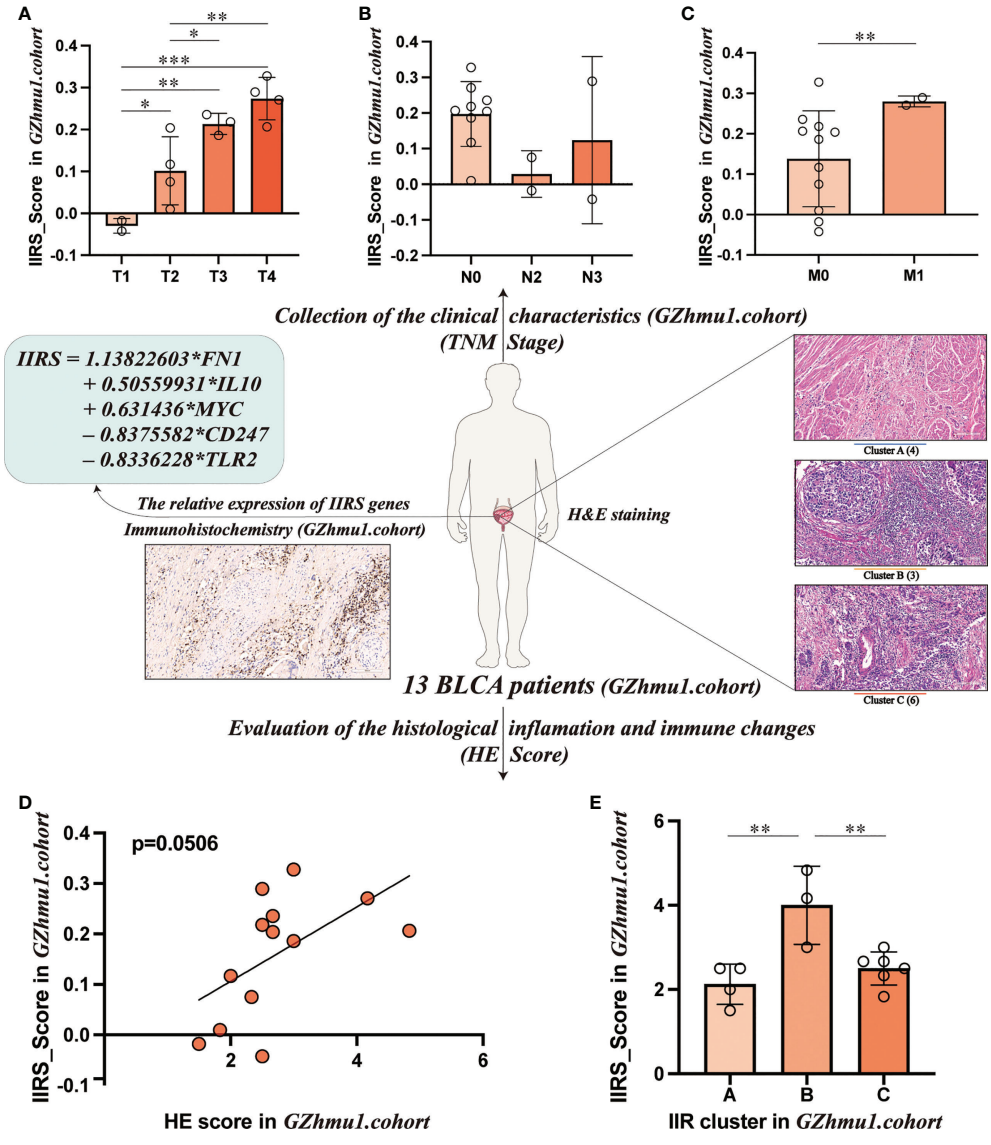

FIGURE 7
Evaluating the clinical application potential of IIRS-score in GZhmu1.cohort. **(A-C)** Differences in the IIRS-score among different TNM groups. **(D)** The correlation between IIRS-score and HE-score. **(E)** Distributions of IIRS-score among clusters. (***P< 0.001; **P< 0.01; *P< 0.05).

poor treatment responses that oncologists often see when treating BLCA. Despite several therapeutic advances in BLCA, the traditional histological subtype usually fails to accurately predict clinical response to immunotherapy and chemotherapy (1, 5). Ever-increasing studies have revealed the critical role of immune and inflammatory responses (IIR) in facilitating or constraining the progression of tumors. Although several immune or inflammatory response-related patterns of BLCA have been identified (15–19), most of these researches seem to ignore the indivisible relationship between immune and inflammation. Thus, comprehensive analyses of IIR patterns in tumor microenvironment (TME) infiltration characteristics of BLCA remain urgently needed.

In the current study, three distinct and stable IIR subtypes have been identified and survival analysis suggested that cluster A and Cluster C had a favorable prognosis while cluster B had a worse prognosis. Previous studies demonstrated that normal controlled inflammation and immunity were correlated with favorable prognosis, while uncontrolled inflammation and immunity can result in disease progression (13, 26–29). Consistent with this, Cluster A and Cluster C may cause the normally controlled inflammation, while cluster B seems to be related to uncontrolled inflammation. H&E-stained histopathology images and immune scores confirmed clusters' distinct infiltration of immune and inflammatory cells. A limited and balanced inflammation can initiate a favorable immune response (13, 26, 27), which is corroborated by the H&E results in cluster A. Patients in cluster C with a favorable prognosis showed massive infiltration of immune and inflammatory cells, which is in agreement with the concept that highly controllable inflammation in tumors is related to increased survival of patients with nearly any type of cancer (5, 27). However, some highly infiltrating cells may be retained in the stroma surrounding tumor nests, suggesting that these cells are ineffective in their duties as anti-tumor agents (5, 28). The stromal status, which is defined as "loose" or "dense," might influence the migration of immune or inflammatory cells and restrict them from interacting with cancer cells (29). Following this, we observed that the high-level immune and inflammatory cells in cluster B were nearly nonexistent in the cancer cells, which might help explain the mismatched survival advantage of cluster B. We first identified cluster-specific and prognosis-related immune cells to further investigate the causes of these differences. Cluster A-specific NK cells resting were the prognosis-related favorable factors, while prognosis-related risk factors consisted of Cluster B-specific Macrophages M0, Mast cells resting, and B cells naïve. Although immature immune cells can help the body struggle with cancer, a recent study demonstrated that these immature cells could aid the metastatic spread, which helps explain the Cluster B-specific unfavorable prognosis (30, 31). Cluster C with a better prognosis was prominently composed of various activated immune cells, suggesting that they play a positive role in BLCA progression. Numerous activated function immune cells contribute to anti-tumor immunity, as they transmigrate across the stroma into the tumor (32).

Furthermore, we noticed that the relative abundance of 11 selected inflammatory activities differed significantly among clusters, suggesting the critical role of IIR in the development of BLCA. PI3K/AKT/mTOR and MAPK were activated in clusters A and B, respectively. Other inflammatory-activities populations were significantly more abundant in cluster C than in the other clusters, confirming the activated inflammatory status in cluster C. A growing number of researches have shown that inflammation plays a vital role in the progression of BLCA through various molecular basis and signaling pathways (14, 33–38). Cytokines, the most pivotal effector and messenger molecules in the immune and inflammatory responses, mediate the interactions between immune and non-immune cells in TME, thereby involving the occurrence, invasion, and migration of BLCA (14, 33). Cyclooxygenase-2 (Cox-2), a key enzyme that catalyzes the synthesis of prostaglandins, is overexpressed in BLCA and plays a pivotal role in inflammation-mediated stem cell proliferation/differentiation, thus promoting the growth of bladder tumors (34, 35). Moreover, the progression of BLCA involves alterations in multiple inflammation-related pathways that determine patients' clinical characteristics and outcomes (5, 36–38). These changes were strongly associated with multiple cellular activities, such as cell proliferation, apoptosis, cycle progression, and angiogenesis. Overall, we observed the heterogeneity of the TME infiltration characteristics of BLCA among three IIR subtypes, which partially explains the distinct clinical outcome of patients among IIR subtypes. These results indicated that TME-associated immune and inflammatory infiltration plays a critical part in the progression of BLCA.

Given the specificity of IIR-modified phenotypes in individuals, we established a scoring model, IIRS, to evaluate the IIR modification pattern of individual patients with BLCA. Intriguingly, we noticed that patients in Cluster B showed the highest IIRS score with the worst prognosis compared to other subtypes, suggesting that the IIRS score was a dependable model for the comprehensive assessment of the IIR modification pattern and predicting the prognosis of patients. The IIRS was constructed based on five filtered genes: FN1, TLR2, IL10, MYC, and CD247. FN1, IL10, and MYC activation were related to the poor prognosis, indicating a pivotal role in cancer progression. FN1 was significantly elevated in several malignant tumors (39), which is in accordance with our results. Evolving lines of evidence have indicated that FN1 played a pivotal role in tumor cell proliferation, migration, invasion, and angiogenesis (39–41). As a crucial anti-inflammatory cytokine, IL10 has profound immunosuppressive functions, such as supporting immune escape and suppressing the expression of antigen-presenting cells, MHC-class II Ags, and costimulatory molecules on macrophages (42). Previous research has

indicated that IL10 was reported to be upregulated in numerous advanced cancers (43), confirmed by the present work. MYC activation has been reported to regulate the expression of several immune checkpoints, inactivate macrophages and DCs, and limit NK and T cells (44, 45). The inactivation of MYC triggers tumor regression through the loss of hallmark features of cancer (45). The upregulation of TLR2 and CD247 in current work was significantly associated with the superior prognosis, suggesting that TLR2 and CD247 activation may be essential for anti-tumor immunity. In agreement with our concept, TLR2 was reported to initiate the innate and sustained adaptive immune responses in cancer (46, 47). Moreover, the downregulation of CD247 in T cells was associated with immunosuppression due to chronic inflammation (11). Taken together, previous research and our results indicated that the IIRS genes might act as potential biomarkers and therapeutic targets for BLCA.

In the last decade, the accumulated interest in immunotherapy and chemotherapy, coupled with a growing understanding of the pathogenesis of BLCA, has dramatically enriched the therapeutic choices against BLCA (1, 3). Accumulating evidence has revealed that TMB can enable oncologists to identify patients who are likely to benefit from immunotherapy (24), which is in line with our finding that high TMB has a significant correlation with favorable prognosis. Additionally, checkpoint blockades significantly impact cancer immunotherapy (48). Preliminary pathway annotation analysis indicated that mutated DEIIRGs were significantly associated with the PD-L1 expression and PD-1 checkpoint pathway in cancer. It was also found that the vast majority of checkpoint molecules were negatively correlated to IIRS-score, indicating that IIRS may play a pivotal role in immunotherapeutic response prediction. With the IMvigor210 cohort and TCIA database, IIRS was further verified to be efficient in predicting the response to immunotherapy. Considering that traditional cisplatin-based chemotherapy still plays a non-negligible role in the personalized medicine era (3), we assessed the IC50 of potential drugs against BLCA. Patients with low IIRS-score were more sensitive to most potential drugs than the high IIRS-score group, suggesting that the low IIRS-score group was more likely to benefit from chemotherapy. Although our analyses provided different therapeutic options for high and low IIRS-score groups, the efficacy and mechanism of these drugs against BLCA still require further demonstration.

The present work is the first to establish the immune and inflammatory phenotype-related prognosis, immunotherapy, and chemotherapy signature for BLCA. Intriguingly, we observed that IIRS could even predict the prognosis of BLCA patients with different subclasses stratified by clinical traits. Moreover, they may effectively improve the prediction of prognosis when compared to conventional staging. To our knowledge, the five-gene prognostic signature described herein has not been reported previously. The current study has certain limitations that deserve mention. On the one hand, this work was a retrospective design with heterogeneity due to comparisons between patients from cross-platform data. A comprehensive prospective study is even more necessary to affirm the complete prediction ability of the IIRS. On the other hand, potential driver molecules in our research require further functional validation, and their detailed molecular mechanisms in the pathogenesis of BLCA need further elucidation.

Data availability statement

Publicly available datasets were used in this study, the names of the repositories/accession numbers are in the article/ Supplementary Materials.

Author contributions

ZC: Conceptualization, Investigation, Writing - Original Draft. RL: Writing - Review and Editing. JZ: Validation. LA: Writing - Review and Editing. GZ: Formal analysis. ML: Visualization. JD: Investigation. RY: Formal analysis. ZS: Visualization. WZ: Funding acquisition. DQ: Funding acquisition. XD: Supervision. SL: Supervision. BS: Supervision. WW: Project administration. All authors contributed to the article and approved the submitted version.

Funding

This work was supported by grants from The National Natural Science Foundation of China (No.61931024), and The Science and Technology Plan Project of Guangzhou (Grant NO. 201804020023).

Acknowledgments

We thank Home for Researchers editorial team (www.home-for-researchers.com) for language editing service.

Conflict of interest

The authors declare that the research was conducted in the absence of any commercial or financial relationships that could be construed as a potential conflict of interest.

Publisher's note

All claims expressed in this article are solely those of the authors and do not necessarily represent those of their affiliated organizations, or those of the publisher, the editors and the reviewers. Any product that may be evaluated in this article, or

claim that may be made by its manufacturer, is not guaranteed or endorsed by the publisher.

Supplementary material

The Supplementary Material for this article can be found online at: https://www.frontiersin.org/articles/10.3389/fimmu.2022.1008865/full#supplementary-material

SUPPLEMENTARY FIGURE 1
Collection of Inflammation-Immunity-related genes. **(A)** Screening out the Inflammation-related union genes using six gene sets. **(B)** The "Immune Cell-Target" network. **(C)** Identification of Inflammation-related core genes. **(D)** Identification of Immune-related core genes after screening. **(E)** The Venn diagram of drug-disease crossover genes.

SUPPLEMENTARY FIGURE 2
Validation of three IIR patterns in two GEO cohorts. **(A, B)** Hierarchical clustering of IIRGs in GEO cohorts and the KM curves of OS for three IIRGs modification patterns.

SUPPLEMENTARY FIGURE 3
Comparison of composition and immune cells infiltration of TME among three subtypes in TCGA-BLCA cohort. **(A-C)** Comparison of the composition of TME (immune score, stromal score, and tumor purity) among three subgroups. **(D)** Comparison of inflammation score among three subgroups. **(I)** Differences in the abundances of the 22 immune cells infiltration in IIRGs subtypes.

SUPPLEMENTARY FIGURE 4
(A-G) KM curves were applied to estimate overall survival for the high- and low-level groups of differentially expressed immune cells. **(H)**The interaction of prognosis-related differentially expressed IIRGs. **(I)** The AUC values were applied to compare models' differences in predicting 1-, 3-, and 5-year OS.

SUPPLEMENTARY FIGURE 5
Tumor mutation analysis of DEIIRGs in TCGA-BLCA cohort. **(A)** The mutation profile of DEIIRGs in TCGA-BLCA patients. **(B)** A visual summary of these mutated genes is displayed as a tag cloud, where more frequent genes are displayed using a larger font size. **(C)** Enrichment analysis of KEGG signal pathway of the mutated DEIIRGs with mutation frequencies higher than 1%. **(D)** Lollipop plot displaying mutation distribution and protein domains for identified genes in cancer with the labeled recurrent hotspots.

SUPPLEMENTARY FIGURE 6
Evaluation of the performance of IIRS in different clinical subgroups of TCGA-BLCA patients. **(A-E)** The KM curves of IIRS in BLCA patients with different ages, gender, stage, T, and N.

SUPPLEMENTARY FIGURE 7
Chemotherapeutic responses of high- and low-risk TCGA-BLCA patients. **(A, B)** The box plots of the estimated IC50 for selected drugs.

References

1. Patel VG, Oh WK, Galsky MD. Treatment of muscle-invasive and advanced bladder cancer in 2020. *CA Cancer J Clin* (2020) 70(5):404–23. doi: 10.3322/caac.21631

2. Afonso J, Santos LL, Longatto-Filho A, Baltazar F. Competitive glucose metabolism as a target to boost bladder cancer immunotherapy. *Nat Rev Urol* (2020) 17(2):77–106. doi: 10.1038/s41585-019-0263-6

3. Felsenstein KM, Theodorescu D. Precision medicine for urothelial bladder cancer: Update on tumour genomics and immunotherapy. *Nat Rev Urol* (2018) 15 (2):92–111. doi: 10.1038/nrurol.2017.179

4. Buttigliero C, Tucci M, Vignani F, Scagliotti GV, Di Maio M. Molecular biomarkers to predict response to neoadjuvant chemotherapy for bladder cancer. *Cancer Treat Rev* (2017) 54:1–9. doi: 10.1016/j.ctrv.2017.01.002

5. Tran L, Xiao JF, Agarwal N, Duex JE, Theodorescu D. Advances in bladder cancer biology and therapy. *Nat Rev Cancer* (2021) 21(2):104–21. doi: 10.1038/s41568-020-00313-1

6. Jiang X, Wang J, Deng X, Xiong F, Ge J, Xiang B, et al. Role of the tumor microenvironment in pd-L1/Pd-1-Mediated tumor immune escape. *Mol Cancer* (2019) 18(1):10. doi: 10.1186/s12943-018-0928-4

7. Hagerling C, Casbon AJ, Werb Z. Balancing the innate immune system in tumor development. *Trends Cell Biol* (2015) 25(4):214–20. doi: 10.1016/j.tcb.2014.11.001

8. Mantovani A, Allavena P, Sica A, Balkwill F. Cancer-related inflammation. *Nature* (2008) 454(7203):436–44. doi: 10.1038/nature07205

9. Setrerrahmane S, Xu H. Tumor-related interleukins: Old validated targets for new anti-cancer drug development. *Mol Cancer* (2017) 16(1):153. doi: 10.1186/s12943-017-0721-9

10. Bonavita E, Bromley CP, Jonsson G, Pelly VS, Sahoo S, Walwyn-Brown K, et al. Antagonistic inflammatory phenotypes dictate tumor fate and response to immune checkpoint blockade. *Immunity* (2020) 53(6):1215–29.e8. doi: 10.1016/j.immuni.2020.10.020

11. Eldor R, Klieger Y, Sade-Feldman M, Vaknin I, Varfolomeev I, Fuchs C, et al. Cd247, a novel T cell-derived diagnostic and prognostic biomarker for detecting disease progression and severity in patients with type 2 diabetes. *Diabetes Care* (2015) 38(1):113–8. doi: 10.2337/dc14-1544

12. Hou J, Karin M, Sun B. Targeting cancer-promoting inflammation - have anti-inflammatory therapies come of age? *Nat Rev Clin Oncol* (2021) 18(5):261–79. doi: 10.1038/s41571-020-00459-9

13. Rossi JF, Lu ZY, Massart C, Levon K. Dynamic Immune/Inflammation precision medicine: The good and the bad inflammation in infection and cancer. *Front Immunol* (2021) 12:595722. doi: 10.3389/fimmu.2021.595722

14. Briukhovetska D, Dörr J, Endres S, Libby P, Dinarello CA, Kobold S. Interleukins in cancer: From biology to therapy. *Nat Rev Cancer* (2021) 21(8):481–99. doi: 10.1038/s41568-021-00363-z

15. Jin K, Qiu S, Jin D, Zhou X, Zheng X, Li J, et al. Development of prognostic signature based on immune-related genes in muscle-invasive bladder cancer: Bioinformatics analysis of tcga database. *Aging (Albany NY)* (2021) 13(2):1859–71. doi: 10.18632/aging.103787

16. Luo Y, Chen L, Zhou Q, Xiong Y, Wang G, Liu X, et al. Identification of a prognostic gene signature based on an immunogenomic landscape analysis of bladder cancer. *J Cell Mol Med* (2020) 24(22):13370–82. doi: 10.1111/jcmm.15960

17. Shen C, Wang L, Yang X, Liu J, Yang Q, Ding X, et al. Construction of a immune-associated genes based prognostic signature in bladder cancer. *Artif Cells Nanomed Biotechnol* (2021) 49(1):108–19. doi: 10.1080/21691401.2020.1865994

18. Xie Z, Cai J, Sun W, Hua S, Wang X, Li A, et al. Development and validation of prognostic model in transitional bladder cancer based on inflammatory response-associated genes. *Front Oncol* (2021) 11:740985. doi: 10.3389/fonc.2021.740985

19. Yan Y, Huang Z, Cai J, Tang P, Zhang F, Tan M, et al. Identification of a novel immune microenvironment signature predicting survival and therapeutic options for bladder cancer. *Aging (Albany NY)* (2020) 13(2):2780–802. doi: 10.18632/aging.202327

20. Newman AM, Steen CB, Liu CL, Gentles AJ, Chaudhuri AA, Scherer F, et al. Determining cell type abundance and expression from bulk tissues with digital cytometry. *Nat Biotechnol* (2019) 37(7):773–82. doi: 10.1038/s41587-019-0114-2

21. Zhong J, Liu Z, Cai C, Duan X, Deng T, Zeng G. M6a modification patterns and tumor immune landscape in clear cell renal carcinoma. *J Immunother Cancer* (2021) 9(2):e001646. doi: 10.1136/jitc-2020-001646

22. Chang Z, An L, He Z, Zhang Y, Li S, Lei M, et al. Allicin suppressed escherichia coli-induced urinary tract infections by a novel Malt1/Nf-Kb pathway. *Food Funct* (2022) 13(6):3495–511. doi: 10.1039/d1fo03853b

23. Chang Z, Zhang J, Lei M, Jiang Z, Wu X, Huang Y, et al. Dissecting and evaluating the therapeutic targets of coptis chinensis franch in the treatment of urinary tract infections induced by escherichia coli. *Front Pharmacol* (2021) 12:794869. doi: 10.3389/fphar.2021.794869

24. Klempner SJ, Fabrizio D, Bane S, Reinhart M, Peoples T, Ali SM, et al. Tumor mutational burden as a predictive biomarker for response to immune

checkpoint inhibitors: A review of current evidence. *Oncologist* (2020) 25(1):e147–e59. doi: 10.1634/theoncologist.2019-0244

25. Zhu H, Jia X, Wang Y, Song Z, Wang N, Yang Y, et al. M6a classification combined with tumor microenvironment immune characteristics analysis of bladder cancer. *Front Oncol* (2021) 11:714267. doi: 10.3389/fonc.2021.714267

26. Steinman RM, Hemmi H. Dendritic cells: Translating innate to adaptive immunity. *Curr Top Microbiol Immunol* (2006) 311:17–58. doi: 10.1007/3-540-32636-7_2

27. Lippitz BE. Cytokine patterns in patients with cancer: A systematic review. *Lancet Oncol* (2013) 14(6):e218–28. doi: 10.1016/s1470-2045(12)70582-x

28. Wang L, Saci A, Szabo PM, Chasalow SD, Castillo-Martin M, Domingo-Domenech J, et al. Emt- and stroma-related gene expression and resistance to pd-1 blockade in urothelial cancer. *Nat Commun* (2018) 9(1):3503. doi: 10.1038/s41467-018-05992-x

29. Salmon H, Franciszkiewicz K, Damotte D, Dieu-Nosjean MC, Validire P, Trautmann A, et al. Matrix architecture defines the preferential localization and migration of T cells into the stroma of human lung tumors. *J Clin Invest* (2012) 122 (3):899–910. doi: 10.1172/jci45817

30. Ouzounova M, Lee E, Piranlioglu R, El Andaloussi A, Kolhe R, Demirci MF, et al. Monocytic and granulocytic myeloid derived suppressor cells differentially regulate spatiotemporal tumour plasticity during metastatic cascade. *Nat Commun* (2017) 8:14979. doi: 10.1038/ncomms14979

31. Rabinovich GA, Gabrilovich D, Sotomayor EM. Immunosuppressive strategies that are mediated by tumor cells. *Annu Rev Immunol* (2007) 25:267–96. doi: 10.1146/annurev.immunol.25.022106.141609

32. Young MR. Endothelial cells in the eyes of an immunologist. *Cancer Immunol Immunother* (2012) 61(10):1609–16. doi: 10.1007/s00262-012-1335-0

33. Schepisi G, Santoni M, Massari F, Gurioli G, Salvi S, Conteduca V, et al. Urothelial cancer: Inflammatory mediators and implications for immunotherapy. *BioDrugs* (2016) 30(4):263–73. doi: 10.1007/s40259-016-0176-3

34. Thanan R, Murata M, Ma N, Hammam O, Wishahi M, El Leithy T, et al. Nuclear localization of cox-2 in relation to the expression of stemness markers in urinary bladder cancer. *Mediators Inflamm* (2012) 2012:165879. doi: 10.1155/2012/165879

35. Wang D, Dubois RN. Prostaglandins and cancer. *Gut* (2006) 55(1):115–22. doi: 10.1136/gut.2004.047100

36. Mitra AP, Bartsch CC, Cote RJ. Strategies for molecular expression profiling in bladder cancer. *Cancer Metastasis Rev* (2009) 28(3-4):317–26. doi: 10.1007/s10555-009-9196-5

37. Benjamin DJ, Lyou Y. Advances in immunotherapy and the tgf-B resistance pathway in metastatic bladder cancer. *Cancers (Basel)* (2021) 13(22):5724. doi: 10.3390/cancers13225724

38. Goriki A, Seiler R, Wyatt AW, Contreras-Sanz A, Bhat A, Matsubara A, et al. Unravelling disparate roles of notch in bladder cancer. *Nat Rev Urol* (2018) 15 (6):345–57. doi: 10.1038/s41585-018-0005-1

39. Wang S, Gao B, Yang H, Liu X, Wu X, Wang W. Microrna-432 is downregulated in cervical cancer and directly targets Fn1 to inhibit cell proliferation and invasion. *Oncol Lett* (2019) 18(2):1475–82. doi: 10.3892/ol.2019.10403

40. Cai X, Liu C, Zhang TN, Zhu YW, Dong X, Xue P. Down-regulation of Fn1 inhibits colorectal carcinogenesis by suppressing proliferation, migration, and invasion. *J Cell Biochem* (2018) 119(6):4717–28. doi: 10.1002/jcb.26651

41. Liu X, Wang Y, Zhu P, Wang J, Liu J, Li N, et al. Human follicular fluid proteome reveals association between overweight status and oocyte maturation abnormality. *Clin Proteomics* (2020) 17:22. doi: 10.1186/s12014-020-09286-7

42. Frei K, Lins H, Schwerdel C, Fontana A. Antigen presentation in the central nervous system. the inhibitory effect of il-10 on mhc class ii expression and production of cytokines depends on the inducing signals and the type of cell analyzed. *J Immunol* (1994) 152(6):2720–8.

43. Cheng Y, Zhu Y, Xu J, Yang M, Chen P, Xu W, et al. Pkn2 in colon cancer cells inhibits M2 phenotype polarization of tumor-associated macrophages *Via* regulating Dusp6-Erk1/2 pathway. *Mol Cancer* (2018) 17(1):13. doi: 10.1186/s12943-017-0747-z

44. Casey SC, Tong L, Li Y, Do R, Walz S, Fitzgerald KN, et al. Myc regulates the antitumor immune response through Cd47 and pd-L1. *Science* (2016) 352 (6282):227–31. doi: 10.1126/science.aac9935

45. Sodir NM, Swigart LB, Karnezis AN, Hanahan D, Evan GI, Soucek L. Endogenous myc maintains the tumor microenvironment. *Genes Dev* (2011) 25 (9):907–16. doi: 10.1101/gad.2038411

46. Haidl ID, Meghnem D, Issekutz TB, Marshall JS. Toll-like receptor 2 activation induces c-c chemokine receptor 2-dependent natural killer cell recruitment to the peritoneum. *Immunol Cell Biol* (2020) 98(10):854–67. doi: 10.1111/imcb.12379

47. Klein JC, Moses K, Zelinskyy G, Sody S, Buer J, Lang S, et al. Combined toll-like receptor 3/7/9 deficiency on host cells results in T-Cell-Dependent control of tumour growth. *Nat Commun* (2017) 8:14600. doi: 10.1038/ncomms14600

48. Kalbasi A, Ribas A. Tumour-intrinsic resistance to immune checkpoint blockade. *Nat Rev Immunol* (2020) 20(1):25–39. doi: 10.1038/s41577-019-0218-4

frontiers | Frontiers in Immunology

TYPE Original Research
PUBLISHED 28 October 2022
DOI 10.3389/fimmu.2022.1006665

OPEN ACCESS

EDITED BY
Beatriz Martín-Antonio,
University Hospital Fundación Jiménez Díaz, Spain

REVIEWED BY
Chi Yan,
Henan Provincial Cancer Hospital, China
Benjamin Bonavida,
University of California, Los Angeles, United States

*CORRESPONDENCE
Apostolos Zaravinos
a.zaravinos@euc.ac.cy

SPECIALTY SECTION
This article was submitted to Cancer Immunity and Immunotherapy, a section of the journal Frontiers in Immunology

RECEIVED 29 July 2022
ACCEPTED 10 October 2022
PUBLISHED 28 October 2022

CITATION
Georgoulias G and Zaravinos A (2022) Genomic landscape of the immunogenicity regulation in skin melanomas with diverse tumor mutation burden.
Front. Immunol. 13:1006665.
doi: 10.3389/fimmu.2022.1006665

Genomic landscape of the immunogenicity regulation in skin melanomas with diverse tumor mutation burden

George Georgoulias [1] and Apostolos Zaravinos [1,2*]

[1]Department of Life Sciences, School of Sciences, European University Cyprus, Nicosia, Cyprus, [2]Cancer Genetics, Genomics and Systems Biology laboratory, Basic and Translational Cancer Research Center (BTCRC), Nicosia, Cyprus

Skin melanoma cells are tightly interconnected with their tumor microenvironment (TME), which influences their initiation, progression, and sensitivity/resistance to therapeutic interventions. An immune-active TME favors patient response to immune checkpoint inhibition (ICI), but not all patients respond to therapy. Here, we assessed differential gene expression in primary and metastatic tumors from the TCGA-SKCM dataset, compared to normal skin samples from the GTEx project and validated key findings across 4 independent GEO datasets, as well as using immunohistochemistry in independent patient cohorts. We focused our attention on examining the expression of various immune receptors, immune-cell fractions, immune-related signatures and mutational signatures across cutaneous melanomas with diverse tumor mutation burdens (TMB). Globally, the expression of most immunoreceptors correlated with patient survival, but did not differ between TMB^{high} and TMB^{low} tumors. Melanomas were enriched in *"naive T-cell", "effector memory T-cell", "exhausted T-cell", "resting Treg T-cell"* and *"Th1-like"* signatures, irrespective of their *BRAF*, *NF1* or *RAS* mutational status. Somatic mutations in *IDO1* and *HLA-DRA* were frequent and could be involved in hindering patient response to ICI therapies. We finally analyzed transcriptome profiles of ICI-treated patients and associated their response with high levels of IFNγ, Merck18, CD274, CD8, and low levels of myeloid-derived suppressor cells (MDSCs), cancer-associated fibroblasts (CAFs) and M2 macrophages, irrespective of their TMB status. Overall, our findings highlight the importance of pre-existing T-cell immunity in ICI therapeutic outcomes in skin melanoma and suggest that TMB^{low} patients could also benefit from such therapies.

KEYWORDS

skin melanoma, tumor mutation burden (TMB), immune signatures, immune checkpoint inhibition therapy, patient response, tumor-infiltrating lymphocytes, tumor microenvironment

Introduction

Cutaneous melanomas are among the most immunogenic cancers (1), with an increasing incidence rate worldwide (2). They have an increased mutation rate as a result of exposure to UV radiation (2, 3) and are very heterogenous with different mutational subtypes, being mainly sorted according to the mutational status of *BRAF*, *NRAS* and *NF1* (4–6). Additionally, skin melanomas can be classified across five main immune subtypes; wound healing, IFN-γ dominant, inflammatory, lymphocyte depleted and TGF-β dominant; whereas very few of them are immunologically quiet (7).

The tumor microenvironment (TME) is the ecosystem surrounding a tumor and includes the extracellular matrix, blood vessels and stromal cells. It also encompasses a diverse number of immune cells, such as dendritic cells (DCs), neutrophils, natural killer (NK) cells, T-cells and B-cells, as well as immunosuppressors, including myeloid-derived suppressor cells (MDSCs), regulatory T (Treg) cells, tumor-associated macrophages (TAMs) or cancer-associated fibroblasts (CAFs). All these, constitute an ecosystem where they interact with the tumor cells bidirectionally, modulating the malignant phenotype (8). An immune-active TME has been shown to favor clinical response to immune checkpoint inhibition (ICI) therapies with anti-CTLA-4 and anti-PD-1 mAbs (9–11). The absence of tumor-infiltrating lymphocytes (TILs) in the TME on the other hand, predicts sentinel lymph node metastasis and survival (12). Combination immunotherapy or dual ICI (anti-PD-1 plus anti-CTLA-4) has recently shown impressive response rates in metastatic patients. However, half of them had significant toxicity from the treatment regimen (13, 14).

The tumor's relationship with immune cells within the TME can remarkably influence cancer cell proliferation, progression, and metastasis (15). This unique immunogenicity renders skin melanoma as a paradigm for tumor-immune interactions and is driven by a high mutational burden (TMB), which can increase the tumor's probability to generate immunogenic neoantigens, making it easier for the immune system to recognize cancer cells and elicit effective immune responses against them (16–18). Patients with high TMB are also likely to be more responsive to immunotherapy (19, 20). However, despite the promising therapeutic outcome that most ICI therapies provide to metastatic patients, most of them will not respond, exhibiting early (primary) or late (adaptive) resistance and relapse (21).

Here, we delved into the expression of a group of activating and inhibitory immune receptors in the TME of skin melanoma patients with diverse TMB. We also examined immune-related signatures, fractions of immune-cells and mutational signatures across tumors with a low or high TMB. Our results indicate that elevated expression levels of *TIGIT*, *IDO1* and *LAG3*, other than *PD-1, PD-L1/2* and *CTLA-4*, associate with the patients' overall and disease-free survival, but not with the TMB, corroborating that immunogenicity in these tumors is affected by other factors as well. In addition, we found that skin melanomas are significantly enriched in the "naive T-cell", "effector memory T-cell", "exhausted T-cell", "resting Treg T-cell" and "Th1-like" signatures, irrespective of their *BRAF*, *NF1* and *RAS* mutational status. We also show that despite the similar immune-cell fractions between TMB^{high} and TMB^{low} tumors, the first have a higher ratio of M1/M2 macrophages. Our data further support that somatic mutations in *IDO1* and *HLA-DRA* are frequent and could be involved in hindering patient response to ICI therapies. We finally provide evidence that TMB alone is not the best predictor of immunotherapy response and therefore, anti-PD-1/anti-CTLA-4 monotherapy or combination ICI therapy could also be applied to TMB^{low} patients.

Materials and methods

NGS data extraction and analysis

We extracted whole exome and RNA-seq data from the TCGA-SKCM dataset, containing 461 primary and metastatic skin melanoma samples, in total. All data, including patient clinicopathological information and MAF files, were assessed from GDC Data Portal (https://portal.gdc.cancer.gov/). Apart from one matched blood sample from the TCGA cohort that was used as control, we included normal skin samples from the GTEx project (https://gtexportal.org/) for differential gene expression analysis, totaling to 557 controls. TCGA and GTEx samples were re-aligned to the hg38 genome and were processed using a uniform bioinformatic pipeline, to eliminate batch effects.

Differential gene expression was identified between skin melanoma and matched TCGA normal and GTEx normal skin data, using limma with cut-off $|\log_2 FC>2|$ for upregulation and $|\log_2 FC<1|$ for downregulation, along with adjusted $p<0.05$. The B-statistic was used to sort the differentially expressed genes. We then performed Gene Ontology (GO) enrichment analysis for the top 250 up- and down-regulated genes in primary (or metastatic) skin melanomas, respectively, using Enrichment Analysis Visualization Appyter. Similar gene sets from GO analysis were clustered together using Uniform Manifold Approximation and Projection (UMAP) (22) and the significantly enriched (adjusted $p<0.05$) GO terms for biological processes (GO-BP), molecular function (GO-MF) and cellular component (GO-CC) were highlighted.

We focused on the expression of some well-known immune checkpoints, including *PD-1, PD-L1/2*, *CTLA-4, TIGIT*, *IDO1/2* and other prospective immunoreceptors (*LAG3, VTCN1*, *VISTA, ILT2* and *ILT4*). To calculate each gene's expression,

we used one-way ANOVA, and the disease state (skin melanoma or matched TCGA normal and GTEx normal skin samples) as variable to calculate differential expression. The expression data were first $\log_2$(TPM+1) transformed for differential analysis and the $|\log_2 FC|$ was defined as median (skin melanoma) - median (matched TCGA normal and GTEx samples), as explained before (23, 24).

Validation of deregulated genes using independent GEO datasets

Four independent studies from the Gene Expression Omnibus (GEO) repository were analyzed for subsequent validation of the top deregulated genes in primary (or metastatic) melanomas against their adjacent normal skin samples, or between primary and metastatic melanomas, depending on the study. In specific, we obtained microarray data from the studies with the following GEO accession numbers: GSE8401, containing 31 primary and 52 metastatic melanomas (25, 26); GSE7553, 2 *in-situ* melanomas, 14 primary, 40 metastatic melanomas and 4 normal skin samples (27); GSE46517, 31 primary, 73 metastatic melanomas and 7 normal skin samples (28); and GSE15605, composed of 46 primary and 12 metastatic melanomas, as well as 16 normal skin samples. Data were analyzed using limma with vooma transformation in R (29). P-values were adjusted using Benjamini & Hochberg (FDR) and the significance threshold was set at $p<0.05$. The top 250 differentially expressed genes (ranked by p-value) were obtained either between primary and metastatic melanomas, or between each of those and their corresponding normal skin samples. UMAP, boxplots, and expression density plots were retrieved to assess normalization status and sample groupings. Volcano plots and mean difference (MD) plots were used to visualize differentially expressed genes. Adjusted p-value histograms were generated using hist to view the distribution of the p-values in the analysis results. Moderated t-statistic quantile-quantile (q-q) plots were used to check the variation in the data.

Immune-related gene signatures

We compared immune-related gene signatures between cutaneous melanoma and control samples (matched TCGA and GTEx normal data), as well as between BRAF hotspot mutants ($BRAF^{mut}$, n=147), NF1 mutants ($NF1^{mut}$, n=27), RAS hotspot mutants (RAS^{mut}, n=91) and triple-wild type ($Triple^{WT}$, n=47) tumors, using GEPIA2 (30). The signatures were specific for naive T-cells (*CCR7, LEF1, TCF7* and *SELL*); effector T-cells (*CX3CR1, FGFBP2* and *FCGR3A*); effector memory T-cells (*PDCD1, DUSP4, GZMK, GZMA* and *IFNG*); central memory T-cells (*CCR7, SELL* and *IL7R*); resident memory T-cells (*CD69, ITGAE, CXCR6* and *MYADM*); exhausted T-cells (*HAVCR2, TIGIT, LAG3, PDCD1, CXCL13* and *LAYN*); resting Tregs (*FOXP3, IL2RA*); effector Tregs (*FOXP3, CTLA-4, CCR8* and *TNFRSF9*); and Th1-like cells (*CXCL13, HAVCR2, IFNG, CXCR3, BHLHE40* and *CD4*). The $|\log_2 FC>1|$ and $p<0.01$ (ANOVA) were used to assess differences with statistical significance between groups. Principal component analysis (PCA) was used to automatically perform dimensionality reduction on data from the TCGA-SKCM dataset and normal suprapubic skin (not exposed to the sun), based on the expression of these signatures in the samples. The expression of specific immune-checkpoints was also explored individually across the different molecular or immune subtypes (C1, wound healing; C2, IFN-gamma dominant; C3, inflammatory; C4, lymphocyte depleted; C5, immunologically quiet; C6, TGF-b dominant) (7).

Commutation analysis and comparison of immunostimulators and immunoinhibitors between TMB^{high} and TMB^{low} tumors

We used iCoMut Beta 0.21 for FireBrowse to categorize skin melanomas into three TMB subgroups, based on the mutational distribution quartiles. The lower quartile contained tumors with a low mutation rate, i.e., <7.4 synonymous and non-synonymous (total) mutations/Mb or <5.14 non-synonymous mutations/MB (also termed as "TMB^{low}"). The upper quartile involved tumors with an increased rate of mutation, i.e., >30 total mutations/Mb or >20 non-synonymous mutations/MB ("TMB^{high}"). Among the TMB^{high} subgroup, 18 tumors with >81 total mutations/Mb were considered as "extremely hypermutated". The rest 50% of samples was termed "TMB-intermediate" (TMB^{int}, >7.42 & <30 total mut/Mb). Tumor stratification based on their TMB (synonymous and non-synonymous mutations) was also reflected on their neoantigen burden, being significantly higher among TMB^{high} tumors (68,263 neoantigens, 734.5 ± 695.7; median ± SD) versus TMB^{int} (34,473 neoantigens, 211 ± 151.2) and TMB^{low} tumors (4,929 neoantigens 57 ± 52.3). Maftools (31) was also used to compare oncoplots between TMB^{high} and TMB^{low} tumors.

The mutation rate was then correlated with the expression of either activating or inhibitory immune receptors within each TMB subgroup. In specific, we compared the expression of 49 immunostimulators (*BTNL2, C10orf54, CD27, CD274, CD276, CD28, CD40, CD40LG, CD48, CD70, CD80, CD86, CXCL12, CXCR4, ENTPD1, HHLA2, ICOS, ICOSLG, IL2RA, IL6, IL6R, KLRC1, KLRK1, LTA, MICA, MICB, NT5E, PDCD1LG2, PVR, RAET1E, TMEM173, TMIGD2, TNFRSF13B, TNFRSF13C, TNFRSF14, TNFRSF17, TNFRSF18, TNFRSF25, TNFRSF4, TNFRSF8, TNFRSF9, TNFSF13, TNFSF13B, TNFSF14, TNFSF15, TNFSF18, TNFSF4, TNFSF9 and ULBP1*) and 23

immunoinhibitors (*ADORA2A, BTLA, CD160, CD244, CD96, CSF1R, CTLA4, HAVCR2, IDO1, IL10, IL10RB, KDR, KIR2DL1, KIR2DL2, KIR2DL3, LAG3, LGALS9, PDCD1, PVRL2, TGFB1, TGFBR1, TIGIT and VTCN1*) across TMB^{high}, TMB^{int} and TMB^{low} melanoma tumors.

Mutational signatures and cancer driver genes

We extracted and analyzed single base substitutions (SBS) and doublet base substitutions (DBS) using SigProfiler's MatrixGenerator and Extractor, as previously described in detail (32, 33). SBS signatures were identified using 96 different contexts, considering also the bases 5' and 3' from the mutated base. DBS signatures were generated after the concurrent modification of two consecutive nucleotide bases (34). The extracted mutational signatures were then compared against the ones found in COSMIC v3.2 (https://cancer.sanger.ac.uk/signatures/). Each signature's contribution was calculated separately for primary and metastatic skin melanomas. Cancer driver mutations were identified using IntOGen (35).

Cell-type fractions

We analyzed each tumor's cell type fraction by extracting data from the Cancer Immunome Database (TCIA) (36). The absolute values and the quanTIseq computational pipeline were used to quantify tumoral immune contexture (37), focusing on B cells, M1/M2 macrophages, neutrophils, monocytes, NK cells, non-regulatory CD4+ and CD8+ T cells, regulatory CD4+ T cells (Tregs) and dendritic cells.

Immunohistochemistry and evaluation of TIL load

An independent cohort of 11 skin melanoma samples from the Human Protein Atlas (https://www.proteinatlas.org/) (38) and tissue microarrays (TMAs), containing 40 cases of malignant melanoma, plus 30 adjacent normal skin tissue and 10 skin tissue (ME803b, US Biomax, Inc.) were used to validate protein expression using IHC and evaluate the TIL load with hematoxylin and eosin (H&E) staining. In brief, FFPE sections (4μm) were heated at 50°C overnight. Then, they were deparaffinized in xylene and rehydrated in graded ethanol to distilled water. During hydration, a 5 min blocking for endogenous peroxidase was done in 0.3% H_2O_2 in 95% ethanol. Prior to immunostaining, the sections were immersed in 10mM citrate buffer (pH 6.0), rinsed in Tris-buffered saline (TBS) and subjected to heat-induced epitope retrieval (HIER) using a pressure boiler. Sections were then incubated overnight at 4°C with mouse monoclonal antibodies (mAbs) against IDO1 (1:150, Sigma-Aldrich Cat# HPA023149, RRID : AB_1846221), PD-1 (1:250, Sigma-Aldrich Cat# HPA035981, RRID : AB_10669664), PD-L1, a marker specific for T-cells, B-cells and tumor cells (1:50 dilution, clone 22C3, Dako, CA), LAG3 (1:15, Sigma-Aldrich), the cytotoxic T-cell markers CD8A The image used in Figures 1-3 has part labels; however, the description is missing in the caption. Could you clarify this? Provide revised files if necessary.and CD8B (CDA, 1:400 dilution, clone C8/144B, Dako, CA; CD8, 1:100, Sigma-Aldrich Cat# HPA029164), and the Treg-specific marker FOXP3 (1:200 dilution, clone 236A/E7, ThermoFischer Scientific). The UltraVision LP HRP polymer®, Ultra V Block and DAB quanto substrate system® (Thermo scientific, CA) were used for detection. Finally, slides were rinsed in tap water, counterstained with hematoxylin, dehydrated in grade ethanol and coverslipped. Slides were then independently assessed by two observers. Sections of hyper-reactive tonsils were used as positive controls for anti-PD-L1 and anti-CD8 staining and preimmune rabbit serum as a negative control for nonspecific staining. Protein staining was scored as 2+ (high (>75% positive cells) or medium (50-75% positive cells) staining), l+ (low staining, 5-25% positive cells) and 0 (staining not detected or <5% positive cells) with strong, medium, weak or negative intensity. The percentage (%) of TILs (200x magnification) in the was also scored. Slide scanning was performed on a VENTANA iScan HT slide scanner v1.1.1 (Roche).

Somatic mutations in the IFN-γ gene expression signature and immune checkpoint genes

We evaluated gene expression along with the detection of SNVs and Indels across an IFN-γ-related signature, composed of *IDO1, CXCL10, CXCL9, HLA-DRA, STAT1* and *IFNG* (39). We also assessed somatic mutations in the IFN-γ pathway genes *IFNGR1/2, JAK1/2* and *IRF1*, as well as across *BRAF, NRAS, NF1, PTEN* and *B2M* in the TCGA-SKCM dataset. The analysis of somatic mutations was performed using MuTect2 Variant Aggregation and Masking (v.4.1) and gene expression was measured in $\log_2$(FPKM-UQ+1) values using the UCSC Xena platform (40). MuPIT Interactive (http://mupit.icm.jhu.edu/) was used to map the SNVs on the crystal structure of each protein, in 3D (hg38).

Detection of immunophenoscores

We calculated IPS scores in TMB^{high} and TMB^{low} tumors (ranging from 0-10) based on the expression of immunomodulators, effector T-cells, effector memory T-cells and immunosuppressors. Their

immunophenotypes were visualized using immunophenograms, as previously described (41, 42).

Patient response to immunotherapy

Tumor Immune Dysfunction and Exclusion (TIDE, http://tide.dfci.harvard.edu/) (43, 44) was used to predict patient response to anti-PD1 or combined anti-PD-1 and anti-CTLA-4 therapy across seven independent skin melanoma datasets (Van Allen et al., 2015 (45), Hugo et al., 2016 (GSE78220) (41), Nathanson et al., 2017 (46), Prat et al., 2017 (GSE93157) (47), Lauss et al., 2017 (GSE100797) (48), Riaz et al., 2017 (GSE91061) (49) and Gide TN, et al., 2019 [PRJEB23709) (50)]. Pre-treatment melanoma tumor expression profiles of patients (log_2(TPM+1) values) were downloaded and normalized towards the control samples. Each gene was normalized by subtracting the expression value in the reference control samples. Higher TIDE values indicate that the patient has higher potentials of tumor immune evasion and is, therefore, less likely to benefit from the corresponding immune-checkpoint blockade. The IFNG values indicate the IFNγ response biomarkers of *IFNγ*, *ACAT1*, *IDO1*, *CXCL10*, *CXCL9* and *HLA-DRA*. From the analysis we also deduced the expression of CD274 (PD-L1), the average expression from CD8A and CD8B genes, the levels of cytotoxic T-lymphocytes, each patient's dysfunction of the tumor, exclusion potential of the tumor, as well as the Pearson's correlation between gene expression and MDSCs, CAFs and M1/M2 TAMs.

Statistical analysis

Differences in gene expression between high and low activating (or inhibitory) immune receptor-expressing tumors or between TMB^{high} and TMB^{low} tumors, were assessed using the nonparametric Mann-Whitney test. Gene expression (log_2 (TPM+1) values were profiled using violin plots across different pathological stages of the tumors. Multivariate analysis of variance (MANOVA) with the F statistic was used to estimate differences across the different stages. We used Kaplan-Meier curves to plot overall and disease-free survival in patients with high or low expression of immune checkpoints or different multi-gene signatures, using the median expression as cut-off. The log-rank test with HR and 95% CI was used for analysis. Adjusted p-values <0.05 were considered statistically significant. Correlations between each patient's TIL or TMB load and the expression of immune receptors were assessed using Pearson's test. All statistical analyses were performed using GraphPad Prism v9.0.0.121. Clusters of similar GO terms were computed using the Leiden algorithm (51) and points were plotted on the first two UMAP dimensions using BokehJS 2.3.2.

Results

Deregulated genes and functional analysis in skin melanoma

We initially detected the significantly deregulated genes, having a broad distribution across all chromosomes, in primary and metastatic skin melanoma (Table S1), and focused on the top 250 up-/down-regulated genes within each subgroup. The upregulated genes in primary melanomas were enriched in regulation of immune response; cytokine-mediated signaling pathway; antigen receptor-mediated signaling pathway; cellular response to interferon-gamma; regulation of T cell proliferation; regulation of T cell activation; T cell receptor signaling pathway; positive regulation of lymphocyte proliferation; positive regulation of T cell activation; and cellular response to cytokine stimulus (GO-BP), in MHC class II receptor activity; MHC class II protein complex binding; CXCR3 chemokine receptor binding; chemokine activity; and cytokine receptor activity (GO-MF), as well as in MHC class II protein complex; T cell receptor complex; lumenal side of endoplasmic reticulum membrane; and integral component of lumenal side of endoplasmic reticulum membrane, among other GO-CC terms (Table S2 and Figure S1).

On the other hand, the top 250 down-regulated genes were enriched in regulation of extrinsic apoptotic signaling pathway; positive regulation of protein localization to cell periphery; maintenance of protein location in nucleus; response to cytokine; positive regulation of protein localization to plasma membrane; regulation of protein localization to plasma membrane; ribosome biogenesis; and positive regulation of NF-kappaB transcription factor activity, among other GO-BP terms. They were also enriched in cytoskeleton-nuclear membrane anchor activity; chloride channel inhibitor activity; nucleoside-diphosphatase activity; chloride channel regulator activity, among other GO-MF terms, as well as in (cytosolic) large ribosomal subunit; melanosome membrane; and chitosome; pigment granule membrane, among other GO-CC terms (Table S3 and Figure S2).

Among metastatic melanomas, the upregulated genes were enriched in regulation of immune response; cytokine-mediated signaling pathway; antigen receptor-mediated signaling pathway; cellular response to interferon-gamma; regulation of T cell proliferation; regulation of T cell activation; and T cell receptor signaling pathway, among other GO-MF terms. Similar to primary tumors, they were also enriched in MHC class II receptor activity; MHC class II protein complex binding; MHC protein binding; CXCR3 chemokine receptor binding; chemokine activity; and cytokine receptor activity, among other GO-MF terms, as well as in MHC protein complex; MHC class II protein complex; T cell receptor complex; lumenal side of endoplasmic reticulum membrane; and

integral component of lumenal side of endoplasmic reticulum membrane, among other GO-CC terms (Table S4 and Figure S3).

Finally, the top 250 down-regulated genes in metastatic melanomas were enriched in the same GO terms as in the primary tumors (Table S5 and Figure S4). Key findings were also validated across four independent GEO datasets (GSE8401, GSE7553, GSE46517 and GSE46517). The top 250 deregulated genes in each dataset were mainly enriched in the GO-BP terms epidermis & skin development, keratinocyte & epidermal cell differentiation, among others.

High expression of immune-checkpoints associates with the TIL load and can be used as a prognostic marker in melanoma

Focusing on immune checkpoints, we found higher expression for *PD-1, PD-L1, CTLA-4, IDO1, LAG3, HAVCR2, TIGIT* and *ILT4*, as well as for *CD8* in skin melanomas against the normal samples, reflecting the immunosuppressive TME in these tumors. On the other hand, *VISTA* and *VTCN1* were downregulated in skin melanoma, whereas, *IDO2*, *PD-L2* and *ADORA2A* did not differ between melanomas and normal samples (Figure 1). Interestingly, the expression of *CD8* and the given immunoreceptors, did not differ stage-wise (Figure S5).

In addition, skin melanoma patients expressing highly *CD8, PDCD1, CD274, PDCD1LG2, CTLA-4, C10orf54 (VISTA), LAG3, HAVCR2, TIGIT, ILT2, ILT4, ADORA2A, IDO1* and *IDO2* had better overall survival versus low-expressing patients. What's more, patients with higher levels of *CD8, VISTA, PD-L2, LAG3, ADORA2A, IDO1, IDO2* and *ILT2* had markedly improved disease-free survival, suggesting that their expression can be used as a prognostic marker, with high levels being favorable in melanoma (Figure S6).

The TIL load is a predictive biomarker for patient response to anti-PD1/PD-L1 immunotherapy (52). We hypothesized that TILs associate with the expression of further immune checkpoints in the TME. To verify this assumption, we conducted Pearson's correlation test with the expression of 11 immune receptors and found that, similar to other cancers (53, 54), the TIL load significantly correlates with *TIGIT* (r=0.503, p=0.05), *IDO1* (r=0.545, p=0.037), *LAG3* (r=0.589, p=0.023) and *ADORA2A* (r=0.589, p=0.037) in skin melanomas, irrespective of their mutation rate.

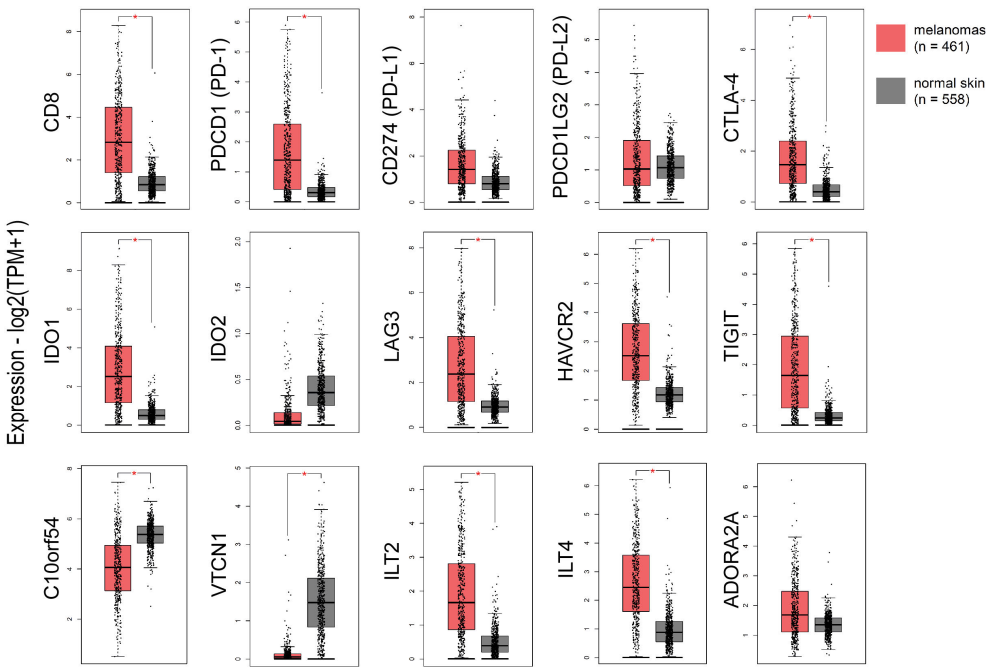

FIGURE 1
The expression of *CD8, PD-1, CTLA-4, IDO1, LAG3, HAVCR2, TIGIT, ILT2* and *ILT4* was significantly higher in skin melanomas; whereas, *C10orf54 (VISTA)* and *VTCN1*, were expressed at markedly lower levels in the tumor samples compared to normal skin samples. Red asterisks (*) denote significant differences ($|\log_2 FC>1|$ and $p<0.01$) between skin melanomas from the TCGA-SKCM dataset and matched normal samples from TCGA and GTEx. One-way ANOVA, using disease state (skin melanoma or normal sample) was used to calculate differential expression. The expression data were first $\log_2(TPM+1)$ transformed for differential analysis and the $\log_2 FC$ was defined as median (skin melanoma) - median (normal skin).

Furthermore, *CD274 (PD-L1)* expression correlated significantly with the rest immune checkpoints (apart from *VTCN1*) in skin melanoma compared to normal skin (not exposed to the sun), especially with *PD-L2, ILT2, HAVCR2* and *TIGIT* (Figure S7A). This finding supports previous evidence that immune response is driven by different immunosuppressive mechanisms within the TME in skin melanoma, which could be tackled using combination immunotherapies, especially in metastatic patients (55, 56). Adding to that, *CD8A* expression correlated significantly with *CD274, PDCD1, PDCD1LG2, IDO1, LAG3, ILT2, HAVCR2, TIGIT, ADORA2A* and *ILT4* expression in the tumor compared to unexposed normal skin, reiterating that CD8 expression is of paramount significance for a successful response to ICI therapies (57, 58) (Figure S7B).

Immune-signatures are activated in skin melanomas irrespective of their molecular subtype

Recent evidence shows that immune signatures are associated with disease prognosis. We thus, investigated 9 immune-related gene signatures in skin melanoma against the normal counterparts, and found a significant enrichment in the "naive T-cell", "effector memory T-cell", "exhausted T-cell", "resting Treg T-cell" and "Th1-like" gene signatures. Naïve T cells are precursors for effector and memory T cell subsets (59). Exhausted T cells are dysfunctional and arise during chronic infection and cancer. Their state is defined by poor effector function, sustained expression of inhibitory receptors and a transcriptional state distinct from that of functional effector or memory T cells (60). Resting Treg cells differentiate as activated Tregs after the antigen exposition (61), whereas, Th1-like cells play a role on inflammatory and autoimmune disorders (62).

On the other hand, the "effector T-cell", "resident memory T-cell", "central memory T-cell" and "effector Treg T-cell" signatures did not differ significantly between melanoma and normal samples, despite being higher in the former. Effector T-cells steer the immune responses to execute immune functions. While they were initially found to promote immunity, recent studies unraveled negative regulatory functions of effector T-cells in modulating adaptive, but also innate immunity (63). Resident memory T-cells are critical for maintaining antitumor immunity (63), whereas central memory T-cells mediate a faster, stronger, and more effective response to secondary challenge from a pathogen, compared to naive T-cells. As for Treg cells, they are quite heterogeneous with distinct phenotypical and functional subsets. Naïve-like thymus-derived Tregs, once stimulated, can differentiate into effector Tregs and migrate to peripheral tissues to control immune homeostasis (64). Interestingly, none of the above immune signatures differed between $BRAF^{mut}$, $NF1^{mut}$, RAS^{mut} and $Triple^{WT}$ tumors (Figure S8). In addition, PCA analysis for the "effector memory T-cell" and "naïve T-cell" signatures discriminated best skin melanomas from the non-sun-exposed (suprapubic) normal skin (Figure 2). Collectively, these findings strongly suggest the activation of several immune-related gene signatures in skin melanoma, irrespective of its molecular subtype, reflecting their link with the disease prognosis.

Mutational signatures causing high TMB associate with UV light exposure and ageing in melanoma

Skin melanoma patient stratification based on their mutation rate revealed that tumors with >30 mutations/Mb had a different mutational signature profile from those having <7.42 mutations/Mb. The former group was mainly characterized of (C/T)p*Cp(C/G)>T and (C/T)p*Cp(A/G)>T mutations, whereas the latter, of transversions, A>G and (A/G)p*C>T mutations (Figure 3). We further analyzed the single-base substitution (SBS) profiles and decomposed each signature to its components and the different percentages of contribution for each of these. As expected, we found that (both primary and metastatic) melanomas were mainly characterized of signatures SBS7a/b (exposure to UV light), SBS1 (spontaneous deamination of 5-methylcytosine; clock-like), SBS5 (clock-like) and SBS10b (*POLE/POLD1* mutations). Interestingly, we found a primary tumor to associate with SBS4 (tobacco smoking) and a metastatic tumor to associate with SBS17b. The latter signature is of unkown aetiology, but previous studies have associated it with 5FU chemotherapy treatment and to damage inflicted by reactive oxygen species (65). As expected, we found ~3.6-times higher number of SBSs among metastatic tumors compared to primary ones (121,175 vs 33,796 SBSs). The mutational signatures exhibiting the highest contribution in primary tumors, were SBS7b (17,220 mutations; 51.9%) SBS7a (13,873 mutations; 41.8%), SBS1 (1,408 mutations; 4.2%) and SBS5 (640 mutations; 1.9%), followed by a small contribution in SBS4 (46 mutations; 0.1%), SBS17b (603 mutations; 0.5%) and SBS7d (6 mutations; 0%). Metastatic tumors on the other hand, were enriched in SBS7b (60,043 mutations; 49.5%) SBS7a (50,904 mutations; 42%), SBS1 (4,124 mutations; 3.4%) and SBS10b (3,823 mutations; 3.2%), followed by a small contribution in SBS5 (1,321 mutations; 1.1%), SBS17b (603 mutations; 0.5%) and SBS17a (357 mutations; 0.3%) (Figures 4A–C). Most of these SBSs were previously reported in skin melanoma and their mutational processes are known to cause a high TMB and hypermutation (32, 42, 66–69). As regards *POLE/POLD1* mutated tumors (SBS10b), they have been shown to have a higher number of neoantigens and infiltrating lymphocytes (70).

We also found a substantial variation in the number of doublet base substitutions (DBS) (range, 0-79 DBSs/sample in

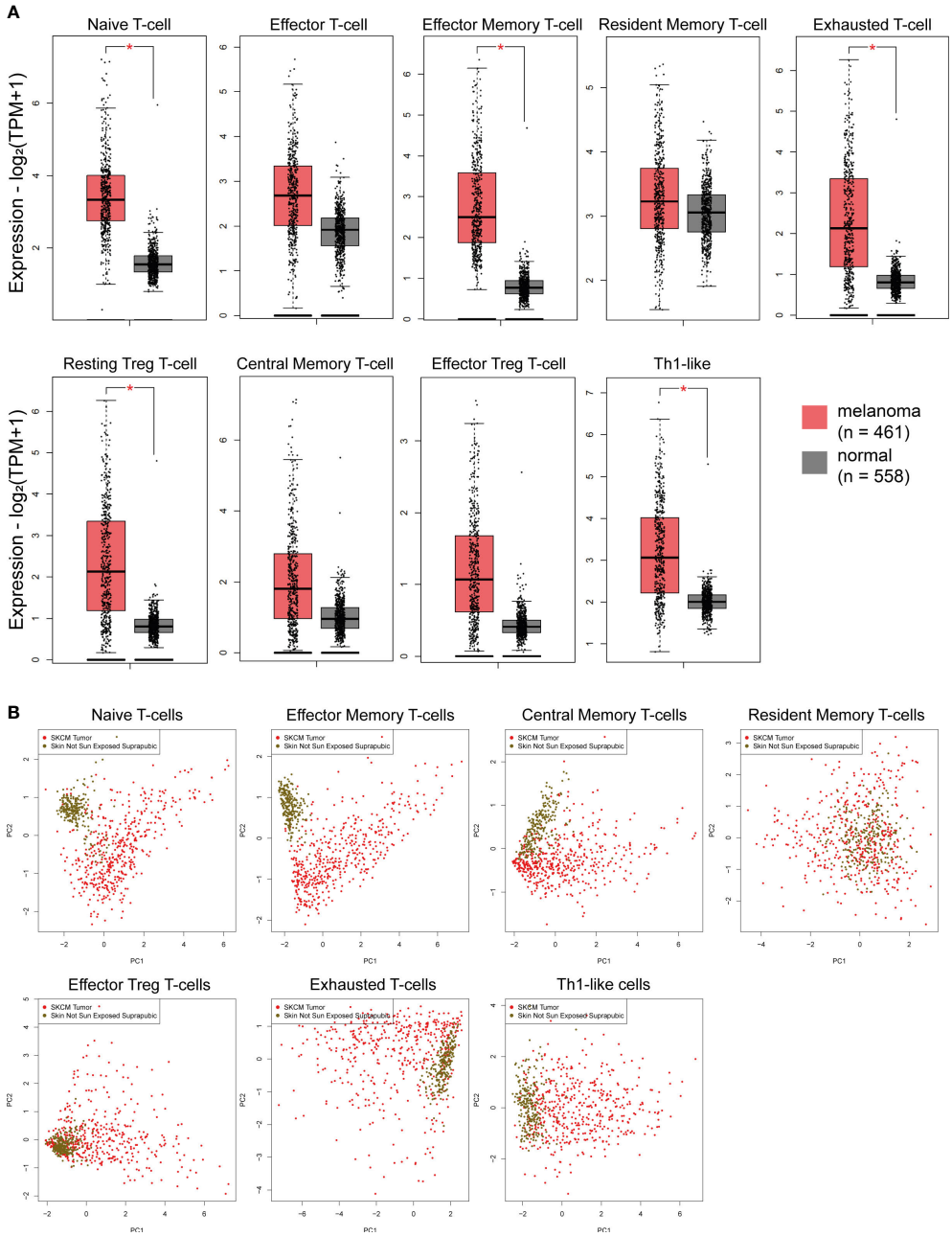

FIGURE 2
(A) Immune-related signatures being upregulated in skin melanomas. The *"naïve T-cell"*, *"effector memory T-cell"*, *"exhausted T-cell"*, *"resting Treg T-cell"* and *"Th1-like"* signatures discriminated best skin melanomas (TCGA-SKCM) from the non-sun-exposed (suprapubic) normal skin (GTEx). Asterisks (*) denote significant differences |Log2FC|>1 and p-value<0.01. **(B)** PCA dimensionality reduction on skin melanoma samples and normal skin tissue not exposed to the sun, based on the expression of each signature.

primary tumors; 0-206 DBSs/sample in metastatic tumors). Among these, we identified a high percentage of DBS1 and ID13, both due to exposure to UV light. DBS1 is mainly composed of CC>TT on the untranscribed strands of genes indicative of damage to cytosine and repair by transcription-coupled nucleotide excision repair (TC-NER), and it associates with SBS7a/SBS7b (71, 72). ID13 is predominantly composed of T deletions at TT dinucleotides, exhibits large numbers of mutations and is also associated with DBS1 (34) (Figure 4D). These data reiterate the strong link between UV light exposure with melanoma and ageing.

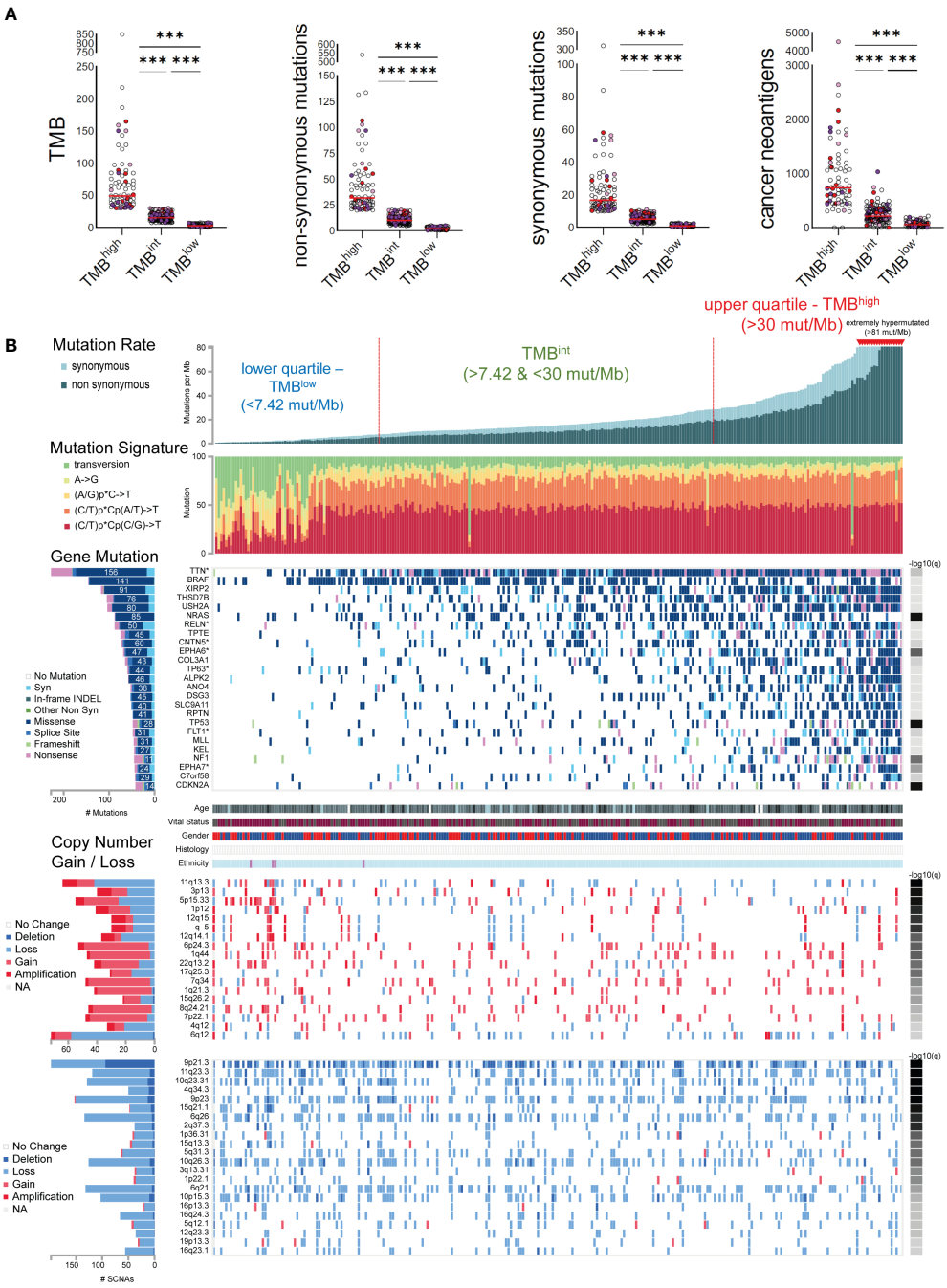

FIGURE 3
(A) Skin melanomas were stratified into upper and lower quartiles. The upper quartile includes TMB^{high} tumors (>30 total mutations/Mb), among which some were extremely hypermutated (>81 total mutations/Mb); whereas the lower quartile contains TMB^{low} tumors (<7.4 total mutations/Mb). Tumors in-between were classified as TMB intermediate (TMB^{int}). The scatterplots in the upper part show the total number of mutations (TMB), non-synonymous and synonymous mutations, as well as cancer neoantigens per TMB subgroup. Melanoma samples overexpressing *CD274* (PD-L1) (>2.44 $\log_2$(TPM+1)) and *CTLA4* (>3.089 $\log_2$(TPM+1)) are highlighted in red and purple color, respectively. Samples overexpressing both *CD274* and *CTLA4* are colored in light purple. Asterisks (***) denote statistically significant differences in the TMB, non-synonymous mutations, synonymous mutations or cancer neoantigens, between the three subgroups ($p<0.0001$). **(B)** The mutational signatures differed between TMB^{high} and TMB^{low} tumors, with the first having a preference for (C/T)p*Cp(C/G)>T and (C/T)p*Cp(A/G)>T mutations, whereas the latter, of transversions, A>G and (A/G)p*C>T mutations. The significantly mutated genes include *TTN, BRAF, XIRP2, THSD7B, USH2A, NRAS, RELN, TPTE, CNTN5, EPHA6, COL3A1*, among others. Copy number gains and losses were observed irrespective of the TMB status of the tumors, mainly across 6q12, 11q13.3, 5p15.33, 6p24.3, 9p21.3, 7q34, 11q23.3, 10q23.31, 4q34.3, 9p23 and 6q26.

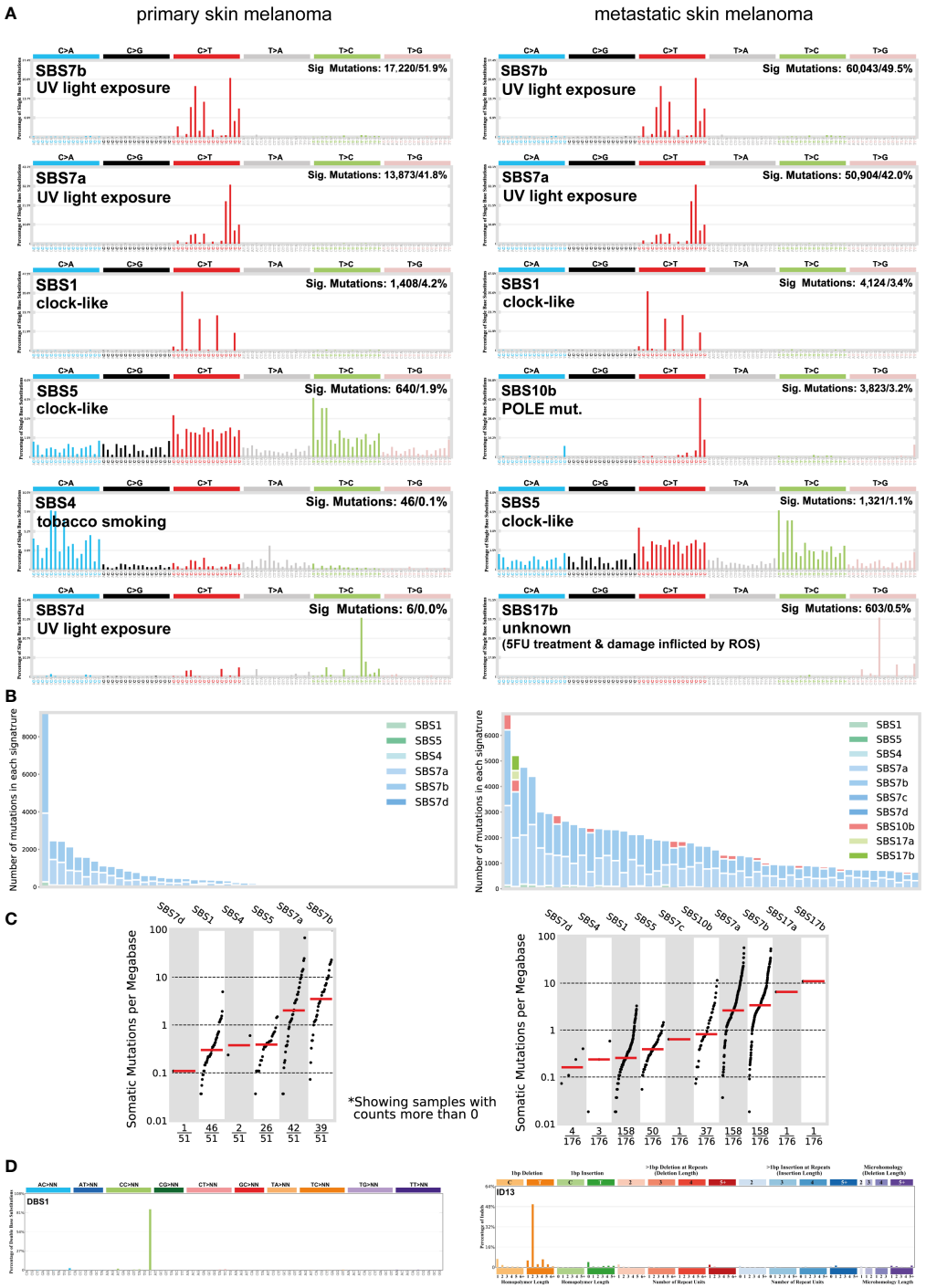

FIGURE 4
(A) The most prevalent single base substitution (SBS) signatures in primary and metastatic skin melanoma. The proposed aetiology of each SBS signature, along with the total number of mutations and corresponding percentage (%) are denoted. SBS signatures were identified using 96 different contexts, considering not only the mutated base, but also the bases immediately 5′ and 3′. **(B)** Activity plots depicting the number of mutations in each signature per skin melanoma patient. **(C)** TMB plots depicting the somatic mutations per Mb. **(D)** The most common doublet base substitutions (DBS) across primary and metastatic skin melanomas, were DBS1 and ID13. DBS signatures were generated after the concurrent modification of two consecutive nucleotide bases.

Genomic landscape in skin melanomas with diverse TMB

In total, 25 genes were recurrently mutated in skin melanoma, including *TTN* (156 missense out of a total of 228 mutations), *BRAF* (141 missense out of a total of 146 mutations), *XIRP2* (91 missense out of a total of 118 mutations), *THSD7B* (76 missense out of a total of 105 mutations), *USH2A* (80 missense out of a total of 104 mutations), *NRAS* (85 missense out of a total of 88 mutations), *RLN* (50 missense out of a total of 88 mutations) and *TPTE* (45 missense out of a total of 75 mutations), among others, having a lower mutation frequency (Figure 3). As expected, BRAF and NRAS mutations were not common among TMB^{high} patients, as only the $BRAF^{V600K}$ mutation is UV-induced and associates with a higher mutational burden (73). Overall, we identified 40 recurrently mutated cancer drivers, including *BRAF*, *NRAS*, *ARID2* and *TP53*, across 466 tumors within the TCGA-SKCM dataset (413,742 total mutations), among which, *BRAF* dominated (35) (Table S6 and Figure S9). As anticipated, we found differences in the top mutated genes between primary and metastatic skin melanomas, apart from the drivers BRAF, NRAS, TP53 and PTEN, being commonly mutated in the two types (Figure S9).

Copy number variations (CNVs) were also observed across all tumor samples, irrespective of their TMB status. In addition, we did not detect any difference in the intra-tumoral genomic heterogeneity between TMB^{high} and TMB^{low} tumors, as reflected by their MATH scores (74). CNVs were mainly located in 6q12 (1.39% deletion, 79% loss, 15.28% gain and 4.17% amplification); 11q13.3 (65.63% loss, 18.75% gain and 15.63% amplification; associated with *WNT11* amplification); 5p15.33 (45.45% loss, 43.64% gain and 10.91% amplification); 6p24.3 (7.55% loss, 84.91% gain and 7.55% amplification); 7q34 (89.58% gain, 4.17% amplification and 6.25% loss; associated with *BRAF* amplification); 8q24.21 (89.13% gain, 6.52% amplification and 4.35% loss; associated with *MYC* amplification); 9p21.3 (47.47% deletion and 52.53% loss); 11q23.3 (7.56% deletion, 92.44% loss); 10q23.31 (10.08% deletion, 89.92% loss; associated with *PTEN* deletion); 4q34.3 (22% deletion, 78% loss); 9p23 (8.50% deletion, 90/20% loss and 1.31% gain), 6q26 (3.73% deletion, 96.27% loss) and 1p22.1 (87.5% loss, 2.5% deletion and 10% gain; associated with *NRAS* reduction) among others (Figure 3). These findings are in good agreement with previous reports (75).

The expression of most immune-receptors is independent of the TMB in skin melanoma

PD-L1 expression and TMB were recently shown to be independent biomarkers in most cancers (76). Here, we evaluated the expression of *CD274* (*PD-L1*) along with other immunoinhibitors and immunostimulators, across TMB^{high}, TMB^{int} and TMB^{low} skin melanomas. Globally, we found that the expression of most immunoreceptors does not differ across the three TMB subgroups ($p>0.05$) (Figures S10–S13). *CD274* expressed higher in TMB^{high} tumors ($p<0.05$), but still without any significant correlation with the TMB (Pearson's rho (r) =0.052, p=0.372). We also noted differences in the expression of *TNFSF18*, *KDR* and *ENTPD1*, which were lower in TMB^{high} tumors ($p<0.05$) but also did not correlate significantly with the TMB (*TNFSF18*, r=-0.043, p= 0.459; *KDR*, r=-0.073, p=0.214; *ENTPD1*, r=0.0002, p=0.997). In contrast, the expression of *TNFSF9* was marginally higher in TMB^{low} melanomas (p=0.06) and correlated negatively with the TMB (r=-0.146, p=0.013). A few other correlations we could note, were between *TNFSF9* and TMB (r=-0.146, p=0.013), *NT5E* and TMB (r=0.134, p=0.023), as well as between *MICA* and TMB (Pearson's r=0.167, p=0.004). Paradoxially, however, the expression of several well-known inhibitory receptors, including *CTLA-4, PDCD1 (PD-1), TIGIT, IDO1, LAG3, ADORA2A* and *VTCN1*, was similar between TMB^{high} and TMB^{low} tumors, corroborating that in general, the expression of immune checkpoints and TMB are independent biomarkers in skin melanoma. This finding was further supported by our IHC data, showing that PD-1, PD-L1, IDO1 and LAG3 protein levels are also similar across melanomas of differential TMB status (Figures 5A, B). In addition, PD-L1+ cells (when expressed) were topologically associated with CD8+ T-cells. The TIL percentage (%) also, did not differ significantly across the three TMB subgroups of tumors (TMB^{high}, 1.77 ± 2.63; TMB^{int}, 2.74 ± 5.46; TMB^{low}, 1.72 ± 3.03); it was higher in the stroma than in the parenchyma of primary tumors, but this percentage decreased in the metastatic cases. Taken together, these data suggest that TMB is not the only factor that affects immunogenicity. In fact, other factors apart from high PD-L1 expression, seem to also affect immunogenicity in skin melanoma and therefore, prevent TMB^{low} patients to benefit from ICI therapies. These include high levels of IFNγ, CD8 and GZMA/PRF1 [intra-tumoral immune cytolytic activity (23, 42, 77)], as well as low levels of MDSCs, CAFs or M2 macrophages in the TME.

To further investigate these factors, we examined the fractions of 10 immune cell types, including B-cells, DCs, M1/M2 macrophages, NK cells, neutrophils, CD4+, CD8+T-cells and Tregs, among the three TMB subgroups of melanomas. Interestingly, we observed a similar immune-cell fraction between TMB^{high} and TMB^{int} tumors, both having a higher ratio of M1/M2 macrophages compared to TMB^{low} tumors. In addition, the CD8+ T-cells/Tregs ratio was similar between the three TMB subgroups (Figure 5C). Other than this, the total number of lymphocytes and the rest immune cells did not differ between TMB^{high} and TMB^{low} melanomas, neither did the number of TIL patches or clusters that they formed

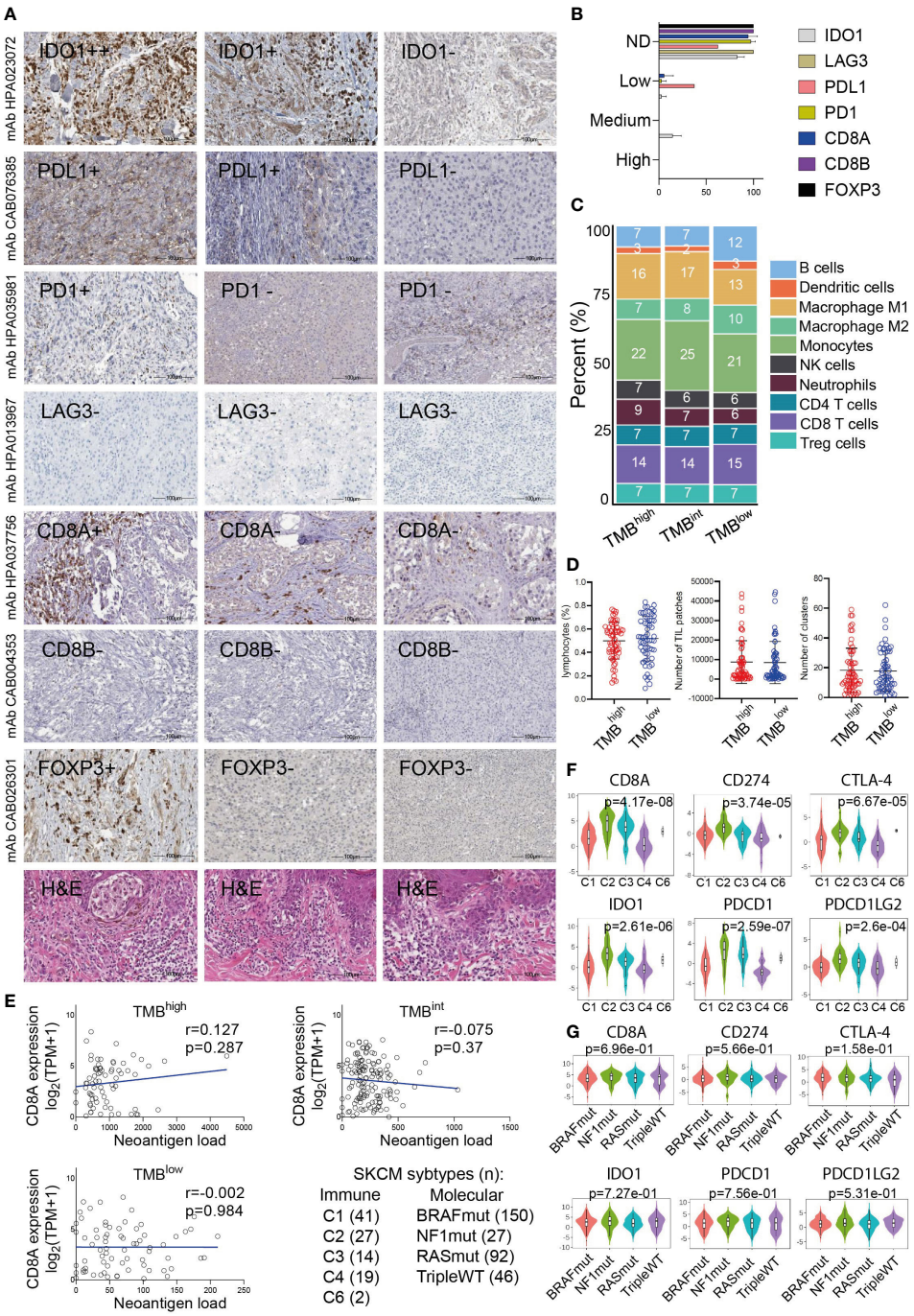

FIGURE 5
(A) Indicative immunohistochemistry (IHC) staining for the inhibitory receptors IDO1, PD-L1, PD-1, LAG3, CD8A/B (marker for cytotoxic T-cells) and FOXP3 (marker for Tregs) in an independent cohort of 11 cutaneous melanomas. H&E, hematoxylin and eosin staining. **(B)** Overall, the protein expression of these markers was either not detected (ND) or low and probably did not differ between TMB^{high} and TMB^{low} tumors. **(C)** Immune-cell fractions across TMB^{high}, TMB^{int} and TMB^{low} skin melanomas, using extracted data (quanTIseq) from The Cancer Immunome Database. **(D)** The scatterplots depict the percentage of lymphocytes (%), average number of TIL patches and clusters (with standard deviation, SD) in TMB^{high} (>30 mut/Mb) and TMB^{low} (<7.4 mut/Mb) skin melanomas. Neither of these differed significantly between the two subgroups of tumors. **(E)** The expression of CD8A (log_2(TPM+1)) did not correlate with the neoantigen load in either TMB subgroup. Expression of CD8A, PDCD1 (PD-1), CD274 (PD-L1), PDCD1LG2 (PD-L2), IDO1 and CTLA-4 across different immune **(F)** and molecular **(G)** subtypes in skin melanoma. Immune subtypes: C1, wound healing (n=41); C2, IFN-gamma dominant (n=27); C3, inflammatory (n=14); C4, lymphocyte depleted (n=19); C5, immunologically quiet (n=0); C6, TGF-b dominant (n=2). Molecular subtypes: $BRAF^{mut}$ (n=150), $NF1^{mut}$ (n=27), RAS^{mut} (n=92), $triple^{WT}$ (n=46).

(Figure 5D), suggesting the existence of other mechanisms allowing or inhibiting response to ICI therapies. These findings also agree with the notion that the content of CD8+ cytotoxic T cells within the TME, along with the TMB, are both crucial factors in determining patient resistance to ICI therapies. In line with this, McGrail et al. showed that CD8+ T-cell levels positively correlate with the neoantigen load in melanoma and that TMB^{high} tumors have a better response to ICI compared to TMB^{low} ones (78). Nevertheless, in terms of CD8A gene expression, our data show that this does not correlate with the neoantigen load in either TMB subgroup (Figure 5E). As regards the number of TIL clusters in different molecular subtypes of skin melanoma, this was recently evaluated in the same cohort and it was found to associate with better survival in $BRAF^{V600E/K}$ patients, but neither in $NRAS^{mut}$ nor $BRAF^{wt}$/$NRAS^{wt}$ patients (79). We also found that CD8A, PDCD1 (PD-1), CD274 (PD-L1), PDCD1LG2 (PD-L2), IDO1 and CTLA-4 are highly expressed in the 'IFN-gamma dominant' (C2) and 'inflammatory' (C3) immune subtypes, but not across the different molecular subtypes ($BRAF^{mut}$, $NF1^{mut}$, RAS^{mut} or $triple^{WT}$) (Figures 5F, G).

Mutations in the IFNγ pathway could affect immunogenicity in melanoma patients

IFNγ-related gene expression signatures have been shown to predict patient response to PD-1 checkpoint blockade in melanoma (39). Motivated by these observations, we hypothesized that mutations in the IFNγ pathway could also affect immunogenicity in melanoma patients, apart from the high IFNγ levels. Therefore, we explored the mutational pattern of genes in the IFNγ pathway signaling, to find whether they associate with T-cell insensitivity, and therefore, resistance to immunotherapy. Notably, we found an increased number of SNVs in *IDO1* and *HLA-DRA* (MHC-II protein). In specific, these contained 28 missense mutations, 1 stop gained and 1 splice acceptor variant in *IDO1* (Figure 6 and Table S7), which however did not seem to disturb the gene's expression, as they did not affect the protein's, heme-ring. Therefore, the ability of IDO1 to catalyze the deoxygenation of tryptophan does not seem to be affected. Kynurenine is the metabolic product of tryptophan, which suppresses T-cell proliferation and promotes the development of Treg cells. Its inhibition could be exploited therapeutically in cancer immunotherapy beyond ICI or adoptive transfer of chimeric antigen receptor (CAR) T-cells, since it may restore T-cell function and reduce the accumulation of Tregs (80, 81).

In *HLA-DRA*, we detected 14 missense variants, corroborating the dynamic role of the function of MHC in the progression of the disease (82). HLA-II expression has also been shown to predict patient response to anti-PD1, but not to anti-CTLA-4 immunotherapy (82). HLA-DRa also exhibited heterogenous expression in melanoma lesions and cell lines, with IFNγ being a strong inducer of HLA class II expression (83).

In addition, we noted 3 missense mutations in *CXCL10* and 5 missense mutations, one 5' UTR and one stop gained variant in *CXCL9*, 6 missense mutations in *STAT1*, as well as 5 missense mutations in *IFNG*, including 1 splice donor, 1 stop-gained, three 5' UTR variants and one 3' UTR variant (Figure 6 and Table S7).

As expected, *BRAF* and *NRAS* were the most frequently mutated genes among all patient samples, hosting hotspot mutations (274 missense mutations, 2 in frame deletions and one 3' UTR variants in *BRAF*; and 121 missense mutations, one frameshift and one splice donor variant in *NRAS*), followed by *NF1* (34 missense, 30 stop gained, 5 frameshift, one 3' UTR, 3 splice acceptor and 1 splice donor variants and 2 splice region; synonymous variants) and *PTEN* (23 missense, 14 frameshifts, 1 in frame insertion, 4 splice donor/acceptor variants and 6 stop gained mutations). Finally, we detected a smaller number of somatic mutations in *B2M* (1 in frame deletion, 2 splice donor and 1 coding sequence variants), *IFNGR1* (4 missense and two 3' UTR variants), *IFNGR2* (1 missense, one 3' UTR and one splice region variant in chr21), *JAK1* (10 missense mutations, one 5' UTR and 1 stop gained variant), *JAK2* (2 frameshift and 6 missense mutations) and *IRF1* (1 missense and one 3'UTR variant) (Table S7). Apart from the activating *NRAS* mutations (linked with high NRAS expression) and the inactivating *NF1* mutations (linked with decreased NF1 expression), all the other mutations were randomly distributed across all melanoma tumors, irrespective of their gene expression (Figure 6). Collectively, these data show that mutations in the IFNγ pathway could affect immunogenicity in melanoma patients.

Patient response to ICI therapies is independent of their TMB status

Tumor immune evasion is based on the infiltration of dysfunctional T-cells in the tumor, but also the prevention of T-cell infiltration into the TME. TIDE scores predict better patient response to anti-PD-1 and anti-CTLA-4 therapies, compared to TMB and PD-L1, and can be used to predict longer patient overall survival (84). Using 7 publicly available transcriptome profiles of ICI-treated melanoma patients, we predicted their response based on their TIDE scores. Overall, patient response rate to ICI ranged between 27-53%, depending on their number in each dataset and the ICI therapy given. Broadly, non-responders (high TIDE score) had significantly lower IFNG, Merck18, CD274 (PD-L1), CD8 and 'dysfunction of the tumor' scores. In contrast, they had higher 'exclusion potential of the tumor' scores, as a result of the higher levels in MDSCs, CAFs and M2 macrophages. As expected, microsatellite instability (MSI) did not associate with melanoma patient

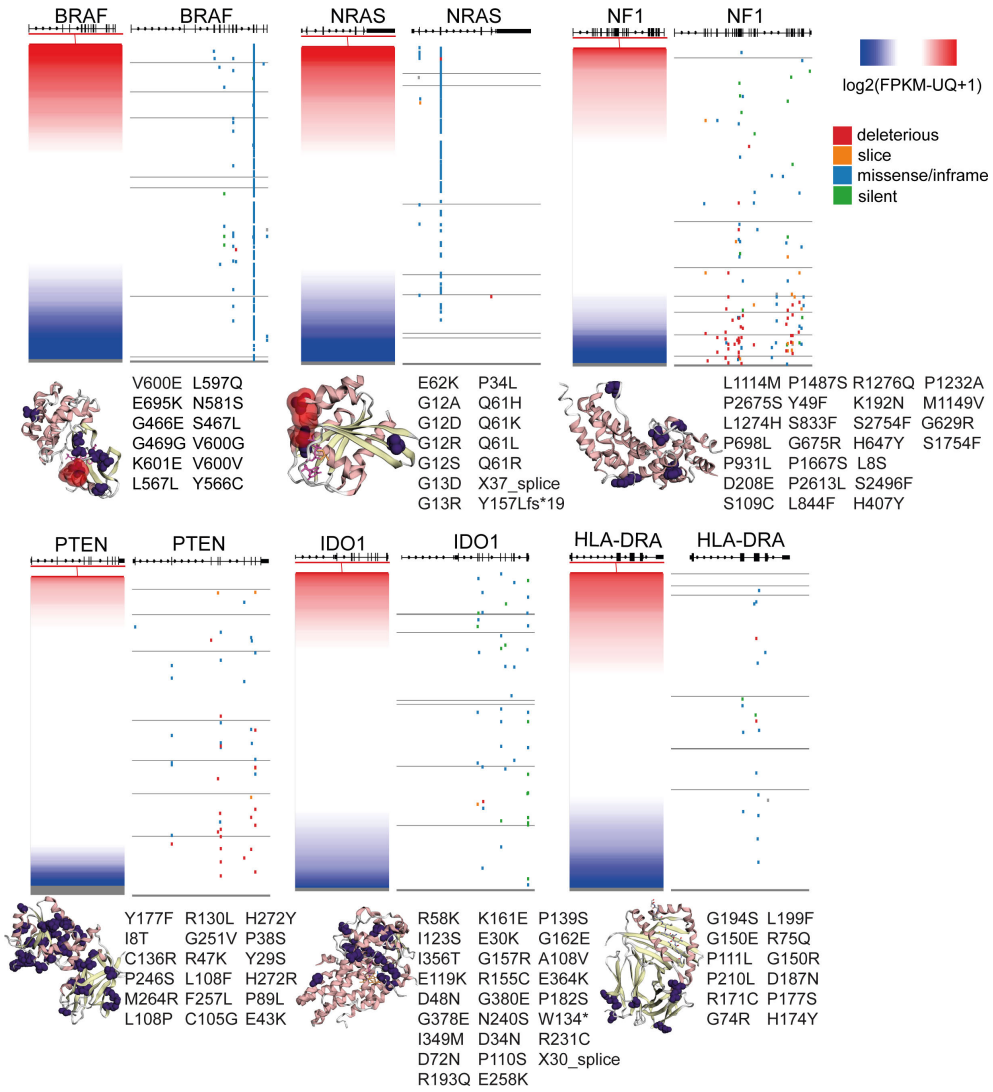

FIGURE 6
Gene expression and somatic mutations (deleterious, slice, missense/inframe or silent) in the genes BRAF, NRAS, NF1, PTEN, IDO1 and HLA-DRA in skin melanoma. The crystal structures (3D) of the genes' encoded proteins along with their somatic mutations detected in the TCGA-SKCM dataset (purple color), were calculated using MuPIT (hg38 coding) and are depicted on the right of each plot. Hotspot BRAF and NRAS mutations are highlighted in red color in the corresponding crystal structures. Apart from BRAF, NRAS, NF1 and PTEN, all of which are well-known to be recurrently mutated in skin melanoma, IDO1 and HLA-DRA were also significantly mutated, but the somatic mutations did not seem to affect their protein expression.

response to ICI therapies, obviously due to its low prevalence in this tumor type. Importantly, we found higher CTL levels among ICI-responders compared to non-responders (Figures 7A, B), recapitulating previous findings (85).

Next, we questioned whether the TMB status associates with the outcome of each ICI therapy. Therefore, we calculated the immunophenoscores between TMB^{high}, TMB^{int} and TMB^{low} patients treated with anti-PD1 or anti-CTLA-4 alone, a combination of both immune checkpoint inhibitors, or any of them. Interestingly, our analysis revealed similar IPS scores across all TMB subtypes (Figures 7C, D), suggesting that ICI therapy is independent of the patient's TMB status alone, and it could thus, also work effectively to treat TMB^{low} patients. Our data also clearly point that the quality of mutations is a more important factor than their quantity, in terms of their immunologic impact on patient response to ICI therapy.

Discussion

In the present study, we explored the expression of various activating or inhibitory immunoreceptors in skin melanomas

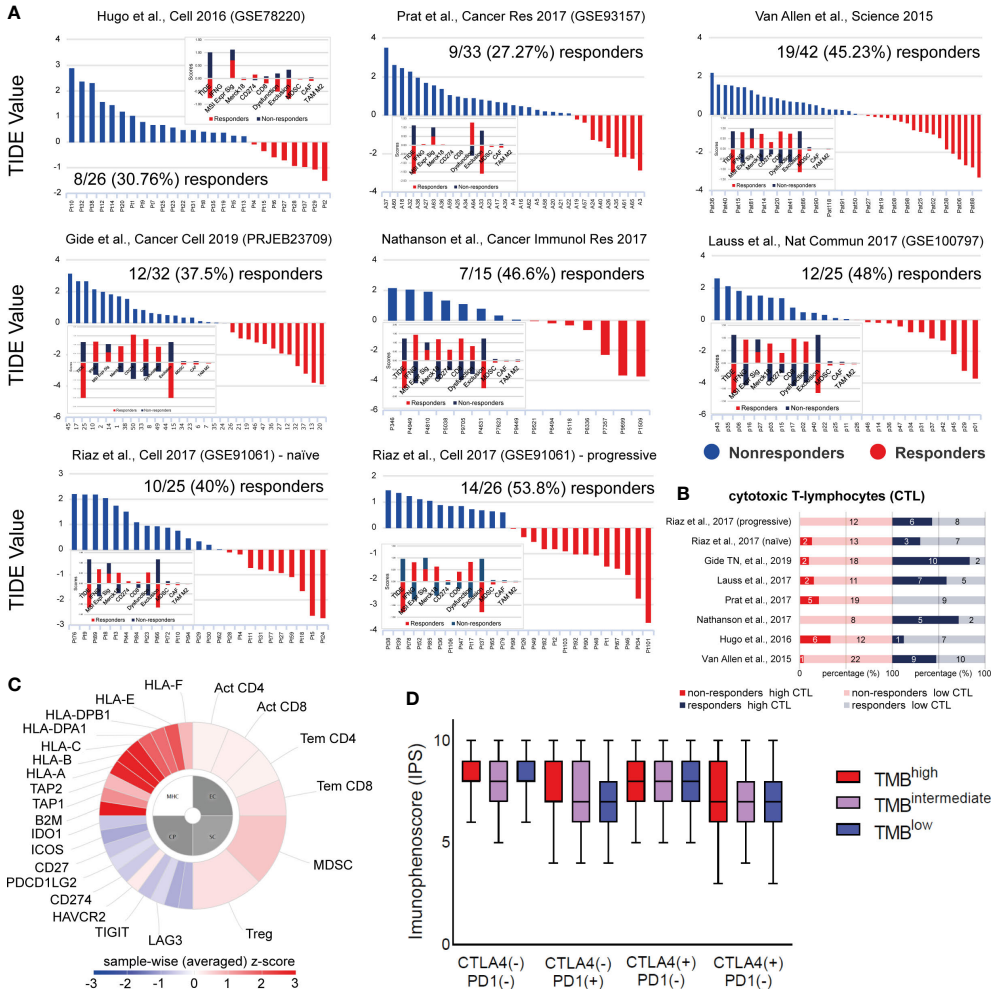

FIGURE 7
(A) TIDE analysis was used to predict patient response to ICI in 7 independent datasets of skin melanoma patients. Higher TIDE score (blue) denotes non-responders to immune-checkpoint blockade, whereas lower TIDE score (red) denotes responders. **(B)** Percentage (%) of high or low cytotoxic T-cell lymphocytes (CTLs) among responders or non-responders to ICI therapies, across all 7 melanoma datasets. Clearly, higher CTL levels were found among ICI-responders. The numbers of ICI-responders or non-responders with high or low CTL levels, are indicated within each bar. **(C)** Indicative immunophenogram depicting the four categories of markers, the expression of which, was used to calculate the immunophenoscores (IPS) for each TMB subgroup of patients. These include: MHC molecules (MHC), immunomodulators (CP), effector cells (EC) and suppressor cells (SC). The outer part of the circle includes individual factors; whereas, the inner part illustrates the weighted average z-scores of the factors included in each category. Sample wise z-scores were positively weighted according to stimulatory cells and negatively weighted according to inhibitory cells and averaged. **(D)** The boxplots indicate the average IPS across the three TMB subgroups, treated with combination ICI therapy [CTLA-4 (+)/PD1 (+)] or with each ICI therapy, alone [CTLA-4 (+)/PD1 (–) or CTLA-4 (–)/PD1 (+)] or none [CTLA-4 (-)/PD1 (-)]. Similar IPS scores were found across all tumors, suggesting that ICI therapy can be applied independently of the patient's TMB status.

with diverse TMB, and evaluated their association with patient survival and the TIL load. Overall, our findings show that high expression of most immunoreceptors, apart from PD-1, PD-L1/L2 and CTLA-4 that have been already tested in the clinical setting, associates with the TIL load and patient survival, but not with the TMB, in contrast to other, less hypermutated and/or non-inflamed tumor types (24, 53).

High TMB was initially noted to correlate with response to anti-CTLA-4 immunotherapy in melanoma (45, 86). During the next years, TMB was employed in many clinical trials of anti-PD-1/PD-L1 agents for treating various cancer types. Patients with higher TMB tended to exhibit better treatment response, but the testing methods and cutoffs of TMB varied across trials (45, 87, 88). In contrast to the widely accepted threshold of ≥10 mut/Mb to define TMB^{high} tumors, in our study we used a more stringent criterion, setting this threshold in the upper 25th quartile (≥30 mut/Mb, TMB^{high}), but we also defined as TMB^{int} those tumors with a mutational burden between 7.42 and 30 mut/Mb.

Overall, our findings suggest that TMB^{high} skin melanomas correlate with high levels of IFNγ, CD8+ T-cells in the TME,

cancer neoepitopes, as well as high expression of PD-L1 and further immune receptors. In addition, TMB^{high} patients experience longer survival and greater response rates after ICI therapy, compared to TMB^{low} ones (89). The number of cytotoxic CD8+ T-cells modulates immunogenicity in the TME. CD8+ T-cells are the most powerful effectors during an anticancer immune response and constitute the backbone of cancer immunotherapy (90, 91). TMB^{high} skin melanomas also correlate with intratumoral immune cytolytic activity (CYT), defined by the expression of granzyme A and perforin 1, both secreted by effector cytotoxic CD8+ T-cells and NK cells against their target cells (72, 87). CYT is significantly elevated upon CD8 + T-cell activation, as well as during a productive clinical response against immune-checkpoint blockade therapies in melanoma patients (23). The presence of several immune-exclusive cells in the TME, such as MDSCs, CAFs and M2 macrophages also affects response to ICI therapies (57).

By stratifying patients based on their TMB, we found that those having a higher mutation rate (>30 mut/Mb) did not express higher *CTLA-4, PD-1, IDO1* or other immunoreceptors, apart from just a few cases (including *CD274* which was upregulated in TMB^{high} tumors). In contrast, *TNFSF18*, *KDR* and *ENTPD1* showed lower expression levels among TMB^{high} tumors, and also did not correlate with the TMB. Collectively, these observations strongly indicate that immunogenicity in these tumors is affected by other factors as well, other than the TMB, and therefore, TMB^{low} patients could also benefit from ICI therapies.

In the KEYNOTE-002 study, pembrolizumab (anti-PD-1) was established as a new standard treatment after progression on ipilimumab (anti-CTLA-4) and other therapies (92). A year later, in the KEYNOTE-006 study, pembrolizumab was shown to prolong progression-free survival and overall survival and had less high-grade toxicity compared to ipilimumab in patients with advanced melanoma (93). In the CheckMate-066 study, nivolumab was also shown to associate with significant improvements in overall survival and progression-free survival, as compared with dacarbazine, among previously untreated metastatic melanoma patients, without a BRAF mutation (94). Similar improvements associated with ICI therapies were reported elsewhere (13, 95).

Our findings also corroborate that the expression of immune checkpoints and the quantification of the mutational burden seem to be independent predictive biomarkers of ICI therapy in melanoma patients. These results are in line with recent reports mentioning that PD-L1 expression and TMB have non-overlapping effects on the response rate to PD-1/PD-L1 inhibitors and can thus, be used to categorize the immunologic subtypes of different tumor types (76, 96). In addition, despite that TMB associates with improved treatment response, the mutation frequency in expressed genes was found to be superior in predicting the outcome. Additionally, the pre-existing T- and B-cell immunity was shown to play a key role in therapeutic outcomes (97).

We also show that, apart from CTLA-4 and PD-1, there are many other immune receptors expressed by T-cells, which influence the TME and act as checkpoints, negatively regulating immune responses in skin melanoma (24, 98). As combination ICI therapy has been proven to provide clinical benefits for patients with advanced metastatic melanoma, as in other cancer types (99, 100), our data further open up new perspectives for combining the currently administered immune checkpoint blockers, ipilimumab, nivolumab and pembrolizumab with mAbs towards additional inhibitory molecules. These include IDO1, IL2RA, TIGIT, LTA, VTCN1, TIM3, KDR, ENTPD1 and LAG3, as well as agonistic mAbs targeting activating immune receptors, such as TNFSF18, CD70, ICOS and KLRK1. In this line, FDA recently approved the combination therapy of nivolumab (anti-PD-1) and relatlimab (anti-LAG-3 mAb, Opdualag), which was shown to provide a greater benefit with regard to progression-free survival than inhibition of PD-1 alone, in patients with previously untreated metastatic or unresectable melanoma (REALITIVY-047, ClinicalTrials.gov number, NCT03470922) (101).

Importantly, we show that the TIL load is significantly higher among TMB^{high} skin melanomas, providing evidence that patients with a high number of immunogenic mutations have an increased survival. Indeed, the lymphocytic score associated with better survival in these patients, in agreement with previous reports (102, 103). The tumors also had higher CTL numbers, as deduced from their *CD8A* expression. To examine further the factors that could contribute to treatment response or resistance among melanoma patients receiving anti-PD-1 and/or anti-CTLA-4 immunotherapy, we evaluated transcriptomic data from 7 independent datasets and found that indeed, the number of CTLs in the TME associates with patient response to ICI therapy, irrespective of the patient TMB status.

In addition, we investigated different immune-related gene signatures. We found several T-cell-related signatures, including those of naive T-cells, effector memory T-cells and exhausted T-cells, all being upregulated in skin melanoma compared to the normal skin (or matched blood). Other signatures involving inhibitory cells (effector Treg T-cell and resting Treg T-cell signatures), or helper T-cells (Th1-like cell signature), were also higher in skin melanoma, underlying the intricate immunological reactions taking place within the tumor's microenvironment. Looking deeper into the fractions of immune-cells within the TME however, we did not observe significant differences between TMB^{high} and TMB^{low} tumors, apart from the ratio of M1/M2 macrophages, which was higher in the TMB^{high} subgroup.

Notably, different genomic events and the immune microenvironment in skin melanoma seem to orchestrate the

patients' resistance to ICI therapies or their relapse (42). Frameshift mutations, indels and splice-site mutations are also believed to generate more immunogenic neoantigens compared with the nonsynonymous SNVs that are more frequently detected upon TMB assessment (104). In addition, cancer neoantigens that are similar to pathogen-derived antigens can affect tumor immunogenicity and thus, patient response to ICI therapy (86). We explored the SNVs and CNVs across the different TMB subgroups of tumors, and also highlighted the mutational signatures contributing more to this mutational burden. Chronic sun exposure over years permits the accumulation of sun damage, and it correlates with the age of melanoma diagnosis. Therefore, is was expected to observe mainly UV-light (SBS7a/b/d) and clock-like signatures (SBS1 and SBS5) across all melanomas. In addition, we found that a small percentage of these tumors also associated with *POLE/POLD1* mutations (SBS10b) and tobacco smoking (SBS4).

Together with granzyme B and perforin, IFN-γ acts as a cytotoxic cytokine that initiates apoptosis in tumor cells (105, 106). IFN-γ also enables the synthesis of immune checkpoint inhibitory molecules and indoleamine-2,3-dioxygenase (IDO), thus stimulating other immune-suppressive mechanisms (107–109). The IFN-γ signaling pathway enhances MHC expression and subsequent tumor antigen presentation. It also induces the recruitment of further immune cells, and inhibits tumor cell proliferation (110). IDO1 associates with adverse clinical outcome in melanoma patients, and its activity promotes an immunosuppressive TME by upregulating trafficking of MDSCs and Tregs (111). Here, we evaluated somatic mutations in *IFNG* and other IFN-γ-related genes in skin melanoma, and questioned whether their presence associates with gene expression. Our data reveal that *IDO1* and *HLA-DRA* are frequently mutated in skin melanoma, but these mutations do not seem to associate with their gene expression. Nevertheless, the frequency of the somatic mutations that we detected both in *IDO1* and *HLA-DRA*, suggests that these are common events taking place in skin melanoma and could be involved in hindering patient response to ICI therapies. Their contribution to immune evasion and resistance to ICI therapies, could take place in parallel with other well-known mutations in *BRAF*, *NRAS*, *NF1*, *PTEN* and *B2M*, as well as in other genes involved in the IFN-γ signaling pathway, being critical in mediating antitumor immunity (112).

We finally showed that non-responders to anti-PD-1 and/or anti-CTLA-4 ICI therapies have lower IFNG, Merck18, CD274 and CD8 scores, and lower dysfunction of the tumor. In addition, they have higher exclusion potential of the tumor and higher levels in the immune suppressive MDSCs, CAFs and M2 macrophages, compared to ICI-responders. The latter cell types, on their own and cooperatively, induce an immune-suppressive TME that prevents anti-tumor cytotoxic and Th1-directed T-cell activities, mainly through the release of cytokines, chemokines, and other soluble mediators (113). In addition, their depletion increases anti-tumor immune responses overcoming innate resistance (114). Non-responders to monotherapy often express alternate immune-checkpoints, such as IDO1, ICOS, and TIGIT, in contrast to combination therapy on non-responders, who rarely express these alternate drug targets (50). Moreover, ICI responders had significantly higher CTL numbers compared to non-responders. Therefore, it seems that IFNγ-associated genes and CTLs in the TME, along with a high TMB (and consequently neoantigen) load, but no specific gene mutation, associate with ICI therapy response. These data provide important insights to facilitate the development of precision immuno-oncology for skin melanoma patients.

Overall, we highlight the associations between various immune receptors, TMB, TILs, patient survival and their response to ICI therapies. Taken together, our data highlight the importance of pre-existing T-cell immunity in the therapeutic outcome. They also corroborate that the expression of most immunoreceptors and TMB are independent biomarkers in predicting treatment response in skin melanoma and that ICI therapies could also be applied to TMB^{low} patients.

Data availability statement

The original contributions presented in the study are included in the article/Supplementary Material. Further inquiries can be directed to the corresponding author.

Author contributions

GG and AZ acquired data and analyzed them. AZ developed the methodology, analyzed data and interpreted them. AZ wrote the manuscript and supervised the study. GG and AZ critically reviewed the manuscript. All authors contributed to the article and approved the submitted version.

Acknowledgments

We would like to acknowledge TCGA, ICGC, HPA, GDAC and TCIA for providing the genetic and clinical data of the skin melanoma patients that were analyzed in this study. We would also like to acknowledge assistance with extracting mutational signatures from Dr. Ilias Georgakopoulos-Soares.

Conflict of interest

The authors declare that the research was conducted in the absence of any commercial or financial relationships that could be construed as a potential conflict of interest.

Publisher's note

Supplementary material

The Supplementary Material for this article can be found online at: https://www.frontiersin.org/articles/10.3389/fimmu.2022.1006665/full#supplementary-material

SUPPLEMENTARY FIGURE 1
The bar charts (left) depict the top 10 enriched Gene Ontology (GO) terms in the top 250 upregulated genes in primary skin melanoma, along with their corresponding p-values. Asterisks (*) indicate the terms with significant adjusted p-values (<0.05). The scatterplots (right) were created using UMAP and are organized so that similar gene sets are clustered together. Larger, black-outlined points represent significantly enriched terms, the associated gene set names and p-values of which, are denoted.

SUPPLEMENTARY FIGURE 2
The bar charts (left) depict the top 10 enriched Gene Ontology (GO) terms in the top 250 downregulated genes in primary skin melanoma, along with their corresponding p-values. Colored bars correspond to terms with significant p-values (<0.05). Asterisks (*) indicate the terms with significant adjusted p-values (<0.05). The scatterplots (right) were created using UMAP and are organized so that similar gene sets are clustered together. Larger, black-outlined points represent significantly enriched terms, the associated gene set names and p-values of which, are denoted.

SUPPLEMENTARY FIGURE 3
The bar charts (left) depict the top 10 enriched Gene Ontology (GO) terms in the top 250 upregulated genes in metastatic skin melanoma, along with their corresponding p-values. Colored bars correspond to terms with significant p-values (<0.05). Asterisks (*) indicate the terms with significant adjusted p-values (<0.05). The scatterplots (right) were created using UMAP and are organized so that similar gene sets are clustered together. Larger, black-outlined points represent significantly enriched terms, the associated gene set names and p-values of which, are denoted.

SUPPLEMENTARY FIGURE 4
The bar charts (left) depict the top 10 enriched Gene Ontology (GO) terms in the top 250 downregulated genes in metastatic skin melanoma, along with their corresponding p-values. Colored bars correspond to terms with significant p-values (<0.05). Asterisks (*) indicate the terms with significant adjusted p-values (<0.05). The scatterplots (right) were created using UMAP and are organized so that similar gene sets are clustered together. Larger, black-outlined points represent significantly enriched terms, the associated gene set names and p-values of which, are denoted.

SUPPLEMENTARY FIGURE 5
Stage-plot analysis of the expression of *CD8* and several immune receptors in skin melanoma, showing no significant differences according to the tumor's stage.

SUPPLEMENTARY FIGURE 6
The Kaplan-Meier curves show the overall and disease-free (DF) survival of melanoma patients, expressing high or low expression levels of *PD-1, PD-L1/L2, CTLA-4, LAG3, IDO1/2, TIGIT, HAVCR2, VISTA, VTCN1, ILT2/4, ADORA2A* and *CD8* (marker for CD8+ T cells). The log-rank test was used to assess statistical differences between the two subgroups of patients. The patients were separated into high expression group (upper 50 percentile, red curve) and low expression group (lower 50 percentile, blue curve) by gene expression levels. The numbers of the patients in each group are provided as "n(high)" and "n(low)", respectively. The log-rank p-value, along with the HR(high) and p(HR) values are also provided in each Kaplan-Meier survival plot. A Bonferroni-corrected cut-off log-rank p-value of <0.05 indicates statistical significance.

SUPPLEMENTARY FIGURE 7
The scatterplots depict the Pearson's correlation coefficient (R and p-values) between the expression of *CD274 (PD-L1)* **(A)** or *CD8A* **(B)** and various immune receptors in skin melanomas (TCGA-SKCM) and normal suprapubic skin sample, not exposed to the sun (GTEx).

SUPPLEMENTARY FIGURE 8
The boxplots depict nine immune-signatures which did not differ across $BRAF^{mut}$, $NF1^{mut}$, RAS^{mut} and $Triple^{WT}$ skin melanoma tumors. Signatures were calculated in $\log_2(TPM+1)$ using the $|\log_2 FC>1|$ and p<0.01 (ANOVA) as thresholds for statistical significance across the different skin melanoma subtypes.

SUPPLEMENTARY FIGURE 9
The comutation plots depict the top 20 significantly mutated genes (SMGs, FDR<0.1) in primary and metastatic **(A)** or TMB^{high} and TB^{low} skin melanomas **(B)**. Green, red, pink, black and orange boxes indicate missense, nonsense, translation start site, multi-hit and splice-site mutations, respectively. The SMGs that correlate with primary or metastatic tumors (p<0.05) are highlighted by red or blue circles, respectively, next to the gene names. Each SMG's q-values (–log10 (FDR)) are plotted as a right-side bar plot in blue color. **(C)** The bar chart depicts the top 30 cancer drivers in skin melanoma. **(D)** The lollipop plots (below) report all the variants affecting the coding region of three drivers in skin melanoma (BRAF, NRAS and ARID2). Diagram circles are colored with respect to the corresponding mutations. Passenger mutations are highlighted in light blue and ad driver mutations in red.

SUPPLEMENTARY FIGURE 10
The scatterplots show mean values in $\log_2(TPM+1)$ with standard deviation (SD) of gene expression across various immunostimulators. Gene expression did not change across TMB^{high}, TMB^{int} and TMB^{low} skin melanomas, apart from *CD274* and *TNFSF18* (*, p<0.05. **, p<0.01).

SUPPLEMENTARY FIGURE 11
The scatterplots show mean values in $\log_2(TPM+1)$ with standard deviation (SD) of gene expression across various immunoinhibitors. Gene expression did not change across TMB^{high}, TMB^{int} and TMB^{low} skin melanomas, apart from *KDR*, which was lower in TMB^{high} tumors (**, p<0.01).

SUPPLEMENTARY FIGURE 12
Pearson's correlation between TMB and the expression of activating immune receptors (immunostimulators), shows that there was no relationship between their gene expression and the TMB in skin melanoma.

SUPPLEMENTARY FIGURE 13
Pearson's correlation between TMB and the expression of inhibitory immune receptors (immunoinhibitors), shows that there was no relationship between the gene expression and the TMB in skin melanoma.

SUPPLEMENTARY TABLE 1
Significantly up- and down-regulated genes in skin melanoma (TCGA-SKCM).

SUPPLEMENTARY TABLE 2
Gene Ontology enrichment for the top 250 up-regulated genes in primary skin melanoma.

SUPPLEMENTARY TABLE 3
Gene Ontology enrichment for the top 250 down-regulated genes in primary skin melanoma.

SUPPLEMENTARY TABLE 4
Gene Ontology enrichment for the top 250 up-regulated genes in metastatic skin melanoma.

SUPPLEMENTARY TABLE 5
Gene Ontology enrichment for the top 250 down-regulated genes in metastatic skin melanoma.

SUPPLEMENTARY TABLE 6
Recurrently mutated cancer drivers in skin melanoma, identified using IntOGen analysis.

SUPPLEMENTARY TABLE 7
Somatic mutation analysis for IDO1, HLA-DRA, CXCL10, CXCL9. STAT1, IFNG, B2M, BRAF, NRAS, NF1, JAK1, JAK2, PTEN, IFNGR1, IFNGR2 and IRF1, in skin melanoma.

References

1. Bittner M, Meltzer P, Chen Y, Jiang Y, Seftor E, Hendrix M, et al. Molecular classification of cutaneous malignant melanoma by gene expression profiling. *Nature* (2000) 406:536–40. doi: 10.1038/35020115

2. Leiter U, Garbe C. Epidemiology of melanoma and nonmelanoma skin cancer–the role of sunlight. *Adv Exp Med Biol* (2008) 624:89–103. doi: 10.1007/978-0-387-77574-6_8

3. Brash DE, Rudolph JA, Simon JA, Lin A, McKenna GJ, Baden HP, et al. A role for sunlight in skin cancer: UV-induced p53 mutations in squamous cell carcinoma. *Proc Natl Acad Sci U.S.A.* (1991) 88:10124–8. doi: 10.1073/pnas.88.22.10124

4. Cancer Genome Atlas Network. Genomic classification of cutaneous melanoma. *Cell* (2015) 161:1681–96. doi: 10.1016/j.cell.2015.05.044

5. Davies H, Bignell GR, Cox C, Stephens P, Edkins S, Clegg S, et al. Mutations of the BRAF gene in human cancer. *Nature* (2002) 417:949–54. doi: 10.1038/nature00766

6. Huang FW, Hodis E, Xu MJ, Kryukov GV, Chin L, Garraway LA. Highly recurrent TERT promoter mutations in human melanoma. *Science* (2013) 339:957–9. doi: 10.1126/science.1229259

7. Thorsson V, Gibbs DL, Brown SD, Wolf D, Bortone DS, Ou Yang T-H, et al. The immune landscape of cancer. *Immunity* (2018) 48:812–30.e14. doi: 10.1016/j.immuni.2018.03.023

8. Villanueva J, Herlyn M. Melanoma and the tumor microenvironment. *Curr Oncol Rep* (2008) 10:439–46. doi: 10.1007/s11912-008-0067-y

9. Ji R-R, Chasalow SD, Wang L, Hamid O, Schmidt H, Cogswell J, et al. An immune-active tumor microenvironment favors clinical response to ipilimumab. *Cancer Immunol Immunother CII* (2012) 61:1019–31. doi: 10.1007/s00262-011-1172-6

10. Topalian SL, Taube JM, Anders RA, Pardoll DM. Mechanism-driven biomarkers to guide immune checkpoint blockade in cancer therapy. *Nat Rev Cancer* (2016) 16:275–87. doi: 10.1038/nrc.2016.36

11. Herbst RS, Soria J-C, Kowanetz M, Fine GD, Hamid O, Gordon MS, et al. Predictive correlates of response to the anti-PD-L1 antibody MPDL3280A in cancer patients. *Nature* (2014) 515:563–7. doi: 10.1038/nature14011

12. Mandalà M, Imberti GL, Piazzalunga D, Belfiglio M, Labianca R, Barberis M, et al. Clinical and histopathological risk factors to predict sentinel lymph node positivity, disease-free and overall survival in clinical stages I-II AJCC skin melanoma: Outcome analysis from a single-institution prospectively collected database. *Eur J Cancer Oxf Engl 1990* (2009) 45:2537–45. doi: 10.1016/j.ejca.2009.05.034

13. Postow MA, Chesney J, Pavlick AC, Robert C, Grossmann K, McDermott D, et al. Nivolumab and ipilimumab versus ipilimumab in untreated melanoma. *N Engl J Med* (2015) 372:2006–17. doi: 10.1056/NEJMoa1414428

14. Larkin J, Hodi FS, Wolchok JD. Combined nivolumab and ipilimumab or monotherapy in untreated melanoma. *N Engl J Med* (2015) 373:1270–1. doi: 10.1056/NEJMc1509660

15. Tucci M, Passarelli A, Mannavola F, Felici C, Stucci LS, Cives M, et al. Immune system evasion as hallmark of melanoma progression: The role of dendritic cells. *Front Oncol* (2019) 9:1148. doi: 10.3389/fonc.2019.01148

16. McGranahan N, Favero F, de Bruin EC, Birkbak NJ, Szallasi Z, Swanton C. Clonal status of actionable driver events and the timing of mutational processes in cancer evolution. *Sci Transl Med* (2015) 7:283ra54. doi: 10.1126/scitranslmed.aaa1408

17. Schumacher TN, Schreiber RD. Neoantigens in cancer immunotherapy. *Science* (2015) 348:69–74. doi: 10.1126/science.aaa4971

18. Riaz N, Morris L, Havel JJ, Makarov V, Desrichard A, Chan TA. The role of neoantigens in response to immune checkpoint blockade. *Int Immunol* (2016) 28:411–9. doi: 10.1093/intimm/dxw019

19. Goodman AM, Kato S, Bazhenova L, Patel SP, Frampton GM, Miller V, et al. Tumor mutational burden as an independent predictor of response to immunotherapy in diverse cancers. *Mol Cancer Ther* (2017) 16:2598–608. doi: 10.1158/1535-7163.MCT-17-0386

20. Lee C-H, Yelensky R, Jooss K, Chan TA. Update on tumor neoantigens and their utility: Why it is good to be different. *Trends Immunol* (2018) 39:536–48. doi: 10.1016/j.it.2018.04.005

21. Christodoulou M-I, Zaravinos A. New clinical approaches and emerging evidence on immune-checkpoint inhibitors as anti-cancer therapeutics: CTLA-4 and PD-1 pathways and beyond. *Crit Rev Immunol* (2019) 39:379–408. doi: 10.1615/CritRevImmunol.2020033340

22. McInnes L, Healy J, Melville J. UMAP: Uniform manifold approximation and projection for dimension reduction. *arXiv preprint* (2018). doi: 10.48550/ARXIV.1802.03426

23. Roufas C, Chasiotis D, Makris A, Efstathiades C, Dimopoulos C, Zaravinos A. The expression and prognostic impact of immune cytolytic activity-related markers in human malignancies: A comprehensive meta-analysis. *Front Oncol* (2018) 8:27. doi: 10.3389/fonc.2018.00027

24. Zaravinos A, Roufas C, Nagara M, de Lucas Moreno B, Oblovatskaya M, Efstathiades C, et al. Cytolytic activity correlates with the mutational burden and deregulated expression of immune checkpoints in colorectal cancer. *J Exp Clin Cancer Res CR* (2019) 38:364. doi: 10.1186/s13046-019-1372-z

25. Xu L, Shen SS, Hoshida Y, Subramanian A, Ross K, Brunet J-P, et al. Gene expression changes in an animal melanoma model correlate with aggressiveness of human melanoma metastases. *Mol Cancer Res MCR* (2008) 6:760–9. doi: 10.1158/1541-7786.MCR-07-0344

26. Jalili A, Mertz KD, Romanov J, Wagner C, Kalthoff F, Stuetz A, et al. NVP-LDE225, a potent and selective SMOOTHENED antagonist reduces melanoma growth. *Vitro vivo. PloS One* (2013) 8:e69064. doi: 10.1371/journal.pone.0069064

27. Riker AI, Enkemann SA, Fodstad O, Liu S, Ren S, Morris C, et al. The gene expression profiles of primary and metastatic melanoma yields a transition point of tumor progression and metastasis. *BMC Med Genomics* (2008) 1:13. doi: 10.1186/1755-8794-1-13

28. Kabbarah O, Nogueira C, Feng B, Nazarian RM, Bosenberg M, Wu M, et al. Integrative genome comparison of primary and metastatic melanomas. *PloS One* (2010) 5:e10770. doi: 10.1371/journal.pone.0010770

29. Smyth GK. Linear models and empirical bayes methods for assessing differential expression in microarray experiments. *Stat Appl Genet Mol Biol* (2004) 3. doi: 10.2202/1544-6115.1027

30. Tang Z, Kang B, Li C, Chen T, Zhang Z. GEPIA2: An enhanced web server for large-scale expression profiling and interactive analysis. *Nucleic Acids Res* (2019) 47:W556–60. doi: 10.1093/nar/gkz430

31. Mayakonda A, Lin D-C, Assenov Y, Plass C, Koeffler HP. Maftools: efficient and comprehensive analysis of somatic variants in cancer. *Genome Res* (2018) 28:1747–56. doi: 10.1101/gr.239244.118

32. Alexandrov LB, Nik-Zainal S, Wedge DC, Aparicio SAJR, Behjati S, Biankin AV, et al. Signatures of mutational processes in human cancer. *Nature* (2013) 500:415–21. doi: 10.1038/nature12477

33. Bergstrom EN, Huang MN, Mahto U, Barnes M, Stratton MR, Rozen SG, et al. SigProfilerMatrixGenerator: A tool for visualizing and exploring patterns of small mutational events. *BMC Genomics* (2019) 20:685. doi: 10.1186/s12864-019-6041-2

34. Alexandrov LB, Kim J, Haradhvala NJ, Huang MN, Tian Ng AW, Wu Y, et al. The repertoire of mutational signatures in human cancer. *Nature* (2020) 578:94–101. doi: 10.1038/s41586-020-1943-3

35. Martínez-Jiménez F, Muiños F, Sentís I, Deu-Pons J, Reyes-Salazar I, Arnedo-Pac C, et al. A compendium of mutational cancer driver genes. *Nat Rev Cancer* (2020) 20:555–72. doi: 10.1038/s41568-020-0290-x

36. Charoentong P, Finotello F, Angelova M, Mayer C, Efremova M, Rieder D, et al. Pan-cancer immunogenomic analyses reveal genotype-immunophenotype relationships and predictors of response to checkpoint blockade. *Cell Rep* (2017) 18:248–62. doi: 10.1016/j.celrep.2016.12.019

37. Finotello F, Mayer C, Plattner C, Laschober G, Rieder D, Hackl H, et al. Molecular and pharmacological modulators of the tumor immune contexture revealed by deconvolution of RNA-seq data. *Genome Med* (2019) 11:34. doi: 10.1186/s13073-019-0638-6

38. Uhlen M, Zhang C, Lee S, Sjöstedt E, Fagerberg L, Bidkhori G, et al. A pathology atlas of the human cancer transcriptome. *Science* (2017) 357:eaan2507. doi: 10.1126/science.aan2507

39. Ayers M, Lunceford J, Nebozhyn M, Murphy E, Loboda A, Kaufman DR, et al. IFN-γ-related mRNA profile predicts clinical response to PD-1 blockade. *J Clin Invest* (2017) 127:2930–40. doi: 10.1172/JCI91190

40. Goldman M, Craft B, Hastie M, Repečka K, Kamath A, McDade F, et al. The UCSC xena platform for public and private cancer genomics data visualization and interpretation. *[preprint]. Cancer Biol* (2018) 326470. doi: 10.1101/326470

41. Hugo W, Zaretsky JM, Sun L, Song C, Moreno BH, Hu-Lieskovan S, et al. Genomic and transcriptomic features of response to anti-PD-1 therapy in metastatic melanoma. *Cell* (2016) 165:35–44. doi: 10.1016/j.cell.2016.02.065

42. Roufas C, Georgakopoulos-Soares I, Zaravinos A. Distinct genomic features across cytolytic subgroups in skin melanoma. *Cancer Immunol Immunother CII* (2021) 70:3137–54. doi: 10.1007/s00262-021-02918-3

43. Fu J, Li K, Zhang W, Wan C, Zhang J, Jiang P, et al. Large-Scale public data reuse to model immunotherapy response and resistance. *Genome Med* (2020) 12:21. doi: 10.1186/s13073-020-0721-z

44. Jiang P, Gu S, Pan D, Fu J, Sahu A, Hu X, et al. Signatures of T cell dysfunction and exclusion predict cancer immunotherapy response. *Nat Med* (2018) 24:1550–8. doi: 10.1038/s41591-018-0136-1

45. Van Allen EM, Miao D, Schilling B, Shukla SA, Blank C, Zimmer L, et al. Genomic correlates of response to CTLA-4 blockade in metastatic melanoma. *Science* (2015) 350:207–11. doi: 10.1126/science.aad0095

46. Nathanson T, Ahuja A, Rubinsteyn A, Aksoy BA, Hellmann MD, Miao D, et al. Somatic mutations and neoepitope homology in melanomas treated with CTLA-4 blockade. *Cancer Immunol Res* (2017) 5:84–91. doi: 10.1158/2326-6066.CIR-16-0019

47. Prat A, Navarro A, Paré L, Reguart N, Galván P, Pascual T, et al. Immune-related gene expression profiling after PD-1 blockade in non-small cell lung carcinoma, head and neck squamous cell carcinoma, and melanoma. *Cancer Res* (2017) 77:3540–50. doi: 10.1158/0008-5472.CAN-16-3556

48. Lauss M, Donia M, Harbst K, Andersen R, Mitra S, Rosengren F, et al. Mutational and putative neoantigen load predict clinical benefit of adoptive T cell therapy in melanoma. *Nat Commun* (2017) 8:1738. doi: 10.1038/s41467-017-01460-0

49. Riaz N, Havel JJ, Makarov V, Desrichard A, Urba WJ, Sims JS, et al. Tumor and microenvironment evolution during immunotherapy with nivolumab. *Cell* (2017) 171:934–949.e16. doi: 10.1016/j.cell.2017.09.028

50. Gide TN, Quek C, Menzies AM, Tasker AT, Shang P, Holst J, et al. Distinct immune cell populations define response to anti-PD-1 monotherapy and anti-PD-1/Anti-CTLA-4 combined therapy. *Cancer Cell* (2019) 35:238–255.e6. doi: 10.1016/j.ccell.2019.01.003

51. Traag VA, Waltman L, van Eck NJ. From louvain to Leiden: Guaranteeing well-connected communities. *Sci Rep* (2019) 9:5233. doi: 10.1038/s41598-019-41695-z

52. Ballot E, Ladoire S, Routy B, Truntzer C, Ghiringhelli F. Tumor infiltrating lymphocytes signature as a new pan-cancer predictive biomarker of anti PD-1/PD-L1 efficacy. *Cancers* (2020) 12:E2418. doi: 10.3390/cancers12092418

53. Kitsou M, Ayiomamitis GD, Zaravinos A. High expression of immune checkpoints is associated with the TIL load, mutation rate and patient survival in colorectal cancer. *Int J Oncol* (2020) 57:237–48. doi: 10.3892/ijo.2020.5062

54. Kitano A, Ono M, Yoshida M, Noguchi E, Shimomura A, Shimoi T, et al. Tumour-infiltrating lymphocytes are correlated with higher expression levels of PD-1 and PD-L1 in early breast cancer. *ESMO Open* (2017) 2:e000150. doi: 10.1136/esmoopen-2016-000150

55. Yu Z, Si L. Immunotherapy of patients with metastatic melanoma. *Chin Clin Oncol* (2017) 6:20. doi: 10.21037/cco.2017.04.01

56. Ott PA, Hodi FS, Kaufman HL, Wigginton JM, Wolchok JD. Combination immunotherapy: A road map. *J Immunother Cancer* (2017) 5:16. doi: 10.1186/s40425-017-0218-5

57. Jenkins RW, Barbie DA, Flaherty KT. Mechanisms of resistance to immune checkpoint inhibitors. *Br J Cancer* (2018) 118:9–16. doi: 10.1038/bjc.2017.434

58. Li F, Li C, Cai X, Xie Z, Zhou L, Cheng B, et al. The association between CD8 + tumor-infiltrating lymphocytes and the clinical outcome of cancer immunotherapy: A systematic review and meta-analysis. *EClinicalMedicine* (2021) 41:101134. doi: 10.1016/j.eclinm.2021.101134

59. Takada K, Jameson SC. Naive T cell homeostasis: From awareness of space to a sense of place. *Nat Rev Immunol* (2009) 9:823–32. doi: 10.1038/nri2657

60. Wherry EJ. T Cell exhaustion. *Nat Immunol* (2011) 12:492–9. doi: 10.1038/ni.2035

61. Ciccocioppo F, Lanuti P, Pierdomenico L, Simeone P, Bologna G, Ercolino E, et al. The characterization of regulatory T-cell profiles in alzheimer's disease and multiple sclerosis. *Sci Rep* (2019) 9:8788. doi: 10.1038/s41598-019-45433-3

62. Kamali AN, Noorbakhsh SM, Hamedifar H, Jadidi-Niaragh F, Yazdani R, Bautista JM, et al. A role for Th1-like Th17 cells in the pathogenesis of inflammatory and autoimmune disorders. *Mol Immunol* (2019) 105:107–15. doi: 10.1016/j.molimm.2018.11.015

63. Wan YY, Flavell RA. How diverse–CD4 effector T cells and their functions. *J Mol Cell Biol* (2009) 1:20–36. doi: 10.1093/jmcb/mjp001

64. Koizumi S-I, Ishikawa H. Transcriptional regulation of differentiation and functions of effector T regulatory cells. *Cells* (2019) 8:E939. doi: 10.3390/cells8080939

65. Secrier M, Li X, de Silva N, Eldridge MD, Contino G, Bornschein J, et al. Corrigendum: Mutational signatures in esophageal adenocarcinoma define etiologically distinct subgroups with therapeutic relevance. *Nat Genet* (2017) 49:317. doi: 10.1038/ng0217-317a

66. Hayward NK, Wilmott JS, Waddell N, Johansson PA, Field MA, Nones K, et al. Whole-genome landscapes of major melanoma subtypes. *Nature* (2017) 545:175–80. doi: 10.1038/nature22071

67. Nik-Zainal S, Alexandrov LB, Wedge DC, Van Loo P, Greenman CD, Raine K, et al. Mutational processes molding the genomes of 21 breast cancers. *Cell* (2012) 149:979–93. doi: 10.1016/j.cell.2012.04.024

68. Saini N, Roberts SA, Klimczak LJ, Chan K, Grimm SA, Dai S, et al. The impact of environmental and endogenous damage on somatic mutation load in human skin fibroblasts. *PloS Genet* (2016) 12:e1006385. doi: 10.1371/journal.pgen.1006385

69. Sha D, Jin Z, Budczies J, Kluck K, Stenzinger A, Sinicrope FA. Tumor mutational burden as a predictive biomarker in solid tumors. *Cancer Discovery* (2020) 10:1808–25. doi: 10.1158/2159-8290.CD-20-0522

70. Wang F, Zhao Q, Wang Y-N, Jin Y, He M-M, Liu Z-X, et al. Evaluation of POLE and POLD1 mutations as biomarkers for immunotherapy outcomes across multiple cancer types. *JAMA Oncol* (2019) 5:1504–6. doi: 10.1001/jamaoncol.2019.2963

71. Chen J-M, Férec C, Cooper DN. Patterns and mutational signatures of tandem base substitutions causing human inherited disease. *Hum Mutat* (2013) 34:1119–30. doi: 10.1002/humu.22341

72. Kucab JE, Zou X, Morganella S, Joel M, Nanda AS, Nagy E, et al. A compendium of mutational signatures of environmental agents. *Cell* (2019) 177:821–836.e16. doi: 10.1016/j.cell.2019.03.001

73. Menzies AM, Haydu LE, Visintin L, Carlino MS, Howle JR, Thompson JF, et al. Distinguishing clinicopathologic features of patients with V600E and V600K BRAF-mutant metastatic melanoma. *Clin Cancer Res Off J Am Assoc Cancer Res* (2012) 18:3242–9. doi: 10.1158/1078-0432.CCR-12-0052

74. Mermel CH, Schumacher SE, Hill B, Meyerson ML, Beroukhim R, Getz G. GISTIC2.0 facilitates sensitive and confident localization of the targets of focal somatic copy-number alteration in human cancers. *Genome Biol* (2011) 12:R41. doi: 10.1186/gb-2011-12-4-r41

75. Guan J, Gupta R, Filipp FV. Cancer systems biology of TCGA SKCM: Efficient detection of genomic drivers in melanoma. *Sci Rep* (2015) 5:7857. doi: 10.1038/srep07857

76. Yarchoan M, Albacker LA, Hopkins AC, Montesion M, Murugesan K, Vithayathil TT, et al. PD-L1 expression and tumor mutational burden are independent biomarkers in most cancers. *JCI Insight* (2019) 4:126908. doi: 10.1172/jci.insight.126908

77. Rooney MS, Shukla SA, Wu CJ, Getz G, Hacohen N. Molecular and genetic properties of tumors associated with local immune cytolytic activity. *Cell* (2015) 160:48–61. doi: 10.1016/j.cell.2014.12.033

78. McGrail DJ, Pilié PG, Rashid NU, Voorwerk L, Slagter M, Kok M, et al. High tumor mutation burden fails to predict immune checkpoint blockade response across all cancer types. *Ann Oncol Off J Eur Soc Med Oncol* (2021) 32:661–72. doi: 10.1016/j.annonc.2021.02.006

79. Klein S, Mauch C, Brinker K, Noh K-W, Knez S, Büttner R, et al. Tumor infiltrating lymphocyte clusters are associated with response to immune checkpoint inhibition in BRAF V600E/K mutated malignant melanomas. *Sci Rep* (2021) 11:1834. doi: 10.1038/s41598-021-81330-4

80. Liu M, Wang X, Wang L, Ma X, Gong Z, Zhang S, et al. Targeting the IDO1 pathway in cancer: From bench to bedside. *J Hematol OncolJ Hematol Oncol* (2018) 11:100. doi: 10.1186/s13045-018-0644-y

81. Platten M, Wick W, Van den Eynde BJ. Tryptophan catabolism in cancer: Beyond IDO and tryptophan depletion. *Cancer Res* (2012) 72:5435–40. doi: 10.1158/0008-5472.CAN-12-0569

82. Degenhardt Y, Huang J, Greshock J, Horiates G, Nathanson K, Yang X, et al. Distinct MHC gene expression patterns during progression of melanoma. *Genes Chromosomes Cancer* (2010) 49:144–54. doi: 10.1002/gcc.20728

83. Meyer S, Handke D, Mueller A, Biehl K, Kreuz M, Bukur J, et al. Distinct molecular mechanisms of altered HLA class II expression in malignant melanoma. *Cancers* (2021) 13:3907. doi: 10.3390/cancers13153907

84. Wang Y, Tong Z, Zhang W, Zhang W, Buzdin A, Mu X, et al. FDA-Approved and emerging next generation predictive biomarkers for immune checkpoint inhibitors in cancer patients. *Front Oncol* (2021) 11:683419. doi: 10.3389/fonc.2021.683419

85. Daud AI, Loo K, Pauli ML, Sanchez-Rodriguez R, Sandoval PM, Taravati K, et al. Tumor immune profiling predicts response to anti-PD-1 therapy in human melanoma. *J Clin Invest* (2016) 126:3447–52. doi: 10.1172/JCI87324

86. Snyder A, Makarov V, Merghoub T, Yuan J, Zaretsky JM, Desrichard A, et al. Genetic basis for clinical response to CTLA-4 blockade in melanoma. *N Engl J Med* (2014) 371:2189–99. doi: 10.1056/NEJMoa1406498

87. Hellmann MD, Ciuleanu T-E, Pluzanski A, Lee JS, Otterson GA, Audigier-Valette C, et al. Nivolumab plus ipilimumab in lung cancer with a high tumor mutational burden. *N Engl J Med* (2018) 378:2093–104. doi: 10.1056/NEJMoa1801946

88. Marabelle A, Fakih M, Lopez J, Shah M, Shapira-Frommer R, Nakagawa K, et al. Association of tumour mutational burden with outcomes in patients with advanced solid tumours treated with pembrolizumab: Prospective biomarker analysis of the multicohort, open-label, phase 2 KEYNOTE-158 study. *Lancet Oncol* (2020) 21:1353–65. doi: 10.1016/S1470-2045(20)30445-9

89. Klempner SJ, Fabrizio D, Bane S, Reinhart M, Peoples T, Ali SM, et al. Tumor mutational burden as a predictive biomarker for response to immune checkpoint inhibitors: A review of current evidence. *Oncologist* (2020) 25:e147–59. doi: 10.1634/theoncologist.2019-0244

90. Raskov H, Orhan A, Christensen JP, Gögenur I. Cytotoxic CD8+ T cells in cancer and cancer immunotherapy. *Br J Cancer* (2021) 124:359–67. doi: 10.1038/s41416-020-01048-4

91. Wellenstein MD, de Visser KE. Cancer-Cell-Intrinsic mechanisms shaping the tumor immune landscape. *Immunity* (2018) 48:399–416. doi: 10.1016/j.immuni.2018.03.004

92. Ribas A, Puzanov I, Dummer R, Schadendorf D, Hamid O, Robert C, et al. Pembrolizumab versus investigator-choice chemotherapy for ipilimumab-refractory melanoma (KEYNOTE-002): A randomised, controlled, phase 2 trial. *Lancet Oncol* (2015) 16:908–18. doi: 10.1016/S1470-2045(15)00083-2

93. Robert C, Schachter J, Long GV, Arance A, Grob JJ, Mortier L, et al. Pembrolizumab versus ipilimumab in advanced melanoma. *N Engl J Med* (2015) 372:2521–32. doi: 10.1056/NEJMoa1503093

94. Robert C, Long GV, Brady B, Dutriaux C, Maio M, Mortier L, et al. Nivolumab in previously untreated melanoma without BRAF mutation. *N Engl J Med* (2015) 372:320–30. doi: 10.1056/NEJMoa1412082

95. Iorgulescu JB, Harary M, Zogg CK, Ligon KL, Reardon DA, Hodi FS, et al. Improved risk-adjusted survival for melanoma brain metastases in the era of checkpoint blockade immunotherapies: Results from a national cohort. *Cancer Immunol Res* (2018) 6:1039–45. doi: 10.1158/2326-6066.CIR-18-0067

96. Cristescu R, Mogg R, Ayers M, Albright A, Murphy E, Yearley J, et al. Pan-tumor genomic biomarkers for PD-1 checkpoint blockade-based immunotherapy. *Science* (2018) 362:eaar3593. doi: 10.1126/science.aar3593

97. Anagnostou V, Bruhm DC, Niknafs N, White JR, Shao XM, Sidhom JW, et al. Integrative tumor and immune cell multi-omic analyses predict response to immune checkpoint blockade in melanoma. *Cell Rep Med* (2020) 1:100139. doi: 10.1016/j.xcrm.2020.100139

98. Topalian SL, Drake CG, Pardoll DM. Immune checkpoint blockade: A common denominator approach to cancer therapy. *Cancer Cell* (2015) 27:450–61. doi: 10.1016/j.ccell.2015.03.001

99. Pardoll DM. The blockade of immune checkpoints in cancer immunotherapy. *Nat Rev Cancer* (2012) 12:252–64. doi: 10.1038/nrc3239

100. Sharma P, Allison JP. The future of immune checkpoint therapy. *Science* (2015) 348:56–61. doi: 10.1126/science.aaa8172

101. Tawbi HA, Schadendorf D, Lipson EJ, Ascierto PA, Matamala L, Castillo Gutiérrez E, et al. Relatlimab and nivolumab versus nivolumab in untreated advanced melanoma. *N Engl J Med* (2022) 386:24–34. doi: 10.1056/NEJMoa2109970

102. Brown SD, Warren RL, Gibb EA, Martin SD, Spinelli JJ, Nelson BH, et al. Neo-antigens predicted by tumor genome meta-analysis correlate with increased patient survival. *Genome Res* (2014) 24:743–50. doi: 10.1101/gr.165985.113

103. Slansky JE, Spellman PT. Alternative splicing in tumors - a path to immunogenicity? *N Engl J Med* (2019) 380:877–80. doi: 10.1056/NEJMcibr1814237

104. Tau GZ, Cowan SN, Weisburg J, Braunstein NS, Rothman PB. Regulation of IFN-gamma signaling is essential for the cytotoxic activity of CD8(+) T cells. *J Immunol Baltim Md 1950* (2001) 167:5574–82. doi: 10.4049/jimmunol.167.10.5574

105. Maimela NR, Liu S, Zhang Y. Fates of CD8+ T cells in tumor microenvironment. *Comput Struct Biotechnol J* (2019) 17:1–13. doi: 10.1016/j.csbj.2018.11.004

106. Mojic M, Takeda K, Hayakawa Y. The dark side of IFN-γ: Its role in promoting cancer immunoevasion. *Int J Mol Sci* (2017) 19:E89. doi: 10.3390/ijms19010089

107. Angelova M, Charoentong P, Hackl H, Fischer ML, Snajder R, Krogsdam AM, et al. Characterization of the immunophenotypes and antigenomes of colorectal cancers reveals distinct tumor escape mechanisms and novel targets for immunotherapy. *Genome Biol* (2015) 16:64. doi: 10.1186/s13059-015-0620-6

108. Zaidi MR, Davis S, Noonan FP, Graff-Cherry C, Hawley TS, Walker RL, et al. Interferon-γ links ultraviolet radiation to melanomagenesis in mice. *Nature* (2011) 469:548–53. doi: 10.1038/nature09666

109. Jorgovanovic D, Song M, Wang L, Zhang Y. Roles of IFN-γ in tumor progression and regression: A review. *biomark Res* (2020) 8:49. doi: 10.1186/s40364-020-00228-x

110. Holmgaard RB, Zamarin D, Li Y, Gasmi B, Munn DH, Allison JP, et al. Tumor-expressed IDO recruits and activates MDSCs in a treg-dependent manner. *Cell Rep* (2015) 13:412–24. doi: 10.1016/j.celrep.2015.08.077

111. Platanias LC. Mechanisms of type-i- and type-II-interferon-mediated signalling. *Nat Rev Immunol* (2005) 5:375–86. doi: 10.1038/nri1604

112. Patel H, Nilendu P, Jahagirdar D, Pal JK, Sharma NK. Modulating secreted components of tumor microenvironment: A masterstroke in tumor therapeutics. *Cancer Biol Ther* (2018) 19:3–12. doi: 10.1080/15384047.2017.1394538

113. Highfill SL, Cui Y, Giles AJ, Smith JP, Zhang H, Morse E, et al. Disruption of CXCR2-mediated MDSC tumor trafficking enhances anti-PD1 efficacy. *Sci Transl Med* (2014) 6:237ra67. doi: 10.1126/scitranslmed.3007974

114. Ngiow SF, Meeth KM, Stannard K, Barkauskas DS, Bollag G, Bosenberg M, et al. Co-Inhibition of colony stimulating factor-1 receptor and BRAF oncogene in mouse models of BRAFV600E melanoma. *Oncoimmunology* (2016) 5:e1089381. doi: 10.1080/2162402X.2015.1089381

frontiers | Frontiers in Immunology

TYPE Original Research
PUBLISHED 07 November 2022
DOI 10.3389/fimmu.2022.1049884

OPEN ACCESS

EDITED BY
Giuseppina Comito,
Universitàdegli Studi di Firenze,
Italy

REVIEWED BY
Baoqing Sun,
First Affiliated Hospital of Guangzhou Medical University, China
Maria Alejandra Garcia Marquez,
University Hospital of Cologne,
Germany

*CORRESPONDENCE
Shao-Gang Wang
sgwangtjm@163.com
Zheng Liu
lz2013tj@163.com
Qi-Dong Xia
qidongxia_md@163.com

†These authors have contributed equally to this work and share first authorship

‡These authors have contributed equally to this work

SPECIALTY SECTION
This article was submitted to Cancer Immunity and Immunotherapy, a section of the journal Frontiers in Immunology

RECEIVED 21 September 2022
ACCEPTED 24 October 2022
PUBLISHED 07 November 2022

CITATION
An Y, Sun J-X, Xu M-Y, Xu J-Z, Ma S-Y, Liu C-Q, Liu Z, Wang S-G and Xia Q-D (2022) Tertiary lymphoid structure patterns aid in identification of tumor microenvironment infiltration and selection of therapeutic agents in bladder cancer.
Front. Immunol. 13:1049884.
doi: 10.3389/fimmu.2022.1049884

Tertiary lymphoid structure patterns aid in identification of tumor microenvironment infiltration and selection of therapeutic agents in bladder cancer

Ye An†, Jian-Xuan Sun†, Meng-Yao Xu, Jin-Zhou Xu, Si-Yang Ma, Chen-Qian Liu, Zheng Liu*‡, Shao-Gang Wang*‡ and Qi-Dong Xia*‡

Department of Urology, Tongji Hospital, Tongji Medical College, Huazhong University of Science and Technology, Wuhan, Hubei, China

Background: Tertiary lymphoid structures (TLSs) are emerging as a potential predictor of prognosis and response to immunotherapy in some solid tumors. However, the comprehensive role of TLSs in bladder cancer remains unclear.

Methods: Eighteen bladder cancer (BCa) datasets were downloaded from The Cancer Genome Atlas (TCGA), Gene Expression Omnibus (GEO), ArratyExpress and IMvigor210. Based on 39 validated TLS signature genes (TSGs), we evaluated the TLS patterns in all patients, and correlated the TLS patterns with prognosis and tumor microenvironment (TME) cell-infiltrating characteristics. The cox regression model and principal component analysis (PCA) algorithms were used to construct the TLS score, which helps to quantify the TLS pattern in individuals.

Results: The landscape of 39 validated TSGs in BCa was assessed first. Five distinct TLS patterns and four gene clusters were determined. TLS cluster C2 and gene cluster A were thought to be characterized by mature TLSs and showed better prognosis and higher immune cells infiltration than other clusters. The TLS score was discovered to be tightly correlated with the infiltration level of immune cells, and could predict the maturation status of TLSs to some extent. We found TLS score was an excellent predictor for prognosis in patients with BCa independent of tumor mutation burden (TMB), and low TLS score was related to better prognosis than high TLS score. Besides, low TLS score was correlated with a better response to immune checkpoint blockade (ICB) immunotherapy and commonly used chemotherapy drugs.

Conclusions: Our work demonstrated the characteristics of TLSs in BCa. By using the TLS score, we could evaluate the TLS pattern in individuals. Better understanding of TLS pattern and the usage of TLS score could help instruct clinical strategy and precision medicine for BCa.

KEYWORDS

tertiary lymphoid structures, tumor microenvironment, bladder cancer, immunotherapy, tumor mutation burden

Introduction

Bladder cancer (BCa) is the tenth most common cancer worldwide with an estimated 573,000 new cases and 213,000 cancer deaths in 2020 (1). Based on the invasion of lamina propria, BCa can be divided into non-muscle invasive bladder cancer (NMIBC) and muscle invasive bladder cancer (MIBC). NMIBC represents approximately 70% of localized BCa and MIBC represents the remaining 30%. For prevention of recurrence or progression to MIBC, tumor resection followed by a scheduled intravesical instillation is the main treatment for NMIBC (2). Treatments for MIBC include neoadjuvant therapy followed by radical cystectomy (RC) and lymphadenectomy or a bladder-sparing project such as chemotherapy (3). With a more comprehensive understanding of tumor microenvironment (TME) and the rise of immune checkpoint blockade (ICB) therapy, immunotherapy offers a new option for patients with metastasized BCa (4). However, not all patients could benefit from immunotherapy. A single-arm phase 2 clinical trial with atezolizumab reported a 30% pathological complete response rate (5), thus, new biomarkers or molecular signatures are urgently needed to predict the efficacy of immunotherapy.

Tertiary lymphoid structures (TLSs) are ectopic lymphoid tissues formed at sites of long-lasting inflammation including tumors. Structurally resembling secondary lymphoid organs (SLOs), TLSs are mainly composed of B cells, T cells, dendritic cells (DCs), neutrophils and macrophages (6). TLSs also consist of high endothelial venules and lymphatic vessels, which help to guide the trafficking of immune cells into TME (7). Thus, TLSs play a nonnegligible role in anti-tumor immune activity, and it is reported that TLSs are correlated with better prognosis of most solid tumors including lung cancer (8, 9), breast cancer (10), colorectal cancer (11), pancreatic cancer (12) and melanoma (13). In addition, studies have revealed that B cells and TLSs are tightly associated with the response to immunotherapy (14), and the presence of TLSs is a predictive factor for the response to ICB therapy in sarcoma and melanoma (15, 16). Based on this, TLSs induction is now regarded as a potential therapeutic strategy for malignancies (17). Several studies have proved that widely used anti-cancer treatments could induce the formation of intratumoral TLSs in mouse models. For BCa, Zhou et al. and Pfannstiel et al. used public databases for bioinformatics analysis and found higher density of TLSs were correlated with a better response to ICB therapy and prognosis (18, 19).

However, the mechanisms behind the interaction between TLSs and BCa, and the crosstalk among immune cells in TLSs remain unclear. Meanwhile, the results of previous studies were based on the subtype of BCa, and none of them focused on the comprehensive effect of TLSs on BCa. Therefore, in this study, we integrated several independent BCa datasets and divided the patients with BCa into five TLS patterns according to TLS signature genes (TSGs). We performed survival analyses and investigated the landscape of TME cell infiltration in each pattern and found significantly different infiltration among five patterns. These were in accordance with the opinion that high heterogeneity existed in the cellular constituents of TLSs and would contribute to different anti-tumor effects and outcomes (14). Then, TLS cluster related differentially expressed genes (DEGs) were discovered, by which patients were classified into four genomic subgroups. The correlation between TLS patterns and gene patterns was evaluated. Finally, we developed a scoring system named TLS score to evaluate the TLS pattern in individuals and correlated it with tumor somatic mutation, TME cell infiltration characteristics, and response to immunotherapy and chemotherapy.

Materials and methods

Data retrieval and preprocessing

Thirty-nine TSGs were obtained from Fridman et al. (6). We selected data sets if they satisfied the following criteria. The inclusion criteria of the data sets are: 1) BCa patients with the results of transcriptome sequencing; 2) biological duplication should be more than 30; and the exclusion criteria is: normal people with transcriptome sequencing results. Transcriptional matrix (FPKM) and corresponding clinical information of 408 BCa patients was downloaded from The Cancer Genome Atlas

(TCGA) (https://portal.gdc.cancer.gov/). Then, we transferred the fragments per kilobase million (FPKM) values into transcripts per kilobase million (TPM) values. EMTAB1803 and EMTAB4321 cohorts were downloaded from ArrayExpress ((https://www.ebi.ac.uk/arrayexpress). Transcriptional profiles and clinical information of 14 cohorts including GSE5287, GSE13507, GSE31684, GSE32548, GSE32894, GSE48075, GSE48276, GSE69795, GSE70691, GSE86411, GSE87304, GSE120736, GSE128192 and GSE128702 were downloaded from the Gene Expression Omnibus database (GEO, https://www.ncbi.nlm.nih.gov/gds). IMvigor210 immunotherapy cohort which investigated the therapeutic efficacy of Atezolizumab in metastatic urothelial carcinoma patients (20) was obtained from R software using R package "IMvigor210CoreBiologies". The basic information of these included cohorts was shown in Table 1. Then we merged these 18 datasets and eliminated the batch effects using the Combat algorithm by R package "sva" (21). The principal components analysis (PCA) was used to check the effectiveness of the mergence. The copy number variation matrix was downloaded from UCSC-Xena (http://xena.ucsc.edu/).

The landscape of TSGs and TLS patterns in BCa

Systematic analyses of copy number variation and mutation of TSGs were conducted. Copy number variation and mutation analysis were visualized as mutation atlas and genome cycle plot respectively. Having merged the gene matrix and eliminated the batch effects, Kaplan–Meier method survival curve and log-rank test of each TSG were performed to investigate the prognostic value of TSGs.

Then, we conducted non-negative matrix factorization (NMF) algorithm based on the 39 TSGs to identify the TLS pattern. MCPCOUNTER and CIBERSORT methods (22) were applied to characterize the TME cell infiltration and quantify their proportion among TLS patterns. The differential overall survival was analyzed by log-rank test and Kaplan–Meier method survival curve to investigate survival benefits among these TLS patterns.

TABLE 1 Data sources and including samples.

Data source	Tumor bulk-seq samples	Samples with survival data
E-MTAB-1803	85	73
E-MTAB-4321	476	0
GSE120736	145	0
GSE128192	112	0
GSE128702	256	0
GSE13507	188	164
GSE31684	93	93
GSE32548	131	0
GSE32894	308	0
GSE48075	142	73
GSE48276	116	73
GSE5287	30	30
GSE69795	61	38
GSE70691	49	49
GSE86411	132	0
GSE87304	305	0
IMvigor	348	348
TCGA	408	407
Meta-cohort	3385	1348

Identification of DEGs among TLS patterns, DEGs based consensus cluster, and development of the TLS score

The DEGs were screened out by R package "limma" with the |log2 fold change (FC)| >0 and adjusted p-value <0.05, and finally visualized as an Upset diagram. Univariate Cox regression was performed to find out the DEGs with prognostic values. Subsequently, Gene Ontology (GO) and Kyoto Encyclopedia of Genes and Genomes (KEGG) enrichment analyses based on these DEGs were conducted. An unsupervised consensus cluster was performed by R package "ConsensusClusterPlus". Similarly, the TME cell infiltration characteristics and the differential overall survival were analyzed among DEGs based consensus clusters. Then we distinguished the molecular characteristics of these DEGs with prognostic value by PCA algorithm and developed a TLS score formula: TLS score = $\sum$ (PC1 + PC2).

In this formula, PC1 and PC1 represent the expression levels of those DEGs with prognostic value in two different dimensions, respectively. TLS score was identified as the summary of PC1 and PC2, which can represent the individual TLS level to some degree.

Validation of TLS score, and the correlation between TME and TLS score

Using the above formula, we calculated the TLS score of each sample. Following this, we checked the best cut-off value of TLS score in TCGA_BLCA cohort to gain the best prognostic predicting efficiency and obtained a threshold. All patients included in these 18 datasets were divided into low score group and high score group according to the threshold. Gene sets enrichment analysis (GSEA) was performed to find the differential function enrichments of TLS between high score group and low score group (23). We performed survival analyses in all patients and the above 18 cohorts separately to check whether the TLS score was a predictor of prognosis for BCa.

Then, we used ssGSEA, ESTIMATE, TIMER, CIBERSORT, CIBERSORT-ABS, QUANTISEQ, MCPCOUNTER, XCELL and EPIC algorithms to investigate the correlation between TME and TLS score. Thus, we could obtain comprehensive characteristics of immune cells infiltration, immune related pathways and immune related functions between high and low groups. The correlation between TLS score and immune cells infiltration in the last seven algorithms was performed by the linear regression test. Besides, we calculated the tumor mutation burden (TMB) of each sample in TCGA_BLCA cohort and further investigated the correlation between TMB and TLS score. We also combined these two factors for prediction of overall survival in patients with BCa. Finally, we collected the mutation atlas of each sample and compared the differences in mutant frequencies between high and low TLS groups by the χ^2 test.

Prediction of response to chemotherapy/immunotherapy by TLS score

As TLSs were proved to be a predictor of response to ICB treatment in many solid tumors, we investigated the relationship between TLS score and drug sensitivity to either chemotherapy or immunotherapy. We used three algorithms to predict the response to immunotherapy: TCIA (24), TIDE (25) and SubMap (26). A novel algorithm called oncoPredict was used to predict the response to chemotherapy (27). All the prediction of response to chemotherapy or immunotherapy was compared between high TLS score group and low TLS score group by Wilcoxon or χ^2 test.

Statistical analysis

All the data processing, analyses and figure plotting were performed by R software vision 4.1.1. A P value less than 0.05 indicates statistical significance.

Results

The landscape of TSGs in BCa

In this study, 39 genes were identified as the gene signatures of TLSs, among which CCL2/3/4/5/8/18/19/21, CXCL9/10/11/13 were chemokine signature genes; CXCL13, CD200, FBLN7, ICOS, SGPP2, SH2D1A, TIGIT, PDCD1 were T follicular helper cell (T_{FH} cell) signature genes; CD4, CCR5, CXCR3, CSF2, IGSF6, IL2RA, CD38, CD40, CD5, MS4A1, SDC1, GFI1, IL1R1, IL1R2, IL10, CCL20, IRF4, TRAF6, STAT5A were T helper 1 cell (T_H1 cell) and B cell signature genes; TNFRSF17 was plasma cell signature gene (6). We first explored the incidence of somatic mutations and copy number variations (CNV) of the 39 TSGs in BCa. These genes are immune-related, and we found low mutation rate (54 samples of 412 samples TCGA_BLCA cohort with a 13.11% frequency) in BCa (Figure 1A). Nevertheless, we found a prevalent alteration of CNV in all TSGs. Compared to the higher frequency of loss in IL10, GFI1, CCR5, ICOX, SGPP2, PDCD1 and CCL20, most TSGs had a greater frequency of CNV gain (Figure 1B). The locations of CNV were presented in Figure 1C.

Then, we used the Combat algorithm by R to eliminate the batch effects of the 18 included cohorts mentioned above and merged them into a new meta-cohort. Before processing, these datasets could easily be distinguished by principal component analysis (PCA) (Figure 1D), while they merged well after processing (Figure 1E). Following this, we divided the samples in the meta-cohort into two subgroups based on the expression level of each TSG and performed survival analyses. As shown in Figures S2A–S, higher expression level of CCL2, CCL8, CD4, CD5, CD38, CD40, CD200, CXCL9, CXCL10, CXCL13, CCR3, GFI1, ICOS, IRF4, MS4AA, PDCD1, SH2D1, STAT5 and TRAF6 showed a better survival advantage, while high expression level of IL1R1, IL10 and SDC1 indicated a worse prognosis (Figures S1A–C). CXCL13 was first described as a key chemokine for B cells migrating to SLOs, and was also regarded as a key regulator for TLSs formation. We found patients with high CXCL13 expression were associated with a significantly better prognosis ($P < 0.001$, Figure S2J).

TLS patterns and the characteristics of TME cell infiltration

We used non-negative matrix factorization (NMF) algorithm for clustering, and could see an optimal clustering effect when k = 5 (Figure 2A). All samples in the meta-cohort were divided into 5 TLS patterns based on choosing k = 5, termed TLS cluster C1 – C5 (Figure 2B). We wondered whether there existed significant differences in immune cells infiltration among five TLS patterns. So we conducted TME infiltration analysis and discovered that TLS cluster C1 was significantly enriched in $CD8^+$ T cell, T follicular helper cell (T_{FH} cell) and macrophage M1; TLS cluster C2 was significantly enriched in B cells (including naïve B cell, memory B cell and plasma B cell), $CD8^+$ T cell, T_{FH} cell and myeloid dendritic cell (DC); TLS cluster C3 was enriched in regulatory T cell (T_{reg}) while other immune cells showed low infiltration levels; cluster C4 showed enrichment in active mast cell and cluster C5 was enriched in macrophage M0, M2, fibroblasts, endothelial and neutrophil (Figures 2C, D). The TME cells infiltration characteristics were consistent with the results of survival analyses that patients from cluster C1 and C2 showed significant survival advantages compared to other clusters (Figure 2E). In addition, we investigated the TSGs signatures among five TLS patterns (Figure 2F), and we could see dramatic differences in 25 TSGs transcriptional profile among five clusters.

10.3389/fimmu.2022.1049884

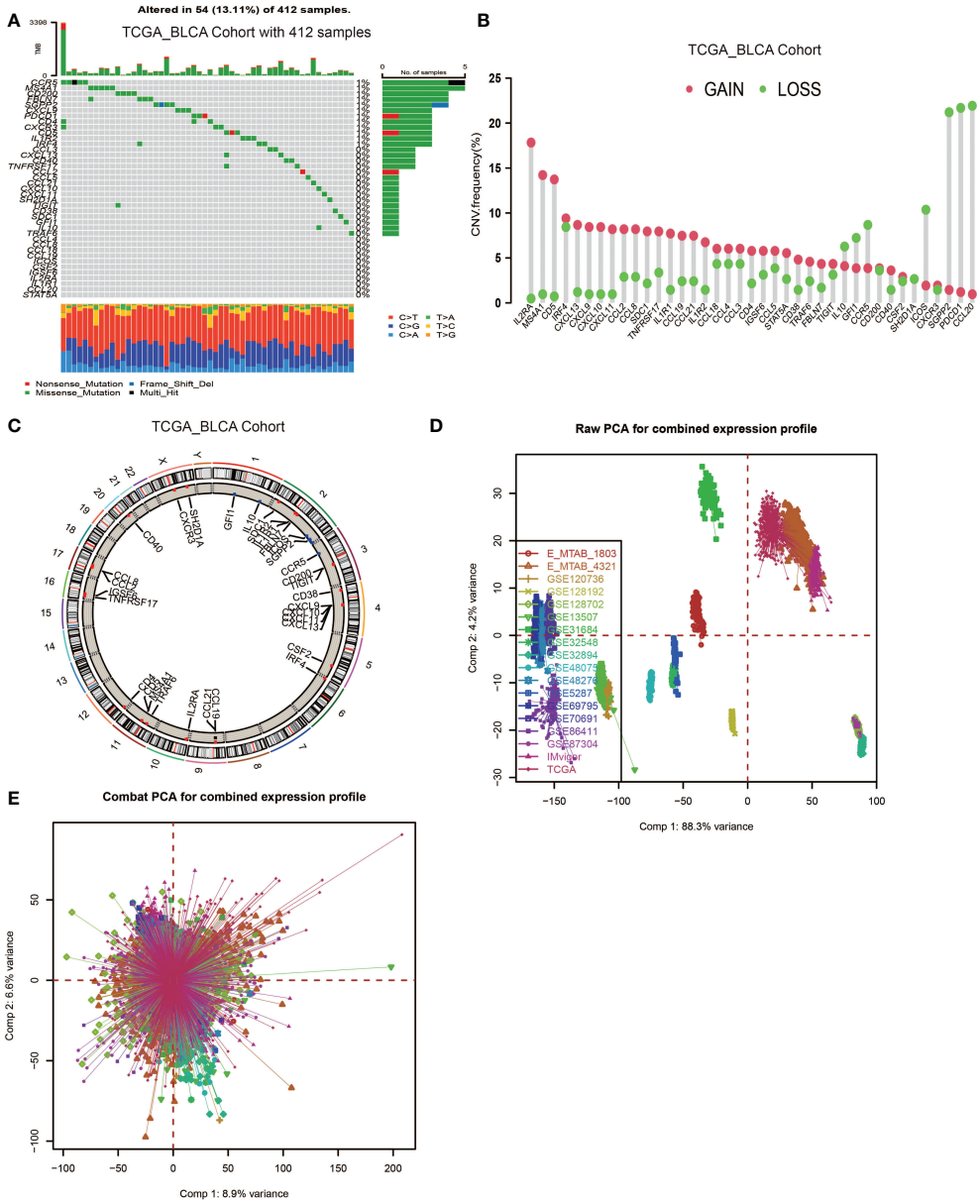

FIGURE 1
Landscape of genetic and expression variation of TLS signature genes in BCa and the combination of 18 datasets. **(A)** Mutation frequency of 39 TLS signature genes in 412 patients with BCa from the TCGA_BLCA cohort. Each column represented individual patients. The upper barplot showed TMB. The number on the right indicated the mutation frequency in each regulator gene. The right barplot showed the proportion of each variant type. The stacked barplot below showed a fraction of conversions in each sample. **(B)** CNV variation frequency of TLS signature genes. The height of the column represented the alteration frequency. The deletion frequency, green dot; The amplification frequency, red dot. **(C)** Location of CNV alteration of TLS signature genes on 23 chromosomes using cohort. **(D, E)** Principal component analysis for the expression profiles of common genes before and after combination of 18 cohorts. Before processing, 18 subgroups without intersection were identified, indicating these datasets samples were well distinguished based on the expression profiles of their common genes, while the 18 datasets merged well after processing.

Cluster C1 was characterized by the significantly increased expression level of CXCL9, CXCL10 and CXCL13; cluster C2 showed remarkable enrichment in CXCL13, ICOS, SH2D1A, CD4, CXCR3, CD38, CD5 and MS4A1; cluster C3 was enriched in SDC1, while other TGSs showed significantly decreased expression; cluster C4 was significantly enriched in CCL20; cluster C5 showed increased expression in CXCL2, CXCL8 and CXCL18 and decreased in SDC1 and CCL20.

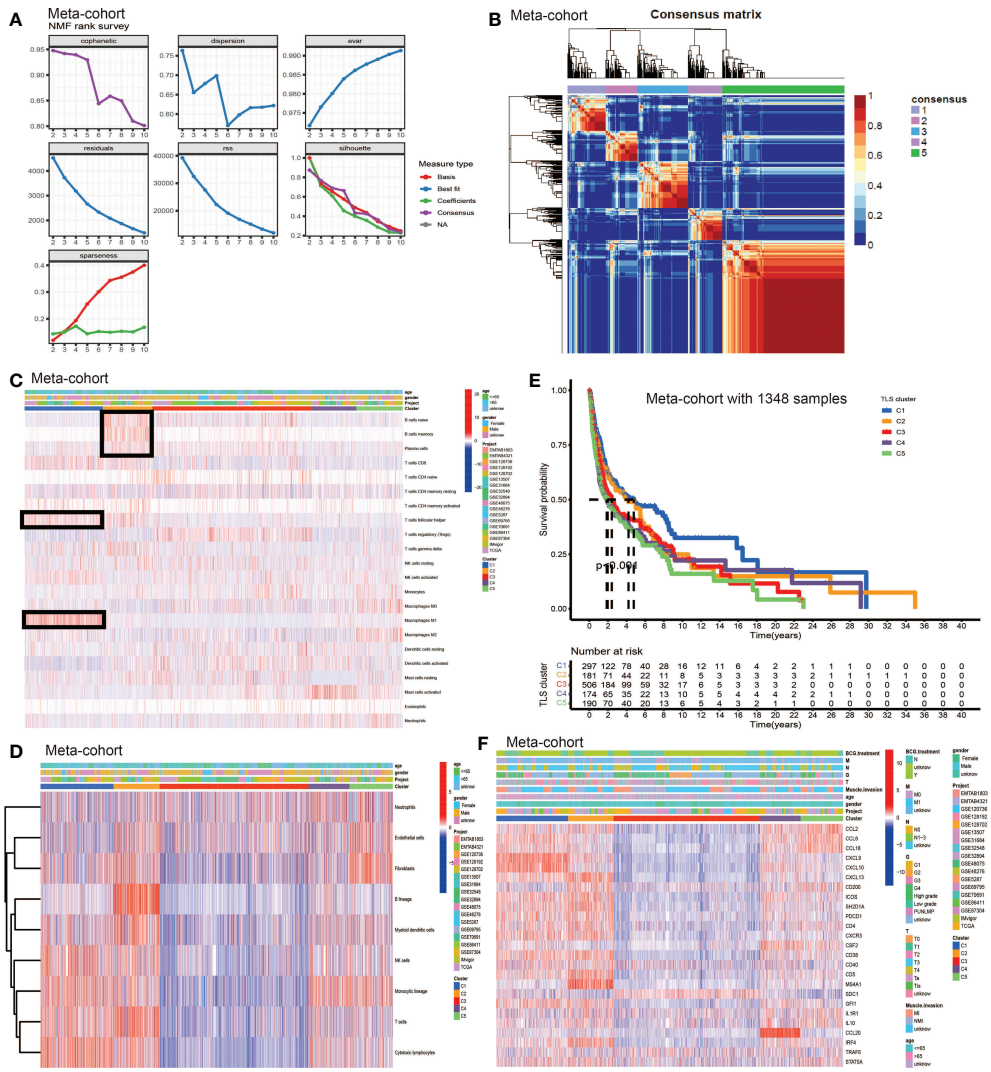

FIGURE 2
The generation of TLS patterns and biological characteristics of each pattern. **(A)** The NMF rank survey. **(B)** Connectivity matrix for patients with bladder cancer in the meta-cohort by NMF when k = 5. **(C)** TME cells infiltration characteristics in five different TLS patterns by CIBERSORT. **(D)** TME cells infiltration characteristics in five different TLS patterns by MCP. **(E)** Kaplan–Meier curves indicated TLS patterns were markedly related to overall survival of patients in meta-cohort. **(F)** TLS signature genes enrichment in each TLS pattern.

Generation of DEGs and the consensus clustering

To further explore the latent mechanism behind the different characteristics among five TLS patterns, we found 77 TLS cluster related DEGs using R software package "limma" (Figure 3A). Cox regression model was used to screen out 33 DEGs with prognostic value. We first performed GO and KEGG enrichment analyses by clusterProfiler R package to find out the biological behavior behind these DEGs. We discovered enrichment in biological process (BP), namely, cell-cell adhesion, immune cell activation and granulocyte chemotaxis; cellular component (CC), plasma membrane, endocytic vesicle; molecular function (MF), namely, cytokine receptor binding, cytokine and chemokine activity (Figure 3B). The KEGG analysis showed similar results which exhibited high enrichment in cytokine-cytokine receptor reaction and T cell signaling pathway (Figure 3C). The above results proved again that TLSs were important in regulating and coordinating the complicated function of TME. Then, these 33 TLS related cluster DEGs were used for clustering analysis by the unsupervised clustering algorithm. By choosing k = 4 as the optimal k value, we finally divided patients into four genomic subgroups, named gene cluster A – D (Figure 3D, Figures S3A–H). Subsequently, we

used the cumulative distribution function (CDF) curve to validate the rationality of grouping (Figures S3I, J), and the details of grouping were presented on the track plot (Figure S3K). Similarly, we investigated the differences in TME cell infiltration among these four gene clusters (Figures 3E, F). We discovered similar infiltration characteristics to TLS patterns that gene cluster A showed significantly high infiltration level of $CD8^+$ T cell, B lineage, T_{FH}, natural killer cell (NK cell) and macrophage M1; gene cluster B had high $CD8^+$ T cell, NK cell, macrophage M1 and neutrophil infiltration; gene cluster C was enriched in T_{reg} while other immune cells showed significantly low level; gene cluster D was enriched in fibroblast, endothelial, and showed a relatively high level of macrophage M2 and B lineage. Survival analysis showed that patients from gene cluster A had the best prognosis than patients in cluster B - D (Figure 3G). Finally, we tested the expression level of TSGs among these five gene clusters (Figure 3H). Gene cluster A showed significantly high expression level of most TSGs except SDC1; cluster B exhibited relatively high expression of CCL8, CCL18, CXCL10, CXCL13, ICOS, SH2D1A, CSF2, CD38 and CCL20; cluster C only showed high SDC1 expression and had significantly decreased level of most TSGs; cluster D had high expression level of CCL2, CD200, IL1R1 and IL10.

Development of TLS score and function annotation

The above analyses elucidated the landscape of TLS characteristics in BCa based on the patient population. However, the TLS patterns and gene clusters may not reveal the true situation of specific individuals due to the heterogeneity among patients. Therefore, we constructed a scoring system to quantify the TLS patterns in individuals. We named the scoring system TLS score, and we could classify patients into high TLS score group or low TLS score group based on this score. Firstly, we used gene sets enrichment analysis (GSEA) to investigate the differentially active pathways between the high and low groups. We discovered immune response, cytokines and antigen-antibody reaction pathways were significantly enriched in low TLS score group, such as adaptive immune response, immune response signaling pathway, lymphocyte mediated immunity, immunoglobulin complex, allograft pathway, inflammatory response, antigen processing, cytokine-receptor interaction (Figures 4A–C). While high TLS score group showed enrichment in metabolic related pathways and cell growth and differentiation related pathways, such as steroid hormone synthesis, retinol metabolism, drug metabolism cytochrome P450, and epidermal cell differentiation (Figures 4D–F). Then, we performed survival analysis in meta-cohort and the 18 cohorts separately (Figures S4A–I). Importantly, we observed a significant survival advantage in patients with low TLS score in the meta-cohort and IMvigor210 immunotherapy cohort (Figures 4G, H).

Tumor mutation burden (TMB) has been demonstrated to be a useful predictor for ICB treatment including BCa (28), and a pan-cancer research indicated that high somatic TMB was correlated with better prognosis of patients receiving ICB treatment than low TMB (29). Our result also revealed patients with high TMB had better prognosis compared to low TMB (Figure S4A). Subsequently, we analyzed the relationship between TLS score and TMB, and we didn't find a significant correlation between them (Figure 4I). Therefore, we combined the TLS score and TMB to predict the prognosis (Figure 4J). We found patients with high TMB and low TLS score had the best overall survival and those with low TMB and high TLS had the worst. Additionally, we discovered patients with high TMB and low TLS score had better survival than high TMB and high TLS score. These analyses revealed TLS score was an excellent predictor of prognosis in patients with BCa independent of TMB, and had better effect than TMB at the same time. Finally, we investigated the distribution differences of somatic mutation between high score and low score groups in the TCGA_BLCA cohort. Generally, no obvious distribution differences were found between the two groups (Figures S4B, C), but significant differences existed in the distribution of gene FAT1, EPG5, AHNAK, ERBB2, PIK3CA, HERC1, RXRA, RNF213 and HYDIN (Table 2).

TLS score and TME cell infiltration

Considering the crucial role of TLSs in anti-tumor immunity, we used nine algorithms to comprehensively investigate the characteristics of TME cell infiltration in two TLS score groups. The Sankey diagram showed the visualizing attribute changes in individual patients (Figure 5A). As shown in Figure 5B, low TLS score group was associated with higher immune score and ESTIMATE score. The ssGSEA showed the differences in immune function between two groups, and we could see low score group has better immune function in almost all the anti-tumor processes except IFN-β response (Figure 5C). TIMER, CIBERSORT, CIBERSORT-ABS, QUANTISEQ, MCPCOUNTER, XCELL and EPIC methods were used for the component analysis of TME cells (Figure 5D). We discovered low score group had significant high infiltration levels of B cells, T cells ($CD4^+$ T cell and $CD8^+$ T cell), macrophages (macrophage M1 and macrophage M2), myeloid dendritic cell and NK cell compared to high score group, and the lower of TLS score, the higher infiltration of immune cells. Figure 5E showed the correlation between TLS score and infiltration level of immune cells. We noticed the value of TLS score showed significantly negative correlation with B cells (Figures 6A, B) including naïve B cells, memory B cells and plasma cells (Figures S5A–E); T cells including various types of $CD4^+$ T cell, $CD8^+$ T cell and T_{FH} cell (Figures 6C–E and Figure S5F–K); macrophages including macrophage M1 and macrophage M2 (Figure 6F and Figures S5L, M). Besides, TLS score had significantly negative

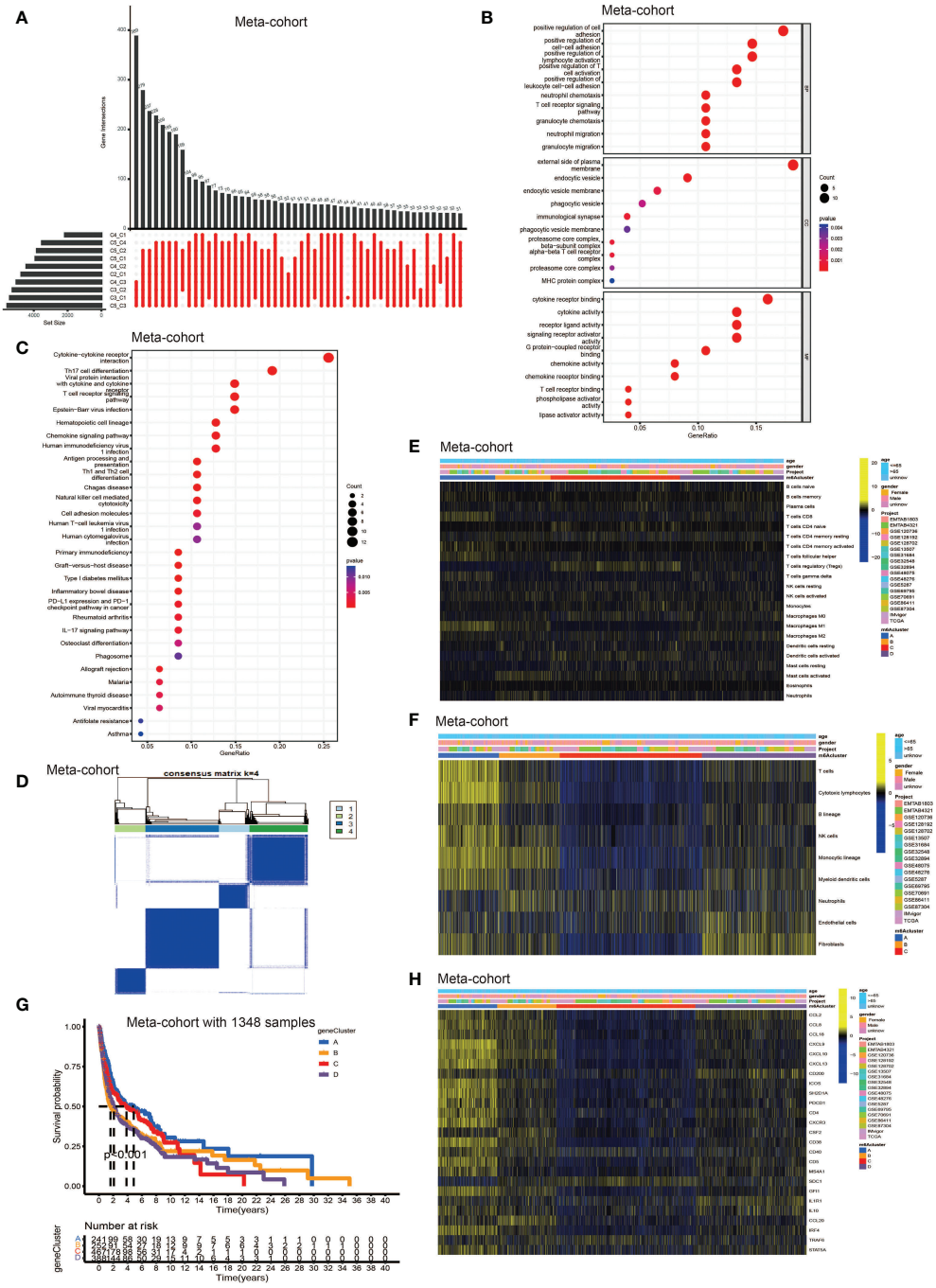

FIGURE 3
Identification of DEGs among TLS patterns and DEGs based consensus cluster. **(A)** 77 TLS cluster-related DEGs shown in the Upset diagram. **(B)** Functional annotation for TLS cluster related DEGs using GO enrichment analysis. The size of the plots represented the number of genes enriched. The pathways were grouped by cellular component (CC), molecular function (MF) and biological process (BP). **(C)** Functional annotation for TLS cluster related DEGs using KEGG enrichment analysis. The size of the plots represented the number of genes enriched. **(D)** Unsupervised clustering of 33 TLS cluster related DEGs with prognostic value in meta-cohort and consensus matrices for k = 4. **(E)** TME cells infiltration characteristics in four different TLS gene cluster by CIBERSORT. **(F)** TME cells infiltration characteristics in four different TLS gene cluster by MCP. **(G)** Kaplan–Meier curves indicated TLS genomic phenotypes were markedly related to overall survival of patients in meta-cohort. **(H)** TLS signature genes enrichment in each TLS gene cluster.

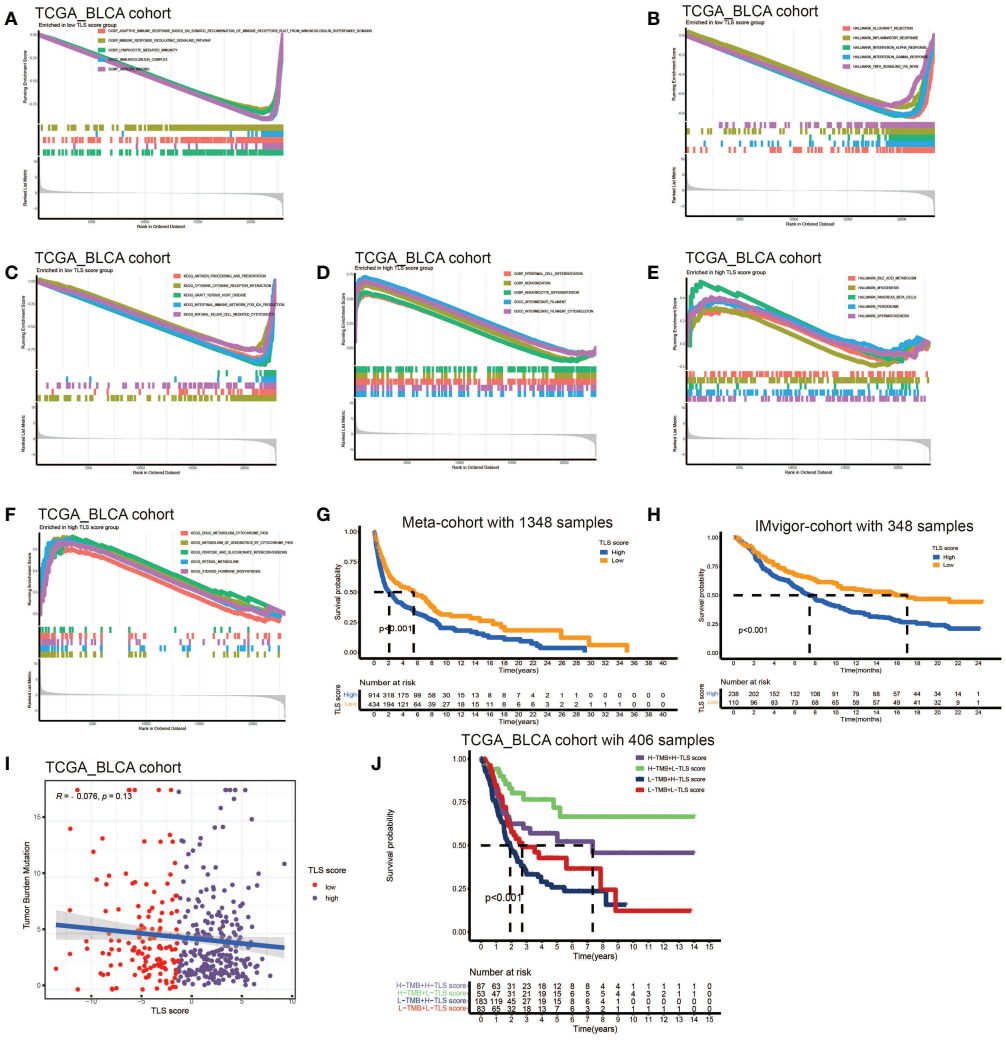

FIGURE 4
Development of TLS score and function annotation. **(A-C)** Gene sets enrichment analysis (GSEA) in low TLS score group by GO, KEGG and HALLMARK. **(D–F)** Gene sets enrichment analysis (GSEA) in high TLS score group by GO, KEGG and HALLMARK. **(G)** Survival analyses for low and high TLS score patient groups in meta-cohort using Kaplan–Meier curves (P <0.001, Log-rank test). **(H)** Survival analyses for low and high TLS score patient groups in IMvigor210 immunotherapy cohort using Kaplan–Meier curves (P <0.001, Log-rank test). **(I)** Linear regression analysis for tumor mutation burden and TLS score. The dot represented each sample. **(J)** Survival analyses for four groups grouped according to tumor mutation burden and TLS score in the TCGA_BLCA cohort using Kaplan–Meier curves.

correlation to myeloid dendritic cells and NK cells (Figures 6G, H). We also noticed that TLS score was positively correlated with endothelial cells (Figure 6I). In general, the TLS score was significantly associated negatively with the infiltration level of most immune cells.

Characteristics of TLS in immunotherapy and chemotherapy

Our above results demonstrated the TLS score was an excellent predictor for prognosis and was tightly correlated with infiltration level of immune cells. Based on this, we proposed that low TLS score might indicate an immune subtype which was more sensitive to immunotherapy. Therefore, we investigated the correlation between the TLS score and the response to ICB treatment. We discovered low TLS score was significantly associated with better response to anti-PD-1 immunotherapy and the significant correlation still existed after Bonferroni correction (Figure 7A). Then, the patients were classified into four subgroups according to their usage of anti-PD-L1 and anti-CTLA-4 treatments: CTLA-4 positive PD-1 positive (Figure 7B), CTLA-4 positive PD-1 negative (Figure 7C), CTLA-4 negative PD-1 positive

TABLE 2 Mutant genes that exist significant differences between high and low TLS score groups.

gene	H-wild	H-mutation	L-wild	L-mutation	p-value
FAT1	253(93.7%)	17(6.3%)	116(85.29%)	20(14.71%)	0.009425
EPG5	262(97.04%)	8(2.96%)	123(90.44%)	13(9.56%)	0.00946
AHNAK	254(94.07%)	16(5.93%)	117(86.03%)	19(13.97%)	0.011132
ERBB2	248(91.85%)	22(8.15%)	114(83.82%)	22(16.18%)	0.022194
PIK3CA	224(82.96%)	46(17.04%)	99(72.79%)	37(27.21%)	0.023353
HERC1	260(96.3%)	10(3.7%)	123(90.44%)	13(9.56%)	0.029162
RXRA	251(92.96%)	19(7.04%)	134(98.53%)	2(1.47%)	0.031326
RNF213	255(94.44%)	15(5.56%)	120(88.24%)	16(11.76%)	0.042807
HYDIN	259(95.93%)	11(4.07%)	123(90.44%)	13(9.56%)	0.046722

(Figure 7D), CTLA-4 negative PD-1 negative (Figure 7E). We found that in all four subgroups, the low TLS score group had significant higher IPS score than low TLS score group, which indicated patients from low TLS score group were associated with better response to anti-PD-1, anti-CTLA-4 or combined immunotherapy compared to high TLS score. We also performed Tumor Immune Dysfunction and Exclusion (TIDE) analysis, and surprisingly found low TLS score was related to higher TIDE score (Figure S6A). This immune evasion effect might be caused by the relatively higher infiltration level of T_{reg} in low TLS score group (Figure 4C).

Additionally, we investigated the relationship between TLS score and response to chemotherapy. We applied R package oncoPredict and examined several commonly used drugs, such as gemcitabine, cisplatin and vinblastine which were used for adjuvant treatment after surgery and epirubicin which was used for intravesical instillation. We found low TLS score was significantly related to lower sensitivity score of gemcitabine, cisplatin, vinblastine and epirubicin (Figures 7F–I), which indicated that low TLS score group was associated with higher sensitivity to chemotherapy. Several other chemotherapy drugs were also screened out, and showed significant association with TLS score (Figure S6B–X and Figures S7A–Y). Although some of them are newly developed and haven't been used for BCa treatment, we could screen out appropriate chemotherapy drugs for patients and instruct clinical medication in the future.

Discussion

TLSs have emerged as a crucial role in the immune response of anti-tumor effect and at the same time as a predictor of prognosis and response to immunotherapy. As mentioned earlier, many researches have been carried out to explore the complex role of TLSs in anti-cancer, but there are still many mysteries. For example, there still lacks accurate and comprehensive biomarkers of TLSs, although many biomarkers have been continuously proposed (17). Meanwhile, the mechanisms how TLSs regulate the immune response and how the immune cells interact with each other (especially B cells and T cells) also remain unclear (30). Therefore, it is necessary and urgent to investigate the comprehensive role of TLSs in malignancies. Although previous studies have explored the predictive value of TLSs in BCa, their results were based on either the immune subtype or limited TLSs signature biomarkers, which may lead to a biased conclusion. For example, Zhou et al. divided patients with MIBC into six MIBC immune classes, and found class F had the best prognosis and highest level of TLSs. In addition, they analyzed the TLS signature in pan-cancer using nine genes validated in metastasized melanoma tumors as TLSs signature genes (19). Pfannstiel et al. quantified the TLSs in intra- and peritumoral stroma, and found the number of TLS and the distance from TLS to tumor were associated with the disease specific survival. These studies paid more attention to the TME of BCa or limited TLSs signature genes and didn't go deep into the effects of TLSs in BCa.

In our study, we enrolled 18 bladder cancer datasets and 39 validated TSGs for further investigation which was the most comprehensive analysis of the role of TLSs in BCa currently reported. Firstly, we summarized the landscape of the 39 validated TSGs in BCa and discovered most TSGs exhibited CNV rather than somatic mutation. Most TSGs including the essential chemokines for the formation of TLSs such as CXCL13 and CCL21 showed greater frequency of CNV gain, which indicated the neogenesis of TLSs in tumor tissue. Recently, Groeneveld et al. proved CXCL13 could also be regarded as the biomarker of TLSs in BCa, and demonstrated CXCL13 was associated with better prognosis of patients with BCa (31). Similarly, CCL21 is crucial for the recruitment of lymphocytes and TLSs formation. Delvecchio et al. elucidated that intratumoral injection of CXCL13 and CCL21 could induce TLSs formation in the orthotopic model of pancreatic tumor, resulting in a better therapeutic effect of gemcitabine (32). Then, we merged the 18 cohorts into a new meta-cohort, and used the NMF clustering to divide all patients into five TLS patterns named TLS pattern C1 – C5 according to the expression level of TSGs. It's not surprising to find there existed huge differences

10.3389/fimmu.2022.1049884

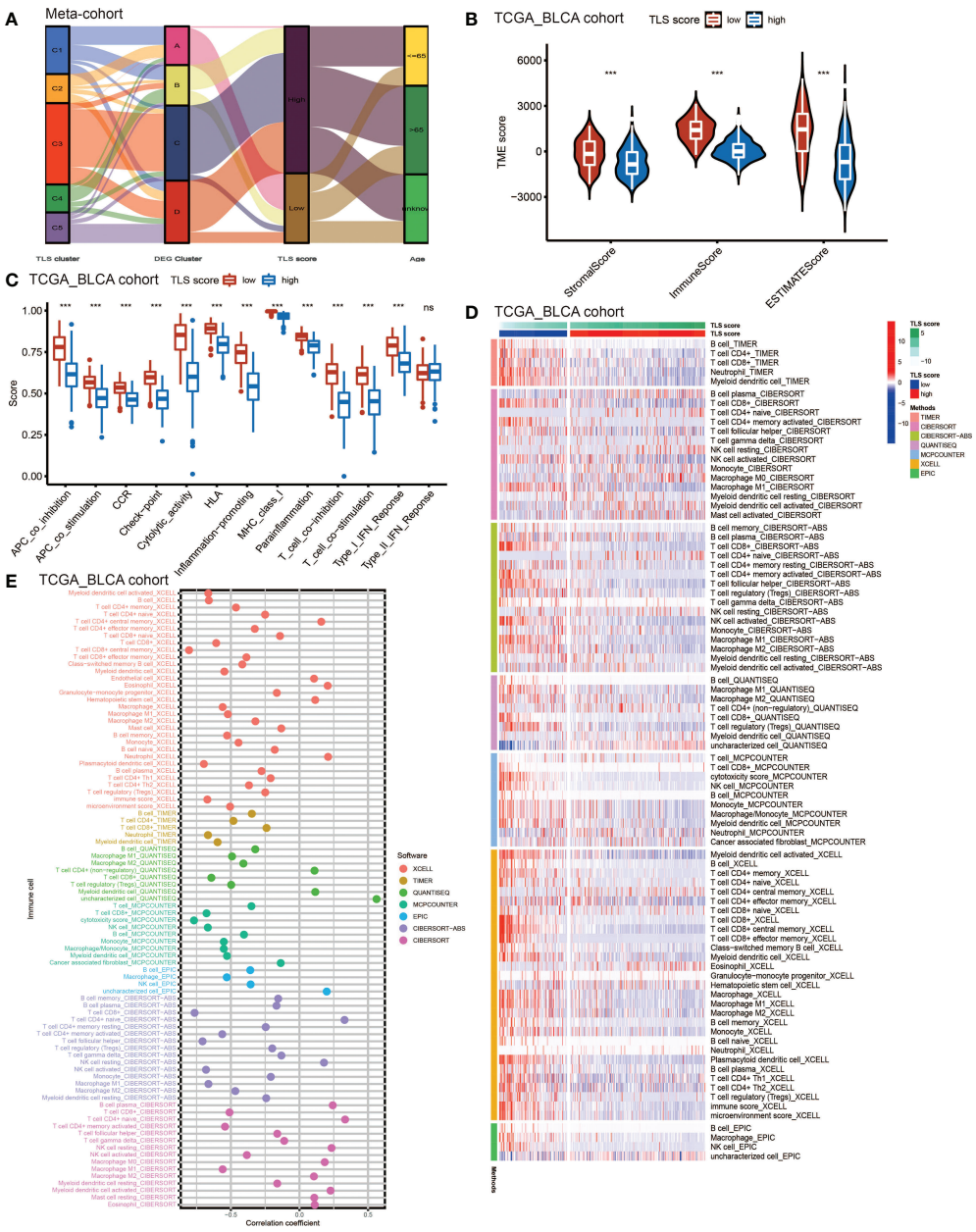

FIGURE 5
The TME cell infiltrating characteristics between high and low TLS score group. **(A)** Sankey diagram showing the changes of TLS clusters, gene clusters and TLS score and final survival status. **(B)** Differences in the stromal, immune and ESTIMATE score between high and low TLS score groups in meta-cohort (***P <0.001, Wilcoxon test). **(C)** The intensity of immune function between high and low TLS score groups. The upper and lower ends of the boxes represented interquartile range of values. The lines in the boxes represented median value, and black dots showed outliers. The asterisks represented the statistical p-value (ns, no significance; ***P < 0.001). **(D)** TME cells infiltration characteristics in high and low score groups by TIMER, CIBERSORT, CIBERSORT-ABS, QUANTISEQ, MCPCOUNTER, XCELL and EPIC methods. **(E)** The correlation between TLS score and infiltration level of immune cells.

between five TLS patterns among the various aspects from TME cell infiltration to prognosis. Cluster C2 showed high infiltration level of B cells (including naïve B cell, memory B cell and plasma B cell), $CD8^+$ T cell, T_{FH} cell and myeloid dendritic cell. It is now considered that TLSs could be divided into three different mature states: early TLS, composed of dense lymphocytic aggregate but lacking DCs; immature TLS, having DCs but lacking germinal center (GC); and mature TLS, having active GC and active B cell (33–35). Therefore, we thought cluster C2 was characterized by mature TLS, and not surprising to find

10.3389/fimmu.2022.1049884

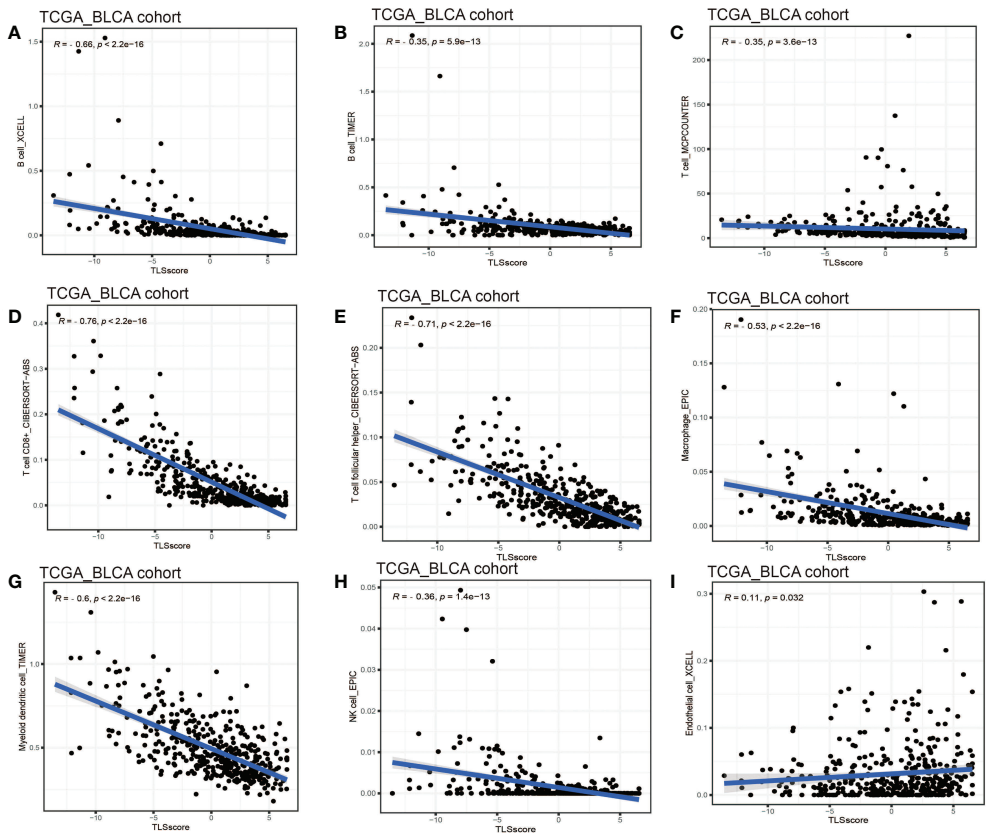

FIGURE 6
Linear regression analysis for TLS score and immune cells. **(A)** Correlation between TME B cells infiltration and TLS score by XCELL. **(B)** Correlation between TME B cells infiltration and TLS score by TIMER. **(C)** Correlation between TME T cells infiltration and TLS score. **(D)** Correlation between TME $CD8^+$ T cell infiltration and TLS score. **(E)** Correlation between TME T cell follicular helper infiltration and TLS score. **(F)** Correlation between TME macrophages infiltration and TLS score. **(G)** Correlation between TME myeloid dendritic cell infiltration and TLS score. **(H)** Correlation between TME NK cell infiltration and TLS score. **(I)** Correlation between TME endothelial cell infiltration and TLS score.

patients from cluster C2 had the best survival advantage. Cluster C1 was significantly enriched in $CD8^+$ T cell, T_{FH} cell and macrophage M1. T_{FH} ($CD4^+$ $CXCL13^+$ T cell) which could produce CXCL13 is also believed crucial in the formation of TLSs (6, 36). Although we didn't see significantly high infiltration level of B cells, cluster C1 showed better prognosis than clusters C3 – C5. We supposed that the survival advantage was due to the significantly high infiltration of T_{FH} which indicated active TLS neogenesis. The following heatmap of TGSs also proved our opinion. Notably, CCL20 was highly enriched in cluster C4 and we observed patients from cluster C4 had the worst survival advantage. Previous studies have proved that the activation of CCL20-CCR6 axis could promote ovarian cancer migration, lung adenocarcinoma progression and impair the function of T cells in prostate cancer (37–39). Thus, our findings could provide a new insight into CCL20 in BCa.

Next, we investigated the mRNA transcriptome differences between distinct TLS patterns and used unsupervised clustering to divide patients into four gene clusters named gene cluster A – D. Consistent with the TLS clusters, gene cluster A was characterized by mature TLS and patients from it had the best prognosis. Interestingly, we found gene clusters B and D had relatively high infiltration levels of immune cells (such as B cells, T cells, macrophages and neutrophils), but didn't show corresponding survival advantages. Thus, we thought gene clusters B and D were characterized by immune-exclude phenotype, also called 'cold' tumor (40). In this phenotype, cytotoxic T lymphocytes (CTLs) were excluded from the core of the tumor and instead present along the margin of the tumor where they could be stuck in the fibrotic stroma. The significantly high infiltration level of fibroblasts and endothelial cells in clusters B and D also proved it.

To further investigate the TLS pattern in individuals, we developed a scoring system named TLS score to quantify the TLS pattern in patients with BCa. Using the TLS score, we divided all patients into two subgroups: high TLS score group and low TLS

10.3389/fimmu.2022.1049884

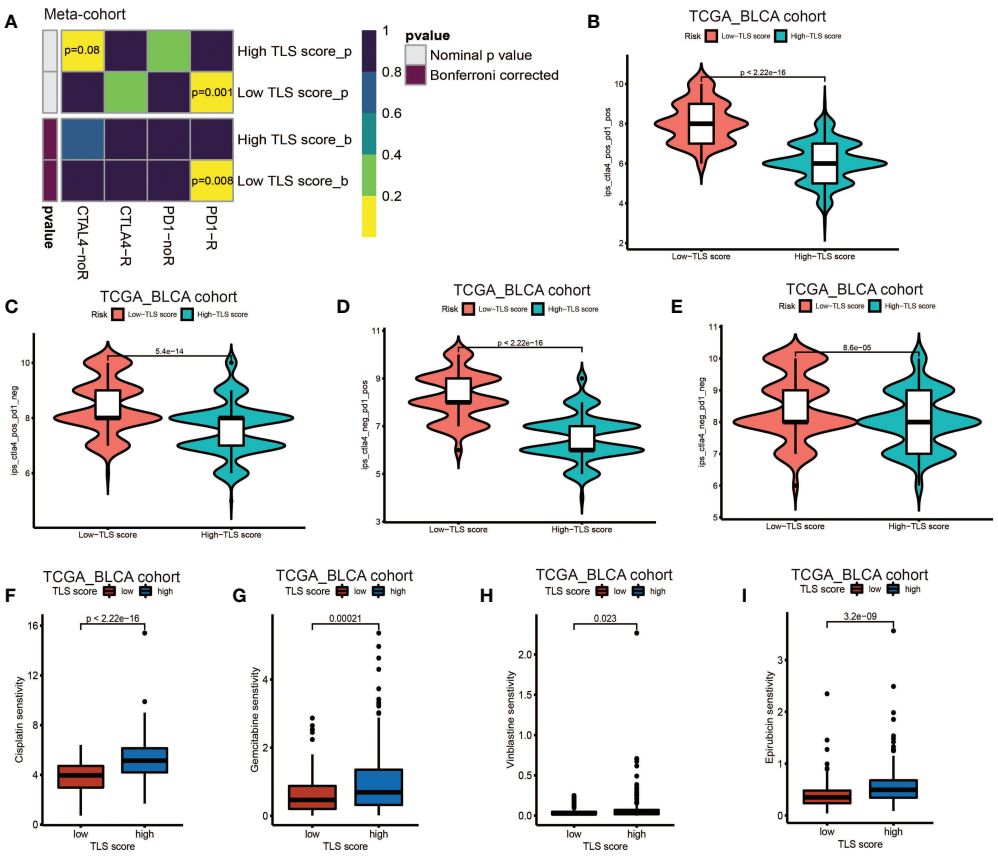

FIGURE 7
Role of TLS patterns in immunotherapy and chemotherapy. **(A)** The similarity of gene expression profiles between TLS score and bladder cancer patients treated with immune checkpoint blockade (ICB). CTLA4-noR, patients no respond to anti-CTLA4 treatment, CTLA4-R, patients respond to anti-CTLA4 treatment, PD1-noR, patients no respond to anti-PD-1 treatment, PD1-R, patients respond to anti-PD-1 treatment. **(B–E)** The violin diagram showed the differences of response index between high and low TLS score groups among four subgroups. **(F–I)** The differences of drug sensitivity (oncoPredict score) between high and low TLS score group. **(F)** Cisplatin for chemotherapy; **(G)** Gemcitabine for chemotherapy; **(H)** Vinblastine for chemotherapy; **(I)** Epirubicin for intravesical instillation.

score group. We first performed GSEA to dig out the latent enrichment of pathways between two subgroups. We found immune response, cytokines and antigen-antibody reaction related pathways were enriched in low score group, while metabolic related pathways and cell growth and differentiation related pathways were enriched in high score group. This result revealed a better anti-tumor potential of low score group compared to high score group. The subsequent survival analysis also proved it that patients from low score group had significantly better prognosis than that in high score group. As TMB has been proved as a biomarker for prediction of response to ICB treatment (29), we further evaluated the relationship between TLS score and TMB. We didn't find significant correlation between TLS score and TMB, which indicated TLS score might be a predictor independent of TMB. So, we combined TMB and TLS score for prognosis prediction. Consistent with our expectations, TLS score showed a better predictive value of prognosis than TMB. Nine genes (FAT1, EPG5, AHNAK, ERBB2, PIK3CA, HERC1, RXRA, RNF213 and HYDIN) showed significant distribution differences of somatic mutation between high and low score groups. Among them, five genes have been reported to be correlated with the development, progression or metastasis of BCa. For example, Wang et al. reported that knockdown of FAT1 promoted the BCa cell apoptosis and inhibit the viability and migration of BCa *in vitro* (41). The overexpression of AHNAK has been reported to promote the proliferation and migration of UMUC3 and T24 cells, while knockdown of AHNAK could inhibit the metabolism and epithelial-mesenchymal transition (EMT) of these cells (42). Besides, RXRA hot-spot mutant was reported to related to upregulated PPAR signaling activity (43), and then contributed to the growth of BCa cells (44). The other genes

(EPG5, HERC1, RNF213 and HYDIN) haven't been reported to correlate with the pathology of BCa, and we think these genes are potential targets for intervention of BCa.

A systematic analysis of immune cell infiltration in the TME was conducted. We found low TLS score group showed better immune functions than high score group and obtained higher ESTIMATE score. Component analysis of infiltrating cells revealed that low score group had significantly high infiltration level of most immune cells: B cells, T cells ($CD4^+$ T cell and $CD8^+$ T cell), macrophages (macrophage M1 and macrophage M2), myeloid dendritic cell and NK cell. However, we noticed T_{reg} cell also showed infiltration in low TLS score group. T_{reg} cell is an important immunosuppressive cell and usually leads to tumor angiogenesis, immune evasion, drug resistance, tumor progression and metastasis (45). Indeed, T_{reg} cell was found within TLSs in breast cancer, lung cancer, colorectal cancer and prostate cancer, and contributed to a negative effect on the capacity of TLSs (46–48). The research results of Joshi et al. demonstrated T_{reg} cells suppressed anti-tumor response in TLSs, while after T_{reg} cell depletion, T cells proliferation rates increased in TLSs and led to tumor destruction (49). These results suggest TLSs play a complicated role in anti-tumor effect, and more researches and accurate biomarkers for TLSs are needed in the future. Correlation analysis of infiltrated immune cells showed the value of TLS score was negatively correlated with B cells (naïve B cell, memory B cell and plasma cell), T cells ($CD4^+$ T cell, $CD8^+$ T cell and T_{FH} cell), macrophages (macrophage M1 and M2), myeloid dendritic cell and NK cell. Therefore, the TLS score could be used to evaluate the infiltration level of immune cells in TME in individual patients with BCa. Considering plasma cells in TLSs were activated and differentiated in GC, the TLS score could also reveal the maturation state of TLSs to some extent. In recent years, humoral immunity has been proposed to be important in anti-tumor effects, and B cells play a key role in this process. A pan-cancer study demonstrated that the presence of memory B cells was associated with poor prognosis in colon, gastric cancers, although TLSs were reported to promote the prognosis of patients in these cancers (50). Another study reported that high density of B cells was related to better prognosis of patients with pancreatic cancer but only if these cells formed TLS (51). Therefore, when considering the anti-tumor effects of B cells, it is important to distinguish the phenotypes or characteristics of B cells. For BCa, Koti et al. reported that well-formed TLS were more common in aggressive high grade MIBC compared to low grade NIMBC (52). More studies are needed to further elucidate the effects of B cells in BCa.

Immunotherapy, led by ICB treatment (PD-1/PD-L1 blockade alone or combined with CTLA-4 checkpoint inhibition) showed great benefit in the second-line therapy of patients with unresectable and metastatic BCa (53). However, the response rate to ICB treatment is low, and there is an urgent need to find new biomarkers to screen out patients who are appropriate for ICB treatment. Previous studies have reported the presence of TLSs was associated with higher response rate to immunotherapy of ICB treatment in the patient population with BCa. Here we wondered whether TLS score could predict the response to ICB treatment in individuals and instruct the clinical treatment strategy. We found low TLS score group was significantly associated with the response to anti-PD-1 treatment. In TCIA method, we discovered patients from low score group showed advantages not only in anti-PD-1/anti-CTLA-4 monotherapy but in combined immunotherapy. Besides, survival analysis revealed that patients from low score group had better prognosis than that from high score group in meta-cohort and IMvigor210 immunotherapy cohort. These results demonstrated that TLS score was an excellent predictor for the response to ICB immunotherapy and prognosis in patients with BCa. To our surprise, in TIDE analysis, low TLS score group had a relatively higher TIDE score than high TLS score group. We thought the result of TIDE might be influenced by the relatively high T_{reg} cell infiltration level and led to bias.

Finally, we investigated the relationship between TLS score and response to chemotherapy by oncoPredict algorithm. For BCa, gemcitabine, cisplatin and vinblastine are usually used for adjuvant treatment after surgery and epirubicin is usually used for intravesical instillation. We found low TLS score group was related to better response to all these drugs. In addition, we screen out a number of other chemotherapy drugs which showed better response in low TLS score group. Our findings revealed that TLS score played a unique role in predicting the response to chemotherapy in BCa. Exhilaratingly, previous studies have reported that widely used anti-cancer drugs could induce the formation of intratumoral TLSs in mice. In patients with cancer, studies revealed the use of chemotherapy was associated with massive TLSs in tumors (54, 55), which strongly indicated that chemotherapy could induce the formation of TLSs. All these results suggest TLSs and chemotherapy are important in tumor destruction, and mutually reinforce anti-tumor effect. Our work plays a key role in this process that help to screen out patients who are appropriate for chemotherapy.

In general, we used the validated TGSs to provide a comprehensive insight into TLSs in BCa and evaluated the comprehensive role of TLSs in prognosis, TMB, TME immune cell infiltration, response to chemotherapy and immunotherapy. The TLS patterns could help to distinguish patients with different statuses of TLSs, and draw the landscape of TME cell infiltration, TSGs expression and prognosis among patients. The TLS score could evaluate the specific TLS pattern in individuals, and was proven to be a good predictor for prognosis, response to immunotherapy and chemotherapy. Besides, TLS score showed a significant correlation with the infiltration level of immune cells and could indicate the maturation status of TLSs to some

extent. Therefore, the TLS score could aid in precision medicine for patients with BCa.

However, there are a few limitations existing in our study. First, though 39 genes were validated as TSGs, there still lacks accurate TSGs. The TSGs we included in this study might not be comprehensive and accurate enough, thus, might lead to bias. Second, the study was performed by bioinformatic analyses, and many cells reported to play a role in TLSs recently such as regulatory B (B_{reg}) cells couldn't be distinguished well by algorithms. Third, although the analysis used data from 18 cohorts and clinical samples size is relatively adequate, our study lacks external verification in clinical trials. Finally, the exact mechanisms behind the interaction between TLSs and BCa remain unclear, and more researches are needed to further unveil the mystery of TLSs.

In conclusion, our work demonstrated the characteristics of TLSs in BCa. By using the TLS score, we could evaluate the TLS pattern in individuals, and predict the TME cell infiltration, TLS maturation, prognosis, response to immunotherapy and chemotherapy in BCa. Thus, better understanding of TLS pattern and the usage of TLS score could help instruct clinical strategy and improve prognosis of patients with BCa.

Data availability statement

The datasets presented in this study can be found in online repositories. The names of the repository/repositories and accession number(s) can be found in the article/Supplementary Material.

Author contributions

Q-DX, S-GW and ZL designed the study. Q-DX collected the data, analyzed the data and drew the figures. YA and J-XS analyzed the data and wrote the manuscript. M-YX, C-QL, J-ZX and S-YM contributed to critical revision of the manuscript. All authors contributed to the article and approved the submitted version.

Funding

This work was supported by the National Natural Science Foundation of China (81772729) and Undergraduate Training Program for Innovation and Entrepreneurship (S202210487014).

Acknowledgments

We thank all the R software package developers.

Conflict of interest

The authors declare that the research was conducted in the absence of any commercial or financial relationships that could be construed as a potential conflict of interest.

Publisher's note

Supplementary material

The Supplementary Material for this article can be found online at: https://www.frontiersin.org/articles/10.3389/fimmu.2022.1049884/full#supplementary-material

SUPPLEMENTARY FIGURE 1
Survival analysis for TLS signature genes that low expression subgroup showed survival advantages. **(A)** Survival analysis for IL1R1. **(B)** Survival analysis for IL10. **(C)** Survival analysis for SDC1.

SUPPLEMENTARY FIGURE 2
Survival analysis for TLS signature genes that high expression subgroup showed survival advantages. (**A–S**) Survival analysis for CCL2, CCL8, CD4, CD5, CD38, CD40, CD200, CXCL9, CXCL10, CXCL13, CCR3, GFI1, ICOS, IRF4, MS4AA, PDCD1, SH2D1, STAT5 and TRAF6.

SUPPLEMENTARY FIGURE 3
The process of generating four distinct TLS cluster related DEGs genomic patterns. **(A–H)** Unsupervised clustering of 33 TLS cluster related DEGs in meta-cohort and consensus matrices for k = 1, 3 - 9. **(I)** The cumulative distribution function (CDF) curve for k = 2 - 9. **(J)** The scree plot for k = 2 - 9. K The track plot for k = 2 - 9.

SUPPLEMENTARY FIGURE 4
Survival analysis between high and low TMB subgroups and somatic mutation between high and low TLS score groups. A Survival analysis between high and low TMB subgroups. B Distribution differences of somatic mutation between high score and low score groups in the TCGA_BLCA cohort.

SUPPLEMENTARY FIGURE 5
Linear regression analysis for TLS score and immune cells. **(A)** B cell memory. **(B)** B cell memory. **(C)** B cell naive. **(D)** B cell plasma. **(E)** B cell plasma. **(F)** T cell $CD4^+$ Th1. **(G)** T cell $CD4^+$ Th2. **(H)** T cell $CD4^+$ memory actived. **(I)** T cell $CD8^+$. **(J)** T cell $CD8^+$ effector memory. **(K)** T cell follicular helper. **(L)** Macrophage M1. **(M)** Macrophage M2.

SUPPLEMENTARY FIGURE 6
23 drugs that are correlated with TLS score.

SUPPLEMENTARY FIGURE 7
25 drugs that are correlated with TLS score.

References

1. Sung H, Ferlay J, Siegel RL, Laversanne M, Soerjomataram I, Jemal A, et al. Global cancer statistics 2020: GLOBOCAN estimates of incidence and mortality worldwide for 36 cancers in 185 countries. *CA Cancer J Clin* (2021) 71(3):209–49. doi: 10.3322/caac.21660

2. Babjuk M, Burger M, Capoun O, Cohen D, Compérat EM, Dominguez Escrig JL, et al. European Association of urology guidelines on non-muscle-invasive bladder cancer (Ta, T1, and carcinoma in situ). *Eur Urol* (2022) 81(1):75–94. doi: 10.1016/j.eururo.2021.08.010

3. Lenis AT, Lec PM, Chamie K, Mshs MD. Bladder cancer: A review. *Jama* (2020) 324(19):1980–91. doi: 10.1001/jama.2020.17598

4. Wu Z, Liu J, Dai R, Wu S. Current status and future perspectives of immunotherapy in bladder cancer treatment. *Sci China Life Sci* (2021) 64 (4):512–33. doi: 10.1007/s11427-020-1768-y

5. Powles T, Kockx M, Rodriguez-Vida A, Duran I, Crabb SJ, van der Heijden MS, et al. Clinical efficacy and biomarker analysis of neoadjuvant atezolizumab in operable urothelial carcinoma in the ABACUS trial. *Nat Med* (2019) 25(11):1706–14. doi: 10.1038/s41591-019-0628-7

6. Sautès-Fridman C, Petitprez F, Calderaro J, Fridman WH. Tertiary lymphoid structures in the era of cancer immunotherapy. *Nat Rev Cancer* (2019) 19(6):307–25. doi: 10.1038/s41568-019-0144-6

7. Ruddle NH. High endothelial venules and lymphatic vessels in tertiary lymphoid organs: Characteristics, functions, and regulation. *Front Immunol* (2016) 7:491. doi: 10.3389/fimmu.2016.00491

8. Dieu-Nosjean MC, Antoine M, Danel C, Heudes D, Wislez M, Poulot V, et al. Long-term survival for patients with non-small-cell lung cancer with intratumoral lymphoid structures. *J Clin Oncol* (2008) 26(27):4410–7. doi: 10.1200/JCO.2007.15.0284

9. Germain C, Gnjatic S, Tamzalit F, Knockaert S, Remark R, Goc J, et al. Presence of b cells in tertiary lymphoid structures is associated with a protective immunity in patients with lung cancer. *Am J Respir Crit Care Med* (2014) 189 (7):832–44. doi: 10.1164/rccm.201309-1611OC

10. Martinet L, Garrido I, Filleron T, Le Guellec S, Bellard E, Fournie JJ, et al. Human solid tumors contain high endothelial venules: association with T- and b-lymphocyte infiltration and favorable prognosis in breast cancer. *Cancer Res* (2011) 71(17):5678–87. doi: 10.1158/0008-5472.CAN-11-0431

11. Di Caro G, Bergomas F, Grizzi F, Doni A, Bianchi P, Malesci A, et al. Occurrence of tertiary lymphoid tissue is associated with T-cell infiltration and predicts better prognosis in early-stage colorectal cancers. *Clin Cancer Res* (2014) 20(8):2147–58. doi: 10.1158/1078-0432.CCR-13-2590

12. Hiraoka N, Ino Y, Yamazaki-Itoh R, Kanai Y, Kosuge T, Shimada K. Intratumoral tertiary lymphoid organ is a favourable prognosticator in patients with pancreatic cancer. *Br J Cancer* (2015) 112(11):1782–90. doi: 10.1038/bjc.2015.145

13. Ladányi A, Kiss J, Somlai B, Gilde K, Fejos Z, Mohos A, et al. Density of DC-LAMP(+) mature dendritic cells in combination with activated T lymphocytes infiltrating primary cutaneous melanoma is a strong independent prognostic factor. *Cancer Immunol Immunother CII.* (2007) 56(9):1459–69. doi: 10.1007/s00262-007-0286-3

14. Helmink BA, Reddy SM, Gao J, Zhang S, Basar R, Thakur R, et al. B cells and tertiary lymphoid structures promote immunotherapy response. *Nature* (2020) 577 (7791):549–55. doi: 10.1038/s41586-019-1922-8

15. Petitprez F, de Reyniès A, Keung EZ, Chen TW, Sun CM, Calderaro J, et al. B cells are associated with survival and immunotherapy response in sarcoma. *Nature* (2020) 577(7791):556–60. doi: 10.1038/s41586-019-1906-8

16. Cabrita R, Lauss M, Sanna A, Donia M, Skaarup Larsen M, Mitra S, et al. Tertiary lymphoid structures improve immunotherapy and survival in melanoma. *NatureS* (2020) 577(7791):561–5. doi: 10.1038/s41586-019-1914-8

17. Fridman WH, Meylan M, Petitprez F, Sun CM, Italiano A, Sautès-Fridman C. B cells and tertiary lymphoid structures as determinants of tumour immune contexture and clinical outcome. *Nat Rev Clin Oncol* (2022) 19(7):441–57. doi: 10.1038/s41571-022-00619-z

18. Pfannstiel C, Strissel PL, Chiappinelli KB, Sikic D, Wach S, Wirtz RM, et al. The tumor immune microenvironment drives a prognostic relevance that correlates with bladder cancer subtypes. *Cancer Immunol Res* (2019) 7(6):923–38. doi: 10.1158/2326-6066.CIR-18-0758

19. Zhou L, Xu B, Liu Y, Wang Z. Tertiary lymphoid structure signatures are associated with survival and immunotherapy response in muscle-invasive bladder cancer. *Oncoimmunology* (2021) 10(1):1915574. doi: 10.1080/2162402X.2021.1915574

20. Balar AV, Galsky MD, Rosenberg JE, Powles T, Petrylak DP, Bellmunt J, et al. Atezolizumab as first-line treatment in cisplatin-ineligible patients with locally advanced and metastatic urothelial carcinoma: a single-arm, multicentre, phase 2 trial. *Lancet (London England)* (2017) 389(10064):67–76. doi: 10.1016/S0140-6736(16)32455-2

21. Xia QD, Sun JX, Xun Y, Xiao J, Liu CQ, Xu JZ, et al. SUMOylation pattern predicts prognosis and indicates tumor microenvironment infiltration characterization in bladder cancer. *Front Immunol* (2022) 13:864156. doi: 10.3389/fimmu.2022.864156

22. Newman AM, Liu CL, Green MR, Gentles AJ, Feng W, Xu Y, et al. Robust enumeration of cell subsets from tissue expression profiles. *Nat Methods* (2015) 12 (5):453–7. doi: 10.1038/nmeth.3337

23. Subramanian A, Tamayo P, Mootha VK, Mukherjee S, Ebert BL, Gillette MA, et al. Gene set enrichment analysis: a knowledge-based approach for interpreting genome-wide expression profiles. *Proc Natl Acad Sci U S A* (2005) 102(43):15545–50. doi: 10.1073/pnas.0506580102

24. Charoentong P, Finotello F, Angelova M, Mayer C, Efremova M, Rieder D, et al. Pan-cancer immunogenomic analyses reveal genotype-immunophenotype relationships and predictors of response to checkpoint blockade. *Cell Rep* (2017) 18 (1):248–62. doi: 10.1016/j.celrep.2016.12.019

25. Jiang P, Gu S, Pan D, Fu J, Sahu A, Hu X, et al. Signatures of T cell dysfunction and exclusion predict cancer immunotherapy response. *Nat Med* (2018) 24(10):1550–8. doi: 10.1038/s41591-018-0136-1

26. Hoshida Y, Brunet JP, Tamayo P, Golub TR, Mesirov JP. Subclass mapping: identifying common subtypes in independent disease data sets. *PloS One* (2007) 2 (11):e1195. doi: 10.1371/journal.pone.0001195

27. Maeser D, Gruener RF, Huang RS. oncoPredict: an r package for predicting in vivo or cancer patient drug response and biomarkers from cell line screening data. *Briefings Bioinf* (2021) 22(6):bbab260. doi: 10.1093/bib/bbab260

28. Chan TA, Yarchoan M, Jaffee E, Swanton C, Quezada SA, Stenzinger A, et al. Development of tumor mutation burden as an immunotherapy biomarker: utility for the oncology clinic. *Ann Oncol* (2019) 30(1):44–56. doi: 10.1093/annonc/mdy495

29. Samstein RM, Lee CH, Shoushtari AN, Hellmann MD, Shen R, Janjigian YY, et al. Tumor mutational load predicts survival after immunotherapy across multiple cancer types. *Nat Genet* (2019) 51(2):202–6. doi: 10.1038/s41588-018-0312-8

30. Trüb M, Zippelius A. Tertiary lymphoid structures as a predictive biomarker of response to cancer immunotherapies. *Front Immunol* (2021) 12:674565. doi: 10.3389/fimmu.2021.674565

31. Groeneveld CS, Fontugne J, Cabel L, Bernard-Pierrot I, Radvanyi F, Allory Y, et al. Tertiary lymphoid structures marker CXCL13 is associated with better survival for patients with advanced-stage bladder cancer treated with immunotherapy. *Eur J Cancer (Oxford Engl 1990)* (2021) 148:181–9. doi: 10.1016/j.ejca.2021.01.036

32. Delvecchio FR, Fincham REA, Spear S, Clear A, Roy-Luzarraga M, Balkwill FR, et al. Pancreatic cancer chemotherapy is potentiated by induction of tertiary lymphoid structures in mice. *Cell Mol Gastroenterol Hepatol* (2021) 12(5):1543–65. doi: 10.1016/j.jcmgh.2021.06.023

33. Posch F, Silina K, Leibl S, Mündlein A, Moch H, Siebenhüner A, et al. Maturation of tertiary lymphoid structures and recurrence of stage II and III colorectal cancer. *Oncoimmunology* (2018) 7(2):e1378844. doi: 10.1080/2162402X.2017.1378844

34. Garaud S, Dieu-Nosjean MC, Willard-Gallo K. T Follicular helper and b cell crosstalk in tertiary lymphoid structures and cancer immunotherapy. *Nat Commun* (2022) 13(1):2259. doi: 10.1038/s41467-022-29753-z

35. Calderaro J, Petitprez F, Becht E, Laurent A, Hirsch TZ, Rousseau B, et al. Intra-tumoral tertiary lymphoid structures are associated with a low risk of early recurrence of hepatocellular carcinoma. *J Hepatol* (2019) 70(1):58–65. doi: 10.1016/j.jhep.2018.09.003

36. Chaurio RA, Anadon CM, Lee Costich T, Payne KK, Biswas S, Harro CM, et al. TGF-β-mediated silencing of genomic organizer SATB1 promotes tfh cell differentiation and formation of intra-tumoral tertiary lymphoid structures. *Immunity* (2022) 55(1):115–28.e9. doi: 10.1016/j.immuni.2021.12.007

37. Liu W, Wang W, Wang X, Xu C, Zhang N, Di W. Cisplatin-stimulated macrophages promote ovarian cancer migration *via* the CCL20-CCR6 axis. *Cancer Letters* (2020) 472:59–69. doi: 10.1016/j.canlet.2019.12.024

38. Kfoury Y, Baryawno N, Severe N, Mei S, Gustafsson K, Hirz T, et al. Human prostate cancer bone metastases have an actionable immunosuppressive microenvironment. *Cancer Cell* (2021) 39(11):1464–78.e8. doi: 10.1016/j.ccell.2021.09.005

39. Fan T, Li S, Xiao C, Tian H, Zheng Y, Liu Y, et al. CCL20 promotes lung adenocarcinoma progression by driving epithelial-mesenchymal transition. *Int J Biol Sci* (2022) 18(11):4275–88. doi: 10.7150/ijbs.73275

40. Binnewies M, Roberts EW, Kersten K, Chan V, Fearon DF, Merad M, et al. Understanding the tumor immune microenvironment (TIME) for effective therapy. *Nat Med* (2018) 24(5):541–50. doi: 10.1038/s41591-018-0014-x

41. Wang F, Liu P, An H, Zhang Y. Sulforaphane suppresses the viability and metastasis, and promotes the apoptosis of bladder cancer cells by inhibiting the expression of FAT–1. *Int J Mol Med* (2020) 46(3):1085–95. doi: 10.3892/ijmm.2020.4665

42. Zhang Z, Yu Y, Li P, Wang M, Jiao W, Liang Y, et al. Identification and validation of an immune signature associated with EMT and metabolic reprogramming for predicting prognosis and drug response in bladder cancer. *Front Immunol* (2022) 13:954616. doi: 10.3389/fimmu.2022.954616

43. The Cancer Genome Atlas Research Network. Comprehensive molecular characterization of urothelial bladder carcinoma. *Nature* (2014) 507(7492):315–22. doi: 10.1038/nature12965

44. Halstead AM, Kapadia CD, Bolzenius J, Chu CE, Schriefer A, Wartman LD, et al. Bladder-cancer-associated mutations in RXRA activate peroxisome proliferator-activated receptors to drive urothelial proliferation. *eLife* (2017) 6:30862. doi: 10.7554/eLife.30862

45. Wing JB, Tanaka A, Sakaguchi S. Human FOXP3(+) regulatory T cell heterogeneity and function in autoimmunity and cancer. *Immunity* (2019) 50 (2):302–16. doi: 10.1016/j.immuni.2019.01.020

46. Gobert M, Treilleux I, Bendriss-Vermare N, Bachelot T, Goddard-Leon S, Arfi V, et al. Regulatory T cells recruited through CCL22/CCR4 are selectively activated in lymphoid infiltrates surrounding primary breast tumors and lead to an adverse clinical outcome. *Cancer Res* (2009) 69(5):2000–9. doi: 10.1158/0008-5472.CAN-08-2360

47. García-Hernández ML, Uribe-Uribe NO, Espinosa-González R, Kast WM, Khader SA, Rangel-Moreno J. A unique cellular and molecular microenvironment is present in tertiary lymphoid organs of patients with spontaneous prostate cancer regression. *Front Immunol* (2017) 8:563. doi: 10.3389/fimmu.2017.00563

48. Schweiger T, Berghoff AS, Glogner C, Glueck O, Rajky O, Traxler D, et al. Tumor-infiltrating lymphocyte subsets and tertiary lymphoid structures in pulmonary metastases from colorectal cancer. *Clin Exp Metastasis* (2016) 33 (7):727–39. doi: 10.1007/s10585-016-9813-y

49. Joshi NS, Akama-Garren EH, Lu Y, Lee DY, Chang GP, Li A, et al. Regulatory T cells in tumor-associated tertiary lymphoid structures suppress anti-tumor T cell responses. *Immunity* (2015) 43(3):579–90. doi: 10.1016/j.immuni.2015.08.006

50. Gentles AJ, Newman AM, Liu CL, Bratman SV, Feng W, Kim D, et al. The prognostic landscape of genes and infiltrating immune cells across human cancers. *Nat Med* (2015) 21(8):938–45. doi: 10.1038/nm.3909

51. Castino GF, Cortese N, Capretti G, Serio S, Di Caro G, Mineri R, et al. Spatial distribution of b cells predicts prognosis in human pancreatic adenocarcinoma. *Oncoimmunology* (2016) 5(4):e1085147. doi: 10.1080/2162402X.2015.1085147

52. Koti M, Xu AS, Ren KYM, Visram K, Ren R, Berman DM, et al. Tertiary lymphoid structures associate with tumour stage in urothelial bladder cancer. *Bladder Cancer* (2017) 3(4):259–67. doi: 10.3233/BLC-170120

53. Witjes JA, Bruins HM, Cathomas R, Compérat EM, Cowan NC, Gakis G, et al. European Association of urology guidelines on muscle-invasive and metastatic bladder cancer: Summary of the 2020 guidelines. *Eur urol* (2021) 79 (1):82–104. doi: 10.1016/j.eururo.2020.03.055

54. Morcrette G, Hirsch TZ, Badour E, Pilet J, Caruso S, Calderaro J, et al. APC germline hepatoblastomas demonstrate cisplatin-induced intratumor tertiary lymphoid structures. *Oncoimmunology* (2019) 8(6):e1583547. doi: 10.1080/2162402X.2019.1583547

55. Benzerdjeb N, Dartigues P, Kepenekian V, Valmary-Degano S, Mery E, Avérous G, et al. Tertiary lymphoid structures in epithelioid malignant peritoneal mesothelioma are associated with neoadjuvant chemotherapy, but not with prognosis. *Virchows Archiv: an Int J pathol* (2021) 479(4):765–72. doi: 10.1007/s00428-021-03099-1

frontiers | Frontiers in Immunology

TYPE Original Research
PUBLISHED 25 November 2022
DOI 10.3389/fimmu.2022.985861

OPEN ACCESS

EDITED BY
Apostolos Zaravinos,
European University Cyprus, Cyprus

REVIEWED BY
Zhi Li,
The First Affiliated Hospital of China Medical University, China
Saitian Zeng,
Cangzhou Central Hospital, China

*CORRESPONDENCE
Kun Fang
k99ftl@163.com

SPECIALTY SECTION
This article was submitted to Cancer Immunity and Immunotherapy, a section of the journal Frontiers in Immunology

RECEIVED 04 July 2022
ACCEPTED 04 November 2022
PUBLISHED 25 November 2022

CITATION
Fang K, Xu Z, Jiang S, Yan C, Tang D and Huang Y (2022) Integrated profiling uncovers prognostic, immunological, and pharmacogenomic features of ferroptosis in triple-negative breast cancer.
Front. Immunol. 13:985861.
doi: 10.3389/fimmu.2022.985861

Integrated profiling uncovers prognostic, immunological, and pharmacogenomic features of ferroptosis in triple-negative breast cancer

Kun Fang[1]*, Zhengjie Xu[1], Suxiao Jiang[1], Changsheng Yan[2], Desheng Tang[2] and Yan Huang[3]

[1]Department of Surgery, Yinchuan Maternal and Child Health Hospital, Yinchuan, China, [2]Department of Surgery, The First Affiliated Hospital of Harbin Medical University, Harbin, Heilongjiang, China, [3]Department of Surgery, Affiliated Hospital of Ningxia Medical University, Yinchuan, China

Objective: Ferroptosis is an iron-dependent type of regulated cell death triggered by the toxic buildup of lipid peroxides on cell membranes. Nonetheless, the implication of ferroptosis in triple-negative breast cancer (TNBC), which is the most aggressive subtype of breast carcinoma, remains unexplored.

Methods: Three TNBC cohorts—TCGA-TNBC, GSE58812, and METABRIC—were adopted. Consensus molecular subtyping on prognostic ferroptosis-related genes was implemented across TNBC. Ferroptosis classification-relevant genes were selected through weighted co-expression network analysis (WGCNA), and a ferroptosis-relevant scoring system was proposed through the LASSO approach. Prognostic and immunological traits, transcriptional and post-transcriptional modulation, therapeutic response, and prediction of potential small-molecule agents were conducted.

Results: Three disparate ferroptosis patterns were identified across TNBC, with prognostic and immunological traits in each pattern. The ferroptosis-relevant scoring system was proposed, with poorer overall survival in high-risk patients. This risk score was strongly linked to transcriptional and post-transcriptional mechanisms. The high-risk group had a higher response to anti-PD-1 blockade or sunitinib, and the low-risk group had higher sensitivity to cisplatin. High relationships of risk score with immunological features were observed across pan-cancer. Two Cancer Therapeutics Response Portal (CTRP)-derived agents (SNX-2112 and brefeldin A) and PRISM-derived agents (MEK162, PD-0325901,

PD-318088, Ro-4987655, and SAR131675) were predicted, which were intended for high-risk patients.

Conclusion: Altogether, our findings unveil prognostic, immunological, and pharmacogenomic features of ferroptosis in TNBC, highlighting the potential clinical utility of ferroptosis in TNBC therapy.

KEYWORDS

triple-negative breast cancer, ferroptosis, prognosis, immunological feature, immunotherapy

Introduction

Female breast cancer is the most commonly diagnosed cancer globally, with an estimated 2.3 million new cases (11.7%), and the major cause of cancer deaths with estimated 0.68 million deaths (6.9%) (1). Triple-negative breast cancer (TNBC) is a subtype of breast cancer with the absence of expression of estrogen receptor (ER) and progesterone receptor (PR) together with human epidermal growth factor receptor type 2 (HER2) (2). TNBC possesses a strong invasive and metastatic ability, easily invading blood vessels, and increased recurrence risk (2). The therapeutic options for TNBC are far more limited in comparison to those for other breast cancer subtypes (3). Surgical resection and chemotherapy remain the first-line regimens against TNBC (3). Immunotherapy has revolutionized the field of oncology over the past few years, primarily with the introduction of immune checkpoint blockade (ICB) into clinical practice. Few patients with TNBC benefit from ICB, and complete and durable responses are rare because most tumors are not immunoreactive (4). Hence, an innovative scheme is required for bringing immunotherapy closer to TNBC. TNBC is highly genetically diverse, which ranges from high proliferation to chemotherapy resistance with low proliferative and luminal features (5). Biomarker selection, drug discovery, and clinical trial design are necessary to match properly targeted therapies to distinct subpopulations of TNBC patients.

Ferroptosis is an iron-dependent type of cell death induced by disruption of membrane integrity because of overproduced lipid peroxides, which is morphologically characterized by cell swelling, pore formation on the cell membrane, smaller mitochondria, and reduced mitochondrial cristae together with enhanced mitochondrial membrane density (6). Induction of ferroptotic cell death involves a few alterations (altered iron metabolism, response to oxidative stress, production of lipid peroxides, etc.) (7). Excessive or deficient ferroptosis correlates to various physiological and pathophysiological processes, especially dysregulated immune responses (8). For instance, CD8+ T cells trigger tumoral ferroptosis during cancer immunotherapy (9). Inducing ferroptosis may elicit an immunostimulatory tumor microenvironment (10). Due to the distinction of ferroptosis from apoptosis and others, inducing ferroptosis may eliminate tumor cells that have resistance to other cell death types (11). Ferroptotic cell death has become a novel direction around which to design TNBC therapy. Nonetheless, the full appearance of ferroptosis in TNBC has not yet been completely clarified.

The current study integrated ferroptosis-related genes (FRGs) and proposed a novel ferroptosis classification in TNBC. Especially, disparate ferroptosis patterns exhibited unique prognostic and immunological traits. Additionally, a ferroptosis-relevant gene signature was established and evaluated its associations with survival, immunological traits, and therapeutic sensitivity. Altogether, our findings suggested the possible implications of ferroptosis in shaping tumor immune microenvironment and immunological features.

Abbreviations: TNBC, triple-negative breast cancer; ICB, immune checkpoint blockade; FRGs, ferroptosis-related genes; K-M, Kaplan–Meier; OS, overall survival; GO, Gene Ontology; KEGG, Kyoto Encyclopedia of Genes and Genomes; FDR, false discovery rate; GSVA, gene set variation analysis; GSEA, gene set enrichment analysis; WGCNA, weighted co-expression network analysis; LASSO, least absolute shrinkage and selection operator; ROC, receiver operating characteristic; AUC, area under the curve; SubMap, Subclass Mapping; GDSC, Genomics of Drug Sensitivity in Cancer.

Materials and methods

Study population and data collection

The current study searched the TNBC cohorts from The Cancer Genome Atlas (TCGA) (https://portal.gdc.cancer.gov/) and GEO (http://www.ncbi.nlm.nih.gov/geo/) together with METABRIC (http://www.cbioportal.org/). The inclusion criteria of TNBC patients comprised the following: i) histopathological diagnosis of TNBC, ii) appropriate transcriptome data, and iii) available follow-up information. As a result, we included 117 patients (tumors, N = 117; normal tissues, N = 113) from TCGA-

TNBC as the training cohort. Meanwhile, 107 patients from the GSE58812 (12) and 299 patients from the METABRIC (13) were adopted as the verification cohorts. The specific clinical information is listed in Supplementary Table 1.

The ensemble IDs of TCGA-TNBC dataset were mapped to gene symbols in accordance with the annotation of "Homo_sapiens.GRCh38.91.chr.gtf". Then, gene expression was normalized utilizing the scale approach of the limma package (14), and the mean RNA expression of duplicates was computed, followed by the removal of genes with low abundance. The probes of GSE58812 expression profiles were mapped in line with the GPL570 annotation file, and the mean RNA expression was computed for duplicates. The METABRIC data were acquired from the cBio Cancer Genomics Portal (http://cbioportal.org) (15). Pan-cancer expression profiles were acquired from TCGA project.

Ferroptosis gene set

Sixty FRGs were collected from previously published literature, which is listed in Supplementary Table 2. The position of chromosomes of FRGs was visualized in the Circos plot *via* the RCircos package (16). The levels of FRGs were compared between TNBC and normal tissues.

Somatic mutation analysis

The somatic variants in Mutation Annotation Format were acquired from the TCGA-TNBC dataset. Overall gene mutation was estimated utilizing the maftools package (17).

Interaction between ferroptosis-related genes

Functional protein–protein interactions among FRGs were conducted *via* the STRING database (https://string-db.org) (18), which were visualized utilizing Cytoscape software (19).

Survival analysis

A univariate or multivariate Cox regression approach was adopted to assess the relationships of variables with overall survival (OS) using the survival package. Kaplan–Meier (K-M) curves with the log-rank test were carried out by utilizing the survminer package.

Functional enrichment analysis

With clusterProfiler package (20), Gene Ontology (GO) together with the Kyoto Encyclopedia of Genes and Genomes (KEGG) pathway enrichment analysis was conducted. False discovery rate (FDR) <0.05 denoted significant enrichment. The "c2.cp.kegg.v7.2.symbols" gene set was downloaded from Molecular Signatures Database, which was adopted for gene set variation analysis (GSVA) (21). Additionally, the activity of known biological processes was inferred through GSVA. Gene set enrichment analysis (GSEA) was conducted to estimate the significant activity of KEGG pathways between groups (22).

Consensus clustering

The consensus clustering method from the ConsensusClusterPlus package was employed to infer the number of unsupervised classes across TNBC (23). This analysis was set as agglomerative "k-means" clustering with Euclidean correlation distance, and 80% of the samples were resampled 1,000 times. The discrimination of transcriptome profiling between diverse patterns was displayed through principal component analysis (PCA) by utilizing the limma package. To validate the reproducibility of ferroptosis classification, the unique upregulated markers of each ferroptosis pattern were selected, and sample clustering was implemented in the verification cohorts *via* the NTP algorithm.

Estimation of immunological features

The relative abundance of tumor-infiltrating immune cells was inferred through the single-sample gene set enrichment analysis (ssGSEA) approach. Tumor purity, immune, and stromal scores were computed *via* the ESTIMATE algorithm (24). RNA expression, methylation, and copy-number alterations of immunomodulators (co-stimulators, co-inhibitors, ligands, receptors, cell adhesion, antigen presentation, and others) were analyzed. Additionally, the activity of common immune checkpoints was computed across TNBC. Seven steps within the cancer-immunity cycle were quantified with ssGSEA in accordance with expression profiling (25).

Weighted co-expression network analysis

The weighted co-expression network analysis (WGCNA) package (26) was adopted for co-expression analysis. First, an appropriate soft threshold power was chosen to transform the adjacency matrix into the topological overlap matrix. Associations of co-expression modules with ferroptosis classification were computed. The genes in the module that exhibited the strongest relationship with ferroptosis classification were regarded as ferroptosis classification-relevant genes.

Construction of a ferroptosis scoring system

A least absolute shrinkage and selection operator (LASSO) regression model was conducted on prognostic ferroptosis pattern-relevant genes by utilizing the glmnet package. The coefficient was computed with a multivariate Cox regression approach, and the remaining genes were chosen for constructing a ferroptosis scoring system (ferroptosis_score). Ferroptosis_score was computed as the sum of the products of gene expression and matched coefficients. TNBC cases were classified as ferroptosis_score-high and ferroptosis_score-low groups in accordance with the median score. Time-dependent receiver operating characteristic (ROC) analysis was implemented, followed by calculation of the area under the curve (AUC) at diverse time points for assessing the discriminative significance. Utilizing the rms package, a nomogram was constructed in accordance with prognostic parameters. The predictive efficiency was estimated with calibration curves.

Evaluation of post-transcriptional events

The miRNA expression profiles were downloaded from TCGA-TNBC dataset. MiRNAs or mRNAs with differential expression were selected between groups in accordance with FDR < 0.05. Targeted mRNAs were inferred through online databases, followed by KEGG pathway enrichment analysis.

Therapeutic response estimation

The expression similarity between groups and patients receiving anti-PD-1/anti-CTLA4 agents was assessed through Subclass Mapping (SubMap) (27). The chemotherapeutic response was inferred on the basis of the largest publicly available pharmacogenomics database: Genomics of Drug Sensitivity in Cancer (GDSC; www.cancerRxgene.org) (28). The prediction process employed the pRRophetic package, and ridge regression was utilized for estimating half of the maximum inhibitory concentration (IC50) (29). The prediction accuracy was evaluated with 10-fold cross-validation. Drug sensitivity profiling of human cancer cell lines was obtained from the Cancer Therapeutics Response Portal (CTRP) (https://portals.broadinstitute.org/ctrp) together with the PRISM project (https://depmap.org/portal/prism/), which was adopted for the prediction of small-molecule agents (30).

Statistical analysis

R software (version 4.1.0) was adopted for statistical analysis. Continuous variables were compared with Student's t-test or Wilcoxon rank-sum test. The relationships between variables were estimated with Pearson's or Spearman's test. Statistical significance was set at $p < 0.05$ (*$p < 0.05$, **$p < 0.01$, and ***$p < 0.001$).

Results

Transcriptional and genetic alterations, survival implication, and interactions of ferroptosis-related genes in triple-negative breast cancer

The present study collected 60 FRGs from previously published literature. Figure 1A illustrates the position of FRGs on chromosomes. Most FRGs exhibited abnormal expression in TNBC in contrast to normal tissues (Figures 1B, C). The extensive somatic mutations of FRGs occurred across TNBC, especially TP53 (Figure 1D). Pearson's correlation test of RNA expression unveiled that most FRGs notably interacted with each other (Figure 1E). Additionally, we investigated the closely functional interactions among products of FRGs (Figure 1F). Among FRGs, MT1G, FADS2, and HMOX1 were notably linked to TNBC cases' OS (Figure 1G). GO and KEGG enrichment results confirmed the implication of FRGs in ferroptosis (Figure 1H).

Definition of ferroptosis classification across triple-negative breast cancer

In accordance with the consensus clustering approach using the transcript levels of prognostic FRGs, the optimal number of clusters was 3, and TCGA-TNBC dataset was categorized as three disparate ferroptosis patterns, namely, C1–3 (Supplementary Figures 1A–C; Figure 2A). Three patterns exhibited disparate OS results, with C3 being the worst, C1 the next, and C2 the best (Figure 2B). PCA unveiled the diverse transcriptome profiling traits among three ferroptosis patterns (Figure 2C). We selected the unique upregulated markers in each ferroptosis pattern that were utilized for sample clustering in the GSE58812 and METABRIC datasets (Supplementary Figure 2A). The reproducibility of ferroptosis classification was confirmed in the two verification datasets (Supplementary Figures 2B–E).

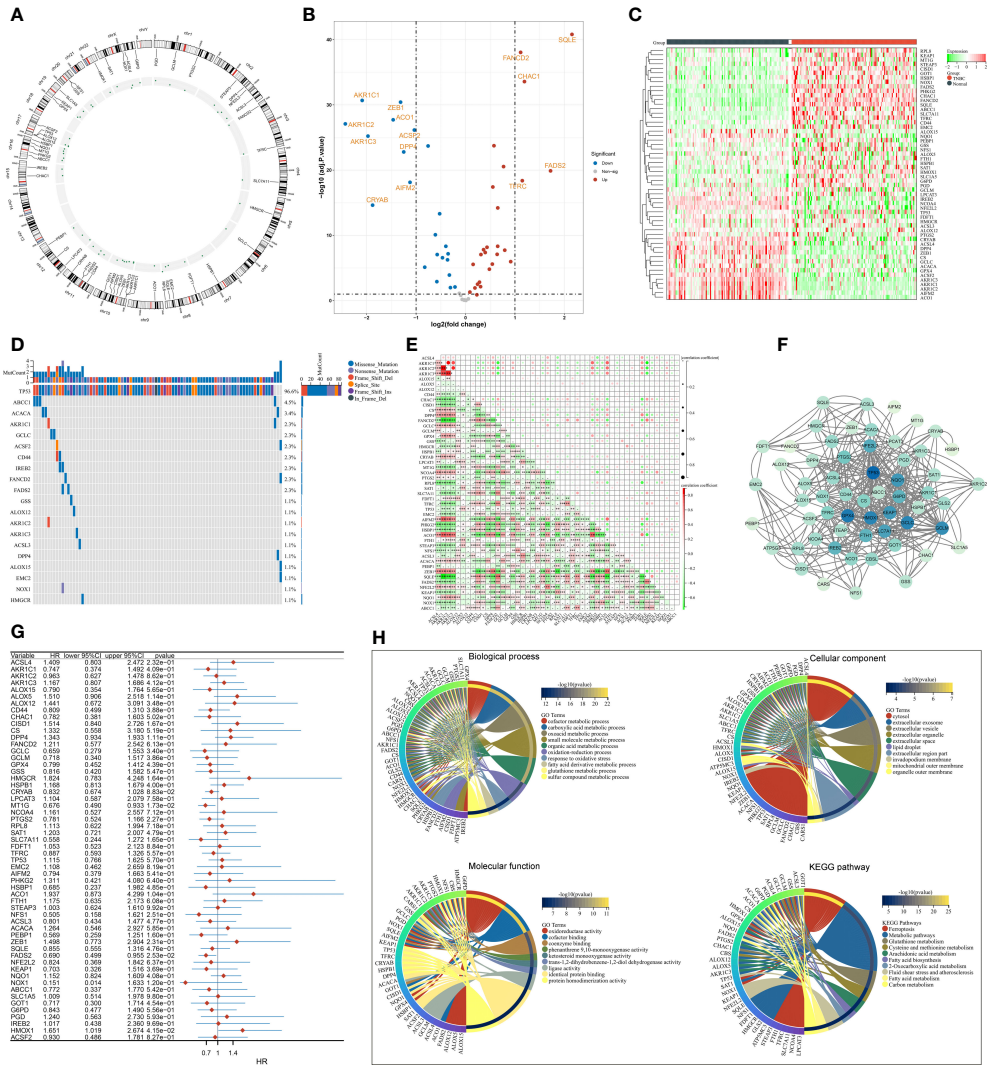

FIGURE 1
Transcriptional and genetic alterations, survival implication, and interactions of FRGs in TNBC. **(A)** Circos plot for the position of FRGs on chromosomes. **(B, C)** Volcano and heatmap for RNA levels of FRGs in TNBC and normal tissues. **(D)** Oncoplot of the somatic landscape of FRGs across TNBC. FRGs are ranked by mutation frequency, and side bar plot shows log10 converted Q-value estimated through MutSigCV. **(E)** Relationships between FRGs at the RNA level. **(F)** An interaction network of products of FRGs. **(G)** Univariate Cox regression results of the relationships of FRGs with OS. **(H)** GO and KEGG enrichment results of FRGs. FRGs, ferroptosis-related genes; TNBC, triple-negative breast cancer; OS, overall survival; GO, Gene Ontology; KEGG, Kyoto Encyclopedia of Genes and Genomes *p<0.05, **p<0.01 and ***p<0.001..

Unique immunological traits in diverse ferroptosis patterns

The notable discrepancy in RNA expression, methylation, and copy-number variations of immunomodulators (co-stimulators, co-inhibitors, ligands, receptors, cell adhesion, antigen presentation, and others) was observed across three ferroptosis patterns (Figure 2D). In addition, the C3 subtype displayed the highest abundance of immune cells and expression of immune checkpoints, followed by C2 and C1 (Figure 2E). The activity of KEGG pathways was compared between ferroptosis patterns. In contrast to C1, higher activity of multiple metabolism pathways (pyrimidine, arginine and proline metabolism, alanine aspartate and glutamate, amino sugar and nucleotide sugar, fructose, and mannose, etc.) was observed in C2 (Figure 2F). C2 displayed the enhanced activity of biosynthesis and degradation of DNA and RNA than C3 (Figure 2G). Additionally, tumorigenic pathways (calcium pathway, apoptosis, ABC transporters, neuroactive ligand–receptor interaction, etc.) possessed increased activity in C3 versus C2 or C1 (Figures 2G, H). In contrast to C1, higher activity of immune response pathways (complement and

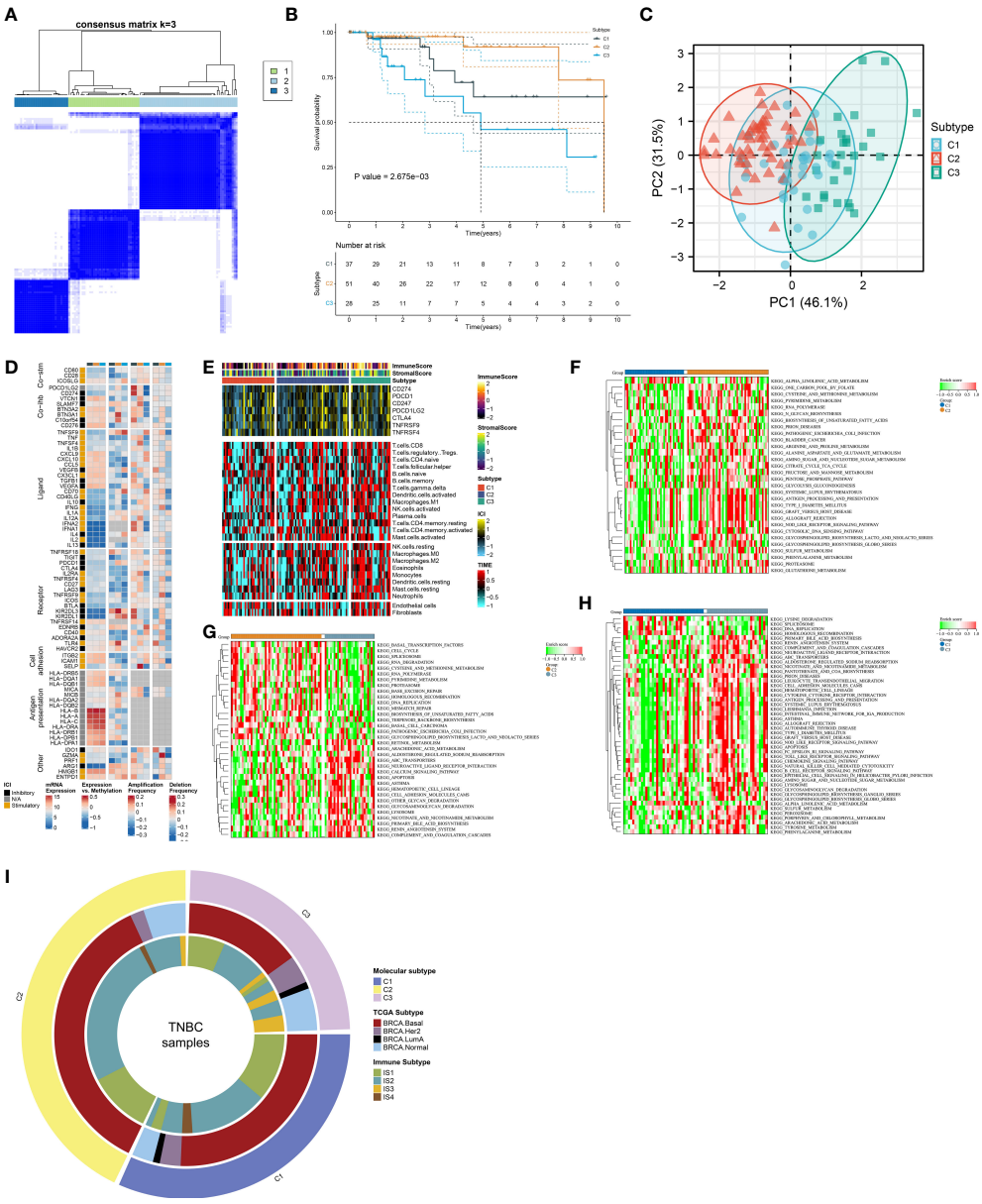

FIGURE 2
Definition of ferroptosis classification with unique immunological traits in TCGA-TNBC cohort. **(A)** Classification of TNBC patients as three patterns through consensus matrix. **(B)** K-M curves for OS among three ferroptosis patterns. **(C)** PCA plots for the notable discrepancy among ferroptosis patterns. **(D)** Distribution of RNA expression, methylation, and copy-number alterations of immunomodulators in three ferroptosis patterns. **(E)** Distribution of immune checkpoint expression, immune cell abundance, and immune and stromal scores across ferroptosis patterns. **(F–H)** KEGG pathways with different activities in C1 versus C2, C2 versus C3, and C3 versus C1. **(I)** Relationships between the ferroptosis classification with TCGA subtypes and immune subtypes. TNBC, triple-negative breast cancer; K-M, Kaplan–Meier; OS, overall survival; PCA, principal component analysis; KEGG, Kyoto Encyclopedia of Genes and Genomes; TCGA, The Cancer Genome Atlas.

coagulation cascades, antigen processing and presentation, chemokine pathway, etc.) was found in C3 (Figure 2H). We compared known molecular subtypes with the ferroptosis classification. Our results demonstrated that the ferroptosis classification was independent of known TCGA subtypes and immune subtypes (Figure 2I).

Selection of ferroptosis pattern-relevant genes in triple-negative breast cancer

A gene co-expression network was conducted by adopting WGCNA to select modules with the strongest correlation to ferroptosis classification. First, no outliers were detected among

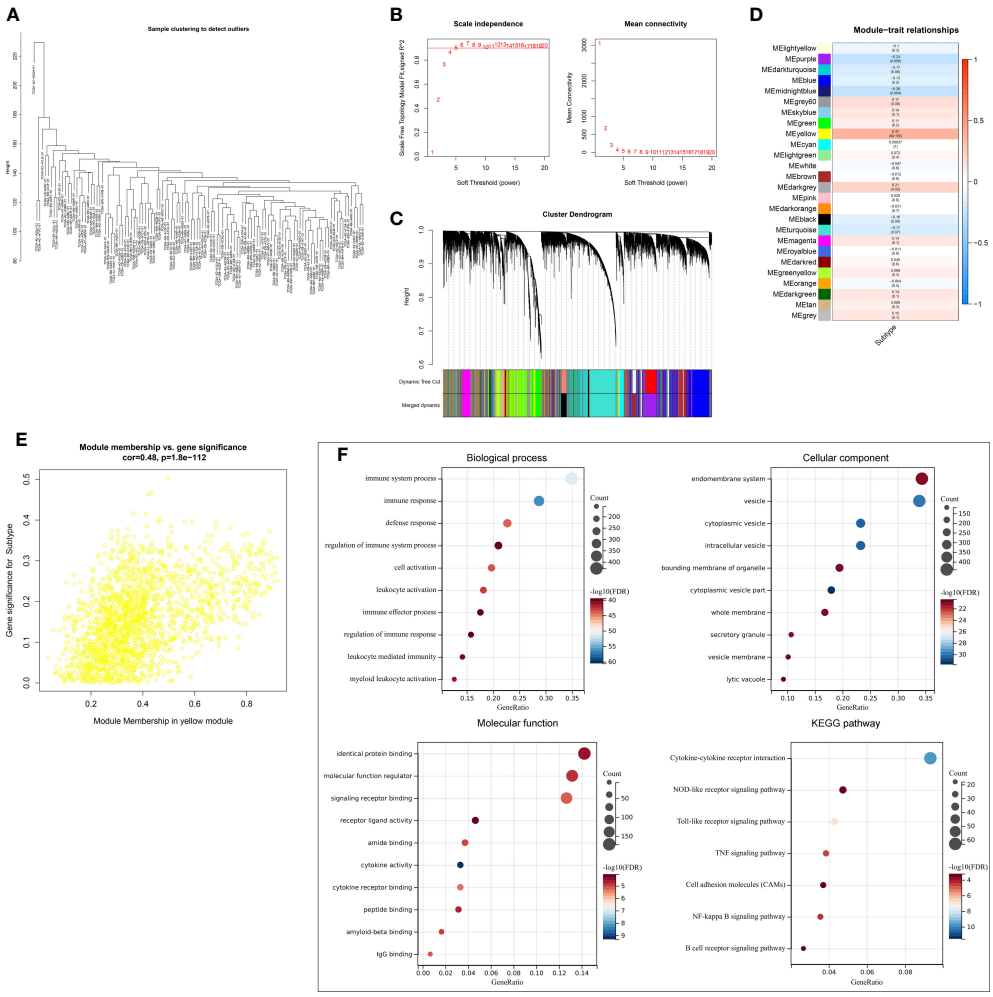

FIGURE 3
Selection of ferroptosis pattern-relevant genes in TCGA-TNBC cohort. **(A)** Removal of outliers *via* sample clustering. **(B)** Selection of the optimal soft threshold through considering scale independence together with mean connectivity. **(C)** The branches of the clustering dendrogram correspond to 26 modules. **(D)** Relationships of modules with ferroptosis classification. Correlation coefficients and p-values are exhibited in boxes. **(E)** Scatter plots for the correlations of module membership in yellow module with gene significance for ferroptosis classification. **(F)** GO and KEGG enrichment results of ferroptosis pattern-relevant genes. GO, Gene Ontology; KEGG, Kyoto Encyclopedia of Genes and Genomes.

TCGA-TNBC samples (Figure 3A). The appropriate soft threshold was set as 10 by considering scale independence together with mean connectivity (Figure 3B). Afterward, a scale-free co-expression network was established. Consequently, 26 co-expression modules were clustered (Figure 3C). Especially, the yellow module displayed the strongest correlation to ferroptosis classification (correlation coefficient = 0.37, p = 6e−05; Figure 3D). In addition, module membership in the yellow module was strongly linked to gene significance for ferroptosis classification (Figure 3E). Thus, genes in the yellow module were regarded as ferroptosis pattern-relevant genes, which primarily participated in modulating immune response and TNBC-relevant pathways (NOD-like/Toll-like receptor/TNF/NF-κB/B cell receptor pathways, etc.) (Figure 3F).

Establishment and external verification of a robust ferroptosis scoring system in triple-negative breast cancer

A total of 145 ferroptosis pattern-relevant genes notably correlated to TNBC cases' OS (Supplementary Table 3), which were adopted for implementing LASSO regression analysis. Increasing λ led to a decrease in the number of independent variables with coefficients close to 0 (Figure 4A). Ten-fold cross-validation was adopted for building the scoring system and estimating the confidence intervals following diverse λ values. The optimal λ value was determined when partial likelihood deviance was the lowest (Figure 4B), and 16 genes were selected for the scoring system following the formula: ferroptosis-

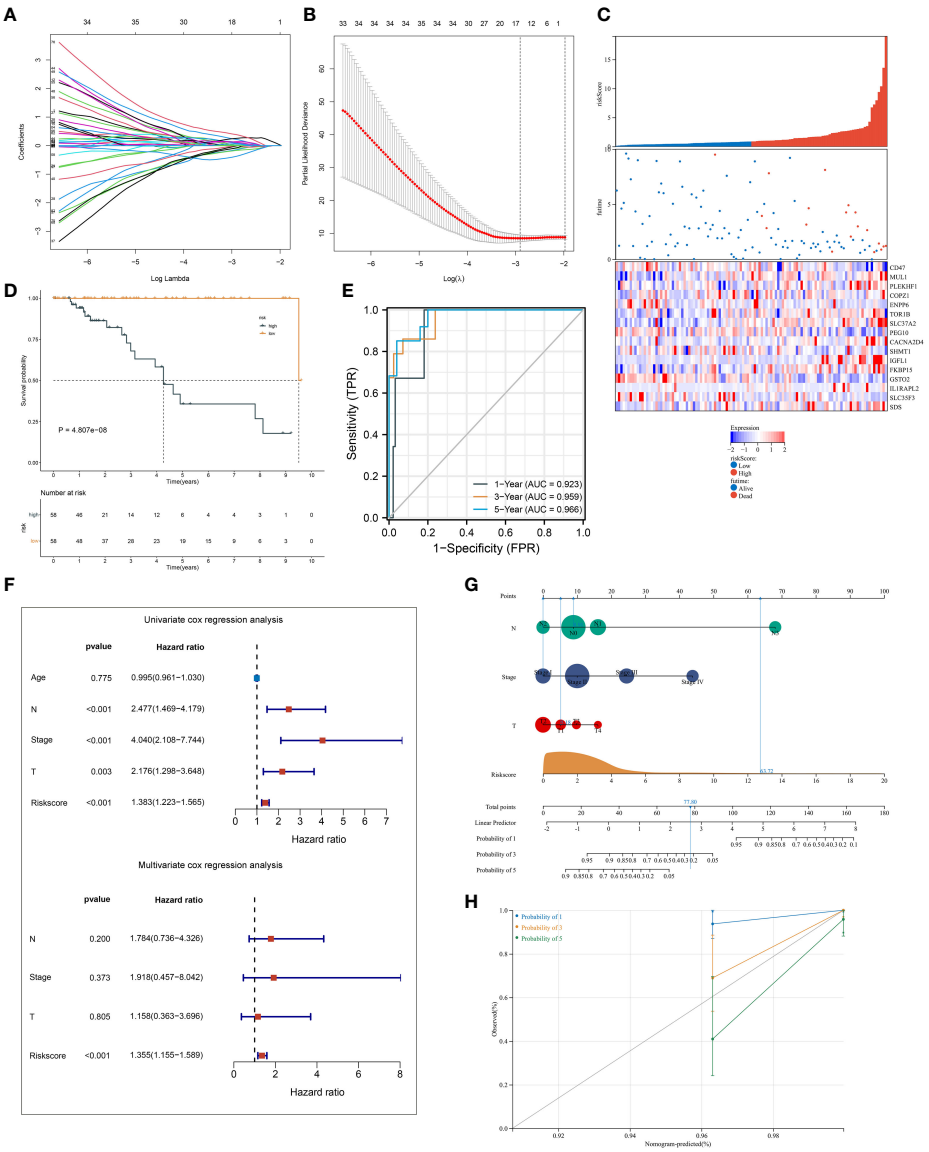

FIGURE 4
Establishment of a ferroptosis scoring system in TCGA-TNBC cohort. **(A)** Changing trajectory of prognostic ferroptosis pattern-relevant genes. The x-axis denotes the log λ values of independent variables, and the y-axis denotes their coefficients. **(B)** Confidence intervals with distinct λ values. **(C)** Distribution of ferroptosis-relevant risk score, survival status, and gene expression across TNBC cases. **(D)** K-M curves of OS between ferroptosis-relevant high- and low-risk groups. **(E)** ROC curves at 1-, 3- and 5-year OS outcomes. **(F)** Univariate and multivariate Cox regression results of ferroptosis-relevant risk score and clinicopathological parameters with TNBC cases' OS. **(G)** Construction of the nomogram by totaling the points determined on the points scale for ferroptosis-relevant risk score, T, N, and M stages. **(H)** Calibration curves of the relationships between observed 1-, 3-, and 5-year OS and nomogram-estimated outcomes. TNBC, triple-negative breast cancer; K-M, Kaplan–Meier; OS, overall survival; ROC, receiver operating characteristic.

relevant risk score = $(-0.142765874605473) * \exp^{CD47} + 0.112505459964827 * \exp^{MUL1} + 0.00538161716022841 * \exp^{PLEKHF1} + 0.215213236835648 * \exp^{COPZ1} + (-0.168998590096113) * \exp^{ENPP6} + 0.0791918658709983 * \exp^{TOR1B} + 0.254809882047955 * \exp^{SLC37A2} + (-0.0946087366980265) * \exp^{PEG10} + 0.139388903981419 * \exp^{CACNA2D4} + (-0.0109640256571299) * \exp^{SHMT1} + 0.385024690538088 * \exp^{IGFL1} + 0.0181238671012704 * \exp^{FKBP15} + (-0.373571481244596) * \exp^{GSTO2} + 0.113747451219178 * \exp^{IL1RAPL2} + (-0.0758300765619583) * \exp^{SLC35F3} + 0.0576459041484211 * \exp^{SDS}$. The risk score of each case in TCGA-TNBC cohort was computed, and cases were classified as ferroptosis-relevant high- and low-risk groups under the median score (Figure 4C). K-M curves showed

poorer OS outcomes in the high-risk score group (Figure 4D). ROC analysis was conducted on the ferroptosis-relevant scoring system for estimating prognostic outcomes. The AUCs at 1-, 3-, and 5-year OS were all >0.9 (Figure 4E), demonstrating the excellent efficiency of the scoring system in prognostic estimation in TCGA-TNBC cohort. The robustness of the ferroptosis-relevant scoring system was proven in GSE58812 and METABRIC cohorts, and the same formula was applied to the two verification cohorts. Notable differences were observed in OS between ferroptosis-relevant high- and low-risk groups, with relatively high AUCs at 1-, 3-, and 5-year OS in GSE58812 and METABRIC cohorts (Supplementary Figures 3A–F). The above data demonstrated that the ferroptosis-relevant scoring system possessed favorable robustness on diverse platforms.

Univariate Cox regression results showed that T, N, and M stages and the ferroptosis-relevant risk score were significantly associated with TNBC OS (Figure 4F). Further multivariate Cox regression analysis demonstrated that the ferroptosis-relevant risk score acted as an independent risk parameter of TNBC prognosis (Figure 4F). To assist in the clinical application of the ferroptosis-relevant scoring system, we proposed a prognostic nomogram by incorporating T, N, and M stages and the ferroptosis-relevant risk score (Figure 4G). Calibration curves confirmed the high accuracy of the nomogram in inferring 1-, 3-, and 5-year OS outcomes (Figure 4H).

Ferroptosis-relevant risk score involved in somatic mutation and transcriptional and post-transcriptional mechanisms

Somatic mutation was compared between ferroptosis-relevant high- and low-risk groups. Figure 5A illustrates the top 20 mutated genes across TCGA-TNBC individuals, with TP53 as the most frequent mutated gene. A higher mutation frequency was observed in low-risk populations. Additionally, *Leishmania* infection, cytokine–cytokine receptor interaction, endocytosis, apoptosis, and MAPK signaling pathway displayed prominently increased activity in high-risk cases in contrast to low-risk cases (Figure 5B). Most genes from the ferroptosis-relevant risk score displayed abnormal expression between TNBC and normal tissues, with upregulated SLC37A2, IGFL1, and SDS and downregulated MUL1, ENPP6, CACNA2D4, SHMT1, GSTO2, IL1RAPL2, and SLC35F3 (Figure 5C). Afterward, the present study assessed

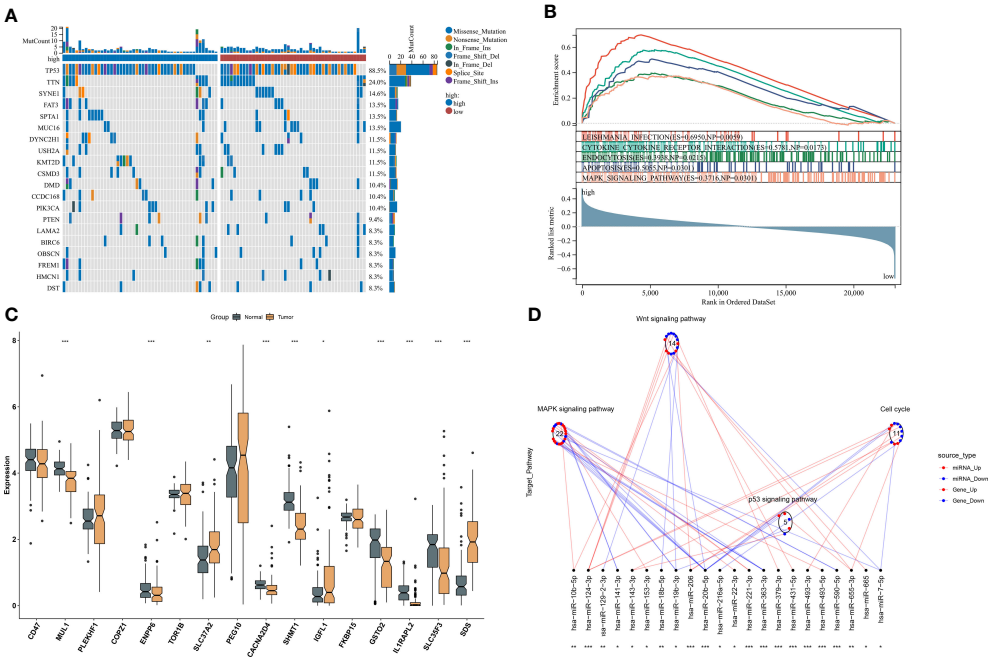

FIGURE 5
Ferroptosis-relevant risk score involved in somatic mutation and transcriptional and post-transcriptional mechanisms in TCGA-TNBC cohort. **(A)** Oncoplot for the somatic landscape of ferroptosis-relevant high- and low-risk patients. Genes are ranked by mutation frequency. **(B)** GSEA for the activity differences in KEGG pathways between groups. **(C)** Levels of the genes from ferroptosis-relevant risk score in TNBC and normal tissues. **(D)** Differences in miRNA-targeted signaling pathways between groups. Red dots denote miRNA-targeted genes that exhibit upregulation in the high-risk group, while blue dots denote miRNA-targeted genes that exhibit downregulation. Red lines indicate low expression of miRNAs in the high-risk group, while blue lines indicate highly expressed miRNAs in the low-risk group. The circle denotes a signaling pathway enriched by targeted genes. GSEA, gene set enrichment analysis; KEGG, Kyoto Encyclopedia of Genes and Genomes; TNBC, triple-negative breast cancer. *p < 0.05, **p < 0.01 and ***p < 0.001.

10.3389/fimmu.2022.985861

differences in miRNA expression between ferroptosis-relevant high- and low-risk groups in TCGA-TNBC dataset. A total of 84 miRNAs notably differentially expressed between groups were selected (Supplementary Table 4). Moreover, an enrichment analysis of their target genes was implemented. The miRNA target genes exhibited observable correlations to cell cycle, MAPK, Wnt, and p53 signaling pathways, which were differentially expressed between groups (Figure 5D), suggesting that the ferroptosis-relevant risk score might correlate to miRNA expression and signaling pathway activity. The survival significance of each gene in the ferroptosis-relevant risk score was assessed. In Figure 6, upregulated CACNA2D4, COPZ1, FKBP15, IGFL1, IL1RAPL2, MUL1, PLEKHF1, SDS, SLC37A2, and TOR1B were correlated to poorer OS outcomes, with opposite effects of CD47, ENPP6, GSTO2, PEG10, SHMT1, and SLC35F3 on OS.

Immunological traits and the immunotherapeutic response of distinct ferroptosis-relevant risk score groups

The activity of steps within the cancer-immunity cycle was computed, which may reflect an anti-tumor immune response. We observed that the ferroptosis-relevant risk score was positively linked to most steps (Figure 7A). In addition, this risk score displayed notably positive

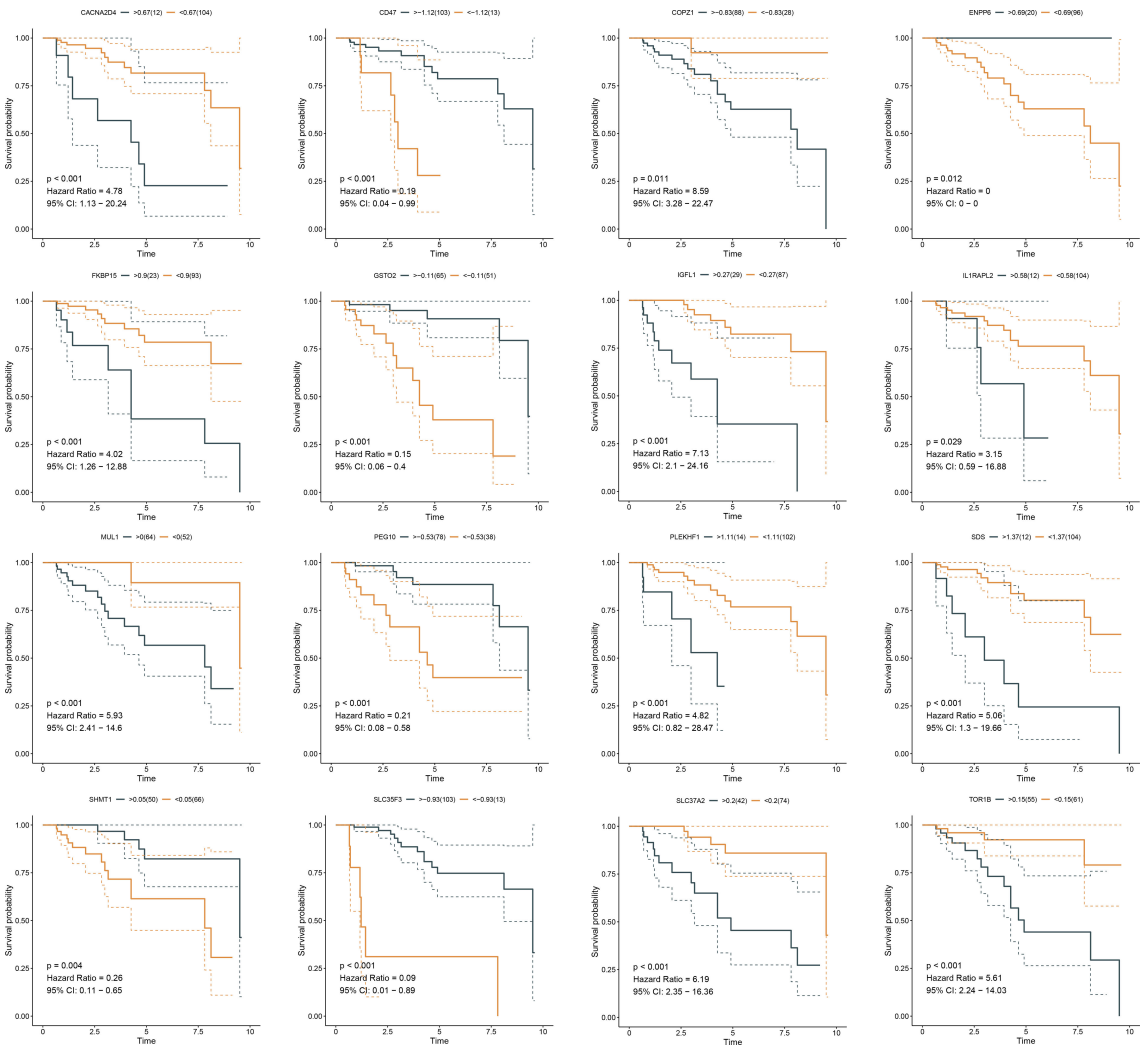

FIGURE 6
K-M curves exhibit OS outcomes in the high and low expression of genes from ferroptosis-relevant risk scores across TCGA-TNBC patients. K-M, Kaplan–Meier; OS, overall survival.

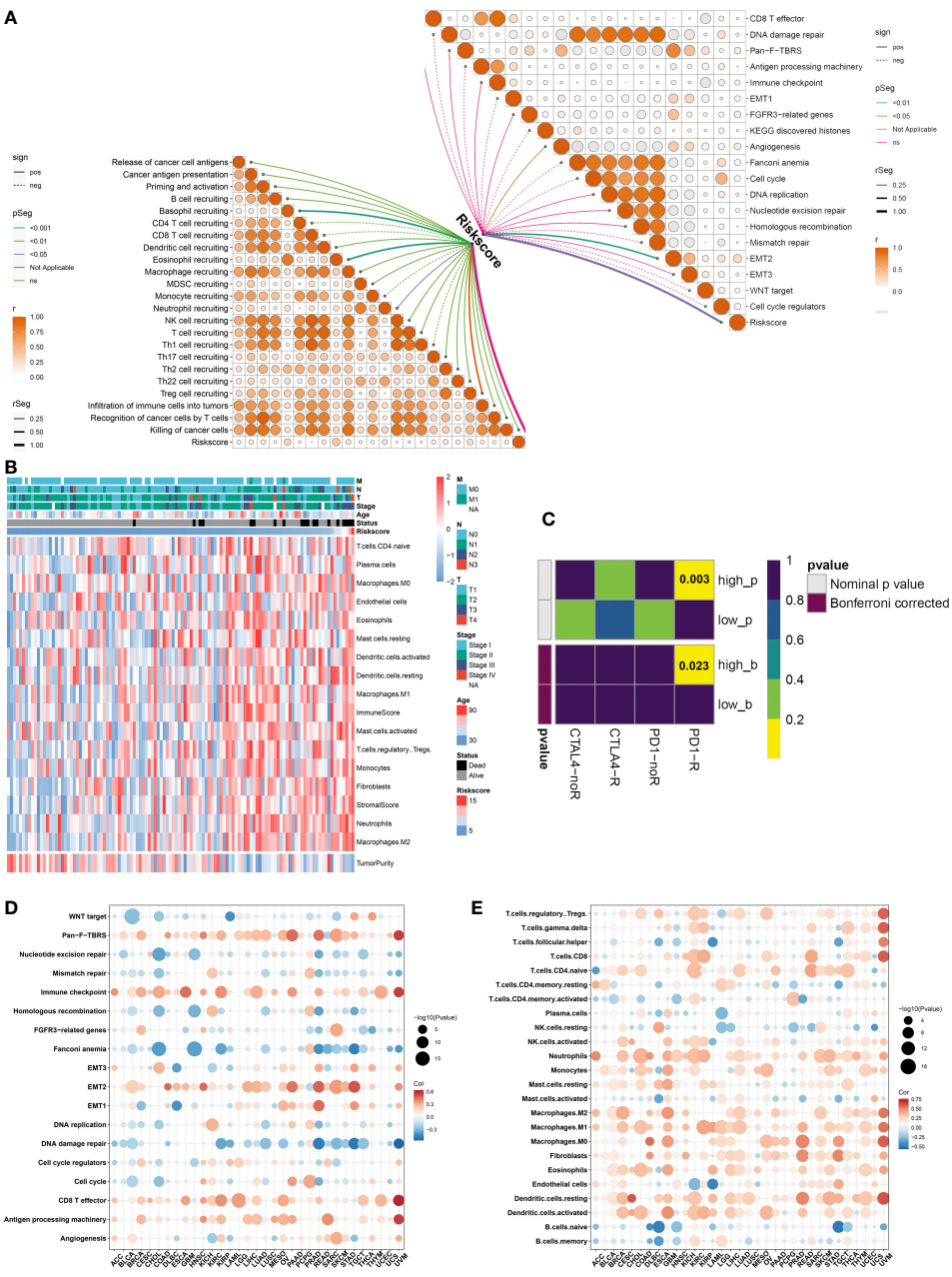

FIGURE 7
Immunological traits and immunotherapeutic response of distinct ferroptosis-relevant risk score groups. **(A)** Relationships between risk score and activity of each step within cancer-immunity cycle and known biological processes in TCGA-TNBC cohort. **(B)** Distribution of immune cell infiltrations, tumor purity, and immune and stromal scores across TCGA-TNBC patients. **(C)** Estimation of immunotherapeutic response of high- and low-risk TCGA-TNBC individuals through SubMap analysis. **(D, E)** Pan-cancer analysis of the relationships between risk score and activity of known biological processes and abundance of immune cell types. SubMap, Subclass Mapping.

interactions with angiogenesis and EMT2. A higher abundance of most immune cells, increased immune and stromal scores, and decreased tumor purity were observed in the high-risk group (Figure 7B). By adopting the SubMap algorithm, the therapeutic response of high- and low-risk cases was inferred. Consequently, high-risk cases possessed a higher possibility of benefitting from anti-PD-1 immunotherapy (Figure 7C).

Immune relevance of ferroptosis-relevant risk score across pan-cancer

Pan-cancer analysis was implemented to further elucidate the immune relevance of the ferroptosis-relevant risk score. This risk score exhibited generally positive relationships with the immune checkpoint, CD8 T effector, and antigen-processing machinery in most cancer types (Figure 7D). In addition, this risk score was positively linked to the abundance of most immune cell types across pan-cancer (Figure 7E). The above data demonstrated the crucial roles of the ferroptosis-relevant risk score in the tumor immune microenvironment across pan-cancer.

Potential therapeutic significance of ferroptosis-relevant gene signature

Estimated IC50 values of chemotherapy or targeted therapeutic agents were compared between ferroptosis-relevant high- and low-risk TNBC cases. Data showed that the low-risk group exhibited significantly lower IC50 of cisplatin, with significantly lower IC50 of sunitinib in the high-risk group (Figure 8A), indicating that low-risk cases had higher sensitivity to cisplatin, with higher sensitivity to sunitinib for high-risk cases. Potential small-molecule agents were predicted aiming at high-risk cases. As a result, two CTRP-derived agents (SNX-2112 and brefeldin A; Figure 8B) and PRISM-derived agents (MEK162, PD-0325901, PD-318088, Ro-4987655, and SAR131675; Figure 8C) were selected for high-risk patients.

Discussion

TNBC is the most aggressive subtype of breast carcinoma, with higher recurrent risk and mortality compared with other subtypes. Due to limited therapeutic options, it is urgently required for ascertaining therapeutic agents with a unique mode of action for surmounting current issues in TNBC therapy (31). Ferroptosis is an iron-dependent cell death form with the traits of accumulated reactive oxygen species together with lipid peroxidation products. Targeting ferroptosis is regarded as a novel anti-TNBC strategy (32). Inducing ferroptosis may sensitize TNBC cells to radiotherapy (33) and neoadjuvant chemotherapy, etc. (34). Nonetheless, FRGs have been rarely studied in patients with TNBC.

On the basis of the expression profiling of prognostic FRGs, a novel ferroptosis classification was proposed for TNBC. Each ferroptosis pattern possessed unique prognostic and immunological traits. Evidence demonstrates the interactions of ferroptosis with tumor immunity. For instance, the interplay between TNBC cells and macrophages modulates ferroptotic cell death, development, and chemoresistance of TNBC (35). Ferroptosis of cancer cells negatively affects antigen-presenting cells and impedes adaptive immune responses, thereby hindering ferroptosis-induced therapeutic application (36). The LASSO approach is a compressed estimate adopted for acquiring a refined model through building a penalty function, which enables to compress several coefficients and set several coefficients to 0 (37). Hence, this approach reserves the preponderance of gene subset choice with shrinkage and is a biased estimator that is appropriate for dealing with complex collinear data, thus helping select variables in parameter estimation for better solving the multicollinearity issue of regression analysis. Based on ferroptosis pattern-relevant genes, a robust ferroptosis scoring system in inferring TNBC survival was proposed. High- and low-risk groups exhibited diverse somatic mutation and transcriptional and post-transcriptional mechanisms. The activation of innate immunity and tumoral ferroptotic cell death may induce anti-PD-1/PD-L1 therapeutic resistance (38). High-risk cases were more likely to benefit from anti-PD-1 immunotherapy.

Neoadjuvant chemotherapy remains a crucial treatment option for patients with locally advanced TNBC, which lowers tumor burden, offers the opportunity for surgery and even breast conservation, and accelerates early evaluation of individual responses (34). Evidence demonstrates that patients achieving pathological complete responses (pCRs) following neoadjuvant chemotherapy have more favorable survival (39). Nevertheless, currently, pCRs remain in low proportions. Improving pCRs represents an important aim of neoadjuvant chemotherapy. Thus, early detection of cases with better responses to neoadjuvant chemotherapy has naturally become the major focus of TNBC therapy. The ferroptosis-relevant gene signature may infer the sensitivity of TNBC to cisplatin and sunitinib. Low-risk cases had higher sensitivity to cisplatin, and high-risk cases were more sensitive to sunitinib. Small-molecule agents exert crucial roles in cancer therapy, combining with specific target molecules in cells for playing specific functions. They have become the focus of research because of their potent specificity, prominent curative effect, and little damage to normal cells. We predicted two CTRP-derived agents (SNX-2112 and brefeldin A) and PRISM-derived agents (MEK162, PD-0325901, PD-318088, Ro-4987655, and SAR131675) for the treatment of high-risk patients.

In summary, our study reported the prognostic, molecular, immunological, and pharmacogenomic features linked to ferroptotic cell death in TNBC. As our awareness of ferroptosis continues to improve, we look forward to more research to unveil the potential mechanisms of ferroptosis in cancer.

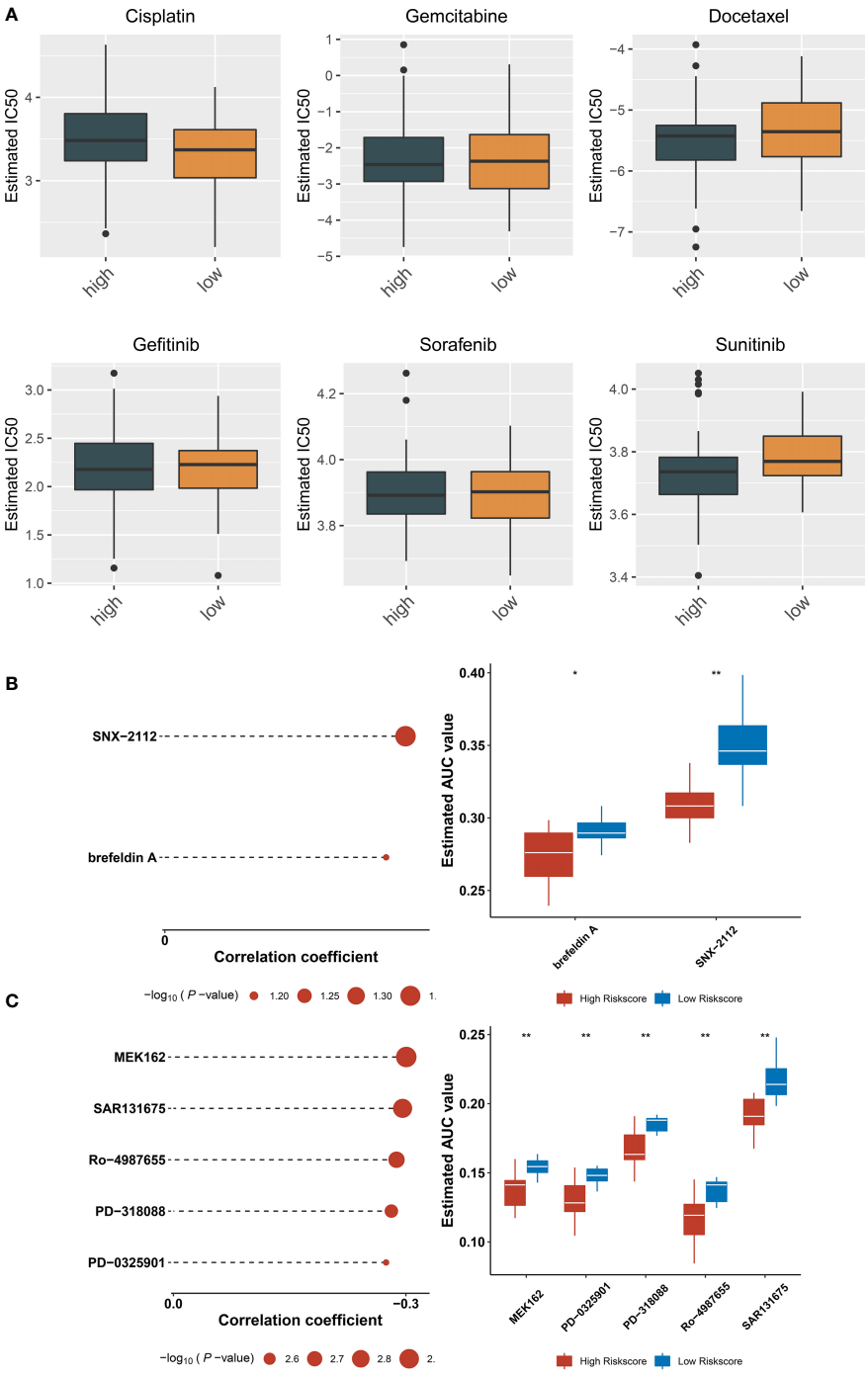

FIGURE 8
Potential therapeutic significance of ferroptosis-relevant gene signature in TCGA-TNBC cohort. **(A)** Comparison of IC50 values of chemotherapy or targeted therapeutic agents between ferroptosis-relevant high- and low-risk TNBC cases. **(B)** Association between CTRP-derived agents and ferroptosis-relevant risk score and comparison of AUC values of agents between groups. **(C)** Association between PRISM-derived agents and ferroptosis-relevant risk score and comparison of AUC values of agents between groups. TNBC, triple-negative breast cancer; CTRP, Cancer Therapeutics Response Portal; AUC, area under the curve. *p < 0.05, **p < 0.01.

Conclusion

Altogether, our findings proposed three disparate ferroptosis patterns across TNBC, which provided a novel insight into the relationships of ferroptosis with prognostic outcomes and immunological features. Additionally, a robust ferroptosis-relevant gene signature was exploited, which enabled us to precisely speculate survival and responses to immunotherapy, chemotherapy, and targeted therapies for TNBC individuals. Several small-molecule agents were also predicted based on ferroptosis-relevant gene signatures. Hence, this study provided a roadmap for patients' stratification and assisted in developing regimens for personalized treatment decisions and follow-up in TNBC.

Data availability statement

The original contributions presented in the study are included in the article/Supplementary Material. Further inquiries can be directed to the corresponding author.

Author contributions

KF conceived and designed the study. ZX and SJ conducted most of the experiments and data analysis, and wrote the manuscript. DT, CY, and YH participated in collecting data and helped to draft the manuscript. All authors contributed to the article and approved the submitted version.

Funding

The research was supported by a Ningxia Hui Autonomous Region Natural Science Foundation Project (2022AAC03748), Ningxia Hui Autonomous Region Natural Science Foundation Project (2021AAC03523), Basic research project of Yinchuan Maternal and Child Health Hospital (2022NYFYCX05).

Conflict of interest

The authors declare that the research was conducted in the absence of any commercial or financial relationships that could be construed as a potential conflict of interest.

Publisher's note

Supplementary material

The Supplementary Material for this article can be found online at: https://www.frontiersin.org/articles/10.3389/fimmu.2022.985861/full#supplementary-material

SUPPLEMENTARY FIGURE 1
Consensus clustering analysis of TCGA-TNBC samples. **(A)** Consensus cumulative distribution function (CDF) curve. **(B)** Relative alterations in the area under the CDF curve. **(C)** Tracking plot of sample classification.

SUPPLEMENTARY FIGURE 2
Verification of reproducibility of ferroptosis classification. **(A)** Heatmap illustrates the unique up-regulated markers in each ferroptosis pattern across TCGA-TNBC samples. **(B)** Sample clustering of the GSE58812 dataset through NTP algorithm based on the unique up-regulated markers. **(C)** K-M curves of OS among three clusters in the GSE58812 dataset. **(D)** Sample clustering of the METABRIC dataset with NTP algorithm on the basis of the unique up-regulated markers. **(E)** K-M curves of OS among three clusters in the METABRIC dataset.

SUPPLEMENTARY FIGURE 3
External validation of the robustness of ferroptosis-relevant gene signature. **(A)** Distribution of ferroptosis_score, survival status, and gene expression in the GSE58812 dataset. **(B)** K-M curves of OS between ferroptosis-relevant high- and low-risk groups in the GSE58812 dataset. **(C)** ROC curves at 1-, 3- and 5-year OS in the GSE58812 dataset. **(D)** Distribution of ferroptosis-relevant risk score, survival status, and gene expression in the METABRIC dataset. **(E)** K-M curves of OS between ferroptosis-relevant high- and low-risk groups in the METABRIC dataset. **(F)** ROC curves at 1-, 3- and 5-year OS in the METABRIC dataset.

SUPPLEMENTARY TABLE 1
The clinical information of TNBC patients from TCGA-TNBC, GSE58812, and METABRIC cohorts.

SUPPLEMENTARY TABLE 2
The list of ferroptosis-related genes.

SUPPLEMENTARY TABLE 3
Univariate cox regression results of ferroptosis pattern-relevant genes.

SUPPLEMENTARY TABLE 4
Differentially expressed miRNAs between ferroptosis-relevant high- and low-risk groups in the TCGA-TNBC dataset.

References

1. Sung H, Ferlay J, Siegel RL, Laversanne M, Soerjomataram I, Jemal A, et al. Global cancer statistics 2020: GLOBOCAN estimates of incidence and mortality worldwide for 36 cancers in 185 countries. *CA Cancer J Clin* (2021) 71(3):209–49. doi: 10.3322/caac.21660

2. Pan Y, He Y, Zhao X, Pan Y, Meng X, Lv Z, et al. Engineered red blood cell membrane-coating salidroside/indocyanine green nanovesicles for high-efficiency hypoxic targeting phototherapy of triple negative breast cancer. *Adv Healthc Mater* (2022) 11:e2200962. doi: 10.1002/adhm.202200962

3. Yamada A, Hayashi N, Kumamaru H, Nagahashi M, Usune S, Asaga S, et al. Prognostic impact of postoperative radiotherapy in patients with breast cancer and with pT1-2 and 1-3 lymph node metastases: A retrospective cohort study based on the Japanese breast cancer registry. *Eur J Cancer* (2022) 172:31–40. doi: 10.1016/j.ejca.2022.05.017

4. Lee JV, Housley F, Yau C, Nakagawa R, Winkler J, Anttila JM, et al. Combinatorial immunotherapies overcome MYC-driven immune evasion in triple negative breast cancer. *Nat Commun* (2022) 13(1):3671. doi: 10.1038/s41467-022-31238-y

5. Liao M, Qin R, Huang W, Zhu HP, Peng F, Han B, et al. Targeting regulated cell death (RCD) with small-molecule compounds in triple-negative breast cancer: a revisited perspective from molecular mechanisms to targeted therapies. *J Hematol Oncol* (2022) 15(1):44. doi: 10.1186/s13045-022-01260-0

6. Niu X, Chen L, Li Y, Hu Z, He F. Ferroptosis, necroptosis, and pyroptosis in the tumor microenvironment: Perspectives for immunotherapy of SCLC. *Semin Cancer Biol* (2022) 273–285. doi: 10.1016/j.semcancer.2022.03.009

7. Gao W, Wang X, Zhou Y, Wang X, Yu Y. Autophagy, ferroptosis, pyroptosis, and necroptosis in tumor immunotherapy. *Signal Transduct Target Ther* (2022) 7 (1):196. doi: 10.1038/s41392-022-01046-3

8. Kumar R, Mendonca J, Owoyemi O, Boyapati K, Thomas N, Kanacharoen S, et al. Supraphysiologic testosterone induces ferroptosis and activates immune pathways through nucleophagy in prostate cancer. *Cancer Res* (2021) 81 (23):5948–62. doi: 10.1158/0008-5472.Can-20-3607

9. Wang W, Green M, Choi JE, Gijón M, Kennedy PD, Johnson JK, et al. CD8 (+) T cells regulate tumour ferroptosis during cancer immunotherapy. *Nature* (2019) 569(7755):270–4. doi: 10.1038/s41586-019-1170-y

10. Hsieh CH, Hsieh HC, Shih FS, Wang PW, Yang LX, Shieh DB, et al. An innovative NRF2 nano-modulator induces lung cancer ferroptosis and elicits an immunostimulatory tumor microenvironment. *Theranostics* (2021) 11(14):7072–91. doi: 10.7150/thno.57803

11. Sui S, Xu S, Pang D. Emerging role of ferroptosis in breast cancer: New dawn for overcoming tumor progression. *Pharmacol Ther* (2022) 232:107992. doi: 10.1016/j.pharmthera.2021.107992

12. Jézéquel P, Loussouarn D, Guérin-Charbonnel C, Campion L, Vanier A, Gouraud W, et al. Gene-expression molecular subtyping of triple-negative breast cancer tumours: importance of immune response. *Breast Cancer Res* (2015) 17:43. doi: 10.1186/s13058-015-0550-y

13. Curtis C, Shah SP, Chin SF, Turashvili G, Rueda OM, Dunning MJ, et al. The genomic and transcriptomic architecture of 2,000 breast tumours reveals novel subgroups. *Nature* (2012) 486(7403):346–52. doi: 10.1038/nature10983

14. Ritchie ME, Phipson B, Wu D, Hu Y, Law CW, Shi W, et al. Limma powers differential expression analyses for RNA-sequencing and microarray studies. *Nucleic Acids Res* (2015) 43(7):e47. doi: 10.1093/nar/gkv007

15. Cerami E, Gao J, Dogrusoz U, Gross BE, Sumer SO, Aksoy BA, et al. The cBio cancer genomics portal: an open platform for exploring multidimensional cancer genomics data. *Cancer Discovery* (2012) 2(5):401–4. doi: 10.1158/2159-8290.Cd-12-0095

16. Zhang H, Meltzer P, Davis S. RCircos: an r package for circos 2D track plots. *BMC Bioinf* (2013) 14:244. doi: 10.1186/1471-2105-14-244

17. Mayakonda A, Lin DC, Assenov Y, Plass C, Koeffler HP. Maftools: efficient and comprehensive analysis of somatic variants in cancer. *Genome Res* (2018) 28 (11):1747–56. doi: 10.1101/gr.239244.118

18. Szklarczyk D, Gable AL, Nastou KC, Lyon D, Kirsch R, Pyysalo S, et al. The STRING database in 2021: customizable protein-protein networks, and functional characterization of user-uploaded gene/measurement sets. *Nucleic Acids Res* (2021) 49(D1):D605–d12. doi: 10.1093/nar/gkaa1074

19. Doncheva NT, Morris JH, Gorodkin J, Jensen LJ. Cytoscape StringApp: Network analysis and visualization of proteomics data. *J Proteome Res* (2019) 18 (2):623–32. doi: 10.1021/acs.jproteome.8b00702

20. Yu G, Wang LG, Han Y, He QY. clusterProfiler: an r package for comparing biological themes among gene clusters. *Omics* (2012) 16(5):284–7. doi: 10.1089/omi.2011.0118

21. Hänzelmann S, Castelo R, Guinney J. GSVA: gene set variation analysis for microarray and RNA-seq data. *BMC Bioinf* (2013) 14:7. doi: 10.1186/1471-2105-14-7

22. Subramanian A, Tamayo P, Mootha VK, Mukherjee S, Ebert BL, Gillette MA, et al. Gene set enrichment analysis: a knowledge-based approach for interpreting genome-wide expression profiles. *Proc Natl Acad Sci U.S.A.* (2005) 102(43):15545–50. doi: 10.1073/pnas.0506580102

23. Wilkerson MD, Hayes DN. ConsensusClusterPlus: a class discovery tool with confidence assessments and item tracking. *Bioinformatics* (2010) 26 (12):1572–3. doi: 10.1093/bioinformatics/btq170

24. Yoshihara K, Shahmoradgoli M, Martínez E, Vegesna R, Kim H, Torres-Garcia W, et al. Inferring tumour purity and stromal and immune cell admixture from expression data. *Nat Commun* (2013) 4:2612. doi: 10.1038/ncomms3612

25. Chen DS, Mellman I. Elements of cancer immunity and the cancer-immune set point. *Nature* (2017) 541(7637):321–30. doi: 10.1038/nature21349

26. Langfelder P, Horvath S. WGCNA: an r package for weighted correlation network analysis. *BMC Bioinf* (2008) 9:559. doi: 10.1186/1471-2105-9-559

27. Hoshida Y, Brunet JP, Tamayo P, Golub TR, Mesirov JP. Subclass mapping: identifying common subtypes in independent disease data sets. *PloS One* (2007) 2 (11):e1195. doi: 10.1371/journal.pone.0001195

28. Yang W, Soares J, Greninger P, Edelman EJ, Lightfoot H, Forbes S, et al. Genomics of drug sensitivity in cancer (GDSC): a resource for therapeutic biomarker discovery in cancer cells. *Nucleic Acids Res* (2013) 41(Database issue): D955–61. doi: 10.1093/nar/gks1111

29. Geeleher P, Cox N, Huang RS. pRRophetic: an r package for prediction of clinical chemotherapeutic response from tumor gene expression levels. *PloS One* (2014) 9(9):e107468. doi: 10.1371/journal.pone.0107468

30. Ghandi M, Huang FW, Jané-Valbuena J, Kryukov GV, Lo CC, McDonald ER3rd, et al. Next-generation characterization of the cancer cell line encyclopedia. *Nature* (2019) 569(7757):503–8. doi: 10.1038/s41586-019-1186-3

31. Ding Y, Chen X, Liu C, Ge W, Wang Q, Hao X, et al. Identification of a small molecule as inducer of ferroptosis and apoptosis through ubiquitination of GPX4 in triple negative breast cancer cells. *J Hematol Oncol* (2021) 14(1):19. doi: 10.1186/s13045-020-01016-8

32. Yang J, Zhou Y, Xie S, Wang J, Li Z, Chen L, et al. Metformin induces ferroptosis by inhibiting UFMylation of SLC7A11 in breast cancer. *J Exp Clin Cancer Res* (2021) 40(1):206. doi: 10.1186/s13046-021-02012-7

33. Zhang Z, Lu M, Chen C, Tong X, Li Y, Yang K, et al. Holo-lactoferrin: the link between ferroptosis and radiotherapy in triple-negative breast cancer. *Theranostics* (2021) 11(7):3167–82. doi: 10.7150/thno.52028

34. Sha R, Xu Y, Yuan C, Sheng X, Wu Z, Peng J, et al. Predictive and prognostic impact of ferroptosis-related genes ACSL4 and GPX4 on breast cancer treated with neoadjuvant chemotherapy. *EBioMedicine* (2021) 71:103560. doi: 10.1016/j.ebiom.2021.103560

35. Li H, Yang P, Wang J, Zhang J, Ma Q, Jiang Y, et al. HLF regulates ferroptosis, development and chemoresistance of triple-negative breast cancer by activating tumor cell-macrophage crosstalk. *J Hematol Oncol* (2022) 15(1):2. doi: 10.1186/s13045-021-01223-x

36. Wiernicki B, Maschalidi S, Pinney J, Adjemian S, Vanden Berghe T, Ravichandran KS, et al. Cancer cells dying from ferroptosis impede dendritic cell-mediated anti-tumor immunity. *Nat Commun* (2022) 13(1):3676. doi: 10.1038/s41467-022-31218-2

37. Chen L, Niu X, Qiao X, Liu S, Ma H, Shi X, et al. Characterization of interplay between autophagy and ferroptosis and their synergistical roles on manipulating immunological tumor microenvironment in squamous cell carcinomas. *Front Immunol* (2021) 12:739039. doi: 10.3389/fimmu.2021.739039

38. Jiang Z, Lim SO, Yan M, Hsu JL, Yao J, Wei Y, et al. TYRO3 induces anti-PD-1/PD-L1 therapy resistance by limiting innate immunity and tumoral ferroptosis. *J Clin Invest* (2021) 131(8):e139434. doi: 10.1172/jci139434

39. Cortazar P, Zhang L, Untch M, Mehta K, Costantino JP, Wolmark N, et al. Pathological complete response and long-term clinical benefit in breast cancer: the CTNeoBC pooled analysis. *Lancet* (2014) 384(9938):164–72. doi: 10.1016/s0140-6736(13)62422-8

frontiers | Frontiers in Oncology

TYPE Original Research
PUBLISHED 02 December 2022
DOI 10.3389/fonc.2022.1058894

OPEN ACCESS

EDITED BY
Julie Decock,
Qatar Biomedical Research Institute,
Qatar

REVIEWED BY
Roberta Castriconi,
Università di Genova,
Italy
Frank M. Cichocki,
University of Minnesota Twin Cities,
United States

*CORRESPONDENCE
Victor H. Engelhard
vhe@virginia.edu

†These authors have contributed equally to this work

SPECIALTY SECTION
This article was submitted to Cancer Immunity and Immunotherapy, a section of the journal Frontiers in Oncology

RECEIVED 30 September 2022
ACCEPTED 15 November 2022
PUBLISHED 02 December 2022

CITATION
Lindsay RS, Melssen MM, Stasiak K, Annis JL, Woods AN, Rodriguez AB, Brown MG and Engelhard VH (2022) NK cells reduce anergic T cell development in early-stage tumors by promoting myeloid cell maturation. *Front. Oncol.* 12:1058894. doi: 10.3389/fonc.2022.1058894

NK cells reduce anergic T cell development in early-stage tumors by promoting myeloid cell maturation

Robin S. Lindsay[1,2], Marit M. Melssen[1,2†], Katarzyna Stasiak[1,2†], Jessica L. Annis[1,2], Amber N. Woods[1,2], Anthony B. Rodriguez[1,2], Michael G. Brown[1,2,3] and Victor H. Engelhard[1,2*]

[1]Beirne B. Carter Center for Immunology Research, University of Virginia School of Medicine, Charlottesville, VA, United States, [2]Department of Microbiology, Immunology and Cancer Biology, University of Virginia School of Medicine, Charlottesville, VA, United States, [3]Division of Nephrology, Department of Medicine, University of Virginia School of Medicine, Charlottesville, VA, United States

Introduction: Studies of NK cells in tumors have primarily focused on their direct actions towards tumor cells. We evaluated the impact of NK cells on expression of homing receptor ligands on tumor vasculature, intratumoral T cell number and function, and T cell activation in tumor draining lymph node.

Methods: Using an implantable mouse model of melanoma, T cell responses and homing receptor ligand expression on the vasculature were evaluated with and without NK cells present during the early stages of the tumor response by flow cytometry.

Results: NK cells in early-stage tumors are one source of IFNγ that augments homing receptor ligand expression. More significantly, NK cell depletion resulted in increased numbers of intratumoral T cells with an anergic phenotype. Anergic T cell development in tumor draining lymph node was associated with increased T-cell receptor signaling but decreased proliferation and effector cell activity, and an incomplete maturation phenotype of antigen presenting cells. These effects of NK depletion were similar to those of blocking CD40L stimulation.

Discussion: We conclude that an important function of NK cells is to drive proper APC maturation *via* CD40L during responses to early-stage tumors, reducing development of anergic T cells. The reduced development of anergic T cells resulting in improved tumor control and T cell responses when NK cells were present.

KEYWORDS

natural killer (Nk) cell, anergic T cells, CD40L blockade, antigen presenting cell (APC), B16 melanoma

Introduction

It has been shown that the adaptive immune system generates anti-tumor responses, particularly T cell responses, that delay tumor growth. The level of T cell infiltrate in tumors is associated with enhanced 5-year survival times (1). Additionally, clinical responses to immunotherapies correlate with the size of the T cell infiltrate in tumors prior to therapy (2, 3) suggesting that the magnitude and quality of the immune response prior to therapy is an important determinant of responsiveness to future therapy. However, the size and quality of the T cell infiltrate in tumors can be determined by many factors.

One key factor is entry into the tumor, which requires expression of appropriate homing receptors (HR) on T cells and homing receptor ligands (HRL) on tumor vasculature (4–7). VCAM-1, ICAM-1, and CXCL9 are key HRL for infiltration of $CD8^+$ T cells in several tumor models (8–10). We also previously established that in late-stage (>14 days) B16 melanoma tumors, expression of these HRL depends on IFNγ produced by $CD8^+$ T cells (9). However, it is unclear what induces HRL expression to promote the initial infiltration of these $CD8^+$ T cells in early-stage tumors. An interesting possibility is that this is due to innate immune cells that produce inflammatory cytokines, including IFNγ, and are present in the tissue prior to tumor formation.

A second factor is the effectiveness of T cell priming in the tumor draining lymph nodes (TDLN). This is dictated by the number and quality of antigens expressed by tumors, how much antigen arrives in the draining lymph node (LN) by direct drainage or transport by migrating dendritic cells (DC), and the maturation state of the antigen presenting DC (11, 12). It has been well-established that the maturation state of DC in tumors is suboptimal and/or immunosuppressive (12–15). This can arise as a consequence of different factors in the tumor microenvironment (TME), including immunosuppressive cells ($CD4^+$ T regulatory cells, myeloid derived suppressor cells, fibroblasts, tumor cells), cytokines such as TGFβ and VEGF, and hypoxia (16).

An interesting and relatively unexplored area is the contribution that NK cells make to the size or quality of the T cell infiltrate in tumors. Studies of NK cell function in tumors have largely focused on their direct actions towards tumor cells. Although tumor cell killing and inflammatory cytokine secretion by NK cells play a role in containing metastatic spread (17–20), NK cells rarely play a significant role in determining the growth rate of primary tumor (21, 22) as they are often dysfunctional in advanced tumors (21, 23) due at least partially to the TME (24). It has been hypothesized that NK cells promote the availability of tumor antigen by killing tumor cells (25, 26). This is supported by observations that functional NK cells can promote DC maturation in murine *in vitro* systems and infection models (27, 28), and in human *in vitro* systems (29, 30) and promote initiation of immune responses through DC crosstalk (31). Recent studies have also demonstrated that NK cells promote larger numbers of DC in tumors (3, 32). NK cells have also been shown to be in close proximity to DCs in murine (3) and human (33) tumors, suggesting possible interactions. However it is also possible that NK cells limit anti-tumor immune responses through their well-established killing of T cells (34, 35) and antigen presenting cells (36). Given these differing NK cell effects on T cell immunity, it is unclear what effect they would have on T cell priming in TDLN and T cell activity over the course of tumor outgrowth.

In the present work, we evaluated the impact of NK cells on HRL expression on tumor vasculature, intratumoral T cell number and activity, and T cell priming and DC maturation in TDLN. Considering the possible loss of NK function over time, we focused our work on tumors harvested 7 days after implantation, the earliest reliable point at which we could locate them. Our results establish that NK cells promote DC maturation and improved quality of T cell activation in TDLN, and their absence leads to an increased number of dysfunctional tumor infiltrating lymphocytes (TIL) that fail to persist. These results illuminate a novel aspect of NK cell function in early-stage tumors.

Materials and methods

Mice

C57BL/6 mice were from Charles River/NCI. Nur77-GFP reporter (C57BL/6-Tg(Nr4a1-EGFP/cre)820^{Khog}/J) (37), OT-I transgenic (C57BL/6-Tg(TcraTcrb)1100^{Mjb}/J) (38), Thy1.1 congenic mice (B6.PL-$Thy1^a$/CyJ) (39), $Rag1^{ko}$ mice (B6.$Rag1^{em10Lutzy}$) and $Perforin^{ko}$ (C57BL/6-Prf1tm1Sdz/J) (40) mice, all from Jackson Laboratories, were bred and maintained in a pathogen-free facility at the University of Virginia. Six to 12-week-old Nur77-GFP x (OT-I x Thy1.1) F1 mice were the source of mice expressing OT-$I^+$$Thy1.1^+$Nur77-$GFP^+$ cells used for adoptive transfer. All procedures were approved by the University of Virginia Animal Care and Use Committee in accordance with the NIH Guide for Care and Use of Laboratory Animals.

Cell lines

B16-F1 cells transfected to express cytoplasmic ovalbumin (ova) have been described (41). Ova-transfected B16-F1 (B16-ova) were cultured in RPMI-1640 (Corning) supplemented with 5% FBS (Sigma), 15 mM HEPES and 2 mM L-glutamine (both from Gibco). Blasticidin (10μg/ml) (Gibco) was added to maintain ova expression in B16-ova. Cells were authenticated by visual confirmation of melanin pigment production *in vitro*

and *in vivo*, and OVA expression confirmed by staining with the H-2K^{b}+ova peptide specific antibody 25-D1.16. Where indicated, B16-ova cells were transduced to express the fluorescent protein IRFP720 (42). All cultured cells injected into mice were within 2–8 passages after thaw and mycoplasma free.

Tumor implantation

B16-ova cells (4×10^{5}) in 200 µL phosphate-buffered saline (PBS) were injected subcutaneously (SC) in the neck scruff. Where indicated B16-ova cells were transduced with IRFP720 fluorescent protein to enable tumor cell identification prior to implantation. Mice were monitored for weight loss, signs of distress and tumor size every 2–3 days. Where indicated, mice were injected intraperitoneally (IP) daily with 5 µg/mL FTY720 (Novartis) or saline control for indicated periods of time during tumor growth. Where indicated mice were treated IP with 250 µg Brefeldin A (Sigma) 4–6 hours prior to harvest. At the time of harvest mice were euthanized and tumor, TDLN, NDLN, and/or spleen were collected and processed as outlined below.

Isolation of CD45^{+} and CD31^{+} tumor infiltrating cells

B16-ova tumors from C57BL/6 or Perforin^{ko} mice were harvested in RPMI-1640 (Corning) supplemented with 2% FBS, 0.05 mM β-mercaptoethanol, 40 µg/mL DNase (all from Sigma), 15 mM HEPES, 2 mM L-glutamine, 10 mM sodium pyruvate, 1X essential and non-essential amino acids, gentamicin (1 µg/mL) (all from Gibco), and liberase^{TM} (76 µg/mL) (Roche). Tumors were digested for 15 min at 37°C, manually homogenized, and filtered through 70 µm mesh (Miltenyi) to prepare single cell suspensions. The CD45^{+} fraction was enriched with CD45 MicroBeads mouse (Miltenyi) using an AutoMACS instrument and analyzed by flow cytometry. Fractions with CD45^{+} cells removed were stained for CD31^{+} cells in selected experiments or a second enrichment was performed using CD31 MicroBeads (Miltenyi).

T cell *ex vivo* restimulation assay

B16-ova tumors from C57BL/6 mice were harvested and CD8^{+} cells isolated using MACS beads (Miltenyi) as described above. Cells were stimulated with CD3/CD28 T activator beads (10 µL/mL, Gibco) for 12 hours in the presence of anti-CD107a antibody (AF488, Biolegend) to mark degranulating cells. Brefeldin A (10 µg/mL) was added during the last 4-6 hours of culture to block secretion of intracellular cytokines.

Isolation of single cells from LN and spleen

LN were manually shredded using needles, and spleens were cut up manually with scissors. Tissue suspensions were digested using liberase^{TM} (76 µg/mL) for 30 min at 37°C and then manually homogenized and filtered through 70 µm mesh (Miltenyi) prior to staining and analysis by flow cytometry.

Nur77-GFP reporter adoptive cell transfers

Single-cell suspensions of splenocytes from naïve Nur77-GFP^{+}OT-I^{+}Thy1.1^{+} mice were prepared smashing spleens between frosted glass slides and filtering cells through a 100 µm filter. Red blood cells were lysed using RBC lysis buffer (Invitrogen). Cells were washed twice, resuspended in PBS, and immediately injected IV ($5x10^{4}$) into Thy1.2^{+} C57BL/6 mice. The next day, recipient mice were implanted SC with B16-ova cells. Seven days post tumor implantation spleen, TDLN, and tumor were isolated and single cell suspensions prepared as described above.

NK cell depletion

Starting 2 days prior to tumor implantation NK cells were depleted by injection of 100 µg anti-NK1.1 (BioXcell) or isotype control (BioXcell) antibody IP into mice. Injections were repeated every 3 days until tumors were harvested. Depletion was confirmed in all mice used for analysis by flow cytometry (example tumor depletion shown in Supplementary Figures 2A–E).

PD-1 blockade

Starting on D3 post tumor implantation 200 µg of anti-PD-1 blocking antibody (BioXcell) or isotype control (BioXcell) was injected IP into tumor bearing mice with or without NK cell depletion. Injections were repeated every 3 days until tumors were harvested.

CD40L blockade

Mice were injected IP on D3 and D5 post tumor injection with 250 µg anti-CD40L blocking antibody (BioXcell) or an isotype control antibody (BioXcell) in 200 µl of PBS.

Flow cytometry

Cells were Fc blocked with 1:1000 anti-CD16/CD32 (2.4G2, BioXcell) and stained with Live/Dead Fixable Aqua (Life Technologies) in PBS for 20 min at 4°C. Subsequently cells were stained with fluorescently labeled antibodies in PBS supplemented with 2% FBS and 0.1% sodium azide for 30 min at 4°C. For extracellular stains only, cells were fixed in 2% paraformaldehyde (Thermo Scientific) for 10 min at 4°C. For intracellular and intranuclear stains, BD Cytofix/Cytoperm and BD Transcription Factor Staining kits were used according to manufacturer's protocol. Data was acquired on Cytoflex (Beckman Coulter) or Attune (BD Biosciences) flow cytometers and analyzed using FlowJo software. In experiments that analyzed Nur77 expression, cells were directly analyzed without fixation. OT-I $CD3^+$ $CD8^+$ T cells were subsequently gated on $Thy1.1^+$ before assessing Nur77 experiments. Normalized MFI values were generated on positive cells by dividing all values generated that day by the average of the isotype control group.

Annexin V staining

Following extracellular staining, cells were stained with Annexin V-APC in Annexin buffer (Biolegend). Cells were immediately run on the cytometer while still in the buffer.

Dextramer staining

Single cell suspensions from tumors or LN were incubated with SIINFEKL-Dextramer or irrelevant dextramer control (Immudex) for 1 h at 37°C. Cells were subsequently stained for other surface or intracellular markers as described above.

Statistical analysis

Data is displayed as mean with error bars representing SEM. Groups were compared using a one-way ANOVA with Tukey's multiple comparisons test or a Students T test with Welch's correction for comparisons only involving two groups. All analysis and graphs were performed using PRISM software (Graphpad).

Results

Early-stage tumors contain $CD31^+$ endothelial cells expressing high levels of HRL and significant T cell infiltrates

To examine differences in early-stage and late-stage TME, we used flow cytometry of single cell suspensions to compare subcutaneous B16-ova tumors on day 7 (D7), the earliest time at which we could consistently locate them, to day 14 (D14) tumors. While the total number of $CD31^+$ tumor vascular endothelial cells was higher in D14 tumors (Figure 1A), the numbers per g of tumor were similar on both days (Figure 1B), indicating that early-stage tumors are well-vascularized. The number and percentage of $CD31^+$ cells expressing ICAM-1 was unchanged between D7 and D14, but VCAM-1 and CXCL9 (gating shown in Supplementary Figure 1A) were expressed by a higher number (Figures 1B, C) and percentage (Figures 1D, E) of these cells on D7, albeit at a similar mean fluorescence intensity (MFI) (Figure 1F). This suggests that effector T cells should be readily able to enter D7 tumors. Indeed, T cell infiltrates were evident, but the numbers per g of tumor were 46% lower for $CD4^+$ cells and 65% lower for $CD8^+$ cells on D7 than D14 (Figure 1G). This is consistent with the possibility that cells other than T cells might upregulate the expression of HRL, particularly VCAM-1 and CXCL9, on early-stage tumor endothelial cells.

Functional NK cells in early-stage tumors promote HRL expression on $CD31^+$ endothelial cells but diminish intratumoral T cell number

In contrast to T cells, we found that NK cells, and $CD11c^+$MHC-II^+, $CD11c^{neg}CD11b^+MHCII^+$, and $CD11c^{neg}CD11b^+MHCII^{neg}$ myeloid cells (gating shown in Supplementary Figure 1B), were present at similar levels per g of tumor at all stages of tumor growth (Figures 1H, I). Innate immune cells can express inflammatory cytokines that upregulate HRL expression, and our previous work implicated IFNγ in controlling expression of both VCAM-1 and CXCL9 (9). To determine if the intratumoral innate cells produced IFNγ, mice were treated with Brefelden A (BFA) prior to tumor harvest. While no myeloid subpopulations in D7 tumors expressed IFNγ directly *ex vivo* (Figure 1J), NK cells in D7 tumors did do so, although this was lost by D14 (Figure 1K, gating shown in Supplementary Figure 1C). We found that B16-ova cells did not express any NK cell ligands (Figure 1L). However, small fractions of B16-ova cells in D7 tumors expressed the NK activating NKG2D ligands Rae1 and H60 and some also upregulated MHCI, an inhibitory ligand for NK cells (Figure 1L). Together these data suggest that the production of IFNγ by NK cells in early-stage tumors is driven by B16-ova tumor cells. Overall, this suggests that IFNγ produced by NK cells increases HRL expression on $CD31^+$ tumor vasculature and promotes T cell infiltration in early-stage tumors.

To test this hypothesis, we depleted NK cells by injection of anti-NK1.1 prior to tumor implantation and maintained depletion with additional injections for the duration of the experiment (Supplementary Figures 2A–E). The fractions of $CD31^+$ cells that expressed ICAM-1 and VCAM-1 were

unchanged by NK cell depletion (Figure 2A), but the expression levels on positive cells were modestly but significantly lower (Figure 2B). Thus, NK cells augment HRL expression on CD31$^+$ early-stage tumor vasculature but are not the only cells responsible. However, despite this reduced HRL expression, the numbers of CD8$^+$ T cells per g of tumor in NK-depleted D7 tumors were significantly increased, and those of CD4$^+$ T cells were trending toward an increase (Figure 2C), while APC and myeloid populations were unchanged (Figure 2D). This was not due to changes in tumor weight as NK cell depletion did not significantly alter tumor weights (Figure 2E). Approximately 80% of CD8$^+$ T cells in D7 tumors were antigen experienced (CD44$^+$) and consisted of CD62L^{neg} effector cells and CD62L$^+$ cells that had either not yet downregulated CD62L after activation or were central memory (Figure 2F, gating shown in Supplementary Figure 2F). CD44^{neg} CD62L$^+$ naïve cells and CD44^{neg} CD62L^{neg} early activated cells were present at lower levels. The distribution of these intratumoral CD8$^+$ T cell subpopulations was unchanged by NK depletion (Figure 2F). This demonstrates that NK cells, despite increasing HRL expression on D7 tumor vasculature, mediate an unexpected reduction in intratumoral CD8$^+$ T cells.

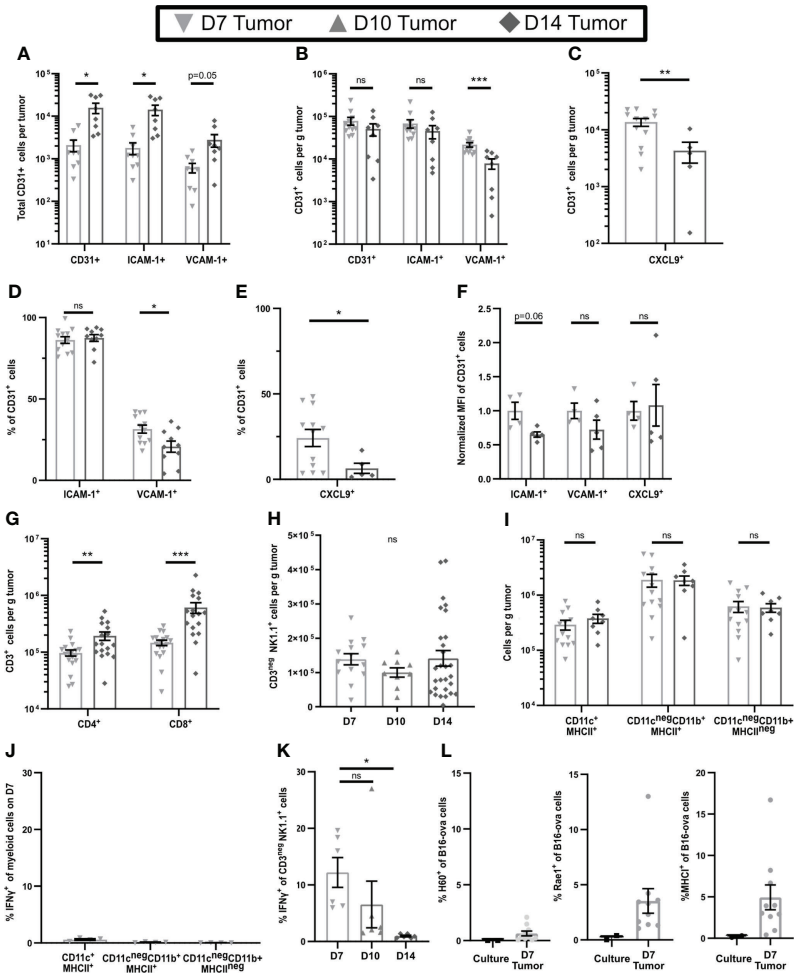

FIGURE 1
Early-stage tumors have high levels of endothelial HRL expression, substantial innate immune cell infiltrates, and functional NK cells. B16-ova tumors **(A–K)**, or B16-ova expressing IRFP720 to identify tumor cells **(L)**, were implanted into WT B6 mice and harvested on D7, D10, or D14. Single cell suspensions were enriched for CD45$^+$ cells using MACS Beads and the CD45^{neg} **(A–F, L)** or CD45$^+$ **(G–K)** fractions were analyzed by flow cytometry. **(J, K)** Mice were treated with BFA for cytokine analysis 4-6 hours prior to tumor harvest. **(L)** B16-ova cells expressing IRFP720 fluorescent protein were analyzed by flow cytometry directly from culture prior to implantation and on D7. Data points represent a single tumor and mean per group with error bars representing SEM. Data are from: **(A, B)** 2 experiments; **(C, E)** 1-3 experiments; **(D)** 3 experiments; **(F)** 1 experiment; **(G)** 3-5 experiments; **(H)** 2-6 experiments; **(I)** 2-3 experiments; **(J)** 1 experiment; **(K)** 2 experiments; **(L)** 3 experiments. Statistics: **(A–G, I)** Unpaired Student's T test with Welch's correction; **(H, J, K)** One-way Anova with Tukey's posttest. *p < 0.05; **p < 0.01; ***p < 0.001; ns, not significant.

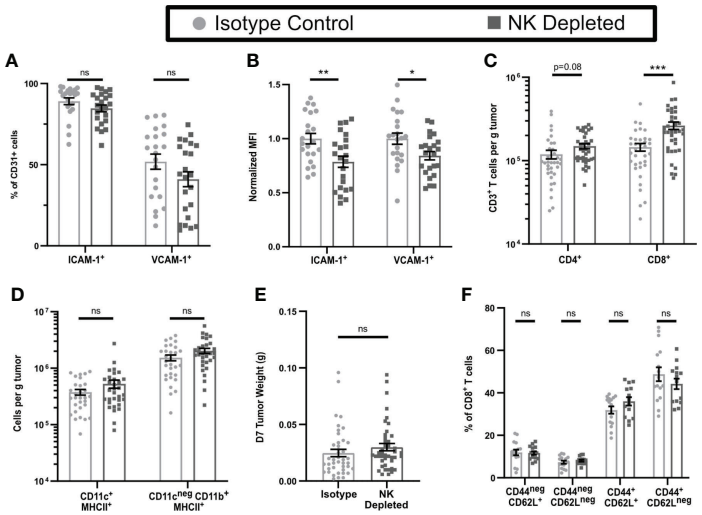

FIGURE 2
Early-stage tumors from mice lacking NK cells have reduced endothelial HRL expression but increased numbers of CD8$^+$ T cells. B16-ova tumors were implanted into WT B6 mice treated with isotype control or anti-NK1.1 depleting antibodies on D-2, D1, and D4, and harvested on D7. Single cell suspensions were enriched for CD45$^+$ cells using MACS Beads and the CD45^{neg} **(A, B)** or CD45$^+$ **(C–F)** fractions were analyzed by flow cytometry. Data points represent a single tumor and mean per group with error bars representing SEM. Data are from: **(A, B)** 4 experiments; **(C)** 7 experiments; **(D)** 6 experiments; **(E)** 9 experiments; **(F)** 4 experiments. Statistics: Unpaired Student's T test with Welch's correction. *p < 0.05; **p < 0.01; ***p < 0.001; ns, not significant.

Antigen-experienced T cells in tumors from NK depleted mice show deficient effector function but are not exhausted

To test the functionality of the antigen-experienced CD8$^+$ T cells in NK-depleted D7 tumors, we examined cytokine production after *in vivo* BFA blockade. In tumors containing NK cells, ~10% of CD8$^+$ T cells produced IFNγ, while only ~5% in tumors from NK-depleted mice did so (Figure 3A gating shown in Supplementary Figure 3A). However, the numbers of IFNγ producing cells per g were the same in both tumors, and there were more than twice as many cells per g not producing IFNγ in NK-depleted tumors (Figure 3B). The majority of IFNγ$^+$ cells were CD44$^+$CD62L^{neg} and were similar per g tumor in isotype and NK depleted mice (Figure 3C). A small portion of IFNγ$^+$ cells were CD44$^+$CD62L$^+$ and these were increased in NK depleted tumors (Figure 3C). The increase in IFNγ^{neg} CD8$^+$ T cells per g in NK-depleted tumors was statistically significant in all subpopulations, but the majority of the increase was in CD44$^+$ antigen-experienced CD8$^+$ T cells (Figure 3D). To determine if this effector deficiency was due to the TME or intrinsic to the T cells, we isolated CD8$^+$ T cells from D7 tumors and re-stimulated them *ex vivo* with anti-CD3 and anti-CD28. All T cells became CD44$^+$ following this restimulation. However, a smaller percentage of restimulated CD8$^+$ T cells from tumors of NK-depleted mice produced IFNγ compared to restimulated CD8$^+$ T cells from tumors of normal mice, and this was evident only in the CD62L^{neg} population (Figure 3E). The percentage of cells showing degranulation marked by CD107a was also decreased in restimulated CD62L^{neg} T cells from tumors of NK-depleted mice (Figure 3E, gating shown in Supplementary Figure 3B), demonstrating that the effector function deficiency is generalized. Thus, depletion of NK cells selectively increases the accumulation in early-stage tumors of antigen-experienced CD8$^+$ T cells that intrinsically lack at least one effector function.

One common mechanism leading to intrinsic T cell dysfunction in tumors is exhaustion, characterized by increased expression of inhibitory molecules, including PD-1. However, the percentages and numbers per g of PD-1$^+$ CD8$^+$ T cells in early-stage tumors of mice containing or lacking NK cells were not significantly different (Figure 3F). To determine whether PD-1 was blocking T cells that might have otherwise expressed IFNγ, we treated mice containing or lacking NK cells with anti-PD-1 starting on D3 after tumor implantation and harvested on D7. There was no significant increase in total CD8$^+$ T cells or IFNγ$^+$ CD8$^+$ T cells per g of tumor as a consequence of anti-PD-1 treatment in mice containing or lacking NK cells (Figures 3G, H). These results suggest that the increase in non-functional CD8$^+$ T cells in tumors from NK depleted mice is not due to PD-1 mediated exhaustion.

Recent studies have identified an exhausted stem-cell-like T cell progenitor population with a SLAMF6^{Hi}TCF7$^+$ phenotype (43). Cells with this phenotype comprised ~13% of the total CD8$^+$ TIL (Figure 3I, gating shown in Supplementary Figure 3C).

However, there was no difference in the percentage or numbers of SLAMF6^{Hi}TCF7^{+} CD8^{+} T cells in D7 tumors from mice containing or lacking NK cells (Figure 3I). This population was also not increased following anti-PD-1 treatment. These results suggest that NK depletion does not influence the development of SLAMF6^{Hi}TCF7^{+} T cell progenitors, and that the population that is increased in D7 tumors of NK-depleted mice is therefore non-progenitor.

CD8^{+} T cells in early-stage tumors from NK-depleted mice are more likely to become anergic

Anergic CD4^{+} and CD8^{+} T cells show reduced responses to TCR engagement and lack resulting effector functions (44–46). While T cell effector cytokine production and proliferation are often linked, anergic T cells continue to proliferate (47–49). To evaluate

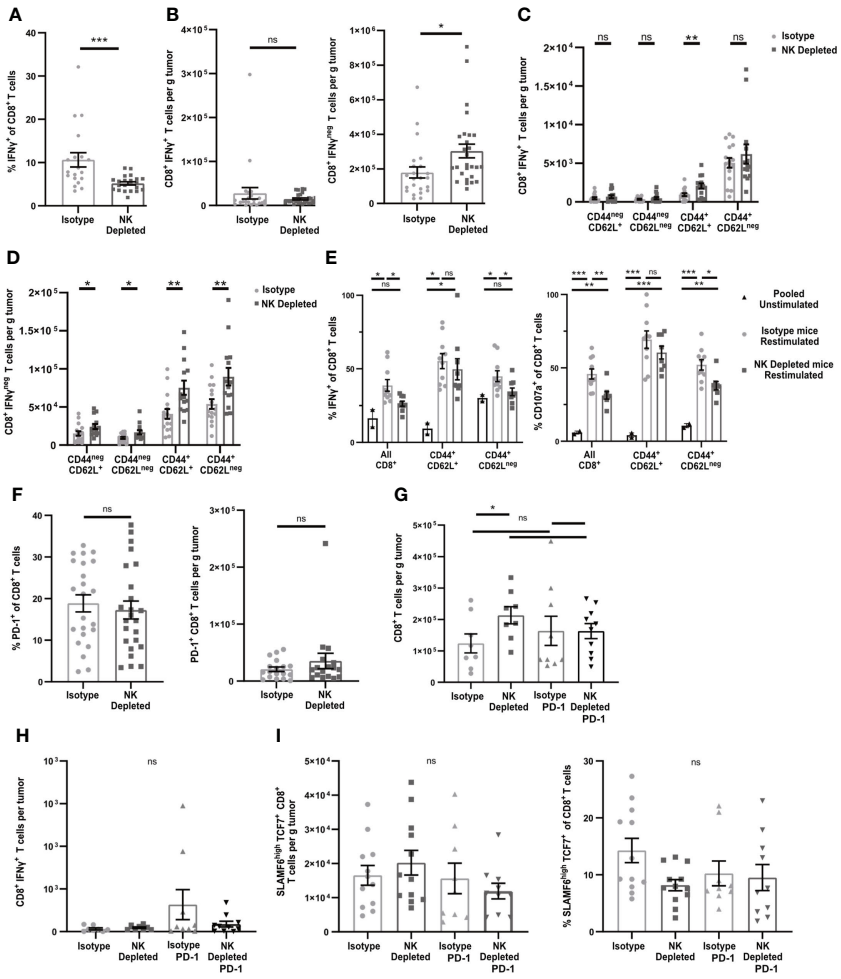

FIGURE 3
Early-stage tumors from mice lacking NK cells have increased numbers of dysfunctional but non-exhausted CD8+ T cells. B16-ova tumors were implanted into WT B6 mice treated with isotype control or anti-NK1.1 depleting antibody on D-2, D1, and D4, and harvested on D7. **(A–D, F–I)** Single cell suspensions were enriched for CD45+ cells using MACS Beads and analyzed by flow cytometry. **(A–D, H)** Mice were treated with BFA for cytokine analysis 4-6 hours prior to tumor harvest. **(E)** CD8+ cells were isolated using MACS beads and restimulated with anti-CD3/28 beads and labeled with anti-CD107a fluorescently labeled antibodies overnight, with unstimulated T cells pooled from all tumors as a control. BFA was added for the final 4-6 h to block cytokine secretion. **(G–H)** Isotype-treated or NK depleted mice were treated with anti-PD-1 or isotype control starting on D3 after tumor implantation. **(A–D, F–I)** Data points represent a single tumor and mean per group with error bars representing SEM. Data are from: **(A–B)** 6 experiments; **(C–D)** 4 experiments; **(E)** 2 experiments, with unstimulated controls pooled from all tumors in each individual experiment. **(F)** 5 experiments; **(G–H)** 3 experiments. Statistics: **(A–D, F)** Unpaired Student's T test with Welch's correction; **(E, G–I)** One-way Anova with Tukey's posttest. *p < 0.05; **p < 0.01; ***p < 0.001; ns, not significant.

whether the non-functional CD8$^+$ T cells in NK depleted tumors were anergic, we first examined their ability to proliferate within the tumor. Using Ki67, there were no changes in the proliferating fractions of CD8$^+$ T cells overall, or of CD8$^+$ T cell subpopulations, in early-stage tumors from mice containing or lacking NK cells (Figure 4A, gating shown in Supplementary Figure 4A). To determine whether sensitivity to TCR signals was reduced in CD8$^+$ T cells in tumors from NK-depleted mice, we transferred congenically marked ovalbumin specific OT-I CD8$^+$ T cells that expressed Nur77-GFP prior to tumor implantation. Nur77 expression is directly tied to TCR signaling (37). The percentage of OT-I T cells that expressed Nur77-GFP was decreased in tumors from NK-depleted mice, and this was most evident in the CD44$^+$CD62L^{neg} effector population (Figure 4B, gating shown in Supplementary Figure 4B). The normalized Nur77-GFP MFI of Nur77$^+$ OT-I cells in tumors from NK-depleted mice was also reduced (Figure 4C). These results indicate that intratumoral CD8$^+$ T cells activated in mice lacking NK cells had reduced sensitivity to TCR signals, but similar levels of proliferation, consistent with an anergic phenotype.

Since CD8$^+$ T cells in tumors from mice containing or lacking NK cells proliferated similarly, this cannot explain

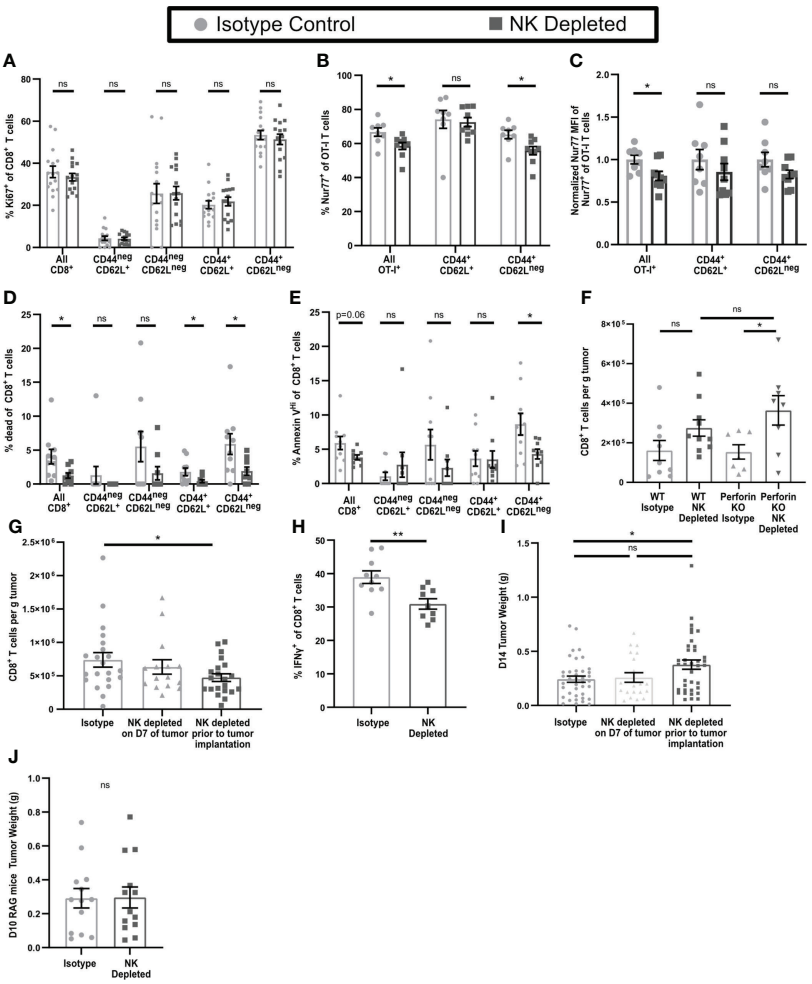

FIGURE 4
Dysfunctional CD8$^+$ T cells in tumors from mice lacking NK cells display an anergic phenotype. B16-ova tumors were implanted into WT B6 **(A–H)** or Perforin^{ko} **(F)** mice, with or without NK cell depletion. Anti-NK1.1 depleting antibody was administered prior to tumor implantation and maintained with additional treatments every three days **(A–J)** or on D7 after tumor implantation **(G, I)**. Single cell suspensions were enriched for CD45$^+$ cells using MACS Beads and analyzed by flow cytometry **(A–H)**. Mice were treated with BFA for cytokine analysis 4-6 hours prior to tumor harvest **(H)**. Tumors were harvested on D7 **(A–F)**, D14 **(G–I)**. **(B, C)** Nur77-GFP$^+$ Thy1.1$^+$ OT-I T cells were adoptively transferred into recipient mice prior to tumor implantation to monitor antigen specific TCR signaling. Nur77 MFI was normalized to the Isotype control average for each individual experiment. **(J)** Tumors were implanted in RAG mice and harvested on D10 by which time tumor size endpoints were reached in some mice. Data is from: **(A)** 4 experiments; **(B, C)** 2 experiments; **(D, E)** 2 experiments; **(F)** 2 experiments; **(G)** 6 experiments; **(H)** 2 experiments; **(I)** 8 experiments; **(J)** 3 experiments. Statistics: **(A–E, H, J)** Unpaired Student's T test with Welch's correction; **(F, G, I)** One-way Anova with Tukey's posttest. *p < 0.05; **p < 0.01; ns, not significant.

their increased numbers in tumors from NK-depleted mice. Anergic T cells have also been shown to have increased resistance to apoptosis (46). Using a viability marker (Live/Dead Aqua), we observed a significant decrease in the percentage of dead $CD8^+$ T cells overall, and of antigen experienced $CD44^+CD62L^+$ and $CD44^+CD62L^{neg}$ subpopulations, in NK-depleted tumors (Figure 4D). We also observed a significant decrease in the percentage of Annexin V^{Hi} (late apoptosis) $CD44^+CD62L^{neg}$ $CD8^+$ T cells (Figure 4E, gating shown in Supplementary Figure 4C). We considered that reduced apoptosis of intratumoral T cells in tumors lacking NK cells might be reflective of direct NK cell killing, which requires perforin (35). To test this hypothesis, WT and $Perforin^{ko}$ mice, with and without NK depletion, were implanted with B16-ova, and tumors analyzed on D7. $CD8^+$ T cell numbers in tumors from WT and $Perforin^{ko}$ mice containing NK cells were comparable, as were the numbers in tumors from NK-depleted mice of both genotypes (Figure 4F). Thus, the increase in $CD8^+$ T cells in tumors from NK-depleted mice is not due to a lack of direct NK cell killing. These results suggest that the increased level of $CD8^+$ T cells in D7 tumors from NK-depleted mice is due to a reduction in apoptotic death in the antigen experienced population, consistent with an anergic phenotype.

NK depletion results in reduced $CD8^+$ T cell numbers and functionality in late-stage tumors

To determine if T cell dysfunction continued in late-stage tumors, we harvested D14 tumors from mice that were NK cell depleted either prior to tumor implantation (D-2) in the same manner as our early-stage tumors, or after initial T cell priming (D7). NK depletion on D7 did not result in any changes in the number of $CD8^+$ T cell in D14 tumors (Figure 4G). However, in D14 tumors from mice depleted of NK cells prior to tumor implantation we observed a significant reduction in $CD8^+$ T cell numbers overall compared to mice with intact NK cells (Figure 4G). This contrasts with the elevated numbers of $CD8^+$ T cells observed in D7 tumors from NK depleted mice. We did not find a significant reduction in the numbers per g of tumor of either $IFN\gamma^{neg}$ or $IFN\gamma^+$ cells in NK depleted mice, although there was a trend toward a reduction for $IFN\gamma^+$ cells although this data showed significant variation (Supplementary Figures 4D, E). However, there was a significant reduction in the percentage of $IFN\gamma^+$ $CD8^+$ T cells in late-stage tumors lacking NK cells (Figure 4H) consistent with what was observed in D7 tumors. It is notable that these changes were accompanied by an overall significant increase in $CD8^+$ T cell numbers per g of tumor from D7 to D14 in both NK depleted (Supplementary Figure 4F) and non-depleted (Figure 1G) mice. While depletion of NK cells prior to tumor implantation had no effect on the size of D7 tumors (Figure 2E), it did result in a significant increase in the size of D14 tumors (Figure 4I). However, there was no change in D14 tumor size when NK cells were depleted starting on D7 (Figure 4I). We utilized RAG mice lacking T cells to determine if this effect was directly mediated by NK cells. There was no increase in late-stage tumor size in RAG mice depleted of NK cells prior to tumor implantation (Figure 4J), suggesting that the impact of NK cell depletion on tumor control in WT B6 mice is mediated by its effect on adaptive immunity. This indicates that NK cell depletion reduces the functionality of intra-tumoral $CD8^+$ T cells in both early and late stage tumors, and that this results in reduced long-term tumor control.

Altered T cell activation in the TDLN of NK-depleted mice

T cell anergy normally develops during initial activation from an imbalance among signals *via* the TCR, costimulatory molecules, and cytokines (46). To determine whether NK depletion altered activation of $CD8^+$ T cells in the TDLN, we treated mice starting on day 3 (D3) post implantation with FTY720 to prevent T cell egress. The overall number of $CD8^+$ T cells in the TDLN or non-draining LN (NDLN) was unchanged by NK depletion (Supplementary Figures 5A, B). However, the percentage (Figures 5A, B) and number (Supplementary Figures 5C, D) of $CD8^+CD44^+CD62L^{neg}$ effector T cells were reduced specifically in the TDLN and not the NDLN. The percentage of $Ki67^+$ proliferating $CD8^+$ T cells was reduced in the TDLN in all populations except the naïve $CD44^{neg}CD62L^+$ cells (Figure 5C). The percentage of endogenous ovalbumin-specific $CD8^+$ T cells, representing tumor antigen specific T cells, among all $CD8^+$ T cells, was also reduced in TDLN but not NDLN of NK-depleted mice (Figure 5D, Supplementary Figure 5E). This was associated with decreased proliferation of ovalbumin specific $CD8^+$ T cells overall (Figure 5E), a reduced number of the $CD44^+CD62L^+$ subpopulation (Figure 5F), and an increased percentage of naïve ($CD44^{neg}CD62L^+$) ovalbumin specific $CD8^+$ T cells (Supplementary Figure 5F). We did not observe a change in the subpopulation distribution of ovalbumin specific T cells in the NDLN, where naïve cells were the primary population (Supplementary Figure 5G). These results demonstrate that NK depletion leads to a reduction in T cell activation, proliferation, and tumor specific effector generation in the TDLN.

The development of anergic T cells has been shown to be promoted by elevated TCR stimulation and/or a lack of co-stimulation (46, 50–53). We therefore tested the hypothesis that the reduced number of proliferating and differentiated effector T cells in the TDLN of NK-depleted mice reflected increased sensitivity to TCR stimulation. We tested this by examining the activation of OT-I T cells expressing the Nur77-GFP reporter that were transferred prior to tumor implantation. OT-I T cells did not show a significant difference in subpopulation

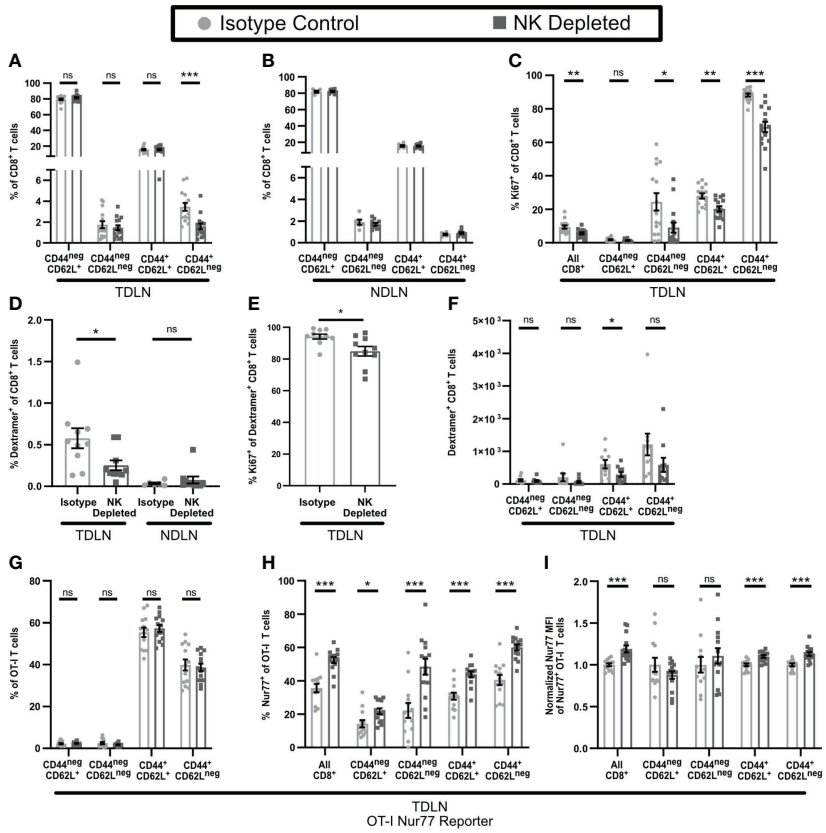

FIGURE 5
T cell activation is altered in the TDLN of mice lacking NK cells. B16-ova tumors were implanted into WT B6 mice treated with isotype control or anti-NK1.1 depleting antibody on D-2, D1, and D4. TDLN **(A–H)** or NDLN **(B, D)** were harvested on D7. **(A–F)** Mice were treated with FTY720 starting on D3 to prevent T cell egress from LN. **(G–I)** Nur77-GFP$^+$ Thy1.1$^+$ OT-I T cells were adoptively transferred into recipient mice prior to tumor implantation to monitor antigen specific TCR signaling. Nur77 MFI was normalized to the isotype control average for each individual experiment. Single cell suspensions were analyzed by flow cytometry. Data is from: **(A, C)** 3 experiments; **(B)** 2 experiments; **(D–F)** 2 experiments; **(G–I)** 2 experiments. Statistics: Unpaired Student's T test with Welch's correction. *p < 0.05; **p < 0.01; ***p < 0.001; ns, not significant.

distribution in TDLN of isotype and NK-depleted mice (Figure 5G). Importantly however, the fraction of Nur77$^+$ OT-I T cells (Figure 5H) and their Nur77 MFI (Figure 5I), were significantly higher, indicating that they had received enhanced TCR signals. Nur77 signaling was specific to the TDLN, as the Nur77 positive signal was nearly absent in the spleens of both isotype and NK depleted mice (Supplementary Figure 5H). Taken together, these results demonstrate that NK depletion leads to enhanced TCR stimulation of CD8$^+$ T cells in TDLN, decreased proliferation, and differentiation of those cells. This is consistent with what others have shown to promote the development of anergic T cells.

APC from tumors and TDLN of NK-depleted mice appear less mature

Based on the changes in CD8$^+$ T cell phenotype that accompanied NK depletion, we examined the phenotypes of APC in both tumor and TDLN. The numbers of intratumoral APC (Figure 2D) and their subsets (Figure 6A) were not altered by NK depletion. While the numbers of CD11b$^+$CD11c^{neg}MHCII$^+$ APC in TDLN of NK-depleted mice were not reduced, the numbers of CD11c$^+$MHCII$^+$ APC were, and this was evident in both CD11b$^+$ and CD103$^+$ subsets (Figure 6B). This was specific for the TDLN, as NDLN APC numbers were unchanged

(Supplementary Figure 6A). The lower numbers of these APC subsets in TDLN could be due to reduced entry of migratory APC, or reduced survival or proliferation of resident APC. Cells with an CD11c^{Hi}MHCII^{Int} phenotype, characteristic of the majority of LN resident APC (54), were selectively reduced in the TDLN of NK-depleted mice, while cells with a CD11c^{Lo}MHCII^{Hi} phenotype, characteristic of migratory DC, were not altered (Figure 6C, Supplementary Figure 6B). This is consistent with the unchanged number of intratumoral APC and suggests that APC migration from the tumor remains unchanged in NK depleted mice. This suggests that one consequence of NK depletion is a reduction in the numbers of CD11b^{+} and CD103^{+} subsets of resident DC in TDLN.

We also examined the maturation status of APC in tumor and TDLN. All subsets of intratumoral APC from NK depleted mice expressed lower levels of MHCII (Figure 6D), suggesting that they are less mature than those from non-depleted mice. As immature APCs in tissues are more phagocytic and have reduced proteolytic capacity (55, 56) we used tumors expressing the fluorescent protein iRFP720 to identify APC that retained unprocessed tumor derived antigen. All subsets of intratumoral APC from NK depleted mice

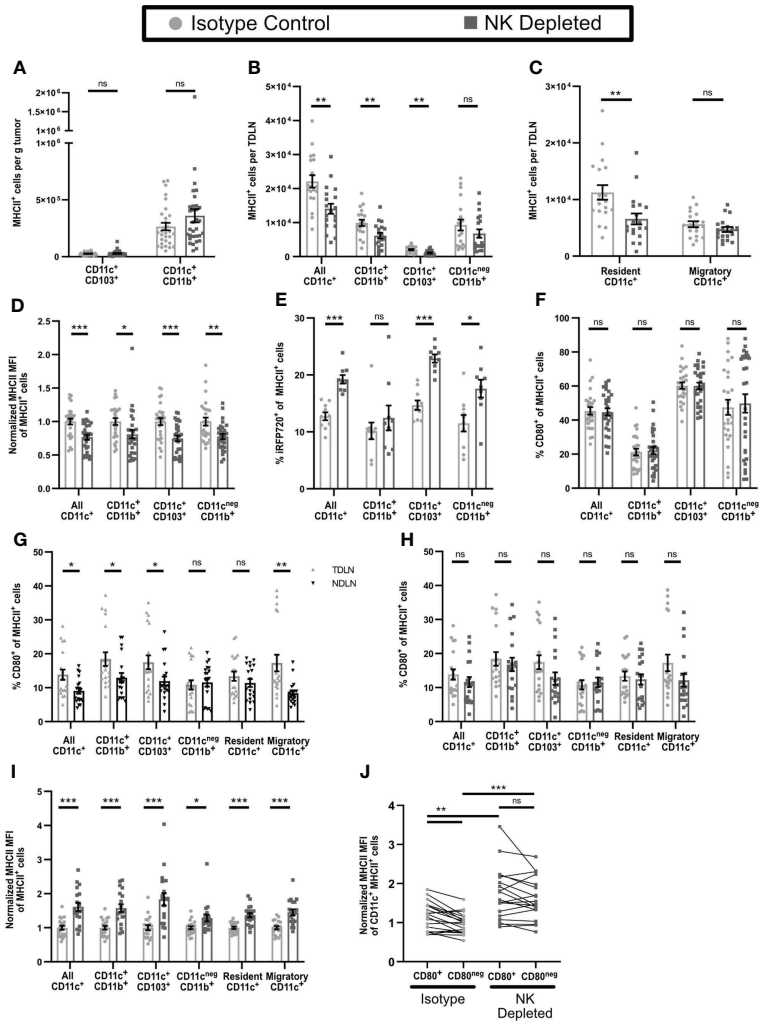

FIGURE 6
Antigen presenting cells in tumors and TDLN of mice lacking NK cells have an altered maturation phenotype. **(A–D, F–J)** B16-ova or **(E)** B16-ova-iRFP720 tumors were implanted into WT B6 mice treated with isotype control or anti-NK1.1 depleting antibody on D-2, D1, and D4. Tumor **(A, D–F)**, TDLN **(B, C, G–J)**, or NDLN **(C)** were harvested on D7. Single cell suspensions were analyzed by flow cytometry. **(C, G–I)** Resident APC were defined as CD11c^{Hi}MHCII^{Int} and Migratory APC as CD11c^{Low}MHCII^{Hi}. **(I, J)** For each APC subset, MHCII MFI was normalized to the isotype control average of that same subset **(I)** or of all CD11c^{+}MHCII^{+} APC **(J)** separately for each experiment. **(B, C, G–J)** Data are from 4 experiments; **(A, D, F)** Data are from 6 experiments; **(E)** Data are from 2 experiments. Statistics: **(A–I)** Unpaired Student's T test with Welch's correction; **(J)** For CD80^{+} vs CD80^{neg} comparisons, a paired T test was used. For comparisons between isotype and NK depleted, an Unpaired Student's T test with Welch's correction was used. *p < 0.05; **p < 0.01; ***p < 0.001; ns, not significant.

showed significantly greater retention of tumor derived antigen (Figure 6E), again consistent with a less mature phenotype. The percentage of intratumoral APC expressing CD80 (Figure 6F) and their level of CD80 expression (Supplementary Figure 6C), which typically increase with APC maturation (55, 56) was unchanged by NK depletion. Overall, this suggests that intratumoral APC from NK depleted mice are less mature.

In APC from TDLN of either NK-depleted or non-depleted mice retention of tumor derived antigen could not be detected. However, compared to APC in NDLN, CD80 was expressed on approximately 25-100% more cells in most $CD11c^+$ APC subsets in TDLN but was not different on $CD11b^+CD11c^{neg}MHCII^+$ cells or resident APC (Figure 6G). Thus, APC in TDLN appear more mature compared to those in NDLN. Neither the percentage of APC expressing CD80 (Figure 6H), nor their CD80 expression level (Supplementary Figure 6D) was changed in any subsets in TDLN of mice lacking NK cells. However, MHCII expression levels were increased in all populations of $CD11c^+$ APC ($CD11b^+$, $CD103^+$, resident, and migratory; gating shown in Supplementary Figure 6E) and in $CD11c^{neg}CD11b^+MHCII^+$ cells (Figure 6I). In TDLN of intact mice, $CD11c^+MHCII^+$ APC that expressed CD80 (gating shown in Supplementary Figure 6F) also expressed higher levels of MHCII (Figure 6J). However, in TDLN from NK depleted mice, both $CD80^+$ and $CD80^{neg}$ APC showed an increase in MHCII MFI, and they were no longer different from one another (Figure 6J). Thus, APC in early stage TDLN of NK depleted mice display increased MHCII expression regardless of CD80 expression. Increased MHCII expression in mature APC usually corresponds with an increased level of costimulatory molecule expression (57). Increased MHCII expression without increased CD80 suggests an incomplete APC maturation, which may have resulted in the aberrant activation and anergic T cell phenotypes we observed in tumor bearing mice lacking NK cells.

Blockade of CD40L results in similar phenotypes of T cell activation and APC in the TDLN as NK depletion

NK cells in tumor bearing mice express elevated levels of CD40L (58), and interactions with CD40 cause increased APC maturation (59). CD40L blockade also results in reduced T cell numbers and function in tumor bearing mice (60). We found that some NK cells, as well as some $CD4^+$ T cells, in early-stage tumors and TDLN expressed CD40L (Supplementary Figure 7). We utilized CD40L blockade to determine if this resulted in an increase in dysfunctional T cells in early-stage tumors similar to NK depletion and resulted in similar effects on APC and T cell phenotypes in the TDLN. In contrast to NK depletion, CD40L blockade beginning on D3 led to almost complete absence of T cells in early-stage tumors (Figure 7A), making it impossible to evaluate changes in T cell function or phenotype. However, in the TDLN, CD40L blockade resulted in a reduction in the numbers of $CD8^+$ T cells overall, naïve ($CD44^{neg}CD62L^+$), and effector ($CD44^+CD62L^{neg}$) T cells, but no change in $CD44^+CD62L^+$ $CD8^+$ T cells (Figure 7B), and similar results were seen with either NK depletion alone or combination NK depletion and CD40L blockade. While the observed reduction in overall and naïve $CD8^+$ T cell numbers was not seen in the TDLN of NK depleted mice in Figure 5A, this is likely because the mice in Figure 7 were not treated with FTY720. We augmented these studies by comparing the effects of CD40L blockade and NK depletion on tumor antigen specific cells. As above, the total number of ova-dextramer$^+$ $CD8^+$ T cells in the TDLN was reduced comparably by NK cell depletion, CD40L blockade, and the combination (Figure 7C). This was primarily due to a reduction in the number of antigen-experienced ($CD44^+$) ova-dextramer$^+$ $CD8^+$ T cells (Figure 7C). As we observed with bulk T cells there was no significant difference in the reduced number of effector cells in the TDLN of CD40L blocked, NK depleted, or dual treated mice. These results suggest that NK cell depletion and CD40L blockade target a common pathway that results in diminished T cell differentiation and that the effect of NK cells on T cell differentiation in the TDLN during early-stage tumor growth is *via* CD40L. However, CD40L blockade has effects beyond those of NK cell depletion as there is complete blockage of T cell infiltration into the early-stage tumors. This suggests that NK cells provide an important source of CD40L during the initial stages of $CD8^+$ T cell activation but are not the only source of CD40L in the microenvironment.

We next determined if CD40L blockade also resulted in incomplete APC maturation in the TDLN similar to that induced by NK depletion. In keeping with Figures 6A, B, CD40L blockade resulted in reduced numbers of $CD11b^+$, $CD103^+$, and resident APC, but unchanged migratory APC, in the early-stage TDLN, and was not significantly different from NK cell depletion alone or combination treatment (Figures 7D, E). In keeping with Figure 6D and Supplementary Figure 6C, neither the percentage (Figure 7F) or expression level (Figure 7G) of CD80 were changed on $CD11c^+MHCII^+$ APC as a consequence of any treatment. Finally, in keeping with Figures 6E, F, and Supplementary Figures 6D, E, MHCII expression on all APC subsets Figures 7H, I, regardless of CD80 expression was increased similarly by CD40L blockade, NK cell depletion, or the combination (Figures 7J, K). This suggests that CD40L blockade during early-stage tumor growth promotes incomplete maturation of APC in TDLN, similar to NK depletion.

Discussion

In this study we determined that NK cells play multiple roles in enhancing the T cell response during the early stages of tumor

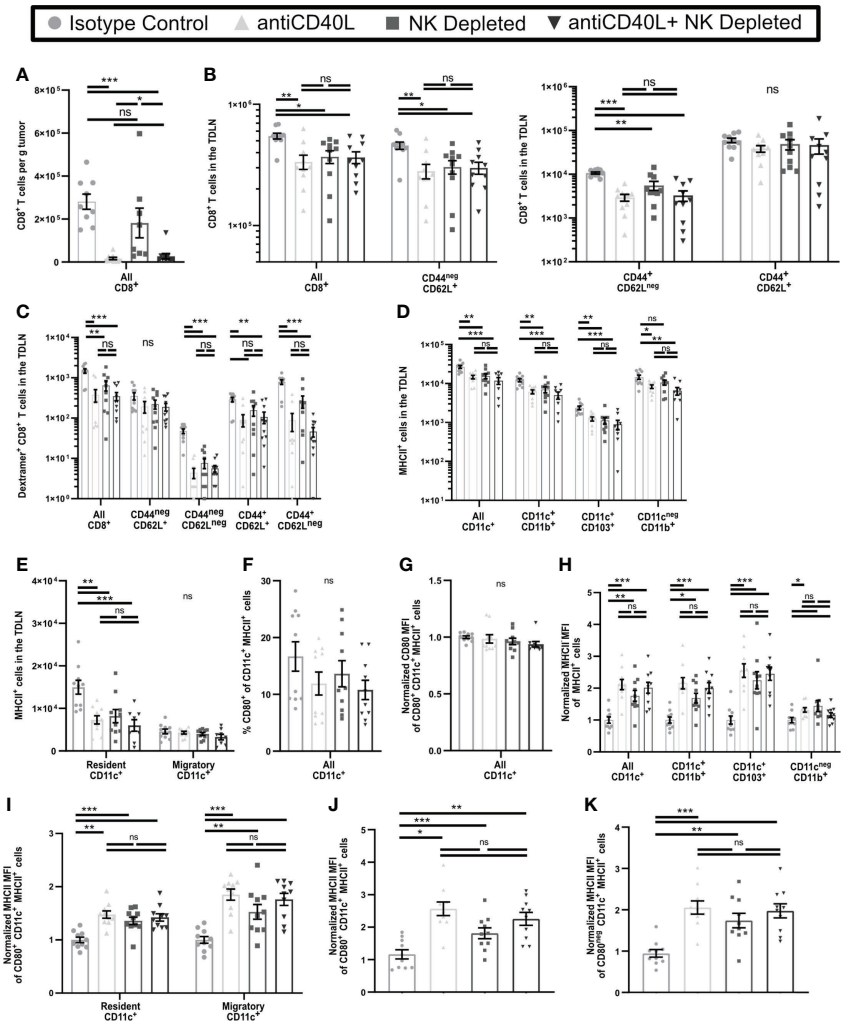

FIGURE 7
Blockade of CD40L and NK Depletion result in similar T cell and APC phenotypes in the TDLN. B16-ova tumors were implanted into WT B6 mice treated with isotype control or anti-NK1.1 depleting antibodies on D-2, D1, and D4, or isotype control or anti-CD40L blocking antibody starting on the day of tumor implantation and then on D2, D4, and D6, or a combination of NK cell depletion and anti-CD40L blockade. Tumor **(A)** or TDLN **(B–K)** were harvested at D7. Single cell suspensions of tumor samples were enriched for $CD45^+$ cells by MACS Beads and analyzed by flow cytometry. Single cell LN samples were analyzed by flow cytometry. **(H–K)** For each APC subset, the indicated MFI was normalized to the isotype control average of that same subset separately for each experiment. **(J, K)** The MHCII MFI was normalized to the isotype control average of all $CD11c^+MHCII^+$ APC separately for each experiment. Data are from: **(A–K)** 2 experiments. Statistics: One-way Anova with Tukey's posttest. *p < 0.05; **p < 0.01; ***p < 0.001; ns, not significant.

development. We showed that NK cells in early-stage tumors are a source of IFNγ and that NK depletion reduced HRL expression on tumor vasculature. However, NK cell depletion resulted in increased intratumoral T cell numbers. Based on their reduced TCR signaling and reduced expression of effector function, but unchanged proliferation and increased resistance to apoptosis, these T cells were functionally anergic. Their development in the TDLN was associated with increased TCR signaling but paradoxically, decreased proliferation and maturation to full effector cells. Additionally, it was associated with an unusual maturation phenotype of APC in the TDLN, characterized by increased MHCII expression but unaltered CD80 expression. The effect of NK depletion on APC phenotype was similar to that of blocking CD40L. This suggests that functional NK cells drive proper APC maturation *via* CD40L during the early tumor response thereby reducing the development of anergic T cells.

Anergic T cells develop in response to increased TCR signaling and/or reduced costimulatory activation (46, 50–53). Characteristics of anergic T cells include proliferation during activation (47–49), reduced production of IL-2 and other cytokines (44–46), resistance to apoptosis (46, 61, 62), and paradoxically, given what drives their development, reduced

response to TCR signals (50). While anergy is best characterized for $CD4^+$ T cells, $CD8^+$ T cells also become anergic (63–65). Anergic $CD4^+$ T cells have been identified by high expression of FR4 and CD73 (66), but there are no known surface markers identifying anergic $CD8^+$ T cells. While anergic $CD8^+$ T cells have been shown to exist in tumors (65, 67), the lack of clear surface markers complicates separating them from exhausted $CD8^+$ T cells (68, 69). With the current focus on exhausted T cells, the presence of anergic intratumoral $CD8^+$ T cells may have been underappreciated. In contrast to exhausted cells, anergic T cells are thought to be immunosuppressive, although the mechanism(s) are not fully understood (51, 70). Preventing anergic cells from developing could increase the number of functional tumor antigen specific cells in the tumor and improve responses to checkpoint blockade therapy.

APC maturation is necessary for T cell activation resulting in generation of effector T cells capable of responding to antigenic stimulation in the periphery. However, a range of distinct maturation phenotypes have been described (71, 72). Fully mature APC most commonly develop in the context of infection or immunization, which include strong stimuli for toll like receptors (73, 74) and CD40 (75). NK cells have also been shown to promote full APC maturation and to improve T cell responses to infections or vaccination (31, 76). NK cell induced maturation of APC *in vitro* partially involves direct contact (29–31) and multiple signaling pathways, including CD40-CD40L interaction (30, 31). NK cells in tumors have been shown to increase the number of APCs (3, 32) and have increased localization near each other (3, 33). However, a direct connection between NK cell induced APC maturation and NK enhanced T cell responses has been questioned because NK cells can also kill activated T cells (34, 35). Here we showed that NK cells incapable of killing T cells did not increase the number of anergic T cells. Instead, when NK cells were depleted, APC in tumor remained immature, while APC in TDLN developed an incomplete maturation phenotype in which elevated MHCII was not accompanied by increased CD80 expression. This was associated with elevated response to TCR signals in the TDLN, but reduced T cell proliferation. This suggests that the increased numbers of anergic T cells in early-stage tumors of mice lacking NK cells is due to the aberrant activation of T cells in the TDLN by incompletely matured APC. Our results provide new evidence that NK cell induced maturation of APC at early stages of tumor responses shapes the outcome of the T cell response by limiting the induction of T cell anergy.

Interactions with CD40 cause increased APC maturation (59, 77), and previous work has shown that NK cells can express CD40L, including during the response to tumors (58). Our data demonstrates that during early-stage tumor responses, NK cell depletion and CD40L blockade result in a similar incomplete APC maturation phenotype. These two treatments also led to similar reductions in the number of effector T cells in the TDLN. Importantly, the combination of NK depletion and CD40L blockade was not additive. This suggests that during the early stages of tumor growth, NK cells are the primary source of CD40L or induce its expression on another cell type such as $CD4^+$ T cells, and this is the principal mechanism by which they drive APC maturation. NK cell expressed CD40L could be operating *via* direct signaling to CD40 but CD40-CD40L interaction may also be necessary for another aspect of NK cell function, such as localized secretion of cytokines to alter APC maturation. It is also important to note that CD40L blockade had a much more profound impact on T cell infiltration into tumor, pointing to a role for another $CD40L^+$ cell in this aspect of the anti-tumor immune response. While the mechanism is uncertain, our data identified CD40L expression on CD4 but not CD8 TIL, and it seems likely that these cells may fulfill this role.

Our results show that systemic depletion of NK cells leads to incomplete maturation of both resident and migratory APC populations in the TDLN but had no effect on APC in NDLN. This selectivity indicates signals provided by the tumor in addition to those provided by NK cells are necessary for APC maturation. It is possible that NK cells in the TDLN drive additional maturation following an initial signal provided by the tumor. This is consistent with the observation that CD40L blockade produced a similar result as NK cell depletion, which suggests that NK cell direct contact with APC in the TDLN promotes complete maturation. An additional possibility is that intratumoral NK cells provide tumor-dependent activation signals, such as DAMPs, that induce complete maturation of APC in the TDLN. Further research into how and where the NK cells drive optimal APC maturation during the early immune response against the tumor will be critical to allow for development of therapeutic intervention strategies in the future.

These results demonstrate that functional NK cells improve the overall quality of tumor-specific T cell responses. However, as NK cell function decreases over time, this effect may be lost, leading to increased development of anergic TIL in association with tumor progression. NK cell dysfunction can thus have effects that resemble those of NK cell depletion in early-stage tumors that we have described here. Our data also demonstrate that the functional effectors that develop in the absence of NK cells are less likely to persist in tumors. Thus, once NK cells have become dysfunctional, new tumor antigens arising as a consequence of ongoing mutation may generate a suboptimal T cell response, resulting in decreased T cell control of the tumor. This study has demonstrated that the long-term impacts of NK cell dysfunction on the T cell response to tumors is an important area for future investigation.

Our work demonstrates that there is a need to evaluate the downstream consequences of NK cell function on both APC maturation and early-stage tumor specific T cell activation in human cancer patients. Based on our work, NK cell adoptive transfer may be able to increase the efficacy of checkpoint blockade therapy by diminishing the generation of anergic T

cells that are unresponsive to checkpoint blockade therapy. NK cell adoptive transfer therapy clinical trials (78–80) have shown promise, but significant challenges remain in *ex vivo* generation of NK cells that retain long-term effector function (81, 82). While combination with other immune therapies is being examined, no trials in combination with checkpoint blockade therapy have been completed. Future examination of the effect of NK cell adoptive transfer therapy on T cell activation in the LN and in tumors will be key to determine if there is synergy with checkpoint blockade therapy.

Data availability statement

The original contributions presented in the study are included in the article/Supplementary Material, further inquiries can be directed to the corresponding author/s.

Ethics statement

The animal study was reviewed and approved by University of Virginia Animal Care and Use Committee.

Author contributions

RL conceptualization, methodology, investigation, analysis, writing – original draft, writing – review & editing; MM: methodology, investigation, writing – review & editing; KS: methodology, investigation; JA: methodology, investigation, analysis; AW: methodology, investigation, analysis; AR: conceptualization, methodology; MB: conceptualization, methodology VE: conceptualization, methodology, writing – review & editing, funding acquisition, supervision. All authors contributed to the article and approved the submitted version.

Funding

This work was supported by USPHS Grants R01 CA78400 and R01 CA181794 (to VE) and R01 AI050072 (to MB). The University of Virginia Histology and Flow Cytometry Cores are supported by USPHS P30 CA44579. RL, JA, AW, and AR were supported by USPHS Training Grant T32 AI007496. AR was the recipient of a Wagner Fellowship from the University of Virginia.

Acknowledgments

We thank Timothy Bender, and the Engelhard and Brown labs for discussion and suggestions.

Conflict of interest

The authors declare that the research was conducted in the absence of any commercial or financial relationships that could be construed as a potential conflict of interest.

Publisher's note

Supplementary material

The Supplementary Material for this article can be found online at: https://www.frontiersin.org/articles/10.3389/fonc.2022.1058894/full#supplementary-material

References

1. Zhang L, Conejo-Garcia JR, Katsaros D, Gimotty PA, Massobrio M, Regnani G, et al. Intratumoral T cells, recurrence, and survival in epithelial ovarian cancer. *N Engl J Med* (2003) 348(3):203–13. doi: 10.1056/NEJMoa020177

2. Tumeh PC, Harview CL, Yearley JH, Shintaku IP, Taylor EJM, Robert L, et al. PD-1 blockade induces responses by inhibiting adaptive immune resistance. *Nature.* (2014) 515(7528):568–71. doi: 10.1038/nature13954

3. Barry KC, Hsu J, Broz ML, Cueto FJ, Binnewies M, Combes AJ, et al. A natural killer-dendritic cell axis defines checkpoint therapy-responsive tumor microenvironments. *Nat Med* (2018) 24(8):1178–91. doi: 10.1038/s41591-018-0085-8

4. Ley K, Laudanna C, Cybulsky MI, Nourshargh S. Getting to the site of inflammation: the leukocyte adhesion cascade updated. *Nat Rev Immunol* (2007) 7 (9):678–89. doi: 10.1038/nri2156

5. Quezada SA, Peggs KS, Simpson TR, Shen Y, Littman DR, Allison JP. Limited tumor infiltration by activated T effector cells restricts the therapeutic activity of regulatory T cell depletion against established melanoma. *J Exp Med* (2008) 205 (9):2125–38. doi: 10.1084/jem.20080099

6. Fisher DT, Chen Q, Skitzki JJ, Muhitch JB, Zhou L, Appenheimer MM, et al. IL-6 trans-signaling licenses mouse and human tumor microvascular gateways for trafficking of cytotoxic T cells. *J Clin Invest.* (2011) 121(10):3846–59. doi: 10.1172/JCI44952

7. Lohr J, Ratliff T, Huppertz A, Ge Y, Dictus C, Ahmadi R, et al. Effector T-cell infiltration positively impacts survival of glioblastoma patients and is impaired by tumor-derived TGF-β. *Clin Cancer Res* (2011) 17(13):4296–308. doi: 10.1158/1078-0432.CCR-10-2557

8. Peske JD, Woods AB, Engelhard VH. Control of CD8 T-cell infiltration into tumors by vasculature and microenvironment. *Adv Cancer Res* (2015) 128:263–307. doi: 10.1016/bs.acr.2015.05.001

9. Woods AN, Wilson AL, Srivinisan N, Zeng J, Dutta AB, Peske JD, et al. Differential expression of homing receptor ligands on tumor-associated vasculature that control CD8 effector T-cell entry. *Cancer Immunol Res* (2017) 5(12):1062–73. doi: 10.1158/2326-6066.CIR-17-0190

10. Sackstein R, Schatton T, Barthel SR. T-Lymphocyte homing: an underappreciated yet critical hurdle for successful cancer immunotherapy. *Lab Investig J Tech Methods Pathol* (2017) 97(6):669–97. doi: 10.1038/labinvest.2017.25

11. Martin-Fontecha A, Lanzavecchia A, Sallusto F. Dendritic cell migration to peripheral lymph nodes. *Handb Exp Pharmacol* (2009) 188):31–49. doi: 10.1007/978-3-540-71029-5_2

12. Gardner A, Ruffell B. Dendritic cells and cancer immunity. *Trends Immunol* (2016) 37(12):855–65. doi: 10.1016/j.it.2016.09.006

13. Yang L, Carbone DP. Tumor-host immune interactions and dendritic cell dysfunction. *Adv Cancer Res* (2004) 92:13–27. doi: 10.1016/S0065-230X(04)92002-7

14. Roberts EW, Broz ML, Binnewies M, Headley MB, Nelson AE, Wolf DM, et al. Critical role for CD103(+)/CD141(+) dendritic cells bearing CCR7 for tumor antigen trafficking and priming of T cell immunity in melanoma. *Cancer Cell* (2016) 30(2):324–36. doi: 10.1016/j.ccell.2016.06.003

15. Wangmo D, Premsrirut PK, Yuan C, Morris WS, Zhao X, Subramanian S. ACKR4 in tumor cells regulates dendritic cell migration to tumor-draining lymph nodes and T-cell priming. *Cancers.* (2021) 13(19):5021. doi: 10.3390/cancers13195021

16. Zong J, Keskinov AA, Shurin GV, Shurin MR. Tumor-derived factors modulating dendritic cell function. *Cancer Immunol Immunother.* (2016) 65 (7):821–33. doi: 10.1007/s00262-016-1820-y

17. Seaman WE, Sleisenger M, Eriksson E, Koo GC. Depletion of natural killer cells in mice by monoclonal antibody to NK-1.1. reduction in host defense against malignancy without loss of cellular or humoral immunity. *J Immunol* (1987) 138 (12):4539–44. doi: 10.4049/jimmunol.138.12.4539

18. Johnson LA, Vaidya SV, Goldfarb RH, Mathew PA. 2B4(CD244)-mediated activation of NK cells reduces metastases of B16F10 melanoma in mice. *Anticancer Res* (2003) 23(5A):3651–5.

19. López-Soto A, Gonzalez S, Smyth MJ, Galluzzi L. Control of metastasis by NK cells. *Cancer Cell* (2017) 32(2):135–54. doi: 10.1016/j.ccell.2017.06.009

20. Dianat-Moghadam H, Mahari A, Heidarifard M, Parnianfard N, Pourmousavi-Kh L, Rahbarghazi R, et al. NK cells-directed therapies target circulating tumor cells and metastasis. *Cancer Lett* (2021) 497:41–53. doi: 10.1016/j.canlet.2020.09.021

21. Pross HF, Lotzová E. Role of natural killer cells in cancer. *Nat Immun* (1993) 12(4–5):279–92.

22. Turner JG, Rakhmilevich AL, Burdelya L, Neal Z, Imboden M, Sondel PM, et al. Anti-CD40 antibody induces antitumor and antimetastatic effects: the role of NK cells. *J Immunol* (2001) 166(1):89–94. doi: 10.4049/jimmunol.166.1.89

23. Whiteside TL, Herberman RB. The role of natural killer cells in immune surveillance of cancer. *Curr Opin Immunol* (1995) 7(5):704–10. doi: 10.1016/0952-7915(95)80080-8

24. Cozar B, Greppi M, Carpentier S, Narni-Mancinelli E, Chiossone L, Vivier E. Tumor-infiltrating natural killer cells. *Cancer Discovery* (2021) 11(1):34–44. doi: 10.1158/2159-8290.CD-20-0655

25. Wu J, Lanier LL. Natural killer cells and cancer. *Adv Cancer Res* (2003) 90:127–56. doi: 10.1016/S0065-230X(03)90004-2

26. Schmidt L, Eskiocak B, Kohn R, Dang C, Joshi NS, DuPage M, et al. Enhanced adaptive immune responses in lung adenocarcinoma through natural killer cell stimulation. *Proc Natl Acad Sci USA* (2019) 116(35):17460–9. doi: 10.1073/pnas.1904253116

27. Kalinski P, Mailliard RB, Giermasz A, Zeh HJ, Basse P, Bartlett DL, et al. Natural killer-dendritic cell cross-talk in cancer immunotherapy. *Expert Opin Biol Ther* (2005) 5(10):1303–15. doi: 10.1517/14712598.5.10.1303

28. Peterson EE, Barry KC. The natural killer-dendritic cell immune axis in anti-cancer immunity and immunotherapy. *Front Immunol* (2021) 11:621254. doi: 10.3389/fimmu.2020.621254

29. Gerosa F, Gobbi A, Zorzi P, Burg S, Briere F, Carra G, et al. The reciprocal interaction of NK cells with plasmacytoid or myeloid dendritic cells profoundly affects innate resistance functions. *J Immunol* (2005) 174(2):727–34. doi: 10.4049/jimmunol.174.2.727

30. Piccioli D, Sbrana S, Melandri E, Valiante NM. Contact-dependent stimulation and inhibition of dendritic cells by natural killer cells. *J Exp Med* (2002) 195(3):335–41. doi: 10.1084/jem.20010934

31. Walzer T, Dalod M, Vivier E, Zitvogel L. Natural killer cell-dendritic cell crosstalk in the initiation of immune responses. *Expert Opin Biol Ther* (2005) 5 Suppl 1:S49–59. doi: 10.1517/14712598.5.1.S49

32. Bottcher JP, Bonavita E, Chakravarty P, Blees H, Cabeza-Cabrerizo M, Sammicheli S, et al. NK cells stimulate recruitment of cDC1 into the tumor microenvironment promoting cancer immune control. *Cell.* (2018) 172(5):1022–1037.e14. doi: 10.1016/j.cell.2018.01.004

33. Melaiu O, Chierici M, Lucarini V, Jurman G, Conti LA, De Vito R, et al. Cellular and gene signatures of tumor-infiltrating dendritic cells and natural-killer cells predict prognosis of neuroblastoma. *Nat Commun* (2020) 11(1):5992. doi: 10.1038/s41467-020-19781-y

34. Rabinovich BA, Li J, Shannon J, Hurren R, Chalupny J, Cosman D, et al. Activated, but not resting, T cells can be recognized and killed by syngeneic NK cells. *J Immunol* (2003) 170(7):3572–6. doi: 10.4049/jimmunol.170.7.3572

35. Waggoner SN, Cornberg M, Selin LK, Welsh RM. Natural killer cells act as rheostats modulating antiviral T cells. *Nature.* (2011) 481(7381):394–8. doi: 10.1038/nature10624

36. Ferlazzo G, Moretta L. Dendritic cell editing by natural killer cells. *Crit Rev Oncog* (2014) 19(1–2):67–75. doi: 10.1615/CritRevOncog.2014010827

37. Moran AE, Holzapfel KL, Xing Y, Cunningham NR, Maltzman JS, Punt J, et al. T Cell receptor signal strength in treg and iNKT cell development demonstrated by a novel fluorescent reporter mouse. *J Exp Med* (2011) 208 (6):1279–89. doi: 10.1084/jem.20110308

38. Hogquist KA, Jameson SC, Heath WR, Howard JL, Bevan MJ, Carbone FR. T Cell receptor antagonist peptides induce positive selection. *Cell.* (1994) 76(1):17–27. doi: 10.1016/0092-8674(94)90169-4

39. Snell GD, Cherry M, McKenzie IF, Bailey DW. Ly-4, a new locus determining a lymphocyte cell-surface alloantigen in mice. *Proc Natl Acad Sci USA* (1973) 70(4):1108–11. doi: 10.1073/pnas.70.4.1108

40. Kagi D, Ledermann B, Burki K, Seiler P, Odermatt B, Olsen KJ, et al. Cytotoxicity mediated by T cells and natural killer cells is greatly impaired in perforin-deficient mice. *Nature.* (1994) 369:31–7. doi: 10.1038/369031a0

41. Hargadon KM, Brinkman CC, Sheasley-O'Neill SL, Nichols LA, Bullock TNJ, Engelhard VH. Incomplete differentiation of antigen-specific CD8 T cells in tumor-draining lymph nodes. *J Immunol* (2006) 177(9):6081–90. doi: 10.4049/jimmunol.177.9.6081

42. Shcherbakova DM, Verkhusha VV. Near-infrared fluorescent proteins for multicolor *in vivo* imaging. *Nat Methods* (2013) 10:751–4. doi: 10.1038/nmeth.2521

43. Miller BC, Sen DR, Al Abosy R, Bi K, Virkud YV, LaFleur MW, et al. Subsets of exhausted CD8+ T cells differentially mediate tumor control and respond to checkpoint blockade. *Nat Immunol* (2019) 20(3):326–36. doi: 10.1038/s41590-019-0312-6

44. Otten GR, Germain RN. Split anergy in a CD8+ T cell: receptor-dependent cytolysis in the absence of interleukin-2 production. *Science* (1991) 251 (4998):1228–31. doi: 10.1126/science.1900952

45. Chai JG, Lechler RI. Immobilized anti-CD3 mAb induces anergy in murine naive and memory CD4+ T cells *in vitro*. *Int Immunol* (1997) 9(7):935–44. doi: 10.1093/intimm/9.7.935

46. Schwartz RH. T Cell anergy. *Annu Rev Immunol* (2003) 21:305–34. doi: 10.1146/annurev.immunol.21.120601.141110

47. Jenkins MK. The role of cell division in the induction of clonal anergy. *Immunol Today* (1992) 13(2):69–73. doi: 10.1016/0167-5699(92)90137-V

48. Perez VL, Van Parijs L, Biuckians A, Zheng XX, Strom TB, Abbas AK. Induction of peripheral T cell tolerance *in vivo* requires CTLA-4 engagement. *Immunity.* (1997) 6(4):411–7. doi: 10.1016/S1074-7613(00)80284-8

49. Colombetti S, Benigni F, Basso V, Mondino A. Clonal anergy is maintained independently of T cell proliferation. *J Immunol Baltim Md 1950* (2002) 169 (11):6178–86. doi: 10.4049/jimmunol.169.11.6178

50. Lechler R, Chai JG, Marelli-Berg F, Lombardi G. T-Cell anergy and peripheral T-cell tolerance. *Philos Trans R Soc Lond B Biol Sci* (2001) 356 (1409):625–37. doi: 10.1098/rstb.2001.0844

51. Appleman LJ, Boussiotis VA. T Cell anergy and costimulation. *Immunol Rev* (2003) 192:161–80. doi: 10.1034/j.1600-065X.2003.00009.x

52. Fathman CG, Lineberry NB. Molecular mechanisms of CD4+ T-cell anergy. *Nat Rev Immunol* (2007) 7(8):599–609. doi: 10.1038/nri2131

53. ElTanbouly MA, Noelle RJ. Rethinking peripheral T cell tolerance: checkpoints across a T cell's journey. *Nat Rev Immunol* (2021) 21(4):257–67. doi: 10.1038/s41577-020-00454-2

54. Merad M, Sathe P, Helft J, Miller J, Mortha A. The dendritic cell lineage: ontogeny and function of dendritic cells and their subsets in the steady state and the inflamed setting. *Annu Rev Immunol* (2013) 31:563–604. doi: 10.1146/annurev-immunol-020711-074950

55. Cella M, Sallusto F, Lanzavecchia A. Origin, maturation and antigen presenting function of dendritic cells. *Curr Opin Immunol* (1997) 9(1):10–6. doi: 10.1016/S0952-7915(97)80153-7

56. Roche PA, Furuta K. The ins and outs of MHC class II-mediated antigen processing and presentation. *Nat Rev Immunol* (2015) 15(4):203–16. doi: 10.1038/nri3818

57. Banchereau J, Steinman RM. Dendritic cells and the control of immunity. *Nature* (1998) 392(6673):245–52. doi: 10.1038/32588

58. Jyothi MD, Khar A. Regulation of CD40L expression on natural killer cells by interleukin-12 and interferon gamma: its role in the elicitation of an effective antitumor immune response. *Cancer Immunol Immunother.* (2000) 49(10):563–72. doi: 10.1007/s002620000151

59. Carbone E, Terrazzano G, Ruggiero G, Zanzi D, Ottaiano A, Manzo C, et al. Recognition of autologous dendritic cells by human NK cells. *Eur J Immunol* (1999) 29(12):4022–9. doi: 10.1002/(SICI)1521-4141(199912)29:12<4022::AID-IMMU4022>3.0.CO;2-O

60. Elgueta R, Benson MJ, de Vries VC, Wasiuk A, Guo Y, Noelle RJ. Molecular mechanism and function of CD40/CD40L engagement in the immune system. *Immunol Rev* (2009) 229(1):152–72. doi: 10.1111/j.1600-065X.2009.00782.x

61. Boussiotis VA, Lee BJ, Freeman GJ, Gribben JG, Nadler LM. Induction of T cell clonal anergy results in resistance, whereas CD28-mediated costimulation primes for susceptibility to fas- and bax-mediated programmed cell death. *J Immunol* (1997) 159(7):3156–67.

62. Mallone R, Kochik SA, Reijonen H, Carson B, Ziegler SF, Kwok WW, et al. Functional avidity directs T-cell fate in autoreactive CD4+ T cells. *Blood.* (2005) 106(8):2798–805. doi: 10.1182/blood-2004-12-4848

63. Sundstedt A, Höidén I, Hansson J, Hedlund G, Kalland T, Dohlsten M. Superantigen-induced anergy in cytotoxic CD8+ T cells. *J Immunol* (1995) 154 (12):6306–13.

64. Gulzar N, Copeland KFT. CD8+ T-cells: function and response to HIV infection. *Curr HIV Res* (2004) 2(1):23–37. doi: 10.2174/1570162043485077

65. Mescher MF, Popescu FE, Gerner M, Hammerbeck CD, Curtsinger JM. Activation-induced non-responsiveness (anergy) limits CD8 T cell responses to tumors. *Semin Cancer Biol* (2007) 17(4):299–308. doi: 10.1016/j.semcancer.2007.06.008

66. Kalekar LA, Schmiel SE, Nandiwada SL, Lam WY, Barsness LO, Zhang N, et al. CD4(+) T cell anergy prevents autoimmunity and generates regulatory T cell precursors. *Nat Immunol* (2016) 17(3):304–14. doi: 10.1038/ni.3331

67. Redmond WL, Linch SN. Combinatorial immunotherapeutic approaches to restore the function of anergic tumor-reactive cytotoxic CD8+ T cells. *Hum Vaccines Immunother.* (2016) 12(10):2519–22. doi: 10.1080/21645515.2016.1193277

68. Crespo J, Sun H, Welling TH, Tian Z, Zou W. T Cell anergy, exhaustion, senescence, and stemness in the tumor microenvironment. *Curr Opin Immunol* (2013) 25(2):214–21. doi: 10.1016/j.coi.2012.12.003

69. Davoodzadeh Gholami M, Kardar GA, Saeedi Y, Heydari S, Garssen J, Falak R. Exhaustion of T lymphocytes in the tumor microenvironment: Significance and effective mechanisms. *Cell Immunol* (2017) 322:1–14. doi: 10.1016/j.cellimm.2017.10.002

70. Macián F, Im SH, García-Cózar FJ, Rao A. T-Cell anergy. *Curr Opin Immunol* (2004) 16(2):209–16. doi: 10.1016/j.coi.2004.01.013

71. Kapsenberg ML. Dendritic-cell control of pathogen-driven T-cell polarization. *Nat Rev Immunol* (2003) 3(12):984–93. doi: 10.1038/nri1246

72. Lutz MB, Backer RA, Clausen BE. Revisiting current concepts on the tolerogenicity of steady-state dendritic cell subsets and their maturation stages. *J Immunol* (2021) 206(8):1681–9. doi: 10.4049/jimmunol.2001315

73. van Vliet SJ, den Dunnen J, Gringhuis SI, Geijtenbeek TB, van Kooyk Y. Innate signaling and regulation of dendritic cell immunity. *Curr Opin Immunol* (2007) 19(4):435–40. doi: 10.1016/j.coi.2007.05.006

74. Cabeza-Cabrerizo M, Cardoso A, Minutti CM, Pereira da Costa M, Reis e Sousa C. Dendritic cells revisited. *Annu Rev Immunol* (2021) 39:131–66. doi: 10.1146/annurev-immunol-061020-053707

75. O'Sullivan B, Thomas R. CD40 and dendritic cell function. *Crit Rev Immunol* (2003) 23(1–2):83–107. doi: 10.1615/CritRevImmunol.v23.i12.50

76. Vivier E, Raulet DH, Moretta A, Caligiuri MA, Zitvogel L, Lanier LL, et al. Innate or adaptive immunity? the example of natural killer cells. *Science.* (2011) 331 (6013):44–9. doi: 10.1126/science.1198687

77. Clatza A, Bonifaz LC, Vignali DAA, Moreno J. CD40-induced aggregation of MHC class II and CD80 on the cell surface leads to an early enhancement in antigen presentation. *J Immunol* (2003) 171(12):6478–87. doi: 10.4049/jimmunol.171.12.6478

78. Ahluwalia P, Ahluwalia M, Mondal AK, Sahajpal NS, Kota V, Rojiani MV, et al. Natural killer cells and dendritic cells: Expanding clinical relevance in the non-small cell lung cancer (NSCLC) tumor microenvironment. *Cancers.* (2021) 13 (16):4037. doi: 10.3390/cancers13164037

79. Liu S, Galat V, Galat Y, Lee YKA, Wainwright D, Wu J. NK cell-based cancer immunotherapy: from basic biology to clinical development. *J Hematol Oncol* (2021) 14(1):7. doi: 10.1186/s13045-020-01014-w

80. Bednarski JJ, Zimmerman C, Berrien-Elliott MM, Foltz JA, Becker-Hapak M, Neal CC, et al. Donor memory-like NK cells persist and induce remissions in pediatric patients with relapsed AML after transplant. *Blood.* (2022) 139(11):1670–83. doi: 10.1182/blood.2021013972

81. Huntington ND, Cursons J, Rautela J. The cancer-natural killer cell immunity cycle. *Nat Rev Cancer.* (2020) 20(8):437–54. doi: 10.1038/s41568-020-0272-z

82. Kundu S, Gurney M, O'Dwyer M. Generating natural killer cells for adoptive transfer: expanding horizons. *Cytotherapy* (2021) 23(7):559–66. doi: 10.1016/j.jcyt.2020.12.002

frontiers | Frontiers in Immunology

TYPE Original Research
PUBLISHED 19 January 2023
DOI 10.3389/fimmu.2022.1054186

OPEN ACCESS

EDITED BY
Julie Decock,
Qatar Biomedical Research Institute, Qatar

REVIEWED BY
Chiranjib Pal,
West Bengal State University, India
Dalina Tanyong,
Mahidol University, Thailand
Abdullahi Aliyu,
A'Sharqiyah University, Oman

*CORRESPONDENCE
Debasish Maiti
debumaiti@gmail.com;
debasish.maiti@tripurauniv.in

SPECIALTY SECTION
This article was submitted to Cancer Immunity and Immunotherapy, a section of the journal Frontiers in Immunology

RECEIVED 26 September 2022
ACCEPTED 19 December 2022
PUBLISHED 19 January 2023

CITATION
Nath P, Modak S, Aktar T, Maiti S, Ghosh A, Singh R, Debnath M, Saha B and Maiti D (2023) Olive leaves extract alleviates inflammation and modifies the intrinsic apoptotic signal in the leukemic bone marrow. *Front. Immunol.* 13:1054186. doi: 10.3389/fimmu.2022.1054186

Olive leaves extract alleviates inflammation and modifies the intrinsic apoptotic signal in the leukemic bone marrow

Priyatosh Nath[1], Snehashish Modak[1], Tamanna Aktar[1], Sharanya Maiti[2], Anisha Ghosh[2], Riddha Singh[3], Mousumi Debnath[4], Bhaskar Saha[5] and Debasish Maiti[1]*

[1]Immunology Microbiology Laboratory, Department of Human Physiology, Tripura University, Agartala, Tripura, India, [2]Delhi Public School Megacity, Kolkata, West Bengal, India, [3]Hariyana Vidyamandir, Kolkata, West Bengal, India, [4]Department of Biosciences, Manipal University Jaipur, Jaipur, Rajasthan, India, [5]National Centre for Cell Science, Pune, Maharashtra, India

Introduction: Current anti-leukemic chemotherapies with multiple targets suffer from side effects. Synthetic drugs with huge off-target effects are detrimental to leukemic patients. Therefore, natural plant-based products are being increasingly tested for new anti-leukemic therapy with fewer or no side effects. Herein, we report the effect of ethanolic olive leaves extract (EOLE) on the K562 cell line and on the bone marrow (BM) of N-ethyl-N-nitrosourea (ENU)-induced leukemic mice.

Methods: Using standard methodologies, we assessed viability, chromatin condensation, and induction of apoptosis in EOLE-treated K562 cells *in-vitro*. The anti-leukemic activity of EOLE was assayed by measuring ROS, levels of various cytokines, expression of iNOS and COX-2 gene, and changes in the level of important apoptosis regulatory and cell signaling proteins *in-vivo*.

Result: K562 cells underwent apoptotic induction after exposure to EOLE. In the BM of leukemic mice, EOLE therapy decreased the number of blast cells, ROS generation, and expression of NF-κB and ERK1/2. IL-6, IL-1β, TNF-α, iNOS, and COX-2 were among the inflammatory molecules that were down-regulated by EOLE therapy. Additionally, it decreased the expression of anti-apoptotic proteins BCL2A1, BCL-xL, and MCL-1 in the BM of leukemic mice.

Discussion: Chronic inflammation and anomalous apoptotic mechanism both critically contribute to the malignant transformation of cells. Inflammation in the tumor microenvironment promotes the growth, survival, and migration of cancer cells, accelerating the disease. The current investigation showed that EOLE treatment reduces inflammation and alters the expression of apoptosis regulatory protein in the BM of leukemic mice, which may halt the progression of the disease.

KEYWORDS

leukemia, olive leaf, ENU, inflammation, apoptosis

1 Introduction

Leukemia, a malignant blood disorder, is characterized by an abnormal hematopoiesis and an accumulation of partially differentiated leukemic blasts in the bone marrow (BM). Entry of these blasts into the circulation alters the composition of normal blood and impairs its functions. The leukemic blasts infiltrate and gradually incapacitate the liver, the kidneys, the lungs, the spleen, and the lymph nodes. Leukemia occurs in individuals of all age groups. Relapse in critical patients and resistance to chemotherapy cause severe hematological complications and therapeutic incompatibility specifically after a chemotherapy eventuating in death of the leukemia patients (1). The leukemic cells and other cells in the BM microenvironment secrete several soluble factors in a dysregulated manner, altering cell signalling and aiding the leukemic cells' survival and resistance to chemotherapy. The leukemic cells become drug resistant by several mechanisms, including inactivation of drug, inhibition of apoptosis, increased drug efflux, decreased drug uptake, altered drug metabolism, enhanced DNA repair and so on (2). The aged leukemia patients cannot sustain intensive chemotherapy due to severe toxicity, or a BM transplant leads to high mortality (3). Overcoming these complications requires the development of therapeutics that will be less toxic, selectively target malignant cells, and strengthen the natural defence mechanism of the individual.

Two important abnormal phenotypes prevalent in leukemia are BM inflammation and apoptotic resistance of malignantly transformed cells (4, 5). The very root of these anomalies lies in the abnormal activation of various signaling molecules, including the nuclear factor-kappa B (NF-κB) and excessive release of various inflammatory cytokines (6, 7). Dysregulation of NF-κB is strongly associated with malignant transformation. It mediates inflammation, accelerates cell proliferation, and makes the cancer cells resistant to apoptosis. It stimulates angiogenesis and promotes metastasis of tumor cells. Constitutive NF-κB activation is commonly seen in Acute Myeloid Leukemia (AML) patients and experimental animal models of AML (7, 8). NF-κB also regulates apoptosis by directly regulating the expression of anti-apoptotic B-cell lymphoma 2-related proteins A1 (BCL2A1) in the murine hematopoietic system (9). Increased anti-apoptotic BCL2A1 and B-cell lymphoma-extra-large (BCL-xL) expression in the mouse hematopoietic system makes the hematopoietic stem and progenitor cells resistant to apoptosis, often leading to hematopoietic transformation and development of leukemia (10, 11). NF-κB is thus an important target for therapeutic intervention in leukemia.

The olive fruit and leaves contain many biologically active polyphenol compounds, including main constituents' oleuropein and hydroxytyrosol. Both oleuropein and hydroxytyrosol are chemopreventive and kill cancer cells by multiple mechanisms (12, 13). The crude olive extract and the olive polyphenols tested in many tumor cell lines and animal tumor models have shown substantial therapeutic benefits (14). The olive leaf extracts induce apoptosis in K-562 leukemia cells and trigger their differentiation into monocyte-macrophage lineage (15). The EOLE potentiates the antioxidant enzyme functions through up-regulation of nuclear factor erythroid 2-related factor 2 (Nrf2) *in vivo* (16). The EOLE treatment also lowers NF-κB expression and the concentration of inflammatory cytokines in inflamed lungs. This observation is consistent with the available literature describing the pharmacologic properties of crude olive leaf extract, or olive polyphenols, which led us to choose EOLE for the current study. Before finalizing this research design, a pilot study with EOLE was conducted on N-ethyl-N-nitrosourea (ENU) induced leukemic mice substantially reduced the total leukocyte and blast count in the peripheral circulation. This study investigated the anti-leukemic effects of EOLE with reference to its anti-inflammatory and cytotoxic activities.

2 Materials and methods

2.1 Preparation of plant extract and phytochemical profiling

The fresh leaves of arbequina olive (*Olea europaea*) were provided by the Rajasthan Olive Cultivation Limited (ROCL), Bassi, Rajasthan, India. The plant was authenticated by the plant taxonomist at the Department of Botany, University of Rajasthan. A herbarium of the plant was preserved along the voucher accession number RUBL211669, dated 06/03/2018. The ethanolic extract of the Olive leaves was prepared according to the previously described method (16). The dried extract was kept at -20°C to prevent degradation.

The chemical formulation of EOLE was determined with liquid chromatography-electrospray ionization tandem mass spectrometry (LC-ESI MS/MS) (Agilent Technologies, Palo Alto, CA, USA) (16). The LC-ESI MS/MS analysis identified around 23 different phytochemicals in EOLE; of which, hydroxytyrosol, oleuropein, and apigenin compose significant fractions (16).

2.2 Cell culture

Human chronic myelogenous leukemia K562 cell was procured from the National Centre for Cell Science (NCCS), Pune, Maharashtra, India, and was expanded in our laboratory. Cells were propagated with fetal bovine serum (FBS) supplemented RPMI 1640 medium (Gibco) inside a humidified cell culture incubator at 37°C temperature and 5% CO_2. On reaching about 80% confluence, the culture was split for use in various experiments *in-vitro* (17).

2.3 Cytotoxicity assay

The cytotoxicity of EOLE on K562 cells and naïve mouse splenocytes was investigated by 3-(4,5-Dimethylthiazol-2-yl)-2,5-diphenyltetrazolium bromide (MTT) (Sigma Aldrich) assay in a 96-well plate with slight modification of a standard protocol (18). To each well of 96 well plates 0.1 ml cell suspensions with a cell density of 2×10^5 cells/ml of RPMI media were seeded and maintained under culture condition. The treated groups of cells were given EOLE (dissolved in cell culture grade dimethyl sulfoxide (DMSO) and successively in RPMI-1640 reducing the final concentration of DMSO to 0.2% only) at the concentrations of 5, 10, 20, 50, and 100 µg/ml of media, whereas the control cells were given 0.2% cell culture grade dimethyl sulfoxide (DMSO). After incubation for 24, 48, and 72 hours the cells were labelled with MTT solution at final concentration of 5mg/ml and incubated for 2-4 hours at 37°C. The resultant formazan crystal formed in control and treated wells was dissolved by the addition of DMSO. The cytotoxic effect of EOLE was calculated as: (%) viability = (absorbance of test-absorbance of blank)/(absorbance of control-absorbance of blank) × 100 (18), [where, the test represents the K562 cells that received EOLE treatment; control represents the untreated K562 cells; and the blank represents only media plus MTT solution and DMSO].

2.4 Cell viability assay

The viability of EOLE treated cells was measured by trypan blue dye exclusion assay with minor modification of a standard protocol. The K562 cells were treated with EOLE at 50 and 100µg/ml, incubated for 24 hours and preceded with trypan blue staining. The numbers of live and dead cells were counted under bright-field microscope using a Neubauer haemocytometer. The calculation was done using the formula:

Viable cells (%) = (1 – number of blue or dead cells/total number of cells) x 100 (19).

2.5 The AO/EtBr and DAPI staining assay

The Acridine orange/Ethidium bromide (AO/EtBr) and 4′, 6-diamidino-2-phenylindole (DAPI) staining were carried out to study the EOLE-induced cell death and chromatin condensation in K562 cells following standard protocols (20, 21). The calculation was done using the formulae:

Non-apoptotic cells(%)

$$= (1 - \text{No. of yellow or orange cells/total no. of cells}) \times 100$$

Nuclear fragmented cells (%)

$$= (1 - \text{No. of bright blue cells/total no. of cells}) \times 100$$

2.6 DNA ladder assay

The nuclear DNA damage by EOLE was studied using a DNA ladder assay (22). In brief, the DNA from the control and treated K562 cells were electrophoretically separated in 1.5% agarose gel. The DNA bands were visualized under ultraviolet (UV) illumination in a Bio-Rad ChemiDoc™ MP imaging system.

2.7 Western blot analysis of apoptosis in K562 cells

Apoptosis induction in EOLE-treated K562 cells was investigated by western blotting (23). An equal amount of protein from the EOLE treated and control K562 cells were separated in SDS-PAGE, transferred to a nitrocellulose membrane, and processed to detect the protein of interest. Primary and secondary antibodies against the target proteins-GAPDH, BCL-2, BCL-xL, BCL2A1, MCL-1, BAX, PUMA, Cytochrome-C, NF-κB, and ERK-1/2 were procured from Abcam (United Kingdom).

2.8 Development of leukemia in mice

The animal experiments were performed with the approval from the institutional animal ethics committee (IAEC), reference no. TU/IAEC/2018/XVII/II dated 18th Dec 2018. The healthy BALB/c mice, of both sexes, same age and body weight, were housed at the institutional animal house, maintained under a standard living condition of 25°C ± 2°C temperature, 45% ± 10% relative humidity, 12h light/dark cycle and food and water *ad libitum*. Leukemia in mice was induced by ENU (24). The development of leukemia was confirmed by blasts in the peripheral blood (24). As per our study, 46% mice developed leukemia within 20 weeks after ENU injection.

2.9 Exclusion and inclusion criteria for leukemic mice

The primary criteria for exclusion and inclusion of mice into the experiment were the status of leukemia. The mice showing more than 20% myeloid or lymphoid blast in the peripheral blood after five months of ENU injection (25) were considered

leukemic. The leukemic mice with excessive weakness or very low body weight were excluded from the studies.

2.10 Mice groups and treatment schedule for *in-vivo* studies

Four different groups of mice were taken for this study (n=6 in each group) (26). Treatment was given by oral gavage for 1 month. Details of animal groups and treatment are: Group-1: Normal control- given sterile water; Group-2: Leukemia control- given sterile water; Group-3: Normal + EOLE- given EOLE in water at 200mg/kg body weight; and Group-4: Leukemia + EOLE- given EOLE dissolved in water at 200mg/kg body weight.

A toxicity study (unpublished) of EOLE was performed in mice before choosing the dose for the *in-vivo* treatment. In brief, the EOLE was orally administered in different groups of mice at the doses of 50, 100, 200, 500, and 1000mg/kg body weight daily for 28 days. During this period the animals were observed for changes in food and water intake, body weight and abnormal symptoms, physical weakness, and death. Notably, the mice group given EOLE at 1000mg/kg body weight developed diarrhoea within 3 to 4 days of continued oral administration. However, no such symptoms were seen in the mice groups given EOLE at 50, 100, and 200mg/kg body weight. The food and water intake, body weight, and physical status in these groups of animals were found similar to the control mice. Therefore, EOLE at 200mg/kg body weight was chosen for *in-vivo* treatment.

2.11 Animal sacrifice and sample collection

On completion of treatment, all the mice under the experiment were sacrificed following the IAEC guidelines. Mice were allowed to inhale chloroform and euthanized by cervical dislocation. The mice assorted in groups were then dissected in aseptic conditions to collect the organs, spleen, and hind limbs to isolate BM from femur bones. Blood was collected before euthanasia by puncturing the retro-orbital sinus with a sterile capillary tube.

2.12 Complete blood count and morphological study

The complete blood count (CBC) of EDTA containing peripheral blood samples was performed in the Trivitron (Celenium-19) digital blood analyzer system (23). The blast cell counting was performed manually under the microscope. Morphology of blood cells was examined conventionally. In brief, a thin smear of blood was prepared and stained using a standard protocol (27). The observation was carried out under 40X and 100X objectives in bright-field microscopy, Leica DM4000B LED fluorescence microscope.

2.13 Serum lactate dehydrogenase activity

The lactate dehydrogenase activity in serum was measured with little modification of the protocol of Simaga et al., 2008 (28). The activity was measured spectrophotometrically at room temperature for 3 min by recording decrease in absorbance of NADH at 340 nm in UV 1900 Shimadzu UV visible double beam spectrophotometer.

2.14 Bone marrow smear preparation and morphological study

The femoral marrow cells were isolated (29). A thin smear of the BM cells was drawn on a grease-free glass slide, stained with Leishman's stain (27) and was observed under a Leica DM4000B LED fluorescence microscope.

2.15 Determination of inflammatory and hematopoietic cytokines in the BM

The indicated cytokines in the BM was measured using the method described by Pino et al., 2010 (30). The supernatants of PBS suspended BM samples were assayed for the indicated cytokines such as IL-1α, IL-1β, TNF-α, TGF-β, VEGF, SCF, G-CSF, GM-CSF, IL-3, and IL-6 by respective cytokine ELISA kits following the manufacturer's protocol (PeproTech, USA and ImmunoTools GmbH, Germany).

2.16 Immunoblots for apoptosis-related and signaling proteins in the BM

The total protein was isolated from the BM cells, resolved on polyacrylamide gels, transferred onto PVDF membrane and probed with the respective primary and secondary antibodies (Abcam, United Kingdom) (31).

2.17 Measurement of ROS production in bone marrow

ROS production in BM was measured following a standard protocol (32). This method used 2-,7-dichlorofluorescein diacetate (DCFDA) as a fluorescence probe. The fluorescence intensity of the samples was taken at $\lambda_{excitation}$ = 488nm and $\lambda_{emission}$ = 530nm in Synergy H1 Hybrid Reader (BioTek Instruments, Inc., Winooski, USA).

2.18 Expression studies of iNOS and COX-2 in bone marrow by real-time PCR

RNA from the BM cells was extracted using Trizol reagent (Ambion by Life Technologies, #15596018). The RNA in equal amount was taken from each sample to synthesize cDNA using the BIO-RAD iScript ™ cDNA synthesis kit (#170-8891). The gene expression was studied in an Applied Biosystem's Step-One Plus real-time PCR system following a standard protocol (16). The sequence of the PCR primer used are: GAPDH Forward: 5′-CAC CAC CCT GTT GCT GTA GCC-3′; GAPDH Reverse: 5′-ACC ACA GTC CAT GCC ATC AC-3′; iNOS Forward: 5'- GCC ACC AAC AAT GGC AAC A-3'; iNOS Reverse: 5'- CGT ACC GGA TGA GCT GTG AAT T-3'; COX-2 Forward: 5'- GAA GAT TCC CTC CGG TGT TT-3'; COX-2 Reverse: 5'- CCC TTC TCA CTG GCT TAT GTA G-3'

2.19 Immunohistochemistry of spleen

Splenic sections were stained for immunohistochemistry and detection of leukemic blast using a standard protocol (10). In brief, thin sections of spleen were deparaffinised and hydrated before incubating in hydrogen peroxide (H2O2) solution to block endogenous peroxidase activity. The sections were blocked with bovine serum albumin (BSA) solution and incubated with anti-mouse rabbit polyclonal antibody to BCL2A1/GRS and MCL-1 antibody for overnight. On the next day, the sections were washed with PBS and incubated with goat anti-rabbit IgG H&L (HRP) (cat. ab97051). Finally, the sections were stained with diaminobenzidine (DAB) and followed by counterstaining with hematoxylin. The sections were then examined and photographed under a Leica DM4000B LED microscope.

2.20 Preparation and isolation of mouse peritoneal macrophage

The peritoneal macrophage from the BALB/c mice was isolated with a slight modification of a standard protocol (33). The macrophage cells were maintained with the serum-supplemented DMEM/F12 medium.

2.21 Macrophage inflammation assay

The effect of EOLE on macrophages- Macrophage + PBS (Normal control); Macrophage + LPS (Inflammation control); Macrophage + LPS &PBS (Treatment-1); Macrophage + LPS and EOLE at 50μg/ml (Treatment-2); Macrophage + LPS and EOLE at 100μg/ml (Treatment-3)- was assayed *in-vitro* (34). Lipopolysaccharide (LPS) was added to the macrophages at the final concentration of 100ng/ml. The LPS stimulates the macrophage to release TNF-α and IL-1β which were studied in the presence and absence of EOLE.

2.22 Statistical analysis

The statistical analysis was performed in GraphPad InStat 3 software. Statistical significance was tested by one-way ANOVA followed by Tukey's multiple comparison tests between the control and treated groups. The p-value $p<0.05$ was considered statistically significant.

3 Results

3.1 EOLE is cytotoxic and induces apoptosis to the K562 cells

MTT assay showed that EOLE (up to 100μg/ml) had significant toxicity against K562 cells but not against naïve mouse splenocytes. At the given dose of EOLE 50 μg/ml, the viability percentage of K562 cells reduced significantly to 59.78 ± 5.46 ($p<0.001$), 29.48 ± 7.2 ($p<0.001$), and 7.16 ± 1.1 ($p<0.001$), respectively, after 24, 48 and 72 hours of incubation. The viability percentage of K562 cells further reduced to 20.42 ± 2.79 ($p< 0.001$), 9.72 ± 3.36 ($p< 0.001$), and 2.64 ± 0.71 ($p< 0.001$), respectively, for 24, 48, and 72 hours at the EOLE dose of 100 μg/ml (Figure 1A i & ii). The trypan blue dye exclusion experiment confirmed the above data (Figure 1B a. i to iv). The control and treated K562 cells were also stained with the AO/EtBr and DAPI and observed under fluorescence microscope to visualize the apoptotic features like membrane blebbing and chromatin condensation. AO/EtBr gives distinctive characteristic features to normal and apoptotic cells. The normal cell fluoresced green; however, the early apoptotic cell showed bright yellow areas in the nucleus. Concurrently, the late apoptotic cell took up EtBr due to loss of membrane integrity and fluoresced orange (Figure 1B b. i to iv). The percentage of non-apoptotic K562 cells presented along a bar diagram showed a significantly ($p<0.001$) less non-apoptotic K562 cells in EOLE treated groups compared to control group (Figure 1B b. iv). The DAPI staining of K562 cells reflects the changes in the nucleus. The control K562 cells showed round to oval-shaped nuclei with diffuse blue staining, whereas many cells in EOLE treated groups fluoresce bright blue indicating chromatin condensation and nuclear fragmentation (Figure 1B c. i to iv). The number of chromatin condensed cell was found significantly higher in 100μg/ml EOLE treated group (Fig- 1Bc. iv). DNA fragmentation in K562 cells was also assayed by DNA ladder assay. The DNA from the control K562 cells produced a thick band in the agarose gel close to the loading well, whereas the DNA from EOLE-treated K562 cells produced a smear due to DNA fragmentation by endonucleases (Figure 1C).

10.3389/fimmu.2022.1054186

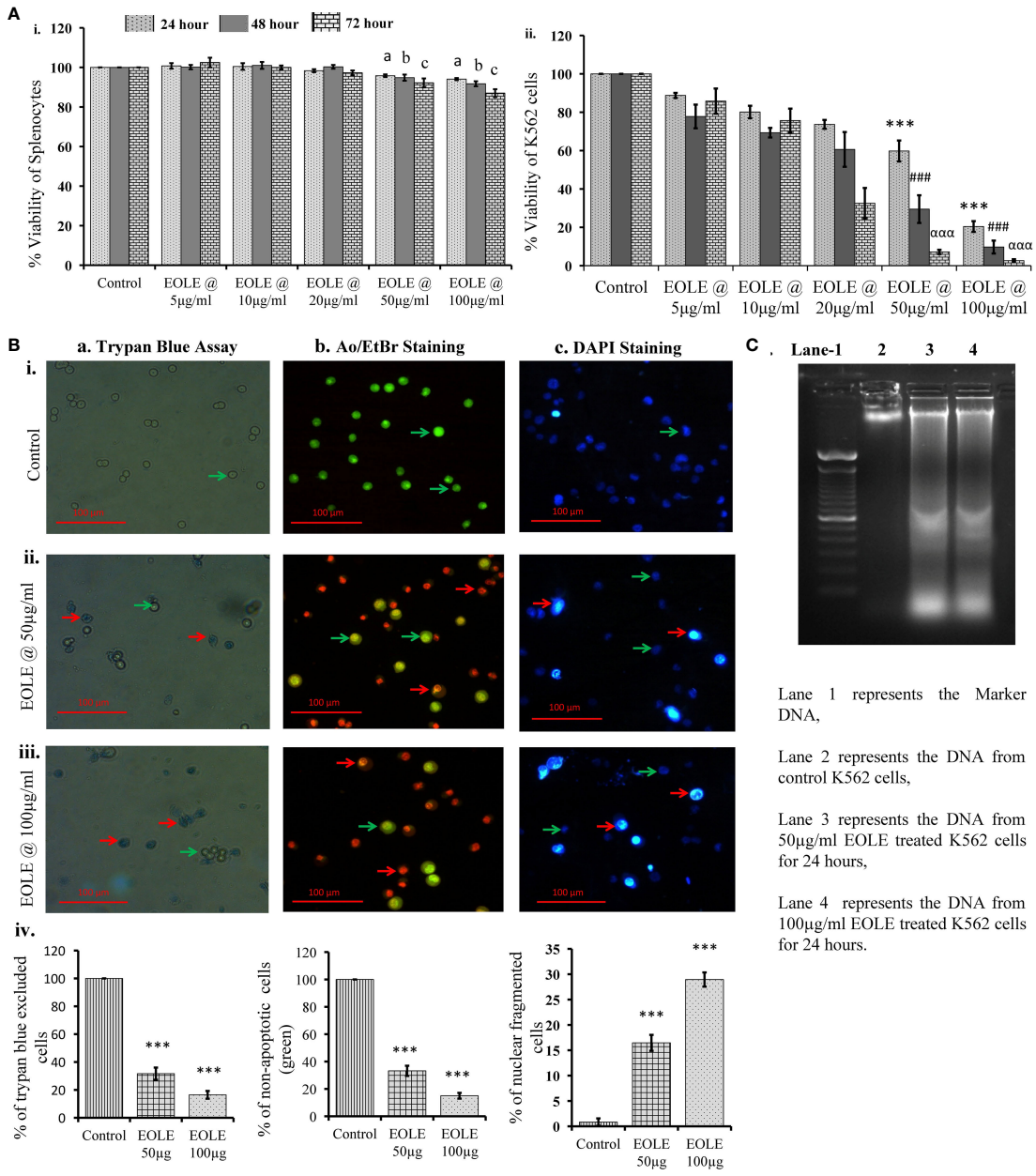

FIGURE 1
Figures showing the cytotoxic activity of EOLE: **(A)** Viability percentage of control and EOLE-treated K562 and splenocytes evaluated through MTT assay, where (i) Viability of mouse splenocytes, (ii) Viability of K562 cells; values are expressed as mean ± SD of 3 observations. The statistical significance was tested using one-way ANOVA following Tukey's multiple comparison tests by comparing the values as, control *vs.* treatments separately for 24 hours, 48 hours, and 72 hours. P value, $p < 0.05$ was considered as statistically significant. When compared between control *vs.* treatment for 24 hours the level of significance is denoted as, a = not significant when $p > 0.05$; * when $p < 0.05$; ** when $p < 0.01$; and *** when $p < 0.001$. When compared between control *vs.* treatment for 48 hours the level of significance is denoted as, b = not significant when $p > 0.05$; # when $p < 0.05$; ## when $p < 0.01$; and ### when $p < 0.001$. When compared between control *vs.* treatment for 72 hours the level of significance is denoted as, c = not significant when $p > 0.05$; α when $p < 0.05$; αα when $p < 0.01$; and ααα when $p < 0.001$; **(B)** Result of the trypan blue dye exclusion assay, AO/EtBr staining, and DAPI staining, where (a) Trypan blue assay, (b) AO/EtBr staining, (c) DAPI staining: (i) Representative images of control group, (ii) Representative images of EOLE-treated (50 µg/ml) group, (iii) Representative images of EOLE-treated (100 µg/ml) group, (iv) Bar diagrams showing results of staining assay. Values are expressed as mean ± SD of 3 different observations. The statistical significance was tested using one-way ANOVA followed by Tukey's multiple comparison tests by comparing the values as, control *vs.* treatments. P-value, $p < 0.05$ was considered as statistically significant and denoted as, a = not significant when $p > 0.05$; * when $p < 0.05$; ** when $p < 0.01$; and *** when $p < 0.001$; **(C)** The representative image of the DNA ladder assay.

3.2 EOLE induces the expression of apoptotic proteins in K562 cells

The cytoplasm of an apoptotic cell always possesses more pro-apoptotic proteins and fewer anti-apoptotic proteins. Therefore, the changes in BCL-2, BCL-xL, BAX, PUMA, and cytochrome c proteins in the control and treated K562 cells were studied by western blotting (Figure 2). The densitometry analysis of protein bands showed a significant reduction in anti-apoptotic proteins BCL-2 (p<0.001) (Figure 2B), BCL-xL (p<0.001) (Figure 2C); and an increase in pro-apoptotic proteins BAX (p<0.01) (Figure 2D), and PUMA (p<0.001) (Figure 2E) in treated K562 cells at the concentration of 50µg and 100 µg EOLE/ml of media. The western blot study also showed significantly more (p<0.01) cytochrome c in the treated K562 cells than the control due to the increased release of cytochrome c from the mitochondria of EOLE-induced apoptotic cells (Figure 2F).

3.3 EOLE reduced leukemic blast cell in blood and bone marrow in mice model

Leukemia was developed in mice within 20 weeks of ENU challenge. In leukemic mice, the leucocyte count increased several folds. A significant part of these leucocyte comprised leukemic blasts characterized by a large nucleus and scant cytoplasm. These blasts accumulated in the BM and blood. The microscopic observation of blood and BM smears revealed a significantly (p<0.05) lesser blast count in EOLE-treated leukemic mice compared to leukemic control (Figures 3A, B). The total count of blood corpuscles and hemoglobin showed a considerable difference among the studied animal groups. The total leukocyte count in the EOLE-treated leukemic group was found significantly (p<0.001) lesser compared to leukemic control mice (Figure 3C). The RBC count, platelet count, and hemoglobin, which were significantly less (p<0.01) in the leukemic control mice, moderately increased in EOLE-treated leukemic mice (Figure 3C).

3.4 EOLE rescues the body weight and improves LDH activity

The average body weight of mice differs among the studied groups of mice. The experiments started by taking mice of almost the same body weight of 11 to 12 gm; however, after the 20th week of ENU administration, the weight of the mice showed a significant difference between the normal and ENU-injected groups. The average weight of ENU-induced leukemic mice was measured

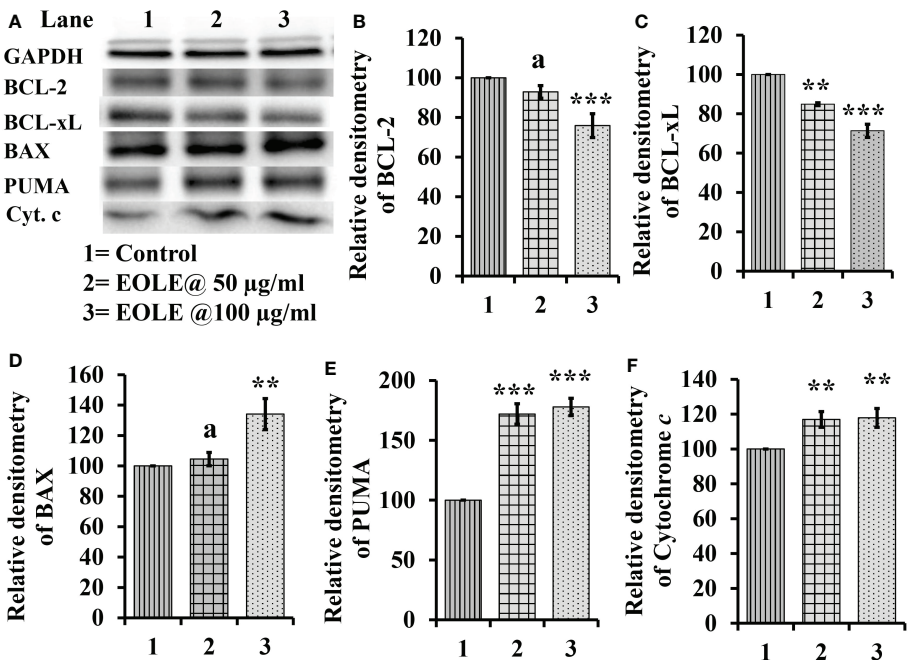

FIGURE 2
Figure showing the expression of many apoptotic pathway proteins in control and EOLE treated K562 cells, where **(A)** Images of protein bands, **(B)** Densitometry plot for BCL-2, **(C)** Densitometry plot for BCL-xL, **(D)** Densitometry plot for BAX, **(E)** Densitometry plot for PUMA, **(F)** Densitometry plot for cytochrome *c* Values are expressed as mean ± SD of 3 observations. The statistical significance was tested using one-way ANOVA following Tukey's multiple comparison tests by comparing the values as, control *vs.* treatments. P-value, p<0.05 was considered as statistically significant and denoted as a= not significant when p > 0.05; * when p < 0.05; ** when p < 0.01; and *** when p < 0.001.

10.3389/fimmu.2022.1054186

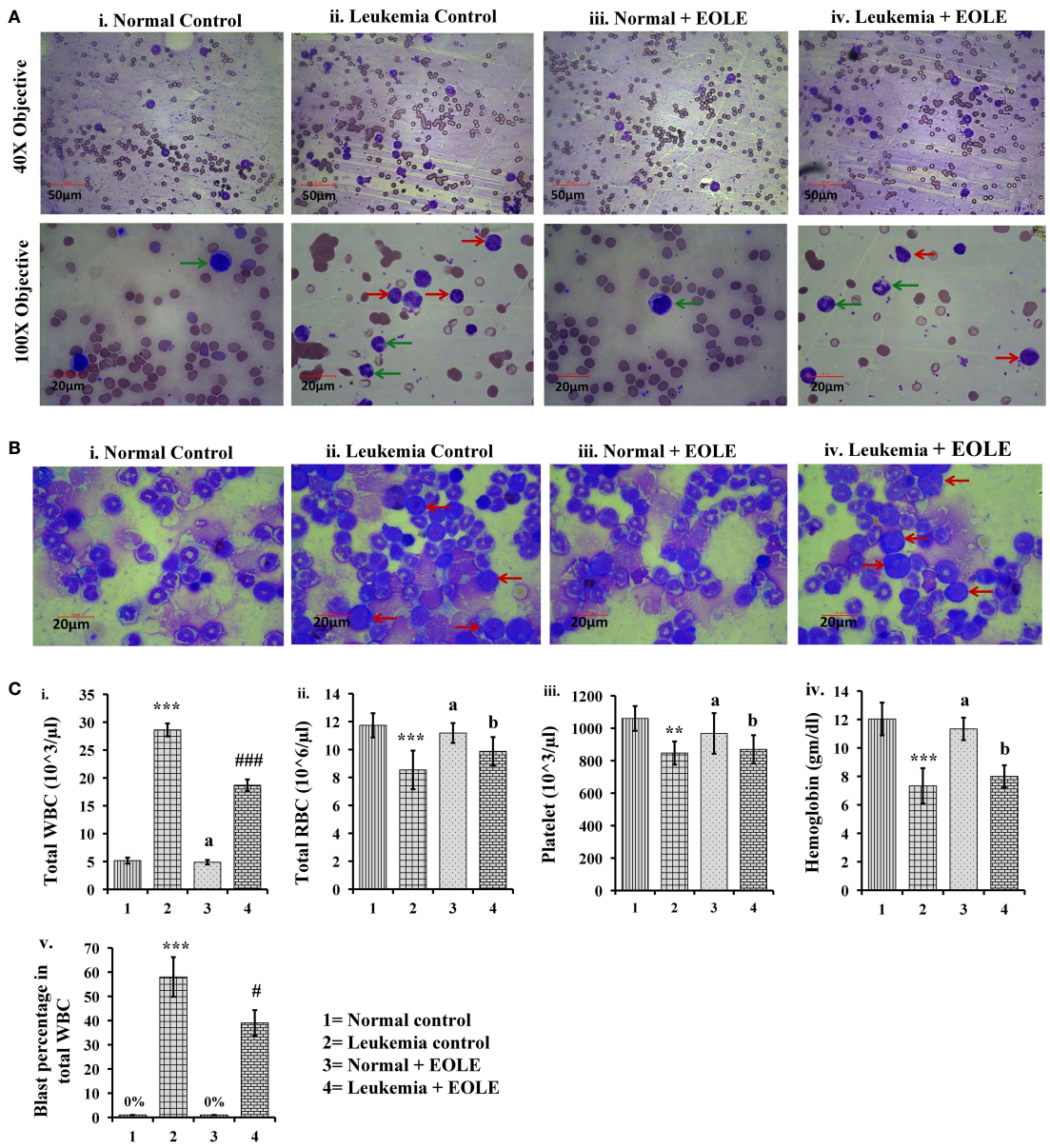

FIGURE 3
Figures showing the morphology of blood bone marrow and various hematologic parameters: **(A)** Representative images of blood smears at different magnifications, where (i) Normal control, (ii) Leukemia control, (iii) Normal + EOLE, (iv) Leukemia+ EOLE. In these figures, the red arrow indicates leukemic blast cells, and the green arrow indicates normal WBCs; **(B)** Representative images of bone marrow, where (i) Normal control, (ii) Leukemia control, (iii). Normal + EOLE, (iv). Leukemia + EOLE. In these figures, the red arrow indicates leukemic blast cells; **(C)** Bar diagrams representing various haematological parameters, where (i) WBC count, (ii) RBC count, (iii) Platelet count, (iv) Hemoglobin concentration, (v) Blast cell count (percentage of total WBC). Values are expressed as mean ± SD of 3 different observations. The statistical significance was tested using one-way ANOVA following Tukey's multiple comparison tests by comparing the values as, Group-1 *vs*. Group-2, 3; Group-2 *vs*. Group- 4. P value, $p < 0.05$ was considered as statistically significant. When compared with Group-1 the level of significance was denoted as, a = not significant when $p > 0.05$; * when $p < 0.05$; ** when $p < 0.01$; and *** when $p < 0.001$. When compared with Group-2 the level of significance was denoted as, b = not significant when $p > 0.05$; # when $p < 0.05$; ## when $p < 0.01$; and ### when $p < 0.001$.

significantly ($p<0.001$) less than the average weight of normal mice at 20th and 24th weeks. After 20 weeks the body weight of the leukemic mice showed slight reduction, however when compared the weight loss was found substantially more in leukemic control mice than EOLE-treated group but not statistically significant ($p>0.05$) (Figure 4A).

LDH is a prognostic marker of cancer progression. In this study, the serum LDH activity was measured significantly

($p<0.01$) higher in leukemic control group than in the normal control. However, in the EOLE-treated leukemic group, it was measured significantly ($p<0.05$) less than in the leukemic control group (Figure 4B).

3.5 EOLE reduces the expression of hematopoietic cytokines- SCF, IL-3, IL-6, GCSF and GM-CSF- in the leukemic bone marrow

Hematopoiesis from the hematopoietic stem cells (HSCs) is a complex process tightly regulated by the hematopoietic cytokines in the BM. The level of major hematopoietic cytokines like G-CSF, GM-CSF, SCF, IL-3, and IL-6 measured in the BM showed variation among different animal groups. The result of ELISA revealed a significantly ($p<0.001$) higher level of these cytokines in the BM of leukemic control mice. However, the leukemic mice that received EOLE treatment had significantly less G-CSF ($p<0.05$), IL-3 ($p<0.001$), and IL-6 ($p<0.01$) (Figure 5).

3.6 EOLE inhibits the inflammation by reducing expression of inflammatory markers

Inflammatory cytokines up-regulate in leukemia support the progression of leukemia. In this study, the protein levels of IL-1α, IL-1β, TNF-α, TGF-β, and VEGF in BM were measured significantly ($p<0.001$) higher in the leukemic control group compared to the normal control. However, the level of these cytokines significantly reduced (IL- 1α ($p<0.001$), TNF-α ($p<0.05$), TGF-β ($p<0.001$), and VEGF ($p<0.01$)) after EOLE treatment (Figure 6A). ROS is an essential mediator of inflammation. The ROS level in the BM was found significantly ($p<0.01$) higher in the leukemic control group compared to normal control. EOLE treatment of leukemic mice significantly ($p<0.05$) reduced ROS production (Figure 6B). Among the other inflammatory markers, the expression of iNOS and the COX-2 gene was measured in the BM of different groups of mice. A significantly higher expression of iNOS ($p<0.05$) and COX-2 ($p<0.01$) was found in the BM of the leukemic control group compared to the normal control. In the EOLE-treated leukemic group, the expression of iNOS and COX-2 was measured moderately less than in the leukemic control group (Figure 6C).

The anti-inflammatory activity of EOLE was further assayed in LPS-induced mouse peritoneal macrophages. LPS stimulates the macrophage to release TNF-α and IL-1β are measured *in-vitro*. The EOLE was found to affect the release of TNF-α and IL-1β from LPS-stimulated macrophages. The culture supernatants assayed through ELISA revealed a significantly ($p< 0.001$) higher TNF-α (Figure 6Di) and IL-1β (Figure 6Dii) levels. However, the release of TNF-α and IL-1β was reduced significantly ($p< 0.001$) in the presence of EOLE.

3.7 EOLE alters intrinsic apoptotic signals in the BM of leukemic mice

Apoptotic resistance is one of the fundamental properties of cancer cells. In this study, the expression of anti-apoptotic

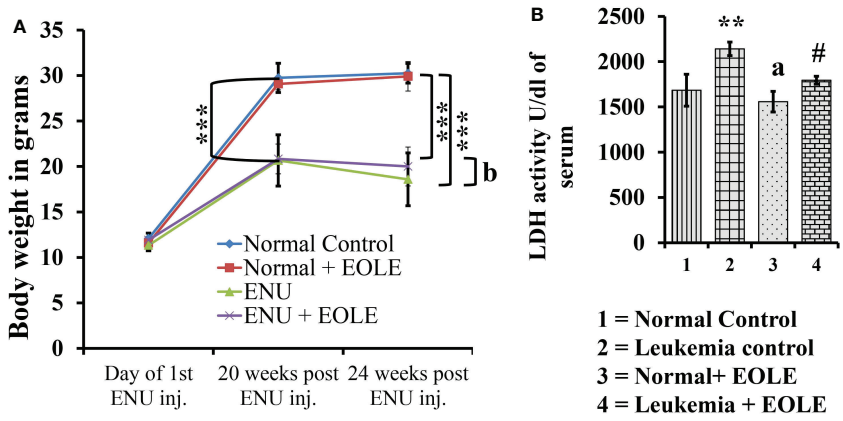

FIGURE 4
The figures show the effect of EOLE treatment on the health parameter of mice, where **(A)** Effect on body weight. Values are expressed as mean ± SD for 6 mice. **(B)** Lactate dehydrogenase activity (LDH) assay. Values are expressed as mean ± SD of 3 different observations. The statistical significance was tested using one-way ANOVA following Tukey's multiple comparison tests by comparing the values as, Group-1 *vs*. Group-2, 3; Group-2 *vs*. Group- 4. P-value, $p < 0.05$ was considered as statistically significant (n = 6).When compared with Group-1 the level of significance was denoted as, a = not significant when $p > 0.05$; * when $p < 0.05$; ** when $p < 0.01$; and *** when $p < 0.001$. When compared with Group-2, b = not significant when $p > 0.05$; # when $p < 0.05$; ## when $p < 0.01$; and ### when $p < 0.001$.

10.3389/fimmu.2022.1054186

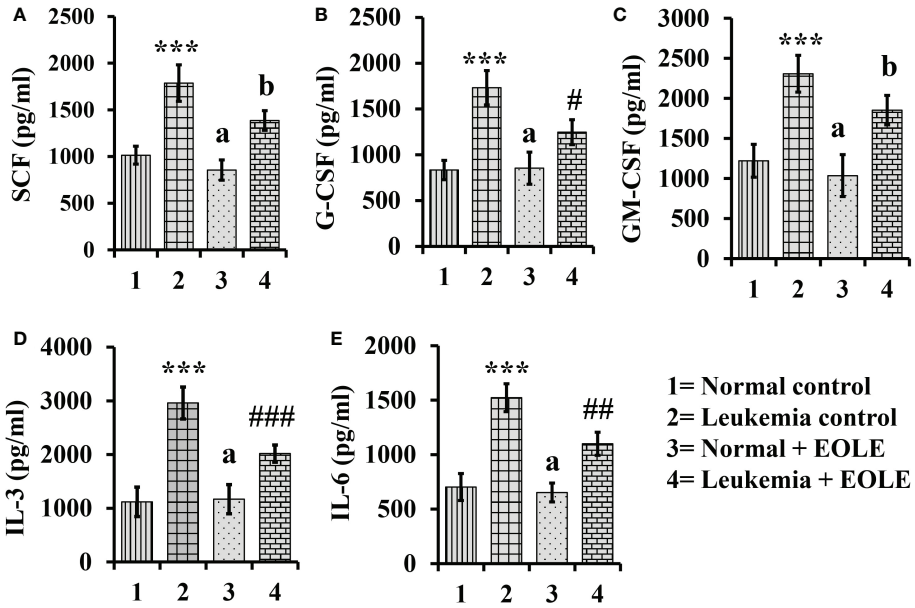

FIGURE 5
Bar diagrams showing the effect of EOLE treatment in the bone marrow concentrations of various hematopoietic cytokines, where **(A)** SCF, **(B)** G-CSF, **(C)** GM-CSF, **(D)** IL-3, **(E)** IL-6; values are expressed as mean ± SD of 3 different observations. The statistical significance was tested using one-way ANOVA and Tukey's multiple comparison tests by comparing the values as, Group-1 *vs*. Group-2, 3; Group-2 *vs*. Group- 4. P value, $p < 0.05$ was considered as statistically significant. When compared with Group-1 the level of significance was denoted as, a = not significant when $p > 0.05$; * when $p < 0.05$; ** when $p < 0.01$; and *** when $p < 0.001$. When compared with Group-2, b = not significant when $p > 0.05$; # when $p < 0.05$; ## when $p < 0.01$; and ### when $p < 0.001$.

BCL2A1, BCL-xL, and MCL-1 proteins was found significantly higher [($p<0.001$), ($p<0.01$), and ($p<0.001$), respectively] in the BM of ENU-induced leukemic mice with lesser expression of pro-apoptotic proteins BAX and PUMA than in control mice. However, following EOLE treatment the expression pattern of the pro-apoptotic and anti-apoptotic proteins was reversed significantly (Figure 7).

3.8 NF-κB and ERK 1/2 were down-regulated by EOLE in leukemic bone marrow

The NF-κB in general induces the expression of several genes that play critical role in cell proliferation and apoptosis, so, the expression of NF-κB in the BM from different groups of mice were assayed. The study revealed a significantly ($p<0.001$) increased expression of NF-κB protein in the BM of leukemic mice. However, it was significantly ($p<0.01$) down-regulated in the EOLE-treated leukemic group (Figures 8A, B).

Similarly the ERK1/2, that transduce extracellular signals to the interior of cell showed aberrant expression. In this study, the western blot analysis of BM cell protein revealed a significantly ($p<0.001$) increased ERK1/2 in leukemic control group compared to normal counterpart. However, in EOLE treated leukemic group, the expression of the same protein was significantly ($p<0.01$) reduced (Figures 8A, C).

3.9 EOLE reduced infiltration of leukemic blast in the spleen

In progressive leukemia, the leukemic blast infiltrates into various bodily organs like the spleen. Therefore, the splenic infiltration of blast cells was investigated in all the groups using immunohistochemical staining (Figure 9). The immunohistochemistry of splenic sections revealed substantially lesser blast cell infiltration in the EOLE-treated leukemic mice compared to the leukemic control mice.

4 Discussion

The life-threatening side effects of existing therapeutics and the acquisition of drug resistance pushing the research globally that is targeted to develop new therapeutics for the treatment of leukemia which is less toxic as well as effective for the treatment of leukemia. The initial development of leukemia starts due to some genetic abnormalities catalysing signaling defects and abnormal cellular function. Chronic inflammation and

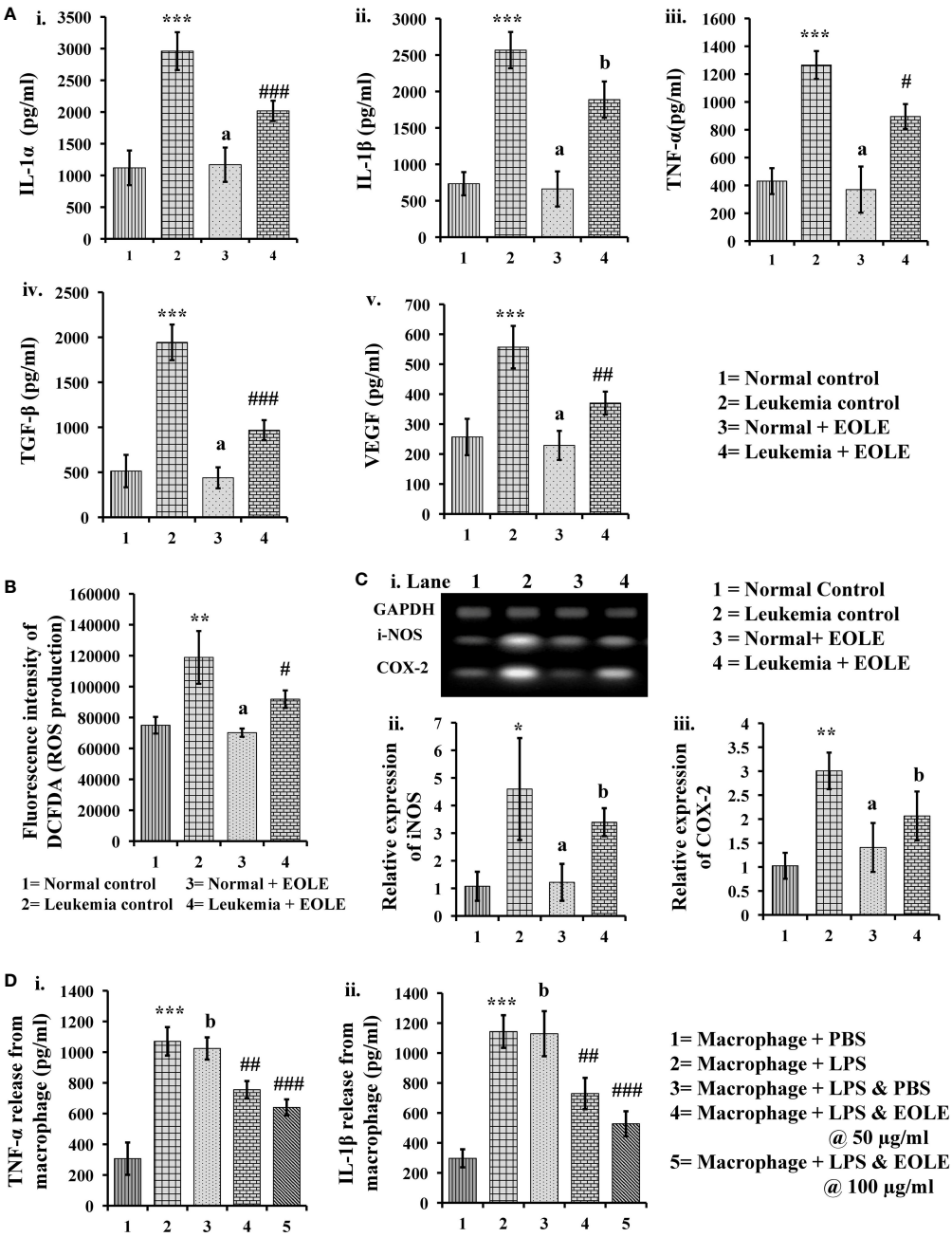

FIGURE 6
Figures showing the result of EOLE treatment on the expression of various inflammatory substances: **(A)** Bar diagrams showing the concentrations of various inflammatory cytokines in BM, where (i) IL-1α, (ii) IL-1β, (iii) TNF-α, (iv) TGF-β, (v) VEGF; **(B)** ROS production by the BM cells; **(C)** Result of gene expression studies, where (i) Bands of PCR amplified products, (ii) Relative expression of iNOS, (iii) Relative expression of COX-2; values are expressed as mean ± SD of 3 different observations. The statistical significance was tested using one-way ANOVA following Tukey's multiple comparison tests by comparing the values as, Group-1 *vs*. Group-2, 3; Group-2 *vs*. Group- 4. P value, $p < 0.05$ was considered as statistically significant. When compared with Group-1 the level of significance was denoted as, a = not significant when $p > 0.05$; * when $p < 0.05$; ** when $p < 0.01$; and *** when $p < 0.001$. When compared with Group-2, b = not significant when $p > 0.05$; # when $p < 0.05$; ## when $p < 0.01$; and ### when $p<0.001$; **(D)** Bar diagrams representing the result of macrophage inflammation assay, where (i) TNF-α release, (ii) IL-1β release; values are expressed as mean ± SD of 3 different observations. The statistical significance was analyzed by comparing the values as, Group-1 *vs*. Group-2; Group-2 *vs*. Group- 3, 4, 5. P value, $p < 0.05$ was considered as statistically significant. When compared with Group-1, a = not significant when $p > 0.05$; * when $p < 0.05$; ** when $p < 0.01$; and *** when $p < 0.001$. When compared with Group-2, b = not significant when $p > 0.05$; # when $p < 0.05$; ## when $p < 0.01$; and ### when $p < 0.001$.

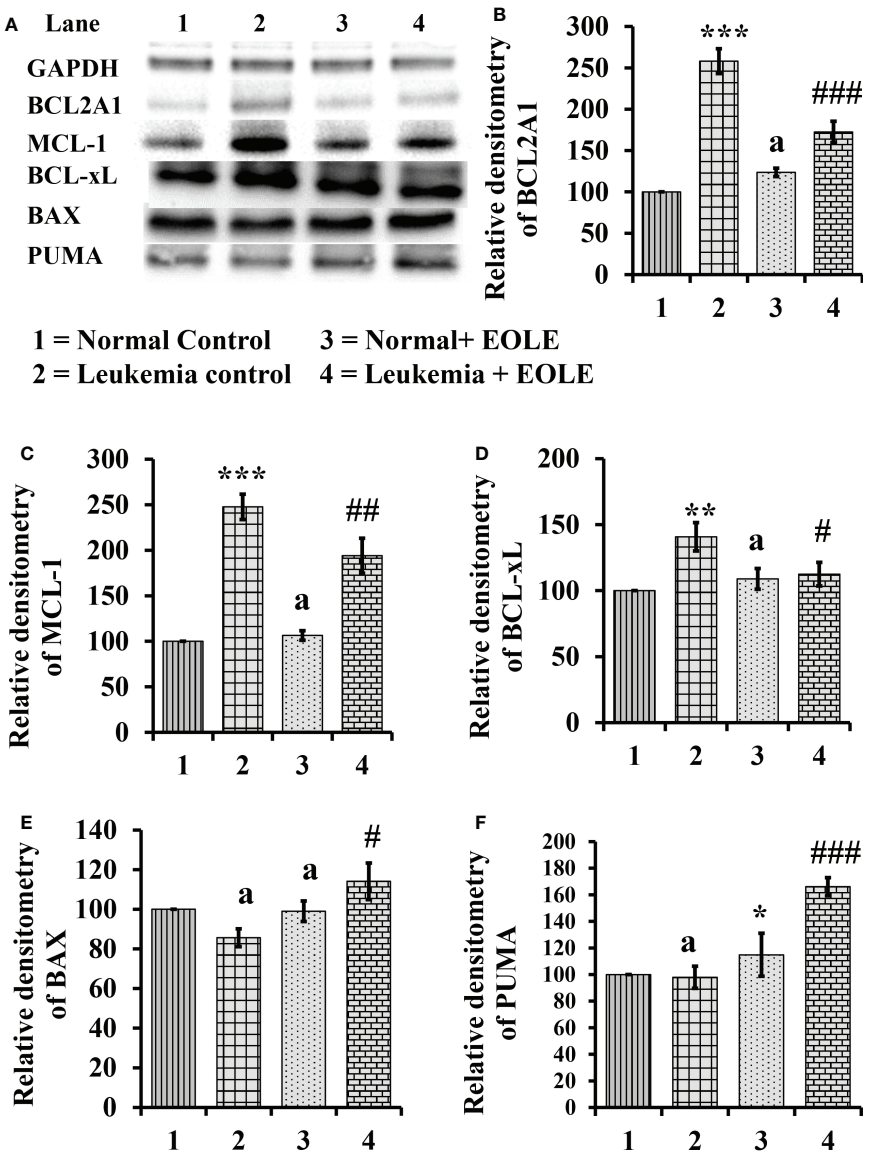

FIGURE 7
Figure showing the result of western blot analysis for many apoptotic pathway proteins in the bone marrow of mice, where **(A)** Image of protein bands, **(B)** Densitometry plot for BCL2A1, **(C)** Densitometry plot for MCL-1, **(D)** Densitometry plot for BCL-xL, **(E)** Densitometry plot for BAX, **(F)** Densitometry plot for PUMA. Values are expressed as mean ± SD of 3 observations. The statistical significance was tested using one-way ANOVA following Tukey's multiple comparison tests by comparing the values as, Group-1 *vs*. Group-2, 3; Group-2 *vs*. Group- 4. P-value, $p < 0.05$ was considered as statistically significant. When compared with Group-1 the level of significance was denoted as, a = not significant when $p > 0.05$; * when $p < 0.05$; ** when $p < 0.01$; and *** when $p < 0.001$. When compared with Group-2, b = not significant when $p > 0.05$; # when $p < 0.05$; ##when $p < 0.01$; and ###when $p < 0.001$.

apoptotic resistance are the two major abnormal functions that aid in the growth of cancer and spread to neighbouring tissues. The drugs that can alter inflammation and induce apoptosis in cancer cells help in preventing cancer growth. Plant phytochemicals are one of the interesting classes of molecules undergoing vigorous checking with the aim to identify novel anticancer molecules. Some noteworthy plant phytochemicals useful against leukemia are curcumin, lupeol, and corydine, isolated from certain herbs and trees (35). Another tree that has drawn the attention of researcher is the olive tree. The olive leaves, fruits, and oils contain many pharmacologically active phytochemicals like oleuropein and hydroxytyrosol (14). The GC-MS analysis of the prepared EOLE revealed the presence of oleuropein and hydroxytyrosol as major chemical structures (16). Both of these phytochemicals exerts anticancer activity through antioxidant, inflammatory, immunomodulatory

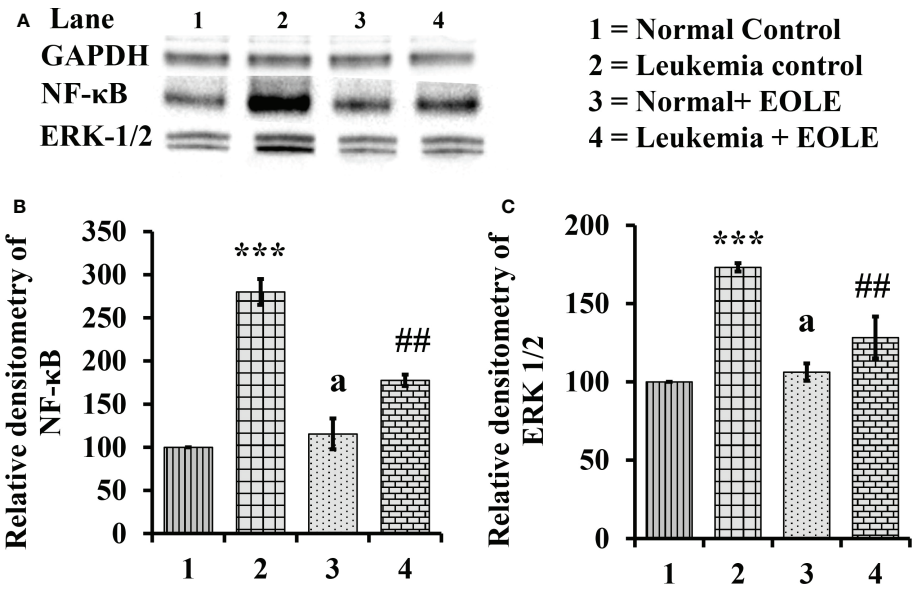

FIGURE 8
Figure showing the expression of NF-κB and ERK1/2 in the bone marrow of mice, where **(A)** Image of NF-κB and ERK1/2 protein bands, **(B)** Densitometry plot for NF-κB, **(C)** Densitometry plot for ERK1/2; values are expressed as mean ± SD of 3 observations. The statistical significance was tested using one-way ANOVA following Tukey's multiple comparison tests by comparing the values as, Group-1 *vs.* Group-2, 3; Group-2 *vs.* Group- 4. P-value, $p < 0.05$ was considered as statistically significant. When compared with Group-1 the level of significance was denoted as, a = not significant when $p > 0.05$; * when $p < 0.05$; ** when $p < 0.01$; and ***when $p < 0.001$. When compared with Group-2, b = not significant when $p > 0.05$; # when $p < 0.05$; ## when $p < 0.01$; ### when $p < 0.001$.

mechanisms (14, 16) encouraged us to hypothesize and test the anti-leukemic activity of EOLE in an animal model of leukemia.

Before beginning with the *in-vivo* studies, the functional activity of EOLE was checked *in-vitro* on the K562 cell line. The EOLE induced apoptosis in K562 cells without any significant toxicity to the normal mouse splenocytes is consistent with the findings of previous studies carried out with olive leaf extracts on HL-60 and K562 cell line (14, 15). As a novel development to the existing literature, this study for the first time determined the effect of EOLE in the expression of apoptosis related proteins BCL-2, BCL-xL, BAX, PUMA and cytochrome c in the K562 cells. These proteins are categorized into pro-apoptotic and anti-apoptotic groups serve essential role in cellular apoptosis program (36). The EOLE was found to up-regulate the pro-apoptotic protein and trigger apoptosis in K562 cells. The results from the *in-vitro* studies sufficiently justify the plans to evaluate the activity of EOLE in leukemic mice.

The leukemia in mice is characterized by appearance of blast and very high WBC count in peripheral blood (24). The normal BM contains about 5% blast cells; however, the number of blast cells significantly increases in leukemic BM. This blast cell from the BM enters into blood stream and then infiltrates to other organs. The blast cell counts in the BM and peripheral blood are markers for the disease progression and the efficacy of any therapy (37). In the current study, the administration of EOLE in leukemic mice slow down the disease progression as indicated by significantly lesser WBC and blast count in the peripheral blood of EOLE-treated leukemic mice compared to the leukemic control. This data is consistent with the result obtained from the studies with standard anti-leukemic drug (38). Loss of body weight is an obvious feature of progressive disease (39). The body weight and serum LDH activity measured indicate better health of the leukemic mice that received EOLE treatment than the untreated mice. The high level of LDH in cancer is associated with inflammation, cell proliferation and survival, metastasis, and immune escape (40).

In order to explore the anti-leukemic mechanism of EOLE, various parameters in the BM that influence normal function of the BM were studied in the included group of mice. The abnormal expression of inflammatory cytokines and apoptosis regulatory proteins is a common phenomenon in leukemia and other hematological malignancies (10, 41, 42). The present study revealed elevated ROS, inflammatory cytokine, high NF-κB, ERK1/2, and high BCL2A1, MCL-1, and BCL-xL in the BM of leukemic mice. ROS is a critical mediator of inflammation and play important role in initiating malignant diseases (43). Elevated levels of ROS induce the expression of COX-2 and cytokines like IL-1β, TNF-α, IL-6, and IL-8, promotes chronic inflammation (44, 45). The increased release of TNF-α and IL-1 in turn induces the expression of NF-κB which then stimulates the expression of inflammation-related genes like iNOS, Cox-2, several

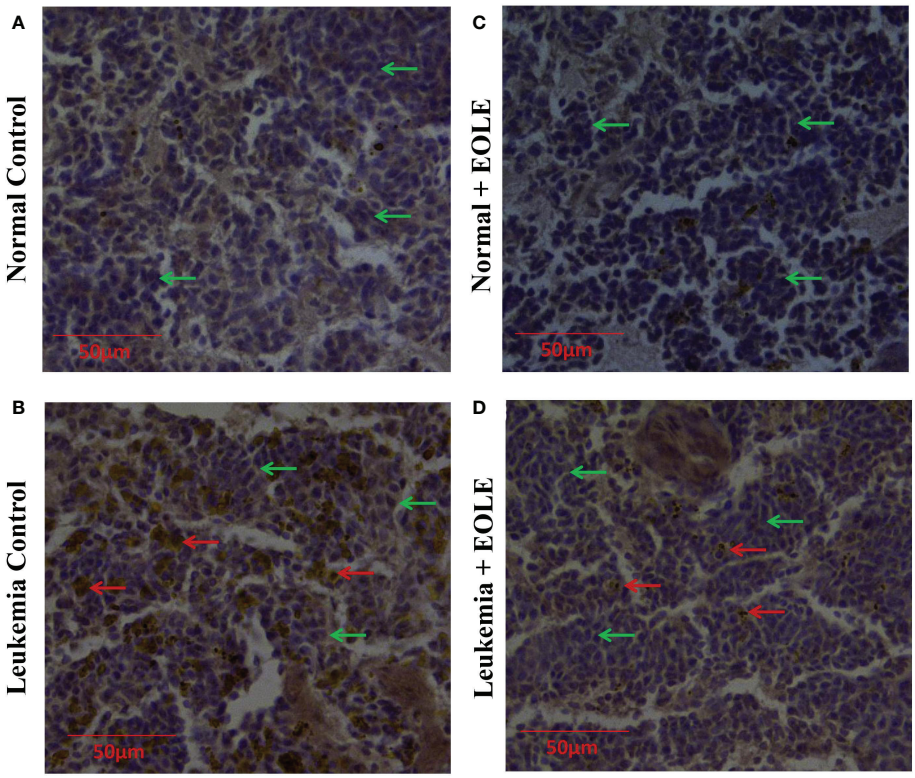

FIGURE 9
Immunohistochemistry images of splenic sections for BCLA1 protein. **(A)** Normal control, **(B)** Leukemia control, **(C)** Normal + EOLE, **(D)** Leukemia + EOLE. In these figures, the brown spots indicate the intensity of BCLA1. The red arrow indicates the BCL2A1positive leukemic blast cells in the spleen, and the green arrow indicates the BCL2A1 negative spleen cells.

inflammatory cytokines and chemokines that contributes in abnormal cell proliferation, and alters normal apoptosis (8). By doing this, the NF-κB and inflammatory cytokine establish an intricate system for cancer growth that plays a seminal role in developing cancer (46). The NF-κB also directly regulates the expression of BCL2A1, an anti-apoptotic protein important for the survival of hematopoietic cells. Other factors like GM-CSF, TNF-α, and IL-1 up-regulates the expression of BCL2A1 protein in the hematopoietic compartment, leading to increased stem cell survival (10). It is evident from the previous studies that the hematopoietic stem and progenitor cells overexpress anti-apoptotic BCL2 family proteins: BCL2A1, BCL-xL become less susceptible or resistant to apoptotic stimulus and transformed into malignant cells (10, 11). Similarly, over-expression of MCL-1 in hematopoietic tissues sustains the growth and progression of AML and develops therapeutic resistance against various chemo-drugs (47). The excessive secretion of cytokine and growth factor caused by the elevated ROS and NF-κB activity leads to hyper-activation of ERK1/2 that influences cellular functions like proliferation and differentiation etc. (48, 49).

The excessive ROS bought up chronic inflammation. In opposite, neutralization of ROS inhibits carcinogenesis and related events (43) made ROS an important therapeutic target. The Oleuropein and Hydroxytyrosol present in EOLE are excellent ROS scavengers (50). In the present study, EOLE treatment to leukemic mice reduce the production of ROS, down-regulate NF-κB, and inflammatory markers like IL-1, TNF-α, iNOS, and COX-2 are consistent with the findings of previous studies (50). In the present study, the EOLE has reduced inflammation in the BM of leukemic mice and the release of TNF-α and IL-1β from LPS-induced inflamed mouse peritoneal macrophages consistently supports the anti-inflammatory activity of EOLE (50). The over-expression of NF-κB in the leukemic BM confers apoptotic resistance to the leukemic cells (8). The olive polyphenols indirectly down-regulates the expression of NF-κB help in alleviating inflammation and apoptotic resistance by regulating the expression of inflammatory cytokines and the proteins of apoptosis pathway. The role of NF-κB in leukemogenesis is evident from the studies where blocking the expression of NF-κB using an inhibitor molecule BMS-345541 altered the expression of genes central to leukemogenesis in patient-derived AML cells (51). The inhibition of NF-κB brings substantial changes in cytokine and interleukin signaling, cellular metabolism, and cell

communication. In the present study, the EOLE-treatment significantly reduced the expression of NF-κB and altered the expression of BCL2A1, BCL-xL, and MCL-1 in the BM of leukemic mice. These are consistent with the available literature on olive polyphenols from previous studies (50). The NF-κB inhibitory and apoptosis-inducing functions of EOLE are also evident from the study of Liu and colleagues (52), where oleuropein, a major polyphenol in EOLE, induced apoptosis in breast cancer cells by abrogating the NF-κB activation cascade. Given the critical role of NF-κB in transcriptional control of a wide array of cellular genes involved in the initiation, maintenance, and progression of malignant diseases, including leukemia, it is not surprising that reducing its expression would significantly change cellular function. Therefore, the reduced inflammatory cytokines and anti-apoptotic proteins in the BM of EOLE-treated leukemic mice may have some association with down-regulated NF-κB in response to EOLE treatment. The reduced production of inflammatory cytokines and ROS further down-regulates the ERK1/2 activity stops cancer progression. It is evident from the studies in which therapeutic inhibition of ERK1/2 reduce the expression of MMPs and delays growth and invasion tumors, including acute myeloid leukemia (AML) (48, 53). The activity of EOLE delays the progression of leukemia and as a result lesser number of blast cell infiltrates in the spleen.

5 Conclusion

Overall, the present study investigated the anti-leukemic activity of EOLE *in-vitro* against K562 cell line and *in-vivo* against ENU-induced leukemia in BALB/c mice. The EOLE treatments to leukemic mice reduce ROS production and down-regulate the expression of NF-κB in the BM. Subsequently, the EOLE reduces the expression of several hematopoietic growth factors and inflammatory cytokines. The EOLE treatment also reverses the expression of apoptosis regulatory proteins in the BM of leukemic mice from an apoptosis-resistant presentation to apoptosis supporting one may indicate apoptosis induction in leukemic cells.

Data availability statement

The original contributions presented in the study are included in the article/Supplementary material. Further inquiries can be directed to the corresponding author.

Ethics statement

The animal study was reviewed and approved by Institutional Animal Ethics Committee Tripura University.

Author contributions

DM: Conceptualization, Validation, Resources, Supervision, Writing- Reviewing and Editing. PN: Methodology, Investigation, Formal analysis, Data Curation, Writing-Original Draft. SMo: Methodology, Data Curation. TA: Methodology, Data Curation. SMa: Methodology, Data Curation. AG: Methodology, Data Curation. RS: Methodology, Data Curation. MD: Material provided and review the manuscript. BS: Review manuscript and edit. All authors contributed to the article and approved the submitted version.

Acknowledgments

The authors acknowledge the State Biotech Hub and Central Instrumentation Centre, Tripura University, for the laboratory and instrumentation support. The authors are thankful to Rajasthan Olive Cultivation Limited for supply of olive leaf to conduct this study.

Conflict of interest

The authors declare that the research was conducted in the absence of any commercial or financial relationships that could be construed as a potential conflict of interest.

Publisher's note

References

1. Kuek V, Hughes AM, Kotecha RS, Cheung LC. Therapeutic targeting of the leukaemia microenvironment. *Int J Mol Sci* (2021) 22(13):6888. doi: 10.3390/ijms22136888

2. Mansoori B, Mohammadi A, Davudian S, Shirjang S, Baradaran B. The different mechanisms of cancer drug resistance: A brief review. *Adv Pharm Bull* (2017) 7(3):339–48. doi: 10.15171/apb.2017.041

3. Ossenkoppele G, Löwenberg B. How I treat the older patient with acute myeloid leukemia. *Blood* (2015) 125(5):767–74. doi: 10.1182/blood-2014-08-551499

4. Cook EK, Luo M, Rauh MJ. Clonal hematopoiesis and inflammation: Partners in leukemogenesis and comorbidity. *Exp Hematol* (2020) 83:85–94. doi: 10.1016/j.exphem.2020.01.011

5. Kitada S, Pedersen IM, Schimmer AD, Reed JC. Dysregulation of apoptosis genes in hematopoietic malignancies. *Oncogene* (2002) 21(21):3459–74. doi: 10.1038/sj.onc.1205327

6. Reikvam H, Aasebø E, Brenner AK, Bartaula-Brevik S, Grønningsæter IS, Forthun RB, et al. High constitutive cytokine release by primary human acute myeloid leukemia cells is associated with a specific intercellular communication phenotype. *J Clin Med* (2019) 8(7):970. doi: 10.3390/jcm8070970

7. Bosman MC, Schuringa JJ, Vellenga E. Constitutive NF-κB activation in AML: Causes and treatment strategies. *Crit Rev Oncol Hematol* (2016) 98:35–44. doi: 10.1016/j.critrevonc.2015.10.001

8. Zhou J, Ching YQ, Chng WJ. Aberrant nuclear factor-kappa b activity in acute myeloid leukemia: from molecular pathogenesis to therapeutic target. *Oncotarget* (2015) 6(8):5490–500. doi: 10.18632/oncotarget.3545

9. Vogler M. BCL2A1: The underdog in the BCL2 family. *Cell Death Diff* (2012) 19(1):67–74. doi: 10.1038/cdd.2011.158

10. Métais JY, Winkler T, Geyer JT, Calado RT, Aplan PD, Eckhaus MA, et al. BCL2A1a over-expression in murine hematopoietic stem and progenitor cells decreases apoptosis and results in hematopoietic transformation. *PloS One* (2012) 7 (10):e48267. doi: 10.1371/journal.pone.0048267

11. Vogler M, Butterworth M, Majid A, Walewska RJ, Sun XM, Dyer MJ, et al. Concurrent up-regulation of BCL-XL and BCL2A1 induces approximately 1000-fold resistance to ABT-737 in chronic lymphocytic leukemia. *Blood* (2009) 113 (18):4403–13. doi: 10.1182/blood-2008-08-173310

12. Ahmad Farooqi A, Fayyaz S, Silva AS, Sureda A, Nabavi SF, Mocan A, et al. Oleuropein and cancer chemoprevention: The link is hot. *Molecules* (2017) 22 (5):705. doi: 10.3390/molecules22050705

13. Fabiani R, De Bartolomeo A, Rosignoli P, Servili M, Montedoro GF, Morozzi G. Cancer chemoprevention by hydroxytyrosol isolated from virgin olive oil through G1 cell cycle arrest and apoptosis. *Eur J Cancer Prev* (2002) 11 (4):351–8. doi: 10.1097/00008469-200208000-00006

14. Imran M, Nadeem M, Gilani SA, Khan S, Sajid MW, Amir RM. Antitumor perspectives of oleuropein and its metabolite hydroxytyrosol: Recent updates. *J Food Sci* (2018) 83(7):1781–91. doi: 10.1111/1750-3841.14198

15. Samet I, Han J, Jlaiel L, Sayadi S, Isoda H. Olive (Olea europaea) leaf extract induces apoptosis and monocyte/macrophage differentiation in human chronic myelogenous leukemia K562 cells: insight into the underlying mechanism. *Oxid Med Cell Longev* (2014) 2014:927619. doi: 10.1155/2014/927619

16. Majumder D, Debnath R, Nath P, Libin Kumar KV, Debnath M, Tribedi P, et al. Bromelain and olea europaea (L.) leaf extract mediated alleviation of benzo(a) pyrene induced lung cancer through Nrf2 and NFκB pathway. *Environ Sci pollut Res Int* (2021) 28(34):47306–26. doi: 10.1007/s11356-021-13803-y

17. Chun-Guang W, Jun-Qing Y, Bei-Zhong L, Dan-Ting J, Chong W, Liang Z, et al. Anti-tumor activity of emodin against human chronic myelocytic leukemia K562 cell lines in vitro and *in vivo*. *Eur J Pharmacol* (2010) 627(1-3):33–41. doi: 10.1016/j.ejphar.2009.10.035

18. Wilson AP. *Cytotoxicity and viability assays in animal cell culture: A practical approach*. Oxford: Oxford University Press (2000).

19. Shahneh FZ, Valiyari S, Azadmehr A, Hajiaghaee R, Yaripour S, Bandehagh A, et al. Inhibition of growth and induction of apoptosis in fibrosarcoma cell lines by echinophora platyloba DC: *In vitro* analysis. *Adv Pharmacol Sci* (2013) 2013:512931. doi: 10.1155/2013/512931

20. Kasibhatla S, Amarante-Mendes GP, Finucane D, Brunner T, Bossy-Wetzel E, Green DR. Acridine Orange/Ethidium bromide (AO/EB) staining to detect apoptosis. *Cold Spring Harb Protoc* (2006) 2006(3):pdb.prot4493. doi: 10.1101/pdb.prot4493

21. Mandelkow R, Gümbel D, Ahrend H, Kaul A, Zimmermann U, Burchardt M, et al. Detection and quantification of nuclear morphology changes in apoptotic cells by fluorescence microscopy and subsequent analysis of visualized fluorescent signals. *Anticancer Res* (2017) 37(5):2239–44. doi: 10.21873/anticanres.11560

22. Rahbar Saadat Y, Saeidi N, Zununi Vahed S, Barzegari A, Barar J. An update to DNA ladder assay for apoptosis detection. *Bioimpacts* (2015) 5(1):25–8. doi: 10.15171/bi.2015.01

23. Debnath R, Majumder D, Nath P, Ghosh D, Maiti D. Bromelain plus peroxidase reduces non-Hodgkin lymphoma progression in in vivo *via* up-regulation of antioxidant enzymes and modulating apoptotic protein expression. *Nutr Cancer* (2020) 72(7):1200–10. doi: 10.1080/01635581.2019.1670217

24. Singha AK, Bhattacharjee B, Saha B, Maiti D. IL-3 and GM-CSF modulate functions of splenic macrophages in ENU induced leukemia. *Cytokine* (2017) 91:89–95. doi: 10.1016/j.cyto.2016.12.009

25. Bloom W, Bloomfield C. Acute leukemia in adults. In: Kellerman R, Rakel D, editors. *Conn's current therapy 2021*. (Philadelphia, United States:Elsevier) (2020). p. 397–402.

26. Arifin WN, Zahiruddin WM. Sample size calculation in animal studies using resource equation approach. *Malays J Med Sci* (2017) 24(5):101–5. doi: 10.21315/mjms2017.24.5.11

27. Gajendra S, Jha B, Goel S, Sahni T, Sharma R, Shariq M, et al. Leishman and giemsa stain: A new reliable staining technique for blood/bone marrow smears. *Int J Lab Hematol* (2015) 37(6):774–82. doi: 10.1111/ijlh.12408

28. Simaga S, Abramić M, Osmak M, Babić D, Ilić-Forko J. Total tissue lactate dehydrogenase activity in endometrial carcinoma. *Int J Gynecol Cancer* (2008) 18 (6):1272–8. doi: 10.1111/j.1525-1438.2008.01196.x

29. Amend SR, Valkenburg KC, Pienta KJ. Murine hind limb long bone dissection and bone marrow isolation. *J Vis Exp* (2016) 110:53936. doi: 10.3791/53936

30. Pino AM, Ríos S, Astudillo P, Fernández M, Figueroa P, Seitz G, et al. Concentration of adipogenic and proinflammatory cytokines in the bone marrow supernatant fluid of osteoporotic women. *J Bone Miner Res* (2010) 25(3):492–8. doi: 10.1359/jbmr.090802

31. Nath P, Majumder D, Debnath R, Debnath M, Singh Sekhawat S, Maiti D. Immunotherapeutic potential of ethanolic olive leaves extract (EOLE) and IL-28B combination therapy in ENU induced animal model of leukemia. *Cytokine* (2022) 156:155913. doi: 10.1016/j.cyto.2022.155913

32. Gupta R, Dubey DK, Kannan GM, Flora SJ. Concomitant administration of moringa oleifera seed powder in the remediation of arsenic-induced oxidative stress in mouse. *Cell Biol Int* (2007) 31(1):44–56. doi: 10.1016/j.cellbi.2006.09.007

33. Zhang X, Goncalves R, Mosser DM. The isolation and characterization of murine macrophages. *Curr Protoc Immunol* (2008) 83:1–14. doi: 10.1002/0471142735.im1401s83

34. Bartosh TJ, Ylostalo JH. Macrophage inflammatory assay. *Bio Protoc* (2014) 4(14):e1180. doi: 10.21769/bioprotoc.1180

35. Iqbal J, Abbasi BA, Mahmood T, Kanwal S, Ali B, Shah SA, et al. Plant-derived anticancer agents: A green anticancer approach. *Asian Pac. J Trop BioMed* (2017) 7(12):1129–50. doi: 10.1016/j.apjtb/j.apjtb.2017.10.016

36. Papaliagkas V, Anogianaki A, Anogianakis G, Ilonidis G. The proteins and the mechanisms of apoptosis: A mini-review of the fundamentals. *Hippokratia* (2007) 11(3):108–13.

37. DiNardo CD, Garcia-Manero G, Pierce S, Nazha A, Bueso-Ramos C, Jabbour E, et al. Interactions and relevance of blast percentage and treatment strategy among younger and older patients with acute myeloid leukemia (AML) and myelodysplastic syndrome (MDS). *Am J Hematol* (2016) 91(2):227–32. doi: 10.1002/ajh.24252

38. Ye L, Gao L, Cheng Q, Guo F, He L, Yuan T, et al. Intermediate dose cytarabine improves survival and relapse-free rate compared with standard-dose cytarabine as post-remission treatment for acute myeloid leukemia: A retrospection study. *Med (Baltimore)* (2021) 100(3):e24273. doi: 10.1097/MD.0000000000024273

39. Talbot SR, Biernot S, Bleich A, van Dijk RM, Ernst L, Häger C, et al. Defining body-weight reduction as a humane endpoint: A critical appraisal. *Lab Anim* (2020) 54(1):99–110. doi: 10.1177/0023677219883319

40. Feng Y, Xiong Y, Qiao T, Li X, Jia L, Han Y. Lactate dehydrogenase a: A key player in carcinogenesis and potential target in cancer therapy. *Cancer Med* (2018) 7(12):6124–36. doi: 10.1002/cam4.1820

41. Pimenta DB, Varela VA, Datoguia TS, Caraciolo VB, Lopes GH, Pereira WO. The bone marrow microenvironment mechanisms in acute myeloid leukemia. *Front Cell Dev Biol* (2021) 9:764698. doi: 10.3389/fcell.2021.764698

42. Aliyu A, Shaari MR, Ahmad Sayuti NS, Reduan MFH, Sithambaram S, Noordin MM, et al. N-Ethyl-n-Nitrosourea induced leukaemia in a mouse model through upregulation of vascular endothelial growth factor and evading apoptosis. *Cancers (Basel)* (2020) 12(3):678. doi: 10.3390/cancers12030678

43. Majumder D, Nath P, Debnath R, Maiti D. Understanding the complicated relationship between antioxidants and carcinogenesis. *J Biochem Mol Toxicol* (2021) 35(2):e22643. doi: 10.1002/jbt.22643

44. Kumar M, Kumar S, Kaur S. Role of ROS and COX-2/iNOS inhibition in cancer chemoprevention: A review. *Phytochem Rev* (2012) 11:309–37. doi: 10.1007/s11101-012-9265-1

45. Reuter S, Gupta SC, Chaturvedi MM, Aggarwal BB. Oxidative stress, inflammation, and cancer: How are they linked? *Free Radic Biol Med* (2010) 49 (11):1603–16. doi: 10.1016/j.freeradbiomed.2010.09.006

46. Chakraborty C, Sharma AR, Sharma G, Lee SS. The interplay among miRNAs, major cytokines, and cancer-related inflammation. *Mol Ther Nucleic Acids* (2020) 20:606–20. doi: 10.1016/j.omtn.2020.04.002

47. Anstee NS, Bilardi RA, Ng AP, Xu Z, Robati M, Vandenberg CJ, et al. Impact of elevated anti-apoptotic MCL-1 and BCL-2 on the development and treatment of

MLL-AF9 AML in mice. *Cell Death Diff* (2019) 26(7):1316–31. doi: 10.1038/s41418-018-0209-1

48. Guo YJ, Pan WW, Liu SB, Shen ZF, Xu Y, Hu LL. ERK/MAPK signalling pathway and tumorigenesis. *Exp Ther Med* (2020) 19(3):1997–2007. doi: 10.3892/etm.2020.8454

49. Serreli G, Deiana M. Extra virgin olive oil polyphenols: Modulation of cellular pathways related to oxidant species and inflammation in aging. *Cells* (2020) 9(2):478. doi: 10.3390/cells9020478

50. Bucciantini M, Leri M, Nardiello P, Casamenti F, Stefani M. Olive polyphenols: Antioxidant and anti-inflammatory properties. *Antiox (Basel)* (2021) 10(7):1044. doi: 10.3390/antiox10071044

51. Reikvam H. Inhibition of NF-κB signaling alters acute myelogenous leukemia cell transcriptomics. *Cells* (2020) 9(7):1677. doi: 10.3390/cells9071677

52. Liu L, Ahn KS, Shanmugam MK, Wang H, Shen H, Arfuso F, et al. Oleuropein induces apoptosis *via* abrogating NF-κB activation cascade in estrogen receptor-negative breast cancer cells. *J Cell Biochem* (2019) 120 (3):4504–13. doi: 10.1002/jcb.27738

53. Lin L, Que Y, Lu P, Li H, Xiao M, Zhu X, et al. Chidamide inhibits acute myeloid leukemia cell proliferation by lncRNA VPS9D1-AS1 downregulation *via* MEK/ERK signaling pathway. *Front Pharmacol* (2020) 11:569651. doi: 10.3389/fphar.2020.569651

frontiers | Frontiers in Immunology

TYPE Original Research
PUBLISHED 27 February 2023
DOI 10.3389/fimmu.2023.1058627

OPEN ACCESS

EDITED BY
Julie Decock,
Qatar Biomedical Research Institute, Qatar

REVIEWED BY
Guanghua Li,
The First Affiliated Hospital of Sun Yat-sen University, China
Congmin Xu,
Georgia Institute of Technology, United States

*CORRESPONDENCE
Jun Deng
dengjun19871106@126.com
Wan Lei
522569951@qq.com
Li Li
lili@email.ncu.edu.cn

†These authors have contributed equally to this work.

SPECIALTY SECTION
This article was submitted to Cancer Immunity and Immunotherapy, a section of the journal Frontiers in Immunology

RECEIVED 30 September 2022
ACCEPTED 13 February 2023
PUBLISHED 27 February 2023

CITATION
Zhong H, Shi Q, Wen Q, Chen J, Li X, Ruan R, Zeng S, Dai X, Xiong J, Li L, Lei W and Deng J (2023) Pan-cancer analysis reveals potential of FAM110A as a prognostic and immunological biomarker in human cancer.
Front. Immunol. 14:1058627.
doi: 10.3389/fimmu.2023.1058627

Pan-cancer analysis reveals potential of FAM110A as a prognostic and immunological biomarker in human cancer

Hongguang Zhong[1†], Qianqian Shi[1†], Qin Wen[1†], Jingyi Chen[1†], Xuan Li[1], Ruiwen Ruan[1], Shaocheng Zeng[1], Xiaofeng Dai[1], Jianping Xiong[1,2], Li Li[1*], Wan Lei[3*] and Jun Deng[1,2*]

[1]Department of Oncology, The First Affiliated Hospital of Nanchang University, Nanchang, Jiangxi, China, [2]Jiangxi Key Laboratory for Individual Cancer Therapy, Nanchang, Jiangxi, China, [3]Department of Pathology, The First Affiliated Hospital of Nanchang University, Nanchang, Jiangxi, China

Background: Despite great success, immunotherapy still faces many challenges in practical applications. It was previously found that family with sequence similarity 110 member A (FAM110A) participate in the regulation of the cell cycle and plays an oncogenic role in pancreatic cancer. However, the prognostic value of FAM110A in pan-cancer and its involvement in immune response remain unclear.

Methods: The Human Protein Atlas (HPA) database was used to detect the expression of FAM110A in human normal tissues, the Tumor Immune Estimation Resource (TIMER) and TIMER 2.0 databases were used to explore the association of FAM110A expression with immune checkpoint genes and immune infiltration, and the Gene Set Cancer Analysis (GSCA) database was used to explore the correlation between FAM110A expression and copy number variations (CNV) and methylation. The LinkedOmics database was used for Gene Ontology (GO) and Kyoto Encyclopedia of Genes and Genomes (KEGG) pathway enrichment analysis. Statistical analysis and visualization of data from the The Cancer Genome Atlas (TCGA) or the Genotype–Tissue Expression (GTEx) databases were performed using the R software (version 3.6.3). Clinical samples were validated using immunohistochemistry.

Results: FAM110A expression was elevated in most tumor tissues compared with that in normal tissues. CNV and methylation were associated with abnormal FAM110A mRNA expression in tumor tissues. FAM110A affected prognosis and was associated with the expression of multiple immune checkpoint genes and abundance of tumor-infiltrating immune cells across multiple types of cancer, especially in liver hepatocellular carcinoma (LIHC). FAM110A-related genes were involved in multiple immune-related processes in LIHC.

Conclusion: FAM110A participates in regulating the immune infiltration and affecting the prognosis of patients in multiple cancers, especially in LIHC. FAM110A may serve as a prognostic and immunological biomarker for human cancer.

KEYWORDS

FAM110A, pan-cancer analysis, bioinformatics, prognosis, immune infiltration

1 Introduction

With the successful application of several immune checkpoint blockers (ICBs), including PD-1, PD-L1, and LAG-3 antagonists, immunotherapy is now a powerful and critical treatment approach (1). However, immunotherapy responders account for only a small fraction of patients with cancer, and resistance to immunotherapy exists in the treatment of most tumor types and patients with cancer (2–4). The tumor microenvironment (TME), which plays a critical role in tumorigenesis and tumor progression, is an important factor influencing the efficacy of immunotherapy (5), and therapeutic strategies targeting the TME have also been regarded as a novel promising modality for the treatment of cancers in recent years (6). However, the complex mechanisms involved in regulating the formation and dynamic variation of TME remain unclear. As a result, the identification of novel prognosis and TME-related genes will help overcome the bottlenecks that immunotherapy is currently facing.

The family with sequence similarity 110 (FAM110), which includes three members, FAM110A, FAM110B, and FAM110C, has been demonstrated to be centrosome-related. They are located in centrosomes and accumulate at spindle poles during mitosis (7). Increasing studies have indicated that FAM110 family protein participates in carcinogenesis. FAM110A exerts an oncogenic role by facilitating malignant biological behaviors of pancreatic cancer cells (8). FAM110B modulates the biologic behavior by inhibiting Wnt/β-catenin signaling in non-small cell lung cancer (9) and has been identified as a potential growth promoting key gene for castration-resistant prostate cancer (10). FAM110C is involved in cell spreading, migration, and filopodia induction (11). Overall, these findings suggest that FAM110 family genes are closely related to malignancies.

Recent studies have revealed that FAM110A expression is regulated by the cell cycle and is highly expressed in the G2 phase; Depletion of FAM110A leads to mitotic defects and delays mitotic progression (12). In lymphoid tissues, proliferation signals from antigen-presenting cells simulated by Dynabeads CD3/CD28 can significantly activate FAM110A expression in CD4+ T lymphocytes (7). These findings indicate a potential role for FAM110A in promoting tumor cell proliferation and immune cell infiltration. However, research on FAM110A, particularly regarding the relevance of immune responses in cancer, is currently inadequate. A more comprehensive analysis of FAM110A is warranted to better understand its functional roles in malignancies.

In this study, we employed a series of bioinformatics approaches to conduct pan-cancer analysis of FAM110A from multiple aspects, including gene expression and genomic alterations, correlation with prognosis, immunological markers, immune infiltration, and gene sets of interest. Moreover, immunohistochemical (IHC) analyses were performed to further confirm the role of FAM110A in LIHC. Our results revealed that FAM110A expression is correlated with immune response and may be a promising prognostic biomarker in multiple cancers.

2 Results

2.1 FAM110A expression in various human normal tissues

To explore the expression levels of FAM110A in various types of normal human tissues, we evaluated the mRNA and protein expression of FAM110A using the Human Protein Atlas (HPA) database. As shown in Figure 1A, the tissues with the highest FAM110A expression were the skin, esophagus, spleen, prostate, and vagina. Next, we examined its expression at the protein level. We found that the expression levels of FAM110A in various tissues were significantly different (Figure 1B). FAM110A mRNA and protein showd different expression patterns in normal tissues, this may be due to the low specificity of the FAM110A antibody, which has not been experimentally validated. Immunohistochemistry showed that FAM110A was expressed in the nucleus and cytoplasm, and representative tissue staining results for different expression levels were shown (Figures 1C–F), including colon (high), spleen (medium), kidney (low), and liver (no expression).

2.2 FAM110A expression in various tumor tissues

We employed TIMER 2.0 website to explore the expression changes of FAM110A between tumor tissues and correspond normal tissues in the TCGA database. As shown in Figure 2A, the mRNA expression of FAM110A was significantly increased in bladder urothelial carcinoma (BLCA), breast invasive carcinoma (BRCA),

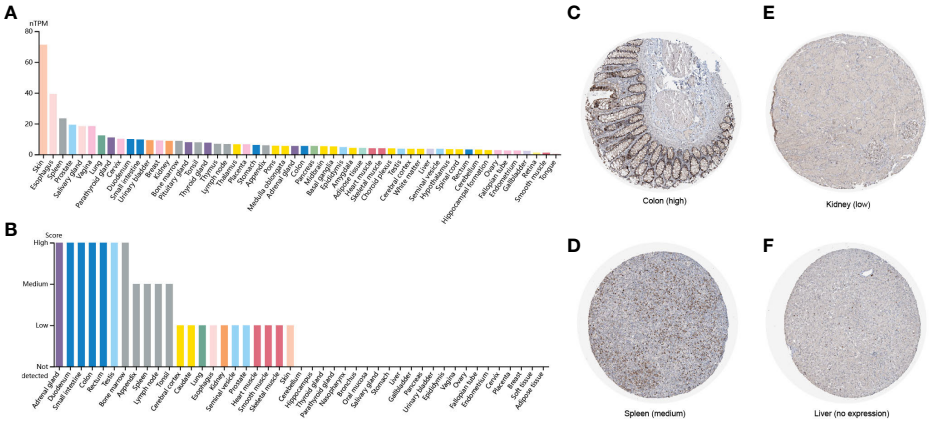

FIGURE 1
FAM110A expression in various human normal tissues. **(A)** FAM110A mRNA expression profiles in normal human tissues. **(B)** FAM110A protein expression data in human normal tissues. **(C–F)** Representative IHC images of FAM110A expression in normal colon, spleen, kidney, and liver tissues.

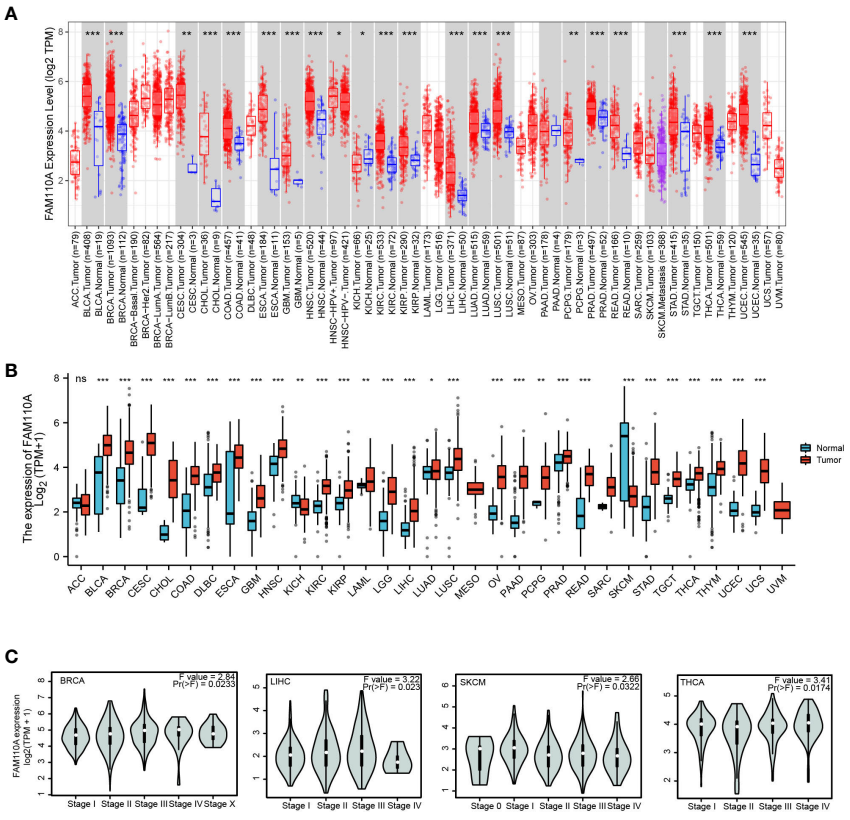

FIGURE 2
FAM110A expression in various tumor tissues. **(A)** FAM110A expression levels in pan-cancer from TCGA database were analyzed by TIMER2.0. (*P<0.05, **P<0.01, ***P<0.001). **(B)** FAM110A expression differences between tumor and normal tissues in pan-cancer from the TCGA and GTEx databases. (*P<0.05, **P<0.01, ***P<0.001). **(C)** The correction between FAM110A expression and the pathological stages of BRCA, LIHC, SKCM and THCA using the GEPIA2 database.

cervical squamous cell carcinoma (CESC), cholangiocarcinoma (CHOL), colon adenocarcinoma (COAD), esophageal carcinoma (ESCA), glioblastoma multiforme (GBM), head and neck squamous cell carcinoma (HNSC), kidney renal clear cell carcinoma (KIRC), kidney renal papillary cell carcinoma (KIRP), LIHC, lung adenocarcinoma (LUAD), lung squamous cell carcinoma (LUSC), pheochromocytoma and paraganglioma (PCPG), prostate adenocarcinoma (PRAD), rectum adenocarcinoma (READ), stomach

adenocarcinoma (STAD), thyroid carcinoma (THCA), uterine corpus endometrial carcinoma (UCEC) and reduced only in kidney chromophobe (KICH).

Due to the small quantity of corresponding normal tissue expression data in the TCGA database, we further conducted a joint analysis with matched normal tissue expression data from the Genotype-Tissue Expression (GTEx) database in a more convincing manner. The expression of FAM110A was elevated in most cancers, including BLCA, BRCA, CESC, CHOL, COAD, diffuse large B-cell lymphoma (DLBC), ESCA, GBM, HNSC, KIRC, KIRP, acute myeloid leukemia (LAML), lower grade glioma (LGG), LIHC, LUAD, LUSC, ovarian serous cystadenocarcinoma (OV), pancreatic adenocarcinoma (PAAD), PCPG, PRAD, READ, STAD, testicular germ cell tumors (TGCT), THCA, thymoma (THYM), UCEC, and uterine carcinosarcoma. In contrast, FAM110A expression in the tumor tissues of KICH and skin cutaneous melanoma (SKCM) was significantly decreased (Figure 2B). In addition, we further explored FAM110A expression across different cancer pathological stages using the GEPIA database and found that FAM110A mRNA expression was correlated with clinicopathological stages in BRCA, LIHC, SKCM, and THCA (Figure 2C).

2.3 Copy number variation and methylation contribute to driving the abnormal expression of FAM110A in pan-cancers

To further explore the mechanisms underlying the abnormal expression of FAM110A mRNA, we analyzed the relationship between gene copy number variation (CNV) and mRNA expression. The results from the GSCA database showed that there was a significant positive correlation between the expression of FAM110A and CNV in patients with COAD, BRCA, HNSC, and LUAD; in contrast, the correlations were not significant in patients with LAML, THCA, GBM, uveal melanoma (UVM), THYM, KICH, KIRC, PCPG, sarcoma (SARC), and DLBC (Figure 3A), suggesting that CNV may not be the only factor responsible for abnormal FAM110A expression, and the underlying mechanisms leading to aberrant expression may be inconsistent in different tumors.

DNA methylation is an epigenetic process that can significantly modulate gene transcription (13); therefore, we found that DNA methylation levels were significantly correlated with mRNA expression in most tumor types, especially in BLCA, CESC, ESCA, LUSC, and SKCM (Figure 3B). To further explore the mechanisms responsible for the discordance in methylation levels in various cancers, we assessed the correlation between FAM110A and four methyltransferase genes, named DNA methyltransferase 1 (DNMT1), DNMT2, DNMT3A, and DNMT3B, and found a significant correlation between them and FAM110A in STAD, KICH, KIRC, KIRP, and LIHC (Figure 3C).

2.4 FAM110A expression level correlates with prognosis in cancers

To further elucidate the effect of FAM110A expression on the prognosis of patients with cancer, we downloaded TCGA RNA-seq and clinical data. Univariate COX regression analysis was performed to explore the relationship between FAM110A expression and overall survival (OS) in 33 cancer types, as shown in Figure 4A. High expression of FAM110 was significantly associated with poorer prognosis in patients with adrenocortical carcinoma (ACC), BLCA, BRCA, COAD, ESCA, KIRC, LAML, LIHC, LUSC, mesothelioma (MESO), OV, and UVM, with LIHC showing the most significant association with FAM110A. In contrast, high CDCA4 expression levels were positively associated with better prognosis in BLCA and LGG (Figures 4C–N).

To exclude the bias caused by non-tumor events, we further evaluated the effect of FAM110A expression levels on disease-specific survival (DSS) (Figure 4B). The results were roughly

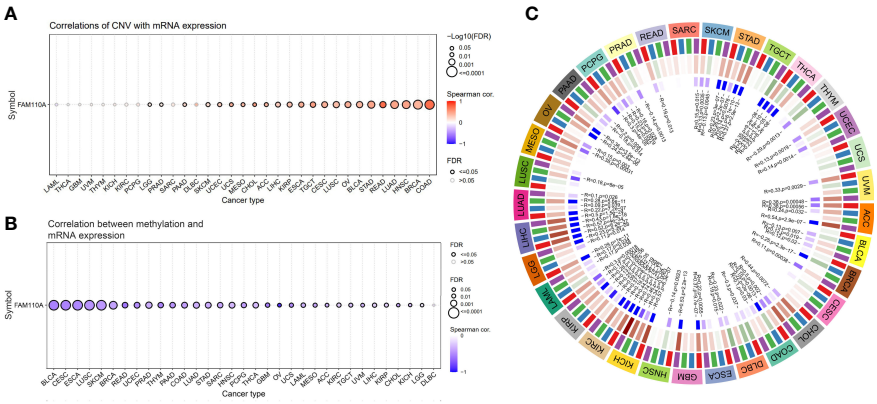

FIGURE 3
CNA and methylation contribute to driving the abnormal expression of FAM110A in pan-cancers. **(A)** Correlation of CNV and FAM110A mRNA expression in the GSCA database. A significant positive correlation was observed in patients with COAD, BRCA, HNSC and LUAD. **(B)** In most tumor types except DLBC, FAM110A mRNA expression was significantly associated with methylation levels, the strongest correlation was observed in BLCA, CESC, ESCA, LUSC, and SKCM. **(C)** Correlation of FAM110A mRNA with four methyltransferases, namely DNMT1 (Red), DNMT2 (Blue), DNMT3A (Green) and DNMT3B (Purple).

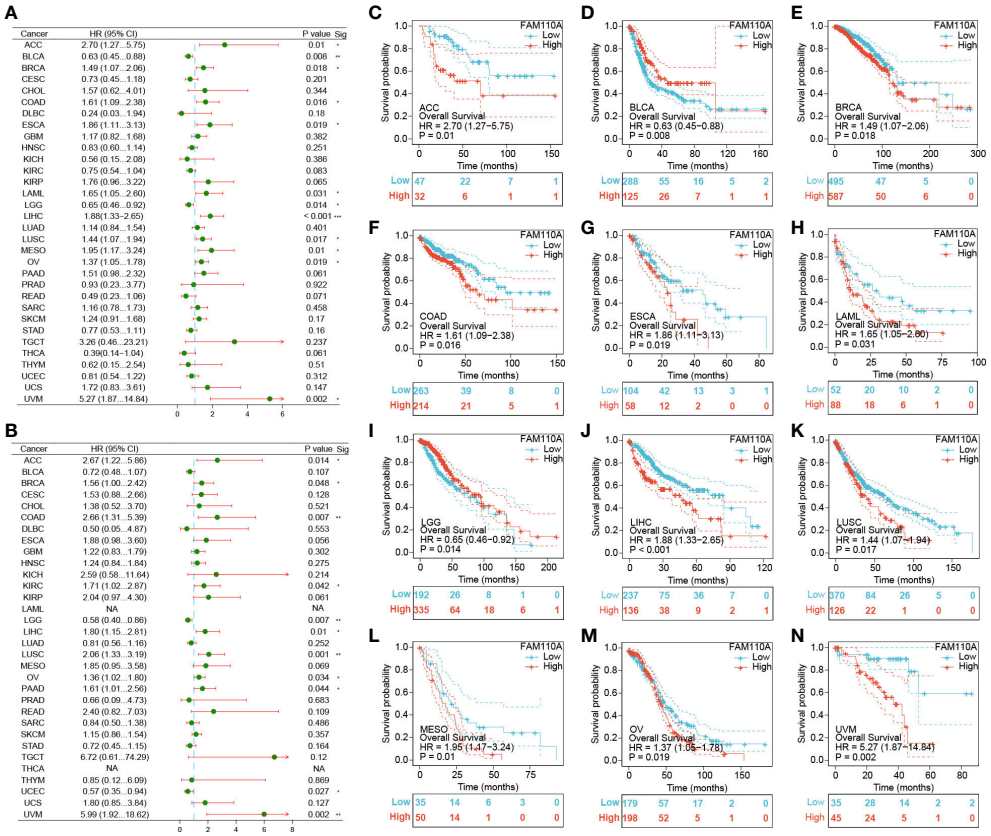

FIGURE 4
Survival analysis of FAM110A in different types of cancer in the TCGA database. **(A, B)** Correlation of FAM110 expression with OS and DSS in patients with different cancers (*P<0.05, **P<0.01, ***P<0.001). **(C-N)** Kaplan–Meier (KM) curves of OS with significance in 12 cancer types (ACC, BLCA, BRCA, COAD, ESCA, KIRC, LAML, LIHC, LUSC, MESO, OV and UVM) in TCGA.

consistent with the OS analysis, demonstrating that high FAM110A expression was associated with poor prognosis in patients with ACC, BRCA, COAD, KIRC, LIHC, LUSC, MESO, OV, PAAD and UVM, while negatively correlated with prognosis in patients with LGG and UCEC (Supplementary Figure 1). These results revealed that FAM110A expression levels are significantly associated with prognosis in patients with multiple tumor types.

2.5 Correlation of FAM110A expression on immune checkpoints and immunotherapy

Since the expression of immune checkpoint genes is closely related to the efficacy of immunotherapy, we first explored the relevance of FAM110A to genes that are recognized as immune response-related checkpoints using the TCGA database. Interestingly, two significant but diametrically opposite trends were observed among the different cancers. FAM110A expression displayed a strong positive correlation with these genes including neuropilin 1 (NRP1), leukocyte-associated immunoglobulin like receptor 1 (LAIR1), CD244, lymphocyte activation gene 3 (LAG3), inducible T cell costimulator (ICOS), CD40 ligand gene (CD40LG), cytotoxic T lymphocyte antigen 4 (CTLA4), CD28, hepatitis A virus cellular receptor 2 (HAVCR2), CD80, programmed cell death 1 (PDCD1 or PD1), programmed cell death 1 ligand 2 (PDCD1LG2), CD27, TNF receptor superfamily member 25 (TNFRSF25), T cell immunoglobulin and ITIM domain (TIGIT), CD274 (PD-L1), and CD86 in ACC, LIHC, SKCM, and UVM. In contrast, FAM110A was negatively correlated with these genes in the BLCA, and LUSC (Figure 5A). Next, we verified the correlations between FAM110A and several immune checkpoint blocker genes, including PD1, PD-L1, CTLA-4, and LAG-3, in the TIMER 2.0 database, and the results were consistent with those of previous studies. The most significant positive correlation between FAM110A and these genes was observed in LIHC and SKCM, and the most significant negative correlation was observed in LGG and BLCA (Figures 5B–E; Supplementary Table 1).

The status of deficient mismatch repair (dMMR)/microsatellite instability-high (MSI-H) together with tumor mutational burden (TMB) are currently considered as promising predictive biomarkers for immunotherapy efficacy (14, 15). Significant correlations were found between FAM110A and several MMR-associated genes, such as MutL homolog 1 (MLH1), MutS homolog 2 (MSH2), and MutS homolog 6 (MSH6) in ACC, GBM, KIRC, LIHC, and STAD (Figure 5F). FAM110A expression was positively correlated with TMB in BRCA, LUAD, MESO, PAAD, STAD, and UCEC and negatively correlated with CDAD, DLBC, ESCA, and THYM (Figure 5G). Moreover, FAM110A expression was positively

10.3389/fimmu.2023.1058627

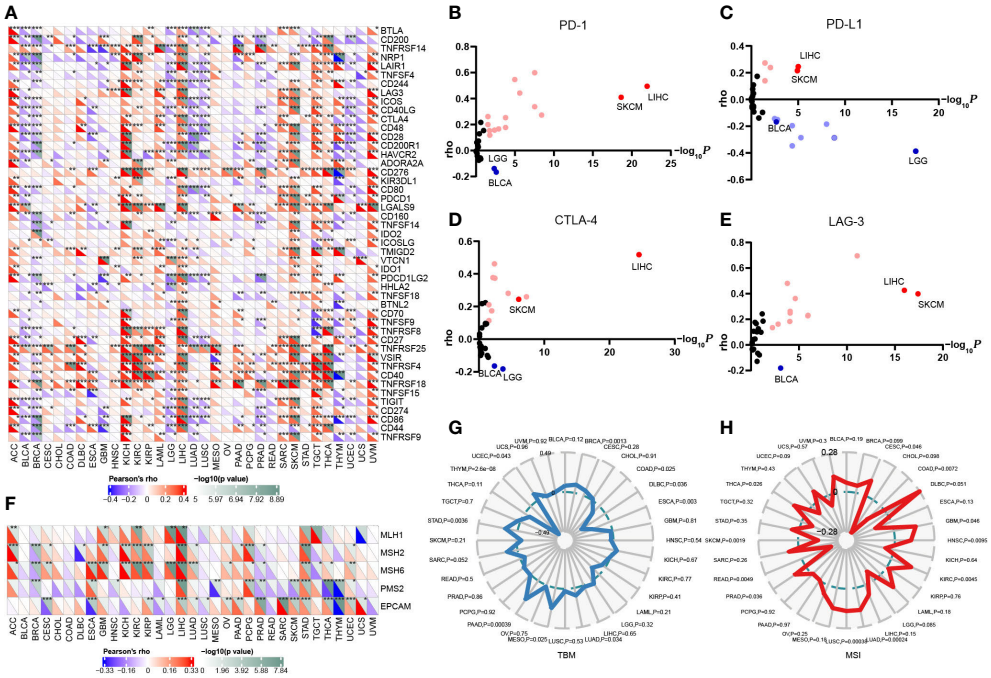

FIGURE 5
Correlation of FAM110A expression on immune checkpoints and immunotherapy. **(A)** The correlation of FAM110A with more than 40 immune checkpoint genes in pan-cancer (*P<0.05, **P<0.01, ***P<0.001). **(B-E)** The correlation of FAM110A with PD-1, PD-L1, CTLA-4 and LAG-3 in the TIMER 2.0 database. **(F)** The correlation of FAM110A with MMR-relate genes, including MLH1, MLH2, MLH6, PMS2 and EPCAM in pan-cancers (*P<0.05, **P<0.01, ***P<0.001). **(G, H)** The correlations of FAM110A expression and TMB, MSI in pan-cancers.

correlated with MSI in CESC, GBM, HNSC, KIRC, LUAD, LUSC, PRAD, and THCA and negatively correlated with MSI in COAD, READ, and SKCM (Figure 5H). However, according to a published result in the TISIDB database, no significant difference of FAM110A mRNA expression level was detected between immunotherapy responders and non-responders (Supplementary Table 2), which could be due to the small sample size in this study. The correlation between FAM110A expression and immunotherapy response still needs further in-depth study.

2.6 Correlation of FAM110A expression with immune infiltration

We used the TIMER database to explore the connection between FAM110A expression levels and the degree of tumor-infiltrating immune cell (TIIC) infiltration in pan-cancer (12). The correlation coefficients of purity and six TIICs (B cells, CD4+ T cells, CD8+ T cells, neutrophils, macrophages, and dendritic cells) collected from the TIMER database are shown in the form of heatmaps (Figure 6A). The most obvious positive correlation between immune cell infiltration and FAM110A was found in LIHC. In contrast, the strongest negative correlation between FAM110A expression and immune cell infiltration was observed in LGG. CD4+ cells exhibited the greatest significant coefficients among all cell types in multiple malignancies, including ACC, CESC, COAD, KIRC, KIRP, LIHC, LUAD, LUSC, MESO, TGCT, and THYM. A significant positive correlation between FAM110A expression and tumor purity was found in BRCA-luminal, GBM, and LGG, while a significant negative correlation was found between KIRC and SKCM.

We further investigated the link between FAM110A expression and tumor purity. We utilized the ESTIMATE algorithm to calculate the stroma score, immune score, and estimate score of relevant tumor samples based on the TCGA database and assessed the correlation between FAM110A expression levels and those scores. Based on our data, the three cancer types that showed the strongest association between FAM110A and the stroma score were PRAD, LGG, and KIRC. The three tumor types that showed the strongest association between FAM110A expression and immune score were LAML, SKCM, and LIHC. The three tumor types that showed the highest association between FAM110A and estimate scores were LAML, SKCM, and PRAD (Figure 6B). These results indicate that FAM110A expression was closely related to the degree of tumor purity and TIIC infiltration.

In addition, we assessed the effect of FAM110A on the infiltration levels of various immune cells in the TME, based on the expression of immune gene markers. Because of the contradictory roles played by FAM110A in prognosis and its association with immune checkpoints, we selected LIHC and BLCA as representative tumor types for subsequent analyses. PRAD served as a negative control because the expression of FAM110A did not seem to have a significant effect on PRAD prognosis. Results from the TIMER 2.0 database revealed a

10.3389/fimmu.2023.1058627

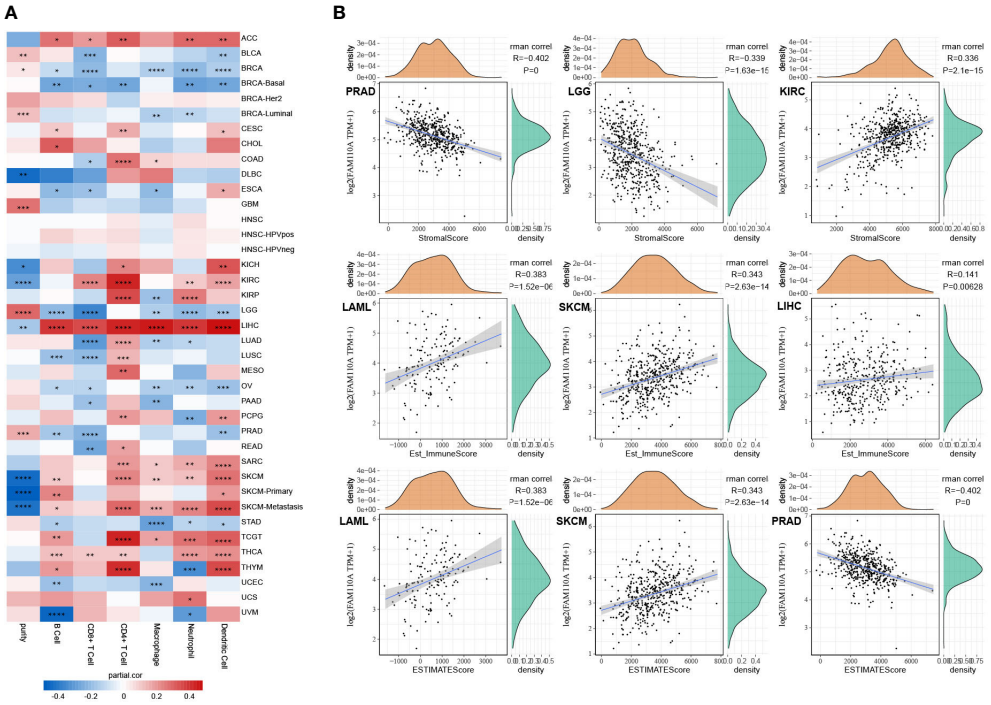

FIGURE 6
Correlation of FAM110A expression with immune infiltration. **(A)** Connection between FAM110A expression and the degree of immune cell infiltration in multiple malignancies using the infiltration scores of six immune cell types (B cell, CD4+ T cell, CD8+ T cell, neutrophil, macrophage, and dendritic cell) accessible in the TIMER database. (*P<0.05, **P<0.01, ***P<0.001, ****P<0.0001) **(B)** The top three tumors with the most significant correlation of FAM110A expression with stroma score, immune score and estimate score.

significant positive correlation between FAM110A expression and the expression of CD8+ T cells, T cells (general), monocytes, tumor-associated macrophages, M2 macrophages, dendritic cells, T helper type 1 (Th1), and exhausted T cells in LIHC. In BLCA, FAM110A and these gene markers were negatively correlated. As expected, no significant correlation was observed between FAM110A expression and TIIC markers in PRAD (Table 1). Analyses of the GEPIA database obtained similar results (Supplementary Table 3).

2.7 FAM110A-related genes are closely correlated with immune response in LIHC

Our previous results revealed that FAM110A is closely related to patient prognosis and immunity in pan-cancer. Since the strongest correlation between FAM110A expression and immune infiltration was observed in LIHC, we used LIHC as an example to verify the potential function of FAM110A using the LinkedOmics

TABLE 1 Correlation analysis between FAM110A and related gene markers of immune cells in TIMER 2.0 (***P<0.001).

Description	Gene markers	LIHC(n=371)				BLCA(n=408)				PRAD(n=498)			
		None		Purity		None		Purity		None		Purity	
		rho	P	rho	P	rho	P	rho	P	rho	P	rho	P
CD8+Tcell	CD8A	0.391	***	0.369	***	-0.194	***	-0.152	0.003	-0.175	***	-0.066	0.180
	CD8B	0.399	***	0.367	***	-0.190	***	-0.151	0.004	0.039	0.383	0.115	0.019
T cell(general)	CD3D	0.537	***	0.535	***	-0.120	0.015	-0.044	0.401	-0.109	0.015	-0.014	0.774
	CD3E	0.442	***	0.442	***	-0.154	0.002	-0.086	0.098	-0.171	***	-0.073	0.137
	CD2	0.458	***	0.452	***	-0.148	0.003	-0.079	0.130	-0.152	***	-0.037	0.448
B cell	CD19	0.405	***	0.363	***	-0.115	0.020	-0.060	0.249	-0.068	0.129	0.004	0.931
	CD79A	0.387	***	0.359	***	-0.100	0.044	-0.034	0.517	-0.123	0.006	-0.050	0.308
Monocyte	CD86	0.526	***	0.526	***	-0.222	***	-0.189	***	-0.249	***	-0.140	0.004

(Continued)

10.3389/fimmu.2023.1058627

TABLE 1 Continued

Description	Gene markers	LIHC(n=371)				BLCA(n=408)				PRAD(n=498)			
		None		Purity		None		Purity		None		Purity	
		rho	P	rho	P	rho	P	rho	P	rho	P	rho	P
	CD115 (CSF1R)	0.436	***	0.419	***	-0.205	***	-0.178	***	-0.242	***	-0.143	0.003
TAM	CCL2	0.415	***	0.383	***	-0.195	***	-0.154	0.003	-0.056	0.213	0.028	0.566
	CD68	0.327	***	0.291	***	-0.165	***	-0.144	0.006	-0.222	***	-0.142	0.004
	IL10	0.410	***	0.379	***	-0.210	***	-0.189	***	-0.207	***	-0.098	0.046
M1 Macrophage	INOS (NOS2)	0.051	0.325	0.037	0.492	0.010	0.840	0.059	0.261	-0.015	0.740	0.067	0.174
	IRF5	0.398	***	0.392	***	0.271	***	0.283	***	0.015	0.732	0.036	0.468
M2 Macrophage	CD163	0.235	***	0.190	***	-0.248	***	-0.230	***	-0.286	***	-0.202	***
	VSIG4	0.310	***	0.268	***	-0.240	***	-0.209	***	-0.258	***	-0.167	***
	MS4A4A	0.269	***	0.231	***	-0.272	***	-0.266	***	-0.286	***	-0.201	***
Neutrophils	CD66b(CEACAMB)	0.071	0.170	0.069	0.202	-0.031	0.528	-0.047	0.364	0.013	0.774	0.033	0.508
	CD11b (ITGAM)	0.461	***	0.441	***	-0.173	***	-0.147	0.005	-0.208	***	-0.108	0.027
	CCR7	0.276	***	0.245	***	0.033	0.508	0.058	0.267	-0.127	0.005	-0.026	0.603
NK cell	KIR2DL1	0.051	0.327	-0.006	0.918	-0.098	0.047	-0.058	0.270	-0.013	0.779	0.042	0.395
	KIR2DL3	0.222	***	0.213	***	-0.110	0.027	-0.074	0.157	-0.006	0.898	-0.008	0.873
	KIR2DL4	0.275	***	0.241	***	-0.110	0.026	-0.069	0.189	0.076	0.091	0.131	0.008
	KIR3DL1	0.054	0.300	0.024	0.664	-0.074	0.137	-0.037	0.475	-0.088	0.049	-0.071	0.151
	KIR3DL2	0.151	0.004	0.123	0.023	-0.093	0.060	-0.053	0.313	0.013	0.772	0.041	0.403
	KIR3DL3	0.084	0.107	0.072	0.179	0.030	0.547	0.058	0.271	-0.082	0.067	-0.135	0.006
	KIR2DS4	0.118	0.023	0.094	0.082	-0.080	0.105	-0.018	0.735	-0.054	0.232	-0.046	0.353
Dendritic cell	HLA-DPB1	0.428	***	0.388	***	-0.140	0.005	-0.096	0.066	-0.063	0.157	0.037	0.452
	HLA-DQB1	0.380	***	0.335	***	-0.095	0.055	-0.032	0.538	-0.122	0.007	-0.055	0.264
	HLA-DRA	0.381	***	0.339	***	-0.107	0.031	-0.060	0.247	-0.209	***	-0.102	0.037
	HLA-DPA1	0.366	***	0.329	***	-0.131	0.008	-0.088	0.091	-0.204	***	-0.092	0.062
	BCDA-1 (CD1C)	0.306	***	0.266	***	-0.103	0.037	-0.052	0.316	-0.135	0.003	-0.008	0.873
	BDCA-4 (NRP1)	0.231	***	0.198	***	-0.331	***	-0.315	***	-0.045	0.313	-0.005	0.912
	CD11c (ITGAX)	0.529	***	0.526	***	-0.204	***	-0.172	***	-0.101	0.025	-0.029	0.551
Th1	TBX21	0.299	***	0.263	***	-0.162	0.001	-0.108	0.038	-0.083	0.064	-0.006	0.908
	STAT4	0.356	***	0.344	***	-0.202	***	-0.143	0.006	-0.141	0.002	-0.037	0.449
	STAT1	0.358	***	0.345	***	-0.070	0.160	-0.017	0.749	-0.175	***	-0.068	0.169
	IFN-g (IFNG)	0.378	***	0.345	***	-0.100	0.043	-0.056	0.285	-0.109	0.015	-0.023	0.642
	TNF-a(TNF)	0.467	***	0.454	***	-0.031	0.527	0.014	0.788	-0.096	0.033	0.022	0.652
Th2	GATA3	0.464	***	0.456	***	0.347	***	0.344	***	0.004	0.924	0.132	0.007
	STAT6	0.005	0.921	0.000	0.997	0.238	***	0.248	***	-0.150	***	-0.099	0.043
	STAT5A	0.421	***	0.385	***	-0.022	0.655	0.016	0.758	-0.138	0.002	-0.027	0.588
	IL13	0.196	***	0.176	0.001	-0.127	0.010	-0.087	0.097	-0.016	0.724	-0.022	0.660
Tfh	BCL6	0.046	0.380	0.058	0.286	0.239	***	0.235	***	-0.222	***	-0.180	***

(Continued)

TABLE 1 Continued

Description	Gene markers	LIHC(n=371)				BLCA(n=408)				PRAD(n=498)			
		None		Purity		None		Purity		None		Purity	
		rho	P	rho	P	rho	P	rho	P	rho	P	rho	P
	IL21	0.093	0.072	0.093	0.084	-0.111	0.024	-0.083	0.113	-0.057	0.206	-0.023	0.646
Th17	STAT3	0.149	0.004	0.121	0.024	0.000	0.994	0.037	0.474	-0.131	0.004	-0.032	0.512
	IL17A	0.009	0.867	0.026	0.625	0.136	0.006	0.159	0.002	-0.114	0.011	-0.036	0.470
Treg	FOXP3	0.268	***	0.279	***	-0.148	0.003	-0.083	0.111	-0.081	0.073	-0.035	0.480
	CCR8	0.410	***	0.405	***	-0.164	***	-0.112	0.032	-0.163	***	-0.081	0.097
	STAT5B	0.090	0.083	0.120	0.025	-0.004	0.935	-0.014	0.795	-0.249	***	-0.148	0.002
	TGFb (TGFB1)	0.481	***	0.472		-0.132	0.007	-0.119	0.022	-0.073	0.104	-0.011	0.824
Tex	PD-1 (PDCD1)	0.495	***	0.487	***	-0.166	***	-0.113	0.030	-0.022	0.624	0.037	0.448
	CTLA4	0.518	***	0.514	***	-0.164	***	-0.097	0.062	-0.049	0.272	0.032	0.513
	LAG3	0.426	***	0.404	***	-0.181	***	-0.131	0.012	-0.033	0.465	0.031	0.523
	TIM-3 (HAVCR2)	0.538	***	0.546	***	-0.219	***	-0.196	***	-0.211	***	-0.107	0.029
	GZMB	0.294	***	0.250	***	-0.181	***	-0.117	0.025	-0.031	0.492	0.060	0.219

database. We analyzed the co-expression of genes associated with FAM110A in LIHC (Figure 7A), and the top 50 genes with the most significant positive or negative correlations with FAM110A are displayed using a heat map (Figure 7B, C).

The Gene Set Enrichment Analysis (GSEA) analysis based on FAM110A-related genes in LIHC showed that GO biological process terms were mainly enriched for interferon-gamma production, interleukin-4 production, interleukin-10 production, T cell activation, B cell activation, myeloid dendritic cell activation, and adaptive immune response (Supplementary Figure 2). Kyoto Encyclopedia of Genes and Genomes (KEGG) pathway enrichment analysis showed that the major enriched pathways were primary immunodeficiency, Th1 and Th2 cell differentiation, antigen processing and presentation, chemokine signaling, NF-kappa B signaling, and T cell receptor signaling (Figure 7D-J).

2.8 FAM110A is associated with poor prognosis, immune infiltration, and immune checkpoints in LIHC

To further verify the expression of FAM110A in LIHC, IHC analysis was performed to detect the expression level of FAM110A protein in 120 randomly selected tumor tissues and paired adjacent non-tumor tissues from patients with LIHC. Our results revealed that FAM110A protein expression was significantly increased in tumor tissues compared to that in matched non-tumor adjacent tissues, the subcellular localization of FAM110A was in the nucleoplasm and cytoplasm (Figure 8A). According to the IHC scoring criteria, the high expression rate of FAM110A in tumor tissues was 56.7% (68/120) and the low expression rate was 43.3% (52/120).

To verify the effect of FAM110A on poor prognosis in patients with LIHC, all randomly selected patients were divided into high and low FAM110A expression groups (Figure 8B), and the clinical follow-up data of those patients were analyzed through Kaplan-Meier survival analysis and log-rank test. Our results showed that patients with high FAM110A expression were associated with worse prognosis than those with low FAM110A expression (Figure 8C).

Next, the correlation between FAM110A and immune infiltration and immune checkpoint genes was verified. We evaluated the degree of immune infiltration and PD-L1 expression in serial sections of the specimens from the same patient. The number of CD8+ lymphocytes infiltrating the tissues of the patients was significantly higher than that of the patients with low FAM110A expression (Figure 8B, D), and the PD-L1 protein expression levels were positively correlated with the FAM110A expression levels (Figure 8B, E).

3 Discussion

FAM110A is a centrosome-associated protein localized at the mitotic spindle and spindle poles during mitosis (7). Perez et al. revealed that aberrant expression of FAM110A may result in dysregulation of the cell cycle (12), which is regarded as a typical characteristic of cancer cells (16). Huang et al. demonstrated that FAM110A is an oncogene that promotes the malignant behavior of cancer cells and tumorigenesis in pancreatic cancer (8). In this study, we conducted a comprehensive bioinformatics analysis of FAM110A using multiple public databases.

Our results showed that FAM110A mRNA is widely distributed and overexpressed in most cancer tissues compared to that in normal tissues. Moreover, the expression level of FAM110A mRNA

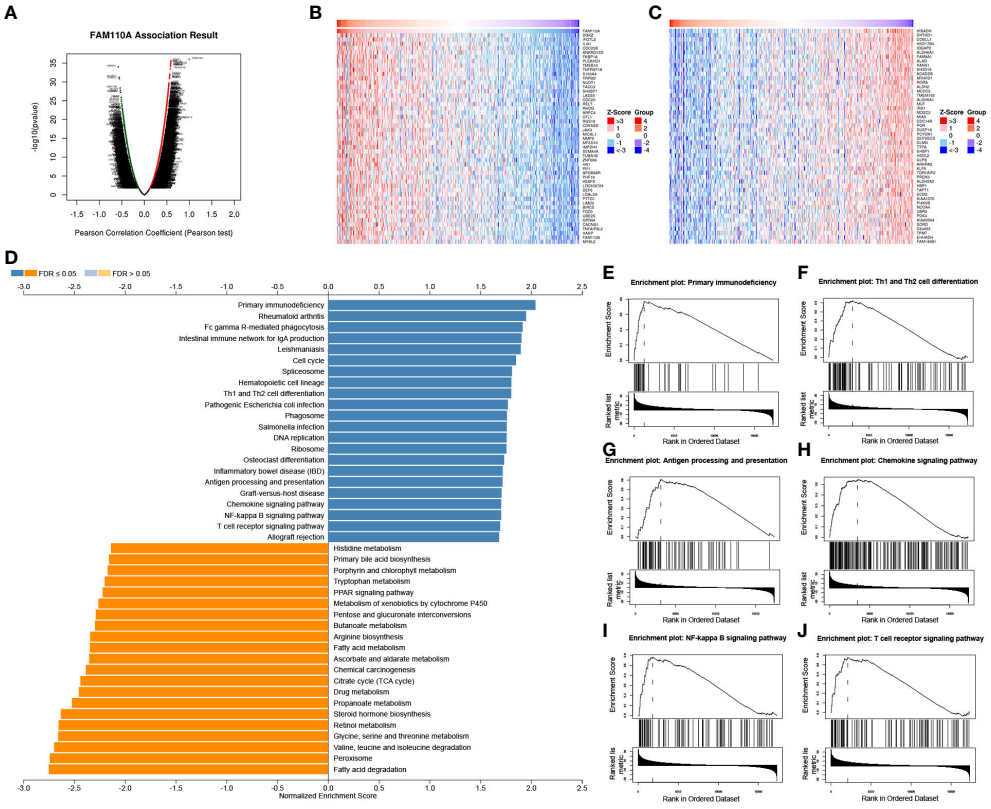

FIGURE 7
GSEA of FAM110A in the TCGA LIHC cohort. **(A)** Correlations between FAM110A and genes differentially expressed in LIHC. **(B, C)** Heat maps of the most 50 significant genes positively and negatively correlated with FAM110A in LIHC. **(D-J)** KEGG enrichment analyses showed that primary immunodeficiency, Th1 and Th2 cell differentiation, antigen processing and presentation, chemokine signaling pathway, NF-kappa B signaling pathway, and T cell receptor signaling pathway were enriched.

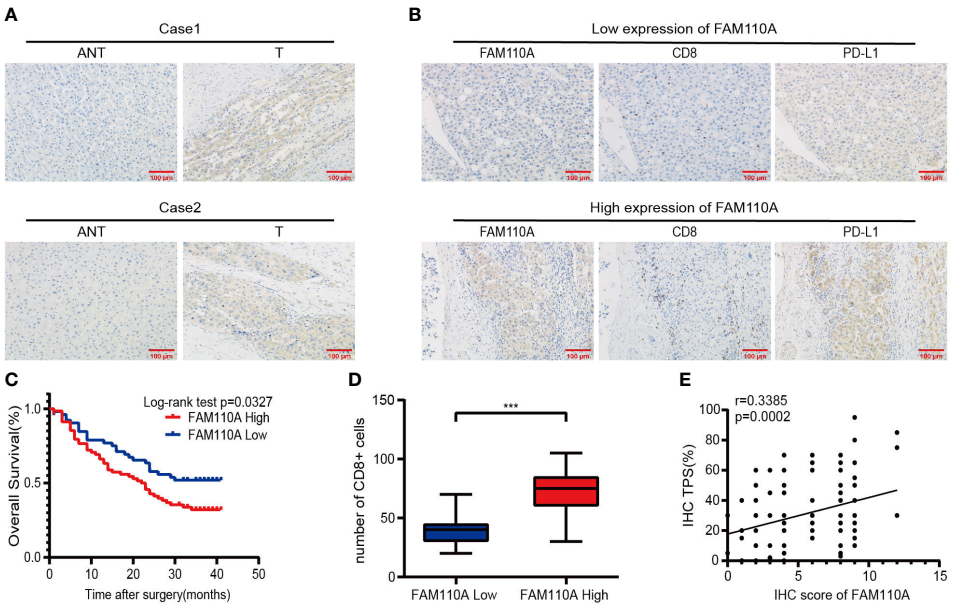

FIGURE 8
FAM110A expression correlated with immune infiltration and poor prognosis in LIHC. **(A)** Representative FAM110A staining image in cancerous and adjacent normal tissues. **(B)** Representative IHC staining images of LIHC tissues with FAM110A-high and low expression. Positive CD8, PD-L1 expression cells were shown. Scale bars, 100 μm. **(C)** Kaplan–Meier survival curves for OS of patients with LIHC based on the expression status of FAM110A.*p < 0.05. **(D)**The number of CD8+ T cells in LIHC tissues with high or low FAM110A expression.***P<0.001. **(E)** The correlation of FAM110A with PD-L1 protein expression was evaluated by Pearson's correlation.

correlated with the clinicopathological stages of BRCA, LIHC, SKCM, and THCA. Our findings also demonstrated a significant correlation between FAM110A mRNA expression and CNV and methylation in pan-cancers. In view of the abnormal expression levels of FAM110A in tumors, the Kaplan–Meier method and COX regression analysis were conducted, and the results demonstrated that FAM110A may serve as a potential prognostic biomarker for a variety of cancers, especially LIHC. FAM110A is closely related to multiple immune checkpoint genes, and its expression levels may indirectly reflect the abundance of these two immune infiltrates in the TME. As a result, we propose that FAM110A plays a delicate role in tumor initiation or development based on differential expression profiles and may affect immunotherapy efficacy to some extent.

Tumor immunotherapy aims to boost the natural immune system and relies on the patients' own immune function to eliminate cancer cells and tumor tissues (17, 18). Through the successful application of monoclonal antibodies, cytokines, cellular immunotherapy, and vaccines, immunotherapy has revolutionized cancer treatment (19). Immune-related gene expression is regarded as a predictive marker for immunotherapy in a variety of cancers (20–22). Here, we analyzed the association of FAM110A with more than 40 immune checkpoint genes in pan-cancer based on the TCGA database and verified the correlation of FAM110A between several immune checkpoint genes, including PD-1, PD-L1, LAG-3, and CTLA-4 in the TIMER 2.0 database. Our data suggested that FAM110A had the strongest positive correlation with these immune checkpoint genes in cancers where FAM110A is considered an important risk factor, such as LIHC and SKCM. Meanwhile, in BLCA and LGG, where FAM110A served as a protective factor, the expression of FAM110A showed the strongest negative correlation with these immune inhibitor checkpoint genes. This may explain the association between FAM110A overexpression and poor prognosis in patients with cancer.

DNA mismatch repair (MMR) is an important DNA repair pathway that plays critical roles in DNA replication fidelity, mutation avoidance, and genome stability. MMR-deficiency leads to a hypermutated phenotype in the genome, which in turn leads to MSI (23). Specifically, MMR-deficient cancers tend to be more sensitive to immune checkpoint blockade (24). We found statistically significant correlations between FAM110A and MSI in several cancers; however, the correlation was not very strong (correlation coefficient<0.6). The association of FAM110A with cancer patient prognosis, especially immunotherapy efficacy, requires further clinical validation.

The immune TME, majorly represented by the TIICs, plays an important role in cancer therapeutics and patient prognosis (20, 25). In fact, a high density of TIICs within the TME is associated with better outcomes in several types of cancers (26–28). A thorough understanding of the factors involved in regulating immune infiltrates will aid in improving response rates and developing new therapeutic strategies (29). Results from the TIMER database showed that infiltration abundance of several TIICs, such as B cells, CD4+ T cells, CD8+ T cells, neutrophils, macrophages, and dendritic cells, were significantly correlated with the expression of FAM110A in multiple malignancies, especially in LIHC. Taking these findings together, we speculated that FAM110A is also significantly associated with immune-related functions and pathways in LIHC. We performed GO and KEGG enrichment analysis of FAM110A-related genes in LIHC and found highly significant enrichment of GO terms associated with immune function, including interferon-γ production, T cell activation, B cell activation, adaptive immune response, mast cell-mediated immunity, and positive regulation of cell activation. We also identified an enrichment of immune-related signaling pathways, including primary immunodeficiency, Th1 and Th2 cell differentiation, antigen processing and presentation, chemokine signaling, NF-kappa B signaling and T cell receptor signaling pathways, through KEGG pathway analysis. Based on our identification, FAM110A is involved in the activation of T cells as well as related immune pathways, which suggests that FAM110A plays an important role in the immune process. These results may explain the possible mechanism by which FAM110A promotes immune infiltration, and provids corroborating support for the role of FAM110A as an immunological biomarker.

Importantly, we further confirmed the abnormal expression of FAM110A in LIHC and the correlation between the expression of immune checkpoint PD-L1 protein and the immune infiltration degree of CD8+ cells by IHC experiments. The Kaplan-Meier plot and log-rank test demonstrated that high FAM110A expression leads to a worse prognosis in patients with LIHC. In addition, previous studies have shown that aberrant expression of FAM110A is associated with cell cycle dysregulation (12), which is considered to be a fundamental mechanism underlying malignant progression (30). And this fact may represent an important cause for the prognostic impact of FAM110A.

Due to the potential prognostic value of FAM110A, the expression level of FAM110A in postoperative tissue specimens can be used as one of the bases for assessing the prognosis of patients in various tumors, particularly in LIHC. Moreover, our fingdings also sets a new path in the field of tumor immunology. Based on the findings, more studies are expected to reveal the underlying mechanism of FAM110A regulating tumor immune microenvironment in the future, which would be beneficial for progresses of cancer immunotherapy.

There are still many limitations in this study. To begin with, some of our results are limited to a single approach or database, lacking mutual validation of data from multiple sources. Moreover, our bioinformatic results show that FAM110A is associated with poor prognosis of liver cancer and immune response. however, we are still uncertain whether FAM110A affects prognosis by regulating immune processes. In addition, although these findings have pointed to new directions for subsequent studies, the potential biological function process and molecular mechanism involved still deserve detailed experimental validation.

In general, we performed a comprehensive analysis of FAM110A using bioinformatics methods, revealing the important role of FAM110A in prognosis and immune infiltration in multiple

cancers, especially in LIHC. More importantly, our study provides a promising candidate for therapeutic targets and a new direction for future research.

4 Materials and methods

4.1 FAM110A expression analysis

The HPA (https://www.proteinatlas.org) database was used to explore the mRNA and protein expression levels of FAM110A in normal human tissues. The expression level of FAM110A gene in a variety of cancer tissues was obtained through the "Gene_DE" module in the TIMER 2.0 (http://timer.cistrome.org/) (31). The RNA-seq data of normal and tumor samples were collected from the TCGA (http://cancergenome.nih.gov) and GTEx (http://commonfund.nih.gov/GTEx/) projects. We used the "Stage plot" function in the Gene Expression Profiling Interactive Analysis (GEPIA; http://gepia.cancer-pku.cn/) (32) database to analyze the correlation between FAM110A expression and tumor stage. The TISIDB (http://cis.hku.hk/TISIDB/) database (33) was used to detect difference of FAM110A mRNA expression level between immunotherapy responders and non-responders.

4.2 CNV and methylation analysis

The Gene Set Cancer Analysis (GSCA; http://bioinfo.life.hust.edu.cn/GSCA/#/) database is a powerful bioinformatics analysis tool which mainly integrates the mRNA expression, mutation, immune infiltrates, methylation data from the TCGA database (34), The "mutation" module in the GSCA database was used to analyze CNVs and methylation of FAM110A as well as their correlation with mRNA expression levels. SangerBox (http://vip.sangerbox.com/) is a comprehensive, user-friendly bioinformatics analysis platform (35). The relationship between FAM110A and methyltransferase genes expression was investigated by Sangerbox platform.

4.3 Survival analysis

We verified the prognostic value of FAM110A based on clinical data from the TCGA database, Xiantao Academic Online Website (https://www.xiantao.love/) was used for bioinformatics analysis based on the R language. In the R environment, RNA sequencing data in fragments per kilobase per million format were transformed into transcripts per million reads format. The "Survival" (version 3.2-10) and "survminer" (version 0.4.9) packages were used for statistical analysis and visualization, respectively. The statistical significance of OS and DSS between the high and low FAM110A expression groups in patients with 33 cancer types was analyzed by univariate Cox regression. Statistical significance was set at $P < 0.05$.

4.4 Immune infiltration analysis

The correlation data between FAM110A expression and six types of TIICs (B cell, CD4+ T cell, CD8+ T cell, neutrophil, macrophage, and dendritic cell) were obtained from the "GENE" module in the TIMER (https://cistrome.shinyapps.io/timer/) database (36). Estimation of Stromal and Immune cells in Malignant Tumor tissues using Expression data (ESTIMATE) is a method that uses gene expression signatures to infer the proportion of mesenchymal and immune cells in tumor samples. We use the "ESTIMATE" package to calculate the immune score, stromal score and estimate score of relate samples respectively. The correlation between those scores and the expression of FAM110A was explored through SangerBox platform.

4.5 Co-expressed genes and gene enrichment analysis

The LinkedOmics (http://www.linkedomics.org/login.php) database (37) is a multi-omics database that integrates multi-omics data and clinical data for 32 cancer types and 11,158 patients from the TCGA project. We selected the data set "LIHC cohort", data type "RNAseq", and the statistical method "Pearson correlation test" to analyze the co-expression genes of FAM110A in LIHC. The "Gene Set Enrichment Analysis (GSEA)" tool was then used to conduct the GO_BP term search and KEGG pathway enrichment analysis to those FAM110A-related genes.

4.6 Patients and tissue specimens

All clinical samples were obtained from the First Affiliated Hospital of Nanchang University, China. Formalin-fixed, paraffin-embedded samples from 120 patients were collected from January 2019 to December 2019. All samples were collected with the consent of the patients and the study was approved by the Ethics Committee of the First Affiliated Hospital of Nanchang University. All patient specimens and clinical data used in this study complied with the principles of the Declaration of Helsinki.

4.7 Immunohistochemistry analysis

Paraffin-embedded tissue sections were degreased by immersion in xylene for 10 min and hydrated in various concentrations of alcohol, followed by antigen retrieval using ethylenediaminetetraacetic acid solution, boiled in a pressure cooker for 1.5 min, and cooled down to room temperature naturally. The slides were then immersed in 3% H_2O_2 for 10 min to eliminate endogenous peroxidase activity. After washing with phosphate-buffered saline (PBS), the sections were incubated with the FAM110A antibody (1:20, sc-376464, SANTA CRUZ), anti-

CD274 antibody (1:200, 66248-1-Ig, Proteintech), or CD8 antibody (1:200, 85336S, Cell Signaling) overnight at 4°C. After three times of washing with PBS, the sections were incubated with secondary antibody for 20 min at 37°C and stained using diaminobenzidine solution. IHC scores were calculated according to the staining intensity and the corresponding percentage of positive cells, tumor proportion score (TPS) were calculated according to the percentage of tumor cells showing partial or complete cell membrane staining of PD-L1. Two blinded, independent pathologists observed the results under a light microscope.

4.8 Statistical analysis

For bioinformatic data, the whole dataset was filtered by deleting missing and duplicated data, and all statistical analyses and visualizations were conducted using the R software (version 3.6.3) (http://www.rproject.org/). The correlation between FAM110A and immune checkpoint and MMR genes was evaluated using Pearson's correlation test. The Wilcoxon rank-sum test was used for differential expression analysis of FAM110A between cancer and normal tissues, and the results were visualized using the "ggplot2" package (version 3.3.3). For clinical data, we compared the two groups using a t-test for continuous variables. GraphPad Prism 8 was used for statistical analysis and visualization and $p < 0.05$ was considered statistically significant.

Data availability statement

The original contributions presented in the study are included in the article/Supplementary Material. Further inquiries can be directed to the corresponding authors.

Ethics statement

The studies involving human participants were reviewed and approved by Ethics Committee of the First Affiliated Hospital of Nanchang University. Written informed consent for participation was not required for this study in accordance with the national legislation and the institutional requirements.

Author contributions

JD, WL, and LL designed the study and guided work. HZ, and QS wrote the manuscript. JC, and QW conducted data collection and analyses. XL assisted in the collection of tissue samples. RR performed immunohistochemistry. SZ, and XD collected clinical information. JX helped the revision. All authors contributed to the article and approved the submitted version.

Funding

This work was supported by the Jiangxi Provincial Young Talents projects (grant number 20204BCJ23016), the Key Laboratory of Jiangxi Province (grant number 20202BCD42011), the Natural Science Foundation of Jiangxi Province (grant number 20192ACB20028), the Health and Family Planning Commission of Jiangxi Province (grant number 20194009), and the Education Department of Jiangxi Province (grant number GJJ190116).

Conflict of interest

The authors declare that the research was conducted in the absence of any commercial or financial relationships that could be construed as a potential conflict of interest.

Publisher's note

Supplementary material

The Supplementary Material for this article can be found online at: https://www.frontiersin.org/articles/10.3389/fimmu.2023.1058627/full#supplementary-material

References

1. Emens LA, Ascierto PA, Darcy PK, Demaria S, Eggermont AMM, Redmond WL, et al. Cancer immunotherapy: Opportunities and challenges in the rapidly evolving clinical landscape. *Eur J Cancer (Oxford England: 1990)* (2017) 81:116–29. doi: 10.1016/j.ejca.2017.01.035

2. Schoenfeld AJ, Hellmann MD. Acquired resistance to immune checkpoint inhibitors. *Cancer Cell* (2020) 37(4):443–55. doi: 10.1016/j.ccell.2020.03.017

3. Pennock GK, Chow LQ. The evolving role of immune checkpoint inhibitors in cancer treatment. *oncol* (2015) 20(7):812–22. doi: 10.1634/theoncologist.2014-0422

4. Bagchi S, Yuan R, Engleman EG. Immune checkpoint inhibitors for the treatment of cancer: Clinical impact and mechanisms of response and resistance. *Annu Rev Pathol* (2021) 16:223–49. doi: 10.1146/annurev-pathol-042020-042741

5. Petitprez F, Meylan M, de Reyniès A, Sautès-Fridman C, Fridman WH. The tumor microenvironment in the response to immune checkpoint blockade therapies. *Front Immunol* (2020) 11:784. doi: 10.3389/fimmu.2020.00784

6. Bejarano L, Jordão MJC, Joyce JA. Therapeutic targeting of the tumor microenvironment. *Cancer Discovery* (2021) 11(4):933–59. doi: 10.1158/2159-8290.Cd-20-1808

7. Hauge H, Patzke S, Aasheim HC. Characterization of the Fam110 gene family. *Genomics* (2007) 90(1):14–27. doi: 10.1016/j.ygeno.2007.03.002

8. Huang H, Li H, Zhao T, Khan AA, Pan R, Wang S, et al. Tspan1-elevated Fam110a promotes pancreatic cancer progression by transcriptionally regulating Hist1h2bk. *J Cancer* (2022) 13(3):906–17. doi: 10.7150/jca.66404

9. Xie M, Cai L, Li J, Zhao J, Guo Y, Hou Z, et al. Fam110b inhibits non-small cell lung cancer cell proliferation and invasion through inactivating Wnt/B-catenin signaling. *OncoTargets Ther* (2020) 13:4373–84. doi: 10.2147/ott.S247491

10. Vainio P, Wolf M, Edgren H, He T, Kohonen P, Mpindi JP, et al. Integrative genomic, transcriptomic, and rnai analysis indicates a potential oncogenic role for Fam110b in castration-resistant prostate cancer. *Prostate* (2012) 72(7):789–802. doi: 10.1002/pros.21487

11. Hauge H, Fjelland KE, Sioud M, Aasheim HC. Evidence for the involvement of Fam110c protein in cell spreading and migration. *Cell signal* (2009) 21(12):1866–73. doi: 10.1016/j.cellsig.2009.08.001

12. Aquino Perez C, Burocziova M, Jenikova G, Macurek L. Ck1-mediated phosphorylation of Fam110a promotes its interaction with mitotic spindle and controls chromosomal alignment. *EMBO Rep* (2021) 22(7):e51847. doi: 10.15252/embr.202051847

13. Kulis M, Esteller M. DNA Methylation and cancer. *Adv Genet* (2010) 70:27–56. doi: 10.1016/b978-0-12-380866-0.60002-2

14. Zhao P, Li L, Jiang X, Li Q. Mismatch repair Deficiency/Microsatellite instability-high as a predictor for anti-Pd-1/Pd-L1 immunotherapy efficacy. *J Hematol Oncol* (2019) 12(1):54. doi: 10.1186/s13045-019-0738-1

15. Jardim DL, Goodman A, de Melo Gagliato D, Kurzrock R. The challenges of tumor mutational burden as an immunotherapy biomarker. *Cancer Cell* (2021) 39 (2):154–73. doi: 10.1016/j.ccell.2020.10.001

16. Schwartz GK, Shah MA. Targeting the cell cycle: A new approach to cancer therapy. *J Clin Oncol* (2005) 23(36):9408–21. doi: 10.1200/jco.2005.01.5594

17. Tan S, Li D, Zhu X. Cancer immunotherapy: Pros, cons and beyond. *Biomed pharmacother = Biomed pharmacother* (2020) 124:109821. doi: 10.1016/j.biopha.2020.109821

18. Yang Y. Cancer immunotherapy: Harnessing the immune system to battle cancer. *J Clin Invest* (2015) 125(9):3335–7. doi: 10.1172/jci83871

19. Baxevanis CN, Perez SA, Papamichail M. Cancer immunotherapy. *Crit Rev Clin Lab Sci* (2009) 46(4):167–89. doi: 10.1080/10408360902937809

20. Xiao Y, Yu D. Tumor microenvironment as a therapeutic target in cancer. *Pharmacol Ther* (2021) 221:107753.

21. Ren D, Hua Y, Yu B, Ye X, He Z, Li C, et al. Predictive biomarkers and mechanisms underlying resistance to Pd1/Pd-L1 blockade cancer immunotherapy. *Mol Cancer* (2020) 19(1):19. doi: 10.1186/s12943-020-1144-6

22. He X, Xu C. Immune checkpoint signaling and cancer immunotherapy. *Cell Res* (2020) 30(8):660–9. doi: 10.1038/s41422-020-0343-4

23. Baretti M, Le DT. DNA Mismatch repair in cancer. *Pharmacol Ther* (2018) 189:45–62. doi: 10.1016/j.pharmthera.2018.04.004

24. Le DT, Durham JN, Smith KN, Wang H, Bartlett BR, Aulakh LK, et al. Mismatch repair deficiency predicts response of solid tumors to pd-1 blockade. *Sci (New York NY)* (2017) 357(6349):409–13. doi: 10.1126/science.aan6733

25. Hinshaw DC, Shevde LA. The tumor microenvironment innately modulates cancer progression. *Cancer research* (2019) 79(18):4557–66.

26. Zhang Y, Zhang Z. The history and advances in cancer immunotherapy: Understanding the characteristics of tumor-infiltrating immune cells and their therapeutic implications. *Cell Mol Immunol* (2020) 17(8):807–21. doi: 10.1038/s41423-020-0488-6

27. Zhang J, Endres S, Kobold S. Enhancing tumor T cell infiltration to enable cancer immunotherapy. *Immunotherapy* (2019) 11(3):201–13. doi: 10.2217/imt-2018-0111

28. Vishwakarma S, Arya N, Kumar A. Regulation of tumor immune microenvironment by sphingolipids and lysophosphatidic acid. *Curr Drug Targets* (2022) 23(6):559–73. doi: 10.2174/1389450122666211208111833

29. Pitt JM, Marabelle A, Eggermont A, Soria JC, Kroemer G, Zitvogel L. Targeting the tumor microenvironment: Removing obstruction to anticancer immune responses and immunotherapy. *Ann Oncol* (2016) 27(8):1482–92. doi: 10.1093/annonc/mdw168

30. Liu J, Peng Y, Wei W. Cell cycle on the crossroad of tumorigenesis and cancer therapy. *Trends Cell Biol* (2022) 32(1):30–44. doi: 10.1016/j.tcb.2021.07.001

31. Li T, Fu J, Zeng Z, Cohen D, Li J, Chen Q, et al. Timer2.0 for analysis of tumor-infiltrating immune cells. *Nucleic Acids Res* (2020) 48(W1):W509–w14. doi: 10.1093/nar/gkaa407

32. Tang Z, Li C, Kang B, Gao G, Li C, Zhang Z. Gepia: A web server for cancer and normal gene expression profiling and interactive analyses. *Nucleic Acids Res* (2017) 45 (W1):W98–w102. doi: 10.1093/nar/gkx247

33. Ru B, Wong CN, Tong Y, Zhong JY, Zhong SSW, Wu WC, et al. Tisidb: An integrated repository portal for tumor-immune system interactions. *Bioinf (Oxford England)* (2019) 35(20):4200–2. doi: 10.1093/bioinformatics/btz210

34. Liu CJ, Hu FF, Xia MX, Han L, Zhang Q, Guo AY. Gscalite: A web server for gene set cancer analysis. *Bioinf (Oxford England)* (2018) 34(21):3771–2. doi: 10.1093/bioinformatics/bty411

35. Shen W, Song Z, Zhong X, Huang M, Shen D, Gao P, et al. Sangerbox: A comprehensive, interaction-friendly clinical bioinformatics analysis platform. *iMeta* (2022) 1(3):e36. doi: 10.1002/imt2.36

36. Li T, Fan J, Wang B, Traugh N, Chen Q, Liu JS, et al. Timer: A web server for comprehensive analysis of tumor-infiltrating immune cells. *Cancer Res* (2017) 77(21): e108–e10. doi: 10.1158/0008-5472.Can-17-0307

37. Vasaikar SV, Straub P, Wang J, Zhang B. Linkedomics: Analyzing multi-omics data within and across 32 cancer types. *Nucleic Acids Res* (2018) 46(D1):D956–d63. doi: 10.1093/nar/gkx1090

frontiers | Frontiers in Immunology

TYPE Review
PUBLISHED 07 March 2023
DOI 10.3389/fimmu.2023.1121285

OPEN ACCESS

EDITED BY
Julie Decock,
Qatar Biomedical Research Institute, Qatar

REVIEWED BY
Wolfram Weckwerth,
University of Vienna, Austria
Pierosandro Tagliaferri,
Magna Græcia University, Italy

*CORRESPONDENCE
Guoxu Zheng
bio_zhengguoxu@163.com
An-Gang Yang
agyang@fmmu.edu.cn

SPECIALTY SECTION
This article was submitted to Cancer Immunity and Immunotherapy, a section of the journal Frontiers in Immunology

RECEIVED 11 December 2022
ACCEPTED 23 February 2023
PUBLISHED 07 March 2023

CITATION
Guo Z, Zhang R, Yang A-G and Zheng G (2023) Diversity of immune checkpoints in cancer immunotherapy. *Front. Immunol.* 14:1121285. doi: 10.3389/fimmu.2023.1121285

Diversity of immune checkpoints in cancer immunotherapy

Zhangyan Guo[1], Rui Zhang[1,2], An-Gang Yang[1*] and Guoxu Zheng[1*]

[1]State Key Laboratory of Cancer Biology, Department of Immunology, Fourth Military Medical University, Xi'an, China, [2]State Key Laboratory of Cancer Biology, Department of Biochemistry and Molecular Biology, Fourth Military Medical University, Xi'an, China

Finding effective treatments for cancer remains a challenge. Recent studies have found that the mechanisms of tumor evasion are becoming increasingly diverse, including abnormal expression of immune checkpoint molecules on different immune cells, in particular T cells, natural killer cells, macrophages and others. In this review, we discuss the checkpoint molecules with enhanced expression on these lymphocytes and their consequences on immune effector functions. Dissecting the diverse roles of immune checkpoints in different immune cells is crucial for a full understanding of immunotherapy using checkpoint inhibitors.

KEYWORDS

immune checkpoint, immunotherapy, T cell, NK cell, macrophage

1 Introduction

It now appears that immunotherapies can elicit durable antitumor responses in metastatic cancer. These immunotherapies include adoptive cell therapy (ACT) and checkpoint inhibitor therapies (1). In particular, recent studies have confirmed that targeting immune checkpoint pathways has remarkable clinical efficiency across several tumor types (2). Immune checkpoint molecules are mainly expressed on immune cells and can maintain immunological homeostasis. Under normal physiological conditions, they can inhibit and prevent immune cells from killing tumor cells (3). In the past few years, studies have mainly focused on finding new immune checkpoint molecules expressed on T cells, which can effectively restore the exhaustion of T cells when blocked. The immune checkpoint targets that have been validated clinically include CTLA4 and PD-1, and many new candidates are being discovered and will undergo clinical evaluation (4). In addition to T cells, Nature Killer cells also express immune checkpoints, but the consequences of these checkpoints on NK cells' functions are much less explored (5). Recently, literature has shown that macrophage-centered blockade of immune checkpoints represents promising therapeutic avenues (6). In this review, we will discuss recent advances in knowledge regarding the diversity of immune checkpoints expressed on different immune cells and their relationships with cancer immunotherapy (Figure 1).

10.3389/fimmu.2023.1121285

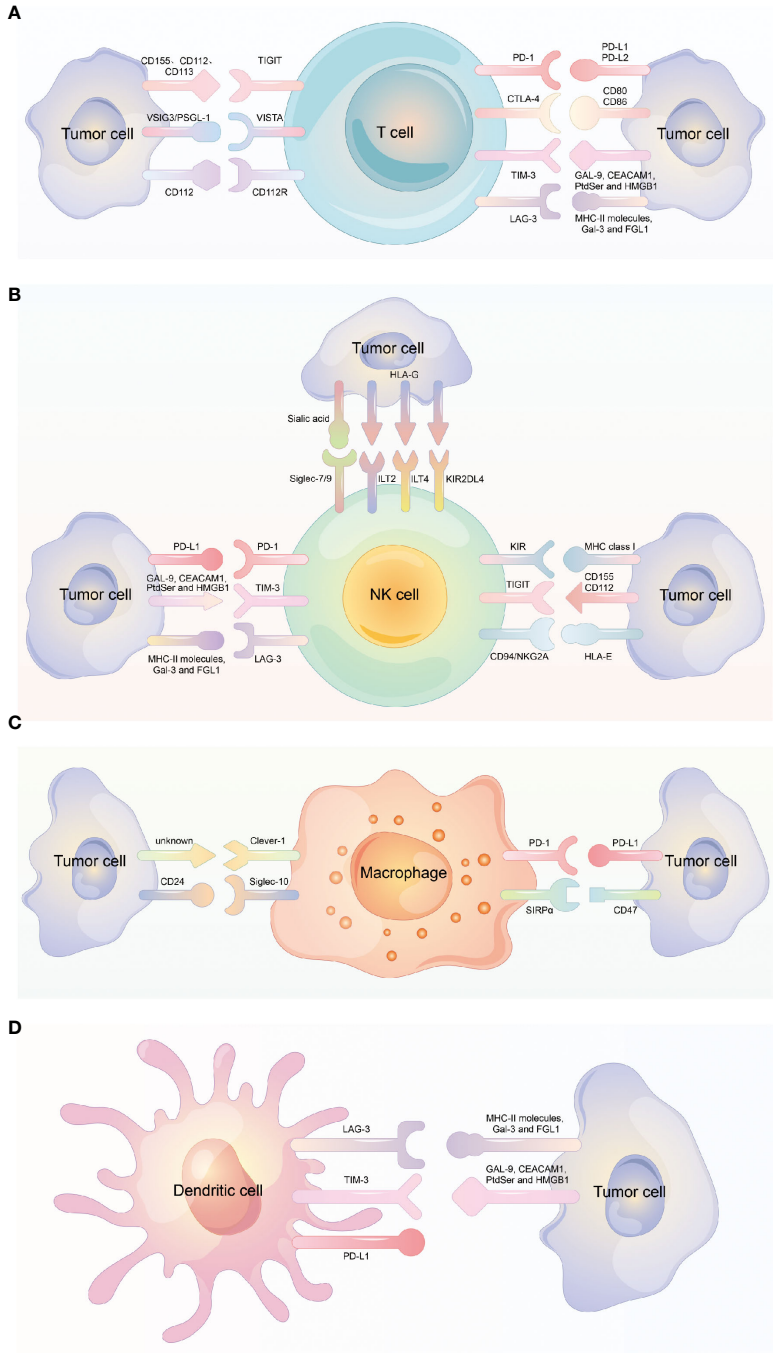

FIGURE 1
Different immune checkpoint molecules expressed on different immune cells. **(A)** Different immune checkpoint molecules expressed on T cell and the corresponding ligand molecules expressed on tumor cells. **(B)** Different immune checkpoint molecules expressed on NK cell and the corresponding ligand molecules expressed on tumor cells. **(C)** Different immune checkpoint molecules expressed on Macrophage and the corresponding ligand molecules expressed on tumor cells. **(D)** Different immune checkpoint molecules expressed on dendritic cell and the corresponding ligand molecules expressed on tumor cells.

2 Checkpoint immunotherapy based on T cells

In the last few decades, the function of tumor-infiltrating lymphocytes (TILs), especially the cytotoxic $CD8^+$ T cells and other subgroups of T cells, such as $CD4^+$ T cells and Tregs on tumor progression and patient prognosis have been deeply explored (7–9).

In immunological homeostasis, the engagement of T-cell antigen receptors (TCRs) with antigenic peptides can result in the activation and proliferation of T cells (10). To prevent overreaction and autoimmunity, inhibitory receptors are upregulated on T cells and other immune cells. These inhibitory receptors are also called immune checkpoints. Because of the presence of the immunoreceptor tyrosine-based inhibitory motif (ITIM), immune

checkpoints can induce inhibitory signals in inhibitory receptor-expressing immune cells (11).

In the immunosuppressive tumor microenvironment, tumor cells make use of the overexpression of inhibitory receptors on immune cells to avoid immune clearance (12). The expression of immune checkpoints can lead to T-cell exhaustion, which is defined by a decline in T-cell proliferation and reduced T-cell function. To date, immune checkpoints that have been explored for their expression by T cells include PD-1 (programmed cell death protein-1), CTLA-4 (cytotoxic T-lymphocyte-associated protein-4), TIM-3 (mucin-domain containing-3), LAG-3 (lymphocyte-activation gene-3), and T cell immunoglobulin and ITIM domain (TIGIT), among others (13).

2.1 PD-1

PD-1 (CD279) is a coinhibitory receptor that is extensively expressed on T cells, NK cells (natural killer cells), and B cells. In particular, PD-1 is expressed on activated T cells at high levels and is considered to be involved in immune tolerance (14). There are two ligands for PD-1, known as PD-L1 and PD-L2, which have low expression in normal tissue but abnormal expression in some tumor types. For example, it has been reported that the expression of PD-L1 is upregulated in melanoma, non-small-cell lung cancer, breast cancer, and squamous cell head and neck cancer (15).

PD-1$^+$ T-cell exhaustion was originally studied in murine models and then extended to human infection and cancer (16). In chronic viral infections, CD8$^+$ T cells are in a state of dysfunction and have abnormal expression of PD-1. Se Jin Im et al. found that in a mouse model chronically infected with lymphocytic choriomeningitis virus, a population of virus-specific CD8$^+$ T cells proliferated after PD-1 blockade, and this proliferative burst occurred only in this type of CD8$^+$ T cell (17). Tim Wartewig et al. found that mono- and biallelic deletions of PDCD1, which encodes PD-1, are recurrently observed in human T-cell lymphomas with frequencies of up to 30%, indicating high clinical relevance; these findings imply that PD-1 is a potent haploinsufficient tumor suppressor in T-cell lymphomas (18). In a study of colorectal cancer, Xiao Albert Zhou et al. identified a major PD-1-associated protein, KLHL22, that can mediate the degradation of PD-1 before its transport to the cell surface. They found that the expression of KLHL22 was markedly decreased in tumor-infiltrating T cells from colorectal cancer patients and suggested the therapeutic potential of 5-FU (which could increase PD-1 expression by inhibiting the transcription of KLHL22) in combination with anti-PD-1 in colorectal cancer patients (19).

Based on previous research, new strategies have emerged that target PD-1 or PD-L1 and block them; as a result, T-cell function is successfully reinvigorated (20). Along these lines, antibodies targeting the PD-1/PD-L1 axis have been used for various tumors. For example, Alexander C Huang et al. found that neoadjuvant anti-PD-1 treatment is effective against high-risk resectable stage III/IV melanoma (21). Edward B Garon et al. assessed the efficacy and safety of PD-1 inhibition with pembrolizumab in patients with advanced non-small-cell lung cancer enrolled in a phase 1 study and found that a blocking antibody targeting PD-1 had an obvious antitumor effect in NSCLC patients and an acceptable side-effect profile (22). Fan Zhang et al. performed scRNA-seq analysis on 3110 peripheral T cells of NSCLC patients before and after the initiation of PD-1 blockade and found a higher cytotoxic activity in tumor-related CD4$^+$ T-cell clones than in CD8$^+$ T-cell clones (23). In a prognostic analysis of advanced renal cell carcinoma, the investigator assessed the efficacy and safety of nivolumab treatment *versus* everolimus treatment over a 3-year follow-up and found that nivolumab treatment was more effective and safer than everolimus (24). Two phase III clinical trials (CheckMate 141 and KEYNOTE 040) analyzed the overall survival (OS) of patients with recurrent or metastatic head-and-neck squamous cell carcinoma (HNSCC) and found that anti-PD-1 monotherapy improved the therapeutic effects of platinum chemotherapy (25, 26).

Although a promising therapeutic effect using a PD-1 blocking antibody was observed in those tumor patients, some patients did not respond to this blocking antibody blocking, or it had limited effects. This implies that there are other inhibitory pathways involved in T-cell dysfunction.

2.2 CTLA-4

CTLA-4 (cytotoxic T-lymphocyte-associated protein 4), also known as CD152, is a protein receptor mainly expressed on T cells that was first identified as a second receptor for the T-cell costimulatory legend B7 and later discovered to be a negative regulator of T-cell activation (27–29). In naïve T cells, the expression of CTLA4 is low, but in phases of TCR engagement and activation, CTLA4 can be rapidly upregulated in both CD4 helper T cells and CD8 effector T cells, while its upregulation is obvious in helper T cells (30). CTLA4 has two ligands, CD80 and CD86, also called B7-1 and B7-2, which can also be recognized by CD28, a T-cell costimulatory protein that is homologous to CTLA4. However, for both ligands, CTLA4 has higher affinity and avidity than CD28, implying that it is an antagonist of CD28-mediated costimulation (31, 32). This mechanism suggests that the CD28/CTLA4 regulatory form can act as a rheostat in T-cell activation.

In mouse models, anti-CTLA4 antibody treatment initially resulted in the rejection of tumors, including preestablished tumors; furthermore, the rejection resulted in immunity to a secondary exposure to tumor cells (33). During the subsequent development of clinical immunotherapy, two CTLA-4 blockade antibodies, ipilimumab and tremelimumab, have been tested in many types of human tumors, and their treatment efficacy has been reported in melanoma (34, 35), non-small-cell lung cancer (36), mesothelioma (37), prostate cancer (38), breast cancer (39) and urothelial cancer (40). Despite the promising therapeutic effects, a broad range of immune-related adverse events (irAEs) occurring in the skin, gastrointestinal tract, liver and endocrine organs have been reported in some trials, with an incidence of 60-65% (41). A landmark clinical trial called the CheckMate 067 clinical trial (ClinicalTrials.gov NCT01844505) used a combination CPI therapy with an anti-CTLA-4 antibody and an anti-PD-1 antibody This study was carried out on 945 patients with stage III

or IV melanoma and evaluated the median overall survival under treatment with nivolumab plus ipilimumab or with nivolumab or ipilimumab monotherapy. Although the results showed that the OS appeared to be improved in the combination treatment cohort compared with the single-treatment cohorts, the trial did not have sufficient power to show a significant difference between the two nivolumab-containing groups, and the incidence of adverse events was increased in the combination therapy cohort in this trial (42, 43).

Additionally, while CTLA4 is expressed at high levels on Tregs and although an important role of conventional T-cell CTLA4 in self-tolerance has been reported, CTLA4 blockade therapy combined with Treg depletion has led to considerable success in tumor treatment as well as autoimmune disease treatment (41). Therefore, more research should be conducted to reveal the pros and cons of CTLA4 blockade immunotherapy.

2.3 TIM-3

TIM-3 (T-cell immunoglobulin and mucin domain containing-3), a member of the TIM family is a coinhibitory receptors. It is expressed on IFN-γ-producing T helper 1 $CD4^+$ and $CD8^+$ T cells and Th17 cells (44). The expression of TIM-3 is regulated by antigenic stimulation and proinflammatory cytokines (45). In early studies, TIM-3 was reported to have an inhibitory function, suppressing effector Th1 responses in EAE and type I diabetes in a mouse model, and the use of an anti-TIM-3 antibody was reported to lead to disease exacerbation in EAE (46). In subsequent studies, the overexpression of TIM-3 has been found to be correlated with T-cell dysfunction and T-cell exhaustion (47). The role of TIM-3 as a suppressive receptor that regulates T-cell activity in some chronic viral infections, such as HIV-1, HBV and HCV infections, has been reported (48–50). In the tumor microenvironment, TIM-3 has also been found to be expressed on $CD8^+$ TILs (tumor-infiltrating leukocytes), which is closely associated with PD-1 expression. Specifically, the expression patterns of TIM-3 and PD-1 indicate the degree of T-cell exhaustion; for example, in mice bearing solid tumors, $TIM\text{-}3^+PD\text{-}1^+$ TILs exhibit the most severely exhausted phenotype, as defined by failure to proliferate and produce cytokines. Additionally, high expression of TIM-3 on $CD8^+$ T cells has been found to be correlated with poor prognosis in certain types of cancers, and blockade of TIM-3 combined with anti-PD-1 antibody treatment has been confirmed to be more effective than blockade of either molecule alone in antitumor immunotherapy (51–53). In a study on medullary thyroid carcinoma (MTC) in 200 MTC patients, TIM-3 positivity was 48%, and TIM-3 expression was positively correlated with PD-1 and CTLA-4 expression. Log-rank tests and multivariate Cox analyses both indicated that TIM-3, CTLA-4 and PD-1/PD-L1 coexpression were associated with poor structural recurrence-free survival (54).

2.4 LAG-3

LAG-3, lymphocyte activation gene 3, is a cell surface protein belonging to the immunoglobulin superfamily that is expressed on CD4+ and CD8+ T cells (55), NK cells (56), B cells and plasmacytoid dendritic cells (57). It is a coinhibitory transmembrane receptor whose ligands are MHC class II and FGL1, and interaction with the ligands can negatively regulate the activation of T cells (58, 59), similar to the case for CTLA4 and PD-1 (60, 61). In particular, LAG-3 has a synergistic effect with PD-1 to regulate immune responses (62). In clinical immunotherapy, a LAG-3 Ig fusion protein named IMP321 was first used in advanced renal cell carcinoma patients and resulted in reduced tumor growth and improved progression-free survival (63). When LAG-3 blockade antibody (BMS-986016) and nivolumab (a PD-1 antibody) were used in combination in melanoma patients, the initial resistance when only blocking of the PD-1/PD-L1 axis was converted (64). In addition, many types of human tumors present aberrant expression of LAG-3, which correlates with poor outcomes (65–69). Kosaku Mimura et al. evaluated the distribution of different inhibitory ligands in 365 GC patients and found coexpression of inhibitory ligands for PD-1, Tim-3 and Lag-3 in the largest proportion (34.7%). Their findings suggest that the expression of inhibitory ligands for Tim-3 and Lag-3 on GC cells serve as potential predictive biomarkers of the response to anti-PD-1 therapy (70).

2.5 TIGIT

TIGIT, T-cell immunoglobulin and ITIM domain, belongs to the immunoglobulin superfamily and is also a T-cell coinhibitory receptor. It is expressed on $CD4^+$ memory and regulatory T cells, $CD8^+$ T cells and NK cells. To date, the ligands that have been discovered to be recognized by TIGIT are CD155 (PVR or poliovirus receptor), CD112 (PVRL2) and CD113 (PVRL3, NECTIN-3), of which CD155 has the highest affinity for TIGIT (71). TIGIT has been implicated in tumor immunosurveillance, and its role is analogous to that of PD-1 in tumor immunosuppression because it is overexpressed in tumor antigen-specific $CD8^+$ T cells and $CD8^+$ TILs and is often coexpressed with PD-1. Therefore, co-blockade of the two checkpoint molecules can enhance the antitumor efficacy of single blockade (72).

2.6 VISTA

VISTA, V-domain Ig-containing suppressor of T-cell activation, also belongs to the transmembrane Ig superfamily (73). It is part of the B7 family and is mainly expressed on T cells and $CD11b^+$ antigen-presenting cells (APCs)/myeloid cells (74). It has been reported that VISTA can act as both a receptor and a ligand on T cells and that it functions as an inhibitor to maintain immune tolerance (75). In tumor-infiltrating lymphocytes, VISTA is overexpressed, especially in myeloid-derived suppressor cells and regulatory T cells. Recently, it has been reported to be highly expressed in human ovarian and endometrial cancers. The abnormal expression of VISTA in tumor cells suppresses T-cell proliferation and cytokine production *in vitro* and decreases the tumor infiltration of $CD8^+$ T cells *in vivo*. VISTA blockade prolongs the survival of tumor-bearing mice (76). In a study on oropharyngeal squamous cell carcinoma (OPSCC) including 241 tumor tissues aiming to describe the expression of LAG-3, Tim-3,

and VISTA in the TME of OPSCC, immunohistochemistry showed that 168 OPSCC samples stained positive for VISTA. The results also revealed that $CD8^+$ T cells were significantly associated with LAG-3, Tim-3 and VISTA expression ($p < 0.001$, $p < 0.001$, $p = 0.007$), so immune checkpoint therapy targeting LAG-3, Tim-3, and/or VISTA could be a promising treatment strategy, especially for HPV-related OPSCC (77).

2.7 Siglec-15

Siglec-15, short for sialic acid-binding immunoglobulin-like lectin 15, belongs to the Siglec gene family because of its sialic acid-binding immunoglobulin-type lectin structure (78). Originally, Siglec-15 was mainly reported to play roles in osteoclast differentiation and bone remodeling (79, 80). Recently, Wang et al. identified Siglec-15 as a potent immunosuppressive molecule. In their study, using a newly developed genome-scale T-cell Activity Array, they identified that the expression of Siglec-15 was upregulated in many human cancer cells and tumor-infiltrating myeloid cells, while under normal physiological conditions, it was limited to cells in the myeloid lineage. In particular, its expression was mutually exclusive with that of B7-H1 in cancer cells and could be regulated by M-CSF and IFN-γ. In thorough *in vitro* and *in vivo* experiments, Siglec-15 was confirmed to suppress antigen-specific T-cell responses and impair antitumor immunity. Conversely, a Siglec-15-blocking mAb reversed T-cell suppression and promoted tumor immunity in multiple tumor models (81). Siglec-15 has unique molecular features compared with those of many other known checkpoint inhibitory ligands; it shows mutually exclusive expression with PD-L1, which suggests that it plays a key role in tumor escape in PD-L1-negative patients. As a new player in cancer immunotherapy, siglec-15 may have potential applications in anti-PD-1/PD-L1-resistant patients (82). Collectively, the evidence suggests that Siglec-15 is an attractive target for cancer immunotherapy.

2.8 CD112R

CD112R is a poliovirus receptor-like protein and has been described as a new coinhibitory receptor for human T cells that can interact with CD112 with higher affinity than CD226 and TIGIT. Recently, it has also been reported to be expressed in subpopulations of NK cells (83). Zhu et al. reported that CD112 is expressed on DCs and many tumor cells and mediates the interaction of CD112R with DCs and tumor cells. When the interaction between CD112R and CD112 is disrupted, human T-cell function is enhanced. These results imply that the CD112R/CD112 axis is a new checkpoint in human T cells (84).

3 Checkpoint immunotherapy based on NK cells

Natural killer (NK) cells are involved in innate immunity and play a significant role in immunological surveillance against various infections and malignant transformation. Unlike that of T cells, the activation of NK cells does not require prior sensitization, and the NK cell function is determined by the balance of a series of activated and inhibitory receptors expressed on the cell surface (85, 86). In the tumor microenvironment, tumor cells often downregulate the expression of major histocompatibility complex (MHC) class I to escape killing by T cells, nevertheless, these "missing self" tumor cells become more susceptible to the immunosurveillance executed by NK cells. Based on these intrinsic properties and accumulating evidence that defects in NK-cell function and number are often associated with viral infections and tumorigenesis (87), increased attention has been given to NK-cell-based immunotherapy to compensate for the lack of T cell immunotherapy.

3.1 KIRs

Killer-cell immunoglobulin-like receptors (KIRs) are a family of type I transmembrane glycoproteins that are expressed on NK cells and a minority of T cells (88). KIRs have dual functions: they can inhibit NK-cell cytotoxicity by interacting with MHC class I molecules but can also activate cytotoxic activity as activating receptors (89). KIR family members have many haplotypes because of their polymorphic genes, such as KIR2DL1 and KIR3DL2, which are named by the number of extracellular immunoglobulin domains and by the length of the cytoplasmic domain they express (90). KIR inhibitory receptors conduct inhibitory signals through the ITIM, which is located in their long cytoplasmic domain. Based on the "missing self" theory, the humanized antagonistic antibody lirilumab (IPH2102), which can target inhibitory KIRs such as KIR2DL1-3 and KIR2DS1-2, has been used in clinical immunotherapy studies (91). Although the use of lirilumab has been shown to promote NK-cell cytotoxicity toward multiple myeloma, lymphoma and leukemia in preclinical studies, its efficacy in some phase I or II trials on multiple myeloma and acute myeloid leukemia was not as good as expected (92–94). Another mAb targeting KIR2DL1/2/3, IPH2102, has failed to exert impressive clinical effects in patients with multiple myeloma (MM) as monotherapy, but when combined with lenalidomide in a dual immunotherapy for MM patients, it has been reported to achieve a median progression-free survival of 24 months, suggesting the promise of combination therapy (95).

3.2 NKG2A

NKG2 belongs to the C-type lectin-like receptor superfamily and has seven types, NKG2A, NKG2B, NKG2C, NKG2D, NKG2E, NKG2F and NKG2H. NKG2 is expressed on NK cells and acts as an activating receptor or inhibitory receptor when dimerized with other molecules. CD94/NKG2A forms a heterodimeric receptor and plays an inhibitory role on both T cells and NK cells by interacting with HLA-E, which is upregulated in many tumors (96, 97). Pascale André et al. reported that the use of an NKG2A blocking antibody, monalizumab, can enhance NK-cell effector functions against various tumor cells and can rescue $CD8^+$ T-cell function in combination with PD-x axis blockade (98). Takahiro

Kamiya et al. constructed NKG2A-null NK cells in which NKG2A expression was abrogated and found that they had increased cytotoxicity against HLA-E-expressing tumor cells. In immunodeficient mice, NKG2A-null NK cells showed an enhanced antitumor effect against HLA-E-expressing tumors (99). In an *in vivo* study on cancer vaccination using mouse tumor models, the impact of therapeutic vaccines was greatly potentiated by disruption of the NKG2A/Qa-1^b (conserved ortholog of HLA-E) axis even in a PD-1-refractory mouse model. However, in this research, the blockade therapy affected CD8 T cells, not NK cells. These findings indicate that NKG2A-blocking antibodies might improve clinical responses to therapeutic cancer vaccines (100). Overall, blockade of the NKG2A axis represents a promising therapeutic approach, but monalizumab monotherapy or combination therapy with another blocking antibody (cetuximab or durvalumab) is still under investigation, and more trials are needed.

3.3 TIGIT

As mentioned above, TIGIT is expressed on some NK cells and can interact with its ligands CD155 and CD112, which are expressed on many tumor cells (71). The binding of TIGIT with its ligands has been reported to result in an inhibitory signal and downregulate NK-cell functions. Qing Zhang et al. reported that TIGIT was associated with NK-cell exhaustion in mouse models and in patients with colon cancer. In mice bearing tumors, including colon tumors, breast tumors and chemically induced fibrosarcomas, treatment with an mAb to TIGIT induced tumor growth inhibition and tumor volume reduction and prevented NK-cell exhaustion. In addition, blockade of TIGIT resulted in potent tumor-specific T-cell immunity in an NK-cell-dependent manner and exerted a synergistic effect with an mAb blocking PD-1 (101).

3.4 PD-1

In addition to being expressed in T cells as mentioned above, PD-1 has also been reported to be expressed in human NK cells from healthy donors and cancer patients and to have an inhibitory effect on NK-cell function (102, 103). Joy Hsu et al. reported that blockade of the PD-1/PD-L1 axis can elicit a strong NK-cell response, which is essential for the therapeutic effect, and implied the importance of PD-1 in inhibiting NK-cell responses *in vivo* and of the coordinating roles of T cells in PD-1/PD-L1 blockade immunotherapy (104). Wenjuan Dong et al. found that some tumors can induce PD-L1 expression on NK cells *via* AKT signaling and that an anti-PD-L1 mAb can directly act on PD-$L1^+$ NK cells to combat PD-L1- tumors *via* a p38 pathway. Their findings reveal a PD-1-independent mechanism of antitumor efficacy through PD-$L1^+$ NK cells that is activated with an anti-PD-L1 mAb (105).

3.5 TIM-3

The expression of TIM-3 is extensive in immune cells, as mentioned above. In addition to T cells, TIM-3 is constitutively expressed on resting human NK cells and is upregulated upon activation (106). The transcriptional levels of TIM-3 are higher in NK cells than in other lymphocytes, and TIM-3 can serve as a maturation marker. Antibodies that crosslink TIM-3 suppress NK-cell-mediated cytotoxicity, indicating that the function of NK cells may be negatively regulated by the interaction of TIM-3 with its cognate ligands, which are expressed on target cells (107). TIM-3 is upregulated in peripheral NK cells of patients with gastric cancer, lung adenocarcinoma and melanoma, while it is upregulated in tumor-infiltrating NK cells of gastrointestinal stromal tumors. This abnormal expression of TIM-3 on NK cells often predicts a poor prognosis, especially in melanoma and lung adenocarcinoma, but blockade of TIM-3 reverses NK-cell exhaustion and improves NK-cell-mediated cytotoxicity (108–111).

3.6 LAG-3

LAG-3 is an inhibitory receptor that is upregulated on activated T cells and NK cells, as mentioned above. It is homologous to CD4 but has a greater affinity for MHC class II molecules; additionally, LAG-3 can bind to LSECtin and FGL1, which are expressed by some tumor cells (112). Unlike in T cells, the function of LAG-3 in NK cells is not clear. Although previous studies have not found that blockade of LAG-3 on human NK cells can influence NK-cell cytotoxicity (113), one study reported that patients with HIV have lower expression of LAG-3 along with other inhibitory molecules involved in viral control, such as PD-1 and TIM-3, than individuals in a low-risk population or progressors (114). IMP321, a soluble recombinant LAG-3-Ig fusion protein, has been reported to induce NK cells to produce IFN-γ and/or TNF-α in healthy donors in an ex vivo short-term experiment, but in metastatic cancer patients, the values are reduced (5, 115). In clinical trials, many anti-LAG-3 monoclonal antibodies have been analyzed either as monotherapies or in combination with other checkpoint-blocking antibodies, such as anti-PD-1 mAb, for the immunotherapy of solid tumors and hematologic malignancies. Two examples are relatlimab (BMS-986016) (NCT01968109) and LAG525 (NCT02460224). However, further work on the effect of LAG-3 on NK cells needs to be explored (116).

3.7 Siglec-7/9

Siglecs, sialic acid-binding immunoglobulin-type lectins, are a subset of the I-type lectins that bind sialic acid and are mainly expressed on the surfaces of immune cells, including neutrophils, eosinophils, monocytes, macrophages, NK cells, dendritic cells, mast cells, B cells and T cells (117). To date, the siglec receptor family comprises 15 members that vary in their expression patterns

and in the specificity of ligand binding. Among the family members, siglec-7 and siglec-9 are reported to be mainly expressed on NK cells and to transport inhibitory signals through the ITIM motifs in their cytoplasmic tails (118). Many studies have reported that changes in sialic acid are correlated with tumorigenesis and cancer progression (119). Therefore, siglec-sialic acid interactions may play an important role in modulating the immune response and can be targeted as useful checkpoints (120). In human cancer, siglec-9 has been found to be upregulated in peripheral NK cells, mainly in $CD56^{dim}CD16^{+}$ NK cells. In an *in vitro* study, blockade of siglec-7 and siglec-9 using Fab fragments increased the cytotoxicity of NK cells against tumor cells, and in an *in vivo* mouse model, sialoglycan-dependent NK-cell inhibition led to the killing of tumor cells (118). In a recent study, Itziar Ibarlucea-Benitez et al. investigated the impacts of siglec-7 and siglec-9 on tumor progression using a humanized immunocompetent murine model and found reduced tumor burden when using Fc-engineered anti–Siglec-7 and anti–Siglec-9 blocking antibodies. This effect may have been mediated by prevention of macrophage polarization into tumor-associated macrophages and thus reprogramming of the immune-suppressive tumor microenvironment (121). In addition, Siglec-9 has been found to be upregulated on tumor-infiltrated CD8 + T cells in non-small-cell lung cancer and ovarian and colorectal cancers, and other inhibitory receptors, such as PD-1, are also coexpressed by T cells expressing siglec-9, implying that combination with other immune checkpoint inhibitors could be used for coinhibition in immunotherapy (122).

3.8 HLA-G

Human leukocyte antigen (HLA)-G is a nonclassical MHC-I molecule that was initially found to be expressed in pregnancies by cells of the trophoblast at the maternal–fetal interface and acts as a mediator of immune tolerance because it protects the fetus from NK-cell-mediated lysis (123, 124). To date, seven isoforms have been found, including HLA-G1 to HLA-G7, some of which are membrane-bound molecules and some of which are soluble forms. Under normal physiological conditions, the expression of HLA-G is restricted to immune-privileged organs, but it is upregulated in some immune-mediated diseases, such as viral infections and cancer. By interacting with different receptor molecules on different immune cells, HLA-G exerts several immunomodulatory effects. In NK cells, the inhibitory receptors ILT2 and ILT4 are responsible for the HLA-G-mediated inhibitory effect (125). One study has found that these two inhibitory receptors are broadly expressed on T cells, B cells and dendritic cells, implying the immunosuppressive effect of HLA-G on these cells (126). The abnormal expression of HLA-G in different cancers is associated with poor clinical outcomes in patients, so increasing attention has been given to HLA-G as an immune checkpoint in cancer (127). Numerous studies have reported that the expression of HLA-G in ovarian carcinoma, hepatocellular carcinoma, glioma and renal cell carcinoma inhibits NK cell-mediated cytolysis of these cancer cells but that this inhibition can be reversed by the use of specific antibodies targeting HLA-G or its receptors. In addition, the modulation of cytokine secretion by sHLA-G/ILT2 binding and the different immunosuppressive functions of HLA-G on T cells, B cells, macrophages, dendritic cells, and neutrophils have been deeply discussed (128–132). Chia-Ing Jan et al. designed and tested a CAR strategy to target HLA-G in solid tumors, and the results showed that HLA-G CAR-transduced NK cells effectively cytolyzed breast, brain, pancreatic and ovarian cancer cells *in vitro* and resulted in reduced xenograft tumor growth with extended median survival in orthotopic mouse models (133). In our study, we found that HLA-G desensitizes breast cancer cells to trastuzumab by binding to the NK-cell receptor KIR2DL4 and the blockade of HLA-G/KIR2DL4 axis improves the vulnerability of HER2-positive breast cancer to trastuzumab treatment *in vivo* (134).

4 Checkpoint immunotherapy based on macrophage

As an essential innate immune population, macrophages are also important components of the tumor microenvironment (TME). Tumor-associated macrophages (TAMs) have been found to be the most abundant immune cell type in solid tumors and to play an important role in orchestrating the immunosuppressive mechanism of the TME (135). Macrophages are highly plastic and generally can be classified into two polarized cell types: classically activated M1 cells and alternatively activated M2 cells. M1 cells have an antitumor function with a proinflammatory phenotype, and M2 cells can promote tumor progression as immunosuppressive cells. The specific phenotype or polarization type a macrophage assumes is dependent on factors released from TME (136). Many studies have revealed that macrophages play key roles in homeostasis and tumor development; thus, they have been regarded as promising targets for immunotherapy in a variety of diseases.

4.1 PD-1

In addition to T cells and NK cells, PD-1 has been found to be expressed in macrophages, and its expression increases over time and with disease progression (137, 138). Previous studies focused on blockade of the PD-1/PD-L1 axis have demonstrated the promising role of PD-1 in rejuvenating T cells, but the influence of axis blockade on macrophages has not been fully revealed. A recent study has reported that the expression of PD-L1 on macrophages is correlated with clinical responses to anti-PD-L1 therapy; moreover, macrophage polarization can have an effect on the suppression of tumor metastasis (139). Genevieve P Hartley et al. used PD-L1 antibodies to treat mouse and human macrophages and found that the treatment increased spontaneous macrophage proliferation, survival and activation, as indicated by evidence including costimulatory molecule expression and cytokine production. In an *in vivo* model, the use of a PD-L1 antibody increased tumor infiltration by activated macrophages and triggered macrophage-mediated antitumor activity (140). On the other hand, macrophages may be regulators participating in the mechanism of PD1/PD-L1 treatment resistance. Arlauckas et al. found that $PD\text{-}1^{+}$ $CD8^{+}$ T cells

bound PD-1 antibody in a transient period, and then the antibody was seized within minutes from the T-cell surface by PD-1$^-$ macrophages, which led to the failure of reactivation of exhausted T cells (141). Therefore, consideration of the macrophage effect and phenotype in checkpoint immunotherapy is very important.

4.2 CTLA-4

In a study analyzing the action of ipilimumab, a CTLA-4 blocking mAb, Emanuela Romano et al. found that unlike nonresponder patients, patients who respond to ipilimumab treatment display higher peripheral frequencies of nonclassical monocytes at baseline and enrichment of tumor-infiltrating CD68+CD16+ macrophages (142). Previously, Tyler R Simpson et al. explored the activity of an anti-CTLA-4 antibody in the treatment of metastatic melanoma and found that blocking CTLA-4 resulted in selective depletion of Treg cells within tumor lesions; remarkably, this depletion was dependent on Fcγ receptor-expressing macrophages in the TME (143). TAM-mediated elimination of anti-CTLA4-sensitized Tregs resulted in effective antitumor immunity. These results suggest that macrophages in the tumor microenvironment may contribute to the action of anti-CTLA-4 antibodies in tumor treatment.

4.3 CD47-SIRPα

Signal regulatory protein alpha (SIRPα) is a receptor expressed on macrophages that can interact with CD47, which is upregulated on some tumor cells, and thus transmit a "don't eat me" signal. This is a strategy that is used by tumor cells to avoid phagocytosis. Based on this, anti-CD47 antibodies or engineered SIRPα-Fc fusion proteins have been used to prevent the immunosuppressive signal and restore macrophage phagocytic ability. Inhibition of the CD47/SIRPα axis can reduce tumor size and metastasis in many tumor models (144, 145). In clinical trials, anti-CD47 antibodies such as Hu5F9-G4 and CC-90002 and engineered high-affinity SIRPα and SIRPα-Fc fusion proteins (ALX148 and TTI-621) have been investigated for their therapeutic effects. However, this strategy has a defect: because of the ubiquitous expression of CD47 on red blood cells, anti-CD47 therapy can also lead to transient anemia (146). However, an alternative method has emerged involving a bispecific antibody that can target CD47 and tumor-associated antigens at the same time (147). Moreover, researchers have found that SIRPα is upregulated in NK cells upon IL-2 stimulation and interacts with target cell CD47 in a threshold-dependent manner. SIRPα deficiency or antibody blockade increases the killing capacity of NK cells, so disruption of the SIRPα-CD47 immune checkpoint may augment NK-cell antitumor responses, and elevated expression of CD47 may prevent NK-cell-mediated killing of allogeneic and xenogeneic tissues (148).

4.4 SFRs

In the study of phagocytic responses of different tumor cells to phagocytic cells when using SIRPα-CD47 blackade, Chen et al. found that phagocytosis of haematopoietic tumor cells during SIRPα–CD47 blockade was strictly dependent on SLAM (signalling lymphocytic activation molecule) family receptors (SFRs) *in vitro* and *in vivo* in mouse model. As the same results obtained in mouse, they also confirmed that this dependence required SLAMF7 (CD319 or CRACC), a SLAM family member which expressed on macrophages and tumor cell targets in human cells. Unlike other SLAM receptors, whose phagocytosis function are dependent on signalling lymphocyte activation molecule-associated protein (SAP) adaptors, SLAMF7 depended on its interaction with integrin Mac-1 and signals involving immunoreceptor tyrosine-based activation motifs. What counts is, their findings suggest that maybe the SIRPα–CD47 blockade therapy are more effective in patients with SLAMF7 expressing (149). Recently, Li et al. reported a critical role of the other two members of SFRs, SLAMF3 and SLAMF4, in constraining macrophage phagocytosis. Because of their ubiquitous expression on hematopoietic cells, the authors knockout SLAMF3 and SLAMF4 and found that the SFRs deficiency increased the ability of macrophages to phagocytose hematopoietic cells. In mouse model, the SFRs knockout lead to hematopoietic tumor rejection. Importantly, in CAR-macrophage therapy of hematopoietic cancer, the SFRs deletion also enhanced the efficacy. Together, their finding pointing to a potential therapeutic target for hematopoietic cancers (150).

4.5 Clever-1

The full name of Clever-1 is common lymphatic endothelial and vascular endothelial receptor-1, and it is also called Stabilin-1 or Feel-1. It is a conserved, multifunctional adhesion and scavenger receptor that is expressed by some endothelial cells and immunosuppressive macrophages and TAMs. Recent studies have found that Clever-1 can promote tumor progression (151–153). Miro Viitala et al. found that removal of Clever-1 from macrophages can significantly impair tumor growth in multiple solid tumor models, and a lack of Clever-1 in macrophages is associated with an increasingly immunostimulatory phenotype and enhanced signaling through the inflammatory mTOR pathway. Then, anti-Clever-1 treatment displays outcomes comparable to those of PD-1 blockade, implying Clever-1 as a novel target in clinical cancer evaluation and immunotherapy (154).

4.6 CD24/Siglec-10

CD24, a surface protein that is also called heat-stable antigen (HSA) or small cell lung carcinoma cluster 4 antigen, can interact with Siglec-10 and elicit inhibitory signals. CD24 has been reported to be expressed in several solid cancer cells (155, 156). As a member of the Siglec family, siglec-10 bears an ITIM within its cytoplasmic domain and can conduct inhibitory signals. Amira A Barkal et al. reported that many tumors overexpress CD24 and that TAMs express high levels of siglec-10. They found that the phagocytosis of all CD-24-expressing human tumors tested was augmented when CD24 or Siglec-10 was ablated genetically or when an antibody was used to block the CD24/Siglec-10 axis. In an *in vivo* study, ablation and blockade of CD24 resulted in both a macrophage-dependent

reduction in tumor growth and extension of survival. These findings reveal the CD24/Siglec-10 axis as a promising new therapeutic target in cancer immunotherapy (157).

5 Checkpoint immunotherapy based on DCs

5.1 LAG-3

LAG-3 was found to be expressed on a subset of circulating human plasmacytoid dendritic cells (pDCs), and its interaction with MHC II can induce TLR-independent activation of pDCs with limited IFN-α and enhanced IL-6 production. The same study also found LAG-3+ pDCs in melanoma-invaded lymph nodes that were IL-6 positive. These results suggest that activation of pDCs induced by LAG-3 could be involved in creating a suppressive environment in tumor sites (158).

5.2 TIM-3

In addition to T cells, TIM-3 is expressed by multiple other cell types, including dendritic cells, and the expression of TIM-3 may inhibit nucleic acid sensing through TLRs (159). A recent study identified TIM-3, which is expressed by intratumoral $CD103^+$ dendritic cells, as a target for therapy in a murine model of breast cancer. In that study, the use of an anti-TIM-3 antibody improved the response to paclitaxel chemotherapy in models of triple-negative and luminal B disease, with no evidence of toxicity. Anti-TIM-3 antibody administration led to enhanced granzyme B expression by $CD8^+$ T cells and increased CXCR3 chemokine ligand expression by tumor conventional dendritic cells (160). Karen O. Dixon et al. demonstrated that loss of TIM-3 on dendritic cells, but not on $CD4^+$ or $CD8^+$ T cells, promotes strong antitumor immunity; moreover, it prevents dendritic cells from expressing a regulatory program and facilitates the maintenance of $CD8^+$ effector and stem-like T cells. Conditional deletion of TIM-3 in dendritic cells leads to increased accumulation of reactive oxygen species, resulting in NLRP3 inflammasome activation, which underscores the potential of TIM-3 blockade for promoting antitumor immunity by regulating inflammasome activation (161). Overall, the immunomodulatory function mediated by TIM-3 is complex because of the broad expression of TIM-3 in different immune cells and the different interactions of this molecule with multiple ligands. Although promising therapeutic results have been reported in patients with anti-PD1-refractory disease in whom TIM-3 is co-blocked with other checkpoint receptors, the potential of TIM-3 as a drug target in different pathological conditions needs further study (162).

5.3 PD-L1

In a study investigating the anti-tumor mechanism of anti–PD-1 or PD-L1 antibodies, Mayoux et al. characterized various ligands on the surface of dendritic cells and found that PD-L1 is expressed much more abundantly than B7.1 on peripheral and tumor-associated dendritic cells in patients with cancer. PD-L1 expressed on dendritic cells can bind B7.1 on the same cell. This binding potentially prevent PD-1 ligation on T cells or B7.1 ligation of its partner CD28. Blocking PD-L1 on DCs relieves B7.1 sequestration in cis by PD-L1, which allows the B7.1/CD28 interaction to enhance T cell priming. This finding revealed that PD-L1 blockade reinvigorates DC function to generate potent anticancer T cell immunity (163).

6 Discussion

Complex communications between different cells and between cells and their surrounding microenvironment manipulate tumor oncogenesis and progression. In the tumor microenvironment, tumor cells create favorable conditions for cancer progression and avoid immunological surveillance through many strategies. For example, they can reduce neoantigen expression and alter the expression of immunoregulatory molecules on themselves. In addition, other extrinsic factors in the TME, such as the composition of tumor-infiltrating lymphocytes (TILs) and the inhibitory receptors expressed by TILs, all determine the ultimate direction of tumor development (164). Based on this, cancer immunotherapy, which mainly includes adoptive cell transfer (ACT) and immune checkpoint (IC) inhibitor (ICI) therapy, has revolutionized cancer treatment. In this review, we mainly discussed the diversity of immune checkpoints which have been found to be widely distributed in different immune cells and play different regulatory role. With the research and application of immunotherapy based on immune checkpoints in various malignant tumors (Figure 2 and Table 1), their anti-tumor prospects are exciting, but there are still many problems in clinical application. The first question is that most patients exhibit primary or acquired resistance, one possible reason is due to compensatory mechanisms, such as upregulation of alternative immune checkpoints in addition to the widely noted PD-1 and CTLA-4, such as TIM-3 and VISTA, or the influence of many factors in the tumor immune microenvironment on T cell function. To explore the diversity of IC and their different effects on different lymphocytes, as well as to identify new therapeutic targets in the tumor microenvironment, will help guide the application of multi-ICI combination in clinical tumor therapy. To explore the key immunosuppressive pathways in different tumor types and different patient populations is particularly important for selecting the right immunotherapy (165). In addition, studies have found that in some refractory tumors (immunologically cold), the combination of antibodies targeting reverse inhibitory immune microenvironment and anti-PD-1 antibody can often improve the therapeutic effect (154). The second question, there is currently no effective method to distinguish ICI responders from non-responders. But with further research, the discovery of more immune checkpoints and their ligands may help predict the PD-1 therapeutic response in some tumors. For example, it has been found that the expression of inhibitory ligands for Tim-3 and Lag-3 on GC cells serve as potential biomarkers to predict the response to anti-PD-1 therapy

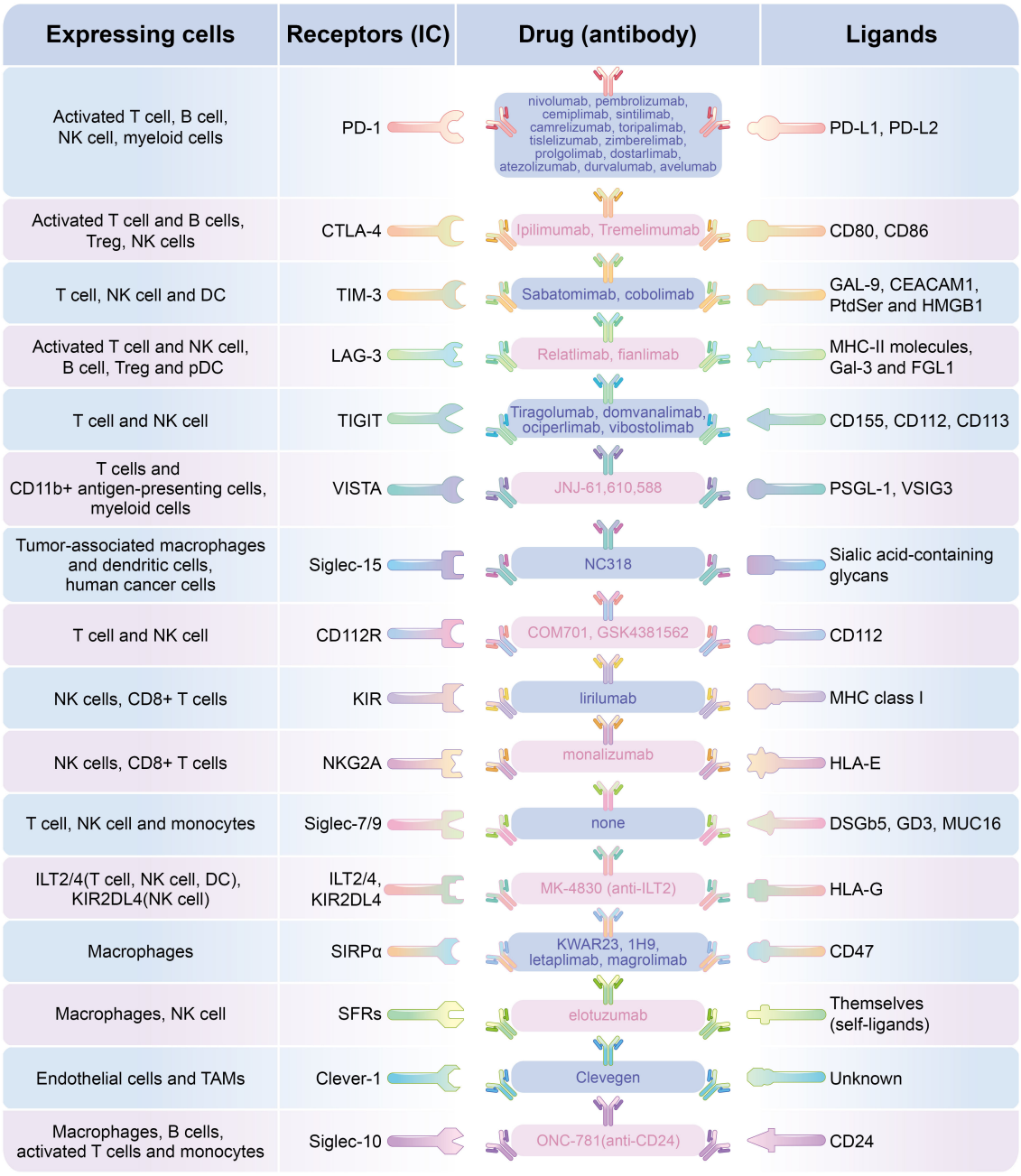

FIGURE 2
Different ICs expressing on different lymphocytes and and the targeted blocking antibody.

and the combinatorial immunotherapy with ICIs targeting for PD-1, Tim-3, and Lag-3 has a therapeutic potential for GC patients (70). Third question, the irAEs present in the clinical ICI treatment is a huge problem, including systemic toxicity, dermotoxicity, gastrointestinal toxicity, endocrine toxicity, pulmonary toxicity, rheumatism, nervous system toxicity, ocular toxicity, renal toxicity, cardiotoxicity and hematological toxicity (166). These side effects will seriously affect the therapeutic effect and prognosis of patients. What's worse, studies have found that the combined use of ICI may lead to a higher incidence of irAEs than single ICI therapy, depending on the type of malignancy and ICI used (167). At present, the cause of irAEs is not clear, but possible causes include non-specific immune stimulation of organ-specific inflammation, tissue damage and autoimmunity (168). Studies have found that the use of some immune checkpoint antibodies can affect the normal immune function of other normal tissues at the same time. For example, the use of CTLA-4 monoclonal antibodies can simultaneously produce an inhibitory effect on Treg cells expressing CTLA-4, leading to the destruction of immune tolerance, and thus an increase in the frequency and severity of irAEs was observed in some cases (169, 170). In view of the wide expression of immune checkpoints in various lymphocytes listed in this paper and the wide distribution of

10.3389/fimmu.2023.1121285

TABLE 1 The description of IC molecules、targeted monoclonal antibody drugs and indications.

IC	Expressing cells	Targeted monoclonal antibody	Indications
PD-1	Activated T cell, B cell, NK cell, myeloid cells	nivolumab, pembrolizumab, cemiplimab, sintilimab, camrelizumab, toripalimab, tislelizumab, zimberelimab, prolgolimab, dostarlimab	Melanoma, NSCLC, RCC, HCC, Hodgkin's lymphoma, primary mediastinal large B cell lymphoma, SCC of the head and neck, urothelial carcinoma, gastric cancer, solid tumors with high MSI, or MRD, Cutaneous squamous cell carcinoma
PD-L1	various malignancies, dendritic cells	atezolizumab durvalumab avelumab	NSCLC, urothelial carcinoma, bladder cancer, Merkel cell carcinoma
CTLA-4	Activated T cell and B cells, Treg, NK cells	Ipilimumab	malignant melanoma, NSCLC, mesothelioma, prostate cancer, breast cancer, urothelial cancer
		Tremelimumab	
Tim-3	T cell, NK cell and DC	Sabatomimab	Advanced Malignancies
		cobolimab	
LAG-3	Activated T cell and NK cell, B cell, Treg and pDC	relatlimab	unresectable or metastatic melanoma
		fianlimab	
TIGIT	T cell and NK cell	tiragolumab	Melanoma, liver cancer, cervical cancer, prostate cancer, ESCC, breast cancer, NSCLC, NHL/DLBCL/B-cell malignancies
		domvanalimab	
		ociperlimab	
		vibostolimab	
VISTA	T cells and CD11b+ antigen-presenting cells, myeloid cells	JNJ-61,610,588	NSCLC, small-cell lung cancer, head and neck, pancreatic, colorectal, cervical cancer
Siglec-15	tumor-associated macrophages and dendritic cells, human cancer cells cells	NC318	advanced solid tumors
CD112R	T cell and NK cell	COM701	Breast cancer, Melanoma, pancreatic cancer
		GSK4381562	
KIR	NK cells, CD8+ T cells	lirilumab	MM, AML, relapsed/refractory lymphomas
NKG2A	NK cells, CD8+ T cells	monalizumab	oral squamous cell carcinoma, gynecological malignancies, relapsed hematological malignancies
Siglec-7/9	T cell, NK cell and monocytes	none	NSCLC, ovarian, colorectal cancers, melanoma
HLA-G	various malignancies	none	Breast cancer
ILT2/4, KIR2DL4	ILT2/4(T cell, NK cell, DC), KIR2DL4(NK cell)	MK-4830 (anti-ILT2)	solid malignancies and hematological malignancies
SIRPα	macrophages	KWAR23	Burkitt's lymphoma, Melanoma
		1H9	
CD47	many tumor cells	letaplimab	Melanoma, AML stem cells, Breast cancer
		magrolimab	
SFRs	Macrophages, NK cell	elotuzumab	MM
Clever-1	Endothelial cells and TAMs	Clevegen	cutaneous and uveal melanoma, hepatobiliary, pancreatic, ovarian, oestrogen-receptor-positive breast, colorectal, gastric, gallbladder cancer and cholangiocarcinoma
Siglec-10	Macrophages, B cells, activated T cells and monocytes	ONC-781(anti-CD24)	Advanced Solid Tumors, Unresectable or metastatic melanoma, Resected HCC

HCC, hepatocellular carcinoma; MRD, minimal residual disease; MSI, microsatellite instability; NSCLC, nonsmall-cell lung carcinoma; RCC, renal cell carcinoma; SCC, squamous cell carcinoma. MM, multiple myeloma; AML, acute myeloid leukemia; ESCC, esophageal squamous cell carcinoma.

the same immune checkpoint in different lymphocytes (Table 1), the immune response caused by the application of ICI in the whole immune system should be fully considered. It will be an urgent topic for ICI treatment in the future to consider avoiding severe irAEs caused by the breakdown of autoimmune balance while achieving good anti-tumor efficacy.

Author contributions

Conceptualization, funding acquisition: ZG. Writing original draft, review and editing: GZ、RZ and A-GY. All authors contributed to the article and approved the submitted version.

Funding

This work was supported by the National Natural Sciences Foundation of China (No. 81872326 to ZG, 82203675 to GZ), the Wu Jieping Medical Foundation (320.6750.2022-19-2 to GZ), the Fund of Air Force Medical University (2022KXKT002 to GZ) and the Fund of State Key Laboratory of Cancer Biology (CBSKL2022ZZ46 to GZ).

Conflict of interest

The authors declare that the research was conducted in the absence of any commercial or financial relationships that could be construed as a potential conflict of interest.

Publisher's note

References

1. Pardoll DM. The blockade of immune checkpoints in cancer immunotherapy. *Nat Rev Cancer* (2012) 12(4):252–64. doi: 10.1038/nrc3239

2. Bagchi S, Yuan R, Engleman EG. Immune checkpoint inhibitors for the treatment of cancer: Clinical impact and mechanisms of response and resistance. *Annu Rev Pathol* (2021) 16:223–49. doi: 10.1146/annurev-pathol-042020-042741

3. Zhang Y, Zheng J. Functions of immune checkpoint molecules beyond immune evasion. *Adv Exp Med Biol* (2020) 1248:201–26. doi: 10.1007/978-981-15-3266-5_9

4. Qin S, Xu L, Yi M, Yu S, Wu K, Luo S. Novel immune checkpoint targets: Moving beyond pd-1 and ctla-4. *Mol Cancer* (2019) 18(1):155. doi: 10.1186/s12943-019-1091-2

5. Khan M, Arooj S, Wang H. Nk cell-based immune checkpoint inhibition. *Front Immunol* (2020) 11:167. doi: 10.3389/fimmu.2020.00167

6. Brom VC, Burger C, Wirtz DC, Schildberg FA. The role of immune checkpoint molecules on macrophages in cancer, infection, and autoimmune pathologies. *Front Immunol* (2022) 13:837645. doi: 10.3389/fimmu.2022.837645

7. Bremnes RM, Busund LT, Kilvaer TL, Andersen S, Richardsen E, Paulsen EE, et al. The role of tumor-infiltrating lymphocytes in development, progression, and prognosis of non-small cell lung cancer. *J Thorac Oncol* (2016) 11(6):789–800. doi: 10.1016/j.jtho.2016.01.015

8. Kroeger DR, Milne K, Nelson BH. Tumor-infiltrating plasma cells are associated with tertiary lymphoid structures, cytolytic T-cell responses, and superior prognosis in ovarian cancer. *Clin Cancer Res* (2016) 22(12):3005–15. doi: 10.1158/1078-0432.CCR-15-2762

9. Schalper KA, Velcheti V, Carvajal D, Wimberly H, Brown J, Pusztai L, et al. *In situ* tumor pd-L1 mrna expression is associated with increased tils and better outcome in breast carcinomas. *Clin Cancer Res* (2014) 20(10):2773–82. doi: 10.1158/1078-0432.CCR-13-2702

10. Thaxton JE, Li Z. To affinity and beyond: Harnessing the T cell receptor for cancer immunotherapy. *Hum Vaccin Immunother* (2014) 10(11):3313–21. doi: 10.4161/21645515.2014.973314

11. Davoodzadeh Gholami M, Kardar GA, Saeedi Y, Heydari S, Garssen J, Falak R. Exhaustion of T lymphocytes in the tumor microenvironment: Significance and effective mechanisms. *Cell Immunol* (2017) 322:1–14. doi: 10.1016/j.cellimm.2017.10.002

12. Schreiber RD, Old LJ, Smyth MJ. Cancer immunoediting: Integrating immunity's roles in cancer suppression and promotion. *Science* (2011) 331 (6024):1565–70. doi: 10.1126/science.1203486

13. Blackburn SD, Shin H, Haining WN, Zou T, Workman CJ, Polley A, et al. Coregulation of Cd8+ T cell exhaustion by multiple inhibitory receptors during chronic viral infection. *Nat Immunol* (2009) 10(1):29–37. doi: 10.1038/ni.1679

14. Keir ME, Butte MJ, Freeman GJ, Sharpe AH. Pd-1 and its ligands in tolerance and immunity. *Annu Rev Immunol* (2008) 26:677–704. doi: 10.1146/annurev.immunol.26.021607.090331

15. Mahoney KM, Freeman GJ, McDermott DF. The next immune-checkpoint inhibitors: Pd-1/Pd-L1 blockade in melanoma. *Clin Ther* (2015) 37(4):764–82. doi: 10.1016/j.clinthera.2015.02.018

16. Zajac AJ, Blattman JN, Murali-Krishna K, Sourdive DJ, Suresh M, Altman JD, et al. Viral immune evasion due to persistence of activated T cells without effector function. *J Exp Med* (1998) 188(12):2205–13. doi: 10.1084/jem.188.12.2205

17. Im SJ, Hashimoto M, Gerner MY, Lee J, Kissick HT, Burger MC, et al. Defining Cd8+ T cells that provide the proliferative burst after pd-1 therapy. *Nature* (2016) 537 (7620):417–21. doi: 10.1038/nature19330

18. Wartewig T, Kurgyis Z, Keppler S, Pechloff K, Hameister E, Ollinger R, et al. Pd-1 is a haploinsufficient suppressor of T cell lymphomagenesis. *Nature* (2017) 552 (7683):121–5. doi: 10.1038/nature24649

19. Zhou XA, Zhou J, Zhao L, Yu G, Zhan J, Shi C, et al. Klhl22 maintains pd-1 homeostasis and prevents excessive T cell suppression. *Proc Natl Acad Sci U.S.A.* (2020) 117(45):28239–50. doi: 10.1073/pnas.2004570117

20. Day CL, Kaufmann DE, Kiepiela P, Brown JA, Moodley ES, Reddy S, et al. Pd-1 expression on hiv-specific T cells is associated with T-cell exhaustion and disease progression. *Nature* (2006) 443(7109):350–4. doi: 10.1038/nature05115

21. Huang AC, Orlowski RJ, Xu X, Mick R, George SM, Yan PK, et al. A single dose of neoadjuvant pd-1 blockade predicts clinical outcomes in resectable melanoma. *Nat Med* (2019) 25(3):454–61. doi: 10.1038/s41591-019-0357-y

22. Garon EB, Rizvi NA, Hui R, Leighl N, Balmanoukian AS, Eder JP, et al. Pembrolizumab for the treatment of non-Small-Cell lung cancer. *N Engl J Med* (2015) 372(21):2018–28. doi: 10.1056/NEJMoa1501824

23. Zhang F, Bai H, Gao R, Fei K, Duan J, Zhang Z, et al. Dynamics of peripheral T cell clones during pd-1 blockade in non-small cell lung cancer. *Cancer Immunol Immunother* (2020) 69(12):2599–611. doi: 10.1007/s00262-020-02642-4

24. Tomita Y, Fukasawa S, Shinohara N, Kitamura H, Oya M, Eto M, et al. Nivolumab versus everolimus in advanced renal cell carcinoma: Japanese subgroup 3-year follow-up analysis from the phase iii checkmate 025 study. *Jpn J Clin Oncol* (2019) 49(6):506–14. doi: 10.1093/jjco/hyz026

25. Ferris RL, Blumenschein GJr., Fayette J, Guigay J, Colevas AD, Licitra L, et al. Nivolumab for recurrent squamous-cell carcinoma of the head and neck. *N Engl J Med* (2016) 375(19):1856–67. doi: 10.1056/NEJMoa1602252

26. Cohen EEW, Soulieres D, Le Tourneau C, Dinis J, Licitra L, Ahn MJ, et al. Pembrolizumab versus methotrexate, docetaxel, or cetuximab for recurrent or metastatic head-and-Neck squamous cell carcinoma (Keynote-040): A randomised, open-label, phase 3 study. *Lancet* (2019) 393(10167):156–67. doi: 10.1016/S0140-6736(18)31999-8

27. Waterhouse P, Penninger JM, Timms E, Wakeham A, Shahinian A, Lee KP, et al. Lymphoproliferative disorders with early lethality in mice deficient in ctla-4. *Science* (1995) 270(5238):985–8. doi: 10.1126/science.270.5238.985

28. Tivol EA, Borriello F, Schweitzer AN, Lynch WP, Bluestone JA, Sharpe AH. Loss of ctla-4 leads to massive lymphoproliferation and fatal multiorgan tissue destruction, revealing a critical negative regulatory role of ctla-4. *Immunity* (1995) 3(5):541–7. doi: 10.1016/1074-7613(95)90125-6

29. Stamper CC, Zhang Y, Tobin JF, Erbe DV, Ikemizu S, Davis SJ, et al. Crystal structure of the B7-1/Ctla-4 complex that inhibits human immune responses. *Nature* (2001) 410(6828):608–11. doi: 10.1038/35069118

30. Perkins D, Wang Z, Donovan C, He H, Mark D, Guan G, et al. Regulation of ctla-4 expression during T cell activation. *J Immunol* (1996) 156(11):4154–9. doi: 10.4049/jimmunol.156.11.4154

31. Greene JL, Leytze GM, Emswiler J, Peach R, Bajorath J, Cosand W, et al. Covalent dimerization of Cd28/Ctla-4 and oligomerization of Cd80/Cd86 regulate T cell costimulatory interactions. *J Biol Chem* (1996) 271(43):26762–71. doi: 10.1074/jbc.271.43.26762

32. Walker LS, Sansom DM. The emerging role of Ctla4 as a cell-extrinsic regulator of T cell responses. *Nat Rev Immunol* (2011) 11(12):852–63. doi: 10.1038/nri3108

33. Leach DR, Krummel MF, Allison JP. Enhancement of antitumor immunity by ctla-4 blockade. *Science* (1996) 271(5256):1734–6. doi: 10.1126/science.271.5256.1734

34. Hodi FS, Mihm MC, Soiffer RJ, Haluska FG, Butler M, Seiden MV, et al. Biologic activity of cytotoxic T lymphocyte-associated antigen 4 antibody blockade in previously vaccinated metastatic melanoma and ovarian carcinoma patients. *Proc Natl Acad Sci U.S.A.* (2003) 100(8):4712–7. doi: 10.1073/pnas.0830997100

35. Hodi FS, O'Day SJ, McDermott DF, Weber RW, Sosman JA, Haanen JB, et al. Improved survival with ipilimumab in patients with metastatic melanoma. *N Engl J Med* (2010) 363(8):711–23. doi: 10.1056/NEJMoa1003466

36. Lynch TJ, Bondarenko I, Luft A, Serwatowski P, Barlesi F, Chacko R, et al. Ipilimumab in combination with paclitaxel and carboplatin as first-line treatment in stage Iiib/Iv non-Small-Cell lung cancer: Results from a randomized, double-blind, multicenter phase ii study. *J Clin Oncol* (2012) 30(17):2046–54. doi: 10.1200/JCO.2011.38.4032

37. Calabro L, Morra A, Fonsatti E, Cutaia O, Amato G, Giannarelli D, et al. Tremelimumab for patients with chemotherapy-resistant advanced malignant mesothelioma: An open-label, single-arm, phase 2 trial. *Lancet Oncol* (2013) 14 (11):1104–11. doi: 10.1016/S1470-2045(13)70381-4

38. Slovin SF, Higano CS, Hamid O, Tejwani S, Harzstark A, Alumkal JJ, et al. Ipilimumab alone or in combination with radiotherapy in metastatic castration-resistant prostate cancer: Results from an open-label, multicenter phase I/Ii study. *Ann Oncol* (2013) 24(7):1813–21. doi: 10.1093/annonc/mdt107

39. Vonderheide RH, LoRusso PM, Khalil M, Gartner EM, Khaira D, Soulieres D, et al. Tremelimumab in combination with exemestane in patients with advanced breast cancer and treatment-associated modulation of inducible costimulator expression on patient T cells. *Clin Cancer Res* (2010) 16(13):3485–94. doi: 10.1158/1078-0432.CCR-10-0505

40. Carthon BC, Wolchok JD, Yuan J, Kamat A, Ng Tang DS, Sun J, et al. Preoperative ctla-4 blockade: Tolerability and immune monitoring in the setting of a presurgical clinical trial. *Clin Cancer Res* (2010) 16(10):2861–71. doi: 10.1158/1078-0432.CCR-10-0569

41. Boutros C, Tarhini A, Routier E, Lambotte O, Ladurie FL, Carbonnel F, et al. Safety profiles of anti-Ctla-4 and anti-Pd-1 antibodies alone and in combination. *Nat Rev Clin Oncol* (2016) 13(8):473–86. doi: 10.1038/nrclinonc.2016.58

42. Hodi FS, Chiarion-Sileni V, Gonzalez R, Grob JJ, Rutkowski P, Cowey CL, et al. Nivolumab plus ipilimumab or nivolumab alone versus ipilimumab alone in advanced melanoma (Checkmate 067): 4-year outcomes of a multicentre, randomised, phase 3 trial. *Lancet Oncol* (2018) 19(11):1480–92. doi: 10.1016/S1470-2045(18)30700-9

43. Willsmore ZN, Coumbe BGT, Crescioli S, Reci S, Gupta A, Harris RJ, et al. Combined anti-Pd-1 and anti-Ctla-4 checkpoint blockade: Treatment of melanoma and immune mechanisms of action. *Eur J Immunol* (2021) 51(3):544–56. doi: 10.1002/eji.202048747

44. Hastings WD, Anderson DE, Kassam N, Koguchi K, Greenfield EA, Kent SC, et al. Tim-3 is expressed on activated human Cd4+ T cells and regulates Th1 and Th17 cytokines. *Eur J Immunol* (2009) 39(9):2492–501. doi: 10.1002/eji.200939274

45. Sakuishi K, Jayaraman P, Behar SM, Anderson AC, Kuchroo VK. Emerging Tim-3 functions in antimicrobial and tumor immunity. *Trends Immunol* (2011) 32 (8):345–9. doi: 10.1016/j.it.2011.05.003

46. Monney L, Sabatos CA, Gaglia JL, Ryu A, Waldner H, Chernova T, et al. Th1-specific cell surface protein Tim-3 regulates macrophage activation and severity of an autoimmune disease. *Nature* (2002) 415(6871):536–41. doi: 10.1038/415536a

47. Wherry EJ, Kurachi M. Molecular and cellular insights into T cell exhaustion. *Nat Rev Immunol* (2015) 15(8):486–99. doi: 10.1038/nri3862

48. Jones RB, Ndhlovu LC, Barbour JD, Sheth PM, Jha AR, Long BR, et al. Tim-3 expression defines a novel population of dysfunctional T cells with highly elevated frequencies in progressive hiv-1 infection. *J Exp Med* (2008) 205(12):2763–79. doi: 10.1084/jem.20081398

49. Golden-Mason L, Palmer BE, Kassam N, Townshend-Bulson L, Livingston S, McMahon BJ, et al. Negative immune regulator Tim-3 is overexpressed on T cells in hepatitis c virus infection and its blockade rescues dysfunctional Cd4+ and Cd8+ T cells. *J Virol* (2009) 83(18):9122–30. doi: 10.1128/JVI.00639-09

50. Wu W, Shi Y, Li J, Chen F, Chen Z, Zheng M. Tim-3 expression on peripheral T cell subsets correlates with disease progression in hepatitis b infection. *Virol J* (2011) 8:113. doi: 10.1186/1743-422X-8-113

51. Sakuishi K, Apetoh L, Sullivan JM, Blazar BR, Kuchroo VK, Anderson AC. Targeting Tim-3 and pd-1 pathways to reverse T cell exhaustion and restore anti-tumor immunity. *J Exp Med* (2010) 207(10):2187–94. doi: 10.1084/jem.20100643

52. Xu Y, Zhang H, Huang Y, Rui X, Zheng F. Role of Tim-3 in ovarian cancer. *Clin Transl Oncol* (2017) 19(9):1079–83. doi: 10.1007/s12094-017-1656-8

53. Li H, Wu K, Tao K, Chen L, Zheng Q, Lu X, et al. Tim-3/Galectin-9 signaling pathway mediates T-cell dysfunction and predicts poor prognosis in patients with hepatitis b virus-associated hepatocellular carcinoma. *Hepatology* (2012) 56(4):1342–51. doi: 10.1002/hep.25777

54. Shi X, Li CW, Tan LC, Wen SS, Liao T, Zhang Y, et al. Immune Co-inhibitory receptors pd-1, ctla-4, Tim-3, lag-3, and tigit in medullary thyroid cancers: A Large cohort study. *J Clin Endocrinol Metab* (2021) 106(1):120–32. doi: 10.1210/clinem/dgaa701

55. Huard B, Gaulard P, Faure F, Hercend T, Triebel F. Cellular expression and tissue distribution of the human lag-3-Encoded protein, an mhc class ii ligand. *Immunogenetics* (1994) 39(3):213–7. doi: 10.1007/BF00241263

56. Triebel F, Jitsukawa S, Baixeras E, Roman-Roman S, Genevee C, Viegas-Pequignot E, et al. Lag-3, a novel lymphocyte activation gene closely related to Cd4. *J Exp Med* (1990) 171(5):1393–405. doi: 10.1084/jem.171.5.1393

57. Workman CJ, Wang Y, El Kasmi KC, Pardoll DM, Murray PJ, Drake CG, et al. Lag-3 regulates plasmacytoid dendritic cell homeostasis. *J Immunol* (2009) 182 (4):1885–91. doi: 10.4049/jimmunol.0800185

58. Huard B, Prigent P, Tournier M, Bruniquel D, Triebel F. Cd4/Major histocompatibility complex class ii interaction analyzed with Cd4- and lymphocyte activation gene-3 (Lag-3)-Ig fusion proteins. *Eur J Immunol* (1995) 25(9):2718–21. doi: 10.1002/eji.1830250949

59. Wang J, Sanmamed MF, Datar I, Su TT, Ji L, Sun J, et al. Fibrinogen-like protein 1 is a major immune inhibitory ligand of lag-3. *Cell* (2019) 176(1-2):334–47 e12. doi: 10.1016/j.cell.2018.11.010

60. Workman CJ, Vignali DA. The Cd4-related molecule, lag-3 (Cd223), regulates the expansion of activated T cells. *Eur J Immunol* (2003) 33(4):970–9. doi: 10.1002/eji.200323382

61. Huang CT, Workman CJ, Flies D, Pan X, Marson AL, Zhou G, et al. Role of lag-3 in regulatory T cells. *Immunity* (2004) 21(4):503–13. doi: 10.1016/j.immuni.2004.08.010

62. Woo SR, Turnis ME, Goldberg MV, Bankoti J, Selby M, Nirschl CJ, et al. Immune inhibitory molecules lag-3 and pd-1 synergistically regulate T-cell function to promote tumoral immune escape. *Cancer Res* (2012) 72(4):917–27. doi: 10.1158/0008-5472.CAN-11-1620

63. Brignone C, Escudier B, Grygar C, Marcu M, Triebel F. A phase I pharmacokinetic and biological correlative study of Imp321, a novel mhc class ii agonist, in patients with advanced renal cell carcinoma. *Clin Cancer Res* (2009) 15 (19):6225–31. doi: 10.1158/1078-0432.CCR-09-0068

64. Ascierto PA, Ignacio M, Bhatia S, Bono P, Sanborn RE, Lipson EJ, et al. Initial efficacy of anti-lymphocyte activation gene-3 (Anti-Lag-3; bms-986016) in combination with nivolumab (Nivo) in pts with melanoma (Mel) previously treated with anti-Pd-1/Pd-L1 therapy. *J Clin Oncol* (2017) 35(15_suppl):9520. doi: 10.1200/JCO.2017.35.15_suppl.9520

65. Shapiro M, Herishanu Y, Katz BZ, Dezorella N, Sun C, Kay S, et al. Lymphocyte activation gene 3: A novel therapeutic target in chronic lymphocytic leukemia. *Haematologica* (2017) 102(5):874–82. doi: 10.3324/haematol.2016.148965

66. Li FJ, Zhang Y, Jin GX, Yao L, Wu DQ. Expression of lag-3 is coincident with the impaired effector function of hbv-specific Cd8(+) T cell in hcc patients. *Immunol Lett* (2013) 150(1-2):116–22. doi: 10.1016/j.imlet.2012.12.004

67. Takaya S, Saito H, Ikeguchi M. Upregulation of immune checkpoint molecules, pd-1 and lag-3, on Cd4+ and Cd8+ T cells after gastric cancer surgery. *Yonago Acta Med* (2015) 58(1):39–44.

68. Yang ZZ, Kim HJ, Villasboas JC, Chen YP, Price-Troska T, Jalali S, et al. Expression of lag-3 defines exhaustion of intratumoral pd-1(+) T cells and correlates with poor outcome in follicular lymphoma. *Oncotarget* (2017) 8(37):61425–39. doi: 10.18632/oncotarget.18251

69. He Y, Yu H, Rozeboom L, Rivard CJ, Ellison K, Dziadziuszko R, et al. Lag-3 protein expression in non-small cell lung cancer and its relationship with pd-1/Pd-L1 and tumor-infiltrating lymphocytes. *J Thorac Oncol* (2017) 12(5):814–23. doi: 10.1016/j.jtho.2017.01.019

70. Mimura K, Kua LF, Xiao JF, Asuncion BR, Nakayama Y, Syn N, et al. Combined inhibition of pd-1/Pd-L1, lag-3, and Tim-3 axes augments antitumor immunity in gastric cancer-T cell coculture models. *Gastric Cancer Off J Int Gastric Cancer Assoc Japanese Gastric Cancer Assoc* (2021) 24(3):611–23. doi: 10.1007/s10120-020-01151-8

71. Harjunpaa H, Guillerey C. Tigit as an emerging immune checkpoint. *Clin Exp Immunol* (2020) 200(2):108–19. doi: 10.1111/cei.13407

72. Chauvin JM, Pagliano O, Fourcade J, Sun Z, Wang H, Sander C, et al. Tigit and pd-1 impair tumor antigen-specific Cd8(+) T cells in melanoma patients. *J Clin Invest* (2015) 125(5):2046–58. doi: 10.1172/JCI80445

73. Wang L, Rubinstein R, Lines JL, Wasiuk A, Ahonen C, Guo Y, et al. Vista, a novel mouse ig superfamily ligand that negatively regulates T cell responses. *J Exp Med* (2011) 208(3):577–92. doi: 10.1084/jem.20100619

74. Le Mercier I, Chen W, Lines JL, Day M, Li J, Sergent P, et al. Vista regulates the development of protective antitumor immunity. *Cancer Res* (2014) 74(7):1933–44. doi: 10.1158/0008-5472.CAN-13-1506

75. Le Mercier I, Lines JL, Noelle RJ. Beyond ctla-4 and pd-1, the generation z of negative checkpoint regulators. *Front Immunol* (2015) 6:418. doi: 10.3389/fimmu.2015.00418

76. Mulati K, Hamanishi J, Matsumura N, Chamoto K, Mise N, Abiko K, et al. Vista expressed in tumour cells regulates T cell function. *Br J Cancer* (2019) 120(1):115–27. doi: 10.1038/s41416-018-0313-5

77. Wuerdemann N, Putz K, Eckel H, Jain R, Wittekindt C, Huebbers CU, et al. Lag-3, Tim-3 and vista expression on tumor-infiltrating lymphocytes in oropharyngeal squamous cell carcinoma-potential biomarkers for targeted therapy concepts. *Int J Mol Sci* (2020) 22(1):379. doi: 10.3390/ijms22010379

78. Angata T, Tabuchi Y, Nakamura K, Nakamura M. Siglec-15: An immune system siglec conserved throughout vertebrate evolution. *Glycobiology* (2007) 17(8):838–46. doi: 10.1093/glycob/cwm049

79. Hiruma Y, Hirai T, Tsuda E. Siglec-15, a member of the sialic acid-binding lectin, is a novel regulator for osteoclast differentiation. *Biochem Biophys Res Commun* (2011) 409(3):424–9. doi: 10.1016/j.bbrc.2011.05.015

80. Shimizu T, Takahata M, Kameda Y, Endo T, Hamano H, Hiratsuka S, et al. Sialic acid-binding immunoglobulin-like lectin 15 (Siglec-15) mediates periarticular bone loss, but not joint destruction, in murine antigen-induced arthritis. *Bone* (2015) 79:65–70. doi: 10.1016/j.bone.2015.05.029

81. Wang J, Sun J, Liu LN, Flies DB, Nie X, Toki M, et al. Siglec-15 as an immune suppressor and potential target for normalization cancer immunotherapy. *Nat Med* (2019) 25(4):656–66. doi: 10.1038/s41591-019-0374-x

82. Sun J, Lu Q, Sanmamed MF, Wang J. Siglec-15 as an emerging target for next-generation cancer immunotherapy. *Clin Cancer Res* (2021) 27(3):680–8. doi: 10.1158/1078-0432.CCR-19-2925

83. Buckle I, Guillerey C. Inhibitory receptors and immune checkpoints regulating natural killer cell responses to cancer. *Cancers* (2021) 13(17):4263. doi: 10.3390/cancers13174263

84. Zhu Y, Paniccia A, Schulick AC, Chen W, Koenig MR, Byers JT, et al. Identification of Cd112r as a novel checkpoint for human T cells. *J Exp Med* (2016) 213(2):167–76. doi: 10.1084/jem.20150785

85. Vivier E, Tomasello E, Baratin M, Walzer T, Ugolini S. Functions of natural killer cells. *Nat Immunol* (2008) 9(5):503–10. doi: 10.1038/ni1582

86. Long EO, Kim HS, Liu D, Peterson ME, Rajagopalan S. Controlling natural killer cell responses: Integration of signals for activation and inhibition. *Annu Rev Immunol* (2013) 31:227–58. doi: 10.1146/annurev-immunol-020711-075005

87. Orange JS. Natural killer cell deficiency. *J Allergy Clin Immunol* (2013) 132 (3):515–25. doi: 10.1016/j.jaci.2013.07.020

88. Bashirova AA, Martin MP, McVicar DW, Carrington M. The killer immunoglobulin-like receptor gene cluster: Tuning the genome for defense. *Annu Rev Genomics Hum Genet* (2006) 7:277–300. doi: 10.1146/annurev.genom.7.080505.115726

89. Rajalingam R. Overview of the killer cell immunoglobulin-like receptor system. *Methods Mol Biol* (2012) 882:391–414. doi: 10.1007/978-1-61779-842-9_23

90. Lanier LL. Nk cell receptors. *Annu Rev Immunol* (1998) 16:359–93. doi: 10.1146/annurev.immunol.16.1.359

91. Benson DMJr., Bakan CE, Zhang S, Collins SM, Liang J, Srivastava S, et al. Iph2101, a novel anti-inhibitory kir antibody, and lenalidomide combine to enhance the natural killer cell versus multiple myeloma effect. *Blood* (2011) 118(24):6387–91. doi: 10.1182/blood-2011-06-360255

92. Korde N, Carlsten M, Lee MJ, Minter A, Tan E, Kwok M, et al. A phase ii trial of pan-Kir2d blockade with Iph2101 in smoldering multiple myeloma. *Haematologica* (2014) 99(6):e81–3. doi: 10.3324/haematol.2013.103085

93. Carlsten M, Korde N, Kotecha R, Reger R, Bor S, Kazandjian D, et al. Checkpoint inhibition of Kir2d with the monoclonal antibody Iph2101 induces contraction and hyporesponsiveness of nk cells in patients with myeloma. *Clin Cancer Res* (2016) 22(21):5211–22. doi: 10.1158/1078-0432.CCR-16-1108

94. Vey N, Bourhis JH, Boissel N, Bordessoule D, Prebet T, Charbonnier A, et al. A phase 1 trial of the anti-inhibitory kir mab Iph2101 for aml in complete remission. *Blood* (2012) 120(22):4317–23. doi: 10.1182/blood-2012-06-437558

95. Benson DMJr., Cohen AD, Jagannath S, Munshi NC, Spitzer G, Hofmeister CC, et al. A phase I trial of the anti-kir antibody Iph2101 and lenalidomide in patients with Relapsed/Refractory multiple myeloma. *Clin Cancer Res* (2015) 21(18):4055–61. doi: 10.1158/1078-0432.CCR-15-0304

96. Braud VM, Allan DS, O'Callaghan CA, Soderstrom K, D'Andrea A, Ogg GS, et al. Hla-e binds to natural killer cell receptors Cd94/Nkg2a, b and c. *Nature* (1998) 391(6669):795–9. doi: 10.1038/35869

97. Sivori S, Vacca P, Del Zotto G, Munari E, Mingari MC, Moretta L. Human nk cells: Surface receptors, inhibitory checkpoints, and translational applications. *Cell Mol Immunol* (2019) 16(5):430–41. doi: 10.1038/s41423-019-0206-4

98. Andre P, Denis C, Soulas C, Bourbon-Caillet C, Lopez J, Arnoux T, et al. Anti-Nkg2a mab is a checkpoint inhibitor that promotes anti-tumor immunity by unleashing both T and nk cells. *Cell* (2018) 175(7):1731–43 e13. doi: 10.1016/j.cell.2018.10.014

99. Kamiya T, Seow SV, Wong D, Robinson M, Campana D. Blocking expression of inhibitory receptor Nkg2a overcomes tumor resistance to nk cells. *J Clin Invest* (2019) 129(5):2094–106. doi: 10.1172/JCI123955

100. van Montfoort N, Borst L, Korrer MJ, Sluijter M, Marijt KA, Santegoets SJ, et al. Nkg2a blockade potentiates Cd8 T cell immunity induced by cancer vaccines. *Cell* (2018) 175(7):1744–55 e15. doi: 10.1016/j.cell.2018.10.028

101. Zhang Q, Bi J, Zheng X, Chen Y, Wang H, Wu W, et al. Blockade of the checkpoint receptor tigit prevents nk cell exhaustion and elicits potent anti-tumor immunity. *Nat Immunol* (2018) 19(7):723–32. doi: 10.1038/s41590-018-0132-0

102. Pesce S, Greppi M, Tabellini G, Rampinelli F, Parolini S, Olive D, et al. Identification of a subset of human natural killer cells expressing high levels of programmed death 1: A phenotypic and functional characterization. *J Allergy Clin Immunol* (2017) 139(1):335–46 e3. doi: 10.1016/j.jaci.2016.04.025

103. Liu Y, Cheng Y, Xu Y, Wang Z, Du X, Li C, et al. Increased expression of programmed cell death protein 1 on nk cells inhibits nk-Cell-Mediated anti-tumor function and indicates poor prognosis in digestive cancers. *Oncogene* (2017) 36 (44):6143–53. doi: 10.1038/onc.2017.209

104. Hsu J, Hodgins JJ, Marathe M, Nicolai CJ, Bourgeois-Daigneault MC, Trevino TN, et al. Contribution of nk cells to immunotherapy mediated by pd-1/Pd-L1 blockade. *J Clin Invest* (2018) 128(10):4654–68. doi: 10.1172/JCI99317

105. Dong W, Wu X, Ma S, Wang Y, Nalin AP, Zhu Z, et al. The mechanism of anti-Pd-L1 antibody efficacy against pd-L1-Negative tumors identifies nk cells expressing pd-L1 as a cytolytic effector. *Cancer Discovery* (2019) 9(10):1422–37. doi: 10.1158/2159-8290.CD-18-1259

106. Gleason MK, Lenvik TR, McCullar V, Felices M, O'Brien MS, Cooley SA, et al. Tim-3 is an inducible human natural killer cell receptor that enhances interferon gamma production in response to galectin-9. *Blood* (2012) 119(13):3064–72. doi: 10.1182/blood-2011-06-360321

107. Ndhlovu LC, Lopez-Verges S, Barbour JD, Jones RB, Jha AR, Long BR, et al. Tim-3 marks human natural killer cell maturation and suppresses cell-mediated cytotoxicity. *Blood* (2012) 119(16):3734–43. doi: 10.1182/blood-2011-11-392951

108. Wang Z, Zhu J, Gu H, Yuan Y, Zhang B, Zhu D, et al. The clinical significance of abnormal Tim-3 expression on nk cells from patients with gastric cancer. *Immunol Invest* (2015) 44(6):578–89. doi: 10.3109/08820139.2015.1052145

109. Xu L, Huang Y, Tan L, Yu W, Chen D, Lu C, et al. Increased Tim-3 expression in peripheral nk cells predicts a poorer prognosis and Tim-3 blockade improves nk cell-mediated cytotoxicity in human lung adenocarcinoma. *Int Immunopharmacol* (2015) 29(2):635–41. doi: 10.1016/j.intimp.2015.09.017

110. da Silva IP, Gallois A, Jimenez-Baranda S, Khan S, Anderson AC, Kuchroo VK, et al. Reversal of nk-cell exhaustion in advanced melanoma by Tim-3 blockade. *Cancer Immunol Res* (2014) 2(5):410–22. doi: 10.1158/2326-6066.CIR-13-0171

111. Komita H, Koido S, Hayashi K, Kan S, Ito M, Kamata Y, et al. Expression of immune checkpoint molecules of T cell immunoglobulin and mucin protein 3/Galectin-9 for nk cell suppression in human gastrointestinal stromal tumors. *Oncol Rep* (2015) 34(4):2099–105. doi: 10.3892/or.2015.4149

112. Xu F, Liu J, Liu D, Liu B, Wang M, Hu Z, et al. Lsectin expressed on melanoma cells promotes tumor progression by inhibiting antitumor T-cell responses. *Cancer Res* (2014) 74(13):3418–28. doi: 10.1158/0008-5472.CAN-13-2690

113. Huard B, Tournier M, Triebel F. Lag-3 does not define a specific mode of natural killing in human. *Immunol Lett* (1998) 61(2-3):109–12. doi: 10.1016/s0165-2478(97)00170-3

114. Taborda NA, Hernandez JC, Lajoie J, Juno JA, Kimani J, Rugeles MT, et al. Short communication: Low expression of activation and inhibitory molecules on nk cells and Cd4(+) T cells is associated with viral control. *AIDS Res Hum Retroviruses* (2015) 31(6):636–40. doi: 10.1089/AID.2014.0325

115. Brignone C, Grygar C, Marcu M, Schakel K, Triebel F. A soluble form of lymphocyte activation gene-3 (Imp321) induces activation of a Large range of human effector cytotoxic cells. *J Immunol* (2007) 179(6):4202–11. doi: 10.4049/jimmunol.179.6.4202

116. Andrews LP, Marciscano AE, Drake CG, Vignali DA. Lag3 (Cd223) as a cancer immunotherapy target. *Immunol Rev* (2017) 276(1):80–96. doi: 10.1111/imr.12519

117. Macauley MS, Crocker PR, Paulson JC. Siglec-mediated regulation of immune cell function in disease. *Nat Rev Immunol* (2014) 14(10):653–66. doi: 10.1038/nri3737

118. Jandus C, Boligan KF, Chijioke O, Liu H, Dahlhaus M, Demoulins T, et al. Interactions between siglec-7/9 receptors and ligands influence nk cell-dependent tumor immunosurveillance. *J Clin Invest* (2014) 124(4):1810–20. doi: 10.1172/JCI65899

119. Adams OJ, Stanczak MA, von Gunten S, Laubli H. Targeting sialic acid-siglec interactions to reverse immune suppression in cancer. *Glycobiology* (2018) 28(9):640–7. doi: 10.1093/glycob/cwx108

120. Lubbers J, Rodriguez E, van Kooyk Y. Modulation of immune tolerance *Via* siglec-sialic acid interactions. *Front Immunol* (2018) 9:2807. doi: 10.3389/fimmu.2018.02807

121. Ibarlucea-Benitez I, Weitzenfeld P, Smith P, Ravetch JV. Siglecs-7/9 function as inhibitory immune checkpoints in vivo and can be targeted to enhance therapeutic antitumor. *Proc Natl Acad Sci USA* (2021) 118(26):e2107424118. doi: 10.1073/pnas.2107424118

122. Stanczak MA, Siddiqui SS, Trefny MP, Thommen DS, Boligan KF, von Gunten S, et al. Self-associated molecular patterns mediate cancer immune evasion by engaging siglecs on T cells. *J Clin Invest* (2018) 128(11):4912–23. doi: 10.1172/JCI120612

123. Kovats S, Main EK, Librach C, Stubblebine M, Fisher SJ, DeMars R. A class I antigen, hla-G, expressed in human trophoblasts. *Science* (1990) 248(4952):220–3. doi: 10.1126/science.2326636

124. Hunt JS, Petroff MG, McIntire RH, Ober C. Hla-G and immune tolerance in pregnancy. *FASEB J* (2005) 19(7):681–93. doi: 10.1096/fj.04-2078rev

125. Pazmany L, Mandelboim O, Vales-Gomez M, Davis DM, Reyburn HT, Strominger JL. Protection from natural killer cell-mediated lysis by hla-G expression on target cells. *Science* (1996) 274(5288):792–5. doi: 10.1126/science.274.5288.792

126. Liu L, Wang L, Zhao L, He C, Wang G. The role of hla-G in tumor escape: Manipulating the phenotype and function of immune cells. *Front Oncol* (2020) 10:597468. doi: 10.3389/fonc.2020.597468

127. Carosella ED, Rouas-Freiss N, Tronik-Le Roux D, Moreau P, LeMaoult J. Hla-G: An immune checkpoint molecule. *Adv Immunol* (2015) 127:33–144. doi: 10.1016/bs.ai.2015.04.001

128. Lin A, Yan WH, Xu HH, Gan MF, Cai JF, Zhu M, et al. Hla-G expression in human ovarian carcinoma counteracts nk cell function. *Ann Oncol* (2007) 18 (11):1804–9. doi: 10.1093/annonc/mdm356

129. Lin A, Chen HX, Zhu CC, Zhang X, Xu HH, Zhang JG, et al. Aberrant human leucocyte antigen-G expression and its clinical relevance in hepatocellular carcinoma. *J Cell Mol Med* (2010) 14(8):2162–71. doi: 10.1111/j.1582-4934.2009.00917.x

130. Wiendl H, Mitsdoerffer M, Hofmeister V, Wischhusen J, Bornemann A, Meyermann R, et al. A functional role of hla-G expression in human gliomas: An alternative strategy of immune escape. *J Immunol* (2002) 168(9):4772–80. doi: 10.4049/jimmunol.168.9.4772

131. Bukur J, Rebmann V, Grosse-Wilde H, Luboldt H, Ruebben H, Drexler I, et al. Functional role of human leukocyte antigen-G up-regulation in renal cell carcinoma. *Cancer Res* (2003) 63(14):4107–11.

132. Lin A, Yan WH. Heterogeneity of hla-G expression in cancers: Facing the challenges. *Front Immunol* (2018) 9:2164. doi: 10.3389/fimmu.2018.02164

133. Jan CI, Huang SW, Canoll P, Bruce JN, Lin YC, Pan CM, et al. Targeting human leukocyte antigen G with chimeric antigen receptors of natural killer cells convert immunosuppression to ablate solid tumors. *J Immunother Cancer* (2021) 9(10): e003050. doi: 10.1136/jitc-2021-003050

134. Zheng G, Guo Z, Li W, Xi W, Zuo B, Zhang R, et al. Interaction between hla-G and nk cell receptor Kir2dl4 orchestrates Her2-positive breast cancer resistance to trastuzumab. *Signal Transduct Target Ther* (2021) 6(1):236. doi: 10.1038/s41392-021-00629-w

135. Solinas G, Schiarea S, Liguori M, Fabbri M, Pesce S, Zammataro L, et al. Tumor-conditioned macrophages secrete migration-stimulating factor: A new marker for M2-polarization, influencing tumor cell motility. *J Immunol* (2010) 185(1):642–52. doi: 10.4049/jimmunol.1000413

136. Najafi M, Hashemi Goradel N, Farhood B, Salehi E, Nashtaei MS, Khanlarkhani N, et al. Macrophage polarity in cancer: A review. *J Cell Biochem* (2019) 120(3):2756–65. doi: 10.1002/jcb.27646

137. Huang X, Venet F, Wang YL, Lepape A, Yuan Z, Chen Y, et al. Pd-1 expression by macrophages plays a pathologic role in altering microbial clearance and the innate inflammatory response to sepsis. *Proc Natl Acad Sci U.S.A.* (2009) 106(15):6303–8. doi: 10.1073/pnas.0809422106

138. Gordon SR, Maute RL, Dulken BW, Hutter G, George BM, McCracken MN, et al. Pd-1 expression by tumour-associated macrophages inhibits phagocytosis and tumour immunity. *Nature* (2017) 545(7655):495–9. doi: 10.1038/nature22396

139. Zou W, Wolchok JD, Chen L. Pd-L1 (B7-H1) and pd-1 pathway blockade for cancer therapy: Mechanisms, response biomarkers, and combinations. *Sci Transl Med* (2016) 8(328):328rv4. doi: 10.1126/scitranslmed.aad7118

140. Hartley GP, Chow L, Ammons DT, Wheat WH, Dow SW. Programmed cell death ligand 1 (Pd-L1) signaling regulates macrophage proliferation and activation. *Cancer Immunol Res* (2018) 6(10):1260–73. doi: 10.1158/2326-6066.CIR-17-0537

141. Arlauckas SP, Garris CS, Kohler RH, Kitaoka M, Cuccarese MF, Yang KS, et al. *In vivo* imaging reveals a tumor-associated macrophage-mediated resistance pathway in anti-Pd-1 therapy. *Sci Transl Med* (2017) 9(389):eaal3604. doi: 10.1126/scitranslmed.aal3604

142. Romano E, Kusio-Kobialka M, Foukas PG, Baumgaertner P, Meyer C, Ballabeni P, et al. Ipilimumab-dependent cell-mediated cytotoxicity of regulatory T cells ex vivo by nonclassical monocytes in melanoma patients. *Proc Natl Acad Sci U.S.A.* (2015) 112(19):6140–5. doi: 10.1073/pnas.1417320112

143. Simpson TR, Li F, Montalvo-Ortiz W, Sepulveda MA, Bergerhoff K, Arce F, et al. Fc-dependent depletion of tumor-infiltrating regulatory T cells Co-defines the efficacy of anti-Ctla-4 therapy against melanoma. *J Exp Med* (2013) 210(9):1695–710. doi: 10.1084/jem.20130579

144. Willingham SB, Volkmer JP, Gentles AJ, Sahoo D, Dalerba P, Mitra SS, et al. The Cd47-signal regulatory protein alpha (Sirpa) interaction is a therapeutic target for human solid tumors. *Proc Natl Acad Sci U.S.A.* (2012) 109(17):6662–7. doi: 10.1073/pnas.1121623109

145. Weiskopf K, Ring AM, Ho CC, Volkmer JP, Levin AM, Volkmer AK, et al. Engineered sirpalpha variants as immunotherapeutic adjuvants to anticancer antibodies. *Science* (2013) 341(6141):88–91. doi: 10.1126/science.1238856

146. Liu J, Wang L, Zhao F, Tseng S, Narayanan C, Shura L, et al. Pre-clinical development of a humanized anti-Cd47 antibody with anti-cancer therapeutic potential. *PloS One* (2015) 10(9):e0137345. doi: 10.1371/journal.pone.0137345

147. Dheilly E, Moine V, Broyer L, Salgado-Pires S, Johnson Z, Papaioannou A, et al. Selective blockade of the ubiquitous checkpoint receptor Cd47 is enabled by dual-targeting bispecific antibodies. *Mol Ther* (2017) 25(2):523–33. doi: 10.1016/j.ymthe.2016.11.006

148. Deuse T, Hu X, Agbor-Enoh S, Jang MK, Alawi M, Saygi C, et al. The sirpalpha-Cd47 immune checkpoint in nk cells. *J Exp Med* (2021) 218(3):e20200839. doi: 10.1084/jem.20200839

149. Chen J, Zhong MC, Guo HJ, Davidson D, Mishel S, Lu Y, et al. Slamf7 is critical for phagocytosis of haematopoietic tumour cells *Via* mac-1 integrin. *Nature* (2017) 544 (7651):493–+. doi: 10.1038/nature22076

150. Li D, Xiong W, Wang YD, Feng J, He YX, Du J, et al. Slamf3 and Slamf4 are immune checkpoints that constrain macrophage phagocytosis of hematopoietic tumors. *Sci Immunol* (2022) 7(67):eabj5501. doi: 10.1126/sciimmunol.abj5501

151. Kzhyshkowska J, Gratchev A, Goerdt S. Stabilin-1, a homeostatic scavenger receptor with multiple functions. *J Cell Mol Med* (2006) 10(3):635–49. doi: 10.1111/j.1582-4934.2006.tb00425.x

152. Algars A, Irjala H, Vaittinen S, Huhtinen H, Sundstrom J, Salmi M, et al. Type and location of tumor-infiltrating macrophages and lymphatic vessels predict survival of colorectal cancer patients. *Int J Cancer* (2012) 131(4):864–73. doi: 10.1002/ijc.26457

153. Karikoski M, Marttila-Ichihara F, Elima K, Rantakari P, Hollmen M, Kelkka T, et al. Clever-1/Stabilin-1 controls cancer growth and metastasis. *Clin Cancer Res* (2014) 20(24):6452–64. doi: 10.1158/1078-0432.CCR-14-1236

154. Viitala M, Virtakoivu R, Tadayon S, Rannikko J, Jalkanen S, Hollmen M. Immunotherapeutic blockade of macrophage clever-1 reactivates the Cd8(+) T-cell response against immunosuppressive tumors. *Clin Cancer Res an Off J Am Assoc Cancer Res* (2019) 25(11):3289–303. doi: 10.1158/1078-0432.CCR-18-3016

155. Kristiansen G, Winzer KJ, Mayordomo E, Bellach J, Schluns K, Denkert C, et al. Cd24 expression is a new prognostic marker in breast cancer. *Clin Cancer Res* (2003) 9 (13):4906–13.

156. Tarhriz V, Bandehpour M, Dastmalchi S, Ouladsahebmadarek E, Zarredar H, Eyvazi S. Overview of Cd24 as a new molecular marker in ovarian cancer. *J Cell Physiol* (2019) 234(3):2134–42. doi: 10.1002/jcp.27581

157. Barkal AA, Brewer RE, Markovic M, Kowarsky M, Barkal SA, Zaro BW, et al. Cd24 signalling through macrophage siglec-10 is a target for cancer immunotherapy. *Nature* (2019) 572(7769):392–6. doi: 10.1038/s41586-019-1456-0

158. Camisaschi C, De Filippo A, Beretta V, Vergani B, Villa A, Vergani E, et al. Alternative activation of human plasmacytoid dcs in vitro and in melanoma lesions: Involvement of lag-3. *J Invest Dermatol* (2014) 134(7):1893–902. doi: 10.1038/jid.2014.29

159. Chiba S, Baghdadi M, Akiba H, Yoshiyama H, Kinoshita I, Dosaka-Akita H, et al. Tumor-infiltrating dcs suppress nucleic acid-mediated innate immune responses through interactions between the receptor Tim-3 and the alarmin Hmgb1. *Nat Immunol* (2012) 13(9):832–42. doi: 10.1038/ni.2376

160. de Mingo Pulido A, Gardner A, Hiebler S, Soliman H, Rugo HS, Krummel MF, et al. Tim-3 regulates Cd103(+) dendritic cell function and response to chemotherapy in breast cancer. *Cancer Cell* (2018) 33(1):60–74 e6. doi: 10.1016/j.ccell.2017.11.019

161. Dixon KO, Tabaka M, Schramm MA, Xiao S, Tang R, Dionne D, et al. Tim-3 restrains anti-tumour immunity by regulating inflammasome activation. *Nature* (2021) 595(7865):101–6. doi: 10.1038/s41586-021-03626-9

162. Wolf Y, Anderson AC, Kuchroo VK. Tim3 comes of age as an inhibitory receptor. *Nat Rev Immunol* (2020) 20(3):173–85. doi: 10.1038/s41577-019-0224-6

163. Mayoux M, Roller A, Pulko V, Sammicheli S, Chen S, Sum E, et al. Dendritic cells dictate responses to pd-L1 blockade cancer immunotherapy. *Sci Trans Med* (2020) 12(534):eaav7431. doi: 10.1126/scitranslmed.aav7431

164. Bilotta MT, Antignani A, Fitzgerald DJ. Managing the tme to improve the efficacy of cancer therapy. *Front Immunol* (2022) 13:954992. doi: 10.3389/fimmu.2022.954992

165. Kraehenbuehl L, Weng CH, Eghbali S, Wolchok JD, Merghoub T. Enhancing immunotherapy in cancer by targeting emerging immunomodulatory pathways. *Nat Rev Clin Oncol* (2022) 19(1):37–50. doi: 10.1038/s41571-021-00552-7

166. Naimi A, Mohammed RN, Raji A, Chupradit S, Yumashev AV, Suksatan W, et al. Tumor immunotherapies by immune checkpoint inhibitors (Icis); the pros and cons. *Cell commun Signaling CCS* (2022) 20(1):44. doi: 10.1186/s12964-022-00854-y

167. Larkin J, Chiarion-Sileni V, Gonzalez R, Grob JJ, Cowey CL, Lao CD, et al. Combined nivolumab and ipilimumab or monotherapy in untreated melanoma. *New Engl J Med* (2015) 373(1):23–34. doi: 10.1056/NEJMoa1504030

168. Poto R, Troiani T, Criscuolo G, Marone G, Ciardiello F, Tocchetti CG, et al. Holistic approach to immune checkpoint inhibitor-related adverse events. *Front Immunol* (2022) 13:804597. doi: 10.3389/fimmu.2022.804597

169. Lisi L, Lacal PM, Martire M, Navarra P, Graziani G. Clinical experience with ctla-4 blockade for cancer immunotherapy: From the monospecific monoclonal antibody ipilimumab to probodies and bispecific molecules targeting the tumor microenvironment. *Pharmacol Res* (2022) 175:105997. doi: 10.1016/j.phrs.2021.105997

170. Larkin J, Hodi FS, Wolchok JD. Combined nivolumab and ipilimumab or monotherapy in untreated melanoma. *New Engl J Med* (2015) 373(13):1270–1. doi: 10.1056/NEJMc1509660

frontiers | Frontiers in Immunology

TYPE Original Research
PUBLISHED 19 April 2023
DOI 10.3389/fimmu.2023.1130513

OPEN ACCESS

EDITED BY
Apostolos Zaravinos,
European University Cyprus, Cyprus

REVIEWED BY
Samit Chatterjee,
University of Rajasthan, India
Zhirui Zeng,
Guizhou Medical University, China
Xing Niu,
China Medical University, China

*CORRESPONDENCE
Xiang Wang
drseanwang@163.com
Shaohua Chen
silverchan1994@163.com
Yuan He
heyuan0963@163.com

†These authors have contributed equally to this work

SPECIALTY SECTION
This article was submitted to Cancer Immunity and Immunotherapy, a section of the journal Frontiers in Immunology

RECEIVED 23 December 2022
ACCEPTED 28 March 2023
PUBLISHED 19 April 2023

CITATION
Wang C, He Y, Zheng J, Wang X and Chen S (2023) Dissecting order amidst chaos of programmed cell deaths: construction of a diagnostic model for KIRC using transcriptomic information in blood-derived exosomes and single-cell multi-omics data in tumor microenvironment.
Front. Immunol. 14:1130513.
doi: 10.3389/fimmu.2023.1130513

Dissecting order amidst chaos of programmed cell deaths: construction of a diagnostic model for KIRC using transcriptomic information in blood-derived exosomes and single-cell multi-omics data in tumor microenvironment

Chengbang Wang[1,2†], Yuan He[3*†], Jie Zheng[1,2†], Xiang Wang[4*] and Shaohua Chen[1,2*]

[1]Department of Urology, The First Affiliated Hospital of Guangxi Medical University, Nanning, China, [2]Guangxi Key Laboratory for Genomic and Personalized Medicine, Center for Genomic and Personalized Medicine, Guangxi Collaborative Innovation Center for Genomic and Personalized Medicine, Guangxi Medical University, Nanning, China, [3]Department of Urology, The Second Nanning People's Hospital, Nanning, China, [4]Department of Urology, Shanghai General Hospital, Shanghai Jiao Tong University School of Medicine, Shanghai, China

Background: Kidney renal clear cell carcinoma (KIRC) is the most frequently diagnosed subtype of renal cell carcinoma (RCC); however, the pathogenesis and diagnostic approaches for KIRC remain elusive. Using single-cell transcriptomic information of KIRC, we constructed a diagnostic model depicting the landscape of programmed cell death (PCD)-associated genes, namely cell death-related genes (CDRGs).

Methods: In this study, six CDRG categories, including apoptosis, necroptosis, autophagy, pyroptosis, ferroptosis, and cuproptosis, were collected. RNA sequencing (RNA-seq) data of blood-derived exosomes from the exoRBase database, RNA-seq data of tissues from The Cancer Genome Atlas (TCGA) combined with control samples from the GTEx databases, and single-cell RNA sequencing (scRNA-seq) data from the Gene Expression Omnibus (GEO) database were downloaded. Next, we intersected the differentially expressed genes (DEGs) of the KIRC cohort from exoRBase and the TCGA databases with CDRGs and DEGs obtained from single-cell datasets, further screening out the candidate biomarker genes using clinical indicators and machine learning methods and thus constructing a diagnostic model for KIRC. Finally, we investigated the underlying mechanisms of key genes and their roles in the tumor microenvironment using scRNA-seq, single-cell assays for transposase-accessible chromatin sequencing (scATAC-seq), and the spatial transcriptomics sequencing (stRNA-seq) data of KIRC provided by the GEO database.

Result: We obtained 1,428 samples and 216,155 single cells. After the rational screening, we constructed a 13-gene diagnostic model for KIRC, which had high diagnostic efficacy in the exoRBase KIRC cohort (training set: AUC = 1; testing set: AUC = 0.965) and TCGA KIRC cohort (training set: AUC = 1; testing set: AUC = 0.982), with an additional validation cohort from GEO databases presenting an AUC value of 0.914. The results of a subsequent analysis revealed a specific tumor epithelial cell of TRIB3^{high} subset. Moreover, the results of a mechanical analysis showed the relatively elevated chromatin accessibility of TRIB3 in tumor epithelial cells in the scATAC data, while stRNA-seq verified that TRIB3 was predominantly expressed in cancer tissues.

Conclusions: The 13-gene diagnostic model yielded high accuracy in KIRC screening, and TRIB3^{high} tumor epithelial cells could be a promising therapeutic target for KIRC.

KEYWORDS

kidney renal clear cell carcinoma, programmed cell death, exosomes, single-cell RNA sequencing, spatial transcriptome, prognosis, biomarkers

Introduction

Renal cell carcinoma (RCC) is the most prevalent solid kidney lesion, accounting for 90% of renal malignancies (1) and 3% of all cancers (2). Kidney renal clear cell carcinoma (KIRC) is the most frequently diagnosed pathological classification, occupying about 80% of RCC (3). Despite the relatively favorable KIRC prognosis, with a 5-year survival rate of 75%, almost 30% of locally advanced cases will relapse with a locoregional recurrence or distant metastases (4, 5). The past decade has certainly witnessed remarkable advances in the characterization of KIRC management and research; nonetheless, much remains to be elucidated regarding the disease's pathogenesis and underlying mechanism, and research into the identification of diagnostic approaches for KIRC is in its infancy. In this scenario, constructing a novel clinical model spanning screening, diagnosis, and prognosis predictions is of tremendous significance to clinical settings and provides novel insights into precision medicine therapeutic decisions.

In recent years, programmed cell deaths (PCDs) have generated holistic attention for researchers due to their inestimable potential in diagnostic biomarkers and therapeutic targets in cancer. Several PCD types have been identified, including apoptosis, necroptosis, autophagy, pyroptosis, ferroptosis, and cuproptosis, all considered cell-dependent and orderly cell death regulated by certain genes, with the purpose of homeostasis preservation and clearance of abnormal cells (6). PCDs are dynamically plastic, exert a dual role in distinct contexts and stages of cancer development (7), and are tightly regulated by spatiotemporal gene expression modulation. Unambiguous evidence suggests that KLF2 deficiency contributes to the suppression of ferroptosis and promotes the progression and metastasis of RCC cells (8). Similarly, Peng et al. demonstrated that silencing key autophagy-related genes could promote anoikis resistance and lung colonization of hepatocellular carcinoma (HCC) cells (9). Recent research advances and efforts in PCDs have predisposed to a significant growth in our understanding of the pathomechanisms of various cancer types, including KIRC. However, such studies have been hampered by a single PCD type or limitations in experimental approaches, which obscure the subtle yet essential regulatory mechanisms underlying the surface.

Encouragingly, the emergence of blood-derived exosomes provides a new perspective on the mechanisms of cellular interactions in the tumor microenvironment (TME) and the search for tumor diagnostic biomarkers. Exosomes are cell-derived nano-vesicles, ranging from 30 to 150 nm in diameter, that transfer RNA, proteins, lipids, and metabolites to recipient cells in the body (10). Initially, exosomes were thought to be the inert debris produced by cells to dispose of wastes. As the study of exosomes deepened, it was gradually discovered that they are involved not only in antigen presentation, cell differentiation, and immune response but also in tissue inflammation, virus transmission, migration, and tumor cell invasion (11–13). A study by Zhang et al. found that the exosomal miR-522 secreted by cancer-associated fibroblasts inhibited ferroptosis in cancer cells by targeting ALOX15 and compromising lipid peroxide accumulation (14). Moreover, a study by Shen et al. reported that exosomes secreted by pancreatic cancer cells were taken up by T lymphocytes, which activated p38 MAPK and then induced endoplasmic reticulum stress-mediated apoptosis, ultimately causing immunosuppression (15). The abovementioned studies demonstrate the intimate association between PCDs and exosomes in TME. Existing studies, however, were conducted in biological assays devoid of a cellular microenvironmental context, which may result in unduly artificial outcomes. The link between

PCDs and exosomes in the TME of KIRC is poorly understood as are the regulating processes.

The emergence of single-cell RNA sequencing (scRNA-seq) technology can partially solve the abovementioned problems. As a high-resolution tool, it overcomes the limitations of traditional bulk sequencing. It enables a breakthrough in the problem of exosomal mRNA traceability at the single-cell level by combining single-cell assays for transposase-accessible chromatin sequencing (scATAC-seq) and spatial transcriptomics sequencing (stRNA-seq) to study epigenetic regulation and observe the spatial distribution of key genes at single-cell resolution, synergistically uncovering molecular mechanisms at higher levels.

In the present study, we collected PCD-related genes, specifically (CDRGs), along with scRNA data and the KIRC cohort from The Cancer Genome Atlas (TCGA) database, to investigate the relationship between KIRC and PCD development. Meanwhile, we deciphered the blood-derived exosome transcriptome data to construct a gene model for clinical diagnosis and validated the diagnostic efficacy in KIRC cohorts by machine learning methods. Finally, we explored the mechanisms of these genes in the KIRC progression by scATAC data and cellular interaction network analysis. The abovementioned results support the clinical diagnosis and treatment decisions in KIRC. The dataset information and workflow of the presented study are shown in Figure 1.

Materials and methods

Acquisition of gene lists and multi-omics datasets

Six PCD categories were included, and their respective related genes, namely CDRGs, were collected. Among these, apoptosis- and necroptosis-related genes were collected from Deathbase (http://deathbase.org/), comprising proteins and corresponding coding genes of typical PCDs. Autophagy-related genes were collected from Human Autophagy Database (HADb; http://www.autophagy.lu). Ferroptosis- and pyroptosis-related genes were collected from Ferroptosis Database (FerrDb; http://www.zhounan.org/ferrdb) and published literature (16). Moreover, Gene Ontology (GO) and Kyoto Encyclopedia of Genes and Genome (KEGG) databases were also used to extract the associated genes in the PCDs mentioned above. The pyroptosis-related genes were derived from the GO database and published literature (17), while the cuproptosis-related genes were only obtained from published literature (18). Details of the CDRGs are listed in Supplementary Table S1.

A total of 11 independent datasets were included in this study, containing eight single-cell datasets, two bulk RNA-seq datasets of tissues, and bulk RNA-seq datasets of blood-derived exosomes. Data from eight single-cell datasets, included five scRNA-seq data

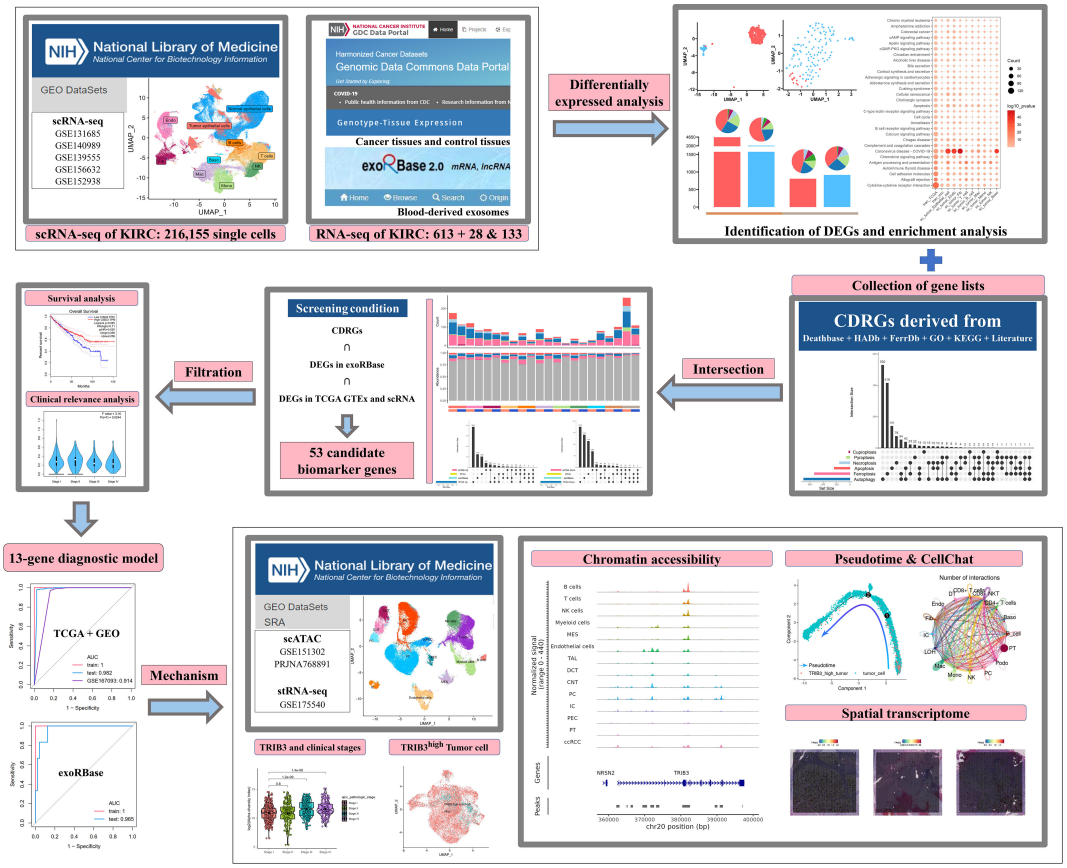

FIGURE 1
The dataset information and workflow of the presented study.

of KIRC, para-carcinoma, and healthy tissues from nephrectomy or biopsies, are shown below: GSE131685 (n = 3), GSE140989 (n = 24), GSE139555 (n = 6), GSE156632 (n = 12), and GSE152938 (n = 3); one spatial transcriptome dataset of KIRC was derived from the GEO database with accession number GSE175540; two datasets contained five scATAC healthy kidney data and three scATAC KIRC data, which were downloaded from GSE151302 and the National Center for Biotechnology Information Sequence Read Archive under accession number PRJNA768891, respectively. Meanwhile, two bulk RNA-seq data of tissues of the TCGA-KIRC cohort with associated clinical information (n = 613) were downloaded from the TCGA (https://portal.gdc.cancer.gov/) databases, combined with the normal kidney tissue data downloaded from the GTEx portal (www.gtexportal.org). The other bulk transcriptomic data of KIRC cohort provided by the GEO database was used as an additional validation cohort with accession number GSE167093 (n = 656); one bulk transcriptomic data of blood-derived exosome was downloaded from the exoRbase database (http://www.exorbase.org/, n = 133).

scRNA-seq data analysis

Fastq files were processed using Cell Ranger (version 6.1.2, 10x Genomics) with default parameters and mapped to 10x human transcriptome GRCh38-2020 (https://support.10xgenomics.com/single-cell-gene-expression/software/downloads/latest). Seurat (version 4.2.0) was used to process single-cell data for the following analyses. We filtered out low-quality cells with less than 400 or more than 5,000 total genes expressed or with more than 30% mitochondrial RNA contents. SCTransform, RunPCA, and RunUMAP functions were used for normalization and dimensionality reduction, respectively (19). In addition, harmony (version 0.1.1) was used to correct batch effects between different arrays (20). FindNeighbors and FindClusters functions were then used to differentiate the cell clusters with the dimensions and resolution parameters of 1:25 and 0.8, respectively. scHCL (version 0.1.1), SingleR (version 1.10.0), and ScType (https://github.com/IanevskiAleksandr/sc-type) packages were used to aid in the identification of cell subpopulations, and cluster-specific marker genes were identified by the FindAllMarkers function of Seurat package (logfc.threshold = 0.25, min.pct = 0.1).

scATAC-seq data analysis

scATAC-seq was processed by Cell Ranger -atac-2.1.0 using default parameters and mapped to 10x human transcriptome GRCh38-2020 (https://support.10xgenomics.com/single-cell-gene-expression/software/downloads/latest). Signac (version 4.2.0, 10x Genomics) was used to analyze the output of the Cell Ranger ATAC pipeline. Low-quality cells were removed based on the following criteria: nucleosome signal score of less than 4 and transcriptional start site enrichment score of more than 3. RunTFIDF function was used for normalization, while RunSVD and RunUMAP were used for linear and nonlinear dimensional reductions, respectively (21). harmony (version 0.1.1) was likewise used to correct batch effects between arrays (20). Gene activity was quantified *via* the GeneActivity function in Signac, including the 2 kb upstream of the transcriptional start site and gene body.

stRNA-seq data analysis

stRNA data was analyzed through Seurat (version 4.2.0). Spatial spots featuring less than 300 genes or more than 30% of mitochondrial genes were filtered out. Raw counts were normalized with the SCTransform function of Seurat with the assay of the spatial parameter. RunPCA and RunUMAP functions were used for dimensionality reduction.

Bulk RNA-seq data processing

We used stringr (version 1.4.1) and stats (version 4.2.1) in R language to integrate the data of KIRC dataset from the TCGA database and the control samples from the GTEx database as well as the raw data matrix of KIRC downloaded from the GEO database. The data were collated and filtered under the following conditions: (1) genes detected in all samples were retained, (2) genes with sum of counts across all samples less than 2.5 were excluded from further analyses, (3) genes with an average expression higher than 0 in at least 80% of the tumor or control samples were retained, (4) the expression levels of duplicated genes in the data matrix were averaged, and (5) batch effects between the TCGA and GTEx databases were corrected using the ComBat function from sva (version 3.44.0) package.

Identification of differentially expressed genes

Differential gene expression analysis in single-cell datasets was performed using the FindMarkers function in the Seurat package with P-value <0.05 and $|\log_2 FC|$ >0.25 as cutoff criteria. DESeq2 (version 1.36.0), limma (version 3.52.4), and edgeR (version 3.38.4) packages were used for the identification of DEGs in the TCGA KIRC cohort, with P-value <0.05 and $|\log_2 FC|$ >1 as the thresholds. In the bulk RNA-seq data of blood-derived exosomes, differentially expressed genes (DEGs) were recruited using $|\log_2 FC|$ >0.5 and P-value <0.05. The intersection analysis of DEGs between different datasets was visualized using the UpSetR (version 1.4.0) package. We then used ggplot2 (version 3.3.6) to visualize the expression differences and expression of key genes by means of bubble plots and heat maps.

Gene Ontology analysis and Kyoto Encyclopedia of Genes and Genomes analysis

GO function enrichment analysis and KEGG pathway enrichment analysis of the target genes in RNA-seq were

performed using R package clusterProfiler (version 4.4.4). The results were filtered with a *P*-value of 0.05.

Correlation analysis between the target genes and clinical parameter

ggpubr (version 0.4.0) package was loaded to perform the correlation analysis of target genes with clinical parameters using the stat_compare_means function, thereby visualizing data with boxplots using ggplot2 package. GEPIA2.0 (http://gepia2.cancer-pku.cn/#index, accessed on December10, 2022), a platform for TCGA data visualization, was also utilized to evaluate the effect of candidate biomarker genes on overall survival in KIRC and to create Kaplan–Meier survival curves. It was also used to analyze the correlations between candidate biomarker genes and clinical indicators.

Machine learning analysis

We used stratified random sampling to divide exoRBase KIRC into a training set and a testing set in a ratio of 3:2. The training set was used to construct the random forest classification model, and the testing set was used to validate the model further. The constructed model's performance was assessed by calculating the area under the curve (AUC) value. The same approach was used for the TCGA KIRC cohort merged with GTEx samples to observe the diagnostic efficacy of key genes in the tissue. The abovementioned process was performed using the tidymodels (version 1.0.0) and pROC (version 1.18.0) R packages.

Cell–cell interaction network analysis

Intercellular interaction analysis was conducted using CellChat (version 1.5.0) (22), based on which we could identify the potential ligand–receptor interactions according to the expression pattern of ligands in one cell subtype and their corresponding receptors in the other cell subtypes.

Reconstructing TRIB3^{high} tumor cell differentiation trajectories by Monocle2

Fate decisions and pseudotime trajectories of TRIB3^{high} tumor cells were reconstructed using the Monocle2 R package (version 2.24.1). First, tumor epithelial cells were selected by Seurat, and 16,747 tumor cells were imported into Monocle2 with a lower detection limit parameter of 0.5. Subsequently, we performed differential gene expression analysis using the differentialGeneTest function and retained DEGs with q-value <0.01 as sorted gene sets and performed descending dimensionality and trajectory analysis. We finally determined the direction of the cell differentiation trajectory by the cell stemness-related gene CD44 and visualized the trajectory results using the plot_cell_trajectory function.

Statistical analysis

The categorized variables between groups were compared using Wilcoxon test, and a correlation analysis between different cell subtypes was performed using Spearman correlation test. A *P*-value less than 0.05 was considered to indicate statistical significance. R language (version 4.2.1; http://www.r-project.org/) was used for data analyses and figure generation unless indicated otherwise.

Results

Transcriptome information of KIRC in multiple tissue sources

We started our investigations with the KIRC expression profiles at single-cell resolutions. We assembled 48 KIRC cases from five independent datasets provided by the GEO database. These were containing cancer, para-carcinoma, and healthy tissues from nephrectomy or biopsies. After the implementation of stringent quality control, 216,155 single cells from five independent datasets were retained for the following analyses. The sample information and quality control data are shown in Supplementary Table S2 and Supplementary Figures S1A, B. Having processed with the Seurat package and removed the batch effect, 54 cell clusters (Supplementary Figures S2A–C) and 10 main cell types were identified, including tumor epithelial cell, normal epithelial cell, endothelial cell (Endo), fibroblast (Fib), T cell, B cell, macrophage (Mac), monocyte (Mono), natural killer cell (NK), and basophil (Baso), thus visualized through uniform manifold approximation and projection (UMAP) (Figure 2A). The marker genes of each cell cluster are shown in Supplementary Table S3. The specific markers and relative abundance for the main cell types are shown in Figure 2B. Specifically, epithelial cells dominated all major cell compartments, with tumor epithelial cells expressing the canonical markers of CA9 coming exclusively from tumor tissues and normal epithelial cells having multiple origins. The distributions for each main cell type and their origins were visualized using UMAP (Figure 2C). Subsequently, we explored the DEGs between the cancer and control samples of various major cell types based on their expression profiles (Supplementary Table S4), with the bar plots indicating the exact counts of upregulated and downregulated DEGs and the pie plots manifesting their corresponding categories in the KEGG pathways (Figure 2D), most of which belong to "human disease". Intriguingly, the highest DEG number was presented between tumor and normal epithelial cells, followed by DEGs between Endo and Fib between cancer and control samples (Figure 2D), demonstrating the dramatic alterations of structural cells in transcriptome and their essential stages in tumorigenesis.

Next, we further dissected the transcriptome landscape of KIRC based upon the TCGA cohort merged with healthy samples in GTEx (Figure 2E), revealing 4,604 upregulated and 2,073 downregulated DEGs in cancer tissues (Figure 2F; Supplementary Table S5). An increasing body of unambiguous evidence denotes

10.3389/fimmu.2023.1130513

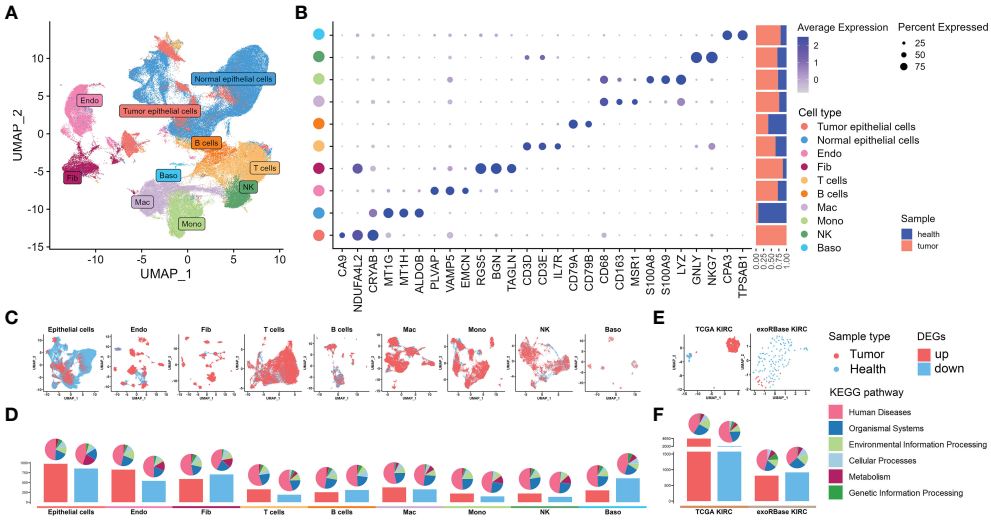

FIGURE 2
Single-cell RNA sequencing (scRNA-seq) and bulk RNA sequencing (RNA-seq) profiling of kidney renal clear cell carcinoma (KIRC). **(A)** Uniform manifold approximation and projection showing the 10 major cell clusters in the scRNA-seq datasets. **(B)** Marker genes and proportions of sample origins for the 10 major cell clusters of the scRNA-seq datasets. **(C)** Distribution characteristics of the 10 major cell clusters in the scRNA-seq datasets. **(D)** Barplots showing the counts of differentially expressed genes (DEGs) between the cancer and control samples of each cell cluster in the scRNA-seq datasets. **(E)** Distribution characteristics of The Cancer Genome Atlas (TCGA) KIRC cohort merged with control cases from the GTEx database (left) and exoRBase KIRC cohort (right) containing the RNA-seq data of blood-derived exosomes of patients. **(F)** Barplots showing the counts of DEGs between the KIRC and healthy cases of TCGA KIRC and exoRBase KIRC cohorts. The pie plots at the top of the bar show the Kyoto Encyclopedia of Genes and Genomes pathway enriched by each group of DEGs.

the role of cancer cell-derived exosomes of patients on the course of epithelial–mesenchymal transition and metastasis in KIRC (23, 24), thus making it a promising diagnostic and prognostic KIRC biomarker. As such, we then analyzed the RNA-seq data of human blood-derived exosomes of healthy controls and KIRC patients using the exoRBase database, with UMAP showing complete separations between cancer and control samples (Figure 2E), and the differential gene expression analysis yielded a total of 1,723 DEGs (Figure 2F; Supplementary Table S6). Notably, the KEGG functional enrichment analyses between groups elucidated that such DEGs were mainly enriched in cell cycle, apoptosis, cancer, and immune-related signaling pathway (Supplementary Figures S3A, B). In a nutshell, we investigated the transcriptome data of tissue- and blood-derived exosomes of KIRC patients and corresponding controls exhaustively, combining them with DEGs of various cell types based on scRNA data, thereby laying the groundwork for a subsequent analysis to identify disease biomarkers.

The expressed pattern of CDRGs in KIRC

As planned, six kinds of PCDs, including apoptosis, necroptosis, autophagy, pyroptosis, ferroptosis, and cuproptosis, and their related genes, namely CDRGs, showing commonalities and specificities were included (Figure 3A). However, we were unable to uncover any genes that were shared by all PCD categories, but the number of genes shared by ferroptosis and autophagy was very high. As depicted in Figure 3B, most CDRGs were upregulated DEGs in single-cell and RNA-seq datasets. However, the proportions of downregulated DEGs were very low in such datasets, with most of them belonging to the autophagy, apoptosis, and ferroptosis pathways. Such a phenomenon raised an illustrative assertion: the expression levels of CDRGs were enhanced in varying degrees. Notwithstanding, this explicit demonstration of the eye-catching alterations of such genes implicitly proposed the question of what specialized roles they played in TME.

Next, we intersected the upregulated (Figure 4A) and downregulated (Figure 4B) DEGs in exoRBase KIRC with CDRGs and DEGs obtained from single-cell and TCGA datasets to screen for the candidate biomarker genes. Herein we retained the differentially expressed CDRGs between the exoRBase and TCGA databases or differentially expressed CDRGs between the exoRBase and single-cell datasets, thereby acquiring 53 candidate biomarker genes. Notably, 20 genes were upregulated (Figure 4C), and 33 genes were downregulated in the blood-derived exosomes of KIRC patients (Supplementary Figure S4A). Concomitantly, such differentially expressed trends of candidate biomarker genes were largely consistent in the TCGA datasets and single-cell datasets of epithelial cells, Endo, and Fib, namely structural cells. Such discoveries denoted the pivotal role of exosomes in orchestrating the dialog with neoplastic cells and profoundly influencing the TME alteration.

Following are the correlations between 53 candidate biomarker genes and clinical markers. The results indicated that 32 out of 53 genes were closely associated with patients' clinical stages or survival outcomes, functioning doubly as a risk or protective factor in KIRC (Figure 4D). Moreover, ferroptosis- and autophagy-related genes account for 32 genes, with a small

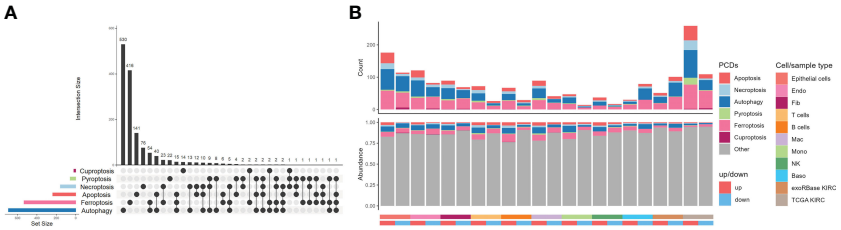

FIGURE 3
Distribution characteristics of programmed cell deaths in kidney renal clear cell carcinoma (KIRC). **(A)** UpSet plot showing the intersection analysis of the six types of cell death-related genes (CDRGs). **(B)** Distribution characteristics of the differentially expressed genes (DEGs) in single-cell RNA sequencing, The Cancer Genome Atlas KIRC, and exoRBase KIRC cohorts and their shared genes with six classes of CDRGs. The top bar plot represents the counts of DEGs shared CDRGs, and the bottom bar plot shows the relative abundance of CDRGs in DEGs of all the groups.

proportion of genes belonging to apoptosis and necroptosis. Thereinto, 13 out of 32 genes were simultaneously related to the clinical stages and survival outcomes of KIRC (Supplementary Figure S4B and Supplementary Figure S5), including PIP4K2C, FIS1, PSAT1, ERBB2, TRIB3, CLU, GABARAPL2, LRBA, PCK2, CDKN1A, FKBP1A, MAP1LC3B, and ITGA6, which are subject to the following analysis.

PSAT1, a risk factor in KIRC, had contradictory expression patterns in blood-derived exosomes and tissues, with the former displaying an elevated expression level and the latter displaying a downregulated expression level. Such phenomena are reminiscent of the connections between exosome releasing and signaling reception of neoplastic cells, possibly contributing to the alteration of expression profiles in TME and the emergence of malignant cancer phenotypes (25). In summary, we comprehensively explored the CDRG expression pattern in KIRC, based on which we carried out the correlation analyses of candidate marker genes with clinical indicators, identifying 13 key genes linked with survival outcomes and clinical stages of KIRC cases.

Validation of the 13-gene diagnostic model and mechanism explorations

Next, we used 13 key genes to construct a diagnostic model for KIRC, as previously described in the "Materials and methods". Specifically, we randomly stratified all samples from the exoRbase database into two groups (training set and the testing set) with a ratio of 3:2 for cross-validation. Encouragingly, the 13-gene diagnostic model presented outstanding discriminatory ability in the KIRC datasets of the exoRbase database (Figure 5A), with AUC values of 1 and 0.965 in the training and testing sets, respectively. Similarly, the model constructed with 13 genes in the TCGA KIRC cohort showed promising diagnostic results, with AUC values of 1

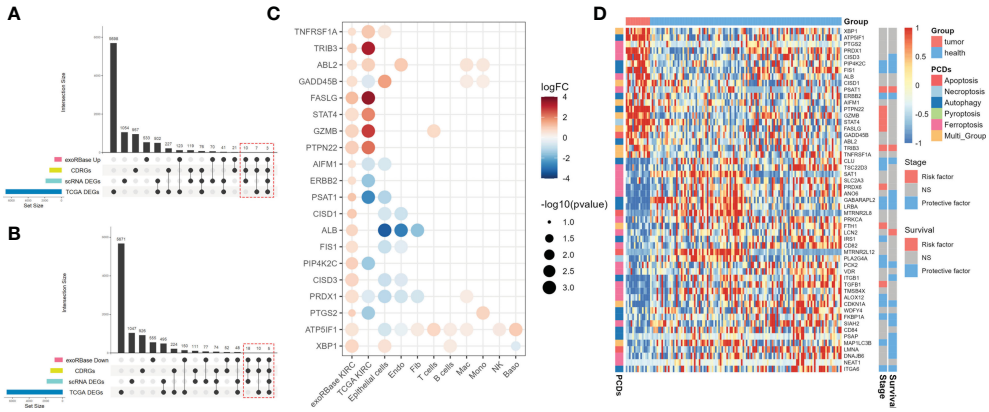

FIGURE 4
Screen for candidate biomarker genes. **(A)** UpSet plots showing the intersection analysis among cell death-related genes (CDRGs), differentially expressed genes (DEGs) in exoRBase kidney renal clear cell carcinoma (KIRC) cohort, upregulated DEGs in The Cancer Genome Atlas (TCGA) KIRC cohort, and scRNA datasets. **(B)** UpSet plots showing the intersection analysis among CDRGs, DEGs in the exoRBase KIRC cohort, downregulated DEGs in the TCGA KIRC cohort, and scRNA datasets. **(C)** The bubble plots show 20 candidate biomarker genes upregulated in the exoRBase KIRC cohort and their expression pattern in other datasets. Red circles represent positive logFC values or upregulated DEGs in corresponding datasets, while blue circles represent negative logFC values or downregulated DEGs in corresponding datasets; the bubble size indicates negative log10(*P*-value). **(D)** Heat map showing the expression levels of 53 candidate biomarker genes in the exoRBase KIRC cohort, with red color indicating relatively high expression and blue color indicating relatively low expression levels. The column annotations on the left side represent the programmed cell death classification of the candidate biomarker genes. The two annotated columns on the right side show the correlation of candidate biomarker gene expression with the survival outcome and clinical stage of the TCGA KIRC cohort, respectively. Red color represents the gene as a risk factor, and blue color represents a protective factor in the prognosis of KIRC cases.

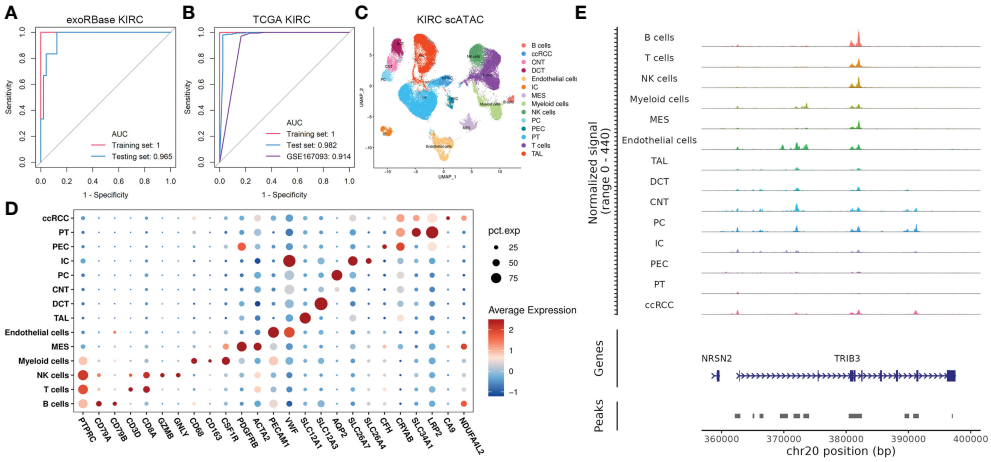

FIGURE 5
Construction of 13-gene diagnostic models and single-cell assays for transposase-accessible chromatin (scATAC-seq) analysis. **(A)** Receiver-operating characteristic (ROC) curve analysis of a 13-gene diagnostic model based on exoRBase kidney renal clear cell carcinoma (KIRC) cohort, with the red curve representing the training set and the blue curve representing the testing set. **(B)** ROC curve analysis of a 13-gene diagnostic model based on The Cancer Genome Atlas KIRC combined with GTEx cohort and KIRC cohort from the GEO database with accession number GSE167093, with the former treated as the training set (red) and the testing set (blue). In contrast, the latter was an additional validation cohort (purple). **(C)** Uniform manifold approximation and projection plot showing the 14 cell clusters in the scATAC-seq analysis **(D)** Bubble plots showing the marker genes for each cell cluster in scATAC-seq. **(E)** CoveragePlot showing the peak–gene links for TIRB3.

and 0.982 in the training and testing sets, respectively (Figure 5B). Furthermore, GSE167093, provided by the GEO database containing 656 KIRC cases, was used as an additional validation cohort, exhibiting a tremendously high diagnostic accuracy with an AUC value of 0.914. The findings unequivocally demonstrated that the 13-gene diagnostic model was very stable and trustworthy in detecting KIRC, regardless of whether the sample was taken from blood-derived exosomes or solid tissue, and ensured high sensitivity and specificity. Moreover, the differentially expressed trend in blood-derived exosomes may provide an instant advantage in liquid biopsy analyses for biomarker evaluations, reducing the sampling inconveniences and hazards.

Nevertheless, the molecular basis for the 13-gene diagnostic model has not been addressed. Such combinations of genes derived from the transcriptomic data of exosomes and various cell subtypes are not as simple as they may seem. The crosstalk behind the cellular identities and their exosomes confers intriguing information about the KIRC pathogenesis. Thus, we then focused on studying the epigenetic profile of KIRC in scRNA and scATAC data to uncover the role of such genes in transcriptome and epigenetic regulation at single-cell resolutions. We discovered the abnormal expression pattern of such genes in distinct cell types based on scRNA data, especially for CLU, CDKN1A, PSAT1, and MAP1LC3B, which are differentially expressed in virtually all cell types (Supplementary Figure S6). Then, we analyzed 63,489 cells in the scATAC datasets of KIRC cases, identifying 15 main cell types based on the average promoter activity of representative marker genes (Figures 5C, D). Of particular interest is the fact that we found that TRIB3 expression was higher in tumor epithelial cells referred to normal epithelial cells. At the same time, its chromatin accessibility was significantly increased compared with the normal PT cell cluster (Figure 5E), a common type of epithelial cell in the kidney.

Comprehensive descriptions of TRIB3^{high} tumor epithelial cells

Next, we investigated the TRIB3 influence in TME and its corresponding cell subset. The subsequent analysis of TRIB3 demonstrated that this gene was positively associated with TNM staging of KIRC (Figures 6A–C), implying its adverse role in the survival outcome of KIRC, which could be the leading contributor to the metastasis of cancer cells. Therefore, our analysis focused on understanding the TRIB3 role in specific phenotypes of tumor epithelial cells, the latter of which was exacted from scRNA datasets and further visualized after dimensionality reduction. Notably, the TRIB3^{high} subset was presented in scattered tumor epithelial cells (Figure 6D) and shared a much higher resemblance to PT (R = 0.864) (Figure 6E). In addition, the pseudotime analysis indicated that such a cell subset could be a primitive cancer stem cell (Figure 6F) as evidenced by the relatively high expression of the cancer stem cell biomarker CD44 (Supplementary Figure S7) (26). The cell–cell communication analysis suggests that TRIB3^{high} tumor cells interact more extensively and strongly than other cell types, particularly for interactions with Mac and T cells (Figure 6G, Supplementary Figure S8). At the same time, the high expression of glyceraldehyde-3-phosphate dehydrogenase (GAPDH) may predict a strong exosome assembly and aggregation capacity for this cell type (Supplementary Figure S7) (27). The results of the cell–cell interaction network analysis disclosed the higher interactions of TRIB3^{high} tumor epithelial cells with other cell types in certain

10.3389/fimmu.2023.1130513

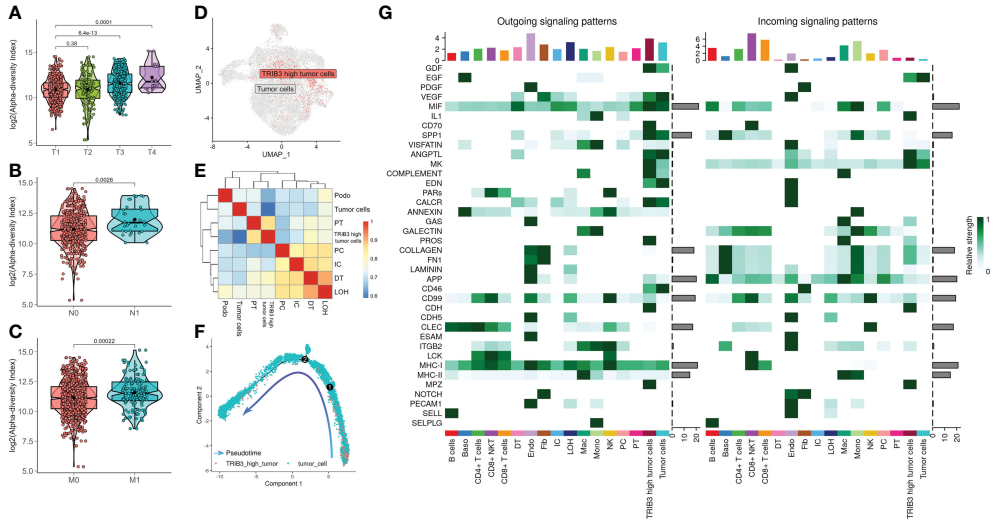

FIGURE 6
Clinical characteristics of TRIB3 expression in kidney renal clear cell carcinoma (KIRC) patients and characterization of the TRIB3^{high} tumor cell subset. **(A–C)** The box plot shows the correlation between TRIB3 expression and T classification, N classification, and M classification in KIRC patients. **(D)** Uniform manifold approximation and projection plot indicating the distribution pattern of TRIB3^{high} tumor cells. **(E)** Heat map showing the correlation between various cell types using the Spearman method; the colors represent the strength of the correlation. **(F)** Pseudotime analysis of TRIB3^{high} tumor cells. The direction of the arrow indicates the differentiation trajectory. **(G)** Signaling role analysis showing the aggregated cell–cell communication networks from all signaling pathways. The shades of color represent the relative strength of cellular communication.

ligand–receptor pairs, spanning CD70-CD27, CLEC2B-KLRB1, CD99-CD99, COL6A2-CD44, COL6A2-SDC4, PGD-VEGFR1, and PROS1-AXL, suggesting that the TRIB3^{high} subset showed stronger local interactions with other major cell types (Supplementary Figure S9), which could predispose to an increased ability of induction and reprogramming of extrinsic phenotypic features, thereby reshaping the overall TME. TRIB3^{high} tumor epithelial cells were mainly enriched in apoptosis, ferroptosis, ribosome, and lysosome signaling pathways compared with other cell clusters (Figures 7A, B). Lastly, the spatial transcriptomic analysis confirmed that the TRIB3^{high} subset is highly enriched in tumor tissues (Figure 7C).

Discussion

PCDs are fundamental and intricate biological processes in various physiological and pathological events. Evidence persuasively denotes that PCDs are critical regulators in cancer development and progression (28, 29), and key factors in various PCDs have been progressively appreciated, thus applying them in the identification of tumor diagnosis and treatment (30–33). Many association studies between KIRC and PCD have emerged in recent years. However, the different types of PCDs are compartmentalized studies, and there is a dearth of pertinent, comprehensive investigations, particularly in KIRC. In this study, we discovered

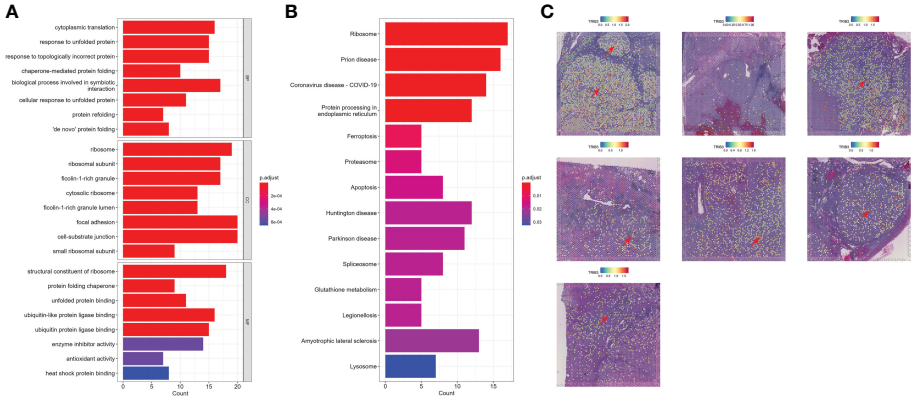

FIGURE 7
Functional analysis and spatial localization of TRIB3^{high} tumor cells. **(A)** Gene Ontology enrichment analysis for upregulated differentially expressed genes (DEGs) in TRIB3^{high} tumor cells. **(B)** Kyoto Encyclopedia of Genes and Genomes pathway analysis for upregulated DEGs in TRIB3^{high} tumor cells. **(C)** Visualization of TRIB3^{high} tumor cells in kidney renal clear cell carcinoma spatial transcriptome tissue sections.

significant alterations in the CDRG expression levels in KIRC tissues. Such changes are not merely present in the tumor epithelial cell emphasized by traditional studies; similar shifts were also observed in other structural cells and immune cells in the TME, most of which belong to autophagy, apoptosis, and ferroptosis. The landscape of diagnostic and therapeutic targets for PCD, as indicated by *in vitro* and *in vivo* data, continues to evolve, making this an unquestionably fruitful area of research. Ma et al. substantiated that silibinin could induce apoptosis by inhibiting the mTOR-GLI1-BCL2 pathway, thus markedly suppressing the tumor growth of RCC (34), with an *in vitro* cell line assay indicating that capsaicin pronouncedly inhibited the migration and invasion of RCC by inducing autophagy through the AMPK/mTOR pathway (35). Similarly, Heiker et al. clarified that silencing the enzymes essential for the biosynthesis of glutathione or glutathione peroxidase could initiate ferroptosis, thus selectively compromising the KIRC cells' viability without any impact on the growth of non-malignant renal epithelial cells (36). The results mentioned above noted that PCDs are highly coordinated and regulate the cells' survival state through various signaling pathways, suggesting its potential as a therapeutic target for RCC.

Currently, the preoperative diagnosis of KIRC heavily relies on MRI/CT. Despite specific enhancement modes for KIRC, misdiagnosis consistently happens in clinical settings (37), imposing a socio-economic burden on healthcare systems globally. Myriads of studies have identified novel diagnostic biomarkers for kidney cancer, spanning long non-coding RNAs, circulating tumor DNA, and circulating tumor cells; despite this, there is still scope for improvement in specificity as well as sensitivity, and the clinical applicability of such emerging biomarkers remains to be further validated (38–41). It is inspiring that blood platelet and blood-derived exosome-based polygenic models manifested excellent diagnostic efficacy, offering an accessible complement to existing screening modalities (42–44). Exosomes are secreted extracellularly by cytosolic fusion with the plasma membrane, which plays an imperative role in shaping the TME (45). Due to the nature of exosomes in mediating intercellular communication and extensive existence in body fluids (*e.g.*, blood, saliva, and urine), they become an optimal surrogate in cancer diagnosis and therapeutic predictions, also presenting encouraging results in clinical application (46–48). Wang et al. found that tumor cells can reduce T cell activity by secreting exosomal PD-L1 and that exosome inhibitors and ferroptosis inducers can effectively counteract these characteristics and create tumor-specific immunity (25). Zhang and colleagues elucidated that adenosine activation of AKT and ERK signaling mediated by exosome secreted by mesenchymal stem cells could contribute to the facilitation of cartilage repair, thereby reducing apoptosis and modulating immune responses (49). These findings demonstrate that PCDs and exosomes are inextricably linked, indicating that further exploration of the reciprocal activity of PCDs and exosomes in the TME could be employed as a unique avenue for future research into the KIRC pathogenesis.

Based on the transcriptome profiling of blood-derived exosomes from KIRC patients, combined with transcriptomic information from the TCGA KIRC cohort and scRNA-seq data of KIRC, we further screened out the candidate biomarker genes among CRDGs by their correlation with clinical indicators, thus uncovering 13 essential genes with diagnostic potential for KIRC. Using machine learning and their cross-validation, the construction of diagnostic models with 13 key genes showed high diagnostic efficacy in both blood-derived exosome samples and tissue samples, with AUC of 0.965 for blood-derived exosomes and AUC = 0.914 for tissue. The traceability analysis based on single-cell omics showed that the expression and alterations of key genes presented in multiple cellular identities in TME, especially in structural cells and macrophages. TME is a highly heterogeneous ecosystem constituted by cancer cells, fibroblasts, adipocytes, endothelial cells, mesenchymal stem cells, and extracellular matrix (45, 50). Notably, cancer cells could secrete exosomes to induce the production of cancer-associated fibroblasts and cancer-associated endothelial cells, thereby contributing to the remodeling of TME (51–53). Comparably, stromal cells are competent in tumor progression by stimulating and reprogramming cancer cells through exosomes (54, 55). From a theoretical perspective, our studies could accelerate the understanding of the identification of a cancer biomarker, simultaneously facilitating the biological interpretation of cancer biology in the multi-omic context.

Our study noted that the high TRIB3 expression, in one of the genes in the 13-gene diagnostic model, was closely linked with advanced clinical stage and worse prognosis in KIRC patients, which is consistent with the findings of Hong et al., collectively revealing its essential role in KIRC development and progression (56). Meanwhile, the relatively elevated chromatin accessibility of TRIB3 in tumor epithelial cells was manifested in the scATAC data. At the same time, the stRNA-seq verified that TRIB3 was predominantly expressed in cancer tissues, further justifying its upregulated expression pattern in KIRC. The biological role of TRIB3 is extensive. In addition to being associated with ferroptosis (57), the upregulation of TRIB3 could suppress the process of autophagy (58, 59). Furthermore, TRIB3 is implicated in the carcinogenesis of a variety of cancers, with evidence indicating that it could inhibit the degradation of FOXO1 and enhance SOX2 transcription, thus contributing to the carcinogenesis of breast cancer (60) and induction of immune evasion by inhibiting the STAT1–CXCL10 axis and impeding the CD8+ T cell infiltration in colorectal cancer (61). Intriguingly, its relationship with exosomes has also been investigated, indicating that TRIB3 could mediate the impairment of autophagy and facilitate the secretion of INHBA/Activin A-enriched exosomes of hepatocellular carcinoma, thus resulting in the occurrence of liver fibrosis (59). On this basis, our further analysis of the $TRIB3^{high}$ subset revealed that such cell subtype interacts more extensively and strongly than the other cell types, representing an optimized remodeling of the TME and maintaining tumor progression. Functionally, the $TRIB3^{high}$ tumor epithelial cell was highly enriched in ribosomes and PCD-related pathways, representing its high metabolic demand, while its high expression of CD44 suggests a high degree of stemness. Such discoveries were validated in a study by Hua et al., elucidating that TRIB3 interacts with β-catenin and TCF4 in intestinal cells, thereby increasing the expression of cancer stem cell-related genes (62).

Meanwhile, it was shown that a high expression of the GAPDH plays a facilitating role in the assembly and secretion of exosomes by cells (27), which is consistent with the TRIB3^{high} tumor epithelial cells, and this is probably a potential mechanism for the regulation of TME of such subset.

To the best of our knowledge, the present study portrays the first landscape of PCDs in KIRC and further explores the identified biomarkers' diagnostic role and biological functions. Nevertheless, our study still has some unavoidable shortcomings. First, the diagnostic model needs to be further validated by expanding the validation cohort; second, additional experimental tools are needed further to investigate the physiopathological mechanisms of the relevant molecules; and finally, the therapeutic potential of such biomarkers remains to be further elucidated. In conclusion, the exosome is an essential mechanism to determine cell fate in addition to cell surface ligand–receptor interaction, which could be the game-changer in shaping the TME. In this study, we constructed a diagnostic model based on PCD-related genes. Furthermore, we validated the diagnostic efficacy in multiple KIRC cohorts, subsequently exploring the mechanism through single-cell omics, thus providing a novel perspective for the early diagnosis of KIRC and facilitating the understanding of the mechanisms of KIRC.

Data availability statement

The datasets presented in this study can be found in online repositories. The names of the repository/repositories and accession number(s) can be found within the article/Supplementary Material.

Ethics statement

Ethical review and approval was not required for the study on human participants in accordance with the local legislation and institutional requirements. Written informed consent for participation was not required for this study in accordance with the national legislation and the institutional requirements.

Author contributions

CW and SC designed this work. CW, YH, and JZ integrated and analyzed the data and wrote this manuscript. CW, XW, and SC edited and revised the manuscript. All authors contributed to the article and approved the submitted version.

Acknowledgments

We thank Home for Researchers editorial team (www.home-for-researchers.com) for language editing service.

Conflict of interest

The authors declare that the research was conducted in the absence of any commercial or financial relationships that could be construed as a potential conflict of interest.

Publisher's note

Supplementary material

The Supplementary Material for this article can be found online at: https://www.frontiersin.org/articles/10.3389/fimmu.2023.1130513/full#supplementary-material

SUPPLEMENTARY FIGURE 1
Quality control (QC) for scRNA-seq data. **(A)** Violin plot showing the number of genes, unique molecular identifiers (UMIs), and the percentage of mitochondrial genes of each sample before QC. **(B)** Violin plot showing the number of genes, UMIs, and the percentage of mitochondrial genes of each sample after QC.

SUPPLEMENTARY FIGURE 2
Single-cell RNA sequencing (scRNA-seq) profiling of kidney renal clear cell carcinoma (KIRC). **(A)** Uniform manifold approximation and projection (UMAP) plot presenting the cell clusters of scRNA-seq. **(B)** UMAP plots showing the data sources of scRNA-seq. **(C)** UMAP plots presenting the 17 cell clusters of scRNA-seq.

SUPPLEMENTARY FIGURE 3
Kyoto Encyclopedia of Genes and Genomes (KEGG) pathway enrichment analysis of differentially expressed genes (DEGs) between different datasets. **(A)** KEGG pathway enrichment for upregulated DEGs. **(B)** KEGG pathway enrichment for downregulated DEGs. The visualized results were the top 30 intersectional enriched terms of the pathways between the datasets. The red bubble represents the enrichment terms of upregulated DEGs (left), and the blue bubble represents the enrichment terms of downregulated DEGs (right). Shades of color in the bubble indicate negative log10(*P*-value), and the bubble sizes indicate the number of genes enriched in the pathway.

SUPPLEMENTARY FIGURE 4
Screen for the candidate biomarker genes. **(A)** Bubble plots showing the 33 candidate biomarker genes that were downregulated in the exoRBase kidney renal clear cell carcinoma (KIRC) cohort and their expression pattern in other datasets. Red circles represent positive logFC values or upregulated DEGs in the corresponding datasets, while blue circles represent positive logFC values or downregulated DEGs in the corresponding datasets. The bubble size indicates negative log10(*P*-value). **(B)** The survival analysis results indicated that 21 candidate biomarker genes were significantly associated with the overall survival of KIRC cases based on the GEPIA database.

SUPPLEMENTARY FIGURE 5
Correlation analysis of the clinical stage of kidney renal clear cell carcinoma patients for candidate biomarker genes. The patients were grouped

according to stages I–IV. The differences in the expression of candidate biomarker genes were compared between groups, and P <0.05 genes were retained.

SUPPLEMENTARY FIGURE 6
A total of 13 genes in 10 main cell clusters. Violin plot showing the differential analysis of key genes in various cell clusters.

SUPPLEMENTARY FIGURE 7
Violin plot showing the differential analysis of CD44 and GAPDH in tumor cells *versus* TRIB3^{high} tumor epithelial cells.

SUPPLEMENTARY FIGURE 8
Analysis of cell–cell signal interaction pathway networks for cell clusters. Circos plot showing putative ligand–receptor interactions between each cell cluster, with the weight of interactions indicated by the thickness of the connecting lines.

SUPPLEMENTARY FIGURE 9
Bubble plot of tumor cell ligand–receptor interactions in the tumor microenvironment. Summary of selected ligand–receptor interactions between different cell clusters between TRIB3^{high} tumor epithelial cells and other cell types. The P-values are indicated by the size of each circle. In contrast, the color gradient indicates the level of interaction.

References

1. Moch H, Cubilla AL, Humphrey PA, Reuter VE, Ulbright TM. The 2016 WHO classification of tumours of the urinary system and Male genital organs-part a: Renal, penile, and testicular tumours. *Eur Urol* (2016) 70(1):93–105. doi: 10.1016/j.eururo.2016.02.029

2. Ferlay J, Colombet M, Soerjomataram I, Dyba T, Randi G, Bettio M, et al. Cancer incidence and mortality patterns in Europe: Estimates for 40 countries and 25 major cancers in 2018. *Eur J Cancer* (2018) 103:356–87. doi: 10.1016/j.ejca.2018.07.005

3. Siegel RL, Miller KD, Jemal A. Cancer statistics, 2019. *CA Cancer J Clin* (2019) 69 (1):7–34. doi: 10.3322/caac.21551

4. Hsieh JJ, Purdue MP, Signoretti S, Swanton C, Albiges L, Schmidinger M, et al. Renal cell carcinoma. *Nat Rev Dis Primers* (2017) 3:17009. doi: 10.1038/nrdp.2017.9

5. Hutson TE, Figlin RA. Renal cell cancer. *Cancer J* (2007) 13(5):282–6. doi: 10.1097/PPO.0b013e318156fe69

6. Fuchs Y, Steller H. Programmed cell death in animal development and disease. *Cell* (2011) 147(4):742–58. doi: 10.1016/j.cell.2011.10.033

7. Li X, He S, Ma B. Autophagy and autophagy-related proteins in cancer. *Mol Cancer* (2020) 19(1):12. doi: 10.1186/s12943-020-1138-4

8. Lu Y, Qin H, Jiang B, Lu W, Hao J, Cao W, et al. KLF2 inhibits cancer cell migration and invasion by regulating ferroptosis through GPX4 in clear cell renal cell carcinoma. *Cancer Lett* (2021) 522:1–13. doi: 10.1016/j.canlet.2021.09.014

9. Peng YF, Shi YH, Ding ZB, Ke AW, Gu CY, Hui B, et al. Autophagy inhibition suppresses pulmonary metastasis of HCC in mice *via* impairing anoikis resistance and colonization of HCC cells. *Autophagy* (2013) 9(12):2056–68. doi: 10.4161/auto.26398

10. Yan W, Jiang S. Immune cell-derived exosomes in the cancer-immunity cycle. *Trends Cancer* (2020) 6(6):506–17. doi: 10.1016/j.trecan.2020.02.013

11. Kalluri R, LeBleu VS. The biology, function, and biomedical applications of exosomes. *Science* (2020) 367(6478). doi: 10.1126/science.aau6977

12. Liu Y, Wang Y, Lv Q, Li X. Exosomes: From garbage bins to translational medicine. *Int J Pharm* (2020) 583:119333. doi: 10.1016/j.ijpharm.2020.119333

13. Crenshaw BJ, Gu L, Sims B, Matthews QL. Exosome biogenesis and biological function in response to viral infections. *Open Virol J* (2018) 12:134–48. doi: 10.2174/1874357901812010134

14. Zhang H, Deng T, Liu R, Ning T, Yang H, Liu D, et al. CAF secreted miR-522 suppresses ferroptosis and promotes acquired chemo-resistance in gastric cancer. *Mol Cancer* (2020) 19(1):43. doi: 10.1186/s12943-020-01168-8

15. Shen T, Huang Z, Shi C, Pu X, Xu X, Wu Z, et al. Pancreatic cancer-derived exosomes induce apoptosis of T lymphocytes through the p38 MAPK-mediated endoplasmic reticulum stress. *FASEB J* (2020) 34(6):8442–58. doi: 10.1096/fj.201902186R

16. Hong Y, Lin M, Ou D, Huang Z, Shen P. A novel ferroptosis-related 12-gene signature predicts clinical prognosis and reveals immune relevancy in clear cell renal cell carcinoma. *BMC Cancer* (2021) 21(1):831. doi: 10.1186/s12885-021-08559-0

17. Song W, Ren J, Xiang R, Kong C, Fu T. Identification of pyroptosis-related subtypes, the development of a prognosis model, and characterization of tumor microenvironment infiltration in colorectal cancer. *Oncoimmunology* (2021) 10 (1):1987636. doi: 10.1080/2162402X.2021.1987636

18. Tsvetkov P, Coy S, Petrova B, Dreishpoon M, Verma A, Abdusamad M, et al. Copper induces cell death by targeting lipoylated TCA cycle proteins. *Science* (2022) 375(6586):1254–61. doi: 10.1126/science.abf0529

19. Butler A, Hoffman P, Smibert P, Papalexi E, Satija R. Integrating single-cell transcriptomic data across different conditions, technologies, and species. *Nat Biotechnol* (2018) 36(5):411–20. doi: 10.1038/nbt.4096

20. Korsunsky I, Millard N, Fan J, Slowikowski K, Zhang F, Wei K, et al. Fast, sensitive and accurate integration of single-cell data with harmony. *Nat Methods* (2019) 16(12):1289–96. doi: 10.1038/s41592-019-0619-0

21. Stuart T, Srivastava A, Madad S, Lareau CA, Satija R. Single-cell chromatin state analysis with signac. *Nat Methods* (2021) 18(11):1333–41. doi: 10.1038/s41592-021-01282-5

22. Jin S, Guerrero-Juarez CF, Zhang L, Chang I, Ramos R, Kuan CH, et al. Inference and analysis of cell-cell communication using CellChat. *Nat Commun* (2021) 12(1):1088. doi: 10.1038/s41467-021-21246-9

23. Wang L, Yang G, Zhao D, Wang J, Bai Y, Peng Q, et al. CD103-positive CSC exosome promotes EMT of clear cell renal cell carcinoma: role of remote MiR-19b-3p. *Mol Cancer* (2019) 18(1):86. doi: 10.1186/s12943-019-0997-z

24. Hu G, Ma J, Zhang J, Chen Y, Liu H, Huang Y, et al. Hypoxia-induced lncHILAR promotes renal cancer metastasis *via* ceRNA for the miR-613/206/ 1-1-3p/Jagged-1/Notch/CXCR4 signaling pathway. *Mol Ther* (2021) 29(10):2979–94. doi: 10.1016/j.ymthe.2021.05.020

25. Wang G, Xie L, Li B, Sang W, Yan J, Li J, et al. A nanounit strategy reverses immune suppression of exosomal PD-L1 and is associated with enhanced ferroptosis. *Nat Commun* (2021) 12(1):5733. doi: 10.1038/s41467-021-25990-w

26. Zhang H, Brown RL, Wei Y, Zhao P, Liu S, Liu X, et al. CD44 splice isoform switching determines breast cancer stem cell state. *Genes Dev* (2019) 33(3-4):166–79. doi: 10.1101/gad.319889.118

27. Dar GH, Mendes CC, Kuan WL, Speciale AA, Conceicao M, Gorgens A, et al. GAPDH controls extracellular vesicle biogenesis and enhances the therapeutic potential of EV mediated siRNA delivery to the brain. *Nat Commun* (2021) 12 (1):6666. doi: 10.1038/s41467-021-27056-3

28. Bertheloot D, Latz E, Franklin BS. Necroptosis, pyroptosis and apoptosis: an intricate game of cell death. *Cell Mol Immunol* (2021) 18(5):1106–21. doi: 10.1038/s41423-020-00630-3

29. Su Z, Yang Z, Xu Y, Chen Y, Yu Q. Apoptosis, autophagy, necroptosis, and cancer metastasis. *Mol Cancer* (2015) 14:48. doi: 10.1186/s12943-015-0321-5

30. Beroske L, Van den Wyngaert T, Stroobants S, van der Veken P, Elvas F. Molecular imaging of apoptosis: The case of caspase-3 radiotracers. *Int J Mol Sci* (2021) 22(8). doi: 10.3390/ijms22083948

31. Alizadeh M, Safarzadeh A, Beyranvand F, Ahmadpour F, Hajiasgharzadeh K, Baghbanzadeh A, et al. The potential role of miR-29 in health and cancer diagnosis, prognosis, and therapy. *J Cell Physiol* (2019) 234(11):19280–97. doi: 10.1002/jcp.28607

32. Tong XP, Chen Y, Zhang SY, Xie T, Tian M, Guo MR, et al. Key autophagic targets and relevant small-molecule compounds in cancer therapy. *Cell Prolif* (2015) 48 (1):7–16. doi: 10.1111/cpr.12154

33. Yan J, Wang ZY, Yang HZ, Liu HZ, Mi S, Lv XX, et al. Timing is critical for an effective anti-metastatic immunotherapy: the decisive role of IFNgamma/STAT1-mediated activation of autophagy. *PloS One* (2011) 6(9):e24705. doi: 10.1371/journal.pone.0024705

34. Ma Z, Liu W, Zeng J, Zhou J, Guo P, Xie H, et al. Silibinin induces apoptosis through inhibition of the mTOR-GLI1-BCL2 pathway in renal cell carcinoma. *Oncol Rep* (2015) 34(5):2461–8. doi: 10.3892/or.2015.4224

35. Que T, Ren B, Fan Y, Liu T, Hou T, Dan W, et al. Capsaicin inhibits the migration, invasion and EMT of renal cancer cells by inducing AMPK/mTOR-mediated autophagy. *Chem Biol Interact* (2022) 366:110043. doi: 10.1016/j.cbi.2022.110043

36. Miess H, Dankworth B, Gouw AM, Rosenfeldt M, Schmitz W, Jiang M, et al. The glutathione redox system is essential to prevent ferroptosis caused by impaired lipid metabolism in clear cell renal cell carcinoma. *Oncogene* (2018) 37(40):5435–50. doi: 10.1038/s41388-018-0315-z

37. Wang P, Pei X, Yin XP, Ren JL, Wang Y, Ma LY, et al. Radiomics models based on enhanced computed tomography to distinguish clear cell from non-clear cell renal cell carcinomas. *Sci Rep* (2021) 11(1):13729. doi: 10.1038/s41598-021-93069-z

38. Guo L, Bi X, Li Y, Wen L, Zhang W, Jiang W, et al. Characteristics, dynamic changes, and prognostic significance of TCR repertoire profiling in patients with renal cell carcinoma. *J Pathol* (2020) 251(1):26–37. doi: 10.1002/path.5396

39. Chao X, Wang P, Ma X, Li Z, Xia Y, Guo Y, et al. Comprehensive analysis of lncRNAs as biomarkers for diagnosis, prognosis, and treatment response in clear cell renal cell carcinoma. *Mol Ther Oncolytics* (2021) 22:209–18. doi: 10.1016/j.omto.2021.08.003

40. Bootsma M, McKay RR, Emamekhoo H, Bade RM, Schehr JL, Mannino MC, et al. Longitudinal molecular profiling of circulating tumor cells in metastatic renal cell carcinoma. *J Clin Oncol* (2022) 40(31):3633–41. doi: 10.1200/JCO.22.00219

41. Koh Y, Nakano K, Katayama K, Yamamichi G, Yumiba S, Tomiyama E, et al. Early dynamics of circulating tumor DNA predict clinical response to immune checkpoint inhibitors in metastatic renal cell carcinoma. *Int J Urol* (2022) 29(5):462–9. doi: 10.1111/iju.14816

42. In 't Veld S, Arkani M, Post E, Antunes-Ferreira M, D'Ambrosi S, Vessies DCL, et al. Detection and localization of early- and late-stage cancers using platelet RNA. *Cancer Cell* (2022) 40(9):999–1009.e6. doi: 10.1016/j.ccell.2022.08.006

43. Li Y, Zhao J, Yu S, Wang Z, He X, Su Y, et al. Extracellular vesicles long RNA sequencing reveals abundant mRNA, circRNA, and lncRNA in human blood as potential biomarkers for cancer diagnosis. *Clin Chem* (2019) 65(6):798–808. doi: 10.1373/clinchem.2018.301291

44. Hoshino A, Kim HS, Bojmar L, Gyan KE, Cioffi M, Hernandez J, et al. Extracellular vesicle and particle biomarkers define multiple human cancers. *Cell* (2020) 182(4):1044–1061 e18. doi: 10.1016/j.cell.2020.07.009

45. Mashouri L, Yousefi H, Aref AR, Ahadi AM, Molaei F, Alahari SK. Exosomes: composition, biogenesis, and mechanisms in cancer metastasis and drug resistance. *Mol Cancer* (2019) 18(1):75. doi: 10.1186/s12943-019-0991-5

46. Chen G, Huang AC, Zhang W, Zhang G, Wu M, Xu W, et al. Exosomal PD-L1 contributes to immunosuppression and is associated with anti-PD-1 response. *Nature* (2018) 560(7718):382–6. doi: 10.1038/s41586-018-0392-8

47. Li Y, Ji J, Lyu J, Jin X, He X, Mo S, et al. A novel urine exosomal lncRNA assay to improve the detection of prostate cancer at initial biopsy: A retrospective multicenter diagnostic feasibility study. *Cancers (Basel)* (2021) 13(16). doi: 10.3390/cancers13164075

48. Wang CB, Chen SH, Zhao L, Jin X, Chen X, Ji J, et al. Urine-derived exosomal PSMA is a promising diagnostic biomarker for the detection of prostate cancer on initial biopsy. *Clin Transl Oncol* (2022) 25(3):758-67. doi: 10.1007/s12094-022-02983-9

49. Zhang S, Chuah SJ, Lai RC, Hui JHP, Lim SK, Toh WS. MSC exosomes mediate cartilage repair by enhancing proliferation, attenuating apoptosis and modulating immune reactivity. *Biomaterials* (2018) 156:16–27. doi: 10.1016/j.biomaterials.2017.11.028

50. Yang E, Wang X, Gong Z, Yu M, Wu H, Zhang D. Exosome-mediated metabolic reprogramming: the emerging role in tumor microenvironment remodeling and its influence on cancer progression. *Signal Transduct Target Ther* (2020) 5(1):242. doi: 10.1038/s41392-020-00359-5

51. Webber J, Steadman R, Mason MD, Tabi Z, Clayton A. Cancer exosomes trigger fibroblast to myofibroblast differentiation. *Cancer Res* (2010) 70(23):9621–30. doi: 10.1158/0008-5472.CAN-10-1722

52. Wang B, Wang X, Hou D, Huang Q, Zhan W, Chen C, et al. Exosomes derived from acute myeloid leukemia cells promote chemoresistance by enhancing glycolysis-mediated vascular remodeling. *J Cell Physiol* (2019) 234(7):10602–14. doi: 10.1002/jcp.27735

53. Zhang PF, Gao C, Huang XY, Lu JC, Guo XJ, Shi GM, et al. Cancer cell-derived exosomal circUHRF1 induces natural killer cell exhaustion and may cause resistance to anti-PD1 therapy in hepatocellular carcinoma. *Mol Cancer* (2020) 19(1):110. doi: 10.1186/s12943-020-01222-5

54. Clement E, Lazar I, Attane C, Carrie L, Dauvillier S, Ducoux-Petit M, et al. Adipocyte extracellular vesicles carry enzymes and fatty acids that stimulate mitochondrial metabolism and remodeling in tumor cells. *EMBO J* (2020) 39(3):e102525. doi: 10.15252/embj.2019102525

55. Garcia Garre E, Luengo Gil G, Montoro Garcia S, Gonzalez Billalabeitia E, Zafra Poves M, Garcia Martinez E, et al. Circulating small-sized endothelial microparticles as predictors of clinical outcome after chemotherapy for breast cancer: an exploratory analysis. *Breast Cancer Res Treat* (2018) 169(1):83–92. doi: 10.1007/s10549-017-4656-z

56. Hong B, Zhou J, Ma K, Zhang J, Xie H, Zhang K, et al. TRIB3 promotes the proliferation and invasion of renal cell carcinoma cells *via* activating MAPK signaling pathway. *Int J Biol Sci* (2019) 15(3):587–97. doi: 10.7150/ijbs.29737

57. Zhang H, Liu X, Zhou L, Deng Z, Wang Y. Identification of RPS7 as the biomarker of ferroptosis in acute kidney injury. *BioMed Res Int* (2022) 2022:3667339. doi: 10.1155/2022/3667339

58. Devis-Jauregui L, Eritja N, Davis ML, Matias-Guiu X, Llobet-Navas D. Autophagy in the physiological endometrium and cancer. *Autophagy* (2021) 17(5):1077–95. doi: 10.1080/15548627.2020.1752548

59. Zhang XW, Zhou JC, Peng D, Hua F, Li K, Yu JJ, et al. Disrupting the TRIB3-SQSTM1 interaction reduces liver fibrosis by restoring autophagy and suppressing exosome-mediated HSC activation. *Autophagy* (2020) 16(5):782–96. doi: 10.1080/15548627.2019.1635383

60. Yu JM, Sun W, Wang ZH, Liang X, Hua F, Li K, et al. TRIB3 supports breast cancer stemness by suppressing FOXO1 degradation and enhancing SOX2 transcription. *Nat Commun* (2019) 10(1):5720. doi: 10.1038/s41467-019-13700-6

61. Shang S, Yang YW, Chen F, Yu L, Shen SH, Li K, et al. TRIB3 reduces CD8(+) T cell infiltration and induces immune evasion by repressing the STAT1-CXCL10 axis in colorectal cancer. *Sci Transl Med* (2022) 14(626):eabf0992. doi: 10.1126/scitranslmed.abf0992

62. Hua F, Shang S, Yang YW, Zhang HZ, Xu TL, Yu JJ, et al. TRIB3 interacts with beta-catenin and TCF4 to increase stem cell features of colorectal cancer stem cells and tumorigenesis. *Gastroenterology* (2019) 156(3):708–721.e15. doi: 10.1053/j.gastro.2018.10.031

Frontiers in Immunology

Explores novel approaches and diagnoses to treat immune disorders.

The official journal of the International Union of Immunological Societies (IUIS) and the most cited in its field, leading the way for research across basic, translational and clinical immunology.

Discover the latest Research Topics

See more →

Frontiers

Avenue du Tribunal-Fédéral 34
1005 Lausanne, Switzerland
frontiersin.org

Contact us

+41 (0)21 510 17 00
frontiersin.org/about/contact